Physics of Atomic Nuclei, Vol. 66, No. 1, 2003, pp. 1–5. Translated from Yadernaya Fizika, Vol. 66, No. 1, 2003, pp. 3–7.

100th ANNIVERSARY OF I.V. KURCHATOV'S BIRTH

Igor' Vasil'evich Kurchatov: The Scientist and Doer (January 12, 1903–February 7, 1960)

I.V. Kurchatov's centenary is a significant date in the history of Russian science, the right time to revere the memory of an outstanding scientist and organizer, one of the founding fathers of nuclear science and industry in Russia.

Igor' Vasil'evich Kurchatov was born in the village of Sim, Ufa province, on January 12, 1903. His father, V.A. Kurchatov, was a forest ranger and surveyor; his mother, M.V. Kurchatova, née Ostroumova, was a parish-school teacher [1]. Soon after the child's birth, the family moved to the Crimea, where Igor' Kurchatov went to a gymnasium and later enrolled at the Faculty of Physics and Mathematics of Tavricheskiĭ University. Having graduated ahead of time in 1924, he decided to give himself to physics. After working in a variety of research laboratories and the Azerbaijan Polytechnic Institute in Baku for a year, he came to the Leningrad Institute for Physics and Technology (the Russian abbreviation of this famous institution is LFTI) in 1925. There, at A.F. Ioffe's famous school, his gift for experimentation and organization gradually came to light. Kurchatov's early work was devoted to the physics of crystals—in particular, dielectric and ferroelectric materials. He was soon at home in what was then a new field and obtained a number of important results there (such as the discovery of the ferroelectric properties of Seignette's salt [2]), for which he was awarded the degree of doctor of physics and mathematics, without presenting a dissertation, in 1934.

However, as early as 1932, the watershed year in nuclear physics, when the positron and neutron were discovered, Kurchatov addressed nuclear physics, which was to become the subject of his life's work. Even his early work [3–5] bears the hallmark of Kurchatov's approach: an all-out attack on a scientific problem, the drive to move to the front echelon as fast as possible, and press the success without delay. He took part, together with K.D. Sinel'nikov, in the work on the first proton accelerator at the Ukrainian Institute for Physics and Technology in Kharkov (1933); headed the organizing committee of the First All-Union Conference on the Atomic Nucleus (1933); studied neutron absorption by nuclei, discovering nuclear isomerism (1935); conducted the famous Kurchatov seminar on neutron physics (1935–1941), while also working (initially with L.V. Mysovskii) at the State Radium Institute (later, Radium Institute of the USSR Academy of Sciences, abbreviated in Russian as RIAN) (1935–1940); investigated resonance neutron absorption by nuclei (1937); and took part in the start of the RIAN cyclotron and the development (jointly with A.I. Alikhanov) of the LFTI cyclotron (before 1941, to be completed after WWII). Finally, with the discovery of the fission process (by O. Hahn and F. Strassman), the Kurchatov group started an in-depth investigation of uranium. This resulted in determining the number of secondary fission neutrons; isolating uranium-235 as a fissile isotope; and, finally, discovering the spontaneous fission of uranium-238 (G.N. Flerov and K.A. Petrzhak, 1941), a world-class result indeed. By 1941, the Kurchatov group had joined the ranks of the leading laboratories in Europe and the United States and, for all intents and purposes, started work on chain reactions. Fully aware of the unique prospects of this new research area, Kurchatov became a member of the Uranium

1063-7788/03/6601-0001$24.00

Committee at the Academy of Sciences (which was headed by V.G. Khlopin, in 1940 and 1941) and wrote to the government, arguing the need to boost uranium research (Kurchatov, Flerov, Petrzhak, and Yu.B. Khariton, 1940).

The outbreak of the war interrupted the Kurchatov group's investigations, and he was assigned the job of degaussing combat vessels (with A.P. Aleksandrov and others, in 1941 and 1942), doing this in Sevastopol, in the Caucasus, at the Caspian flotilla, and in the town of Polyarnyi. However, in October 1942, under the State Defense Committee decree of September 28, 1942, which initiated research into the military use of atomic energy, Kurchatov, on Ioffe's initiative, returned to nuclear subjects, first as head of a special laboratory in Kazan (1942) and afterward as head of Laboratory no. 2 (LIPAN, later Institute of Atomic Energy; now, Russian Research Centre Kurchatov Institute) in Moscow. It was during his work on the Soviet atomic project that Kurchatov's talents as a physicist and leader of large research teams flourished. There, he worked for the rest of his life, giving himself up to the development of atomic weapons, the atomic industry, and the development of nuclear science in his country.

Kurchatov's work on the atomic project is surrounded by legends. For more than fifty years, this chapter of our history was shrouded in secrecy. It was not until recently that it began to open up step by step [6–16]. As real facts come to light, Kurchatov's outstanding role in Soviet nuclear history becomes increasingly apparent. From the end of 1942 to 1955, when the Soviet Union built its H-bomb, and throughout the successive years to his death in 1960, Kurchatov actually participated in, and was a scientific leader of, a vast organizational and managerial effort to coordinate a multitude of research and engineering teams targeted at a uniquely complex task, the creation of the Soviet Union's nuclear weapons.

The Soviet nuclear project under Kurchatov falls easily into three broad periods: the research phase (1943 to 1945); the building of the atomic industry and atomic weapons (1946 to August 1949); and the progress of the atomic industry, the creation of hydrogen weapons, and the birth of atomic power generation and the atomic fleet in the Soviet Union (1950 to 1957).

With the publication of new, once strictly confidential, documents [6–16], we can now see the real caliber of Kurchatov as a scientist and creative personality. At the first, research, phase, he assembled the Ioffe school's physicists and his own pupils and enlisted the support of the familiar schools of the RIAN, the Institute of Chemical Physics, and the Institute of Physics of the Academy of Sciences (known in the Soviet Union as FIAN) to work out physical problems, viz., to obtain nuclear data needed for the startup of a physical reactor and the modeling of nuclear-blast physics, to obtain plutonium in "impulse" and microgram quantities, and to develop a process for obtaining ultrapure graphite and metallic uranium. From early 1945, his team began to prepare for the second, engineering and industrial, phase of the project, and Kurchatov was not caught nodding when a new political situation arose after the atomic bombing of Hiroshima and Nagasaki in August 1945.

With the State Defense Committee decision of August 20, 1945, to set up a Special Committee, a Technical Board, and the First Main Administration, put in charge of the implementation of the atomic project, the second phase of the atomic project began, when Kurchatov and his research team had to solve absolutely new problems theretofore unknown to science. It was at that phase that they acted as research supervisors of major engineering projects: the startup of the first physical reactor, Ph (1946); the design, construction, and startup of plants for plutonium production, radiochemical extraction, and metallurgy (Kurchatov, plants A, B, V, Chelyabinsk-40, in 1948 and 1949); the development of a physical reactor and an industrial heavy-water one (Alikhanov, Laboratory no. 3, 1949; OK-180, Chelyabinsk-40, 1951); the development of a manufacturing technology of diffusion separation of uranium-235 and uranium-238 (I.K. Kikoin, plant D-1, Sverdlovsk-65, 1949–1951); the development of industrial mass separators for the electromagnetic separation of isotopes of uranium (L.A. Artsimovich, SU-20, Sverdlovsk-45, 1950); and, finally, the design calculation, modeling, construction, and production of the first atomic bomb (Khariton, Arzamas-16, 1946–1949). While, at the first phase (the selection of principal work directions and the design of the bomb), Kurchatov and his team were able to avail themselves of data gleaned by Soviet intelligence through its brilliant operations in England and the United States [11], at the second, industrial, phase, it was only thanks to the superb engineering level of the Kurchatov team; the talent of the body of engineers he had brought together; the heroic dedication and commitment of every worker at construction sites, plant floors, and research laboratories that they could complete this mission within the same time, three years, as the team of Nobel prizewinners and other outstanding scientists and engineers from many countries of Europe and the United States that Roosevelt and Churchill had brought together in the United States in 1942–1945. The net result of the first Soviet nuclear test was the solution of the main political task of the time, that of the nation's nuclear safety.

Kurchatov's special, outstanding role follows from the USSR Council of Ministers Decree no. 5070-

1944ss/op, signed by Stalin (October 29, 1949), concerning the award of atomic project participants [13], in which Kurchatov's name tops the list: "In view of his exceptional service to the Soviet Fatherland in the matter of solving the problem of utilization of atomic energy and pursuant to the Council of Ministers Decree no. 626-258, of March 21, 1946, the Council of Ministers of the Union of Soviet Socialist Republics hereby DECREES: I. 1. KURCHATOV, Igor' Vasil'evich, academician, scientific leader of the atomic reactor and atomic bomb project: to be nominated for the title of Hero of Socialist Labor; to be awarded a bonus of 500 000 rubles . . . "to bestow upon Academician I.V. Kurchatov the title of Laureate of the Stalin Prize First Class; to build . . . and transfer to Academician I.V. Kurchatov a town house and a dacha . . .."

At the end of 1949, the third period of Kurchatov's work on the atomic problem began. On one hand, he acted as the scientific leader of the project to perfect nuclear weapons and create hydrogen weapons; on the other hand, he acted as a scientist with a vision, building the foundation for the future advance of nuclear science and engineering. The group that made a special contribution to solving the first problem was composed of FIAN researchers (I.E. Tamm, Z.S. Belenky, V.L. Ginzburg, A.D. Sakharov, Yu.A. Romanov, and others) whose services Kurchatov had enlisted in 1948. It was this group that brought forth the idea of a unique design of a nuclear–thermonuclear weapon, Sakharov Puff (project RDS-6, 1953). In 1950, I.Ya. Pomeranchuk, V.N. Klimov, N.N. Bogolyubov, and D.V. Shirkov were included in this group. Then, a joint team headed by Khariton (it included Ya.B. Zel'dovich, Yu.A. Trutnev, and Sakharov) independently discovered the basic physical principle of modern thermonuclear weapons, radiation implosion, and carried out a successful test in 1955 [14]. This effectively solved the strategic task of securing the Soviet Union's nuclear parity with the United States. A real basis was created for stopping the atomic arms race, both sides beginning slowly to move toward each other and seeking new political solutions that could lead to the discontinuance of the nuclear race and cessation of nuclear tests, and Kurchatov was alive to the necessity and importance of that next step.

There was more than one reason to make the years from 1953 to 1957 a summarizing and watershed period for Kurchatov and his teammates: series AB and heavy-water reactors were constructed and commercialized to service the atomic industry; an atomic power plant—the Soviet Union's or Europe's first—went into operation in Obninsk (1954); atomic-powered submarines and icebreakers began to be built (1958, 1959); series D uranium-isotope-separation plants began to work to capacity; and a solution was finally found for a critical problem, that of prospecting for, and production of, uranium ore [10]. Kurchatov ranked as the highest authority in government circles, which gave him the opportunity to advance a number of new initiatives, first and foremost, in the development of new research centers. Those years saw the birth of nuclear research institutes in Obninsk, Dubna, Dmitrovgrad, Tomsk, Krasnoyarsk, and Snezhinsk and the rapid expansion of the scope of the FIAN, Institute of Chemical Physics, Institute of Physical Problems, TTL (Institute of Theoretical and Experimental Physics), RIAN, Leningrad Nuclear Physics Institute, NIIYaF MGU (Institute of Nuclear Physics at Moscow State University), and many others, whose research efforts were not confined to the nuclear area. Soviet science brought in young talent (Moscow Engineering Physics Institute, Moscow Institute for Physics and Technology, NIIYaF MGU, and specialized departments of many institutions of higher learning), gained momentum, and rose to the world level in coping not only with applied but also with fundamental problems. Kurchatov became its recognized leader, who supported, through the Academy of Sciences, the development of science in many directions. In 1949, it was his authority that helped save quantum and relativistic physics from ideological persecution; from the early 1950s, the atomic industry became the breeding ground for cybernetics, which had been noisily condemned before. From the mid-1950s, Kurchatov was seriously preoccupied with the fate of biology in the Soviet Union, which had been wrecked in the Lysenkoism years, and, by way of backing it, established a radiobiology department at LIPAN in 1958, which is now the Institute of Molecular Genetics, Russian Academy of Sciences.

As soon as the formidable tasks of the third phase had been solved by 1956 to 1957, Kurchatov was in the position to pose new problems, this time not only as a scientist, but also as a prominent, foresighted politician. He worked on these strategic tasks, which he formulated and handled on a scale all his own, in the closing stages of his life, despite a sharp decline in his health. They constitute his testament. The most important of these are the following:

(i) International cooperation of scientists and the establishment of international control authorities in the atomic field under the aegis of the United Nations. The first steps in this directions were the First and Second Geneva Conferences on the Peaceful Uses of Atomic Energy (1955, 1958), Kurchatov's talk at Harwell during Khrushchev's visit to England (1956), and the establishment of an international nuclear research institute at Dubna (1956). These initiatives led to the creation of the IAEA and a number of international committees to coordinate means of inspection

of atomic tests and atomic weapons' proliferation. Kurchatov personally supervised the work of Soviet representatives; determined the composition of delegations and experts; and discussed reports, presentations, and decisions. Simultaneously, he began to engage, in nuclear research, academies of sciences in Union republics and socialist countries.

(ii) Setting up new physical problems associated with the harnessing of thermonuclear energy and with the development of acceleration engineering and of transuranic-element physics. Direct evidence of Kurchatov's initiatives along these lines is the launch of a project for the utilization of fusion power at LIPAN in 1951 (Golovin's recollections [1, 17]) and Kurchatov's numerous talks on its behalf [18, 19]; the construction of high-power cyclotrons in Dubna (synchrocyclotron, 1949; cyclotron U-300, 1960); his support of Flerov's work on transuranium-element synthesis (Flerov's recollections [1])—a totally new field in nuclear physics, which is rapidly developing today; and, finally, Kurchatov's backing of the designs for a proton synchrotron at the Joint Institute for Nuclear Research and a high-current accelerator (ITEP–Protvino), as well as G.I. Budker's innovative ideas concerning colliding-beam accelerators—these ideas were born at LIPAN and materialized later on in the Siberian Division of Russian Academy of Sciences. Kurchatov was distinctly aware of the major role of accelerator technology in particle physics.

(iii) Finally, his realization of the tangible environmental threat of nuclear tests and encouragement of early nuclear-ecology research, which was done, in response to Kurchatov's suggestion, by Sakharov (1958) [20], leading to a major initiative, proposals for the signing of the Limited Test Ban Treaty (1963), and being the first step in the shaping of Sakharov's personality as an original researcher-cum-politician.

Therefore, beginning in the mid-1950s, Kurchatov started to create a base for the development of Soviet science in new directions, which opened right after WWII and which were associated with revolutions in quantum physics, nuclear physics, and biophysics. Regrettably, these new tasks for Soviet science, initiating its shift of focus from tactical, immediate questions to strategic problems, which would radically change the role of science in society in the new era and which Kurchatov saw very clearly, were still far from a solution in those years. They were handed down, as Kurchatov's testimony, by his teammates and scientific school to the next generations of Soviet scientists and their pupils. He himself had only just had time to begin their realization. In 1956, Kurchatov suffered his first stroke, recovered, and again plunged into work not sparing himself. But his health could no longer withstand permanent overloads, and Kurchatov passed away on February 7, 1960.

His services to the nation were highly prized: he had been three times Hero of Socialist Labor, winner of a multitude of state prizes, holder of numerous awards, elected an academician (1943) and member of the Presidium of the Academy of Sciences (1946), and a deputy of the Supreme Soviet. As an outstanding statesman, he was buried near the Kremlin wall—the ultimate honor accorded to heroes of his time.

His life's work is alive and developing in Russia. Russian nuclear science and the atomic industry, created under his stewardship, is continuing to serve his Fatherland.

REFERENCES

1. *Memoirs on Igor Vasil'evich Kurchatov,* Ed. by A. P. Aleksandrov (Nauka, Moscow, 1988).
2. I. V. Kurchatov, *Ferroelectrics* (GTTI, Leningrad; Moscow, 1933); I. V. Kurchatov, D. N. Nasledov, N. N. Semenov, and Yu. B. Khariton, *Electron Phenomena* (ONTI, Leningrad, 1935).
3. I. V. Kurchatov, *Splitting of Atomic Nuclei* (Moscow, 1935), Vol. 2, p. 159.
4. I. V. Kurchatov, *Fission of Heavy Nuclei,* Usp. Fiz. Nauk **25**, 159 (1941).
5. I. V. Kurchatov and L. I. Rusinov, *Isomerism of Atomic Nuclei: Anniversary Collection* (Akad. Nauk SSSR, Moscow, 1947), p. 285.
6. *Creation of the First Soviet Nuclear Bomb,* Ed. by V. N. Mikhaĭlov (Énergoatomizdat, Moscow, 1995).
7. A. K. Kruglov, *How the Atomic Industry Was Created in USSR* (TsNIIatominform, Moscow, 1995).
8. *Atomic Project in USSR. Documents and Materials,* Vol. I: *1938-1945,* Ed. by L. D. Ryabev (Nauka, Moscow, 1998), Part 1.
9. *Atomic Project in USSR. Documents and Materials,* Vol. II: *Atomic Bomb, 1945–1954,* Ed. by L. D. Ryabev (Nauka, Moscow, 1999), Part 1.
10. *Atomic Project in USSR. Documents and Materials,* Vol. II: *Atomic Bomb, 1945–1954,* Ed. by L. D. Ryabev (Nauka, Moscow, 2000), Part 2.
11. *Proceedings of the International Symposium "Science and Society: History of Soviet Atomic Project (1940–1950th Years)," Dubna, 1996* (IZDAT, Moscow, 1997), Vol. 1.
12. *Proceedings of the International Symposium "Science and Society: History of Soviet Atomic Project (40–50th Years)," Dubna, 1996* (IZDAT, Moscow, 1999), Vol. 2.
13. *Atomic Project in USSR. Documents and Materials,* Vol. II: *Atomic Bomb, 1945–1954,* Ed. by L. D. Ryabev (Nauka, Moscow, 1999), Part 1, p. 531.
14. Phys. Today **49** (11) (1996).
15. *Kurchatov Institute. History of Atomic Project: Selected Works of Kurchatov* (Moscow, 1996), Vol. 8.

16. *Kurchatov Institute. History of Atomic Project: Archives of Kurchatov Institute* (Moscow, 1998), Vol. 16.
17. I. N. Golovin, *I. V. Kurchatov* (Atomizdat, Moscow, 1973).
18. I. V. Kurchatov, At. Énerg., No. 3, 5 (1956).
19. I. V. Kurchatov, At. Énerg., No 3, 65 (1956); *Talk of I. V. Kurchatov on XX Congress of C.P.S.U.,* Pravda (February 20, 1956).
20. A. D. Sakharov, *Memoirs* (Publ. in the name of Chekhov, New York, 1990).

Yu. V. Gaponov

Russian Research Centre

Kurchatov Institute, Moscow

Physics of Atomic Nuclei, Vol. 66, No. 1, 2003, pp. 105–109. From Yadernaya Fizika, Vol. 66, No. 1, 2003, pp. 107–111.

ELEMENTARY PARTICLES AND FIELDS
Experiment

Study of the $K^- \to \mu^-\nu\pi^0$ Decay*

I. V. Ajinenko[1], S. A. Akimenko[1], G. I. Britvich[1], I. G. Britvich[1], K. V. Datsko[1], A. P. Filin[1], A. V. Inyakin[1], A. S. Konstantinov[1], V. F. Konstantinov[1], I. Ya. Korolkov[1], V. M. Leontiev[1], V. P. Novikov[1], V. F. Obraztsov[1], V. A. Polyakov[1], V. I. Romanovsky[1], V. I. Shelikhov[1], N. E. Smirnov[1], M. M. Soldatov[1], O. G. Tchikilev[1], E. A. Usenko[1], M. V. Vasiliev[1], E. V. Vlasov[1], V. I. Yakimchuk[1], O. P. Yushchenko[1], V. N. Bolotov[2], S. V. Laptev[2], V. A. Lebedev[2], A. R. Pastsjak[2], A. Yu. Polyarush[2], and R. Kh. Sirodeev[2]

Received April 11, 2002

Abstract—The decay $K^- \to \mu^-\nu\pi^0$ has been studied using in-flight decays detected with the ISTRA+ setup operating in the 25-GeV negative secondary beam of the U-70 PS. About 112K events were used for the analysis. The λ_+ and λ_0 slope parameters of the decay form factors $f_+(t)$ and $f_0(t)$ have been measured: $\lambda_+ = 0.0321 \pm 0.004(\text{stat.}) \pm 0.002(\text{syst.})$, $\lambda_0 = 0.0209 \pm 0.004(\text{stat.}) \pm 0.002(\text{syst.})$; the correlation $d\lambda_0/d\lambda_+ = -0.46$. The limits on the possible tensor and scalar couplings have been derived: $f_T/f_+(0) = -0.021 \pm 0.028(\text{stat.}) \pm 0.014(\text{theor.})$, $f_S/f_+(0) = 0.004 \pm 0.005(\text{stat.}) \pm 0.005(\text{theor.})$.

1. INTRODUCTION

The decay $K \to \mu\nu\pi^0(K_{\mu 3})$ is known to be a key one in hunting for phenomena beyond the Standard Model (SM). In particular, significant efforts have been invested into T-violation searches, by the measurements of the muon transverse polarization σ_T. In our analysis, based on ~112K events of the decay, we present a new search for S and T interactions by fitting the $K_{\mu 3}$ Dalitz plot distribution, similar to that as was done for the K_{e3} decay [1]. Another subject of our study is the measurement of the $V - A$ $f_+(t), f_0(t)$ form-factor slopes: λ_+, λ_0.

2. EXPERIMENTAL SETUP

The experiment is performed at the IHEP 70-GeV proton synchrotron U-70. The experimental setup ISTRA+ has been described in some detail in our paper on K_{e3} decay [1]. The setup is located in the 4-A negative unseparated secondary beam. The beam momentum is ~25 GeV with $\Delta p/p \sim 2\%$. The admixture of K^- in the beam is ~3%. The beam intensity is $\sim 3 \times 10^6$ per 1.9 s U-70 spill.

3. EVENT SELECTION

During a 3-week physics run in March–April 2001, when the muon identification was in full operation, 363M events were logged on tapes. This information is supported by about 100M MC events generated with GEANT 3 [2]. Some information on the reconstruction procedure is presented in [1]; here, we touch only points relevant for the $K_{\mu 3}$-event selection.

The muon identification is based on the information from the SP_1, a 576-cell lead-glass calorimeter, and HC, a scintillator-iron sampling hadron calorimeter, subdivided into seven longitudinal sections 7×7 cells each [3]. The calorimeters are located at the very end of the setup, after the main magnet (M_2) and the last elements of the tracking system: drift tubes (DT) and the matrix scintillation hodoscope (MH). The first requirement is that the energy of the SP_1 cluster, associated with the charged track, is less than ~2.5 MIPs; the HC energy associated with the track should also be less than 2.5 MIPs. The last selection requires that more than 10% of the HC associated energy be deposited in last two layers (out of seven) of the HC. The efficiency of the algorithm to muons is tested on $K \to \mu\nu$ events and is found to be ~70%. The $\pi \to \mu$ misidentification is measured on $K^- \to \pi^-\pi^0$ decay and is ~3%. After the muon identification, the selection of the events with two extra showers results in the $M_{\gamma\gamma}$ spectrum shown in Fig. 1. The π^0 peak has a mass

*This article was submitted by the authors in English.

[1]Institute for High Energy Physics, Protvino, Moscow oblast, 142284 Russia.

[2]Institute for Nuclear Research, Russian Academy of Sciences, pr. Shestidesyatiletiya Oktyabrya 7a, Moscow, 117312 Russia.

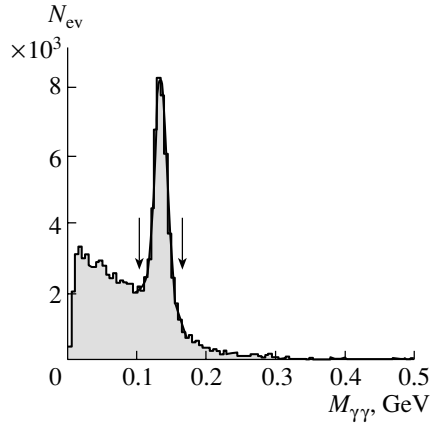

Fig. 1. The $\gamma\gamma$ mass spectrum for the events with the identified muon and two extra showers. Arrows indicate the cut value.

of $M_{\pi 0} = 134.8$ MeV and a resolution of 8.6 MeV. The missing mass squared $(P_K - P_\mu - P_{\pi^0})^2$, where P are the corresponding 4-momenta, is presented in Fig. 2. The cut is ± 0.01 GeV^2. The further selection is done by the requirement that the event pass the $2C$ $K \to \mu\nu\pi^0$ fit. The missing energy $E_K - E_\mu - E_{\pi^0}$ after this selection is shown in Fig. 3. The peak at low $E_{\rm miss}$ corresponds to the remaining $K^- \to \pi^-\pi^0$ background. The corresponding cut is $E_{\rm miss} > 1.4$ GeV. The surviving background is estimated from MC to be less than 4%. The detailed data reduction information is shown in Table 1.

4. ANALYSIS

The event selection described in the previous section results in selected 112K events in the 2001 data. The distribution of the events over the Dalitz plot is shown in Fig. 4. The variables $y = 2E_\mu/M_K$ and $z = 2E_{\pi^0}/M_K$, where E_μ and E_{π^0} are the energies of the muon and π^0 in the kaon c.m.s., are used. The most general Lorentz-invariant form of the matrix element for the decay $K^- \to \mu^-\nu\pi^0$ is [4]

$$M = \frac{G_{\rm F}V_{us}}{2}\bar{u}(p_\nu)(1+\gamma^5) \times \left[2m_K f_S - [(P_K+P_\pi)_\alpha f_+ + (P_K-P_\pi)_\alpha f_-]\gamma^\alpha + i\frac{2f_T}{m_K}\sigma_{\alpha\beta}P_K^\alpha P_\pi^\beta\right]v(p_\mu). \quad (1)$$

It consists of scalar, vector, and tensor terms; f_S, f_T, $f_\pm$ are functions of $t = (P_K - P_\pi)^2$. In the SM, the W-boson exchange leads to the pure vector term. The "induced" scalar and/or tensor terms due to EW radiative corrections are negligibly small; i.e., the nonzero scalar/tensor form factors indicate physics beyond the SM.

The term in the vector part proportional to f_- is reduced (using the Dirac equation) to a scalar form factor. In the same way, the tensor term is reduced to a mixture of scalar and vector form factors. The redefined f_+ (V) and f_S (S), and the corresponding Dalitz plot density in the kaon rest frame $(\rho(E_\pi, E_\mu))$ are [5]

$$\rho(E_\pi, E_\mu) \sim A|V|^2 + B{\rm Re}(V^*S) + C|S|^2; \quad (2)$$

$$V = f_+ + (m_\mu/m_K)f_T,$$

$$S = f_S + (m_\mu/2m_K)f_- + \left(1 + \frac{m_\mu^2}{2m_K^2} - \frac{2E_\mu}{m_K} - \frac{E_\pi}{m_K}\right)f_T,$$

$$A = m_K(2E_\mu E_\nu - m_K\Delta E_\pi) - m_\mu^2\left(E_\nu - \frac{1}{4}\Delta E_\pi\right), \quad (3)$$

$$B = m_\mu m_K(2E_\nu - \Delta E_\pi),$$

$$C = m_K^2\Delta E_\pi, \quad \Delta E_\pi = E_\pi^{\max} - E_\pi, \quad E_\pi^{\max} = \frac{m_K^2 - m_\mu^2 + m_\pi^2}{2m_K}.$$

Following [6], a scalar form factor f_0 is introduced,

$$f_0(t) = f_+(t) + \frac{t}{m_K^2 - m_\pi^2}f_-(t),$$

and a linear dependence of f_+ and f_0 on t is assumed: $f_+(t) = f_+(0)(1 + \lambda_+ t/m_\pi^2)$ and $f_0(t) = f_+(0)(1 + \lambda_0 t/m_\pi^2)$. Then,

$$f_- = f_+(0)(\lambda_0 - \lambda_+)\frac{m_K^2 - m_\pi^2}{m_\pi^2}.$$

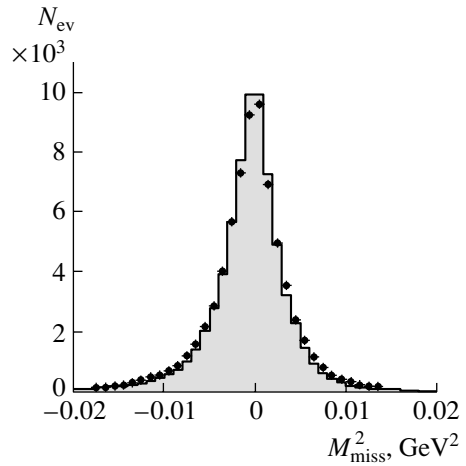

Fig. 2. The missing 4-momentum squared $(P_K - P_\mu - P_{\pi^0})^2$ for the selected events. The points with errors are the data; the histogram is MC.

The procedure for the experimental extraction of the parameters λ_+, λ_0, f_S, and f_T starts from the subtraction of the MC estimated background from the Dalitz plot of Fig. 4. The background normalization was determined by the ratio of the real and generated $K^- \to \pi^-\pi^0$ events. Then the Dalitz plot was subdivided into 20×20 cells. The background-subtracted distribution of the numbers of events in the cells (i, j) over the Dalitz plot, for example, in the case of simultaneous extraction of λ_+, λ_0, and $f_S/f_+(0)$, was fitted with the function

$$\rho(i,j) \sim \sum_{k_i;\, k_1+k_2+k_3=0,1,2} W_{k_1k_2k_3}(i,j)\lambda_+^{k_1}\lambda_0^{k_2}(f_S/f_+(0))^{k_3}. \quad (4)$$

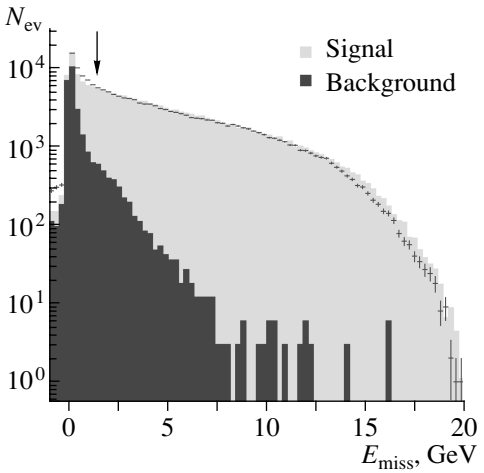

Fig. 3. The missing energy for the $\mu\pi^0$ events. The points with errors are the data; the histograms are MC. The dark (gray) peak at zero value corresponds to the MC-predicted $K \to \pi^-\pi^0$ background. The arrow indicates the cut value.

Here, $W_{k_1k_2k_3}$ are MC-generated functions, which are built up as follows: the MC events are generated with constant density over the Dalitz plot and reconstructed with the same program as for the real events. Each event carries the weight w determined by the corresponding term in (2), calculated using the MC-generated ("true") values for y and z. The radiative corrections according to [7] were taken into account. Then $W_{k_1k_2k_3}$ is constructed by summing up the weights of the events in the corresponding Dalitz plot cell. This procedure allows one to avoid the systematic errors due to the "migration" of events over the Dalitz plot because of the finite experimental resolution.

5. RESULTS

The results of the fit are summarized in Table 2. The first line corresponds to the pure $V - A$ SM fit. The first column is an independent fit of our $K_{\mu 3}$ data. The λ_+–λ_0 correlation parameter is $\frac{d\lambda_0}{d\lambda_+} = -0.2$. The λ_+ value $\lambda_+^\mu = 0.0321 \pm 0.004$ is in good agreement with that extracted from the analysis of our K_{e3} data [1]: $\lambda_+^e = 0.0293 \pm 0.0015$; i.e., our data do not contradict the μ–e universality. In the second column, the results of the joined fit of our K_{e3} and $K_{\mu 3}$ data are presented (this is practically equivalent to fixing the λ_+ to its K_{e3} value). This fit, of course, assumes the μ–e universality. The λ_0 value $\lambda_0 = 0.0209 \pm 0.0042$ is in good agreement with the calculations in the framework of the chiral perturbation theory (ChPT) [6]: $\lambda_0^{\rm th} = 0.017 \pm 0.004$. All

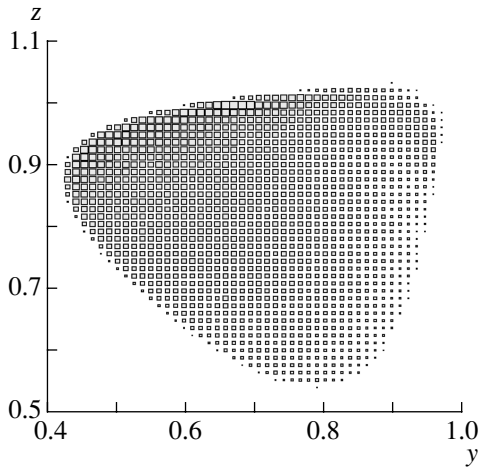

Fig. 4. Dalitz plot ($y = 2E_\mu/M_K$, $z = 2E_{\pi^0}/M_K$) for the selected $K \to \mu\nu\pi^0$ events after the $2C$ fit.

Table 1. Event reduction statistics

Run	April 2001
$N_{\rm ev}$ on tapes	363 002 105
Beam track reconstructed	268 564 958 = 74%
One secondary track found	134 227 095 = 37%
Written to DST	107 215 783 = 30%
μ^- identified and π^0 identified	218 813
$\lvert M^2_{\rm miss}\rvert < 0.01$ GeV^2	195 799
$K \to \mu\nu\pi^0$ accepted	166 495
$E_{\rm miss} > 1.4$ GeV	112.157

Table 2. Results of the fit

	$\mu^-\nu\pi^0$	$\mu^-\nu\pi^0 + e^-\nu\pi^0$
λ_+	$0.0321^{+0.0040}_{-0.0040}$	$0.0296^{+0.0014}_{-0.0014}$
λ_0	$0.0197^{+0.0046}_{-0.0047}$	$0.0209^{+0.0042}_{-0.0042}$
λ_+	$0.0321^{+0.0040}_{-0.0040}$	$0.0297^{+0.0014}_{-0.0014}$
λ_0	0.017	0.017
$f_S/f_+(0)$	$0.0034^{+0.0058}_{-0.0058}$	$0.0039^{+0.0052}_{-0.0052}$
λ_+	$0.0338^{+0.0037}_{-0.0037}$	$0.0299^{+0.0014}_{-0.0014}$
λ_0	0.017	0.017
$f_T/f_+(0)$	$-0.0240^{+0.0330}_{-0.0326}$	$-0.0210^{+0.0278}_{-0.0274}$
χ^2/ndf	1.5	1.5
$N_{\rm bins}$	275	

the errors presented are from the MINOS procedure of the MINUIT program [8] and are larger than the Gaussian ones. At present, we estimate an additional systematic error in λ_+ and λ_0 to be ± 0.002. The estimate is made by varying cuts, cell size during the fit of the Dalitz plots, etc.

In the second and in the third lines, the scalar and the tensor terms are added into the fit. As is seen from the second line of (2), the f_S term is 100% anticorrelated with the $V-A$ contribution $(m_\mu/2m_K)f_-$; i.e., an independent estimate of this term is necessary. By definition, $f_- = f_+(0)(\lambda_0 - \lambda_+)(m_K^2 - m_\pi^2)/m_\pi^2$. The λ_+ is, in fact, defined by the K_{e3} data, and the λ_0 is calculated by ChPT: $\lambda_0^{\rm th} = 0.017 \pm 0.004$. In our f_S fit, we fix λ_0 to this, theoretical, value. The error (± 0.004) in the theoretical prediction induces an additional error in f_S equal to ± 0.005.

A possible example of theories that give nonzero f_S are the 2HDM [9] and the Weinberg 3HDM model [10]. In these theories, the f_S comes from the diagram with the charged Higgs boson exchange H^-. The calculation of the contributions gives [11]

$$f_S^{\rm 2HDM}/f_+(0) = \frac{m_\mu}{2m_K}\frac{m_K^2}{m_H^2}\tan^2\beta, \qquad (5)$$

$$f_S^{\rm 3HDM}/f_+(0) = \frac{m_\mu}{2m_K}\frac{m_K^2}{m_{H_1}^2}{\rm Re}(\alpha_1^*\gamma_1). \qquad (6)$$

Here, m_H is the charged Higgs boson mass (mass of the lightest $H^\pm$ in case of 3HDM); $\tan\beta = v_2/v_1$ is the ratio of the vacuum expectation values for two Higgs doublets; α and γ are complex couplings of the 3HDM Higgs boson to d quarks and leptons. From our limit for f_S,

$$\frac{\tan\beta}{m_H} = 0.39 \pm 0.2({\rm stat.}) \pm 0.2({\rm theor.})\ {\rm GeV}^{-1};$$

$$\mathrm{Re}(\alpha_1^*\gamma_1)\frac{m_K^2}{m_{H_1}^2}$$

$$= 0.036 \pm 0.047({\rm stat.}) \pm 0.047({\rm theor.}).$$

Our 2HDM limit is comparable with that from LEP searches for the decay $b \to \tau\nu_\tau$ [12]: 90% C.L. limit is $\tan(\beta)/m_H < 0.4{-}1$ GeV^{-1} (depending on the collaboration).

The results of the fit with the tensor term are presented in the third line. The tensor term is also correlated with the λ_0, $df_T/d\lambda_0 = -3.5$. That is why we decided to apply the same approach for the tensor term as for the scalar one; i.e., λ_0 is fixed to its theoretical value, and the induced error in f_T, due to the theoretical error in λ_0, is calculated. The error equals ± 0.02 for the single $K_{\mu 3}$ fit and ± 0.014 for the combined one. The tensor coupling f_T appears naturally in the leptoquark models, as a result of the Fierz transformation [11]. Unfortunately, we have not found complete theoretical consideration for this contribution.

6. SUMMARY AND CONCLUSIONS

The $K^-_{\mu 3}$ decay has been studied using in-flight decays of 25-GeV K^-, detected by the ISTRA+ magnetic spectrometer. Due to the high statistics, adequate resolution of the detector, and good sensitivity over all the Dalitz plot space, the measurement errors are significantly reduced as compared with the previous measurements. The λ_+^μ parameter of the vector form factor $f_+(t)$ is measured to be

$$\lambda_+^\mu = 0.0321 \pm 0.004({\rm stat.}) \pm 0.002({\rm syst.})$$

and is in agreement with that obtained from our K^-_{e3} data:

$$\lambda_+^e = 0.0293 \pm 0.0015({\rm stat.}) \pm 0.002({\rm syst.}).$$

The combined fit of both sets of data assuming the μ–e universality gives

$$\lambda_+ = 0.0296 \pm 0.0014(\text{stat.}) \pm 0.002(\text{syst.}).$$

The λ_0 parameter of the scalar form factor $f_0(t)$ is measured to be

$$\lambda_0 = 0.0209 \pm 0.004(\text{stat.}) \pm 0.002(\text{syst.}).$$

It is, at present, the best measurement of this parameter. It is in good agreement with the ChPT prediction as well as with a recent λ_0 measurement from the $\Gamma(K_{\mu 3})/\Gamma(K_{e3})$ ratio [13].

The limits on the possible scalar and tensor couplings are derived:

$$f_S/f_+(0) = 0.004 \pm 0.005(\text{stat.}) \pm 0.005(\text{theor.}),$$
$$f_T/f_+(0) = -0.021 \pm 0.028(\text{stat.}) \pm 0.014(\text{theor.}).$$

The second (theoretical) error comes from the uncertainty in the ChPT prediction for λ_0. Again, these are the current best estimates for these parameters.

ACKNOWLEDGMENTS

We would like to thank V.V. Braguta, A.E. Chalov, A.A. Likhoded, A.K. Likhoded, R.N. Rogalyov, and S.R. Slabospitsky for discussions.

The INR part of the collaboration is supported by the Russian Foundation for Basic Research, project no. 00-02-16074.

REFERENCES

1. I. V. Ajinenko *et al.*, Preprint No. 2001-051, IHEP (Protvino, 2001); hep-ex/0112023.
2. R. Brun *et al.*, CERN-DD/EE/84-1.
3. V. N. Bolotov *et al.*, Preprint No. 802/93, INR (Moscow, 1993).
4. H. Steiner *et al.*, Phys. Lett. B **36B**, 521 (1971).
5. M. V. Chizhov, hep-ph/9511287.
6. J. Gasser and H. Leutwyler, Nucl. Phys. B **250**, 517 (1985).
7. E. S. Ginsberg, Phys. Rev. **162**, 1570 (1967).
8. F. James and M. Roos, CERN D506 (1989).
9. J. F. Gunion *et al.*, *The Higgs Hunter's Guide* (Addison-Wesley, Redwood City, 1990).
10. S. Weinberg, Phys. Rev. Lett. **37**, 657 (1976).
11. G. Belanger and C. Q. Geng, Phys. Rev. D **44**, 2789 (1991).
12. DELPHI Collab., Phys. Lett. B **496**, 43 (2000); ALEPH Collab., Eur. Phys. J. C **19**, 213 (2001); OPAL Collab., Phys. Lett. B **520**, 1 (2001); L3 Collab., Phys. Lett. B **332**, 201 (1994).
13. K. Horie *et al.*, hep-ex/0106006.

Physics of Atomic Nuclei, Vol. 66, No. 1, 2003, pp. 110–113. Translated from Yadernaya Fizika, Vol. 66, No. 1, 2003, pp. 112–115.

ELEMENTARY PARTICLES AND FIELDS
Experiment

Measurement of the Total and Differential Cross Sections for the Reaction $\pi^- p \to \eta n$ with the Crystal Ball Detector

N. G. Kozlenko[1)*], V. V. Abaev[1)], V. S. Bekrenev[1)], S. P. Kruglov[1)], A. A. Koulbardis[1)], I. V. Lopatin[1)], A. B. Starostin[1),2)], B. Draper[3)], S. Hayden[3)], J. Huddleston[3)], D. Isenhower[3)], C. Robinson[3)], M. Sadler[3)], C. Allgower[4)], R. Cadman[4)], H. Spinka[4)], J. Comfort[5)], K. Craig[5)], A. Ramirez[5)], T. Kycia[†6)], M. Clajus[2)], A. Marusic[2)], S. McDonald[2)], B. M. K. Nefkens[2)], N. Phaisangittisakul[2)], S. Prakhov[2)], J. W. Price[2)], W. B. Tippens[2)], J. Peterson[7)], W. J. Briscoe[8)], A. Shafi[8)], I. I. Strakovsky[8)], H. Staudenmaier[9)], D. M. Manley[10)], J. Olmsted[10)], D. Peaslee[11)], N. Knecht[12)], G. Lolos[12)], Z. Papandreou[12)], I. Supek[13)], I. Slaus[13)], A. Gibson[14)], D. Grosnic[14)], D. Koetke[14)], R. Manweiler[14)], and S. Stanislaus[14)]

Received November 23, 2001

Abstract—The first results obtained in 1998 by the Crystal Ball collaboration from a measurement of the total and differential cross sections for the reaction $\pi^- p \to \eta n$ are presented. These new experimental results for the total cross sections are compared with the predictions of the K-matrix model for pion–nucleon scattering. The angular distribution at momenta near the reaction threshold (685 MeV/c) is determined by the S-wave contribution. The P-wave contribution begins to manifest itself from a momentum of 720 MeV/c. © *2003 MAIK "Nauka/Interperiodica".*

Until now, experimental information about the cross sections for the reaction $\pi^- p \to \eta n$ has remained scanty and contradictory, especially near the reaction threshold (685 MeV/c). There have been no publications devoted to this subject since 1975. At the same time, it would be of paramount importance to obtain accurate experimental data in the threshold region for testing theoretical models of η-meson production. Such data would also be useful for evaluating the ηN scattering length and for obtaining deeper insight into the properties of the $S_{11}(1535)$ resonance, which decays through the ηn channel with a probability of 35–55% (according to the last Review of Particle Properties).

In order to measure $\pi^- p \to \eta n$ cross sections, it is necessary to detect either a neutron or photons from the η-meson decay modes $\eta \to 2\gamma$ or $\eta \to 3\pi^0 \to 6\gamma$, and the Crystal Ball [1], which is now on the C6 pion-beam line at the Brookhaven National Laboratory (BNL), where the measurements described in this article were performed, is an ideal detector for these purposes. The layout of the Crystal Ball detector is shown in Fig. 1. The detector consists of 672 separate NaI(Tl) crystals shaped as a truncated triangular pyramid, which cover 93% of 4π steradians, each crystal being of 16 radiation lengths. A liquid-hydrogen target was arranged at the center of the Crystal Ball detector. The target was surrounded by a veto barrel made from four scintillation counters and

[†]Deceased.
[1)]Petersburg Nuclear Physics Institute, Russian Academy of Sciences, Gatchina, 188350 Russia.
[2)]University of California (Los Angeles), 405 Hilgard Avenue, Los Angeles, CA 90095-1547, USA.
[3)]Abilene Christian University, ACU Station, Box 7963, Abilene, TX 79699, USA.
[4)]Argonne National Laboratory, 9700 S. Cass Ave., Argonne, IL 60439-4815, USA.
[5)]Arizona State University, Box 871504, Tempe, AZ 85287-1504, USA.
[6)]Brookhaven National Laboratory, PO Box 5000, Upton, NY 11973, USA.
[7)]University of Colorado, Campus Box 390, Boulder, CO 80309, USA.
[8)]The George Washington University, Washington, DC 20052, USA.
[9)]Universität Karlsruhe, PO Box 6980, D-76128 Karlsruhe, Germany.
[10)]Kent State University, Kent, OH 44242-0001, USA.
[11)]University of Maryland, College Park, MD 20742-3255, USA.
[12)]University of Regina, Regina, SK S4S OA2, Canada.
[13)]Rudjer Bošković Institute, PO Box 1016, Bijenička 54, HR-10001 Zagreb, Croatia.
[14)]Valparaiso University, Valparaiso, IN 46383, USA.
[*]e-mail: kozlenko@pnpi.spb.ru

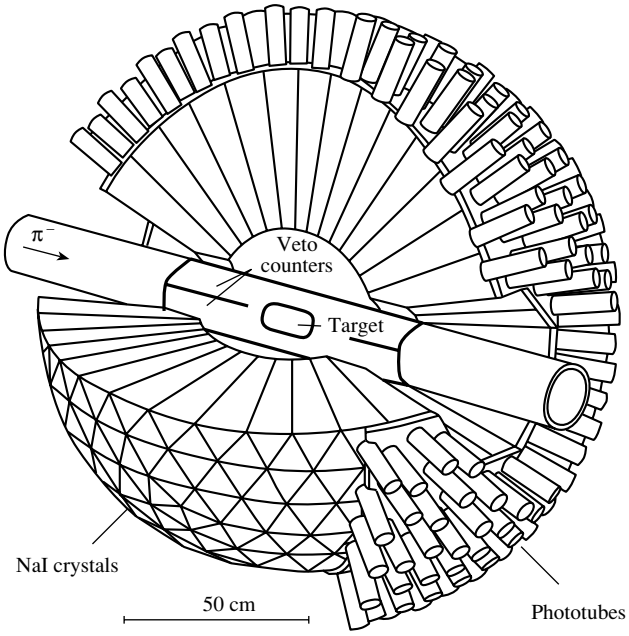

Fig. 1. Layout of the Crystal Ball detector.

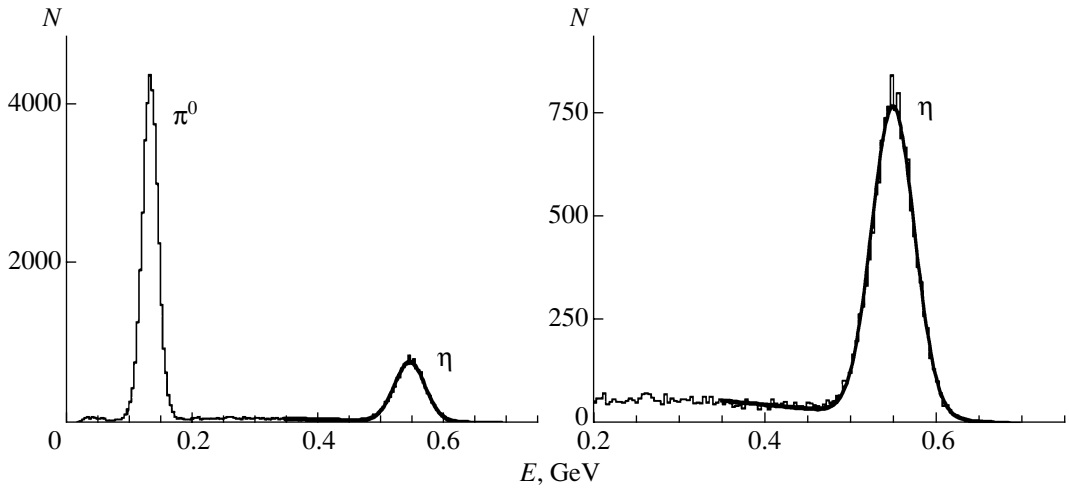

Fig. 2. Invariant-mass spectrum of two photons (N is the number of events). The right panel displays the η-meson region on an enlarged scale.

intended for rejecting events that involve the emission of charged particles.

The yield of the reaction $\pi^- p \to \eta n$ was measured in the threshold region at incident pion momenta of up to 720 MeV/c. The absolute error in the pion momentum was $\pm 0.4\%$, while the momentum spread $\Delta P/P$ (FWHM) in the beam was 2.3%. The invariant mass of the η meson (for the case where two photons from its decay were detected in the Crystal Ball detector) was calculated as

$$M_{2\gamma}^{\mathrm{inv}} = \sqrt{2E_{\gamma_1}E_{\gamma_2}(1-\cos\theta_{\gamma_1\gamma_2})},$$

where $E_{\gamma_1}(E_{\gamma_2})$ is the energy of the first (second) photon and $\theta_{\gamma_1\gamma_2}$ is the angle between the momenta of the first and the second photon. A typical invariant mass distribution for 2γ events is shown in Fig. 2. The background under the η peak (right panel in Fig. 2) was less than 6% and was subtracted in calculating the yield. The background from an empty target was about 2%.

The total cross section σ_{tot} was evaluated by the formula

$$\sigma_{\mathrm{tot}} = \frac{N_\eta}{N_{\pi^-} N_p A \cdot \mathrm{BR}},$$

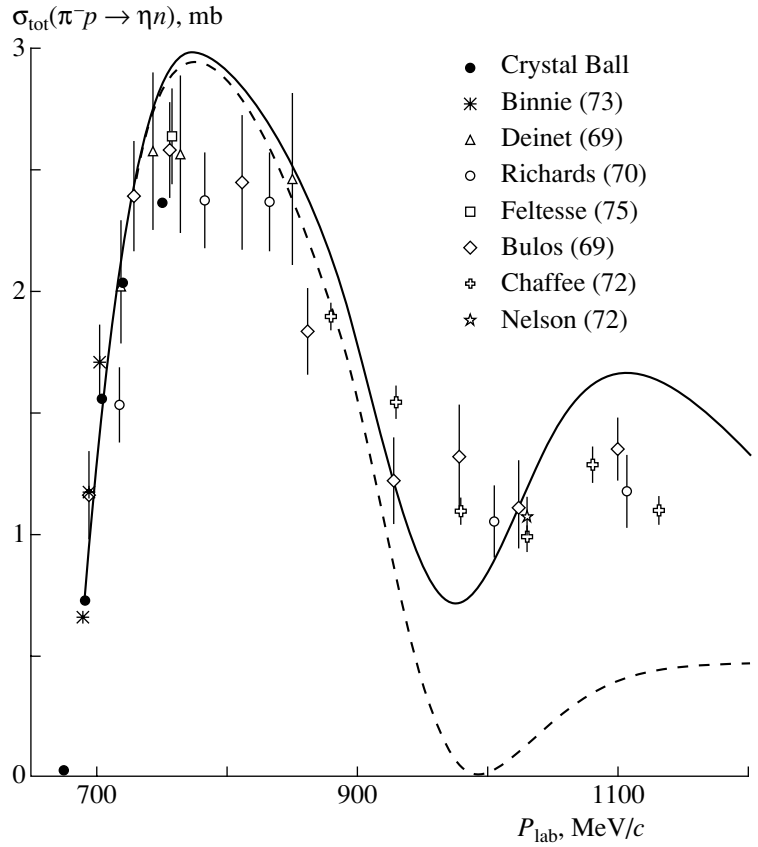

Fig. 3. Total cross sections for the reaction $\pi^- p \to \nu n$. Points represent experimental data. The solid curve corresponds to the calculations from [9], which include S and P waves. The dashed curve was computed by taking into account only the S-wave contribution.

where $N_{\pi^-} = N_{\rm tot}(1-n_e)(1-n_\mu)$; N_η is the number of events under the peak of $M_{2\gamma}^{\rm inv}$ (after the background subtraction); N_{π^-} is the number of pions incident on the target per cycle; N_p is number of protons in the target ($1/{\rm cm}^2$); A is the acceptance of the Crystal Ball for the detection of 2γ from the decay $\eta \to 2\gamma$ (the quantity A also includes the efficiency of the analysis)—at a momentum of 720 MeV/c, the acceptance is approximately equal to 0.45; $N_{\rm tot}$ is the beam monitor (the total number of particles, including e, μ, and π, detected over a cycle); and n_e and n_μ are the fractions of the electron and muon admixtures, respectively.

In determining N_{π^-} and N_p, we used information from proportional chambers in order to reconstruct the tracks of incident particles. The target had the shape of a cylinder of diameter 10 cm and length 10 cm. The cylinder axis was aligned with the incident beam. In data processing, we applied the cuts $|x| <$ 3 cm and $|y| < 2$ cm at the entrance of the target, whereby we selected only those tracks that traversed the central part of the target.

Photon conversion in the scintillator of the veto barrel and in the vacuum pipe was automatically taken into account in calculating the acceptance A by the Monte Carlo method. The uncertainty in the veto-barrel energy threshold could change the acceptance by not more than 1%.

The systematic error (standard deviation) in the total cross sections was 4.5%. The most important contributions to this error are the following: (i) the uncertainty in the electron and muon admixture in the beam (4%); (ii) errors in the Monte Carlo calculation of the acceptance (1%); (iii) errors in determining the number of protons in the target (1%); (iv) the inaccuracy of the procedure for subtracting the physical background under the peak of the η-meson invariant mass $M_{2\gamma}^{\rm inv}$(1%); and (v) the uncertainty in the veto-barrel energy threshold (1%), this uncertainty affecting the calculation of the acceptance A.

The total cross sections obtained in this study are in good agreement with data from previous experiments (see [2–8]), but the statistical accuracy achieved here is higher than that of all published experimental data (see Fig. 3).

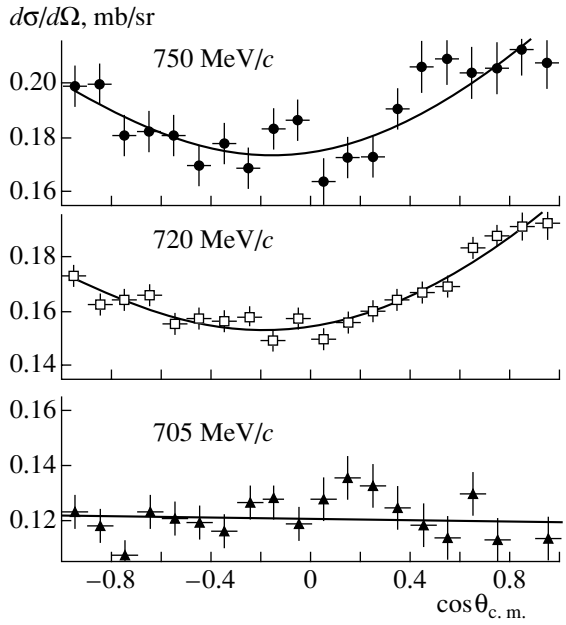

Fig. 4. Differential cross section for the reaction $\pi^- p \to \eta n$. The coefficients in the relevant Legendre polynomial are (lower panel) $A_0 = 0.120$, $A_1 = -0.002$, and $A_2 = 0.0$; (middle panel) $A_0 = 0.165$, $A_1 = 0.013$, and $A_2 = 0.022$; and (upper panel) $A_0 = 0.188$, $A_1 = 0.013$, and $A_2 = 0.024$.

As can be seen from Fig. 3, our results do not completely agree with the predictions of the K-matrix model of pion–nucleon scattering [9] (this model takes into account the S- and P-wave contributions to η-meson production).

The differential cross sections for the process $\pi^- p \to \eta n$ that were measured at the incident-pion momenta of 705, 720, and 750 MeV/c are shown in Fig. 4. At 720 MeV/c, the statistical accuracy is higher than at 705 and 750 MeV/c. This is because, at 720 MeV/c, we summed the results of 48 cycles of measurements (in all, 6×10^5 η mesons produced on the hydrogen target were detected). The errors shown in the figure for the momentum of 720 MeV/c are determined predominantly by the statistical errors of the Monte Carlo evaluation of the acceptance A.

The distributions were approximated by a second-order Legendre polynomial. One can see that, at the momentum of 705 MeV/c, the main contribution to the differential cross sections comes from the S-wave amplitude. At the same time, higher waves must be taken into account in order to describe the differential cross sections at 720 and 750 MeV/c.

It can be seen from Fig. 3 that it is necessary to investigate the reaction $\pi^- p \to \eta n$ at momenta above 750 MeV/c. It is planned to perform such measurements with a beam of momentum 2 GeV/c.

ACKNOWLEDGMENTS

This work was supported by the Russian Foundation for Basic Research and the Ministry for Industry, Sciences, and Technologies of the Russian Federation, as well as by US DOE, NSF, NSERC, and Volkswagen Stiftung.

REFERENCES

1. M. E. Sadler, πN Newsletter **13**, 123 (1997).
2. D. M. Binnie *et al.*, Phys. Rev. D **8**, 2789 (1973).
3. W. Deinet *et al.*, Nucl. Phys. B **11**, 495 (1969).
4. W. B. Richards *et al.*, Phys. Rev. D **1**, 10 (1970).
5. J. Feltesse *et al.*, Nucl. Phys. B **93**, 242 (1975).
6. F. Bulos *et al.*, Phys. Rev. **187**, 1827 (1969).
7. R. B. Chaffee, Thesis LBL 1060 (1972).
8. J. E. Nelson, Thesis LBL 1019 (1972).
9. A. B. Gridnev and N. G. Kozlenko, Eur. Phys. J. A **4**, 187 (1999).

Translated by S. Slabospitsky

Physics of Atomic Nuclei, Vol. 66, No. 1, 2003, pp. 114–122. From Yadernaya Fizika, Vol. 66, No. 1, 2003, pp. 116–124.

ELEMENTARY PARTICLES AND FIELDS
Experiment

The A Dependence of Fast-Particle Spectra in π^+, K^+, and p Interactions with Al and Au Targets at 250 GeV/c*

N. M. Agababyan[1], M. R. Atayan[1], E. A. De Wolf[2], K. Dziunikowska[3], A. M. F. Endler[4], Z. Sh. Garutchava[5], G. R. Gulkanyan[1], R. Sh. Hakobyan[1], D. Kisielewska[3], W. Kittel[6], S. S. Mehrabyan[1], Z. V. Metreveli[5], K. Olkiewicz[3], F. K. Rizatdinova[7], N. A. Sotnikova[7], L. N. Smirnova[7], L. G. Sveshnikova[7], M. D. Tabidze[5], L. A. Tikhonova[7], A. V. Tkabladze[5], A. G. Tomaradze[5], F. Verbeure[2], Sh. M. Yandarbiev[7], and S. A. Zotkin[7]**
The EHS/NA22 Collaboration

Received July 17, 2001; in final form, January 16, 2002

Abstract—The A dependence of charged-particle spectra in π^+, K^+, and p interactions with Al and Au targets at 250 GeV/c are presented and compared to predictions of the Quark–Gluon String Model (QGSM). It is shown that the A dependence of invariant inclusive charged-particle spectra on the Feynman variable x is very weak between Al and Au targets. The QGSM shows a larger difference between fast-particle spectra for both Al and Au targets and different beam particles. The QGSM prediction for the leading-particle spectrum over an energy range from 250 GeV to 10 TeV in pAu(Pb) reactions is in a reasonable agreement with the results of NA22 data and a cosmic-ray experiment.

1. INTRODUCTION

Hadron–nucleus interactions show a particular sensitivity to the space-time structure of the multiparticle production mechanism. With these type of reactions, the hadron-formation process and the fragmentation of relatively-low-energy quark–gluon jets or strings can be studied in nuclear matter. Secondary-particle production shows a different dependence on the atomic number A for different inclusive reactions and different kinematical regions.

There is no clear understanding of a possible difference in the A dependence of leading-particle spectra for meson–nucleus and proton–nucleus interactions. However, if it exists, this effect is very important for the calculation of cosmic-ray cascade processes in the atmosphere and for the interpretation of the results of cosmic-ray experiments.

A detailed model description of hadron–nucleus interactions is important in understanding the dynamics of the interaction and in making quantitave predictions for the reactions of interest. Often, existing models are compared with experimental multiplicity or rapidity distributions, which are not sensitive enough in the beam-fragmentation region.

In this paper, the A dependence of fast secondary-particle yields was studied for π^+, K^+, and p beams with a 250-GeV/c momentum on Al and Au targets. Both the inclusive and leading-particle spectra were analyzed. The 4π geometry and the complete event information of the NA22 experiment grant the possibility of investigating the full p_t region and the particular role that coherent inelastic interactions play for the A dependence of fast-particle spectra [1].

Furthermore, a comparison of the experimental data with the Quark–Gluon String Model (QGSM) was performed for an incident-particle momentum of 250 GeV/c, as well as for cosmic-ray experiments at an energy of 10 TeV.

The paper is organized as follows. In Section 2 we present the experiment and the criteria used for

*This article was submitted by the authors in English.

[1)]Institute of Physics, Yerevan, Armenia.
[2)]Department of Physics, Universitaire Instelling Antwerpen, Wilrijk, Belgium.
[3)]Department of Physics and Nuclear Techniques of the Academy of Mining and Metallurgy and the Institute of Nuclear Physics, Krakow, Poland.
[4)]Centro Brasileiro de Pesquisas Fisicas, Rio de Janeiro, Brazil.
[5)]Institute for High Energy Physics of Tbilisi State University, Georgia.
[6)]High Energy Physics Institute Nijmegen (HEFIN), University of Nijmegen/NIKHEF, the Netherlands.
[7)]Institute of Nuclear Physics, Moscow State University, Russia.
**e-mail: smirnova@npi.msu.su

data selection. The QGSM is described in Section 3. The inclusive-particle and leading-particle analyses are presented in Sections 4 and 5, respectively. The data on associated multiplicity are given in Section 6, and model extrapolations to cosmic-ray experiments, in Section 7. The conclusions of the analysis are summarized in Section 8.

2. EXPERIMENTAL DATA

The experimental data presented here were obtained by the NA22 collaboration using the European Hybrid Spectrometer (EHS), which was exposed to a beam of π^+, K^+, and p with a momentum of 250 GeV/c. An Al and Au foil of thickness 0.5% and of an interaction length were inserted in the Rapid Cycling Bubble Chamber (RCBC), filled with H_2 and used as an active vertex and track detector. The foils were placed at a distance of 15.5 cm from the entrance window. The main advantages of such a vertex detector are the possibility of registering slow particles and of identifying protons of laboratory momentum $p_{\text{lab}} < 1.2$ GeV/c, as well as electrons with $p_{\text{lab}} <$ 200 MeV/c. The pion mass was assigned to all other particles. The angular acceptance for all inelastic interactions in foils was equal to 4π. The experimental conditions were identical for the two targets.

The experimental setup, the minimum bias trigger, and the selection criteria for nuclear interactions are described in more detail in [2, 3]. The aim of the selection criteria was to isolate a set of well-measured and reconstructed inelastic interactions in the foils, eliminating both quasi-elastic and coherent interactions.

The average momentum resolution $\Delta p/p$ varies from a maximum of 2.5% at 30 GeV/c to 1.5% for momenta larger than 100 GeV/c.

Multiplicity-dependent weights are introduced to correct for the loss of events that is caused by the selection criteria. Furthermore, each event is weighted to correct for the losses induced by the interaction trigger [2]. This weight strongly depends on the spatial characteristics of the event. It is determined for each reconstructed event from the overall azimuthal symmetry around the beam axis. An x-dependent systematic error on the trigger weight is added in quadrature to the statistical error. Results of the multiplicity distribution for the selected event sample were presented in [3, 4], and those on rapidity and transverse-momentum distributions in [5]. General features of coherent inelastic meson–nucleus interactions obtained in this experiment are presented in [1], those of target-diffractive interactions, in [6].

The present analysis is based on the following samples of events passing the selection criteria:

$$\pi^+ + \text{Al} \to C^\pm + X \quad (3301), \qquad (1)$$

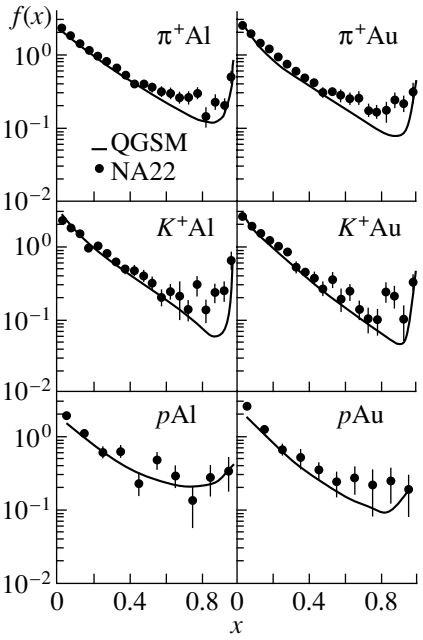

Fig. 1. The invariant inclusive spectra $f(x)$ (7) for reactions (1)–(6) in comparison with QGSM predictions: π^+Al, π^+Au, K^+Al, K^+Au, pAl, and pAu.

$$\pi^+ + \text{Au} \to C^\pm + X \quad (2694), \qquad (2)$$

$$K^+ + \text{Al} \to C^\pm + X \quad (1198), \qquad (3)$$

$$K^+ + \text{Au} \to C^\pm + X \quad (966), \qquad (4)$$

$$p + \text{Al} \to C^\pm + X \quad (181), \qquad (5)$$

$$p + \text{Au} \to C^\pm + X \quad (178). \qquad (6)$$

Hadron–proton interactions taking place in the hydrogen of the bubble chamber [2] are used for comparison.

3. THE QGSM MODEL

The QGSM, used for comparison with the experimental data in this paper, is the Monte Carlo version of the multiparticle production model, where hadrons are produced in the fragmentation of quark–gluon strings, or color "tubes," created as a result of a hadron–hadron collision [7, 8]. This model qualitatively describes both the inclusive charged-particle spectra and the global correlation phenomena observed [9–11] in the hadron–proton interactions at 250 GeV/c measured in the same experiment.

The QGSM Monte Carlo version for hadron–nucleus interactions was developed in [12]. In this model, two quark–gluon strings are formed between the valence quarks of the projectile particle and the quarks of intranuclear nucleons. A part of the forward-moving (i.e., in the direction of the projectile hadron) string is excited and can fragment into hadrons. This

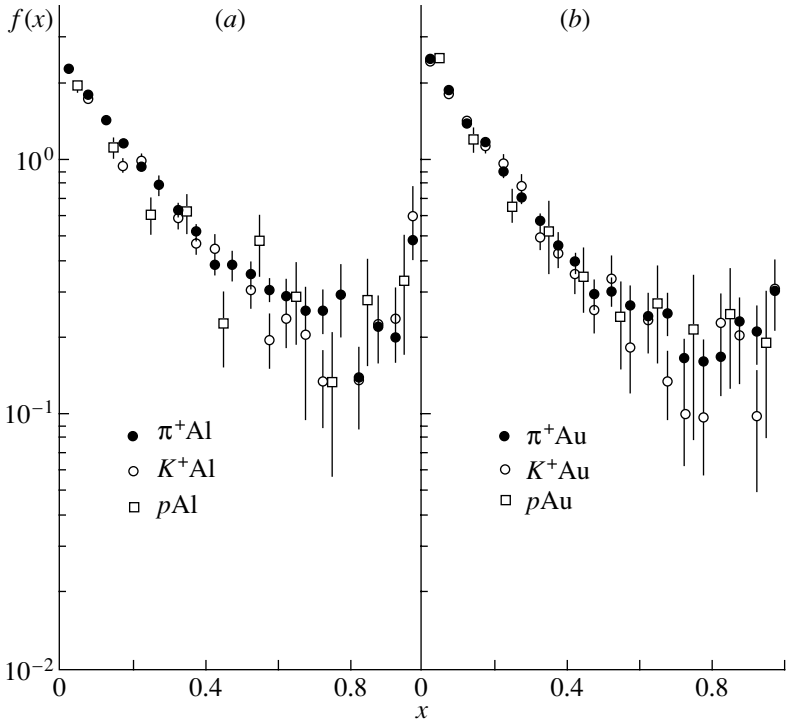

Fig. 2. Comparison of the invariant inclusive spectra $f(x)$ (7) for interactions of different types of projectiles on (a) Al and (b) Au targets.

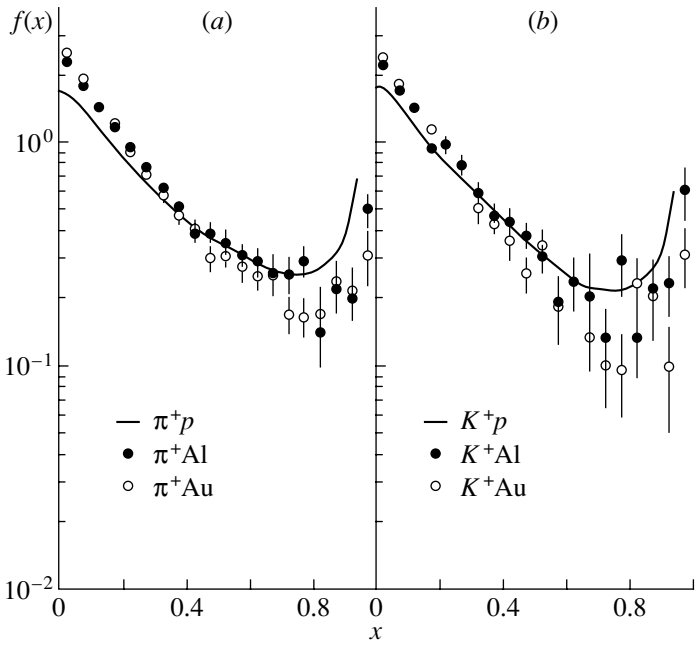

Fig. 3. Comparison of the invariant inclusive spectra $f(x)$ (7) for (a) π^+ and (b) K^+ interactions with different targets.

fragmentation can take place inside, as well as outside the nucleus. The other part of the string is unexcited and forms a "leading front" of the string which can interact inside the nucleus. The same processes take place in the second string, which moves in the target direction.

The model includes all of the main diagrams of hadron–nucleon interactions [9], the possibility of meson–meson interactions, interactions between

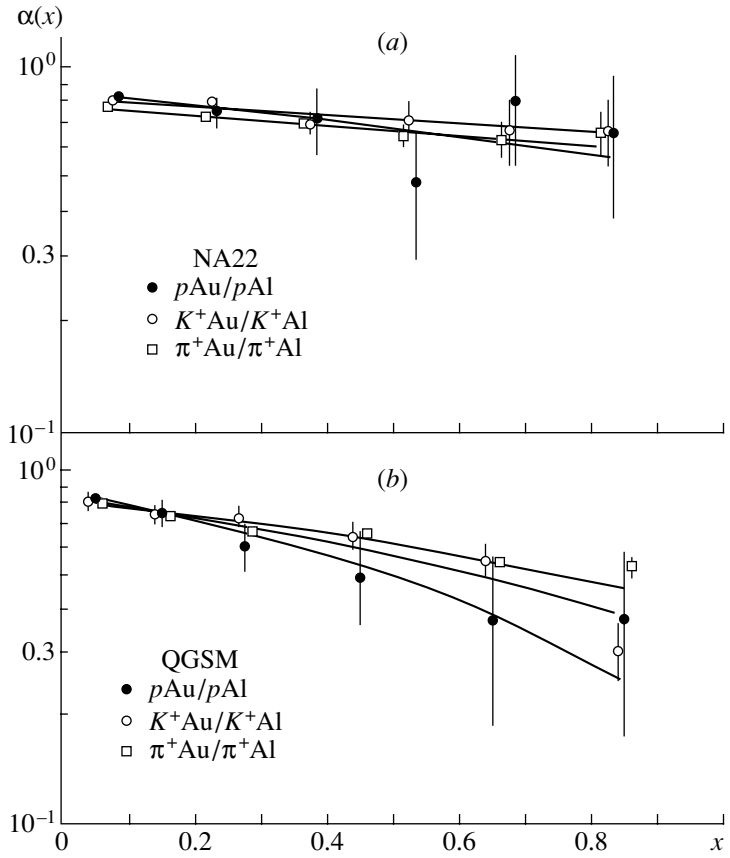

Fig. 4. The function $\alpha(x)$ as calculated from a comparison of $F(x)$ spectra according to (8) for Au with Al targets: (a) NA22 data and (b) QGSM.

strings, and resonance production [12]. As will be seen below, the introduction of diagrams for diffractive interactions reproduces the particle spectra at high x. Coherent hadron interaction was not included in the model. A comparison with the experimental data was performed in [12] on proton–nucleus interactions at projectile momenta of 4.2 and 200 GeV/c. In the present paper, the model predictions are compared with the meson–nucleus and proton–nucleus data at 250 GeV/c, but the model predictions are also extrapolated to much higher energies.

The choice of the QGSM parameters for this experiment was made in [13], where the multiplicity and charged-particle rapidity distributions from previous NA22 publications were compared with the model. Two possible four-dimensional coordinates of hadron formation (when the scattered hadron regains the ability to interact) are the "constituent" hadron formation time, corresponding to the point of string breaking, and the "yo-yo" hadron formation time, which corresponds to the intersection point of the quark trajectories. Of these two, the "yo-yo" hadron formation time was favored by our data.

The so-called "hot-cascade" process of particles produced in string fragmentation was switched on in the model. The coefficient of string tension was set to 0.9 GeV/fm. Using these parameters, a compromise in the agreement with both our Al and Au results was reached, but the particle multiplication in the cascade process was slightly underestimated for Au and slightly overestimated for Al.

4. INVARIANT INCLUSIVE FAST-PARTICLE SPECTRA

The normalized invariant inclusive spectra,

$$f(x) = \frac{1}{N_{\rm ev}} \frac{2E^*}{\sqrt{s}} \frac{dN}{dx}, \qquad (7)$$

of charged particles produced in reactions (1)–(6) are presented in Fig. 1 for $x > 0$, together with the corresponding QGSM predictions. The variable x is calculated in the hadron–nucleon c.m.s. of each reaction; dN is the total number of charged particles in bin dx; $N_{\rm ev}$ is the total number of events in the given reaction; E^* is the energy of the particle, and $\sqrt{s}$ is the total energy, both in the hadron–nucleon c.m.s. A reasonable agreement is observed between the experimental data and the QGSM predictions in the region

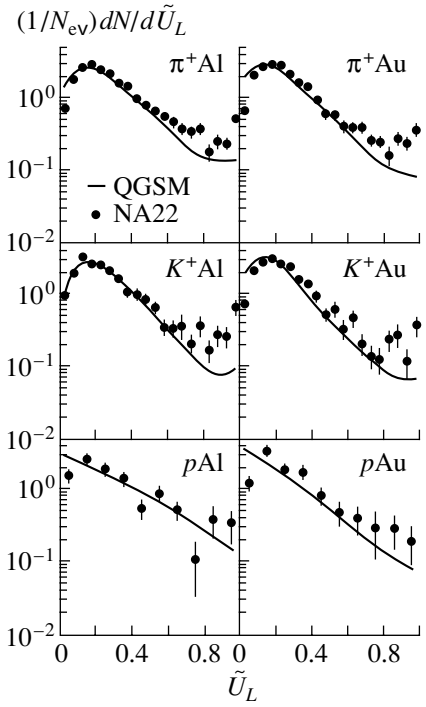

Fig. 5. Leading charged-particle spectra for reactions (1)–(6) in comparison with QGSM predictions: π^+Al, π^+Au, K^+Al, K^+Au, pAl, and pAu.

$x = 0$–0.8. It was noted that the QGSM underestimates the number of fast particles at $x > 0.8$. As the contribution of such fast particles in the inclusive cross section is small (less than 5%), the average value of $\langle x \rangle$ is in rather good agreement with the experiment.

In Fig. 2*a* the $f(x)$ spectra for the three types of projectile are compared on the Al target, in Fig. 2*b*, those on the Au target. No significant differences are observed between the proton, pion, and kaon-induced inclusive spectra. This result is in agreement with those of previous experiments [14].

To demonstrate the effect of the size of the nuclear target on the spectrum, the experimental data on π^+p reactions, obtained in the same experiment [2], are compared in Fig. 3*a* to the spectra for pion–nucleus interactions. The corresponding spectra are shown for the kaon projectile in Fig. 3*b*. A clear difference in the spectra for proton and nuclear targets can be seen at $x > 0.6$ (the deficiency of very fast particles) and at $x < 0.3$ (an excess due to intranuclear cascading).

Table 1. Inelastic cross sections (in mb) for hadron–nucleus interactions interpolated to 250 GeV/c [15]

Beam particle	Al	Au	α
π^+	327 ± 10	1420 ± 50	0.74 ± 0.03
K^+	291 ± 10	1360 ± 50	0.76 ± 0.03
p	415 ± 10	1702 ± 50	0.72 ± 0.01

For a quantitative analysis of the A dependence, the following parametrization of the invariant inclusive spectra was used:

$$F_{hA}(x) = A^{\alpha(x)} F_{hp}(x), \qquad (8)$$

where $F(x) = \sigma_{\text{in}} f(x)$, σ_{in} being the inelastic cross section of the hadron–nucleus interaction.

First, the $\alpha(x)$ functions were calculated from a comparison of the $F(x)$ spectra in h^+Al and h^+Au collisions using the inelastic hA cross sections presented in Table 1 [15]. The results are shown in Fig. 4*a* for proton, pion, and kaon projectiles, separately. Figure 4*a* suggests that $\alpha(x)$ is nearly constant for mesons and perhaps slowly decreasing with increasing x for protons, but the statistical errors are too large to make any conclusion. The corresponding QGSM predictions (Fig. 4*b*) show a more significant A dependence. The parameters of a linear parametrization of $\alpha(x)$ are presented in the Table 2. The parameter a defining the A dependence of the x distribution shape between Al and Au seems to be higher (in absolute value) in the QGSM than in the data. The parameter b is well reproduced by the QGSM simulation.

Second, the $\alpha(x)$ functions were calculated by a fit of the corresponding hp, hAl, and hAu points by (8), for each x bin. The fits are often bad, but the trend observed in Fig. 4*a* (the difference in the parameter $\alpha(x)$ for proton and meson projectiles) is supported with higher statistical significance. Better agreement is observed with the QGSM than above (see Table 2).

It was verified that $\alpha(x)$ does not change when coherent events are included.

5. LEADING-PARTICLE SPECTRA

The physical definition of a leading particle is a fast particle that has survived the collision with the same quantum numbers as the projectile. The spectrum of the leading particle reflects the number of interactions of the projectile with the nucleons inside the nucleus, but should not be sensitive to multiplication by intranuclear secondary-particle interactions.

For a pion projectile this definition loses its meaning because of two reasons: (1) many charged pions produced in the interaction have the same quantum numbers as the projectile pion and (2) the fast pion can carry an electric charge opposite to that of the projectile. Furthermore, the electric charge is not determined in cosmic-ray experiments. So, for all

Table 2. Parameters of the linear fit $\alpha(x) = ax + b$ of experimental data and QGSM predictions

	NA22		QGSM	
	a	b	a	b
pAu/pAl	-0.34 ± 0.22	0.85 ± 0.04	-0.71 ± 0.17	0.86 ± 0.03
π^+Au/π^+Al	-0.22 ± 0.06	0.78 ± 0.01	-0.43 ± 0.03	0.83 ± 0.04
K^+Au/K^+Al	-0.19 ± 0.10	0.82 ± 0.02	-0.54 ± 0.08	0.85 ± 0.03
pp/Al/Au	-0.44 ± 0.03	0.98 ± 0.02	-0.43 ± 0.02	0.88 ± 0.02
π^+p/Al,Au	-0.33 ± 0.01	0.96 ± 0.01	-0.23 ± 0.01	0.86 ± 0.01
K^+p/Al/Au	-0.31 ± 0.01	0.99 ± 0.01	-0.27 ± 0.01	0.89 ± 0.01

cases, the leading particle is simply defined here as the charged (positive or negative) particle with the largest momentum in the laboratory system.

The distribution in the fraction $\tilde{U}_L$ of incident energy carried away by the charged leading particle in the laboratory system is shown in Fig. 5 for reactions (1)–(6), together with the corresponding QGSM predictions. An agreement between the experimental and the predicted leading-particle spectra is observed for hadron–Al reactions, but for hadron–Au reactions the QGSM slightly underestimates the number of leading particles in the range $\tilde{U}_L = 0.6$–0.9.

The average values of $\tilde{U}_L$ are presented in Table 3. The experimental values of $\langle \tilde{U}_L \rangle$ are slightly larger for Al than for Au. The QGSM clearly predicts larger energy losses in Au than in Al.

Table 3. Average values of the part of the incident energy carried away by leading particles, $\langle \tilde{U}_L \rangle$, for experimental spectra and for QGSM predictions

Target	Projectile		
	p	π^+	K^+
Al (NA22)	0.310 ± 0.018	0.300 ± 0.004	0.284 ± 0.006
Al (QGSM)	0.323 ± 0.005	0.304 ± 0.003	0.280 ± 0.005
Au (NA22)	0.281 ± 0.017	0.278 ± 0.004	0.274 ± 0.006
Au (QGSM)	0.246 ± 0.004	0.265 ± 0.003	0.248 ± 0.005

6. ASSOCIATED CHARGED-PARTICLE MULTIPLICITIES

The charged-particle multiplicity associated with a leading particle reflects the rate of particle cascading in a nucleus. The model predictions are sensitive to the particular form of the cascade multiplication of secondary particles, since different mechanisms of cascade multiplication can contribute to associated multiplicities differently. Their relative contribution depends on the leading-particle energy.

To compare associated multiplicities, it is important to know whether the total charge–multiplicity distributions $P_{N_{\rm ch}}$ are in agreement with the corresponding model predictions. In Fig. 6, the total charge–multiplicity distributions (including protons with a momentum larger than 200 MeV/c [16]) are shown for π^+, K^+, and p interactions on Al and Au, in comparison to the QGSM predictions with the same acceptance criteria. We do indeed find good agreement between experiment and QGSM predictions.

In Fig. 7, the average associated multiplicity $\langle N_{\rm ch}^{\rm ass} \rangle$ is presented as a function of $\tilde{U}_L$. The solid curves correspond to the QGSM predictions. One can see that for Al the associated multiplicity is

Table 4. Energy dependence of $\langle U_L \rangle$, calculated in frames of the QGSM for two variants of the hadron formation time

Formation time	Energy	$\langle U_L \rangle$
"Yo-yo"	250 GeV	0.289 ± 0.005
"Constituent"	250 GeV	0.266 ± 0.007
"Yo-yo"	10 TeV	0.260 ± 0.007
"Constituent"	10 TeV	0.262 ± 0.007

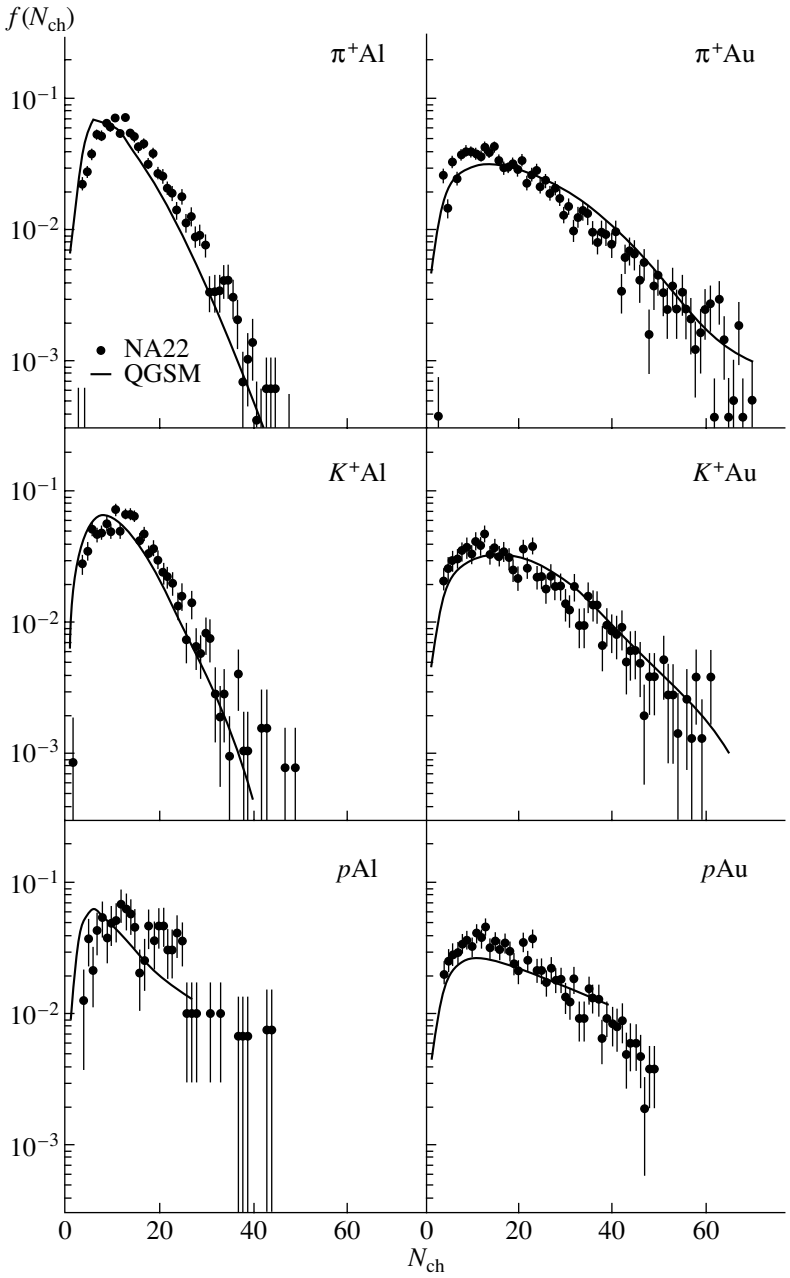

Fig. 6. The multiplicity distribution of charged particles for reactions (1)–(6) in comparison with the QGSM predictions: π^+Al, π^+Au, K^+Al, K^+Au, pAl, and pAu.

underestimated at $\tilde{U}_L > 0.5$. For Au it is slightly overestimated at low values of $\tilde{U}_L$.

7. COMPARISON WITH COSMIC-RAY EXPERIMENTS

To estimate the energy dependence of the leading-particle spectrum, we compare our simulation with the data obtained in a unique cosmic-ray experiment at energies of 1–3 and >7 TeV. The experiment was carried out at the Tien-Shan complex with a lead ionization calorimeter [17]. The most energetic particle produced in an interaction was selected as the leading particle. This definition includes neutrals, because it was imposible to distinguish protons and neutrons in this setup. The experimental value of the energy fraction U_L carried by this most energetic particle was determined by an analysis of fluctuations in the shape of the individual cascades produced by high-energy particles.

The distribution in $U_L dN/dU_L$ obtained in this experiment is shown in Fig. 8, together with the spectrum calculated from the QGSM at an energy of

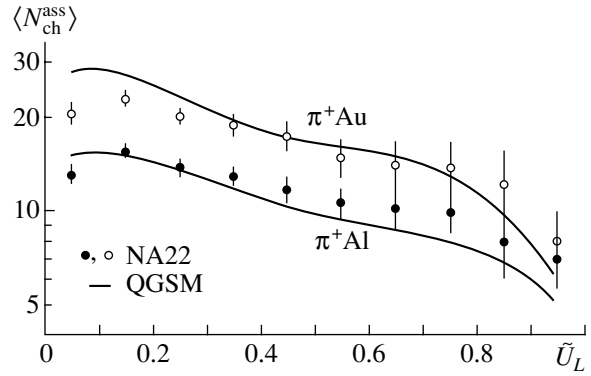

Fig. 7. The associated multiplicity of charged particles for reactions (1), (2) in comparison with the QGSM predictions.

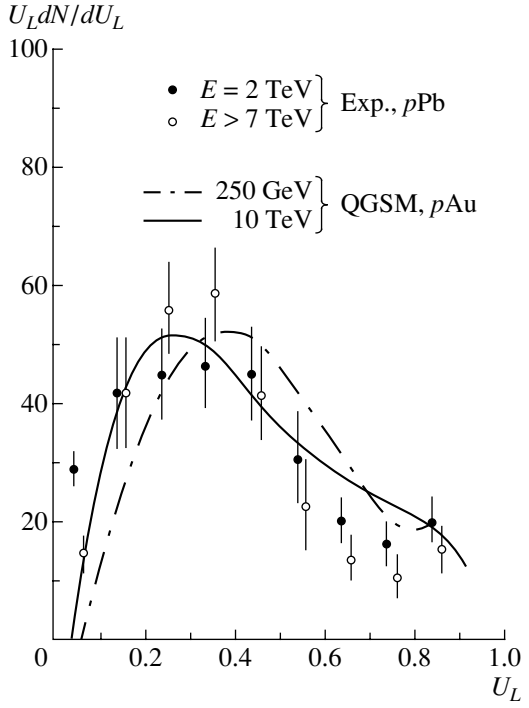

Fig. 8. Cosmic-ray data on the leading-particle spectrum from [17] in comparison with the QGSM predictions.

10 TeV. There are no clear contradictions between the experimental data and the QGSM predictions.

To estimate the model energy dependence of the leading-particle spectrum, we calculated the average value of U_L in frames of the QGSM for two variants of the hadron fomation time: "yo-yo" and "constituent" for 250 GeV and 10 TeV (see Table 4). U_L decreases about 10% over the energy range from 250 GeV to 10 TeV, if we select the "yo-yo" hadron formation time. For the "constituent" hadron formation time, the energy dependence is practically absent. As was shown in Fig. 5 for the "yo-yo" formation time (main variant of calculation), the QGSM describes the yield of leading particles in pAu collisions at energy 250 GeV, but for "constituent" formation time, the QGSM gives a smaller value of U_L at 250 GeV/c than the "yo-yo" variant. One can conclude that experimental data over an energy range from 250 GeV to 10 TeV in pAu(Pb) reactions is in a reasonable agreement with the QGSM "yo-yo" variant prediction.

8. SUMMARY AND CONCLUSIONS

An analysis of inclusive charged-particle spectra is presented for π^+-, K^+-meson, and proton interactions with Al and Au targets at 250 GeV/c. The experimental data were compared with predictions of the QGSM. The following conclusions could be drawn from this analysis.

(i) In agreement with earlier experimental data, the A dependence of the invariant inclusive charged-particle spectra on the Feynman variable x is very weak in interactions with Al and Au targets.

(ii) A small difference may be present in the A dependence of fast-particle inclusive spectra for meson- and proton-induced reactions, as can be expected from the fact that a larger inelastic cross section for protons implies a larger number of intranuclear collisions.

(iii) The coherent interactions do not influence the $\alpha(x)$ parameter of the A dependence of the invariant inclusive spectra.

(iv) The QGSM shows a larger difference between fast-particle spectra on Al and Au targets and for meson and proton projectiles than is observed in the experiment.

(v) The QGSM prediction for the leading-particle spectrum over an energy range from 250 GeV to 10 TeV in pAu(Pb) reactions is in reasonable agreement with the results of NA22 data and with a cosmic-ray experiment [17].

(vi) The associated charged-particle multiplicities are reproduced by QGSM with some underestimation for Al at large $\tilde{U}_L$ and some overestimation for Au at low $\tilde{U}_L$ values.

ACKNOWLEDGMENTS

We are grateful to the III Physikalisches Institut B, RWTH Aachen, Germany; the DESY-Institut für Hochenergiephysik, Berlin-Zeuthen, Germany; the Institute for High Energy Physics, Protvino, Russia; the Department of High Energy Physics, Helsinki University, Finland; and the University of Warsaw and Institute of Nuclear Problems, Poland, for early contributions to this experiment.

This work is part of the research program of the "Stichting voor Fundamenteel Onderzoek der

Materie" (FOM), which is financially supported by the "Nederlandse Organisatie voor Wetenschappelijk Onderzoek" (NWO). We further thank the NWO for support of this project within the program for subsistence to the former Soviet Union (07-13-038).

REFERENCES

1. NA22 Collab. (N. M. Agababyan *et al.*), Z. Phys. C **70**, 233 (1996).
2. NA22 Collab. (M. Adamus *et al.*), Z. Phys. C **32**, 475 (1986).
3. NA22 Collab. (I. V. Ajinenko *et al.*), Z. Phys. C **42**, 377 (1989).
4. NA22 Collab. (I. V. Ajinenko *et al.*), Z. Phys. C **46**, 569 (1990).
5. NA22 Collab. (N. M. Agababyan *et al.*), Z. Phys. C **50**, 361 (1991).
6. NA22 Collab. (N. M. Agababyan *et al.*), Z. Phys. C **72**, 65 (1996).
7. A. B. Kaidalov, in *Proceedings of the X ITEP Physics School, Moscow, 1983,* Issue 2, p. 3; Yad. Fiz. **45**, 1452 (1987) [Sov. J. Nucl. Phys. **45**, 902 (1987)].
8. A. Capella *et al.*, Z. Phys. C **3**, 389 (1980); in *Proceedings of the Europhysics Conference, Erice, Italy, 1981,* p. 1999.
9. N. S. Amelin, L. V. Bravina, and L. N. Smirnova, Yad. Fiz. **52**, 567 (1990) [Sov. J. Nucl. Phys. **52**, 362 (1990)].
10. NA22 Collab. (V. V. Aivazyan *et al.*), Z. Phys. C **51**, 167 (1991); NA22 Collab. (N. M. Agababyan *et al.*), Z. Phys. C **64**, 381 (1994).
11. NA22 Collab. (I. V. Ajinenko *et al.*), Z. Phys. C **58**, 357 (1993).
12. N. S. Amelin, K. K. Gudima, S. Yu. Sivoklokov, and V. D. Toneev, Yad. Fiz. **52**, 272 (1990) [Sov. J. Nucl. Phys. **52**, 172 (1990)].
13. Sh. M. Yandarbiev, F. K. Rizatdinova, L. G. Sveshnikova, *et al.*, Yad. Fiz. **56** (10), 153 (1993) [Phys. At. Nucl. **56**, 1389 (1993)].
14. D. S. Barton *et al.*, Phys. Rev. D **27**, 2580 (1983).
15. A. S. Carroll *et al.*, Phys. Lett. B **80B**, 319 (1979).
16. NA22 Collab. (N. M. Agababyan *et al.*), Z. Phys. C **56**, 371 (1992).
17. S. I. Nikolskiy *et al.*, in *Proceedings of the 17th International Cosmic Ray Conference, ICRC, Paris, 1981,* Vol. 5, p. 94.

Physics of Atomic Nuclei, Vol. 66, No. 1, 2003, pp. 123–129. From Yadernaya Fizika, Vol. 66, No. 1, 2003, pp. 125–132.

ELEMENTARY PARTICLES AND FIELDS
Experiment

Study of Single Muons with the Large Volume Detector at the Gran Sasso Laboratory*

M. Aglietta[1], E. D. Alyea[2], P. Antonioli[3], G. Badino[1], G. Bari[3], M. Basile[3], V. S. Berezinsky[4], F. Bersani[3], M. Bertaina[5], R. Bertoni[1], G. Bruni[3], G. Cara Romeo[3], C. Castagnoli[1], A. Castellina[1], A. Chiavassa[1], J. A. Chinellato[6], L. Cifarelli[a),3)], F. Cindolo[3], A. Contin[3], V. L. Dadykin[4], L. G. Dos Santos[6], R. I. Enikeev[4], W. Fulgione[1], P. Galeotti[1], P. Ghia[1], P. Giusti[3], F. Gomez[1], R. Granella[1], F. Grianti[3], V. I. Gurentsov[4], G. Iacobucci[3], N. Inoue[7], E. Kemp[6], F. F. Khalchukov[4], E. V. Korolkova[,4)], P. V. Korchaguin[4], V. B. Korchaguin[4], V. A. Kudryavtsev[b),4)], M. Luvisetto[3], A. S. Malguin[4], T. Massam[3], N. Mengotti Silva[6], C. Morello[1], R. Nania[3], G. Navarra[1], L. Periale[1], A. Pesci[3], P. Picchi[1], I. A. Pless[5], O. G. Ryazhskaya[4], O. Saavedra[1], K. Saitoh[8], G. Sartorelli[3], M. Selvi[3], N. Taborgna[9], V. P. Talochkin[4], G. C. Trinchero[1], S. Tsuji[10], A. Turtelli[6], P. Vallania[1], S. Vernetto[1], C. Vigorito[1], L. Votano[11], T. Wada[10], R. Weinstein[12], M. Widgoff[13], V. F. Yakushev[4], I. Yamamoto[10], G. T. Zatsepin[4], and A. Zichichi[3]**

The LVD Collaboration

Received December 18, 2001

Abstract—The present study is based on the sample of 2.9×10^6 single muons observed by the Large Volume Detector (LVD) at the underground Gran Sasso Laboratory during 36 500 live hours from June 1992 to February 1998. We have measured the muon intensity at slant depths from 3 to 20 km w.e. Most events are high-energy downward muons produced by meson decay in the atmosphere. The analysis of these muons has revealed the power index γ of the π and K spectrum: $\gamma = 2.76 \pm 0.05$. The remainders are horizontal muons produced by the neutrino interactions in the rock surrounding the LVD. The value of this flux near 90° is $(6.1 \pm 2.7) \times 10^{-13}$ cm^{-2} s^{-1} sr^{-1}. The results are compared with the Monte Carlo simulations and the world data. © *2003 MAIK "Nauka/Interperiodica".*

1. INTRODUCTION

The study of atmospheric muons at large underground depths is the subject of experimental investigations because of the following reasons. First, muons and muon-produced secondary particles are the background for underground detectors designed to search for rare events, including the tasks of neutrino and gamma-ray astronomy. Second, the calculations of atmospheric muon and neutrino fluxes are based on a hypothesis about the primary cosmic-ray spectrum and hadron–hadron interactions. The existing deep underground detectors are not able to measure muon energy for the direct deduction of energy spectrum. But they are able to measure the muon "depth–intensity" curve. This curve shows the vertical–muon flux as a function of the rock (water, ice) depth and is related to the muon propagation through the rock, the muon energy spectrum at sea level, and then, to the primary cosmic-ray spectrum.

*This article was submitted by the authors in English.
[1)]University of Torino and INFN (Torino); Institute of Cosmo-Geophysics, CNR, Italy.
[2)]Indiana University, Bloomington, USA.
[3)]University of Bologna and INFN (Bologna), Italy.
[4)]Institute for Nuclear Research, Russian Academy of Sciences, Moscow.
[5)]Massachusetts Institute of Technology, Cambridge, USA.
[6)]University of Campinas, Campinas, Brazil.
[7)]Saitama University of Science, Japan.
[8)]Ashikaga Institute of Technology, Japan.
[9)]INFN–LNGS, Assergi, Italy.
[10)]Okayama University, Japan.
[11)]INFN–LNF, Frascati, Italy.
[12)]University of Houston, USA.
[13)]Brown University, Providence, USA.
[a)]Now at the University of Salerno and INFN (Salerno), Italy.
[b)]Now at the University of Sheffield, UK.
[**]e-mail: korolkova@sheffield.ac.uk

The connection to the muon propagation allows the tests of the cross sections of the muon interactions with the rock which have been used in the program for the muon transport.

The measurements of muon intensity are made using the single detector and technique from a relatively small depth to a large depth, where neutrino-induced muons dominate and are of special interest. Such an experiment observes muons at zenith angles from the vertical to the horizontal direction. The statistics for the measurement of neutrino-induced flux in the horizontal direction are small enough, but the uncertainties in detecting the muon direction are absent. There is no need to suppress the flux of atmospheric muons by a factor of about 10^6 using accurate time measurements.

The Large Volume Detector (LVD) structure and the complicated profile of the Gran Sasso mountains provide an opportunity to measure the muon depth–intensity curve for slant depths from 3 to 20 km w.e. and the neutrino-induced muon flux in the horizontal direction, where the atmospheric muon flux is suppressed due to the large slant depth. The expected number of horizontal events caused by neutrino-induced muons is small (about one—two events per one LVD tower per year), therefore we cannot at the moment make any conclusions about neutrino oscillations.

In our previous paper [1] we have presented our first results on the measurement of the muon depth–intensity curve for the depth range of 3–20 km w.e. Since that time we have improved the criteria for event selection and increased the statistics. The analysis of [2] was based on the events with all multiplicities. Multiple muon events, especially for large depths, are more difficult to reconstruct than single muons. To avoid this problem, we have also performed the analysis of single muons using stronger criteria for the run and event selection. This analysis is based on increased statistics, compared with our previous publications.

In Section 2, the detector and the procedure of data analysis and conversion of the muon intensity to the vertical are briefly described. In Section 3, the results of the analysis of the depth–vertical muon intensity relation ($I_\mu(x)$) are shown. In Section 4 we present the analysis of neutrino-induced events. Section 5 contains our conclusions.

2. DETECTOR AND DATA SELECTION

The LVD has been extensively described elsewhere [1, 3, 4]. The detector is located at the Gran Sasso Laboratory, Italy. The minimal rock overburden is 3 km w.e. The LVD consists of three towers. Each tower is made of 38 modules with dimensions of $2.1 \times 6.2 \times 1.0$ m^3. Data were obtained using the first LVD tower from June 1992, when it was put into operation, until February 1998. The total live time was 36 500 h. The tower is $13 \times 6.6 \times 12$ m^3. Each module contains eight scintillator counters with the active volume of $1.0 \times 1.5 \times 1.0$ m^3 and the mass of liquid scintillator of 1.2 tons, and a tracking detector is attached to the bottom and one vertical side of the supporting structure. Each tracking detector is made up of four layers of tubes operating in limited streamer mode. Each layer has independent x and y readout strips. These established the x and y coordinates of the hits. The tracking system allows the measurements of particle direction to be taken with an accuracy better than 0.5°.

The mountain structure above the Gran Sasso Laboratory allows the measurements of muons which traversed a slant depth from 3 to more than 12 km w.e. The depths correspond to the median muon energies at sea level from 1.5 to 40 TeV at zenith angles from 0° to 90°. In this analysis we have used the sample of events containing only single muons. Events with all multiplicities are usually studied in the experiments with cosmic-ray muons. Such an analysis supposes the accurate reconstruction of each event. The study of depth–intensity curve with all muon events observed by the LVD has been presented in [2]. The multiple muons have been considered as independent muons and the acceptance both single and multiple muons has been assumed the same. This is a good and well-proven approximation for the derivation of the all-particle primary spectrum. The task requires, however, the reconstruction of muon events with all multiplicities and the measurements of the direction and slant depths with good accuracy. This is a more difficult task for multiple muon events than for single ones. Most muons traverse small rock thicknesses. If the slant depth for a small fraction of these events is incorrectly defined, then the intensity in this direction will not change much. However, these erroneously reconstructed events can significantly contribute to the muon intensity at large depths. To be sure of the precise event reconstruction, in this analysis we have dealt with single muons only. The size of one LVD tower is small enough, and more than 90% of muon events are single muons. The number of muons in bundles is about 10–12% of the total number of muons. Possible uncertainties from neglecting multiple muons are less than or comparable to the errors from including multiple-muon events with erroneous reconstruction. In the case of single-muon analysis we need to correct the absolute intensity for the number of unreconstructed events (multiple muons and muon-induced cascades).

The trigger for muon events has been defined as follows: (i) the energy deposition is greater than

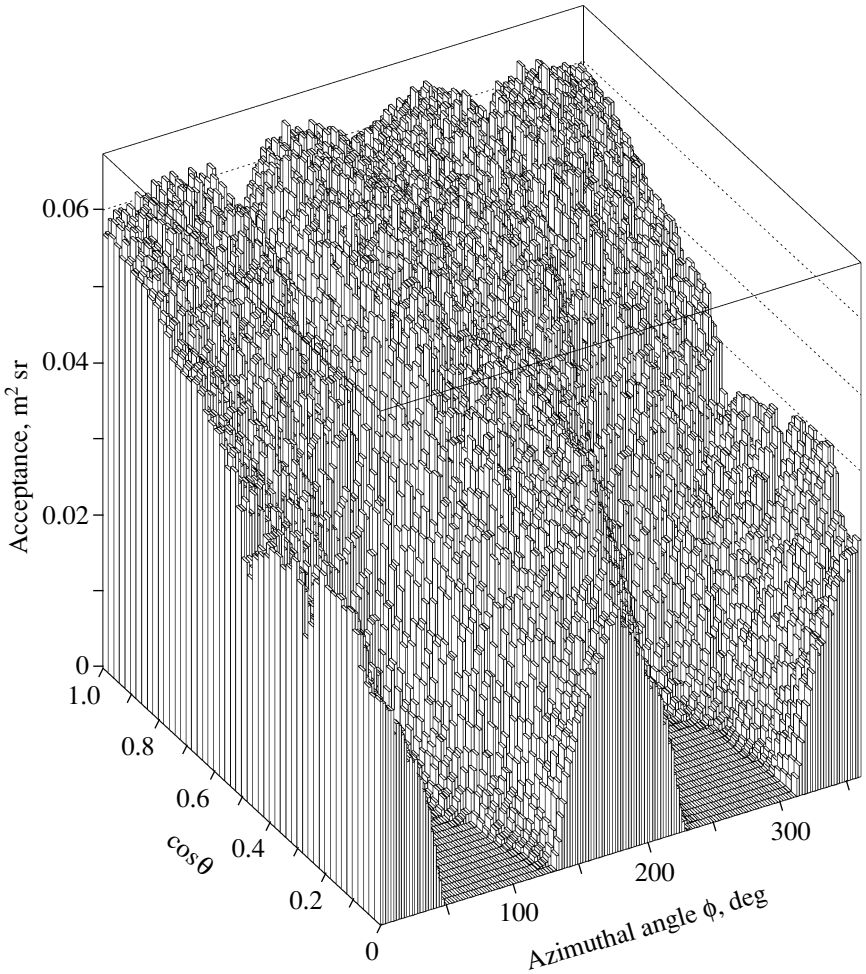

Fig. 1. The LVD acceptance for single muons as a function of the cosine of the zenith angle θ and azimuthal angle ϕ. The angular cell for this plot was chosen as 0.02 ($\cos\theta$) $\times$ 2° (ϕ).

30 MeV in at least two scintillator counters in two different modules and (ii) hits in at least three layers in any three tracking detectors (hits in at least one layer per detector). The data runs have been selected as follows: runs have been accepted if they lasted longer than an hour and the counting rate is within a 15% range around the mean value for the set of runs. Moreover, we have required at least 36 of 38 tracking modules and 240 of 304 scintillator counters of the first tower to be operated during any particular run. These criteria ensured the full and uniform acceptance of the detector. The final muon sample after these cuts consisted of 3 151 580 events. 2 877 659 (91%) events have been reconstructed as single muons. Multiple muons and muons accompanied by cascades constituted 9%. All reconstructed single muons were binned in a two-dimensional array with a cell size of 1° at azimuthal angle ϕ and 0.01 at $\cos\theta$, where θ is the zenith angle. The accuracy of the reconstruction has been checked by observation of the Moon shadowing effect with single-muon data [5]. It is better than 0.65°.

The acceptance for each angular bin has been calculated using the simulation of muons traversing the LVD, taking into account the detector response. The thickness of the rock crossed by the muon was determined from the mountain map.

The angular distribution $N_\mu(\phi, \cos\theta)$ obtained in the experiment has been converted to the depth–intensity relation using the formula

$$I_\mu(x_m) = \frac{\sum_{ij} N_\mu(x_m(\phi_j, \cos\theta_i))}{\sum_{ij}(S(x_m(\phi_j, \cos\theta_i))\epsilon(x_m(\phi_j, \cos\theta_i))\Omega_{ij}T)}, \quad (1)$$

where the summing up has been done over all angular bins $(\phi_j, \cos\theta_i)$ contributing to the depth x_m, $S(x_m(\phi_j, \cos\theta_i))$ is the cross section of the detector in the plane perpendicular to the muon track at the angle $(\phi_j, \cos\theta_i)$, $\epsilon(x_m(\phi_j, \cos\theta_i))$ is the efficiency of

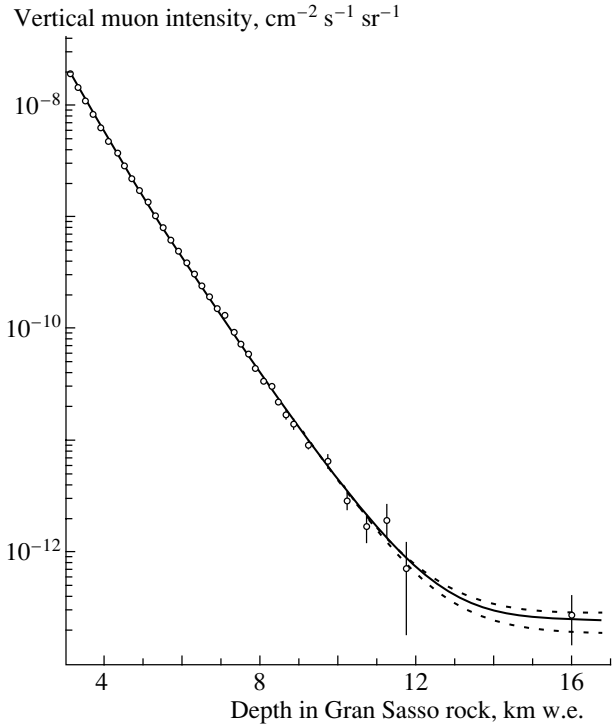

Fig. 2. Depth–vertical muon intensity relation in Gran Sasso rock. The LVD data are presented together with the best fit (solid curve). Dashed curves show the calculated intensities for the maximal and minimal contributions from neutrino-induced muons (see text for details).

muon detection and reconstruction, Ω_{ij} is the solid angle for the angular bin, and T is the live time. Angular bins with ϵ less than 0.03 were excluded from the analysis. The acceptance A is defined as

$$A(\cos\theta,\phi) = \epsilon(\cos\theta,\phi)\Omega(\cos\theta,\phi)S(\cos\theta,\phi) \quad (2)$$

and is shown in Fig. 1.

The intensity of muons at zenith angle θ was assumed to be related to the vertical intensity I_0 through the relation

$$I(x_m,\theta) = I_0(x_m,\theta=0^\circ)/\cos\theta_i^*, \quad (3)$$

where

$$\cos\theta_i^* = \frac{I_\mu^c(x_m,\cos\theta=1)}{I_\mu^c(x_m,\cos\theta_i)} \quad (4)$$

is the ratio of the calculated muon intensity at $\cos\theta = 1$ to that at $\cos\theta_i$. This relation is valid for muons of atmospheric origin if we neglect the contribution of the prompt muons from charmed particles. According to the LVD data, the ratio of prompt muons to pions does not exceed 2×10^{-3} at a 95% confidence level [6].

For the depth–intensity relation, the bin width of 200 m w.e. has been chosen. For a depth more than 9 km w.e., we have chosen bins with the width of 500 km w.e. to increase the statistics for each bin. The conversion of muon intensity to the middle points of each depth bin has been done using formula

$$I_\mu^m(x_i) = I_\mu^m(x_m)\frac{I_\mu^c(x_i)}{I_\mu^c(x_m)}, \quad (5)$$

where $I_\mu^m(x_m)$ and $I_\mu^c(x_m)$ are the measured and calculated muon intensities at the weighted average depth x_m, which corresponds to the depth bin with the middle value of x_i; and $I_\mu^m(x_i)$ and $I_\mu^c(x_i)$ are the derived and calculated muon intensities at the depth x_i, which is the middle point of the depth bin. The values of x_m have been obtained by averaging the depths for all angular bins contributing to the given depth bin with a weight equal to the detected number of muons. To calculate the muon intensities at x_m and x_i, we have used the muon spectrum at sea level with previously estimated parameters [1, 2] (see also Eq. (7)) and the simulated muon survival probabilities. Since the width of depth bins is quite small (200 m w.e. for depth bins with high statistics) and the number of angular bins contributing to each depth bin is quite large (several hundreds), the conversion factor does not exceed 10%.

3. DEPTH–VERTICAL INTENSITY RELATION IN GRAN SASSO ROCK

To calculate the intensity of muons underground requires the intensity of muons at the surface as a function of energy and zenith angle, and the survival probability as a function of slant depth of rock traversed:

$$I_\mu(x,\cos\theta) = \int_0^\infty P(E_{\mu0},x)\,\frac{dI_{\mu0}(E_{\mu0},\cos\theta)}{dE_{\mu0}}\,dE_{\mu0}, \quad (6)$$

where $P(E_{\mu0},x)$ is the probability of a muon with an initial energy $E_{\mu0}$ at sea level to reach the depth x and $dI_{\mu0}(E_{\mu0},\cos\theta)/dE_{\mu0}$ is the muon spectrum at sea level at zenith angle θ. The intensity at the surface in the units of (cm^2 s sr GeV)$^{-1}$ can be approximated by [7]

$$\frac{dI_{\mu0}(E_{\mu0},\cos\theta)}{dE_{\mu0}} = A\cdot0.14\cdot E_{\mu0}^{-\gamma} \times\left(1\Big/\left(1+\frac{1.1E_{\mu0}\cos\theta^*}{115\ \text{GeV}}\right)\right. + 0.054\Big/\left.\left(1+\frac{1.1E_{\mu0}\cos\theta^*}{850\ \text{GeV}}\right)\right), \quad (7)$$

where the values of $\cos\theta$ have been substituted by $\cos\theta^*$, which have been taken from [8]. According to [8], $\cos\theta^* = E_{\pi,K}^{\rm cr}(\cos\theta=1)/E_{\pi,K}^{\rm cr}(\cos\theta)$,

Table 1. The value of power index of meson spectrum for various depth ranges (the errors are statistical only)

Depth interval, km w.e.	γ	χ^2/d.o.f.
3–12	2.76 ± 0.02	25.8/34
4–12	2.78 ± 0.03	19.0/29
5–12	2.79 ± 0.04	16.8/24
6–12	2.82 ± 0.06	14.8/19
7–12	2.94 ± 0.14	11.4/14
8–12	2.76 ± 0.22	6.7/9
9–12	2.60 ± 0.50	3.3/4

where $E^{\rm cr}_{\pi,K}$ are the critical energies of pions and kaons. Equation (7) has been obtained under a simple assumption of scaling in the high-energy hadron–nucleus interactions. Under this assumption, the power index of the primary spectrum, γ, is expected to be equal to that of the meson (pion + kaon) spectrum, $\gamma_{\pi,K}$.

The muons were tracked through the rock using the propagation code MUSIC [9] to calculate the muon survival probabilities $P(E_{\mu 0}, x)$. The randomness of all processes of muon interaction with matter (nuclear interaction, pair production, bremsstrahlung, and ionization) has been taken into account. The cross sections were taken from [10–12]. The muon intensities calculated with a bremsstrahlung cross section from [12] are lower than those with a bremsstrahlung cross section from [13], which was used in our previous paper [1]. Using the cross section from [13] will result in a higher power index (softer muon spectrum) compared to the cross section from [12]. The difference in power index is of the order of 0.01.

The measured depth–intensity curve is shown in Fig. 2 together with the best fit. The underground muon flux observed at a slant depth x and zenith angle θ has a two-component nature and can be presented as:

$$I_\mu(x,\theta) = I^{(\mu)}_\mu(x,\theta) + I^{(\nu)}_\mu(\theta), \qquad (8)$$

where $I^{(\mu)}_\mu(x,\theta)$ is the contribution of atmospheric muons and $I^{(\nu)}_\mu(\theta)$ denotes the contribution of muons from neutrino interactions in the rock surrounding the detector. For slant depths of 13–20 km w.e. the muons seen in the LVD are of later origin. The last experimental point in Fig. 2 corresponds to the neutrino-induced muon flux. This flux was measured at the depth of 13–20 km w.e. To convert the flux of neutrino-induced muons to vertical intensity, we used the calculated ratio of horizontal and vertical fluxes of neutrino-induced muons, which is equal to 2.1 at an energy threshold of 1 GeV for most models of atmospheric neutrino production:

$$I^\nu_\mu(x, \theta = 0^\circ) = I^\nu_\mu(x, \theta = 90^\circ)/2.1. \qquad (9)$$

Table 2. The number of muons at large depths h observed by LVD ($N_{\rm obs}$) and the calculated values ($N^{\rm atm}_\mu$ are atmospheric muons, N^ν_μ are neutrino-induced muons, and $N^{\rm tot}_\mu = N^{\rm atm}_\mu + N^\nu_\mu$)

h, km w.e.	$N^{\rm atm}_\mu$	N^ν_μ	$N^{\rm tot}_\mu$	$N_{\rm obs}$
$h > 13$	0.45	3.75	4.20	5
$h > 14$	0.31	2.92	3.23	4
$h > 15$	0.03	1.50	1.53	2

The depth–intensity curve has been fitted to the calculated function with two free parameters: the additional normalization constant, A, and the power index of the atmospheric pion and kaon spectrum, γ. As a result of the fitting procedure, the following values of the free parameters have been obtained: $A = 1.59 \pm 0.50$ and $\gamma = 2.76 \pm 0.05$ for muon energies at sea level from 1.5 to 40 TeV. The errors of the parameters include both statistical and systematic uncertainties. The latter takes into account possible uncertainties in the depth, rock composition, and density and the uncertainty in the cross sections used to simulate muon transport through the rock. These values are in good agreement with the results of a similar analysis performed for the muon events with all multiplicities observed by the first LVD tower during 21 804 h of live time: $A = 1.95 \pm 0.50$ and $\gamma = 2.78 \pm 0.05$. Note that the estimates of the parameters A and γ are strongly correlated. The larger the value of γ is, the larger the normalization factor A should be.

We have repeated the fitting procedure for restricted depth ranges. The results of this test are presented in Table 1. The results show that the power index is the same within errors for all depth ranges.

Neutrino-induced muon flux has not been included in the fit procedure but has been added to the best fit at the 2.5×10^{-13} cm^{-2} s^{-1} sr^{-1} level. Dashed curves in Fig. 2 show the possible values of the muon intensities if we take into account the uncertainties in the calculation of atmospheric neutrino spectrum at sea level and structure functions and the corrections for quasielastic scattering, and the energy threshold of the detector. The experimental value $(2.9 \pm 1.3) \times 10^{-13}$ cm^{-2} s^{-1} sr^{-1} is in agreement with the calculated one $(2.5 \pm 0.5) \times 10^{-13}$ cm^{-2} s^{-1} sr^{-1}. It also agrees with the compiled world results on underground muon intensities presented by Crouch

in [14], where the flux of neutrino-induced muons is equal to $(2.17 \pm 0.21) \times 10^{-13}$ cm^{-2} s^{-1} sr^{-1}.

If the formula from [15] is used for the muon spectrum at sea level instead of Eq. (7), the best-fit value of γ will be decreased by 0.04–0.05.

The value of γ obtained with the LVD data is in reasonable agreement with the results of other surface and underground experiments: DEIS [16], MUTRON [17], MIPhI [18] (the energies of these experiments correspond to first few points of our depth–intensity curve), ASD [19], NUSEX [20], MACRO [21], and MSU [22] (if we consider the muon spectrum from [15] in the latter case). The LVD data disagree with the results of the Baksan Scintillator Telescope and the KGF [23, 24]. The difference here is likely due to the different measurement methods, the applied analysis procedure in each experiment, and uncertainties in the knowledge of overburden composition.

4. NEUTRINO-INDUCED MUONS

Let us describe the evaluation of the horizontal neutrino-induced muon flux in more details. High-energy neutrinos will produce high-energy muons in the rock. These muons will have enough energy to traverse the entire detector. The reconstructed muons that traversed rock thickness greater than 12 km w.e. have been considered as candidates for neutrino-induced muons. These depths correspond to zenith angles of more than 85°. We have recorded 95 such candidates during 36 500 h of the LVD lifetime. A careful visual scan of all of these tracks eliminated five candidates from the sample because of confusion in the pattern recognition.

Since the timing of the LVD experiment (12.5 ns) is not sufficient to determine the direction of a track crossing one tower, there is a twofold ambiguity in the direction for each measured track. In other words, the LVD cannot discriminate between muon direction (θ, ϕ) and $(180^\circ - \theta, 180^\circ + \phi)$. For $\theta < 90^\circ$, it is reasonable to assume that muons come from above, since the rock thickness is smaller above the horizon. Gran Sasso mountain has a very complicated profile, and for many bins at $\theta \approx 90^\circ$ with $x > 12$ km w.e. the slant depth for inverse direction x_1 appears to be less than 8 km w.e. The muon intensity for 8 km w.e. is 80 times greater than the intensity for 12 km w.e. In this case we assume that the muon came from the direction with the smaller slant depth. Near-horizontal muons with reconstructed slant depths greater than 12 km w.e. and slant depth less than 8 km w.e. in the opposite direction were excluded as neutrino-induced candidates and considered as bins $(\theta, 180^\circ + \phi)$. Totally, we had 67 such events.

Some angular bins with slant depths greater than 12 km w.e. are surrounded by bins with smaller slant depths. According to the calculations of [9], the average angular deviation of muons is 0.45° at 10 km w.e. and it is mainly caused by multiple Coulomb scattering. The probability of muon coming from the direction with smaller slant depth is greater. We have considered such a muon as coming from the direction with smaller depth, assuming that it had been recorded into the bin with greater depth due to the reconstruction error or scattering.

Five muons produced in neutrino interactions with surrounding rock have survived all cuts for slant depths $x > 13$ km w.e.; for $x > 14$ km w.e., we have found four such events; and for $x > 15$ km w.e., there are two neutrino-induced muons.

A Monte Carlo has been used to estimate the expected number of neutrino-induced muons. The spectrum of neutrino-induced muons has been calculated following the formula

$$\frac{dN_\mu}{dE_\mu} = \int_{E_\mu}^{\infty} \frac{dN_\nu}{dE_\nu} \frac{P(E_\nu, E_\mu)}{dE_\mu} dE_\nu. \qquad (10)$$

dN_ν/dE_ν represents the neutrino spectrum and $P(E_\nu, E_\mu)/dE_\mu$ is the probability that a neutrino produces a muon in the interval $(E_\mu, E_\mu + dE_\mu)$. We have used the Bartol neutrino flux [25], which has a systematic uncertainty ±14%, and the Morfin and Tang [26], as well as Duke and Owens [27] parton distribution functions, which result in a less than 1% difference in muon spectra. The major sources of uncertainties in the neutrino-induced muon flux are the uncertainty in the neutrino fluxes and neutrino cross sections because of required extrapolations of the structure functions to small $x \ll 10^{-4}$. For neutrino-induced muons, the calculations of atmospheric neutrino flux by various authors differ by as much as 17%. Different standard parametrizations of charged current cross sections also differ by as much as 13% [28]).

Table 2 shows the number of muons observed by the LVD during 36 500 h, as well as calculated values (the uncertainty of calculations is 20%).

The observed number of muons at large slant depths agrees with the predictions within errors. The measured neutrino-induced horizontal muon flux is $(6.1 \pm 2.7) \times 10^{-13}$ cm^{-2} s^{-1} sr^{-1}, while the calculated one is $(5.2 \pm 1.1) \times 10^{-13}$ cm^{-2} s^{-1} sr^{-1}. Our measured value agrees with the results of other experiments: Soudan-2, $(5.00 \pm 0.55 \pm 0.51) \times 10^{-13}$ cm^{-2} s^{-1} sr^{-1} [29]; Frejus (the flux recalculated for our energy threshold), $(4.77 \pm 0.86) \times 10^{-13}$ cm^{-2} s^{-1} sr^{-1} [30]; and

in a South African mine, $(4.59 \pm 0.42) \times 10^{-13}$ cm^{-2} s^{-1} sr^{-1} [31].

5. CONCLUSIONS

We have measured the underground muon intensity as a function of the slant depth in the range of 3–20 km w.e. The analysis of depth–intensity relation in the depth range of 3–12 km w.e. has been done to obtain the power index of the differential energy spectrum of the pions and kaons in the atmosphere, $\gamma = 2.76 \pm 0.05$ in the energy range of 1–40 TeV. The errors include both statistical and systematic uncertainties with the systematic error due to the dominating uncertainty of the muon interaction cross sections. Our results are in good agreement with other experiments. Muons that traversed a slant depth more than 13 km w.e. were analyzed to obtain the horizontal flux of neutrino-induced muons. This flux is equal to $(6.1 \pm 2.7) \times 10^{-13}$ cm^{-2} s^{-1} sr^{-1} and is consistent with our calculations and the reported results of other experiments. Our fit of the depth–intensity curve to this data is in good agreement with the fit of Crouch, which is a summary of various experiments.

ACKNOWLEDGMENTS

The Collaboration wishes to thank the staff of the Gran Sasso Laboratory for assistance. This work is supported by the Russian Ministry of Industry, Science, and Technologies; the Italian Institute for Nuclear Physics; and the Russian Foundation for Basic Research (project no. 00-02-16112).

REFERENCES

1. LVD Collab. (M. Aglietta, B. Alpat, D. E. Alyea, *et al.*), Astropart. Phys. **3**, 311 (1995).
2. LVD Collab. (M. Aglietta, B. Alpat, D. E. Alyea, *et al.*), Phys. Rev. D **58**, 092005 (1998).
3. LVD Collab. (G. Bari, M. Basile, G. Bruni *et al.*), Nucl. Instrum. Methods Phys. Res. A **264**, 5 (1988).
4. LVD Collab. (G. Bari, M. Bazile, G. Bruni, *et al.*), Nucl. Instrum. Methods Phys. Res. A **277**, 11 (1989).
5. LVD Collab. (M. Aglietta *et al.*), in *Proceedings of the 26th International Cosmic Ray Conference, Salt Lake City, 1999,* Vol. 7, p. 218.
6. LVD Collab. (M. Aglietta, B. Alpat, D. E. Alyea, *et al.*), Phys. Rev. D **60**, 112001 (1999).
7. T. K. Gaisser, *Cosmic Rays and Particle Physics* (Cambridge Univ. Press, Cambridge, 1990.)
8. L. V. Volkova, Preprint No. 72, FIAN (Lebedev Institute of Physics, Academy of Sciences of USSR, Moscow, 1969).
9. P. Antonioli, C. Ghetti, E. V. Korolkova, *et al.*, Astropart. Phys. **7**, 357 (1997).
10. L. B. Bezrukov and E. V. Bugaev, in *Proceedings of the 17th International Cosmic Ray Conference, Paris, 1981,* Vol. 7, p. 90.
11. R. P. Kokoulin and A. A. Petrukhin, in *Proceedings of the 12th International Cosmic Ray Conference, Hobart, 1971,* Vol. 6, p. 2436.
12. S. R. Kelner, R. P. Kokoulin, and A. A. Petrukhin, Yad. Fiz. **60**, 657 (1997) [Phys. At. Nucl. **60**, 576 (1997)].
13. L. B. Bezrukov and E. V. Bugaev, in *Proceedings of the 17th International Cosmic Ray Conference, Paris, 1981,* Vol. 7, p. 102.
14. M. Crouch, in *Proceedings of the 20th International Cosmic Ray Conference, Moscow, 1987,* Vol. 6, p. 165.
15. L. V. Volkova, G. T. Zatsepin, and L. A. Kuzmichev, Yad. Fiz. **29**, 1252 (1979) [Sov. J. Nucl. Phys. **29**, 645 (1979)].
16. O. C. Allkofer, K. Carstensen, G. Bella, *et al.*, in *Proceedings of the 17th International Cosmic Ray Conference, Paris, 1981,* Vol. 10, p. 321.
17. S. Matsuno, F. Kajino, Y. Kawashima, *et al.*, Phys. Rev. D **29**, 1 (1984).
18. V. D. Ashitkov, T. M. Kirina, A. P. Klimakov, *et al.*, in *Proceedings of the 19th International Cosmic Ray Conference, La Jolla, 1985,* Vol. 8, p. 77.
19. F. F. Khalchukov, E. V. Korolkova, V. A. Kudryavtsev, *et al.*, in *Proceedings of the 19th International Cosmic Ray Conference, La Jolla, 1985,* Vol. 8, p. 12; R. I. Enikeev, G. T. Zatsepin, E. V. Korolkova, *et al.*, Yad. Fiz. **47**, 1044 (1988) [Sov. J. Nucl. Phys. **47**, 665 (1988)].
20. G. Battistoni, E. Belotti, C. Bloise, *et al.*, Nuovo Cimento C **9**, 196 (1986).
21. M. A. Ambrosio, R. Antolini, G. Auriemma, *et al.* (MACRO Collab.), Phys. Rev. D **52**, 3793 (1995).
22. N. P. Il'ina, N. N. Kalmykov, I. V. Rakobolskaya, and G. T. Zatsepin, in *Proceedings of the 24th International Cosmic Ray Conference, Rome, 1995,* Vol. 1, p. 524.
23. Yu. M. Andreyev, V. I. Gurentsov, and I. M. Kogai, in *Proceedings of the 20th International Cosmic Ray Conference, Moscow, 1987,* Vol. 6, p. 200.
24. M. R. Krishnaswami, M. G. K. Menon, N. K. Mondal, and V. S. Narasimham, in *Proceedings of the 18th International Cosmic Ray Conference, Bangalore, 1983,* Vol. 11, p. 450.
25. V. Agraval, T. K. Gaisser, P. Lipari, and T. Stanev, Phys. Rev. D **53**, 1314 (1996).
26. J. G. Morfin and W. K. Tang, Z. Phys. C **52**, 13 (1991).
27. D. W. Duke and J. F. Owens, Phys. Rev. D **30**, 49 (1984).
28. T. Gaisser, F. Halzen, and T. Stanev, Phys. Rep. **258**, 173 (1995).
29. D. Demuth and M. Goodman, in *Proceedings of the 27th International Cosmic Ray Conference, Hamburg, 2001,* Vol. 3, p. 1090.
30. W. Rhode, K. Daum, P. Bareyre, *et al.*, Astropart. Phys. **4**, 217 (1996).
31. M. F. Crouch, P. B. Landesker, J. F. Lathrop, *et al.*, Phys. Rev. D **18**, 2239 (1978).

Physics of Atomic Nuclei, Vol. 66, No. 1, 2003, pp. 130–134. Translated from Yadernaya Fizika, Vol. 66, No. 1, 2003, pp. 133–137.

ELEMENTARY PARTICLES AND FIELDS
Experiment

Measurement of Energy of Medium-Mass and Heavy Cosmic-Ray Nuclei by a Specific Energy Deposition at the Maximum of Hadron Showers in Dense Matter

I. D. Rapoport, A. N. Turundaevsky*, and V. Ya. Shestoperov

Institute of Nuclear Physics, Moscow State University, Vorob'evy gory, Moscow, 119899 Russia

Received October 10, 2001

Abstract—The possibility of measuring the energy of cosmic-ray nuclei (for energies higher than 1 TeV) by means of recording the greatest specific energy deposition in hadron showers generated in dense matter is investigated. This method makes it possible to improve the accuracy of energy measurements by thin calorimeters in studying high-energy cosmic rays at high altitudes. Attainable accuracies in measuring energy are considered for the cases of light and heavy nuclei. The results of a relevant simulation are compared with data from the Kosmos-1713 satellite-borne experiment. © *2003 MAIK "Nauka/Interperiodica"*.

The ionization-calorimeter method [1] became a traditional means for measuring the energy of high-energy particles. Along with the use of a considerable thickness of absorbers (whose mass may restrict the potential of relevant experiments at high altitudes), thin ionization calorimeters are also applied, which incompletely record hadron showers initiated by a primary particle [2]. With increasing energy, the corresponding cascade depth also increases [3]. As a method appropriate for reconstructing the primary-particle energy in this case, it was proposed to measure a specific energy deposition at the cascade maximum $K_m = (dE/dX)_{\max}$. A high potential of the new approach was demonstrated by a mathematical simulation of hadronic showers initiated by protons and helium nuclei in iron and lead absorbers [4]. The simulation was performed with the aid of the GEANT package [5], including the GHEISHA [5, 6], FLUKA [5, 7, 8], and QGSM [9, 10] generators of inelastic hadron interactions.

In order to extend the scale of charge of the nuclear component of high-energy cosmic rays, a mathematical simulation of hadron showers initiated by carbon and iron nuclei in the iron absorber is performed here with the aim of investigating the specific energy deposition at the cascade maximum. The simulation of showers from heavy nuclei has some special features. The large part of the energy carried away by spectator nucleons in nucleus–nucleus interaction leads to a strong dependence of the shape of the cascade curve on the fragmentation of the residual nucleus. The decay of such a nucleus into individual nucleons leads to the smoothing of the cascade curve. Reinteractions of heavy fragments may give rise to additional maxima. This is why the simulation of hadron interactions was based here on the QGSJET code [11] taking into account, along with fragmentation, the production of hadronic jets, which are peculiar to the region of ultrahigh energies.

Thereupon, in analyzing simulated cascade curves and in determining the maximum specific energy deposition, we traced the segment of 17 shower lengths after the first inelastic interaction. The resulting average values $\langle K_m \rangle$ in an iron absorber are shown in Fig. 1 versus the energy of (*a*) C and (*b*) Fe nuclei. Also presented there for the sake of comparison are data from the Kosmos-1713 satellite-borne experiment with Sokol-2 equipment [12, 13], which were analyzed with allowance for transition effects [14] caused by the structure of the absorber used in this experiment. As can be seen, the results of the calculations are close to these experimental data. For Fe nuclei, the calculated value of $\langle K_m \rangle$ is somewhat in excess (by 15–20%) of the experimental result. This may be due to the presence of a thin aluminum layer (3 cm) above the iron absorber in the experimental facility, because the number of nucleons from the incident nucleus that participate in the interaction with aluminum is less than that in the interaction with iron, so that the inelasticity factor becomes smaller. The dependence of $(dE/dX)_{\max}$ on the primary energy E for various incident particles could be approximated by a linear ($\langle K_m \rangle = CE + c$) or an exponential ($\langle K_m \rangle = AE^a$) function, with the parameters being set to the values given in Table 1 (the data for protons and helium nuclei were taken from [4]). The parameter values depend only slightly

*e-mail: ant@eas.npi.msu.ru

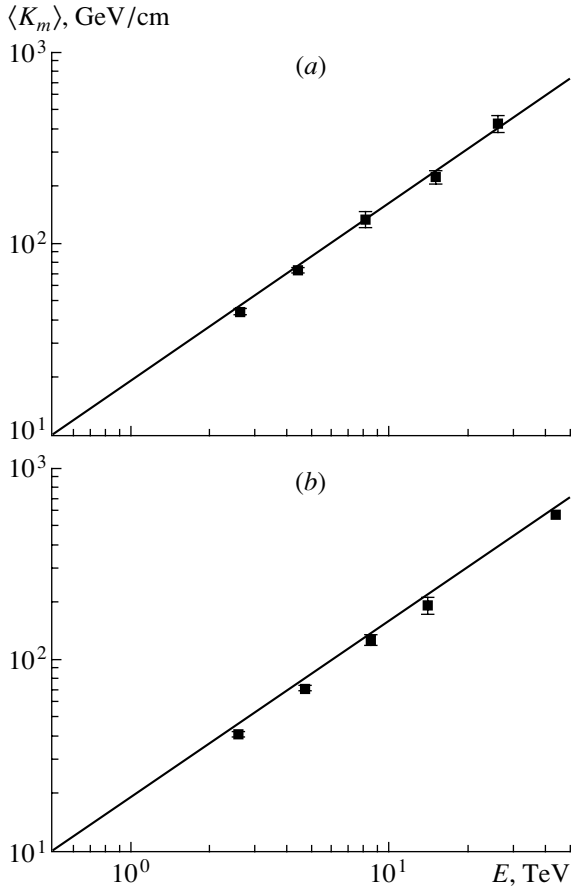

Fig. 1. Average specific energy deposition at the maximum of a hadron shower, $\langle K_m \rangle = \langle (dE/dX)_{\max} \rangle$, versus the energy of primary particles [(*a*) C and (*b*) Fe nuclei] in an iron absorber according to calculations on the basis of the QGSJET model. The experimental points were obtained from an analysis of the data presented in [12, 13].

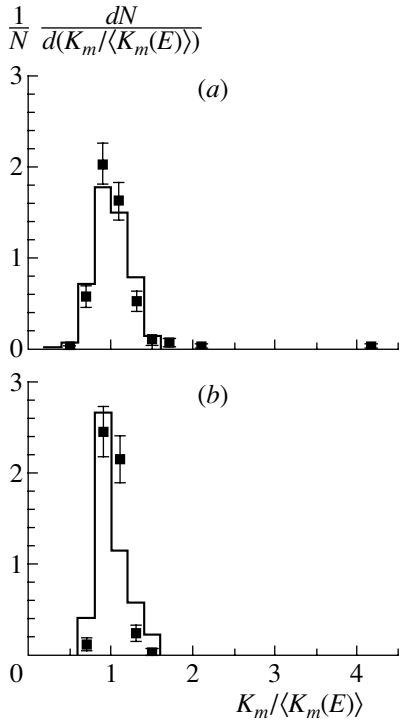

Fig. 2. Distribution of the energy deposition at the maximum of a shower, $(1/N)(dN/d(K_m/\langle K_m(E)\rangle))$, induced by (*a*) C and (*b*) Fe nuclei. The experimental points were obtained from an analysis of the data presented in [12, 13].

on the primary-particle type. The energy deposition at the cascade maximum is determined by the total energy of the primary nucleus. The parameter values derived for carbon and iron can be applied to the nuclei of the M and the VH group, respectively. These approximations can be used to determine the primary energy as $E = (K_m/A)^{1/a}$ or as $E = (K_m - c)/C$.

Table 2 presents the calculated values of the relative fluctuation $D(K_m) = \langle (K_m - \langle K_m \rangle)^2 \rangle^{1/2} / \langle K_m \rangle$. At energies in excess of about 2 TeV per nucleus, these values show only a weak dependence on energy. This makes it possible to compare the K_m distributions calculated at a fixed energy value with generalized experimental data for a relatively wide energy region. For the case of an iron absorber, Fig. 2 displays the $K_m/\langle K_m(E) \rangle$ distributions obtained for the nuclei of the (*a*) M and (*b*) VH groups by using the formula $\langle K_m(E) \rangle = AE^a$ to approximate, for energies of $E > 2.5$ TeV, the experimental data reported in [12, 13]. In this figure, the corresponding results of a simulation for (*a*) C and (*b*) Fe nuclei at an energy of 8 TeV are also given for the sake of comparison.

Figure 3 shows the energy spectra deduced for the nuclei of the (closed symbols) M group and (open symbols) VH group from the data of the Sokol-2 experiment by means of the traditional method—that is, by exploring the total energy deposition in an iron absorber of thickness 85 cm—and by means of the new method—that is, by using the specific energy deposition at the cascade maximum (the maximum was determined over a segment of 30 cm after the first interaction vertex). An analysis reveals that the two methods in question yield results that agree within the statistical errors of the experiment.

The potential of the new method and the potential of the traditional one can be assessed in relation to each other by comparing the root-mean-square deviations $D(E)$ in determining the energy E from the specific energy deposition K_m and from the total energy deposition E_b in an absorber. Such a comparison is illustrated in Fig. 4, which shows the quantities $D(E)$ versus the depth of evolution of the shower ($L = X - X_0$) initiated by 8-TeV (*a*) C and (*b*) Fe nuclei in an iron absorber. It can be seen

Table 1. Parameters in the approximation of the average energy deposition at the shower maximum, $K_m = (dE/dX)_{\max}$: $\langle K_m \rangle = AE^a$ or $\langle K_m \rangle = CE + c$ (E and K_m are given in TeV and GeV/cm, respectively, while A is the average energy deposition at $E = 1$ TeV)

Reaction	Model, experiment	A	a	C	c
pFe	FLUKA	22.9	0.941	19.4	2.7
	GHEISHA	20.9	0.961	18.9	1.5
	QGSM	23.6	0.938	19.9	2.8
	experiment	19.7	0.949	16.1	13.3
HeFe	QGSM + FLUKA	20.4	0.937	17.1	2.4
	experiment	18.7	0.948	13.5	22.7
CFe	QGSJET	19.5	0.931	15.6	5.0
	experiment	17.0	0.965	14.0	10.2
FeFe	QGSJET	19.6	0.919	14.9	6.9
	experiment	16.6	0.938	12.9	9.0

Table 2. Relative fluctuation of the energy deposition at the shower maximum, $D(K_m) = \langle (K_m - \langle K_m \rangle)^2 \rangle^{1/2} / \langle K_m \rangle$ (E is given in TeV)

Reaction	Model	$E = 0.5$	$E = 2$	$E = 8$	$E = 32$
pFe	FLUKA	0.37	0.36	0.38	0.38
	GHEISHA	0.41	0.40	0.40	0.39
	QGSM	0.38	0.38	0.39	0.38
HeFe	QGSM + FLUKA	0.30	0.30	0.30	0.29
CFe	QGSJET	0.26	0.20	0.20	0.18
FeFe	QGSJET	0.33	0.17	0.17	0.16

that the energy E is determined more precisely by using the quantity K_m at small shower depths (where the shower grows) and by using E_b at large depths. In the boundary region, the methodological errors become equal at $L = 42$ cm (23.9 shower lengths from the first-interaction vertex) for C nuclei. This depth corresponds to the relative error of $D(E) = 0.23$ in determining energy. For Fe nuclei, the respective values are $L = 37$ cm (21.0 shower lengths) and $D(E) = 0.20$. The boundary region corresponds to the depth of the cascade maximum and exhibits only a weak energy dependence. Since the energy of photons from the decays of π^0 mesons generated in the first inelastic interaction is determined by energy per nucleon, the depth L is smaller for heavier nuclei at the same total energy. It is worth noting that, in the case of C and Fe nuclei, the new method is more precise than the traditional one up to greater depths in relation to the case of protons and helium nuclei. This is explained by fluctuations of the cascade curve that are associated with the fragmentation of the primary nucleus. Such fluctuations have a more pronounced effect on the longitudinal development of the cascade curve than on the maximum specific energy deposition. Therefore, the new method is more efficient in studying heavy nuclei by means of "short" calorimeters.

The specific energy deposition at the maximum of the hadron shower initiated by various high-energy nuclei is well described on the basis of the package

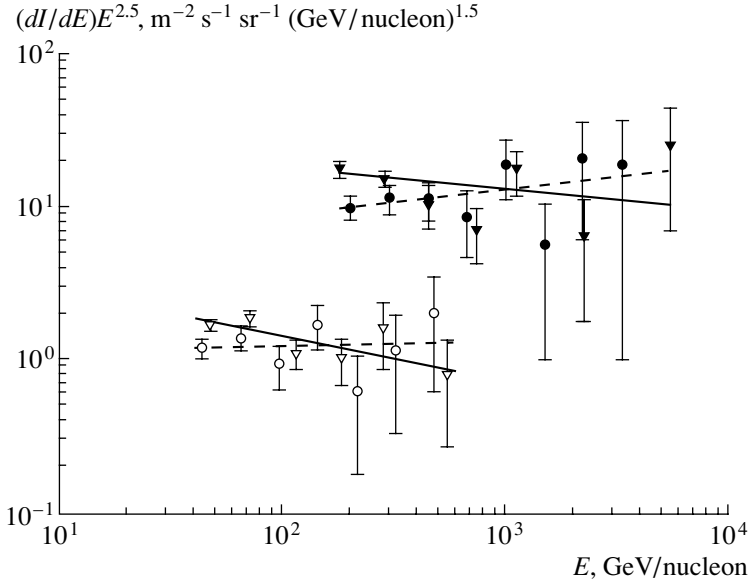

Fig. 3. Energy spectra of (▼, ●) C and (▽, ○) Fe nuclei according to an analysis of experimental data from [12, 13] on the total energy deposition [(▼, ▽) experimental data; (solid lines) exponential approximation] and on the specific energy deposition at the maximum [(●, ○) experimental data; (dashed lines) exponential approximation].

of codes used. The results of the simulations are confirmed by experimental data. This makes it possible to use the quantity in question as a methodological basis for reconstructing, at cascade depths less than L, the primary-particle energy to a precision higher than that of the traditional method. For a fixed precision of reconstruction of the primary energy E, this method enables one to use absorbers of smaller thickness and mass. Similar energy dependences of the specific energy deposition at the cascade maximum for different nuclear components (from protons to iron nuclei) make it possible to apply this method to studying the chemical composition of cosmic rays. The possibility of using a thin absorber, together with one ionization detector arranged below the absorber (in the case where the first interaction can be localized in a thin target above the absorber), is an experimental advantage of the proposed method.

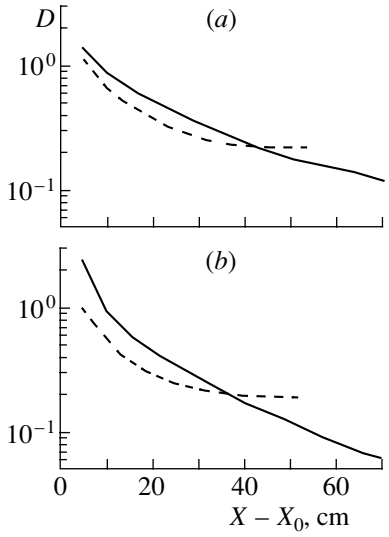

Fig. 4. Relative root-mean-square deviation D in determining energy from the (solid curve) total and (dashed curve) maximum energy deposition versus the depth of evolution of the shower induced by 8-TeV (*a*) C and (*b*) Fe nuclei.

REFERENCES

1. N. L. Grigorov, V. S. Murzin, and I. D. Rapoport, Zh. Éksp. Teor. Fiz. **34**, 506 (1958) [Sov. Phys. JETP **7**, 348 (1958)].
2. I. P. Ivanenko, D. M. Podorozhnyĭ, I. D. Rapoport, *et al.*, in *Shower Theory* (Mosk. Gos. Univ., Moscow, 1996), p. 102.
3. T. G. Guzik, J. Adams, J. Ampe, *et al.*, in *Proceedings of the 26th International Cosmic Ray Conference, ICRC, Salt Lake City, 1999,* Vol. 5, p. 9.
4. I. D. Rapoport, A. N. Turundaevsky, and V. Ya. Shestoperov, Yad. Fiz. **65**, 176 (2002) [Phys. At. Nucl. **65**, 170 (2002)].
5. GEANT User's Guide, CERN DD/EE/83/1 (1983).
6. H. C. Fesefeldt, Technical Report PITHA 85-02 (III Physikalisches Institut, RWTH Aachen Physikzentrum, 1985).
7. J. Ranft and S. Ritter, Z. Phys. C **20**, 347 (1983).
8. A. Fasso, A. Ferrari, J. Ranft, *et al.*, Nucl. Instrum. Methods Phys. Res. A **332**, 459 (1993).
9. N. S. Amelin, K. K. Gudima, S. Yu. Sivoklokov, and V. D. Toneev, Yad. Fiz. **52**, 272 (1990) [Sov. J. Nucl. Phys. **52**, 172 (1990)].

10. N. S. Amelin, K. K. Gudima, and V. D. Toneev, Yad. Fiz. **51**, 512 (1990) [Sov. J. Nucl. Phys. **51**, 327 (1990)].
11. N. N. Kalmykov and S. S. Ostapchenko, Preprint No. 98-36/537, NIIYaF MGU (Institute of Nuclear Physics, Moscow State University, Moscow, 1998).
12. I. P. Ivanenko, I. D. Rapoport, V. Ya. Shestoperov, *et al.*, Preprint No. 89-29/106, NIIYaF MGU (Institute of Nuclear Physics, Moscow State University, Moscow, 1989).
13. I. P. Ivanenko, I. D. Rapoport, V. Ya. Shestoperov, *et al.*, Preprint No. 88-6/83, NIIYaF MGU (Institute of Nuclear Physics, Moscow State University, Moscow, 1988).
14. A. M. Kolchuzhkin and V. I. Bespalov, in *Proceedings of the 16th International Cosmic Ray Conference, ICRC, Kyoto, 1979,* Vol. 9, p. 222.

Translated by S. Slabospitsky

Physics of Atomic Nuclei, Vol. 66, No. 1, 2003, pp. 135–142. From Yadernaya Fizika, Vol. 66, No. 1, 2003, pp. 138–145.

ELEMENTARY PARTICLES AND FIELDS
Theory

Spacetime Symplectic Extension*

Yu. F. Pirogov

Institute for High Energy Physics, Protvino, Moscow oblast, 142284 Russia

Received May 28, 2001

Abstract—It is conjectured that in the origin of spacetime there lies a symplectic rather than metric structure. The complex symplectic symmetry $Sp(2l, C), l \geq 1$ instead of the pseudoorthogonal one $SO(1, d-1)$, $d \geq 4$ is proposed as the spacetime local structure group. A discrete sequence of the metric spacetimes of the fixed dimensionalities $d = (2l)^2$ and signatures, with $l(2l-1)$ timelike and $l(2l+1)$ spacelike directions, defined over the set of Hermitian second-rank spin tensors, is considered as an alternative to the pseudo-Euclidean extra dimensional spacetimes. The basic concepts of the symplectic framework are developed in general, and the ordinary and next-to-ordinary spacetime cases with $l = 1, 2$, respectively, are elaborated in more detail. In particular, the scheme provides the rationale for the four-dimensionality and $1 + 3$ signature of the ordinary spacetime. © *2003 MAIK "Nauka/Interperiodica".*

1. INTRODUCTION

At present, the ordinary spacetime is postulated to be locally the Minkowski space, i.e., the pseudo-Euclidean space of the dimensionality $d = 4$ with the Lorentz group $SO(1, 3)$ as the local symmetry group. Nevertheless, the spinor analysis in the Minkowski space heavily relies on the isomorphism for the proper noncompact groups $SO(1, 3) \simeq SL(2, C)/Z_2$, as well as that $SO(3) \simeq SU(2)/Z_2$ for their maximal compact subgroups (see, e.g., [1]). Moreover, the whole relativistic field theory in four spacetime dimensions can equivalently be formulated (and in a sense it is even preferable) entirely in the framework of spinors of the $SL(2, C)$ group [2]. In this approach, to a spacetime point there corresponds a Hermitian tensor of the second rank.

From this point of view, a description of the ordinary spacetime by means of the real four-vectors of the $SO(1, 3)$ group, rather than by the Hermitian tensors of $SL(2, C)$, is nothing but the (historically settled) tradition of the spacetime parametrization. Nevertheless, just this parametrization underlies the proposed and widely discussed spacetime extensions into the (locally) pseudo-Euclidean spaces of the larger dimensionalities $d > 4$ in the Kaluza–Klein fashion (see, e.g., [3]). These extensions assume the embedding of the local symmetry groups as $SO(1, 3) \subset SO(1, d-1)$. The pseudo-Euclidean extensions play the crucial role in the attempts to construct a unified theory of all the interactions including gravity [4].

In what follows, we stick to the viewpoint that spinors are more fundamental objects than vectors. Thus the spacetime structure group with spinors as defining representations, i.e., the complex symplectic group $Sp(2, C)$, is considered to be more appropriate than the pseudoorthogonal group $SO(1, 3)$ with vectors as defining representations and spinors just as a kind of artifact. In other words, we assume that the symplectic structure of the spacetime has a deeper physical origin than the metric one, though both approaches, symplectic and pseudoorthogonal, are formally equivalent at an effective level in the ordinary spacetime. Then, in searching for the spacetime extradimensional extensions, a natural step would be to look for the extensions in the symplectic framework with the structure group $Sp(2l, C), l > 1$. The reason is that the descriptions equivalent at $l = 1$ and $d = 4$ can result in principally different extensions at $l > 1$ and $d > 4$. This is the problem dealt with in the present paper. We develop the basic concepts of the general symplectic framework and elaborate in more detail the ordinary and next-to-ordinary spacetime cases with $l = 1, 2$, respectively.[1)]

2. STRUCTURE GROUP

It is assumed that an underlying physics described effectively by a local symmetry (structure group) constitutes the basis for the local properties of the spacetime, i.e., for its dimensionality and signature. Hence, to find possible types of spacetime extensions, it is necessary first of all to find all the structure groups isomorphic to each other at $d = 4$. In addition to the well-known isomorphism of the real and complex groups $SO(1, 3) \simeq SL(2, C)/Z_2$ relevant

*This article was submitted by the author in English.

[1)]An early version of the study can be found in [5].

1063-7788/03/6601-0135$24.00

to the ordinary spacetime, there exist the following isomorphisms (up to Z_2) for the proper complex Lie groups: $SL(2,C) \simeq SO(3,C) \simeq Sp(2,C)$ and, respectively, for their maximal compact (real) subgroups: $SU(2) \simeq SO(3) \simeq Sp(2)$. In other terms, these isomorphisms look like $A_1 \simeq B_1 \simeq C_1$, where the groups considered are the first ones from the complex Cartan series: $A_l = SL(l+1,C)$, $B_l = SO(2l+1,C)$, $C_l = Sp(2l,C)$ and similarly for their maximal compact subgroups $SU(l+1)$, $SO(2l+1)$, $Sp(2l)$ (see, e.g., [6]). Here, $l \geq 1$ means the rank of the corresponding Lie algebras. It is equal to the half-rank of the proper noncompact Lie groups and coincides with the rank of their maximal compact subgroups. As the structure groups, all the groups from the above series result in (locally) isomorphic descriptions at $l = 1$. Therefore, at $l > 1$, the extended structure groups may a priori be looked for in each of the series with properly extended spinor space. But the physical requirement for the existence of an invariant bilinear product in the extended spinor space restricts the admissible types of extension.

Namely, for all the complex groups, the complex conjugate fundamental representations $\bar{\psi}$ are not equivalent to the representations ψ themselves. In addition, for all the complex series, there is no invariant tensor in the spinor space that would match a spinor representation and its complex conjugate. Hence, the invariant bilinear product of Grassmann fields in the form $\psi\psi$ (and $\bar{\psi}\bar{\psi}$) is the only possible one (if any). Such a product is admissible just for the symplectic series C_l. This is due to the fact that, by definition, there exists in this case the invariant (antisymmetric) second-rank tensor. It is to be noted that the spinor representations of the orthogonal groups B_l are realized by the embedding of the latter ones into the symplectic groups $C_{2^{l-1}}$ over the 2^l-dimensional spinor space. Only at $l = 1, 2$ do the isomorphisms $B_l \simeq C_l$ take place. The spinors being assumed to be more fundamental objects than vectors, it is natural to consider directly the symplectic groups that are self-sufficient for spinors, instead of the pseudoorthogonal ones, which inevitably should appeal to symplectic groups for justification of the spinor representations.

Just the existence of the alternating second-rank tensor in the $SL(2,C)$ group is, in essence, the *raison d'etre* for the spinor analysis in four spacetime dimensions being based traditionally on this group. The symmetry structure that provides the alternating tensor and, as a result, the invariant inner product for spinors proves to be crucial for the whole physical theory. But this structure survives in $Sp(2l,C)$ and is absent in $SL(l+1,C)$ at $l > 1$. This is why, namely, the first groups, and not the second ones, are to be considered as the structure groups of the extended spacetime. Therefore, while constructing extradimensional spacetimes we retain symplectic structure, i.e., consider extensions in the series C_l.

To summarize, two alternative ways of spacetime extension can be pictured schematically as

$$\begin{array}{ccc} SO(1,3) & \simeq & Sp(2,C) \\ \downarrow & & \downarrow \\ SO(1,d-1) & \not\simeq & Sp(2l,C). \end{array} \qquad (1)$$

The first commonly adopted way of extension corresponds to the real structure groups, while the second one relies on the complex groups. The scheme shows that the isomorphism of the real and complex groups, valid at $d = 4$ and $l = 1$, is no longer fulfilled at $d > 4$ and $l > 1$. In the first way of extension, the local metric properties of the spacetime (i.e., dimensionality and signature) are put in ab initio. In the second way, these properties should not be considered as the primary ones, but, instead, they have to emerge as a manifestation of the inherent symplectic structure.

3. THE COMPLEX SYMPLECTIC SYMMETRY $Sp(2l,C)$

Let ψ_A and $\bar{\psi}^{\bar{A}} \equiv (\psi_A)^*$, as well as their respective duals ψ^A and $\bar{\psi}_{\bar{A}} \equiv (\psi^A)^*$, $A, \bar{A} = 1, \ldots, n\,(n = 2l)$, be the spinor representations of $Sp(2l,C)$. It is well known that there exist in the spinor space the nondegenerate invariant second-rank spin tensors $\epsilon_{AB} = -\epsilon_{BA}$ and $\epsilon^{AB} = -\epsilon^{BA}$ such that $\epsilon_{AC}\epsilon^{CB} = \delta_A{}^B$, with $\delta_A{}^B$ being the Kronecker symbol (and similarly for $\epsilon_{\bar{A}\bar{B}} \equiv (\epsilon^{BA})^*$ and $\epsilon^{\bar{A}\bar{B}} \equiv (\epsilon_{BA})^*$). Owing to these invariant tensors, the spinor indices of the upper and lower positions are pairwise equivalent ($\psi_A \sim \psi^A$ and $\bar{\psi}_{\bar{A}} \sim \bar{\psi}^{\bar{A}}$), so that there are left just two inequivalent spinor representations (generically, ψ and $\bar{\psi}$). Let us call ψ and $\bar{\psi}$ the spinors of the first and second kind, respectively, and similarly for the corresponding indices A and $\bar{A}$.[2)]

Let us put in correspondence to an event point P a second-rank spin tensor $X_A{}^{\bar{B}}(P)$, which is Hermitian, i.e., $X_A{}^{\bar{B}} = (X_B{}^{\bar{A}})^* \equiv \bar{X}^{\bar{B}}{}_A$, or in other terms

[2)] Note that both the kind and the position of the indices are changed under complex conjugation, contrary to the traditional definition of the dotted indices for $SL(2,C)$ without the position change: $(\psi_A)^* \equiv \psi^*_{\dot{A}}$, etc. The advantage of the definition adopted in the present paper is that, relative to the maximal compact subgroup $Sp(2l)$, the two kinds of indices A and $\bar{A}$ in the same position are completely indistinguishable, while the similar A and $\dot{A}$ would enjoy this property only after the implicit position change for $\dot{A}$.

$X^{A\bar{B}} = (X_{B\bar{A}})^*$. One can define the quadratic scalar product as

$$\begin{aligned} \mathrm{tr}X\bar{X} \equiv & X_A{}^{\bar{B}}\bar{X}_{\bar{B}}{}^A = X_A{}^{\bar{B}}X^A{}_{\bar{B}} \\ & = -X_{A\bar{B}}X^{A\bar{B}} = -X_{A\bar{B}}(X_{B\bar{A}})^*, \end{aligned} \tag{2}$$

the last equality being due to the Hermiticity of X. Clearly, $\mathrm{tr}X\bar{X}$ is real, though not sign-definite. In addition, the spin tensor $X\bar{X}$ is antisymmetric, $(X\bar{X})_{AB} = -(X\bar{X})_{BA}$, and hence it can be decomposed into the trace relative to ϵ and a traceless part. Under $S \in Sp(2l, C)$, one has in compact notation

$$\begin{aligned} X &\to SXS^\dagger, \\ \bar{X} &\to S^{\dagger -1}\bar{X}S^{-1}, \end{aligned} \tag{3}$$

so that $X\bar{X} \to SX\bar{X}S^{-1}$ and $\mathrm{tr}X\bar{X}$ is invariant, indeed. In fact, the invariant (2) is at $l > 1$ just the first one in a series of independent invariants $\mathrm{tr}(X\bar{X})^k$, $k = 1, \ldots, l$. By definition, set $\{X\}$ endowed with the structure group $Sp(2l, C)$ and the interval between points X_1 and X_2 defined as $\mathrm{tr}(X_1 - X_2)(\bar{X}_1 - \bar{X}_2)$ constitutes the symplectic spacetime. The noncompact transformations from the $Sp(2l, C)$ are counterparts of the Lorentz boosts in the ordinary spacetime, while transformations from the compact subgroup $Sp(2l) = Sp(2l, C) \cap SU(2l)$ correspond to rotations. With allowance for translations $X_A{}^{\bar{B}} \to X_A{}^{\bar{B}} + \Xi_A{}^{\bar{B}}$, where $\Xi_A{}^{\bar{B}}$ is an arbitrary constant Hermitian spin tensor, the whole theory in the flat symplectic spacetime should be covariant under the inhomogeneous symplectic group.

Let us now fix for a while the extended boosts and restrict ourselves to the extended rotations, i.e., to the maximal compact subgroup $Sp(2l)$. Relative to the latter, the indices of the first and second kinds are indistinguishable in their transformation properties ($\psi_A \sim \bar{\psi}_{\bar{A}}$), and one can temporarily label $X_{A\bar{B}}$ in this case as X_{XY}, where $X, Y, \ldots = 1, \ldots, n$ generically mean spinor indices irrespective of their kind. Hence, while restricting oneself to the compact subgroup, one can reduce the tensor X_{XY} into two irreducible parts, symmetric and antisymmetric ones: $X_{XY} = \sum_\pm (X_\pm)_{XY}$, where $(X_\pm)_{XY} = \pm(X_\pm)_{YX}$ have $d_\pm = n(n \pm 1)/2$ dimensions, respectively. One gets from (2) the following decomposition for the scalar product:

$$\mathrm{tr}X\bar{X} = \sum_\pm (\mp 1)(X_\pm)_{XY}[(X_\pm)_{XY}]^*. \tag{4}$$

At $l > 1$, one can further reduce spin tensor X_- to the trace $X_-^{(0)}$ relative to ϵ and a traceless part $X_-^{(1)}$ as $(X_-)_{XY} = (1/\sqrt{n})X_-^{(0)}\epsilon_{XY} + (X_-^{(1)})_{XY}$ so that

$$\begin{aligned} \mathrm{tr}X\bar{X} = & X_-^{(0)2} + (X_-^{(1)})_{XY}[(X_-^{(1)})_{XY}]^* \\ & - (X_+)_{XY}[(X_+)_{XY}]^*. \end{aligned} \tag{5}$$

As a result, the whole extended spacetime can be decomposed with respect to the rotation subgroup into three irreducible subspaces of 1, $(n-2)(n+1)/2$, and $n(n+1)/2$ dimensions. According to their signature and transformation properties, the first two subspaces correspond to the time dimensions, the rotationally invariant and noninvariant ones, while the third subspace corresponds to the spatial extra dimensions. It is to be noted that the number of components in the extended space, and hence that in the spatial momentum, is equal to the number of the noncompact transformations (boosts). Thus, for a massive particle, there exists a rest frame with zero spatial momentum. In the case $n = 2$, there is a unique antisymmetric tensor $(X_-)_{XY} \sim \epsilon_{XY}$ such that the noninvariant time subspace is empty.

Of course, the particular decomposition of X into two parts $X_\pm$ is noncovariant with respect to the whole $Sp(2l, C)$ and depends on the boosts. Nevertheless, the decomposition being valid at any boost, the number of positive and negative components in $\mathrm{tr}X\bar{X}$ is invariant under the whole $Sp(2l, C)$. In other words, the metric signature of the symplectic spacetime

$$\sigma_d = (\underbrace{+1, \ldots}_{d-}; \underbrace{-1, \ldots}_{d+}) \tag{6}$$

is invariant. Hence, at $n = 2l > 2$ the structure group $Sp(2l, C)$ of the nth rank and the $n(n+1)$th order, acting on the Hermitian second-rank spin tensors with $d = n^2$ components, is just a restricted subgroup of the embedding pseudoorthogonal group $SO(d_-, d_+)$, of the rank $n^2/2$ and the order $n^2(n^2 - 1)/2$, acting on the pseudo-Euclidean space of dimensionality $d = n^2$. What distinguishes $Sp(2l, C)$ from $SO(d_-, d_+)$ is the total set of independent invariants $\mathrm{tr}(X\bar{X})^k$, $k = 1, \ldots, l$. The isomorphism between the groups is achieved only at $l = 1$, i.e., for the ordinary spacetime $d = 4$, where there is just one invariant $\mathrm{tr}X\bar{X}$.

It should be stressed that, in the approach under consideration, neither the discrete set of dimensionalities, $d = (2l)^2$, of the extended spacetime, nor its signature, nor the existence of the rotationally-invariant one-dimensional time subspace is postulated ab initio. Rather, they are the immediate consequences of the underlying symplectic structure. In particular, the latter seems to provide a unique rationale for the four-dimensionality of the ordinary spacetime, as well as for its signature $(+ - - -)$. Namely, these properties

directly reflect the existence of one antisymmetric and three symmetric second-rank Hermitian spin tensors at $l = 1$. The set of such tensors, in turn, is the lowest admissible Hermitian space to accommodate the symplectic structure, the case $l = 0$ being trivial ($d = 0$). On the other hand, just the existence of the one-dimensional time subspace allows one to (partially) order the events at any fixed boosts, which serves as a basis for the causality description. Hence, the latter may ultimately be attributed to the underlying symplectic structure too. At $l > 1$, because of the extra times being mixed via boosts with the one-dimensional time, the causality should approximately be valid only at small boosts.

4. C, P, T SYMMETRIES

Let us charge double the spinor space, i.e., for each ψ_A, $(\psi_A)^\dagger \equiv \bar{\psi}^{\bar{A}}$ introduce two copies $\psi^\pm_A$, $(\psi^\pm_A)^\dagger \equiv (\bar{\psi}^\mp)^{\bar{A}}$, with $\pm$ being the "charge" sign.[3)] In analogy to the ordinary case of $SL(2, C)$ [1], one can define the following discrete symmetries:

$$\begin{aligned} C &: \psi^\pm_A \to \psi^\mp_A, \\ P &: \psi^\pm_A \to (\psi^\mp_A)^\dagger \equiv (\bar{\psi}^\pm)^{\bar{A}}, \\ T &: \psi^\pm_A \to (\psi^\pm_A)^\dagger \equiv (\bar{\psi}^\mp)^{\bar{A}}, \end{aligned} \tag{7}$$

and hence $CPT : \psi^\pm_A \to \psi^\pm_A$ (all up to the phase factors). Under CPT invariance, only two of the discrete operations (7) are independent ones. Without charge doubling, just one combination $CP \equiv T : \psi_A \to \bar{\psi}^{\bar{A}}$ survives.

Now, let us introduce the Hermitian spin-tensor current $J = J^\dagger$ as follows:

$$J_A{}^{\bar{B}} \equiv \sum_\pm (\pm 1)\psi^\pm_A(\psi^\pm_B)^\dagger = \sum_\pm (\pm 1)\psi^\pm_A(\bar{\psi}^\mp)^{\bar{B}} \tag{8}$$

(ψ's are the Grassmann fields). Under (7), the current $J_A{}^{\bar{B}}$ transforms as follows:

$$\begin{aligned} C &: J_A{}^{\bar{B}} \to -J_A{}^{\bar{B}}, \\ P &: J_A{}^{\bar{B}} \to -J_B{}^{\bar{A}}, \\ T &: J_A{}^{\bar{B}} \to J_B{}^{\bar{A}}. \end{aligned} \tag{9}$$

Fixing boosts and decomposing current $J_{A\bar{B}}$ into the symmetric and antisymmetric parts, $J_{XY} = \sum_\pm (J_\pm)_{XY}$, one gets from (9)

$$\begin{aligned} C &: (J_\pm)_{XY} \to -(J_\pm)_{XY}, \\ P &: (J_\pm)_{XY} \to \mp(J_\pm)^{XY}, \\ T &: (J_\pm)_{XY} \to \pm(J_\pm)^{XY}. \end{aligned} \tag{10}$$

This is in complete agreement with the signature association for the symmetric (antisymmetric) part of the Hermitian spin tensor X as the extended spatial (time) components.

5. THE CASE $l = 1$

The noncompact group $Sp(2l, C)$ has $n(n+1)$ generators $M_{AB} = (L_{AB}, K_{AB})$, $A, B = 1, \ldots, n$ ($n = 2l$), so that $L_{AB} = L_{BA}$ and similarly for K_{AB}. The generators L_{AB} are Hermitian and correspond to the extended rotations, whereas those K_{AB} are anti-Hermitian and correspond to the extended boosts. In the space of the first-kind spinors ψ_A, these generators can be represented as $(\sigma_{AB}, i\sigma_{AB})$ with $(\sigma_{AB})_{CD} = 1/2(\epsilon_{AC}\epsilon_{BD} + \epsilon_{AD}\epsilon_{BC})$, so that $\sigma_{AB} = \sigma_{BA}$ and $(\sigma_{AB})_{CD} = (\sigma_{AB})_{DC}$, $(\sigma_{AB})_C{}^C = 0$. Similar expressions hold true in the space of the second-kind spinors $\bar{\psi}_{\bar{A}}$. In these terms, a canonical formalism can be developed at arbitrary $l \geq 1$.

In the simplest case $l = 1$ corresponding to the ordinary four-dimensional spacetime, there exists the isomorphism $B_1 \simeq C_1$ (or $SO(3, C) \simeq Sp(2, C)/Z_2$). Due to this property, the structure of $Sp(2, C)$ can be brought to a mathematically equivalent but more physically familiar form.[4)] Namely, let us introduce for the $SO(3, C)$ group the double set of the Pauli matrices, $(\sigma_i)_A{}^{\bar{B}}$ and $(\bar{\sigma}_i)_{\bar{A}}{}^B$, $i = 1, 2, 3$. They should satisfy the anticommutation relations $\sigma_i\bar{\sigma}_j + \sigma_j\bar{\sigma}_i = 2\delta_{ij}\sigma_0$ and $\bar{\sigma}_i\sigma_j + \bar{\sigma}_j\sigma_i = 2\delta_{ij}\bar{\sigma}_0$, where $(\sigma_0)_A{}^B \equiv \delta_A{}^B$, $(\bar{\sigma}_0)_{\bar{A}}{}^{\bar{B}} \equiv \delta_{\bar{A}}{}^{\bar{B}}$ are the Kronecker symbols and δ_{ij} is the metric tensor of $SO(3, C)$. Among these matrices, σ_0 and $\bar{\sigma}_0$ are the only independent ones which can be chosen antisymmetric, $(\sigma_0)_{AB} \equiv \epsilon_{AB}$ and $(\bar{\sigma}_0)_{\bar{A}\bar{B}} \equiv \epsilon_{\bar{A}\bar{B}}$. On the other hand, with respect to the maximal compact subgroup $SO(3)$, all the matrices σ_i, $\bar{\sigma}_i$ can be chosen both Hermitian and symmetric as $(\sigma_i)_X{}^Y = [(\sigma_i)_Y{}^X]^*$ and $(\sigma_i)_{XY} = (\sigma_i)_{YX}$ (and the same for $\bar{\sigma}_i$). The matrices $\sigma_{ij} \equiv (-i/2)(\sigma_i\bar{\sigma}_j - \sigma_j\bar{\sigma}_i)$ such that $\sigma_{ij} = -\sigma_{ji}$ and $(\sigma_{ij})_{AB} = (\sigma_{ij})_{BA}$ (and similarly for $(\bar{\sigma}_{ij})_{\bar{A}\bar{B}} \equiv (i/2)(\bar{\sigma}_i\sigma_j - \bar{\sigma}_j\sigma_i)_{\bar{A}\bar{B}}$) are not linearly independent from σ_i. They can be brought to the form $(\sigma_{ij})_{XY} = \epsilon_{ijk}(\sigma_k)_{XY}$, with ϵ_{ijk} being the Levi-Civita $SO(3, C)$ symbol.

The matrices $(\sigma_{ij}, i\sigma_{ij})$ can be identified as the generators $M_{ij} = (L_{ij}, K_{ij})$ of the noncompact

[3)] We use here a dagger sign for complex conjugation to show that the Grassmann fields should undergo the change of the order in their products.

[4)] We use here the complex group $SO(3, C)$ instead of the real one $SO(1, 3)$ to show the close similarity with the next case $l = 2$ where there is no real structure group. Because of the complexity of $SO(3, C)$ one should distinguish vectors and their complex conjugate, the latter ones being omitted for simplicity in what follows. The same remains true for the $SO(5, C)$ case corresponding to $l = 2$.

$SO(3,C)$ group in the space of the first-kind spinors. Respectively, in the space of the second-kind spinors, they are $(-\bar{\sigma}_{ij}, i\bar{\sigma}_{ij})$. The generators L_{ij} of the maximal compact subgroup $SO(3) \simeq Sp(2)/Z_2$ correspond to rotations, while those K_{ij} of the noncompact transformations describe Lorentz boosts. Relative to $SO(3)$, one has $\bar{\sigma}_0 = \sigma_0$, $\bar{\sigma}_i = \sigma_i$, and $\bar{\sigma}_{ij} = -\sigma_{ij}$. When restricted by the maximal compact subgroup $SO(3)$, the Hermitian second-rank spin tensor can be decomposed into the complete set of Hermitian matrices (σ_0, σ_{ij}) with real coefficients $X = (1/\sqrt{2})(x_0\sigma_0 + (1/2)x_{ij}\sigma_{ij})$, so that $\mathrm{tr}X\bar{X} = x_0^2 - (1/2)x_{ij}^2$. With identification $x_{ij} \equiv \epsilon_{ijk}x_k$, one gets, as usual, $\mathrm{tr}X\bar{X} = x_0^2 - x_i^2$. Both time and spatial representations being irreducible under $SO(3)$, there takes place the usual decomposition $\underline{4} = \underline{1} \oplus \underline{3}$ relative to the embedding $SO(3,C) \supset SO(3)$.

6. THE CASE $l = 2$

This case corresponds to the next-to-ordinary spacetime symplectic extension. Similarly to the case $l = 1$, there takes place the isomorphism $B_2 \simeq C_2$, or $SO(5,C) \simeq Sp(4,C)/Z_2$. Cases $l = 1, 2$ are the only ones where the structure of the symplectic group gets simplified in terms of the complex orthogonal groups. The double set of Clifford matrices $(\Sigma_I)_A{}^{\bar{B}}$ and $(\overline{\Sigma}_I)_{\bar{A}}{}^B$, $I = 1, \ldots, 5$, satisfies equations $\Sigma_I\overline{\Sigma}_J + \Sigma_J\overline{\Sigma}_I = 2\delta_{IJ}\Sigma_0$ and $\overline{\Sigma}_I\Sigma_J + \overline{\Sigma}_J\Sigma_I = 2\delta_{IJ}\overline{\Sigma}_0$, where $(\Sigma_0)_A{}^B \equiv \delta_A{}^B$, $(\overline{\Sigma}_0)_{\bar{A}}{}^{\bar{B}} \equiv \delta_{\bar{A}}{}^{\bar{B}}$ are the Kronecker symbols and δ_{IJ} is the metric tensor of $SO(5,C)$. Relative to the maximal compact subgroup $SO(5)$, they can be chosen Hermitian, $(\Sigma_I)_X{}^Y = [(\Sigma_I)_Y{}^X]^*$, but antisymmetric, $(\Sigma_I)_{XY} = -(\Sigma_I)_{YX}$ (and similarly for $\overline{\Sigma}_I$), like $(\Sigma_0)_{AB} = \epsilon_{AB}$ and $(\overline{\Sigma}_0)_{\bar{A}\bar{B}} = \epsilon_{\bar{A}\bar{B}}$. One can also require that $(\Sigma_I)_X{}^X = 0$. Therefore, under restriction by $SO(5)$, six matrices Σ_0, Σ_I provide the complete independent set of antisymmetric matrices in the four-dimensional spinor space. After introducing matrices $\Sigma_{IJ} = (-i/2)(\Sigma_I\overline{\Sigma}_J - \Sigma_J\overline{\Sigma}_I)$, so that $\Sigma_{IJ} = -\Sigma_{JI}$, one gets the symmetry condition for them: $(\Sigma_{IJ})_{AB} = (\Sigma_{IJ})_{BA}$ (and similarly for $(\overline{\Sigma}_{IJ})_{\bar{A}\bar{B}} = (i/2)(\overline{\Sigma}_I\Sigma_J - \overline{\Sigma}_J\Sigma_I)_{\bar{A}\bar{B}}$). Hence, ten matrices Σ_{IJ} (or $\overline{\Sigma}_{IJ}$) make up the complete set of symmetric matrices in the spinor space. Under $SO(5)$, one has $\overline{\Sigma}_0 = \Sigma_0$, $\overline{\Sigma}_I = \Sigma_I$, and $\overline{\Sigma}_{IJ} = -\Sigma_{IJ}$.

With respect to $SO(5)$, the Hermitian second-rank spin tensor X can be decomposed into the complete set of matrices Σ_0, Σ_I, and Σ_{IJ} with real coefficients $X = 1/2(x_0\Sigma_0 + x_I\Sigma_I + (1/2)x_{IJ}\Sigma_{IJ})$. In these terms, one gets

$$\mathrm{tr}X\bar{X} = x_0^2 + x_I^2 - \frac{1}{2}x_{IJ}^2. \qquad (11)$$

There is one more independent invariant combination of x_0, x_I, and x_{IJ} stemming from the invariant $\mathrm{tr}(X\bar{X})^2$.

Relative to the embedding $SO(5,C) \supset SO(5)$, one has the following decomposition in the irreducible representations:

$$\underline{16} = \underline{1} \oplus \underline{5} \oplus \underline{10}. \qquad (12)$$

Under discrete transformations (7), one gets

$$P : x_0 \to x_0,\ x_I \to x_I,\ x_{IJ} \to -x_{IJ}, \qquad (13)$$
$$T : x_0 \to -x_0,\ x_I \to -x_I,\ x_{IJ} \to x_{IJ}.$$

This means that, from the point of view of $SO(5)$, x_I is the axial vector, whereas x_{IJ} is the pseudotensor (a counterpart of $x_{ij} = \epsilon_{ijk}x_k$ in three spatial dimensions). The matrices $(\Sigma_{IJ}, i\Sigma_{IJ})$ or $(-\overline{\Sigma}_{IJ}, i\overline{\Sigma}_{IJ})$ represent the $SO(5,C)$ generators $M_{IJ} = (L_{IJ}, K_{IJ})$ in the spaces of the spinors, respectively, of the first and second kinds. A particular expression for the matrices Σ_I, Σ_{IJ} in terms of σ_0, σ_i depends on the fashion of the embedding $SO(3,C) \subset SO(5,C)$.

The rank of the algebra C_2 being $l = 2$, an arbitrary irreducible representation of the noncompact group $Sp(4,C)$ is uniquely characterized by two complex Casimir operators I_2 and I_4, respectively, of the second and fourth order, i.e., by four real quantum numbers. Otherwise, an irreducible representation of $Sp(4,C)$ can be described by the mixed spin tensor $\Psi_{A_1\ldots}^{\bar{B}_1\cdots}$ of a proper rank. This spin tensor should be traceless in any pair of indices of the same kind, and its symmetry in each kind of indices should correspond to a two-row Young tableau. In fact, there exists the completely antisymmetric invariant tensor of the fourth rank $\epsilon_{A_1A_2A_3A_4} \equiv \epsilon_{A_1A_2}\epsilon_{A_3A_4} - \epsilon_{A_1A_3}\epsilon_{A_2A_4} + \epsilon_{A_1A_4}\epsilon_{A_2A_3}$ which corresponds to the embedding $SL(4,C) \supset Sp(4,C)$ (and similarly for $\epsilon_{\bar{A}_1\bar{A}_2\bar{A}_3\bar{A}_4}$). By means of these invariant tensors, three indices of the same kind with antisymmetry are equivalent to one index, whereas four indices with antisymmetry can be omitted altogether. Hence, antisymmetry is possible in no more than pairs of indices of the same kind. Therefore, an irreducible representation of $Sp(4,C)$ can unambiguously be characterized by a set of four integers $(r_1, r_2; \bar{r}_1, \bar{r}_2)$, $r_1 \geq r_2 \geq 0$ and $\bar{r}_1 \geq \bar{r}_2 \geq 0$. Here, $r_{1,2}$ (respectively, $\bar{r}_{1,2}$) are the numbers of boxes in the first or second rows of the proper Young tableau. The rank of the maximal compact subgroup $SO(5) \simeq Sp(4)/Z_2$ (the rotation group) being equal to $l = 2$, a state in a representation is additionally characterized under fixed boosts by two additive quantum numbers, namely, the eigenvalues of the mutually commuting momentum components of L_{IJ} in two different planes, say, L_{12} and L_{45}. Note that, in the $Sp(2,C)$ case, the Young

tableaux are at most one-rowed, and an irreducible representation is characterized by a pair of integers $(r;\bar{r})$, with the complex dimensionality of the representation being $(r+1)(\bar{r}+1)$. In this case, there remains just one diagonal component of the total angular momentum, say, $L_{12} \equiv L_3$.

7. $\Delta l = 1$ REDUCTION

The ultimate attribute of the dimensionality in the given approach is the discrete number $l = 1, 2, \ldots$ corresponding to the dimensionality $n = 2l$ of the spinor space. The dimensionality $d = (2l)^2$ of the spacetime appears just as a secondary quantity. In reality, the extended spacetime with $l > 1$ should compactify to the ordinary one with $l = 1$ by means of the symplectic gravity. Let us restrict ourselves to the next-to-ordinary spacetime case with $l = 2$. Three generic inequivalent types of spinor decomposition relative to the embedding $Sp(4, C) \supset Sp(2, C)$ are conceivable: (i) $\underline{4} = \underline{2} \oplus \underline{2}$, (ii) $\underline{4} = \underline{2} \oplus \bar{\underline{2}}$, and (iii) $\underline{4} = \underline{2} \oplus \underline{1} \oplus \underline{1}$.

(i) Chiral spinor doubling

$$\underline{4} = \underline{2} \oplus \underline{2} \tag{14}$$

results in the decomposition of the Hermitian second-rank spin tensor $\underline{16} \sim \underline{4} \times \bar{\underline{4}}$ as

$$\underline{16} = 4 \cdot \underline{4}, \tag{15}$$

i.e., in a collection of four four-vectors [more precisely, of three vectors and one axial vector, as follows from (12) and (13)]. As for matter fermions, according to (14), the number of two-component fermions after compactification is twice that of the number of four-component fermions prior to compactification. If a kind of family structure reproduces itself during the compactification, it is necessary that there should be at least two copies of the four-component fermions in the extended spacetime with at least four two-component copies of them in the ordinary spacetime. For phenomenological reasons, the fermions in excess of three families should acquire rather large effective Yukawa couplings as a manifestation of the curled-up spacetime background. This is not in principle impossible because the two-component fermions in (14) distinguish extra dimensions. Note that the requirement for the renormalization group consistency of the Standard Model (SM) disfavors the fourth heavy chiral family in the model without a rather low cutoff [7]. But if due to decomposition (15) for the gauge bosons, there appeared the additional moderately heavy vector bosons with mass comparable to that of the heavy fermions, this constraint could in principle be evaded and the compactification scale Λ could be envisaged to be both rather moderate and high without conflict with the SM consistency. On the other hand, the extra timelike dimensions violate causality and the proper compactification scale Λ in the pseudoorthogonal case is stated to be not less than the Planck scale [8]. Nevertheless, one may hope that the latter restriction could somehow be abandoned in the symplectic approach due to approximate causality here. The causality should be valid at small boosts or gravitational fields, so that the compactification scale Λ could possibly be admitted to be not very high. For this reason, the given compactification scenario could still survive at any Λ.

(ii) Vectorlike spinor doubling

$$\underline{4} = \underline{2} \oplus \bar{\underline{2}} \tag{16}$$

results in the decomposition

$$\underline{16} = 2 \cdot \underline{4} \oplus (\underline{3} + \text{h.c.}) \oplus 2 \cdot \underline{1}. \tag{17}$$

In the traditional four-vector notation, one has $X \sim (x_\mu^{(1,2)},\ x_{[\mu\nu]},\ x^{(1,2)})$, $\mu, \nu = 0, \ldots, 3$, with the tensor $x_{[\mu\nu]}$ being antisymmetric and all the components x being real. According to (16), after compactification there should emerge pairs of ordinary and mirror matter fermions. For phenomenological reasons, one should require the mirror fermions to have masses supposedly of the order of the compactification scale Λ. Modulo reservations for the preceding case, this compactification scenario could be valid at any Λ too.

(iii) Spinor-scalar content

$$\underline{4} = \underline{2} \oplus \underline{1} \oplus \underline{1} \tag{18}$$

results in

$$\underline{16} = \underline{4} \oplus \left(2 \cdot \underline{2} + \text{h.c.}\right) \oplus 4 \cdot \underline{1} \tag{19}$$

or in the mixed four-vector and spinor notations $X \sim (x_\mu,\ x_A^{(1,2)},\ x^{(1,2,3,4)})$, $A = 1, 2$. Due to (18), there would take place the violation of the spin-statistics connection for matter fields in the four-dimensional spacetime if this connection was fulfilled in the extended spacetime. The scale of this violation should be determined by the compactification scale Λ which, in contrast with the two preceding cases, must safely be high enough not to violate causality within the experimental precision.

8. GAUGE INTERACTIONS

Let $D_A{}^{\bar{B}} \equiv \partial_A{}^{\bar{B}} + igG_A{}^{\bar{B}}$ be the generic covariant derivative, with g being the gauge coupling, the Hermitian spin tensor $G_A{}^{\bar{B}}$ being the gauge fields,

and $\partial_A{}^{\bar{B}} \equiv \partial/\partial X^A{}_{\bar{B}}$ being the ordinary derivative. Now let us introduce the strength tensor[5)]

$$F^{[\bar{B}_1\bar{B}_2]}_{\{A_1A_2\}} \equiv \frac{1}{ig} D^{[\bar{B}_1}_{\{A_1} D^{\bar{B}_2]}_{A_2\}} \tag{20}$$

$$= \frac{1}{4ig}\Big(D^{\bar{B}_1}_{A_1} D^{\bar{B}_2}_{A_2} - D^{\bar{B}_2}_{A_2} D^{\bar{B}_1}_{A_1} + D^{\bar{B}_1}_{A_2} D^{\bar{B}_2}_{A_1} - D^{\bar{B}_2}_{A_1} D^{\bar{B}_1}_{A_2}\Big)$$

and similarly for $\bar{F}^{\{\bar{B}_1\bar{B}_2\}}_{[A_1A_2]} \equiv (F^{[\bar{A}_2\bar{A}_1]}_{\{B_2B_1\}})^*$, where $\{\dots\}$ and $[\dots]$ mean the symmetrization and antisymmetrization, respectively. One gets

$$F^{[\bar{B}_1\bar{B}_2]}_{\{A_1A_2\}} = \partial^{[\bar{B}_1}_{\{A_1} G^{\bar{B}_2]}_{A_2\}} + igG^{[\bar{B}_1}_{\{A_1} G^{\bar{B}_2]}_{A_2\}} \tag{21}$$

and similarly for $\bar{F}^{\{\bar{B}_1\bar{B}_2\}}_{[A_1A_2]}$. These tensors are clearly gauge-invariant. The total number of real components in the tensor $F^{[\bar{B}_1\bar{B}_2]}_{\{A_1A_2\}}$ is $2(n(n-1)/2)n(n+1)/2 = n^2(n^2-1)/2$, and it exactly coincides with the number of components of the antisymmetric second-rank tensor $F_{[\alpha\beta]}$, $\alpha,\beta = 0,1,\dots,n^2-1$, defined in the pseudo-Euclidean space of the $d = n^2$ dimensions. But in the symplectic case, tensor F is reducible and splits into a trace relative to ϵ and a traceless part, $F = F^{(0)} + F^{(1)}$, where $F^{(0)[\bar{B}_1\bar{B}_2]}_{\{A_1A_2\}} \equiv F^{(0)}_{\{A_1A_2\}}\epsilon^{\bar{B}_1\bar{B}_2}$ and $F^{(1)[\bar{B}_1\bar{B}_2]}_{\{A_1A_2\}}\epsilon_{\bar{B}_1\bar{B}_2} = 0$ (and similarly for $\bar{F}^{\{\bar{B}_1\bar{B}_2\}}_{[A_1A_2]}$). Hence, one has two independent irreducible representations with the real dimensionalities $d_0 = n(n+1)$ and $d_1 = n(n-2)(n+1)^2/2$. At $n = 4$, one has in terms of the complex tensors of $SO(5,C)$ $F^{(0)}_{[IJ]} \equiv (\Sigma_{IJ})^{A_1A_2}F^{(0)}_{\{A_1A_2\}}$ and $F^{(1)[\bar{B}_1\bar{B}_2]}_{[IJ]} \equiv (\Sigma_{IJ})^{A_1A_2}F^{(1)[\bar{B}_1\bar{B}_2]}_{\{A_1A_2\}}$. At $n = 2$, in terms of $SO(3,C)$ there remains only $F^{(0)}_{[ij]} \equiv (\sigma_{ij})^{A_1A_2}F^{(0)}_{\{A_1A_2\}}$ or, equivalently, $F^{(0)}_i \equiv 1/2\epsilon_{ijk}F^{(0)}_{[jk]}$.

For an unbroken gauge theory with fermions, the generic gauge, fermion, and mass terms of the Lagrangian $\mathcal{L} = \mathcal{L}_G + \mathcal{L}_F + \mathcal{L}_M$ are, respectively,

$$\mathcal{L}_G = \sum_{s=0,1}(c_s + i\theta_s)F^{(s)}F^{(s)} + \text{h.c.}, \tag{22}$$

$$\mathcal{L}_F = \frac{i}{2}\sum_{\pm}(\psi^{\pm})^\dagger \overset{\leftrightarrow}{D}\psi^{\pm},$$

$$\mathcal{L}_M = \psi^+ m_0\psi^- + \sum_{\pm}\psi^{\pm}m_{\pm}\psi^{\pm} + \text{h.c.},$$

where $F^{(s)}F^{(s)} \equiv F^{(s)[\bar{B}_1\bar{B}_2]}_{\{A_1A_2\}}F^{(s)\{A_2A_1\}}_{[\bar{B}_2\bar{B}_1]}$ and $\overset{\leftrightarrow}{D}$ is the covariant derivative acting to the right and to the left with different signs. In the Lagrangian, m_0 is the generic Dirac mass, $m_\pm$ are Majorana masses, and c_s and θ_s are the real gauge parameters. One of the parameters c_s, supposedly $c_0 \neq 0$, can be normalized at will. Equation (22) results in the following generalization of the Dirac equation,

$$iD^C{}_{\bar{B}}\psi^{\pm}_C = m_0^\dagger\bar{\psi}^{\pm}_{\bar{B}} + \sum_{\pm} m^\dagger_{\pm}\bar{\psi}^{\mp}_{\bar{B}}, \tag{23}$$

and the pair of Maxwell equations ($c_0 \equiv 1$ and $c_1 = \theta_1 = 0$, for simplicity)

$$(1+i\theta_0)D^{C\bar{B}}F^{(0)}{}_{\{CA\}} - \text{h.c.} = 0, \tag{24}$$

$$(1+i\theta_0)D^{C\bar{B}}F^{(0)}{}_{\{CA\}} + \text{h.c.} = 2gJ_A{}^{\bar{B}},$$

with the fermion Hermitian current J given by (8).

The tensors $F^{(s)}$, $s = 1,2$, are non-Hermitian, but under restriction by the maximal compact subgroup $Sp(2l)$ (when there is no distinction between the indices of different kinds), they split into a pair of the Hermitian ones $E^{(s)}$ and $B^{(s)}$ as follows: $F^{(s)} = E^{(s)} + iB^{(s)}$. Here, one has $E^{(s)[Y_1Y_2]}_{\{X_1X_2\}} \equiv (1/2)\big[F^{(s)[Y_1Y_2]}_{\{X_1X_2\}} + \big(F^{(s)\{X_2X_1\}}_{[Y_2Y_1]}\big)^*\big]$ and $B^{(s)[Y_1Y_2]}_{\{X_1X_2\}} \equiv (1/2i)\big[F^{(s)[Y_1Y_2]}_{\{X_1X_2\}} - \big(F^{(s)\{X_2X_1\}}_{[Y_2Y_1]}\big)^*\big]$ with $E^{(s)[Y_1Y_2]}_{\{X_1X_2\}} = (E^{(s)\{X_2X_1\}}_{[Y_2Y_1]})^*$ and similarly for $B^{(s)}$. Introducing the duality transformation $F^{(s)} \to \tilde{F}^{(s)} \equiv -iF^{(s)}$, so that $\tilde{E}^{(s)} = B^{(s)}$ and $\tilde{B}^{(s)} = -E^{(s)}$, one gets $\text{Re}F^{(s)}F^{(s)} = E^{(s)2} - B^{(s)2}$ and $\text{Im}F^{(s)}F^{(s)} = \text{Re}\tilde{F}^{(s)}F^{(s)} = 2E^{(s)}B^{(s)}$. Though the splitting into $E^{(s)}$ and $B^{(s)}$ is noncovariant with respect to the whole $Sp(2l,C)$, the duality transformation is covariant. The tensors $E^{(s)}$ and $B^{(s)}$ are the counterparts of the ordinary electric and magnetic strengths, and θ_0 is the counterpart of the ordinary T-violating θ parameter for the $n = 2$ case. Thus, θ_1 is an additional T-violating parameter at $n > 2$. Note that, in the framework of symplectic extension, the electric and magnetic strengths stay on equal footing. This is to be compared with the pseudoorthogonal extension where these strengths have an unequal number of components at $d \neq 4$, and hence there is no natural duality relation between them. The electric–magnetic duality of the gauge fields (for imaginary time) plays an important role in the study of the topological structure of the gauge vacuum in four spacetime dimensions. Therefore, a similar study might be applicable to the case of extended symplectic spacetimes with arbitrary $l > 1$.

Field equations (23) and (24) are valid in the flat extended spacetime or, otherwise, refer to the inertial

[5)]For simplicity, we do not distinguish in what follows the relative column positions of the indices of different kinds.

local frames. To go beyond, one can introduce the Hermitian local frames $e_{\alpha A}{}^{\bar{B}}(X)$, $e_{\alpha A}{}^{\bar{B}} = (e_{\alpha B}{}^{\bar{A}})^*$, with $\alpha = 0, 1, \ldots, n^2 - 1$ being the world vector index, and the real world coordinates $x_\alpha \equiv e_\alpha{}^{A}{}_{\bar{B}} X_A{}^{\bar{B}}$, as well as the generally covariant derivative $\nabla_\alpha(e)$. Now, (22) can be adapted to the $d = n^2$ dimensional curved spacetime equipped with a pseudo-Riemannian structure (the real symmetric metrics $g_{\alpha\beta}(x) = e_\alpha{}^{A}{}_{\bar{B}} e_{\beta A}{}^{\bar{B}}$) or to the curved coordinates. In line with [9], one can also supplement gauge equations by the generalized gravity equations in the curved symplectic spacetime. But now the group of equivalence of the local frames (structure group) is not the whole pseudoorthogonal group $SO(d_-, d_+)$ but only its part isomorphic to $Sp(2l, C)$. It leaves more independent components in the local symplectic frames compared to the pseudo-Riemannian frames. The number of components in the latter ones being equal to that in the metrics, the symplectic gravity is not in general equivalent to the metric one. The curvature tensor in the symplectic case, like the gauge strength one, splits additionally into irreducible parts which can a priori enter the gravity Lagrangian with independent coefficients. The ultimate reason for this may be that, in the symplectic approach, the spacetime is likely to be not a fundamental entity. Therefore, gravity as a generally covariant theory of the spacetime distortions is to be meant just as an effective theory. The latter admits the existence of a number of free parameters, the choice of which should be determined, in principle, by the physical contents of the effective theory and should ultimately be clarified by an underlying theory.

9. CONCLUSION

The hypothesis that the symplectic structure of spacetime is superior to the metric one provides, in particular, the rationale for the four-dimensionality and $1 + 3$ decomposition of the ordinary spacetime. When looking for the extradimensional spacetime extensions, the hypothesis predicts the discrete sequence of metric spacetimes of fixed dimensionalities and signatures. The symplectic spacetime extension proves to be not a priori inconsistent and provides a viable alternative to the pseudoorthogonal one. The emerging dynamics in the extended spacetime is largely unorthodox and possesses a lot of new features. The physical contents of the scheme require further investigation. But beyond the physical adequacy of the extradimensional spacetimes, by generalizing from the basic case $l = 1$ to its counterpart for general $l > 1$, a deeper insight into the nature of the four-dimensional spacetime itself may be attained.

ACKNOWLEDGMENTS

The author is grateful to V.V. Kabachenko for useful discussions.

REFERENCES

1. R. F. Streater and A. F. Wightman, *PCT, Spin and Statistics, and All That* (Benjamin, New York, 1964).
2. R. Penrose and W. Rindler, *Spinors in Spacetime* (Cambridge Univ. Press, Cambridge, 1984).
3. *An Introduction to Kaluza–Klein Theory,* Ed. by H. C. Lee (World Sci., Singapore, 1982).
4. M. B. Green, J. H. Schwartz, and E. Witten, *Superstring Theory* (Cambridge Univ. Press, Cambridge, 1982).
5. Yu. F. Pirogov, Preprint No. 88-199, IHEP (Protvino, 1988).
6. S. Helgason, *Differential Geometry and Symmetric Spaces* (Academic, New York, 1962).
7. Yu. F. Pirogov and O. V. Zenin, Eur. Phys. J. C **10**, 629 (1999); hep-ph/9808396.
8. F. J. Yndurain, Phys. Lett. B **256**, 15 (1991).
9. R. Utiyama, Phys. Rev. **101**, 1597 (1956).

Physics of Atomic Nuclei, Vol. 66, No. 1, 2003, pp. 143–151. Translated from Yadernaya Fizika, Vol. 66, No. 1, 2003, pp. 146–154.

ELEMENTARY PARTICLES AND FIELDS
Theory

Relativistic Treatment of the Hard-Bremsstrahlung Process $pp \to pp\gamma$ and Possibility of Discriminating between Different Types of Nucleon–Nucleon Interaction

N. A. Khokhlov[1)], V. G. Neudatchin[*], and V. A. Knyr[1)]

Institute of Nuclear Physics, Moscow State University, Vorob'evy gory, Moscow, 119899 Russia

Received June 6, 2001; in final form, November 16, 2001

Abstract—Previous results of the present authors, who showed that observables of the hard-bremsstrahlung process $pp \to pp\gamma$ at beam energies ranging between 350 and 500 MeV are highly sensitive to the type of nucleon–nucleon potential (meson-exchange potentials versus the Moscow potential), are generalized by means of a relativistic analysis, which includes, above all, a modified current operator. As a result, the relevant cross sections decrease, while their angular dependence changes. However, the above high sensitivity to the type of potential survives and becomes quite significant even at the lowest beam energy of 280 MeV considered here, for which there are experimental data. They seem to favor one of the versions of the Moscow potential. © *2003 MAIK "Nauka/Interperiodica"*.

1. INTRODUCTION

There are two radically different types of models of the nucleon–nucleon interaction. The first type, a traditonal one, employs phenomenological meson-exchange potentials, which date back to the famous idea put forth by Yukawa. They involve a repulsive core associated with vector-meson exchange. We will consider two currently employed potentials of this type, the Paris and the Nijmegen one (see [1] and [2], respectively). Potentials that are close to them in a pragmatic aspect were obtained in some quark models either on the basis of the resonating-group method [3] or on the basis of a superposition of different $6q$ shell configurations [4].

The second type relies on the deep-attraction Moscow potential involving forbidden states [5–8]. The Moscow potential features no repulsive core, but, for S and P partial waves, there is a node in the place of it, along with a loop of the radial wave function to the left of this node. In terms of such a potential supplemented with an imaginary part, it is possible to describe data on nucleon–nucleon scattering (differential cross sections and polarizations) up to a laboratory-energy value of 5 to 6 GeV [6] (with a meson-exchange potential, one can do this only up to 2 GeV [9]), the S- and P-wave phase shifts having positive values throughout this range (in accordance with the generalized Levinson theorem, the triplet S-wave phase shift at zero energy is equal to 2π and so on). Microscopically, the Moscow potential corresponds to the situation where, owing to a nonperturbative instanton-induced strong quark–quark interaction [10], the nucleon–nucleon system at short distances is dominated, for example, by the excited quark configuration $s^4p^2[42]_X[42]_{ST}$ (the notation for the types of symmetry is identical to that in [10, 11]). This interaction is attractive if the wave function is symmetric with respect to the interchange of the coordinates of two quarks in ST space, but it is repulsive if the wave function is antisymmetric. In the region of nucleon overlap, the above configuration can therefore have a much lower energy than the $s^6[6]_X[2^3]_{ST}$ configuration. Other reasons for the dominance of the s^4p^2 configuration are also possible (for example, the effect of the virtual color-excitation channel $NN \leftrightarrow cc$ featuring a very strong attraction of color dipoles) [11, 12]. Such a situation, should it be prevalent, will manifest itself in various processes probing the baryon–baryon composition of the deuteron [13], since the components involved in that case will include $N^*(1/2^-, 3/2^-)N^*(1/2^-, 3/2^-)$, $N^{**}(1/2^+)N$ [$N^{**}(1/2^+)$ is the Roper resonance of S-wave relative motion], and $N^*(1/2^-, 3/2^-)N$ in the P wave.

In our preceding studies [14–16], we showed that the hard-bremsstrahlung process $pp \to pp\gamma$ occurring at rather modest beam energies, those between 350 to 500 MeV, must clearly distinguish between meson-exchange potentials, on one hand, and the Moscow potential, on the other hand. In formal terms, this is because potentials belonging to these two

[1)]Khabarovsk State University of Technology, Tikhookeanskaya ul. 136, Khabarovsk, 680034 Russia.
[*]e-mail: neudat@nucl-th.sinp.msu.ru

types are not phase-equivalent—that is, the S matrix for the Moscow potential has a pole corresponding to a strongly bound forbidden state, and the corresponding S- and P-wave phase shifts at low energies differ by π from those for the meson-exchange potentials. As was indicated above, these distinctions could be recognized [5, 6] by analyzing elastic-scattering data over the widest energy region extending up to 5 or 6 GeV, but by no means is this circumstance alone sufficient for the purposes pursued here—fortunately, the hard-bremsstrahlung process $pp \to pp\gamma$ opens an independent possibility for this.

At the same time, it was indicated in [17] that the hard-bremsstrahlung process in question furnishes virtually no evidence (and much less the corresponding soft process) for recognizing different meson-exchange-potential versions, which are nearly phase-equivalent.

Here, we pursue further investigations begun in [14–16], going over from a nonrelativistic to a relavistic treatment. This makes it possible to remove the ambiguity in nonrelativistic results for the Moscow potential, which were different in two different c.m. frames of two protons, the primary and secondary ones. This ambiguity was insignificant at the beam energy of $E_0 = 280$ MeV, but it became quite pronounced at $E_0 = 450$ MeV and very large at $E_0 = 500$ MeV. This suggests that relativistic effects are of great importance there. On one hand, the removal of the above ambiguity does not change our conclusion that the observables of the above hard-bremsstrahlung process are highly sensitive to the form of nucleon–nucleon interaction, thereby strengthening the argument behind this conclusion; on the other hand, relativistic effects do indeed prove to be of great importance (they are quite significant even at the minimum beam-energy value of $E_0 = 280$ MeV considered here).

2. DESCRIPTION OF FORMALISM

We rely on the relativistic quasipotential equation introduced in [18]. In the c.m. frame, it has the form

$$\left(\frac{\hat{\mathbf{p}}^2}{m} + \hat{V}\right)\chi(\mathbf{r}) = \frac{M^2 - 4m^2}{4m}\chi(\mathbf{r}) = \frac{1}{2}E_{\rm lab}\chi(\mathbf{r}). \quad (1)$$

Here, $\hat{V}$ is the phenomenological nucleon–nucleon potential being discussed (in general, it is nonlocal), $M(\mathbf{q}^2) = 2w(\mathbf{q}) = 2(m^2 + \mathbf{q}^2)^{1/2}$ in the mass of the system under consideration (m is the nucleon mass), and $\mathbf{q}$ is the momentum of the relative motion of the nucleons involved; in the following, we employ the well-known relation [19] $E = \sqrt{M^2 + \mathbf{P}^2}$, where the total energy $E = \sqrt{m^2 + \mathbf{p}_1^2} + m$ of the system in the laboratory frame, the total momentum $\mathbf{P} = \mathbf{p}_1$, and the kinetic energy $E_{\rm lab} = \sqrt{m^2 + \mathbf{p}_1^2} - m$ of the incident nucleon are expressed in terms of its laboratory momentum $\mathbf{p}_1$. The quasipotential representation [20] corresponds to the realization specified by the equations $\hat{\mathbf{p}} = -i\partial/\partial\mathbf{r}$ and $\hat{V} = \hat{V}(\mathbf{r})$. This enables us to use partly the formalism of our previous investigations reported in [14–16]. As to the main relativistic effects, they are absorbed in the current operator, which we now proceed to discuss.

The bremsstrahlung amplitude A_{if} is given by the well-known expression [14–16]

$$\delta(E_i - E_f - k_0)\delta^3(\mathbf{P}_i - \mathbf{P}_f - \mathbf{k})A_{if} \quad (2)$$
$$= \sqrt{\frac{2\pi}{k_0}}\int d^3x\, \langle P_f\chi_f|\varepsilon_\mu^* \hat{J}^\mu(x)\,|P_i\chi_i\rangle\, e^{-i\mathbf{k}\cdot\mathbf{x}}.$$

Our further analysis is based on the pointlike form of relativistic dynamics [21–23], where the interaction is present only in the components of the operator of the 4-momentum P of the two-nucleon system in question.

The formulas for the matrix elements of the current have an especially simple form in the reference frame where the sum of the 3-vectors representing the velocities of the centers of mass of the initial and the final nucleon–nucleon system vanishes; that is,

$$\mathbf{G}_i + \mathbf{G}_f = 0 \quad (3)$$

with $\mathbf{G} = \mathbf{P}/M$. In this reference frame, we have [23]

$$\langle P_f\chi_f|\,\hat{J}_\mu(x)\,|P_i\chi_i\rangle \quad (4)$$
$$= 2\sqrt{M_iM_f}e^{i(P_f - P_i)x}\,\langle\chi_f|\,\hat{j}_\mu(\mathbf{k})\,|\chi_i\rangle\,,$$

where $k = (k_0, \mathbf{k})$ is the photon 4-momentum. Thus, we can recast the amplitude in (2) into the form

$$A_{if} = \sqrt{\frac{2\pi}{k_0}}\cdot 16\pi^3\sqrt{M_iM_f}\,\langle\chi_f|\,\varepsilon_\mu^*\hat{j}^\mu(\mathbf{h})\,|\chi_i\rangle\,, \quad (5)$$

where integration is performed only with respect to the internal variables of the proton–proton system. In the transverse gauge, where

$$\varepsilon = (0, \boldsymbol{\varepsilon}), \quad (\boldsymbol{\varepsilon}\cdot\mathbf{k}) = 0, \quad (6)$$

the situation is simplified in that the component $j_0(\mathbf{k})$ ceases to play any significant role. As is shown in Appendix 1, the expression for the current $\hat{\mathbf{j}}(\mathbf{k})$ in the reference frame specified by Eq. (3) has the form

$$\hat{\mathbf{j}}(\mathbf{k}) = 2iF_m e \quad (7)$$
$$\times\left(\frac{m}{w}[\mathbf{S}\times\mathbf{h}] + \frac{w-m}{w\mathbf{q}^2}[\mathbf{q}\times\mathbf{h}](\mathbf{q}\cdot\mathbf{S})\right)$$
$$+ 2ie\left(\frac{F_m}{mw} + \frac{F_e}{w(w+m)}\right)(\mathbf{h}\cdot[\mathbf{q}\times\mathbf{S}])\mathbf{q}$$

$$+\frac{F_e e}{w}\mathbf{q}(I_1(\mathbf{h})-I_2(\mathbf{h}))-\frac{2F_e e(\mathbf{h}\cdot\mathbf{q})}{wm}\mathbf{q}$$
$$+\frac{M_i-M_f}{M_i+M_f}\cdot 2ie\left(\frac{F_m}{m}+\frac{F_e}{w+m}\right)[\mathbf{q}\times\mathbf{T}],$$

where, by virtue of relation (6), there are no vector terms parallel to $\mathbf{k}$; $(w-m)/w\mathbf{q}^2=\mathbf{q}^2/w(w+m)\mathbf{q}^2=1/w(w+m)$; $\mathbf{S}=\mathbf{s}_1+\mathbf{s}_2$; $\mathbf{T}=\mathbf{s}_1-\mathbf{s}_2$; $F_e(\mathbf{k})$ and $F_m(\mathbf{k})$ are, respectively, the electric and the magnetic form factor for the proton; $\mathbf{h}=2(M_iM_f)^{1/2}(M_i+M_f)^{-2}\mathbf{k}$; and

$$I_j(\mathbf{h})\chi(\mathbf{q}) \tag{8}$$
$$=\begin{cases}\chi(\mathbf{d}_1)=\chi\left(\mathbf{q}-\dfrac{2\mathbf{h}}{1-\mathbf{h}^2}\{w(\mathbf{q})-\mathbf{h}\cdot\mathbf{q}\}\right), j=1,\\ \chi(\mathbf{d}_2)=\chi\left(\mathbf{q}+\dfrac{2\mathbf{h}}{1-\mathbf{h}^2}\{w(\mathbf{q})-\mathbf{h}\cdot\mathbf{q}\}\right), j=2.\end{cases}$$

The nonrelativistic limit of formula (7), where $|\mathbf{h}|\ll m$ and $|\mathbf{q}|\ll m$, was used in our previous studies reported in [14–16].

The way in which the operator $I_j(\mathbf{h})$ acts in the coordinate representation can be expressed as

$$I_j(\mathbf{h})\chi(\mathbf{r})=\exp[\mp 2i(\boldsymbol{\rho}\cdot\mathbf{h})\sqrt{m^2+\hat{\mathbf{p}}^2}]\chi(\mathbf{r})|_{\boldsymbol{\rho}=\mathbf{r}} \tag{9}$$

($\hat{\mathbf{p}}=-i\boldsymbol{\nabla}$), which can be verified by applying this operator to a plane wave. Of course, we use the series expansion

$$I_j(\mathbf{h})=e^{\mp 2i(\boldsymbol{\rho}\cdot\mathbf{h})}\left[1+i(\boldsymbol{\rho}\cdot\mathbf{h})\frac{\hat{\mathbf{p}}^2}{m}+\ldots\right]\Big|_{\boldsymbol{\rho}=\mathbf{r}} \tag{10}$$

(the substitution $\boldsymbol{\rho}\to\mathbf{r}$ is made upon applying the Laplace operator).

It is convenient to transform the matrix element appearing in (5) as follows:

$$\langle\chi_f|\,\varepsilon_\mu^*\hat{j}^\mu(\mathbf{h})\,|\chi_i\rangle=\langle\chi_f|\,\boldsymbol{\varepsilon}^*\hat{\mathbf{j}}(\mathbf{h})\,|\chi_i\rangle \tag{11}$$
$$=(\langle\chi_f|-\langle\phi_f|)\boldsymbol{\varepsilon}^*\hat{\mathbf{j}}(\mathbf{h})(|\chi_i\rangle-|\phi_i\rangle)$$
$$+\langle\phi_f|\,\boldsymbol{\varepsilon}^*\hat{\mathbf{j}}(\mathbf{h})\,|\chi_i\rangle+\langle\chi_f|\,\boldsymbol{\varepsilon}^*\hat{\mathbf{j}}(\mathbf{h})\,|\phi_i\rangle\,.$$

Here, $|f_i\rangle$ and $|\phi_f\rangle$ are the wave functions that describe the relative motion for noninteracting particles (plane waves), the corresponding relative momenta being $\mathbf{q}_i$ for the former and $\mathbf{q}_f$ for the latter. On the whole, this representation makes it possible improve the convergence of the partial-wave expansions of the functions $\chi(\mathbf{r})-\phi(\mathbf{r})$ (see our analysis in [14]). Other matrix elements in (11), where the function $\phi_i(\mathbf{r})$ [$\phi_f(\mathbf{r})$] appears on the left- or on the right-hand side, are calculable quite straightforwardly. The action of the operator $\hat{\mathbf{p}}I_j(\mathbf{h})$, for example, on the function $|\chi_i(\mathbf{r})-\phi_i(\mathbf{r})\rangle$ in the coordinate representation can be written in the form

$$\hat{\mathbf{p}}I_j(\mathbf{h})\,|\chi_i-\phi_i\rangle \tag{12}$$
$$=-i\boldsymbol{\nabla}\left[\exp[\mp 2i\mathbf{h}\cdot\mathbf{r}\sqrt{m^2+\mathbf{q}_i^2-mV_{\tilde{E}}(\mathbf{r})}]\chi_i\right.$$
$$\left.-\exp[\mp 2i\mathbf{h}\cdot\mathbf{r}\sqrt{m^2+\mathbf{q}_i^2}]\phi_i\right],$$

which is the most convenient for applications in Eq. (1).

Further, relevant radial integrals are broken down into two parts as $\int_0^R$ and $\int_R^\infty$, where R is chosen to be a minimal large value at which the inequality $|mV_{\tilde{E}}(R)|\ll m^2+\mathbf{q}^2$ is satisfied (for example, $R=3$ fm for the Moscow potential). In evaluating $\int_0^R$ integrals, use is made of the expansion of, for example, the first exponential in powers of $(\mathbf{q}_i^2-mV_{\tilde{E}}(r))^n$ in the spirit of formula (10). The convergence is fast, and quite an acceptable level of precision is achieved at values as low as $n\sim 3$. In Appendices 1 and 2, we illustrate the technique for computing the matrix elements of other components of the current operator. Although this computational scheme seems cumbersome, it is not more involved than a calculation in the momentum representation, where there is also an unwieldy technical element associated with integration over the solid angles specifying the orientations of the vectors $\mathbf{q}$ and $\mathbf{q}\pm 2\mathbf{h}w(\mathbf{q})$ that has to be performed in going over to one-dimensional radial integrals.

3. RESULTS OF THE CALCULATION AND DISCUSSION

The differential cross sections for the bremsstrahlung process $pp\to pp\gamma$ are displayed in Figs. 1–6 for six values of energy. Here, the geometry (it was realized in experiments reported in [24]) corresponds to nearly the hardest photons.

No calculations within the full relativistic formalism used here [22, 23] have been performed thus far with the current operator (7)—the relativistic corrections introduced in [25] concerned only spin variables, their inclusion reducing the cross section by approximately 25%.

We would like to highlight the following special features of the results displayed in Figs. 1–6. First, relativistic effects are significant even at the beam energy of $E_0=280$ MeV; at higher energies, their impact is so strong that the general pattern changes completely, the cross section becoming by and large much smaller. Specifically, the distinct forward and backward maxima that arise in the differential cross sections computed on the basis of the nonrelativistic

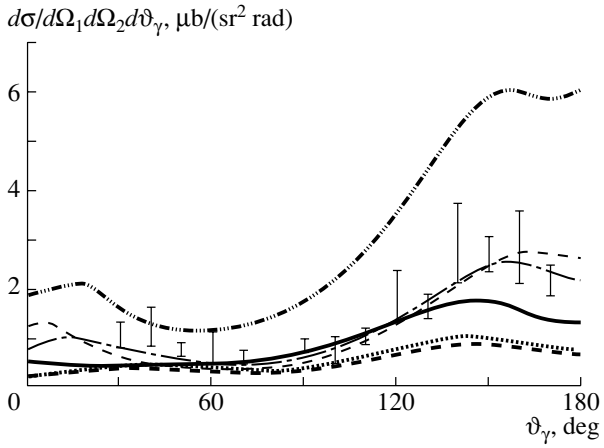

Fig. 1. Differential cross section for the process $pp \to pp\gamma$ as a function of the photon emission angle at $E_0 = 280$ MeV for $\theta_1 = 12.4°$ and $\theta_2 = 12.0°$ in coplanar geometry (the product photon is emitted toward the angle θ_2). The results of the nonrelativistic calculations are shown by the thin short-dashed curve for the Moscow potential MP-92 and by the thin dash-and-dot curve for the Paris potential (here, the results of nonrelativistic calculations in the c.m. frame of primary protons are very close to those in the c.m. frame of secondary protons). The results of the relativistic calculations are represented by the thick solid curve for the Moscow potential MP-92, by the thick dash-and-three-dot curve for the Moscow potential MP-97, by the thick long-dashed curve for the Paris potential, and by the thick dotted curve for the Nijmegen potential.

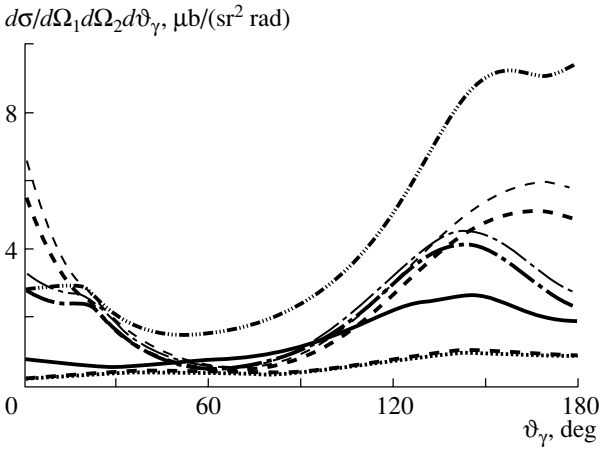

Fig. 2. As in Fig. 1, but for the beam energy of $E_0 = 320$ MeV. Here, two curves are presented for each version of the nonrelativistic calculation, the upper (lower) one being computed in the c.m. frame of secondary (primary) protons.

approach [14–16] with the Moscow potential MP-92 [7] and which stem from the nodal character of the radial wave function for the P-wave state of relative motion survive in the results of the relativistic calculation only for the Moscow potential MP-97 [8], which features the maximum possible amplitude of the aforementioned short-range oscillation in the P wave. Second, there remains a large distinction between the cross sections for meson-exchange potentials, on one hand, and the cross sections for the Moscow potential, on the other hand. This distinction is also associated with the special features of the P wave in the Moscow potential that were mentioned above; that is, these features still strongly manifest themselves, but their manifestations in the relativistic consideration differ from those in the nonrelativistic treatment. Naturally, the problem of distinctions in the nonrelativistic treatment between the cross sections in the c.m. frame of primary protons and those in the c.m. frame of secondary protons [14–16] becomes nonexistent in the relativistic approach.

The results for the beam energy of $E_0 = 280$ MeV in Fig. 1 are of particular importance, since experimental data already available at this energy value [24] become critical to the choice of nucleon–nucleon potential within the relativistic treatment. Specifically, we can see that, while, in the nonrelativistic approach [14–16], the theoretical results for the Moscow potential MP-92 are very close to those for the meson-exchange potentials considered here, in the relativistic approach, the cross section in the backward hemisphere for MP-92 is twice as large as those for the meson-exchange potentials, thereby being much closer to the experimental value. Nevertheless, it is instructive to compare the cross sections for the Moscow potentials MP-92 and MP-97. As can be seen from Fig. 1, the results for MP-97 are in sharp disagreement with experimental data, but these results are of great value from the methodological point of view, furnishing a measure of the formidable effect that can arise in response to a purposely increasing the amplitude of the short-range oscillation (loop) of the wave function in the P wave to an extent that is

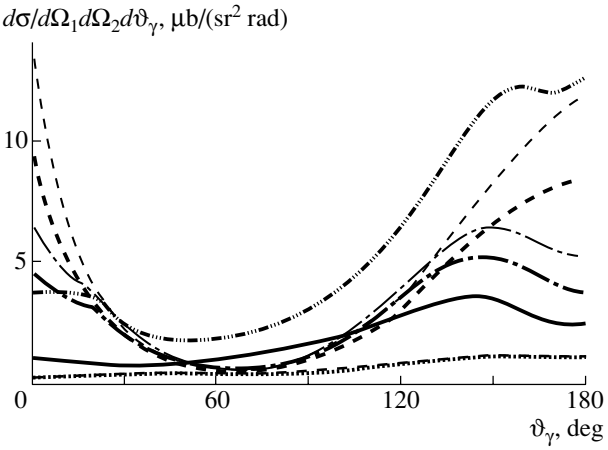

Fig. 3. As in Fig. 2, but for the beam energy of $E_0 = 350$ MeV.

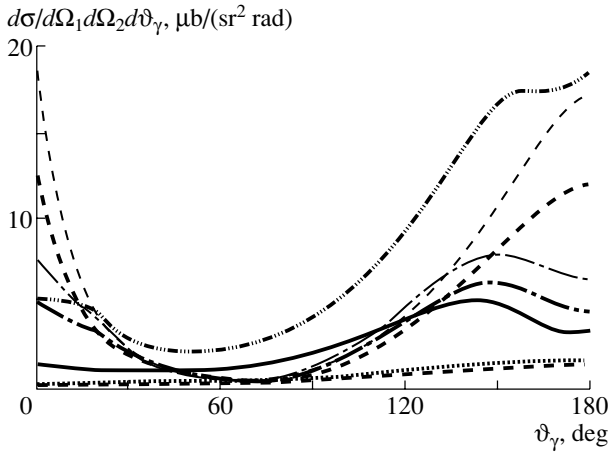

Fig. 4. As in Fig. 2, but for the beam energy of $E_0 =$ 400 MeV.

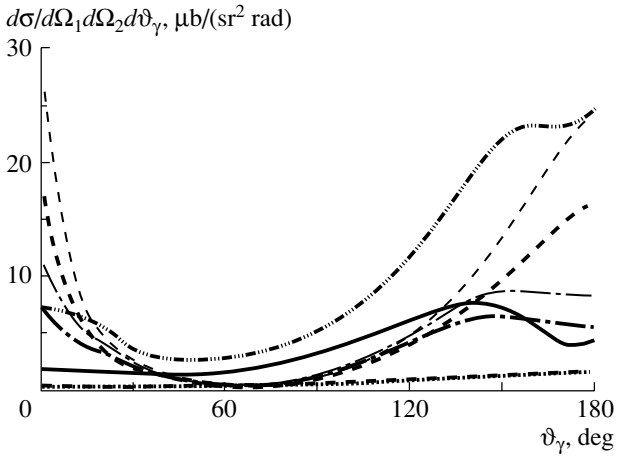

Fig. 5. As in Fig. 2, but for the beam energy of $E_0 =$ 450 MeV.

still compatible with obtaining a correct description of the energy dependence of the P-wave phase shifts for nucleon–nucleon scattering. It can be seen that a moderate increase in the depth of the potentials for the P waves in the MP-92 version—this leads to a comparatively small increase in the amplitude of this loop—fits the theoretical curve to experimental data. It should be emphasized that meson-exchange potentials do not possess such a resource. Yet, these considerations are of only a preliminary character, and of greatest theoretical interest is of course a thorough test of the above theoretical concepts at different energies. Thus, the problem of experimentally investigating the hard-bremsstrahlung process in question at intermediate energies of $E_0 = 300$–500 MeV remains pressing in the context of a comparison of potentials belonging to the above two radically different types.

The hard-bremsstrahlung process in question is virtually insensitive to the node that the S wave develops at $R = 0.5$–0.6 fm in the Moscow potential [5–8], and this important issue is worthy of experimental investigation by a completely different method, that which would employ the quasielastic-knockout reaction $^2\mathrm{H}(e, e'p)n$ at high energies over a wide region of spectator-neutron recoil momenta that extends up to 1 GeV/c (such data are already available [26]). In analyzing experimental data with the aim of extracting the momentum distribution of nucleons in the deuteron, it should be borne in mind, however, that the Moscow potential leads here to a strong final-state neutron–proton interaction.

In all probability, the important experiments of a different type that were reported in [27] and which were aimed at studying the reaction $^2\mathrm{H} + \gamma \to n + p$ at energies as high as those in the region $E_\gamma \geq$ 2 GeV, where the contribution of meson-exchange currents is suppressed and where the wave function describing the relative motion in the neutron–proton system can therefore be probed directly, are sensitive (the inclusion of final-state interaction is mandatory here) to the presence of wave-function nodes both in the initial S-wave state and in the important final-state partial P wave. We are going to analyze both types of the above experiments in the future.

In conclusion, we note that our previous articles [15, 16] contained the erroneous conclusion that, within the nonrelativistic treatment, the results for the hard-bremsstrahlung process $pp \to pp\gamma$ that are obtained with the nucleon–nucleon potential proposed in [28] comply with those for the earlier versions of the Moscow potential that were discussed here and which are characterized, as was indicated above, by a large amplitude of the short-range oscillation in the P wave. In fact, the short-range oscillation of the wave function describing the relative motion of nucleons in

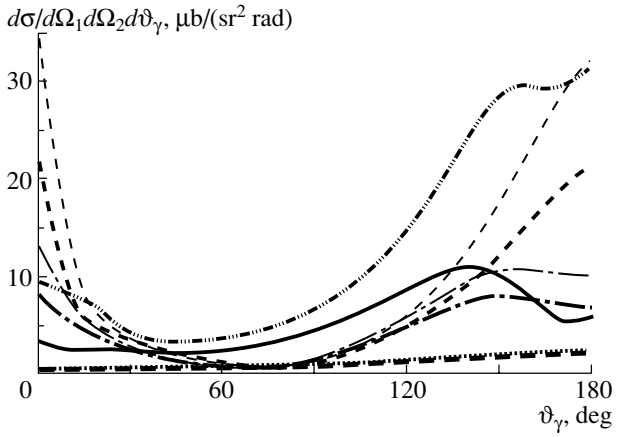

Fig. 6. As in Fig. 2, but for the beam energy of $E_0 =$ 500 MeV.

the P-wave state of the continuum is very strongly suppressed in the nonlocal potential from [28], and the differential cross section for the above process treated with this potential is close to that computed with the Nijmegen potential. This circumstance was pointed out by M.A. Shikhalev, to whom we also owe a valuable discussion on the role of different partial waves in the formation of the amplitude for the process $pp \to pp\gamma$.

ACKNOWLEDGMENTS

This work was supported in part by the Contest Center for Basic Research in Natural and Exact Sciences at St. Petersburg State University (grant no. E00-3.3-67).

APPENDIX 1

Here, we will derive formula (7), relying on the results presented in [23] and supplementing them. For a particle of 4-momentum p, we define the Lorentz transformation associated with a boost g as $p \to L(\alpha(g))p$, where [29]

$$\alpha(g) = \frac{g^0 + 1 + \boldsymbol{\sigma}\cdot\boldsymbol{g}}{\sqrt{2(g^0+1)}}. \tag{A.1}$$

Here, g is the 4-velocity, while $\boldsymbol{\sigma} = (\sigma_x, \sigma_y, \sigma_z)$ are the Pauli matrices. The transformation in question is realized in the following way [29]: associating the matrix $\check{p} = \sigma^\mu p_\mu$ with the vector p, we have

$$p_0 = (\check{p}_{11} + \check{p}_{22})/2, \quad p_1 = (\check{p}_{12} + \check{p}_{21})/2, \quad p_2 = (-\check{p}_{12} + \check{p}_{21})/2i, \quad p_3 = (\check{p}_{11} - \check{p}_{22})/2. \tag{A.2}$$

The transformation

$$\check{p} \to \alpha(g)\check{p}\alpha(g)^+, \tag{A.3}$$

together with formulas (A.2), describes the action of the boost $p \to L(\alpha(g))p$.

Further, we define the Poincaré group transformation characterized by a 4-shift a and a 4-rotation l as [23]

$$U(a,l)\varphi(g) = \exp(img'a)D(\mathbf{s};\alpha(g)^{-1}l\alpha(g'))\varphi(g'), \tag{A.4}$$

where $\varphi(g)$ is a normalizable spinor function, $\mathbf{s}$ is the spin operator, and $g' = L(l)g$. In our case of spin-1/2 particles, we are dealing with the fundamental representation [29]; that is,

$$D(\mathbf{s}; l\alpha(g)^{-1}l\alpha(g')) = \alpha(g)^{-1}l\alpha(g'). \tag{A.5}$$

We specify the operator l by going over to a two-particle system. Here, we have the particle 4-momenta $p_i = m_i g_i$ $(i = 1, 2)$ and the c.m. 4-velocity G. In the c.m. frame, the particle momenta are given by [23]

$$q_i = L[\alpha(G)]^{-1}m_i g_i, \quad \mathbf{q}_1 = \mathbf{q} = -\mathbf{q}_2. \tag{A.6}$$

Bearing in mind that the reaction $pp \to pp\gamma$ is the main subject of our analysis and choosing the coordinate frame specified by Eq. (3), we consider the general expression for the current within the pointlike form of dynamics [23]:

$$\begin{aligned} j^\nu(\mathbf{h}) = \sum_{i=1,2} L\left(L[\alpha(f)]\frac{q_i}{m_i}, L[\alpha(f')]\frac{d_i}{m_i}\right)^\mu_\nu D\left[\mathbf{s}_k; \alpha\left(\frac{q_k}{m_k}\right)^{-1}\alpha(f)^{-1}\alpha(f')\alpha\left(\frac{d_{ki}}{m_k}\right)\right] \\ \times D\left[\mathbf{s}_i; \alpha\left(\frac{q_i}{m_i}\right)^{-1}\alpha(f)^{-1}\alpha\left(L[\alpha(f)]\frac{q_i}{m_i}, L[\alpha(f')]\frac{d_i}{m_i}\right)\alpha(f_i)\right] j_i^\nu(\mathbf{h}) \\ \times D\left[\mathbf{s}_i; \alpha(f_i')^{-1}\alpha\left(L[\alpha(f)]\frac{q_i}{m_i}, L[\alpha(f')]\frac{d_i}{m_i}\right)\alpha(f')\alpha\left(\frac{d_i}{m_i}\right)\right]\frac{m_i w_i(\mathbf{q}_i)}{w_i(\mathbf{d}_i)}\left(\frac{M(\mathbf{d}_i)}{M(\mathbf{q}_i)}\right)^{3/2} I_i(\mathbf{h}). \end{aligned} \tag{A.7}$$

In this formula, $k = 2$ if $i = 1$ and $k = 1$ if $i = 2$.

The quantities f are defined as

$$f = L(G,G')^{-1}G, \quad f' = L(G,G')^{-1}G'. \tag{A.8}$$

These are the 4-velocities of the center of mass in the initial and the final state in the coordinate frame specified by Eq. (3). We also have $f^2 = f'^2 = 1$, $\mathbf{f} + \mathbf{f}' = 0$, $f_0 = f_0' = (1 + \mathbf{f}^2)^{1/2}$; $L(G,G') = L(\alpha(G,G'))$, $\alpha(G,G') = \alpha((G+G')/|G+G'|)$; and $d_1 = (\omega_1(\mathbf{d}_1), \mathbf{d}_1)$, $d_2 = (\omega_2(\mathbf{d}_2), \mathbf{d}_2)$, $d_{12} = L[\alpha(f')^{-1}\times\alpha(f)]q_2 = (\omega_2(\mathbf{d}_1), -\mathbf{d}_1)$, $d_{21} = L[\alpha(f')^{-1}\alpha(f)]q_1 = (\omega_1(\mathbf{d}_2), \mathbf{d}_2)$, where $\mathbf{d}_1$ and $\mathbf{d}_2$ are given by (8). Finally, $j_i^\nu(\mathbf{h})$ is the current of particle i. Specifically, we have

$$j_i^0(\mathbf{h}_i) = eF_e\left(-\frac{4m^2\mathbf{h}_i^2}{\sqrt{1-\mathbf{h}_i^2}}\right), \tag{A.9}$$

$$\mathbf{j}_i(\mathbf{h}_i) = -\frac{ie}{\sqrt{1-\mathbf{h}_i^2}} F_m\left(-\frac{4m^2\mathbf{h}_i^2}{\sqrt{1-\mathbf{h}_i^2}}\right)[\mathbf{h}_i \times \mathbf{s}_i],$$

where F_e and F_m are, respectively, the electric and the magnetic form factor, while the vectors $\mathbf{h}_i$ are defined below.

Expression (A.7) does not involve a contribution from particle interaction because, in the pointlike form of dynamics, such a contribution is absorbed in $j_{||}(\mathbf{h})$ [23]; however, this component is removed by the transverse gauge, as was indicated in the main body of the text.

Photon energies E_γ below 500 MeV, which are actually considered in this study, correspond to $|\mathbf{h}| \ll 1$. In this approximation, $F_e(\mathbf{h}) \ll F_e(0) = 1$ and $F_m(\mathbf{h}) \approx F_m(0) = 2.793/m$; we also have

$$d_1 = (w - 2hq_z, q_x, q_y, q_z - 2hw),$$

$$d_2 = (w + 2hq_z, -q_x, -q_y, -q_z - 2hw)$$

($\mathbf{h}$ is directed along the z axis, and $w = w(q) = (m^2 + \mathbf{q}^2)^{1/2}$),

$$d_{12} = (w - 2hq_z, -q_x, -q_y, -q_z + 2hw),$$
$$d_{21} = (w + 2hq_z, q_x, q_y, q_z + 2hw),$$

$$\frac{1}{\omega(\mathbf{d}_1)}\left(\frac{M(\mathbf{d}_1)}{M(\mathbf{q})}\right)^{3/2} = \frac{w - hq_z}{w^2},$$
$$\frac{1}{\omega(\mathbf{d}_2)}\left(\frac{M(\mathbf{d}_2)}{M(\mathbf{q})}\right)^{3/2} = \frac{w + hq_z}{w^2};$$

$$h_1 = h_2 = f_1 = f_2 = \left(1, -\frac{2hq_zq_x}{m(w+m)}, -\frac{2hq_zq_y}{m(w+m)}, \frac{2h(m(w+m)+q_x^2+q_y^2)}{m(w+m)}\right),$$
$$f_1' = f_2' = \left(1, \frac{2hq_zq_x}{m(w+m)}, \frac{2hq_zq_y}{m(w+m)}, -\frac{2h(m(w+m)+q_x^2+q_y^2)}{m(w+m)}\right);$$

$$\left.\begin{aligned} L[\alpha(f)]\frac{q_1}{m} &= m^{-1}(w + hq_z, q_x, q_y, q_z + hw), \\ L[\alpha(f')]\frac{q_1}{m} &= m^{-1}(w - 3hq_z, q_x, q_y, q_z - 3hw); \end{aligned}\right\} \tag{A.10}$$

$$z_1 = \frac{L[\alpha(f)]\frac{d_1}{m} + L[\alpha(f')]\frac{d_1}{m}}{\left|L[\alpha(f)]\frac{q_1}{m} + L[\alpha(f')]\frac{d_1}{m}\right|} = (w - hq_z, q_x, q_y, q_z - hw).$$

For z_2, there is the analogous formula where it is necessary to make the substitution $\mathbf{q} \to -\mathbf{q}$.

Going over to a general notation, where, for example,

$$d_i \cong (w \mp 2(\mathbf{h}\cdot\mathbf{q}), \pm\mathbf{q} - 2\mathbf{h}w), \tag{A.11}$$

we can write the following approximate expression:

$$L\left(L[\alpha(f)]\frac{q_i}{m_i}, L[\alpha(f')]\frac{d_i}{m_i}\right) j_i(h_i) \equiv L(z_i)j_i(h_i) \tag{A.12}$$
$$\cong \left(\frac{F_e e}{m}(w \mp (\mathbf{h}\cdot\mathbf{q})) \pm \frac{4iF_m e}{m^2}(\mathbf{h}\cdot[\mathbf{q}\times\mathbf{s}_i])w, \pm\frac{F_e e}{m}(\mathbf{q} \mp w\mathbf{h})\right.$$
$$\left. + 4iF_m e\left([\mathbf{s}_i\times\mathbf{h}] + \frac{(\mathbf{h}\cdot[\mathbf{q}\times\mathbf{s}_i])\mathbf{q}}{m^2} + \frac{(\mathbf{q}\cdot\mathbf{s}_i)[\mathbf{q}\times\mathbf{h}]}{m(w+m)}\right)\right).$$

Employing, finally, the realization in (A.5), we obtain

$$D\left[s_k, \alpha\left(\frac{q_k}{m_k}\right)^{-1}\alpha(f)^{-1}\alpha\left(\frac{d_{ki}}{m_k}\right)\right] \cong 1 \pm \frac{i}{w+m}(\mathbf{h}\cdot[\boldsymbol{\sigma}_k\times\mathbf{q}]), \tag{A.13}$$

$$D\left[s_k,\alpha\left(\frac{q_i}{m_i}\right)^{-1}\alpha(f)^{-1}\alpha\left(L[\alpha(f)]\frac{q_i}{m_i},L[\alpha(f')]\frac{d_i}{m_i}\right)\alpha(f_i)\right] \tag{A.14}$$

$$\cong D\left[s_k,\alpha(f_i')^{-1}\alpha\left(L[\alpha(f)]\frac{q_i}{m_i},L[\alpha(f')]\frac{d_i}{m_i}\right)^{-1}\alpha(f')\alpha\left(\frac{d_i}{m_i}\right)\right]\cong 1\pm\frac{i(m+2w)}{2m(w+m)}(\mathbf{h}\cdot[\boldsymbol{\sigma}_i\times\mathbf{q}]).$$

Substituting all the above into formula (A.7), we arrive at expression (7) (apart from terms parallel to **h**, which are of little importance).

APPENDIX 2

For a few examples, we will illustrate here the technique for computing the matrix elements of various components of the relativistic current operator. We have

$$(\boldsymbol{\nabla}\cdot\mathbf{S})\boldsymbol{\nabla}_\mu=-\frac{1}{\sqrt{3}}\left[[\boldsymbol{\nabla}\times\boldsymbol{\nabla}]^{(0)}\times\mathbf{S}\right]^{(1)}_\mu \tag{A.15}$$
$$-\sqrt{\frac{5}{3}}\left[[\boldsymbol{\nabla}\times\boldsymbol{\nabla}]^{(2)}\times\mathbf{S}\right]^{(1)}_\mu,$$

$$(\mathbf{h}\cdot[\boldsymbol{\nabla}\times\mathbf{S}])\boldsymbol{\nabla}_\mu=-i\frac{\sqrt{6}}{3} \tag{A.16}$$
$$\times\left(\frac{\sqrt{15}}{2}\left[[[\boldsymbol{\nabla}\times\boldsymbol{\nabla}]^{(2)}\times\mathbf{S}]^{(2)}\times\mathbf{h}\right]^{(1)}_\mu\right.$$
$$+\left[[[\boldsymbol{\nabla}\times\boldsymbol{\nabla}]^{(0)}\times\mathbf{S}]^{(1)}\times\mathbf{h}\right]^{(1)}_\mu$$
$$\left.-\frac{\sqrt{5}}{2}\left[[[\boldsymbol{\nabla}\times\boldsymbol{\nabla}]^{(2)}\times\mathbf{S}]^{(1)}\times\mathbf{h}\right]^{(1)}_\mu\right),$$

$$\langle L_f,S_f=1;J_fM_f|\left[[\boldsymbol{\nabla}\times\boldsymbol{\nabla}]^{(k)}\times\mathbf{S}\right]^{(n)}_\mu \tag{A.17}$$
$$\times f(r)\,|L_i,S_i=1;J_iM_i\rangle=$$
$$C^{J_fM_f}_{J_iM_in\mu}\begin{Bmatrix}L_f & 1 & J_f\\ L_i & 1 & J_i\\ k & 1 & n\end{Bmatrix}\sqrt{6(2(J_i+1)(2n+1))}$$
$$\times\langle L_f|\,|[\boldsymbol{\nabla}\times\boldsymbol{\nabla}]^{(k)}f(r)|\,|L_i\rangle,$$

$$\left\langle L_f\left|\left|[\boldsymbol{\nabla}\times\boldsymbol{\nabla}]^{(2)}\frac{f(r)}{r}\right|\right|L_i\right\rangle \tag{A.18}$$
$$=\frac{\sqrt{2L_f+1}}{\sqrt{6}C^{L_f0}_{L_i020}}\frac{1}{r}\left(\delta_{L_iL_f}\left(-1+\frac{3(2L_i^2+2L_i-1)\sqrt{2(2L_i+1)}}{(2L_i-1)(2L_i+1)(2L_i+3)}\right)\left(\frac{d^2}{dr^2}-\frac{L_i(L_i+1)}{r^2}\right)f(r)\right.$$
$$+\delta_{L_iL_f-2}\frac{3(L_i+1)(L_i+2)\sqrt{2(2L_i+1)}}{(2L_i+1)(2L_i+3)(2L_i+5)}\left(\frac{d^2}{dr^2}-\frac{(2L_i+3)}{r}\frac{d}{dr}+\frac{(L_i+3)(L_i+1)}{r^2}\right)f(r)$$
$$\left.+\delta_{L_iL_f+2}\frac{3L_i(L_i-1)\sqrt{2(2L_i+1)}}{(2L_i+1)(2L_i-3)(2L_i-1)}\left(\frac{d^2}{dr^2}+\frac{(2L_i-1)}{r}\frac{d}{dr}+\frac{L_i(L_i-2)}{r^2}\right)f(r)\right).$$

Here, the upper index in parentheses stands for the tensor rank of an operator.

REFERENCES

1. M. Lacomb, B. Loiseau, J. M. Richard, *et al.*, Phys. Rev. C **21**, 861 (1980).
2. V. G. J. Stocks, R. A. M. Klomp, C. P. F. Terheggen, and J. J. de Swart, Phys. Rev. C **49**, 2950 (1994).
3. M. Oka and S. Takeuchi, Phys. Rev. Lett. **63**, 1780 (1989); Z.-Y. Zhang, A. Faessler, U. Straub, and L. Ya. Glozman, Nucl. Phys. A **578**, 573 (1994); W. Koepf, L. Wilets, S. Pepin, and F. Stancu, Phys. Rev. C **50**, 614 (1994); D. R. Entem, A. I. Machavariani, A. Valcarce, *et al.*, Nucl. Phys. A **602**, 308 (1996).
4. D. A. Liberman, Phys. Rev. D **16**, 1542 (1977); C. De Tar, Phys. Rev. D **17**, 302 (1978).
5. V. G. Neudatchin, I. T. Obukhovsky, and Yu. F. Smirnov, Phys. Lett. B **43B**, 13 (1973); V. G. Neudatchin, I. T. Obukhovsky, V. I. Kukulin, and N. F. Golovanova, Phys. Rev. C **11**, 128 (1975).
6. V. G. Neudatchin, N. P. Yudin, Yu. L. Dorodnykh, and I. T. Obukhovsky, Phys. Rev. C **43**, 2499 (1991).
7. V. I. Kukulin and V. N. Pomerantsev, Prog. Theor. Phys. **88**, 159 (1992).

8. S. B. Dubovichenko, Yad. Fiz. **60**, 499 (1997) [Phys. At. Nucl. **60**, 425 (1997)].
9. T.-S. H. Lee and A. Matsuyama, Phys. Rev. C **36**, 1459 (1987); M. Batinic, A. Svarc, and T.-S. H. Lee, Phys. Scr. **56**, 321 (1997).
10. A. M. Kusainov, V. G. Neudatchin, and I. T. Obukhovsky, Phys. Rev. C **44**, 2343 (1991)
11. V. G. Neudatchin, Yu. F. Smirnov, and R. Tamagaki, Prog. Theor. Phys. **58**, 1072 (1977); Yu. F. Smirnov, I. T. Obukhovskiĭ, V. G. Neudachin, and R. Tamagaki, Yad. Fiz. **27**, 860 (1978) [Sov. J. Nucl. Phys. **27**, 456 (1978)]; I. T. Obukhovsky, V. G. Neudatchin, Yu. F. Smirnov, and Yu. M. Tchuvil'sky, Phys. Lett. B **88B**, 231 (1979); V. G. Neudachin, I. T. Obukhovskiĭ, and Yu. F. Smirnov, Fiz. Élem. Chastits At. Yadra **15**, 1165 (1984) [Sov. J. Part. Nucl. **15**, 519 (1984)].
12. V. G. Neudatchin and I. T. Obukhovsky, in *Relativistic Nuclear Physics and QCD Proceedings of XII International Seminar, Dubna, 1994,* Ed. by A. M. Baldin and V. V. Burov, Preprint No. E1,2-97-79, OIYaI (Joint Institute for Nuclear Research, Dubna, 1997), Vol. II, p. 3.
13. L. Ya. Glozman, V. G. Neudatchin, I. T. Obukhovsky, and A. A. Sakharuk, Phys. Lett. B **252**, 23 (1990); Phys. Rev. C **48**, 389 (1993); L. Ya. Glozman and A. Faessler, Phys. Lett. B **348**, 270 (1995); M. P. Rekalo and I. M. Sitnik, Phys. Lett. B **356**, 434 (1995); B. Kuehn, C. F. Perdrisat, and E. A. Strokovsky, Yad. Fiz. **58**, 1898 (1995) [Phys. At. Nucl. **58**, 1795 (1995)].
14. V. G. Neudachin, N. A. Khokhlov, A. M. Shirokov, and V. A. Knyr, Yad. Fiz. **60**, 1086 (1997) [Phys. At. Nucl. **60**, 971 (1997)]; V. G. Neudatchin, V. A. Knyr, N. A. Khokhlov, and A. M. Shirokov, Nucl. Phys. A **629**, 218c (1998).
15. N. A. Khokhlov, V. A. Knyr, V. G. Neudatchin, and A. M. Shirokov, Phys. Rev. C **62**, 054003 (2000).
16. V. A. Knyr, V. G. Neudachin, and N. A. Khokhlov, Yad. Fiz. **63**, 1988 (2000) [Phys. At. Nucl. **63**, 1895 (2000)].
17. M. Jetter and H. W. Fearing, Phys. Rev. C **51**, 1666 (1995); H. W. Fearing and S. Scherer, nucl-th/9909076.
18. A. A. Logunov and A. N. Tavkhelidze, Nuovo Cimento **29**, 380 (1963); A. A. Logunov and O. A. Khrustalev, Fiz. Élem. Chastits At. Yadra **1**, 70 (1970) [Sov. J. Part. Nucl. **1**, 39 (1970)]; V. O. Galkin, A. Yu. Mishurov, and R. N. Faustov, Yad. Fiz. **55**, 2175 (1992) [Sov. J. Nucl. Phys. **55**, 1207 (1992)]; G. E. Brown and A. D. Jackson, *The Nucleon–Nucleon Interaction* (North-Holland, Amsterdam, 1975; Atomizdat, Moscow, 1979); F. Coetler, S. C. Pieper, and F. J. D. Serduke, Phys. Rev. C **11**, 1 (1975); E. Pace, G. Salme, and F. M. Lev, nucl-th/9802020.
19. J. Werle, *Relativistic Theory of Reactions* (Polish Scientific Publ., Warsaw, 1966; Atomizdat, Moscow, 1969).
20. I. T. Todorov, Phys. Rev. D **3**, 2351 (1971); V. A. Rizov and I. T. Todorov, Fiz. Élem. Chastits At. Yadra **6**, 669 (1975) [Sov. J. Part. Nucl. **6**, 269 (1975)]; A. P. Martynenko and R. N. Faustov, Teor. Mat. Fiz. **64**, 179 (1985).
21. P. A. M. Dirac, Rev. Mod. Phys. **21**, 392 (1949); B. D. Keister and W. Polyzou, Adv. Nucl. Phys. **21**, 225 (1991).
22. F. M. Lev, Riv. Nuovo Cimento **16**, 1 (1993); Nucl. Phys. A **567**, 797 (1994).
23. F. M. Lev, hep-ph/9403222.
24. K. Michaelian, P. Kitching, D. A. Hutcheon, *et al.*, Phys. Rev. D **41**, 2689 (1990).
25. V. Hermann and K. Nakayama, Phys. Rev. C **46**, 2199 (1992); G. H. Martinus, O. Scholten, and J. A. Tjon, Phys. Rev. C **56**, 2945 (1997).
26. K. I. Blomqvist, W. U. Boeglin, R. Boehm, *et al.*, Phys. Lett. B **424**, 33 (1998).
27. J. E. Belz, Phys. Rev. Lett. **74**, 646 (1995); C. Bochna, Phys. Rev. Lett. **81**, 4576 (1998); L. L. Frankfurt, G. A. Miller, M. M. Sargsian, and M. I. Strikman, Phys. Rev. Lett. **84**, 3045 (2000).
28. V. I. Kukulin, V. N. Pomerantsev, A. Faessler, *et al.*, Phys. Rev. C **57**, 535 (1998); V. I. Kukulin, V. N. Pomerantsev, and A. Faessler, Phys. Rev. C **59**, 3021 (1999).
29. P. Moussa and R. Stora, in *Methods in Subnuclear Physics,* Ed. by N. Nicolic (Gordon and Breach, New York, 1968), Vol. 2, p. 265; S. Gaziorovicz, *Elementary Particle Physics* (Wiley, New York, 1967; Nauka, Moscow, 1969); Yu. V. Novozhilov, *Introduction to Elementary Particle Theory* (Nauka, Moscow, 1972; Pergamon, Oxford, 1975).

Translated by A. Isaakyan

Physics of Atomic Nuclei, Vol. 66, No. 1, 2003, pp. 152–171. From Yadernaya Fizika, Vol. 66, No. 1, 2003, pp. 155–174.

ELEMENTARY PARTICLES AND FIELDS
Theory

Near-Threshold Production of $a_0(980)$ Mesons in πN and NN Collisions and a_0-f_0 Mixing*

L. A. Kondratyuk, E. L. Bratkovskaya[1)], V. Yu. Grishina[2)], M. Büscher[3)], W. Cassing[4)], and H. Ströher[3)]

Institute of Theoretical and Experimental Physics, Bol'shaya Cheremushkinskaya ul. 25, Moscow, 117259 Russia

Received April 8, 2002

Abstract—We consider near-threshold $a_0(980)$-meson production in πN and NN collisions. An effective Lagrangian approach with one-pion exchange is applied to analyze different contributions to the cross section for different isospin channels. The Reggeon exchange mechanism is also evaluated for comparison. The results from πN reactions are used to calculate the contribution of the a_0 meson to the cross sections and invariant $K\bar{K}$ mass distributions of the reactions $pp \to pnK^+\bar{K}^0$ and $pp \to ppK^+K^-$. It is found that the experimental observation of a_0^+ mesons in the reaction $pp \to pnK^+\bar{K}^0$ is much more promising than the observation of a_0^0 mesons in the reaction $pp \to ppK^+K^-$. Effects of isospin violation in the reactions $pN \to da_0$, $pd \to {}^3\mathrm{He}({}^3\mathrm{H})a_0$, and $dd \to {}^4\mathrm{He}a_0$, which are induced by $a_0(980)-f_0(980)$ mixing, are also analyzed. © *2003 MAIK "Nauka/Interperiodica".*

1. INTRODUCTION

The structure of the lightest scalar mesons $a_0(980)$ and $f_0(980)$ is still under discussion (see, e.g., [1–7] and references therein). Different authors interpreted them as unitarized $q\bar{q}$ states, as four-quark cryptoexotic states, as $K\bar{K}$ molecules, or even as vacuum scalars (Gribov's minions). Although it has been possible to describe them as ordinary $q\bar{q}$ states (see [8–10]), other options cannot be ruled out up to now. Another problem is the possible strong mixing between the uncharged $a_0(980)$ and the $f_0(980)$ due to a common coupling to $K\bar{K}$ intermediate states [11–17]. This effect can influence the structure of the uncharged component of the $a_0(980)$- and implies that it is important to perform a comparative study of a_0^0 and a_0^+ (or a_0^-). There is no doubt that new data on a_0^0 and $a_0^+(a_0^-)$ production in πN and NN reactions are quite important to shed new light on the a_0 structure and the dynamics of its production.

In our recent paper [18], we have considered a_0 production in the reaction $\pi N \to a_0 N$ near the threshold and at GeV energies. An effective Lagrangian approach and the Regge pole model were applied to investigate different contributions to the cross section of the reaction $\pi N \to a_0 N$. In [19], we have employed the latter results for an analysis of a_0 production in NN collisions. Furthermore, in [17], we have considered the a_0-f_0 mixing in reactions involving the lightest nuclei d, ${}^3\mathrm{H}$, ${}^3\mathrm{He}$, and ${}^4\mathrm{He}$. Here, we give an overview of those results and present a comparative analysis of $a_0(980)$-resonance production and nonresonant background channels in the reactions $\pi N \to a_0 N \to K\bar{K}N$ and $NN \to a_0 NN \to K\bar{K}NN$. Our study is particularly relevant to the current experimental program at COSY (Jülich) [20–22].

Our paper is organized as follows. In Section 2, we discuss the $K\bar{K}$ and $\pi\eta$ decay channels of the $a_0(980)$. An analysis of $a_0(980)$-resonance production and nonresonant background in the reactions $\pi N \to K\bar{K}N$ and $NN \to a_0 NN \to K\bar{K}NN$ is presented in Section 3. Section 4 is devoted to the calculation of the cross sections for the reactions $NN \to NNa_0$ and $NN \to a_0 NN \to K\bar{K}NN$ in comparison to nonresonant $K\bar{K}$ production. In Section 5, we consider $a_0(980)-f_0(980)$ mixing and isospin violation in the reactions $pN \to da_0$, $pd \to {}^3\mathrm{He}({}^3\mathrm{H})\,a_0$, and $dd \to {}^4\mathrm{He}a_0$.

*This article was submitted by the authors in English.

[1)]Institut für Theoretische Physik, Universität Frankfurt, Germany.

[2)]Institute for Nuclear Research, Russian Academy of Sciences, pr. Shestidesyatiletiya Oktyabrya 7a, Moscow, 117312 Russia.

[3)]Institut für Kernphysik, Forschungszentrum Jülich, Germany.

[4)]Institut für Theoretische Physik, Universität Giessen, Germany.

2. THE $K\bar{K}$ AND $\pi\eta$ DECAY CHANNELS OF THE $a_0(980)$

The $a_0(980)$ invariant mass distribution in the $K\bar{K}$ and $\pi\eta$ modes can be parametrized by the well-known Flatté formula [23] which follows from analyticity and unitarity for the two-channel T matrix.

For example, in the case of the reaction $NN \to a_0 NN \to K\bar{K}NN$, the mass distribution of the final $K\bar{K}$ system can be written as a product of the total cross section for a_0 production (with the "running" mass M) in the $NN \to NNa_0$ reaction and the Flatté mass distribution function

$$\frac{d\sigma_{K\bar{K}}}{dM^2}(s,M) = \sigma_{a_0}(s,M) \times C_{\rm F}\frac{M_R\Gamma_{a_0K\bar{K}}(M)}{(M^2-M_R^2)^2+M_R^2\Gamma_{\rm tot}^2(M)} \quad (1)$$

with the total width $\Gamma_{\rm tot}(M) = \Gamma_{a_0K\bar{K}}(M) + \Gamma_{a_0\pi\eta}(M)$. The partial widths

$$\Gamma_{a_0K\bar{K}}(M) = g_{a_0K\bar{K}}^2\frac{q_{K\bar{K}}}{8\pi M^2}, \quad \Gamma_{a_0\pi\eta}(M) = g_{a_0\pi\eta}^2\frac{q_{\pi\eta}}{8\pi M^2} \quad (2)$$

are proportional to the decay momenta in the c.m.s. (in case of scalar mesons)

$$q_{K\bar{K}} = \frac{[(M^2-(m_K+m_{\bar{K}})^2)(M^2-(m_K-m_{\bar{K}})^2)]^{1/2}}{2M},$$

$$q_{\pi\eta} = \frac{[(M^2-(m_\pi+m_\eta)^2)(M^2-(m_\pi-m_\eta)^2)]^{1/2}}{2M}$$

for a meson of mass M decaying to $K\bar{K}$ and $\pi\eta$, respectively. The branching ratios $\mathrm{Br}(a_0 \to K\bar{K})$ and $\mathrm{Br}(a_0 \to \pi\eta)$ are given by the integrals of the Flatté distribution over the invariant mass squared $dM^2 = 2MdM$:

$$\mathrm{Br}(a_0 \to K\bar{K}) = \int\limits_{m_K+m_{\bar{K}}}^{\infty} dM\frac{2MC_{\rm F}M_R\Gamma_{a_0K\bar{K}}(M)}{(M^2-M_R^2)^2+M_R^2\Gamma_{\rm tot}^2(M)}, \quad (3)$$

$$\mathrm{Br}(a_0 \to \pi\eta) = \int\limits_{m_K+m_{\bar{K}}}^{\infty} dM\frac{2MC_{\rm F}\,M_R\Gamma_{a_0\pi\eta}(M)}{(M^2-M_R^2)^2+M_R^2\Gamma_{\rm tot}^2(M)} + \int\limits_{m_\pi+m_\eta}^{m_K+m_{\bar{K}}} dM\frac{2MC_{\rm F}M_R\Gamma_{a_0\pi\eta}(M)}{(M^2-M_R^2-M_R\Gamma_{a_0K\bar{K}}(M))^2+M_R^2\Gamma_{a_0\pi\eta}^2(M)}. \quad (4)$$

The parameters $C_{\rm F}$, $g_{K\bar{K}}$, and $g_{\pi\eta}$ have to be fixed under the constraint of the unitarity condition

$$\mathrm{Br}(a_0 \to K\bar{K}) + \mathrm{Br}(a_0 \to \pi\eta) = 1. \quad (5)$$

Choosing the parameter $\Gamma_0 = \Gamma_{a_0\pi\eta}(M_R)$ in the interval 50–100 MeV (as given by the PDG [24]), one can fix the coupling $g_{\pi\eta}$ according to (2). In [25], a ratio of branching ratios has been reported,

$$R_{a_0(980)} = \frac{\mathrm{Br}(a_0 \to K\bar{K})}{\mathrm{Br}(a_0 \to \pi\eta)} = 0.23 \pm 0.05, \quad (6)$$

for $m_{a_0} = 0.999$ GeV, which gives $\mathrm{Br}(a_0 \to K\bar{K}) = 0.187$. In another recent study [26], the WA102 collaboration reported the branching ratio

$$\Gamma(a_0 \to K\bar{K})/\Gamma(a_0 \to \pi\eta) = 0.166 \pm 0.01 \pm 0.02, \quad (7)$$

which was determined from the measured branching ratio for the $f_1(1285)$ meson. In our present analysis, we use the results from [25], however, keeping in mind that this branching ratio $\mathrm{Br}(a_0 \to K\bar{K})$ more likely gives an "upper limit" for the $a_0 \to K\bar{K}$ decay.

Thus, the other two parameters in the Flatté distribution $C_{\rm F}$ and $g_{a_0K\bar{K}}$ can be found by solving the system of integral equations, for example, Eq. (3) for $\mathrm{Br}(a_0 \to K\bar{K}) = 0.187$ and the unitarity condition (5). For our calculations, we choose either $\Gamma_{a_0\pi\eta}(M_R) = 70$ or 50 MeV, which gives two sets of independent parameters $g_{a_0K\bar{K}}$, $g_{a_0\pi\eta}$, and $C_{\rm F}$ for a fixed branching ratio $\mathrm{Br}(a_0 \to K\bar{K}) = 0.187$:

set 1 $(\Gamma_{a_0\pi\eta} = 70\ \mathrm{MeV})$: (8)

$g_{a_0K\bar{K}} = 2.3$ GeV, $g_{a_0\pi\eta} = 2.2$ GeV, $C_{\rm F} = 0.365$;

set 2 $(\Gamma_{a_0\pi\eta} = 50\ \mathrm{MeV})$: (9)

$g_{a_0K\bar{K}} = 1.9$ GeV, $g_{a_0\pi\eta} = 1.9$ GeV, $C_{\rm F} = 0.354$.

Note that, for the K^+K^- or $K^0\bar{K}^0$ final state, one has to take into account an isospin factor for the coupling constant, i.e., $g_{a_0K^+K^-} = g_{a_0K^0\bar{K}^0} = g_{a_0K\bar{K}}/\sqrt{2}$, whereas $g_{a_0K^+\bar{K}^0} = g_{a_0K^-\bar{K}^0} = g_{a_0K\bar{K}}$.

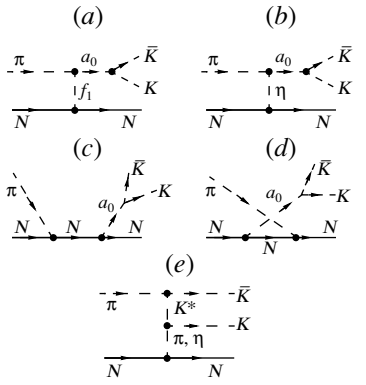

Fig. 1. (a–d) Diagrams for a_0 production in the reaction $\pi N \to a_0 N \to \bar{K}K$ near the threshold and (e) diagram for nonresonant $\bar{K}K$ "background" production.

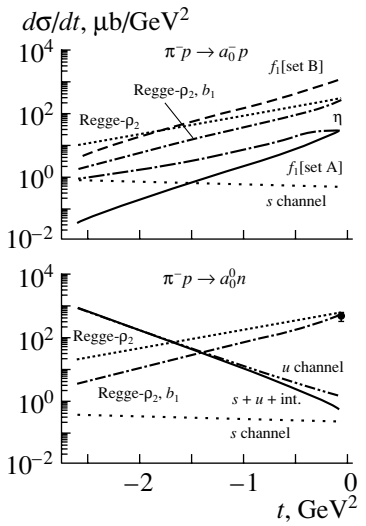

Fig. 2. The differential cross sections $d\sigma/dt$ for the reactions $\pi^- p \to a_0^- p$ and $\pi^- p \to a_0^0 n$ at 2.4 GeV/c. The long-dash-dotted line corresponds to the η exchange, and the solid and long-dashed lines (upper part) show the f_1 contributions within sets A and B, respectively. The rare-dotted and dash-double-dotted lines indicate the s and u channels, while the solid line (lower part) describes the coherent sum of s- and u-channel contributions including interference. The dotted and short-dash-dotted lines present the results within the ρ_2 and ρ_2, b_1 Regge exchange model, respectively (see text).

3. THE REACTIONS $\pi N \to a_0 N$ AND $\pi N \to K\bar{K}N$

3.1. An Effective Lagrangian Approach

The simplest mechanisms for a_0 production in the reaction $\pi N \to a_0 N$ near the threshold are described by the pole diagrams shown in Figs. 1a–1d. It is known experimentally that a_0 couples strongly to the channels $\pi\eta$ and $\pi f_1(1285)$ because $\pi\eta$ is the dominant decay channel of a_0, while πa_0 is one of the most important decay channels of $f_1(1285)$ [24]. The amplitudes, which correspond to the t-channel exchange of $\eta(550)$ and $f_1(1285)$ mesons (see Figs. 1b and 1a), can be written as

$$M_\eta^t(\pi^- p \to a_0^- p) = g_{\eta\pi a_0} g_{\eta NN} \bar{u}(p_2')\gamma_5 u(p_2) \quad (10)$$
$$\times \frac{1}{t - m_\eta^2} F_{\eta\pi\, a_0}(t) F_{\eta NN}(t),$$

$$M_{f_1}^t(\pi^- p \to a_0^- p) = g_{f_1\pi a_0} g_{f_1 NN} \quad (11)$$
$$\times (p_1 + p_1')_\mu \left(g_{\mu\nu} - \frac{q_\mu q_\nu}{m_{f_1}^2} \right) \bar{u}(p_2')\gamma_\nu\gamma_5 u(p_2)$$
$$\times \frac{1}{t - m_{f_1}^2} F_{f_1\pi\, a_0}(t) F_{f_1 NN}(t).$$

Here, p_1 and p_1' are the 4-momenta of π^- and a_0^-, whereas p_2 and p_2' are the 4-momenta of the initial and final protons, respectively; furthermore, $q = p_2' - p_2$ and $t = (p_2' - p_2)^2$. The functions F_j present form factors at the different vertices j ($j = f_1 NN, \eta NN$), which are taken of the monopole form

$$F_j(t) = \frac{\Lambda_j^2 - m_j^2}{\Lambda_j^2 - t}, \quad (12)$$

where Λ_j is a cutoff parameter. In the case of η exchange, we use $g_{\eta NN} = 6.1$ and $\Lambda_{\eta NN} = 1.5$ GeV from [27] and $g_{a_0\pi_\eta}$ is defined by (8). The contribution of the f_1 exchange is calculated for two parameter sets:
set A: $g_{f_1 NN} = 11.2$, $\Lambda_{f_1 NN} = 1.5$ GeV [28],
set B: $g_{f_1 NN} = 14.6$, $\Lambda_{f_1 NN} = 2.0$ GeV [29],
and $g_{f_1 a_0 \pi}$=2.5 for both cases. The latter value for $g_{f_1 a_0 \pi}$ corresponds to $\Gamma(f_1 \to a_0\pi) = 24$ MeV and $\mathrm{Br}(f_1 \to a_0\pi) = 34\%$.

In Fig. 2 (upper part), we show the differential cross sections $d\sigma/dt$ for the reaction $\pi^- p \to a_0^- p$ at 2.4 GeV/c corresponding to η (long-dash-dotted line) and f_1 exchanges with set A (solid line) and set B (long-dashed line). A soft cutoff parameter (set A) close to the mass of f_1 implies that all the contributions related to f_1 exchange become negligibly small. On the other hand, for the parameter values given by set B, the f_1-exchange contribution is much larger than that from η exchange. Note that this large uncertainty in the cutoff presently cannot be controlled by data, and we will discuss the relevance of the f_1-exchange contribution for all reactions separately throughout this study. For set B, the total cross section for the reaction $\pi^- p \to a_0^- p$ is about 0.5 mb at 2.4 GeV/c [cf. Fig. 3 (upper part)], while the forward differential cross section is about 1 mb/GeV^2.

The η and f_1 exchanges, however, do not contribute to the amplitude of the charge-exchange reaction $\pi^- p \to a_0^0 n$. In this case, we have to consider the contributions of the s- and u-channel diagrams (Figs. 1*c* and 1*d*):

$$M_N^s(\pi^- p \to a_0^0 n) = g_{a_0 NN} \frac{f_{\pi NN}}{m_\pi} \frac{1}{s - m_N^2} F_N(s) \quad (13)$$
$$\times\, p_{1\mu} \bar{u}(p_2')[(p_1 + p_2)_\alpha \gamma_\alpha + m_N]\gamma_\mu \gamma_5 u(p_2),$$

$$M_N^u(\pi^- p \to a_0^0 n) = g_{a_0 NN} \frac{f_{\pi NN}}{m_\pi} \frac{1}{u - m_N^2} F_N(u) \quad (14)$$
$$\times\, p_{1\mu} \bar{u}(p_2')\gamma_\mu \gamma_5 [(p_2 - p_1')_\alpha \gamma_\alpha + m_N] u(p_2),$$

where $s = (p_1 + p_2)^2$, $u = (p_2 - p_1')^2$, and m_N is the nucleon mass.

The πNN coupling constant is taken as $f_{\pi NN}^2/4\pi = 0.08$ [27], and the form factor for each virtual nucleon is taken in the so-called monopole form

$$F_N(u) = \frac{\Lambda_N^4}{\Lambda_N^4 + (u - m_N^2)^2}. \quad (15)$$

Following [18], we adopt here a cutoff parameter $\Lambda_N = 1.24$ GeV (see also discussion below).

The rare-dotted and dash-double-dotted lines in the lower part of Fig. 2 show the differential cross section for the charge-exchange reaction $\pi^- p \to a_0^0 n$ at 2.4 GeV/c corresponding to s- and u-channel diagrams, respectively. Due to isospin constraints, only the s channel contributes to the $\pi^- p \to a_0^- p$ reaction (rare-dotted line in the upper part of Fig. 2). In these calculations, the cutoff parameter $\Lambda_N = 1.24$ GeV and $g_{a_0 NN}^2/4\pi \simeq 1$ have been employed in line with the Bonn potential [27]. The solid line in the lower part of Fig. 2 describes the coherent sum of the s- and u-channel contributions, including the interference of the amplitudes. Except for the very forward region, the s-channel contribution (rare-dotted line) is rather small compared to the u channel for the charge-exchange reaction $\pi^- p \to a_0^0 n$, which may give a backward differential cross section of about 1 mb/GeV^2. The corresponding total cross section can be about 0.3 mb at this energy (cf. Fig. 3, middle part).

There is a single experimental point for the forward differential cross section of the reaction $\pi^- p \to a_0^0 n$ at 2.4 GeV/c ([30], lower part of Fig. 2),

$$\left.\frac{d\sigma}{dt}(\pi^- p \to a_0^0 n)\right|_{t \approx 0} = 0.49 \text{ mb/GeV}^2.$$

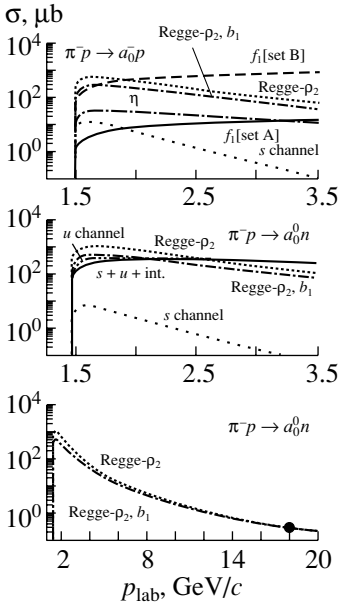

Fig. 3. The total cross sections for the reactions $\pi^- p \to a_0^- p$ and $\pi^- p \to a_0^0 n$ as a function of the incident momentum. The assignment of the curves is the same as in Fig. 2. The experimental data point at 18 GeV/c (lower part) is taken from [35].

Since in the forward region ($t \approx 0$) the s- and u-channel diagrams only give a smaller cross section, the charge-exchange reaction $\pi^- p \to a_0^0 n$ is most probably dominated at small t by the isovector $b_1(1^{+-})$- and $\rho_2(2^{--})$-meson exchanges (see, e.g., [11]). Though the couplings of these mesons to πa_0 and NN are not known, we can estimate $d\sigma(\pi^- p \to a_0^0 n)/dt$ in the forward region using the Regge pole model as developed by Achasov and Shestakov [12]. Note that the Regge pole model is expected to provide a reasonable estimate for the cross section at medium energies of about a few GeV and higher (see, e.g., [31, 32] and references therein).

3.2. The Regge Pole Model

The s-channel helicity amplitudes for the reaction $\pi^- p \to a_0^0 n$ can be written as

$$M_{\lambda_2' \lambda_2}(\pi^- p \to a_0^0 n) = \bar{u}_{\lambda_2'}(p_2') \quad (16)$$
$$\times \left[-A(s,t) + (p_1 + p_1')_\alpha \gamma_\alpha \frac{B(s,t)}{2}\right] \gamma_5 u_{\lambda_2}(p_2),$$

where the invariant amplitudes $A(s,t)$ and $B(s,t)$ do not contain kinematical singularities and (at fixed t and large s) are related to the helicity amplitudes as

$$M_{++} \approx -sB, \quad M_{+-} \approx \sqrt{t_{\min} - t}\, A. \quad (17)$$

The differential cross section then can be expressed through the helicity amplitudes in the standard way as

$$\frac{d\sigma}{dt}(\pi^- p \to a_0^0 n) = \frac{1}{64\pi s}\frac{1}{(p_1^{\text{c.m.}})^2}(|M_{++}|^2 + |M_{+-}|^2). \quad (18)$$

Usually, it is assumed that the reaction $\pi^- p \to a_0^0 n$ at high energies is dominated by the b_1 Regge pole exchange. However, as shown by Achasov and Shestakov [12], this assumption is not compatible with the angular dependence of $d\sigma(\pi^- p \to a_0^0 n)/dt$ observed at Serpukhov at 40 GeV/c [33, 34] and Brookhaven at 18 GeV/c [35]. The reason is that the b_1 Regge trajectory contributes only to the amplitude $A(s,t)$, giving a dip in differential cross section at forward angles, while the data show a clear forward peak in $d\sigma(\pi^- p \to a_0^0 n)/dt$ at both energies. To interpret this phenomenon, Achasov and Shestakov [12] introduced a ρ_2 Regge pole exchange conspiring with its daughter trajectory. Since the ρ_2 Regge trajectory contributes to both invariant amplitudes, $A(s,t)$ and $B(s,t)$, its contribution does not vanish at the forward scattering angle $\theta = 0$, thus giving a forward peak due to the term $|M_{++}|^2$ in $d\sigma/dt$. At the same time, the contribution of the ρ_2 daughter trajectory to the amplitude $A(s,t)$ is necessary to cancel the kinematical pole at $t = 0$ introduced by the ρ_2 main trajectory (conspiracy effect). In this model, the s-channel helicity amplitudes can be expressed through the b_1 and the conspiring ρ_2 Regge trajectories exchange as

$$M_{++} \approx M_{++}^{\rho_2}(s,t) = \gamma_{\rho_2}(t)\exp\left[-i\frac{\pi}{2}\alpha_{\rho_2}(t)\right]\left(\frac{s}{s_0}\right)^{\alpha_{\rho_2}(t)}, \quad (19)$$

$$M_{+-} \approx M_{+-}^{b_1}(s,t) = \sqrt{(t_{\min}-t)/s_0}\,\gamma_{b_1}(t) \times i\exp\left[-i\frac{\pi}{2}\alpha_{b_1}(t)\right]\left(\frac{s}{s_0}\right)^{\alpha_{b_1}(t)}, \quad (20)$$

where $\gamma_{\rho_2}(t) = \gamma_{\rho_2}(0)\exp(b_{\rho_2}t)$, $\gamma_{b_1}(t) = \gamma_{b_1}(0) \times \exp(b_{b_1}t)$, $t_{\min} \approx -m_N^2(m_{a_0}^2 - m_\pi^2)/s^2$, and $s_0 \approx 1$ GeV^2, while the meson Regge trajectories have the linear form $\alpha_j(t) = \alpha_j(0) + \alpha_j'(0)t$.

Achasov and Shestakov describe the Brookhaven data on the t distribution at 18 GeV/c for $-t_{\min} \le -t \le 0.6$ GeV^2 [35] by the expression

$$\frac{dN}{dt} = C_1\left[e^{\Lambda_1 t} + (t_{\min}-t)\frac{C_2}{C_1}e^{\Lambda_2 t}\right], \quad (21)$$

where the first and second terms describe the ρ_2 and b_1 exchanges, respectively. They found two fits: (i) $\Lambda_1 = 4.7$ GeV^{-2}, $C_2/C_1 = 0$; (ii) $\Lambda_1 = 7.6$ GeV^{-2}, $C_2/C_1 \approx 2.6$ GeV^{-2}, $\Lambda_2 = 5.8$ GeV^{-2}. This implies that at 18 GeV/c the b_1 contribution yields only 1/3 of the integrated cross section. Moreover, using the available data on the reaction $\pi^- p \to a_2^0(1320)n$ at 18 GeV/c and comparing them with the data on the $\pi^- p \to a_0^0 n$ reaction, they estimated the total and forward differential cross sections $\sigma(\pi^- p \to a_0^0 n \to \pi^0\eta n) \approx 200$ nb and $[d\sigma(\pi^- p \to a_0^0 n \to \pi^0\eta n)/dt]_{t=0} \approx 940$ nb/GeV^2. Taking $\text{Br}(a_0^0 \to \pi^0\eta) \approx 0.8$, we find $\sigma(\pi^- p \to a_0^0 n) \approx 0.25\,\mu$b and $[d\sigma(\pi^- p \to a_0^0 n)/dt]_{t=0} \approx 1.2\,\mu$b/GeV^2.

In this way, all the parameters of the Regge model can be fixed, and we will employ it for the energy dependence of the $\pi^- p \to a_0^0 n$ cross section to obtain an estimate at lower energies too.

The mass of $\rho_2(2^{--})$ is expected to be about 1.7 GeV (see [36] and references therein), and the slope of the meson Regge trajectory in the case of light (u,d) quarks is 0.9 GeV^{-2} [37]. Therefore, the intercept of the ρ_2 Regge trajectory is $\alpha_{\rho_2}(0) = 2 - 0.9m_{\rho_2}^2 \approx -0.6$. Similarly—in the case of the b_1 trajectory—we have $\alpha_{b_1}(0) \approx -0.37$. At forward angles, we can neglect the contribution of the b_1 exchange (see discussion above) and write the energy dependence of the differential cross section in the form

$$\left.\frac{d\sigma_{\text{Regge}}}{dt}(\pi^- p \to a_0^0 n)\right|_{t=0} \approx \left.\frac{d\sigma_{\rho_2}}{dt}\right|_{t=0} \sim \frac{1}{(p_1^{\text{c.m.}})^2}\left(\frac{s}{s_0}\right)^{-2.2}. \quad (22)$$

This provides the following estimate for the forward differential cross section at 2.4 GeV/c,

$$\left.\frac{d\sigma_{\text{Regge}}}{dt}(\pi^- p \to a_0^0 n)\right|_{t=0} \approx 0.6\ \text{mb/GeV}^2, \quad (23)$$

which is in agreement with the experimental data point [30] (lower part of Fig. 2). Since the b_1 and ρ_2 Regge trajectories have isospin 1, their contribution to the cross section for the reaction $\pi^- p \to a_0^- p$ is a factor of 2 smaller,

$$\frac{d\sigma_{\text{Regge}}}{dt}(\pi^- p \to a_0^- p) = \frac{1}{2}\frac{d\sigma_{\text{Regge}}}{dt}(\pi^- p \to a_0^0 n). \quad (24)$$

In Fig. 2, the dotted lines show the resulting differential cross sections for $d\sigma_{\text{Regge}}(\pi^- p \to a_0^- p)/dt$ (upper part) and $d\sigma_{\text{Regge}}(\pi^- p \to a_0^0 n)/dt$ (lower part) at 2.4 GeV/c corresponding to ρ_2 Regge exchange, whereas the short-dash-dotted lines indicate the contribution for ρ_2 and b_1 Regge trajectories. For $t \to 0$, both Regge parametrizations agree; however,

at large $|t|$ the solution including the b_1 exchange gives a smaller cross section. The cross section $d\sigma_{\rm Regge}(\pi^- p \to a_0^- p)/dt$ in the forward region exceeds the contributions of η, f_1 (set A), and s-channel exchanges, but is a few times smaller than the f_1-exchange contribution for set B. On the other hand, the cross section $d\sigma_{\rm Regge}(\pi^- p \to a_0^0 n)/dt$ is much larger than the s- and u-channel contributions in the forward region, but much smaller than the u-channel contribution in the backward region.

The integrated cross sections for $\pi^- p \to a_0^- p$ (upper part) and $\pi^- p \to a_0^0 n$ (middle and lower part) for the Regge model are shown in Fig. 3 as a function of the pion laboratory momentum by dotted curves for ρ_2 exchange and by short-dash-dotted curves for ρ_2, b_1 trajectories. In the few-GeV region, the cross sections are comparable with the u-channel contribution. At higher energies, the Regge cross section decreases as $s^{-3.2}$ in contrast to the non-Reggeized f_1-exchange contribution, which increases with energy and seems to be too large at 2.5 GeV/c for parameters from the set B. We thus expect parameter set B to be unrealistic.

The main conclusions of this subsection are as follows. In the region of a few GeV, the dominant mechanisms of a_0 production in the reaction $\pi N \to a_0 N$ is the u-channel nucleon exchange (cf. middle part of Fig. 3). A similar cross section ($\simeq 0.4$–1.0 mb) is predicted by the Regge model with conspiring ρ_2 (or ρ_2 and b_1) exchanges, normalized to the Brookhaven data at 18 GeV/c (lower part of Fig. 3). The contributions of s-channel nucleon and t-channel η-meson exchanges are small (cf. upper and middle parts of Fig. 3).

3.3. Possible Signals of a_0 Production in the Reaction $\pi N \to K\bar{K}N$

In Fig. 4, we show the existing experimental data on the reactions $\pi^- p \to nK^+K^-$, $\pi^- p \to nK^0\bar{K}^0$, $\pi^+ p \to pK^+\bar{K}^0$, and $\pi^- p \to pK^0K^-$ taken from [38]. The solid curves describe s- and u-channel contributions, calculated using the dipole nucleon form factor $(F_N^2(u))$ with $\Lambda_N = 1.35$ GeV. The short-dashed and long-dashed curves describe η and f_1 t-channel exchanges, respectively. Two different choices of the Regge pole model are shown by the dash-dotted curves, which describe ρ_2 exchange (upper) and ρ_2, b_1 exchange (lower). The crossed solid curves display the background contribution (see Fig. 1*e*), which was calculated using parameters of the K^* exchange from the Jülich model [3]. It is important that, for the reactions $\pi^+ p \to pK^+\bar{K}^0$ and $\pi^- p \to pK^0K^-$, where the $K\bar{K}$ pair has isospin 1, the main contributions come from P-wave $K\bar{K}$-pair production from the $\pi\pi$ state and from S-wave $K\bar{K}$-pair production from the $\eta\pi$ state. These selection rules follow from G-parity conservation (note that the G parity of the $K\bar{K}$ system with orbital momentum L and isospin I is given by $(-1)^{L+I}$). At the same time, for the reactions $\pi^- p \to nK^+K^-$ and $\pi^- p \to nK^0\bar{K}^0$, the essential contribution to the background stems from S-wave $K\bar{K}$-pair production from the isoscalar $\pi\pi$ state. Let us note that the parametrization of the total cross sections for the reactions $\pi N \to K\bar{K}N$ has been discussed previously in [39]. Here, we also analyze contributions from different channels to the total cross sections.

The most important point is that for all the reactions the background is essentially below the data at the c.m. energy release $Q \leq 300$ MeV. In the case of the reactions $\pi^+ p \to pK^+\bar{K}^0$ and $\pi^- p \to pK^0K^-$ this, in our opinion, can only be due to a contribution of a_0. Of course, in the reactions $\pi^- p \to nK^+K^-$ and $\pi^- p \to nK^0\bar{K}^0$, both scalar mesons, f_0 and a_0, can contribute. In a series of bubble chamber experiments performed in the 1960–1970s, a structure was reported in the mass distribution of the $K_S^0K_S^0$ system produced in the reaction $\pi^- p \to nK_S^0K_S^0$ (see, e.g., [40] and references therein). Usually, this structure was attributed to $f_0(980)$. In our previous work, we used the data on $\pi^- p \to nf_0 \to nK_S^0K_S^0$ to find a restriction on the branching $\mathrm{Br}(f_0 \to K\bar{K})$ [41]. We see here from Fig. 4 (upper right) that an important contribution to the cross section of the reaction $\pi^- p \to nK^0\bar{K}^0$ at $Q \leq 300$ MeV also comes from a_0. We cannot exclude that there can also be some contribution from $a_0(980)$ at $Q \geq 300$ MeV. If this is really the case, our restriction on $\mathrm{Br}(f_0 \to K\bar{K})$ [41] has to be corrected. This problem, however, requires further analysis.

Let us note that the amplitude corresponding to the Feynman diagram in Fig. 1*e* would predict a sharply rising cross section for $Q \geq 400$ MeV. To suppress this unrealistic behavior, we used a Reggeized K^* propagator multiplying the Feynman propagator of the vector meson in all the amplitudes by the Regge power $(s/s_0)^{(\alpha_{K^*}(0)-1)}$ with $\alpha_{K^*}(0) \simeq 0.25$ and $\sqrt{s_0} = 2m_K + m_N$. The background curves are in reasonable agreement with the data on the reactions $\pi^+ p \to pK^+\bar{K}^0$ and $\pi^- p \to pK^0K^-$ at $Q \geq 400$ MeV (see the crossed solid curves in the two lower panels of Fig. 4).

The Regge pole model for a_0 production, especially the set with b_1 and ρ_2 exchange, is in good agreement with the data for all the reactions at $Q \leq 300$ MeV, giving a cross section of the reaction $\pi N \to a_0 N \to K\bar{K}N$ of about 20–30 μb at $Q \simeq 100$–300 MeV. At

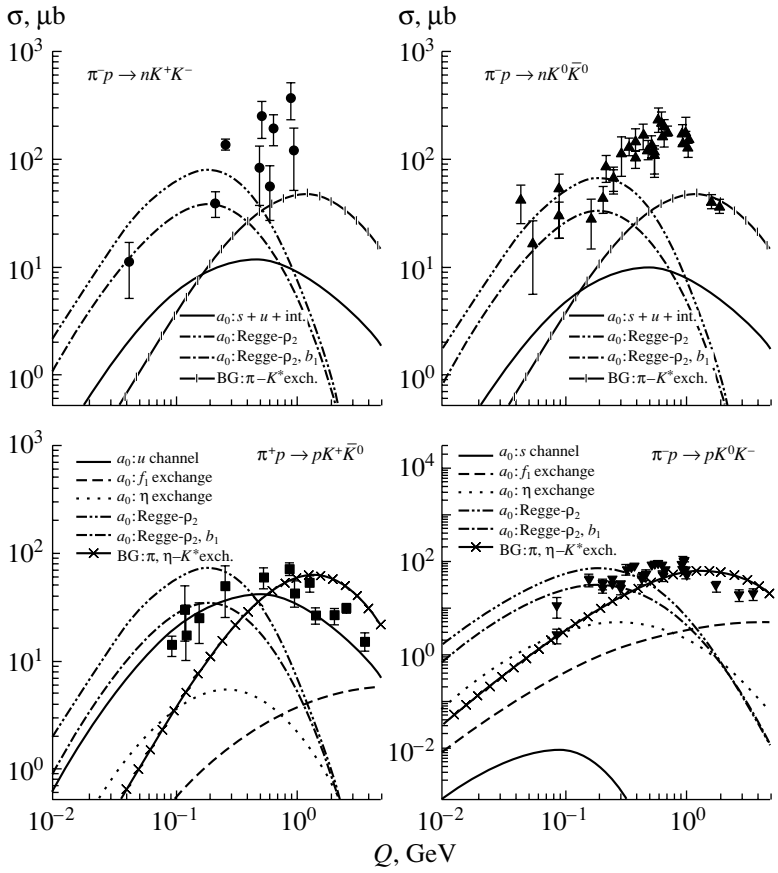

Fig. 4. The total cross sections for the reactions $\pi^- p \to nK^+K^-$, $\pi^- p \to nK^0\bar{K}^0$, $\pi^+ p \to pK^+\bar{K}^0$, and $\pi^- p \to pK^0K^-$ as a function of $Q = \sqrt{s} - \sqrt{s_0}$. Experimental data are taken from [38]. The solid curves describe s- and u-channel contributions, calculated with the dipole nucleon form factor $F_N^2(u)$ with $\Lambda_N = 1.35$ GeV. The short-dashed and long-dashed curves describe η and f_1 t-channel exchanges, respectively. Two different choices of the Regge pole model are shown by the dash-dotted curves which describe ρ_2 exchange (upper) and conspiring ρ_2, b_1 exchange (lower). The crossed solid curves show the background contribution from diagram in Fig. 1*e*.

larger Q, it drops very fast. The u-channel contribution is also in good agreement with the data on the reaction $\pi^+ p \to pK^+\bar{K}^0$, but the coherent sum of the u- and s-channel contributions is below the data for the reactions $\pi^- p \to nK^+K^-$ and $\pi^- p \to nK^0\bar{K}^0$. The t-channel η- and f_1-exchange contributions are small and can be neglected.

Note that both invariant mass distributions of the $K^-\bar{K}^0$ and $K_S^0 K_S^0$ systems presented in [40] show a resonance-like structure near the $K\bar{K}$ threshold at $Q \leq 300$ MeV. However, because of a comparatively small number of events for each fixed initial momentum, those distributions are averaged over a large interval of about 1 GeV/c in $p_{\rm lab}$. Unfortunately, those distributions cannot be directly compared with theoretical ones at any fixed Q, especially in the near-threshold region. In order to give another strong argument that the a_0 contribution is really necessary to explain the existing experimental data, let us consider the energy dependence of the total cross section of the reaction $\pi^- p \to pK^-\bar{K}^0$. Averaging the existing data from [38] versus $p_{\rm lab}$ over the intervals 2.0 ± 0.15 and 3.0 ± 0.15 GeV/c, we find $\sigma_{\rm av} = 34.9 \pm 3.3$ and 73.8 ± 7.6 μb, respectively. The ratio of those cross sections is equal to $R_{21} \simeq 2.1 \pm 0.05$. The energy behavior of the background contribution in our model is $\sigma_{\rm bg} \sim Q^{2.3}$. If we assume that, in the interval of $Q =$ 250–630 MeV (which corresponds to the interval of $p_{\rm lab} = 2$–3 GeV/c), the background contribution is present only, we get $R_{21}^{\rm bg} \simeq 5.5$. This means that at 3 GeV/c we should expect a cross section of $\simeq 200$ μb instead of ~ 70 μb. Evidently, experimental data are inconsistent with this assumption.

Let us formulate the main conclusions of this subsection. The existing data on the reactions $\pi^+ p \to pK^+\bar{K}^0$ and $\pi^- p \to pK^0K^-$ give rather strong evidence that, at low energy above threshold ($Q \leq$ 300 MeV), they are dominated by a_0 production. The same is also true for the reactions $\pi^- p \to nK^+K^-$

Coefficients in Eq. (25) for different mechanisms of the $pp \to ppa_0^0$, $pp \to pna_0^+$, $pn \to ppa_0^-$, and $pn \to pna_0^0$ reactions

Reaction j	Mechanism α	$\xi^{\pi}_{j(\alpha)}[ab;cd]$	$\xi^{\pi}_{j(\alpha)}[ab;dc]$	$\xi^{\pi}_{j(\alpha)}[ba;dc]$	$\xi^{\pi}_{j(\alpha)}[ba;cd]$
$pp \to ppa_0^0$	$t(\eta), t(f_1)$	$+1/\sqrt{2}$	$-1/\sqrt{2}$	$+1/\sqrt{2}$	$-1/\sqrt{2}$
	$s(N)$	$+1/\sqrt{2}$	$-1/\sqrt{2}$	$+1/\sqrt{2}$	$-1/\sqrt{2}$
	$u(N)$	$+1/\sqrt{2}$	$-1/\sqrt{2}$	$+1/\sqrt{2}$	$-1/\sqrt{2}$
	Regge	0	0	0	0
$pp \to pna_0^+$	$t(\eta), t(f_1)$	$-\sqrt{2}$	0	0	$+\sqrt{2}$
	$s(N)$	0	$+\sqrt{2}$	$-\sqrt{2}$	0
	$u(N)$	$+2\sqrt{2}$	$-\sqrt{2}$	$+\sqrt{2}$	$-2\sqrt{2}$
	Regge	-1	$+1$	-1	$+1$
$pn \to ppa_0^-$	$t(\eta), t(f_1)$	$+1$	-1	0	0
	$s(N)$	-2	$+2$	-1	$+1$
	$u(N)$	0	0	$+1$	-1
	Regge	$+1/\sqrt{2}$	$-1/\sqrt{2}$	$-1/\sqrt{2}$	$+1/\sqrt{2}$
$pn \to pna_0^0$	$t(\eta), t(f_1)$	-1	0	$+1$	0
	$s(N)$	-1	-2	$+1$	$+2$
	$u(N)$	-1	$+2$	$+1$	-2
	Regge	0	$+\sqrt{2}$	0	$-\sqrt{2}$

and $\pi^- p \to nK^0\bar{K}^0$, where some smaller contribution of f_0 may also be present. The value of the a_0-production cross section is reasonably described by the Regge pole model with ρ_2, b_1 exchange as proposed by Achasov and Shestakov [12]. The u-channel exchange mechanism also gives a reasonable value of the cross section.

4. THE REACTION $NN \to NNa_0$

4.1. An Effective Lagrangian Approach with One-Pion Exchange

We consider a_0^0, a_0^+, a_0^- production in the reactions $j = pp \to ppa_0^0$, $pp \to pna_0^+$, $pn \to ppa_0^-$, and $pn \to pna_0^0$ using the effective Lagrangian approach with one-pion exchange (OPE). For the elementary $\pi N \to Na_0$ transition amplitude, we take into account different mechanisms α corresponding to t-channel diagrams with $\eta(550)$- and $f_1(1285)$-meson exchanges ($\alpha = t(\eta), t(f_1)$) as well as s- and u-channel graphs with an intermediate nucleon ($\alpha = s(N), u(N)$) (cf. [18]). The corresponding diagrams are shown in Fig. 5. The invariant amplitude of the $NN \to NNa_0$ reaction then is the sum of the four basic terms (diagrams in Fig. 5) with permutations of nucleons in the initial and final states

$$\mathcal{M}^{\pi}_{j(\alpha)}[ab;cd] = \xi^{\pi}_{j(\alpha)}[ab;cd]\,\mathcal{M}^{\pi}_{\alpha}[ab;cd] \qquad (25)$$
$$+ \xi^{\pi}_{j(\alpha)}[ab;dc]\,\mathcal{M}^{\pi}_{\alpha}[ab;dc] + \xi^{\pi}_{j(\alpha)}[ba;dc] \times \mathcal{M}^{\pi}_{\alpha}[ba;dc] + \xi^{\pi}_{j(\alpha)}[ba;cd]\,\mathcal{M}^{\pi}_{\alpha}[ba;cd],$$

where the coefficients $\xi^{\pi}_{j(\alpha)}$ are given in the table. The amplitudes for the t-channel exchange with $\eta(550)$ and $f_1(1285)$ mesons are given by

$$\mathcal{M}^{\pi}_{t(\eta)}[ab;cd] = g_{a_0\eta\pi}F_{a_0\eta\pi} \qquad (26)$$
$$\times \left((p_a-p_c)^2,(p_d-p_b)^2\right) g_{\eta NN}F_{\eta}\left((p_a-p_c)^2\right) \times \frac{1}{(p_a-p_c)^2-m_{\eta}^2}\bar{u}(p_c)\gamma_5 u(p_a)\Pi(p_b;p_d),$$

$$\mathcal{M}^{\pi}_{t(f_1)}[ab;cd] = -g_{a_0f_1\pi}F_{a_0f_1\pi} \qquad (27)$$
$$\times \left((p_a-p_c)^2,(p_d-p_b)^2\right) g_{f_1NN}F_{f_1}\left((p_a-p_c)^2\right) \times \frac{1}{(p_a-p_c)^2-m_{f_1}^2}(p_a-p_c+2(p_b-p_d))_{\mu} \times \left(g_{\mu\nu}-\frac{(p_a-p_c)_{\mu}(p_a-p_c)_{\nu}}{m_{f_1}^2}\right) \times \bar{u}(p_c)\gamma_5\gamma_{\nu}u(p_a)\Pi(p_b;p_d),$$

with

$$\Pi(p_b;p_d) = \frac{f_{\pi NN}}{m_{\pi}}F_{\pi}\left((p_b-p_d)^2\right)(p_b-p_d)_{\beta} \qquad (28)$$

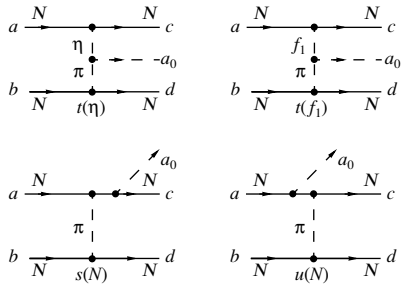

Fig. 5. Diagrams for a_0 production in the reaction $NN \to a_0 NN$.

$$\times\, \bar{u}(p_d)\gamma_5\gamma_\beta u(p_b)\frac{1}{(p_b-p_d)^2-m_\pi^2}.$$

The amplitudes for the s and u channels (lower part of Fig. 5) are given as

$$\mathcal{M}^{\pi}_{s(N)}[ab;cd] = \Pi(p_b;p_d) \tag{29}$$
$$\times\, \frac{f_{\pi NN}}{m_\pi} F_\pi\left((p_d-p_b)^2\right) g_{a_0 NN}$$
$$\times\, \frac{F_N\left((p_a+p_b-p_d)^2\right)}{(p_a+p_b-p_d)^2-m_N^2}(p_d-p_b)_\mu\, \bar{u}(p_c)$$
$$\times\, [(p_a+p_b-p_d)_\delta\gamma_\delta + m_N]\gamma_5\gamma_\mu u(p_a),$$

$$\mathcal{M}^{\pi}_{u(N)}[ab;cd] = \Pi(p_b;p_d) \tag{30}$$
$$\times\, \frac{f_{\pi NN}}{m_\pi} F_\pi\left((p_d-p_b)^2\right) g_{a_0 NN}$$
$$\times\, \frac{F_N\left((p_c+p_d-p_b)^2\right)}{(p_c+p_d-p_b)^2-m_N^2}(p_d-p_b)_\mu \bar{u}(p_c)\gamma_5\gamma_\mu$$
$$\times\, [(p_c+p_d-p_b)_\delta\gamma_\delta + m_N]u(p_a).$$

Here, p_a, p_b and p_c, p_d are the 4-momenta of the initial and final nucleons, respectively. As in the previous section, we mostly employ coupling constants and form factors from the Bonn–Jülich potentials (see, e.g., [27, 28, 42]).

For the form factors at the $a_0 f_1 \pi$ (as well as $a_0\eta\pi$) vertex, factorized forms are applied following the assumption from [43, 44],

$$F_{a_0 f_1\pi}(t_1,t_2) = F_{f_1 NN}(t_1)F_{\pi NN}(t_2), \tag{31}$$

where $F_{f_1 NN}(t), F_{\pi NN}(t)$ are taken in the monopole form (see previous section). Usually, the cutoff parameter $\Lambda_{\pi NN}$ is taken in the interval 1–1.3 GeV. Here, we take $\Lambda_{\pi NN} = 1.05$ GeV (see also the discussion in [19]).

As shown in the analysis of [18], the contribution of the η exchange to the amplitude $\pi N \to a_0 N$ is small (cf. also Section 3). Note that in [45] only this mechanism was taken into account for the reaction $pn \to pp\, a_0^-$. Here, we also include the η exchange

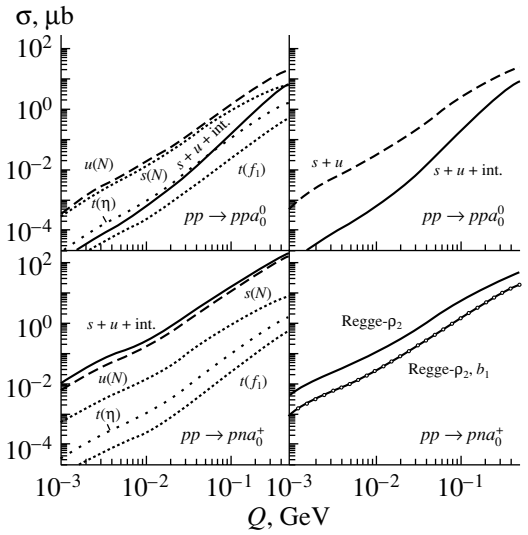

Fig. 6. The total cross sections for the reactions $pp \to ppa_0^0$ and $pp \to pna_0^+$ as a function of the excess energy $Q = \sqrt{s} - \sqrt{s_0}$ calculated with FSI.

because it might be noticeable in those isospin channels where a strong destructive interference of u- and s-channel terms can occur (see below).

Since we have two nucleons in the final state, it is necessary to take into account their final-state interaction (FSI), which has some influence on meson production near the threshold. For this purpose, we adopt the FSI model from [46] based on the (realistic) Paris potential. We use, however, the enhancement factor $F_{NN}(q_{NN})$—as given by this model—only in the region of small relative momenta of the final nucleons $q_{NN} \le q_0$, where it is larger than 1. Having in mind that this factor is rather uncertain at larger q_{NN}, where, for example, contributions of nonnucleon intermediate states to the loop integral might be important, we assume that $F_{NN}(q_{NN}) = 1$ for $q_{NN} \ge q_0$.

In Fig. 6, we show the total cross section as a function of the energy excess $Q = \sqrt{s} - \sqrt{s_0}$ for the reactions $pp \to ppa_0^0$ (upper part) and $pp \to pna_0^+$ (lower part). As seen from Fig. 6, the u and s channels give the dominant contribution; the $t(f_1)$ channel is small for both isospin reactions. For the reaction $pp \to pna_0^+$, the Regge exchange contribution (extended to low energies) becomes important. For the $pp \to ppa_0^0$ channel, the Regge model predicts no contribution from ρ_2 and ρ_2, b_1 exchanges due to isospin arguments (i.e., the vertex with a coupling of three neutral components of isovectors vanishes); thus, only s, u, $t(\eta)$, and $t(f_1)$ channels are plotted in the upper part of Fig. 6.

Here, we have to point out the influence of the interference between the s and u channels. According to the isospin coefficients from the OPE model presented in the table, the phase (of interference α) between the s and u channels $\mathcal{M}^{\pi}_{s(N)} + \exp(-i\alpha)\mathcal{M}^{\pi}_{u(N)}$ is equal to zero; i.e., the sign between $\mathcal{M}^{\pi}_{s(N)}$ and $\mathcal{M}^{\pi}_{u(N)}$ is "plus." The solid curves in Fig. 6 indicate the coherent sum of $s(N)$ and $u(N)$ channels including the interference of the amplitudes ($s + u +$ int.). One can see that, for the $pp \to pna_0^+$ reaction, the interference is positive and increases the cross section, whereas, for the $pp \to ppa_0^0$ channel, the interference is strongly destructive since we have identical particles in the initial and final states and the contributions of s and u channels are very similar.

Here, we would like to comment on an extension of the OPE model to a one-boson exchange (OBE) approximation, i.e., accounting for the exchange of σ, ρ, ω, ... mesons as well as for multimeson exchanges. Generally speaking, the total cross section of a_0 production should contain the sum of all the contributions:

$$\sigma(NN \to NNa_0) = \sum_j \sigma_j,$$

where $j = \pi, \sigma, \rho, \omega, \ldots$. Depending on their cutoff parameters, the heavier meson exchanges might give a comparable contribution to the total cross section for a_0 production. An important point, however, is that, near threshold (e.g., $Q \leq 0.3$–0.6 GeV), the energy behavior of all those contributions is the same, i.e., it is proportional to the three-body phase space $\sigma_j \sim Q^2$ (when the FSI is switched off and the narrow resonance width limit is taken). In this respect, we can consider the OPE as an effective one and normalize it to the experimental cross section by choosing an appropriate value of Λ_π. The most appropriate choice for Λ_π is about 1–1.3 GeV. Another question is related to the isospin of the effective exchange. As is known from a series of papers on the reactions $NN \to NNX, X = \eta, \eta', \omega, \phi$, the most important contributions to the corresponding cross sections near the threshold come from π and ρ exchanges (see, e.g., the review [47] and references therein). In line with those results, we assume here that the dominant contribution to the cross section of the reaction $NN \to NNa_0$ also comes from the isovector exchanges (like π and ρ). In principle, it is also possible that some baryon resonances may contribute. However, there is no information about resonances that couple to the a_0N system. Our assumptions thus enable us to make exploratory estimates of the a_0-production cross section without introducing free parameters that would be out of control by existing data. The model can be extended accordingly when new data on a_0 production become available.

Another important question is related to the choice of the form factor for a virtual nucleon, which—in line with the Bonn–Jülich potentials—we choose as given by (15), which corresponds to monopole form factors at the vertices. In the literature, furthermore, dipole-like form factors (at the vertices) are also often used (cf. [44, 47, 48]). However, there are no strict rules for the "correct" power of the nucleon form factor. In physics terms, the actual choice of the power should be irrelevant; we may have the same predictions for any reasonable choice of the power if the cutoff parameter Λ_N is fixed accordingly. Note that Λ_N may also depend on the type of mesons involved at the vertices. In our previous work [18], we have fixed Λ_N for the monopole related form factor (15) in the interval 1.2–1.3 GeV fitting the forward differential cross section of the reaction $pp \to da_0^+$ from [49]. On the other hand, the same data can be described rather well using a dipole form factor (at the vertices) with $\Lambda_N = 1.55$–1.6 GeV. If we employ this dipole form factor with $\Lambda_N = 1.55$–1.6 GeV in the present case, we obtain practically identical predictions for the cross sections of the channels $pp \to pna_0^+$, $pn \to pna_0^0$, and $pn \to ppa_0^-$, where the u-channel mechanism is dominant and u–s interference is not too important. In the case of the channel $pp \to ppa_0^0$, we obtain cross sections up to a factor of 2 larger for the dipole-like form factor in comparison to the monopole one. This is related to the strong destructive interference of the s- and u-exchange mechanisms, which slightly depends on the type of form factor used. However, our central result, that the cross section for the pna_0^+ final channel is about an order of magnitude higher than the ppa_0^0 channel in pp collisions, is robust (within less than a factor of 2) with respect to different choices of the form factor.

As seen from Fig. 6, we get the largest cross section for the $pp \to pna_0^+$ isospin channel. For this reaction, the u channel gives the dominant contribution; the s-channel cross section is small such that the interference is not so essential as for the $pp \to pp\,a_0^0$ reaction.

As was already discussed in our previous study [18], an effective Lagrangian model (ELM) cannot be extrapolated to high energies because it predicts the elementary amplitude $\pi N \to a_0 N$ to rise fast. Therefore, such a model can only be employed not far from the threshold. On the other hand, the Regge model is valid at large energies and we have to worry about how close to the threshold we can extrapolate corresponding amplitudes. According to duality arguments, one can expect that the Regge amplitude can be applied at low energy, too, if the reaction

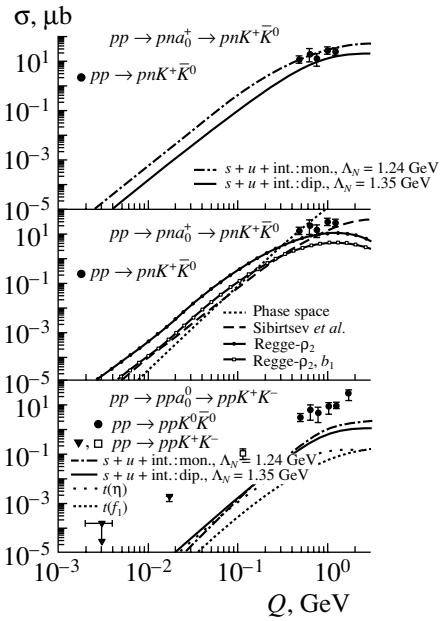

Fig. 7. The calculated total cross sections for the reactions $pp \to ppa_0^+ \to ppK^+\bar{K}_0$ and $pp \to pna_0^0 \to ppK^+K^-$ in comparison to the experimental data as functions of $Q = \sqrt{s} - \sqrt{s_0}$. For more details, see the text.

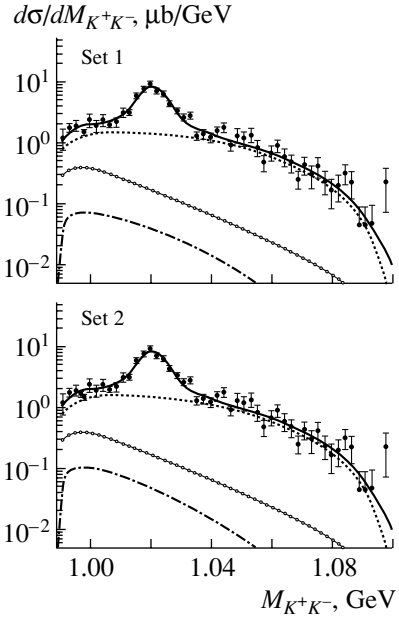

Fig. 8. The K^+K^- invariant mass distribution for the $pp \to ppK^+K^-$ reaction at $p_{\rm lab} = 3.67$ GeV/c. The dotted curves indicate the 4-body phase space with constant interaction amplitude, the dash-dotted curves show the coherent sum of $s(N)$ and $u(N)$ channels with interference. The solid curves with open circles correspond to the f_0 contribution from [41]. The thick solid curves show the sum of all contributions including the decay $\phi \to K^+K^-$. The experimental data are taken from [50].

$\pi N \to a_0 N$ does not contain essential s-channel resonance contributions. In this case, the Regge model might give a realistic estimate of the $\pi N \to a_0 N$ and $NN \to NNa_0$ amplitudes even near the threshold.

Anyway, as we have shown in [18] (see also Section 3), the Regge and u-channel model give quite similar results for the $\pi^- p \to a_0^0 n$ cross section in the threshold region; some differences in the cross sections of the reactions $NN \to NNa_0$—as predicted by those two models—can be attributed to differences in the isospin factors and effects of NN antisymmetrization, which is important near the threshold (the latter was ignored in the Regge model formulated for larger energies).

4.2. Reaction $NN \to NNa_0 \to NNK\bar{K}$

4.2.1. Numerical results for the total cross section. In the upper part of Fig. 7, we display the calculated total cross section [within parameter set 1 (8)] for the reaction $pp \to pna_0^+ \to pnK^+\bar{K}^0$ in comparison to the experimental data for $pp \to pnK^+\bar{K}^0$ (dots) from [38] as a function of the excess energy $Q = \sqrt{s} - \sqrt{s_0}$. The dash-dotted and solid curves in Fig. 7 correspond to the coherent sum of $s(N)$ and $u(N)$ channels with interference ($s + u +$ int.), calculated with a monopole form of the form factor (15) with $\Lambda_N = 1.24$ GeV and with a dipole form $(F_N(u)^2)$ with $\Lambda_N = 1.35$ GeV, respectively. We mention that the latter (dipole) result is in better agreement with the constraints on the near-threshold production of a_0 in the reaction $\pi^+ p \to K^+\bar{K}^0 p$ (see Section 3). In the middle part of Fig. 7, the solid curves with full dots and with open squares present the results within the ρ_2 and ρ_2, b_1 Regge exchange model. The dotted curve shows the 4-body phase space (with constant interaction amplitude), while the dashed curve is the parametrization from Sibirtsev *et al.* [39]. We note, that the cross sections for parameter set 2 (9) are similar to set 1 (8) and larger by a factor of about 1.5.

In the lower part of Fig. 7, we show the calculated total cross section (within parameter set 1) for the reaction $pp \to ppa_0^0 \to ppK^+K^-$ as a function of $Q = \sqrt{s} - \sqrt{s_0}$ in comparison to the experimental data. The closed circles indicate the data for $pp \to ppK^0\bar{K}^0$ from [38], the open square for $pp \to ppK^+K^-$ is from the DISTO collaboration [50], and the closed triangles show the data from COSY-11 [51].

For the $pp \to ppa_0^0 \to ppK^+K^-$ reaction (as for $pp \to ppa_0^0$), there is no contribution from meson Regge trajectories; s and u channels give similar contributions such that their interference according to the effective OPE model (curve $s + u +$ int.) is

strongly destructive (cf. upper part of Fig. 6). The $t(f_1)$ contribution (dotted curve) is practically negligible, while the $t(\eta)$ channel (rare-dotted curve) becomes important closer to the threshold.

Thus, our model gives quite small cross sections for a_0^0 production in the $pp \to ppK^+K^-$ reaction, which complicates its experimental observation for this isospin channel. The situation looks more promising for the $pp \to pna_0^+ \to pnK^+\bar{K}^0$ reaction since the a_0^+-production cross section is an order of magnitude larger than the a_0^0 one. Moreover, as has been pointed out with respect to Fig. 6, the influence of the interference is not as strong as that for the $pp \to pp\,a_0^0 \to ppK^+K^-$ reaction.

Here, we stress again the limited applicability of the ELM at high energies. As seen from the upper part of Fig. 7, the ELM calculations at high energies go through the experimental data, which is not realistic since other channels also contribute to $K^+\bar{K}^0$ production in pp reactions (cf. dashed curve from [39], Fig. 7, middle part). Moreover, the ELM calculations are higher than the Regge model predictions, which indicates that the ELM amplitudes at high energies have to be Reggeized.

4.2.2. Numerical results for the invariant mass distribution. As follows from the lower part of Fig. 7, the a_0 contribution to the K^+K^- production in the $pp \to ppK^+K^-$ reaction near the threshold is hardly seen. With increasing energy, the cross section grows; however, even at $Q = 0.111$ GeV, the full cross section with interference ($s + u + \text{int.}$) gives only a few percent contribution to the $0.11 \pm 0.009 \pm 0.046$ μb "nonresonant" cross section (without $\phi \to K^+K^-$) from the DISTO collaboration [50].

To clarify the situation with the relative contribution of a_0^0 to the total K^+K^- production in pp reactions, we calculate the K^+K^- invariant mass distribution for the $pp \to ppK^+K^-$ reaction at $p_{\text{lab}} = 3.67$ GeV/c, which corresponds to the kinematical conditions for the DISTO experiment [50]. The differential results are presented in Fig. 8. The upper part shows the calculation within parameter set 1, whereas the lower part corresponds to set 2. The dash-dotted curves indicate the coherent sum of $s(N)$ and $u(N)$ channels with interference for the a_0 contribution. However, one has to consider also the contribution from the f_0 scalar meson, i.e., the $pp \to ppf_0 \to ppK^+K^-$ reaction. The f_0 production in pp reactions has been studied in detail in [41]. Here, we use the result from [41] and show in Fig. 8 the contribution from the f_0 meson (calculated with parameter set A from [41]) as the solid curve with open circles.

We find that, when adding the f_0 contribution to the phase space of nonresonant K^+K^- production (the dotted curves in Fig. 8) and the contribution from ϕ decays (resonance peak around 1.02 GeV), the sum (thick solid) curves almost perfectly describe the DISTO data. This means that there is no visible signal for an a_0^0 contribution in the DISTO data according to our calculations, while the f_0 meson gives some contribution to the K^+K^- invariant mass distribution at low invariant masses M, that is, about 12% of the total "nonresonant" cross section from the DISTO collaboration [50]. Thus, the reaction $pp \to pnK^+\bar{K}^0$ is more promising for a_0 measurements, as has been pointed out above.

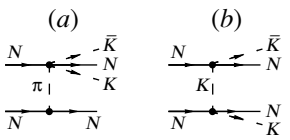

Fig. 9. Diagrams describing different mechanisms of nonresonant $K\bar{K}$ production in the reaction $NN \to NNK\bar{K}$.

4.2.3. Nonresonant background. Following [39], we consider two mechanisms of nonresonant $K\bar{K}$ production, related to pion and kaon exchanges, which are described by the diagrams in Fig. 9. The pion-exchange amplitude can be calculated using the results of Section 3. As concerning the kaon-exchange mechanism, the amplitude of the reaction $NN \to NNa_0 \to NNK\bar{K}$ can be written as

$$\begin{aligned} &\mathrm{M}_{\text{K-exch}}(p_a, p_b; p_c, p_d, k_1, k_2) \qquad (32)\\ &= \frac{F_K^2(q^2)}{q^2 - m_K^2}\bar{u}(p_c)A_{KN\to KN}(p_c, k_1; p_a, q)u(p_a)\\ &\quad \times \bar{u}(p_d)A_{\bar{K}N\to\bar{K}N}(p_d, k_2; p_b, q)u(p_b) \end{aligned}$$

with permutations of nucleons in the initial and final states. Here, p_a, p_b and p_c, p_d are the 4-momenta of the initial and final nucleons, respectively; k_1 and k_2 are the momenta of the final kaons; q is the momentum of the virtual kaon; and $F_K(q^2)$ is the kaon form factor, which we take in the monopole form with the cutoff parameter $\Lambda = 1.2$ GeV.

The antikaon–nucleon amplitude $A_{\bar{K}N\to\bar{K}N}$ has been taken from [52] explicitly. Since near threshold the $KN \to KN$ cross section depends mainly on the normalization of the amplitude, but not on its spin dependence, we adopt the simplest approximation that the amplitude $A_{KN\to KN}$ is a Lorentz scalar. This allows us to connect the $A_{KN\to KN}$ amplitude (squared) by simple kinematical factor to the $KN \to KN$ cross section, where the parametrization for the elastic $K^+p \to K^+p$ cross section has been taken from [53] and the $K^0p \to K^+n$ cross section has been parametrized according to the existing data [38, 54].

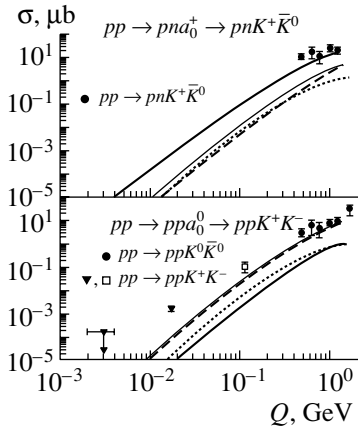

Fig. 10. Comparison of the a_0-resonance contribution (thick solid curves) and nonresonant background (thin solid curves) in the reactions $pp \to pnK^+\bar{K}^0$ and $pp \to ppK^+K^-$. The contribution of the pion-exchange mechanism is shown by the dotted curves, and the dashed curves describe the K-exchange mechanism. The thin solid curves show the sum of the pion- and kaon-exchange mechanisms. The experimental data are taken from [50].

The results of our calculations are shown in Fig. 10 in comparison to the experimental data. The contribution of the pion-exchange mechanism is shown by the dotted curves. The dashed curves describe the K-exchange mechanism. The thin solid curves show the total background, which in our model is the sum of pion- and kaon-exchange contribution. This background can be compared with the a_0-production cross section shown by the thick solid curves. In the case of the reaction $pp \to pnK^+\bar{K}^0$ (upper part), the a_0-production cross section is much larger than the background, while, in the case of the reaction $pp \to ppK^+K^-$ (lower part), the $a_0(980)$-resonance contribution appears to be much smaller than the nonresonant background. We mention that the disagreement with the DISTO ($Q \simeq 100$ MeV) and COSY–11 ($Q \simeq 17$ MeV) data should be related to the K^-pp FSI, which is known to be strong.

4.2.4. Concluding remarks on a_0 production in pN reactions. In this section, we have estimated the cross sections of a_0 production in the reactions $pp \to ppa_0^0$ and $pp \to pna_0^+$ near the threshold and at medium energies. Using an effective Lagrangian approach with OPE, we have analyzed different contributions to the cross section corresponding to t-channel diagrams with $\eta(550)$- and $f_1(1285)$-meson exchanges as well as s- and u-channel graphs with an intermediate nucleon. We additionally have considered the t-channel Reggeon exchange mechanism with parameters normalized to the Brookhaven data for $\pi^-p \to a_0^-p$ at 18 GeV/c [35]. These results have been used to calculate the contribution of a_0 mesons to the cross sections of the reactions $pp \to pnK^+\bar{K}^0$ and $pp \to ppK^+K^-$. Due to unfavorable isospin Clebsh–Gordan coefficients as well as rather strong destructive interference of the s- and u-channel contributions, our model gives quite small cross sections for a_0^0 production in the $pp \to ppK^+K^-$ reaction. However, the a_0^+-production cross section in the $pp \to pna_0^+ \to pnK^+\bar{K}^0$ reaction should be larger by about an order of magnitude. Therefore, the experimental observation of a_0^+ in the reaction $pp \to pnK^+\bar{K}^0$ is much more promising than the observation of a_0^0 in the reaction $pp \to ppK^+K^-$. We note in passing that the $\pi\eta$ decay channel is experimentally more challenging since, due to the larger nonresonant background [55], the identification of the η meson (via its decay into photons) in a neutral-particle detector is required.

We have also analyzed invariant mass distributions of the $K\bar{K}$ system in the reaction $pp \to pNa_0 \to pNK\bar{K}$ at different excess energies Q not far from the threshold. Our analysis of the DISTO data on the reaction $pp \to ppK^+K^-$ at 3.67 GeV/c has shown that the a_0^0 meson is hardly seen in $d\sigma/dM$ at low invariant masses; however, the f_0 meson gives some visible contribution. In this respect, the possibility of measuring the a_0^+ meson in $d\sigma/dM$ for the reaction $pp \to pnK^+\bar{K}^0$ (or $\to dK^+\bar{K}^0$) looks much more promising not only due to a much larger contribution for the a_0^+, but also due to the absence of the f_0 meson in this channel. It is also very important that the nonresonant background is expected to be much smaller than the a_0 signal in the $pp \to pnK^+\bar{K}^0$ reaction.

Experimental data on a_0 production in NN collisions are practically absent (except for the a_0 observation in the reaction $pp \to dX$ [49]). Such measurements might give new information on the a_0 structure. According to Atkinson *et al.* [56], a relatively strong production of a_0 [the same as for the $b_1(1235)$] in nondiffractive reactions can be considered as evidence for a $q\bar{q}$ state rather than a $qq\bar{q}\bar{q}$ state. For example, the cross section of a_0 production in γp reactions at 25–50 GeV is about 1/6 of the cross sections for ρ and ω production. Similar ratios are found in the two-body reaction $pp \to dX$ at 3.8–6.3 GeV/c, where $\sigma(pp \to da_0^+) = (1/4\text{–}1/6)\sigma(pp \to d\rho^+)$.

In our case, we can compare a_0 and ω production. Our model predicts $\sigma(pp \to pna_0^+) = 30\text{–}70$ μb at $Q \simeq 1$ GeV, which can be compared with $\sigma(pp \to ppp\omega) \simeq 100\text{–}200$ μb at the same Q. If such a large cross section could be detected experimentally, this would be a serious argument in favor of the $q\bar{q}$ model for a_0.

To distinguish between the threshold cusp scenario and a resonance model, one can exploit different analytical properties of the a_0-production amplitudes. In case of a genuine resonance, the amplitude of $\eta\pi$ and $K\bar{K}$ production through a_0 has a pole and satisfies the factorization property. This implies that the shapes of the invariant mass distributions in the $\eta\pi$ and $K\bar{K}$ channels should not depend on the specific reaction in which a_0 resonance is produced (for $Q \geq \Gamma_{\rm tot}$). On the other hand, for the threshold cusp scenario, the a_0 bump is produced through the $\pi\eta$ FSI. The corresponding amplitude has a square root singularity and in general cannot be factorized (see, e.g., [46], where the factorization property was disproven for pp FSI in the reaction $pp \to ppM$). This implies that, for a threshold bump, the invariant mass distributions in the $\eta\pi$ and $K\bar{K}$ channels are expected to be different for different reactions and will depend on kinematical conditions (i.e., momentum transfer) even at the same value of excess energy, e.g., $Q \simeq 1$ GeV.

5. $a_0(980)$–$f_0(980)$ MIXING AND ISOSPIN VIOLATION IN THE REACTIONS $pN \to da_0$, $pd \to {}^3\mathrm{He}({}^3\mathrm{H})a_0$, AND $dd \to {}^4\mathrm{He}\,a_0$

5.1. Hints for $a_0(980)$–$f_0(980)$ Mixing

As was suggested long ago in [11], the dynamical interaction of the $a_0(980)$ and $f_0(980)$ mesons with states close to the $K\bar{K}$ threshold may give rise to a significant $a_0(980)$–$f_0(980)$ mixing. Different aspects of this mixing and the underlying dymanics, as well as the possibilities of measuring this effect, have been discussed in [3, 12–17]. Furthermore, it has been suggested by Close and Kirk [16] that the new data from the WA102 collaboration at CERN [26] on the central production of f_0 and a_0 in the reaction $pp \to p_s X p_f$ provide evidence for a significant f_0–a_0-mixing intensity as large as $|\xi|^2 = (8 \pm 3)\%$. In this section, we will discuss possible experimental tests of this mixing in the reactions

$$pp \to da_0^+ \quad \text{(a)}, \quad pn \to da_0^0 \quad \text{(b)},$$
$$pd \to {}^3\mathrm{H}\,a_0^+ \quad \text{(c)}, \quad pd \to {}^3\mathrm{He}\,a_0^0 \quad \text{(d)},$$
$$dd \to {}^4\mathrm{He}\,a_0^0 \quad \text{(e)}$$

near the corresponding thresholds. We recall that the a_0 meson can decay to $\pi\eta$ or $K\bar{K}$. Here, we only consider the dominant $\pi\eta$-decay mode. Note that the isospin-violating anisotropy in reaction (b) due to the $a_0(980)$–$f_0(980)$ mixing is very similar to that which might arise in the reaction $pn \to d\pi^0$ because of the π^0–η mixing (see [57]). Recently, measurements of the charge-symmetry breaking in the reactions $\pi^+ d \to pp\eta$ and $\pi^- d \to nn\eta$ near the η-production threshold were performed at BNL [57]. A similar experiment, comparing the reactions $pd \to {}^3\mathrm{He}\pi^0$ and $pd \to {}^3\mathrm{H}\pi^+$ near the η-production threshold, is now being performed at COSY (Jülich) (see, e.g., [58]).

5.2. Reactions $pp \to da_0^+$ and $pn \to da_0^0$

5.2.1. Phenomenology of isospin violation. In reactions (a) and (b), the final da_0 system has isospin $I_f = 1$; for $l_f = 0$ (S-wave production close to threshold), it has spin-parity $J_f^P = 1^+$. The initial NN system cannot be in the state $I_i = 1$, $J_i^P = 1^+$ due to the Pauli principle. Therefore, near threshold, the da_0 system should be dominantly produced in the P wave with quantum numbers $J_f^P = 0^-$, 1^-, or 2^-. The states with $J_i^P = 0^-$, 1^-, or 2^- can be formed by an NN system with spin $S_i = 1$ and $l_i = 1$ and 3. At the beginning, for qualitative discussion, we neglect the contribution of the higher partial wave ($l_i = 3$).[5] In this case, we can write the amplitude of reaction (a) in the following form:

$$T(pn \to d\,a_0^+) = \alpha^+(\mathbf{p}\cdot\mathbf{S})(\mathbf{k}\cdot\mathbf{e}^*) \qquad (33)$$
$$+ \beta^+(\mathbf{p}\cdot\mathbf{k})(\mathbf{S}\cdot\mathbf{e}^*) + \gamma^+(\mathbf{S}\cdot\mathbf{k})(\mathbf{p}\cdot\mathbf{e}^*),$$

where $\mathbf{S} = \phi_N^T \sigma_2 \boldsymbol{\sigma} \phi_N$ is the spin operator of the initial NN system; $\mathbf{p}$ and $\mathbf{k}$ are the initial and final c.m. momenta; $\mathbf{e}$ is the deuteron polarization vector; and α^+, β^+, and γ^+ are three independent scalar amplitudes that can be considered as constants near threshold (at $k \to 0$).

Due to the mixing, a_0^0 may also be produced via f_0. In this case, the $a_0^0 d$ system will be in the S wave and the amplitude of reaction (b) can be written as

$$T(pn \to da_0^0) = \alpha^0(\mathbf{p}\cdot\mathbf{S})(\mathbf{k}\cdot\mathbf{e}^*) \qquad (34)$$
$$+ \beta^0(\mathbf{p}\cdot\mathbf{k})(\mathbf{S}\cdot\mathbf{e}^*) + \gamma^0(\mathbf{S}\cdot\mathbf{k})(\mathbf{p}\cdot\mathbf{e}^*) + \xi F(\mathbf{S}\cdot\mathbf{e}^*),$$

where ξ is the mixing parameter and F is the f_0 production amplitude. In the limit $k \to 0$, F is again a constant. The scalar amplitudes α, β, and γ for reactions (a) and (b) are related to each other by a relative factor of $\sqrt{2}$ as $\alpha^+ = \sqrt{2}\alpha^0$, $\beta^+ = \sqrt{2}\beta^0$, and $\gamma^+ = \sqrt{2}\gamma^0$.

The differential cross sections for reactions (a) and (b) have the form (up to terms linear in ξ)

$$\frac{d\sigma(pp \to da_0^+)}{d\Omega} = 2\frac{k}{p}\left(C_0 + C_2\cos^2\theta\right), \qquad (35)$$

[5] See, e.g., phenomenological analysis in [59], where this partial wave was also taken into account.

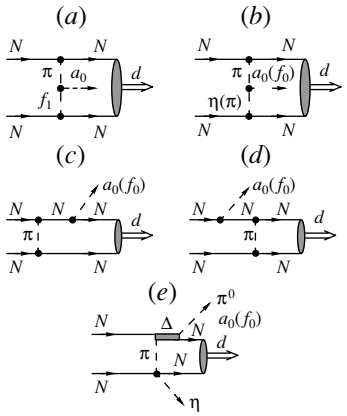

Fig. 11. Diagrams describing (a–d) different mechanisms of a_0- and f_0-meson production in the reaction $NN \to da_0(f_0)$ within the framework of the TSM and (e) the nonresonant $\pi\eta$ production.

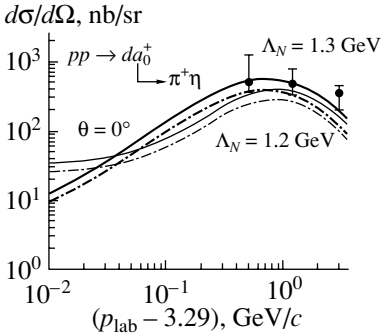

Fig. 12. Forward differential cross section of the reaction $pp \to da_0^+$ as a function of ($p_{\rm lab} - 3.29$ GeV/c). The dots are the experimental data from [49], while the thick dash-dotted and solid curves describe the results of the TSM for $\Lambda_N = 1.2$ and 1.3 GeV, respectively. The thin curves are calculated using the Flatté mass distribution for the a_0 meson with a cut $M_{\pi^+\eta} \geq 0.85$ GeV and $\Lambda_N = 1.2$ GeV (dash-dotted curve) or 1.3 GeV (solid curve).

$$\frac{d\sigma(pn \to da_0^0)}{d\Omega} = \frac{k}{p}\left(C_0 + C_2\cos^2\theta + C_1\cos\theta\right), \tag{36}$$

where

$$C_0 = \frac{1}{2}p^2k^2\left[|\alpha^0|^2 + |\gamma^0|^2\right], \tag{37}$$

$$C_1 = pk\mathrm{Re}((\xi F)^*(\alpha^0 + 3\beta^0 + \gamma^0)),$$

$$C_2 = \frac{1}{2}p^2k^2\left[3|\beta^0|^2 + 2\mathrm{Re}(\alpha^0\beta^{0*} + \alpha^0\gamma^{0*} + \beta^0\gamma^{0*})\right].$$

Similarly, the differential cross section of the reaction $pn \to df_0$ can be written as

$$\frac{d\sigma(pn \to df_0)}{d\Omega} = \frac{3k}{2p}|F|^2. \tag{38}$$

The mixing effect—described by the term $C_1\cos\theta$ in Eq. (36)—then leads to an isospin violation in the ratio $R_{\rm ba}$ of the differential cross sections for reactions (b) and (a),

$$R_{\rm ba} = \frac{1}{2} + \frac{1}{2}\frac{C_1\cos\theta}{C_0 + C_2\cos^2\theta}, \tag{39}$$

and to the forward–backward asymmetry for reaction (b),

$$A_{\rm b}(\theta) = \frac{\sigma_{\rm b}(\theta) - \sigma_{\rm b}(\pi-\theta)}{\sigma_{\rm b}(\theta) + \sigma_{\rm b}(\pi-\theta)} = \frac{C_1\cos\theta}{C_0 + C_2\cos^2\theta}. \tag{40}$$

The latter effect has been already discussed in [60], where it was argued that the asymmetry $A_{\rm b}(\theta = 0)$ can reach 5–10% at an energy excess of $Q = 5$–10 MeV. However, if we adopt a mixing parameter $|\xi|^2 = (8 \pm 3)\%$, as follows from the WA102 data, we can expect a much larger asymmetry. We note explicitly that the coefficient C_1 in (37) depends not only on the magnitude of the mixing parameter ξ, but also on the relative phases with respect to the amplitudes of f_0 and a_0 production, which are unknown so far. This uncertainty has to be kept in mind for the following discussion.

If a_0 and f_0 were very narrow particles, then near threshold the differential cross section (35), dominated by the P wave, would be proportional to k^3 or $Q^{3/2}$, where Q is the c.m. energy excess. Due to S-wave dominance in the reaction $pn \to df_0$, one would expect that the cross section scales like $\sim k$ or $\sim\sqrt{Q}$. In this limit, the a_0–f_0 mixing leads to an enhancement of the asymmetry $A_{\rm b}(\theta)$ as $1/k$ near the threshold. In reality, however, both a_0 and f_0 have widths of about 40–100 MeV. Therefore, at fixed initial momentum, their production cross section should be averaged over the corresponding mass distributions. This will essentially change the threshold behavior of the cross sections. Another complication is that broad resonances are usually accompanied by background lying underneath the resonance signals. These problems will be discussed below in the following subsections.

5.2.2. Model calculations. In order to estimate isospin-violation effects in the differential cross-section ratio $R_{\rm ba}$ and in the forward–backward asymmetry $A_{\rm b}$, we use the two-step model (TSM), which was successfully applied earlier to the description of η-, η'-, ω-, and ϕ-meson production in the reaction $pN \to dX$ in [61, 62]. Recently, this model has been also used for an analysis of the reaction $pp \to da_0^+$ [18].

The diagrams in Fig. 11 describe the different mechanisms of a_0- and f_0-meson production in the

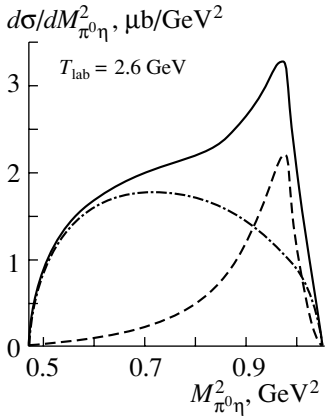

Fig. 13. $\pi^0\eta$ Invariant mass distribution for the reaction $pn \to d\pi^0\eta$ at 3.4 GeV/c. The dashed and dash-dotted curves describe the a_0 resonance contribution and nonresonance background, respectively; the solid curve is the sum of both contributions.

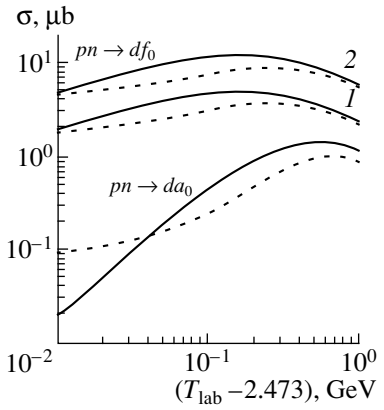

Fig. 14. Total cross sections for the reactions $pn \to da_0$ and $pn \to df_0$ as functions of ($T_{\rm lab} - 2.473$ GeV). The solid and dashed curves are calculated using narrow and finite resonance widths, respectively. The curves denoted by *1* and *2* correspond to the choices $R(f_0/a_0) = 1.46$ and 2.3, respectively.

reaction $NN \to da_0(f_0)$ within the framework of the TSM. In the case of a_0 production, the amplitude of the subprocess $\pi N \to a_0 N$ contains three different contributions: (i) the $f_1(1285)$-meson exchange (Fig. 11a), (ii) the η-meson exchange (Fig. 11b), and (iii) s- and u-channel nucleon exchanges (Figs. 11c and 11d). As it was shown in [18], the main contribution to the cross section for the reaction $pp \to d\,a_0^+$ stems from the u-channel nucleon exchange (i.e., from the diagram of Fig. 11d) and all other contributions can be neglected. In order to preserve the correct structure of the amplitude under permutations of the initial nucleons (which is antisymmetric for the isovector state and symmetric for the isoscalar state), the amplitudes of a_0 and f_0 production can be written as the following combinations of the t- and u-channel contributions:

$$T_{pn\to da_0^0}(s,t,u) = A_{pn\to da_0^0}(s,t) - A_{pn\to da_0^0}(s,u), \quad (41)$$

$$T_{pn\to df_0}(s,t,u) = A_{pn\to df_0}(s,t) + A_{pn\to df_0}(s,u),$$

where $s = (p_1+p_2)^2$; $t = (p_3-p_1)^2$; $u = (p_3-p_2)^2$; and p_1, p_2, p_3, and p_4 are the 4-momenta of the initial protons, meson M, and the deuteron, respectively. The structure of the amplitudes (41) guarantees that the S-wave part vanishes in the case of direct a_0 production since it is forbidden by angular momentum conservation and the Pauli principle. Also, higher partial waves are included in (41) (in contrast to the simplified discussion in Subsection 5.1).

In the case of f_0 production, the amplitude of the subprocess $\pi N \to f_0 N$ contains two different contributions: (i) the π-meson exchange (Fig. 11b) and (ii) s- and u-channel nucleon exchanges (Figs. 11c and 11d). Our analysis has shown that, similar to the case of a_0 production, the main contribution to the cross section of the reaction $pn \to df_0$ is due to the u-channel nucleon exchange (i.e., from the diagram of Fig. 11d); the contribution of the combined $\pi\pi$ exchange (Fig. 11b) as well as the s-channel nucleon exchange can be neglected. In this case, we get for the ratio of the squared amplitudes

$$\frac{|A_{pn\to df_0}(s,t)|^2}{|A_{pn\to da_0}(s,t)|^2} = \frac{|A_{pn\to df_0}(s,u)|^2}{|A_{pn\to da_0}(s,u)|^2} = \frac{|g_{f_0NN}|^2}{|g_{a_0NN}|^2}. \quad (42)$$

If we take $g_{a_0NN} = 3.7$ (see, e.g., [27]) and $g_{f_0NN} = 8.5$ [28], then we find for the ratio of the amplitudes $R(f_0/a_0) = g_{f_0NN}/g_{a_0NN} = 2.3$. Note, however, that Mull and Holinde [28] give a different value for the ratio of the coupling constants $R(f_0/a_0) = 1.46$, which is lower by about 37%. In the following, we use $R(f_0/a_0) = 1.46$–2.3.

The forward differential cross section for reaction (a) as a function of the proton beam momentum is presented in Fig. 12. The thick dash-dotted and solid curves (taken from [18] and calculated for the zero width limit) describe the results of the TSM for different values of the nucleon cutoff parameter, $\Lambda_N = 1.2$ and 1.3 GeV, respectively.

In order to take into account the finite width of a_0, we use a Flatté mass distribution with the same parameters as in [19]: the K-matrix pole at 999 MeV, $\Gamma_{a_0\to\pi\eta} = 70$ MeV, and $\Gamma(K\bar{K})/\Gamma(\pi\eta) = 0.23$ (see also [24] and references therein). The thin dash-dotted and solid curves in Fig. 12 are calculated within TSM using this mass distribution with the cut $M_{\pi^+\eta} \geq 0.85$ GeV and $\Lambda_N = 1.2$ and 1.3 GeV, respectively. The corresponding $\pi^0\eta$ invariant mass

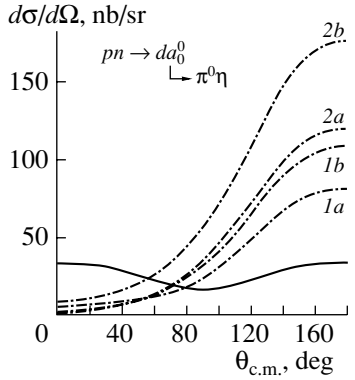

Fig. 15. Differential cross section of the reaction $pn \to da_0^0$ at $T_{\rm lab} = 2.6$ GeV as a function of $\theta_{\rm c.m.}$. The solid curve corresponds to the case of isospin conservation, i.e., $|\xi|^2 = 0$. The dash-dotted curves include the mixing effect with $|\xi|^2 = 0.05$ for the lower curves (*1a* and *2a*) and $|\xi|^2 = 0.11$ for the upper curves (*1b* and *2b*). The curves *1a, 1b* and *2a, 2b* have been calculated for $R(f_0/a_0) = 1.46$ and 2.3, respectively.

distribution for the reaction $pn \to da_0^0 \to d\pi^0\eta$ at 3.4 GeV/c is shown in Fig. 13 by the dashed curve.

In the case of the f_0 meson, where $\mathrm{Br}(K\bar{K})$ is not yet fixed [24], we use the Breit–Wigner mass distribution with $M_R = 980$ MeV and $\Gamma_R \simeq \Gamma_{f_0\to\pi\pi} = 70$ MeV.

The calculated total cross sections for the reactions $pn \to da_0$ and $pn \to df_0$ (as a function of $T_{\rm lab}$ for $\Lambda_N = 1.2$ GeV) are shown in Fig. 14. The solid and dashed curves describe the calculations with zero and finite widths, respectively. In the case of f_0 production in the $\pi\pi$ mode, we take the same cut in the invariant mass of the $\pi\pi$ system, $M_{\pi\pi} \geq 0.85$ GeV. The curves denoted by *1* and *2* are obtained for $R(f_0/a_0) = 1.46$ and 2.3. Comparing the solid and dashed curves, we see that near the threshold the finite-width corrections to the cross sections are quite important. The most important changes are introduced to the energy behavior of the a_0-production cross section. (Compare also thick and thin curves in Fig. 12.)

In principle, mixing can modify the mass spectrum of the a_0 and f_0. However, in this case, the effect is expected to be less spectacular than for the ρ–ω case where the widths of ρ and ω are very different (see, e.g., the discussion in [57] and references therein). Nevertheless, the modification of the a_0^0 spectral function due to a_0–f_0 mixing can be measured comparing the invariant mass distributions of a_0^0 with that of a_0^+. According to our analysis, a much cleaner signal for isospin violation can be obtained from the measurement of the forward–backward asymmetry in the reaction $pn \to da_0^0 \to d\pi^0\eta$ for the integrated strength of the a_0. That is why, for all calculations on isospin-violation effects below, the strengths of f_0 and a_0 are integrated over the invariant masses in the interval 0.85–1.02 GeV.

The magnitude of the isospin-violation effects is shown in Fig. 15, where we present the differential cross section of the reaction $pn \to da_0^0$ at $T_{\rm lab} = 2.6$ GeV as a function of $\theta_{\rm c.m.}$ for different values of the mixing intensity $|\xi|^2 = 0.05$ and 0.11. For reference, the solid curve shows the case of isospin conservation, i.e., $|\xi|^2 = 0$. The dash-dotted curves include the mixing effect. Note that all curves in Fig. 15 were calculated assuming maximal interference of the amplitudes describing the direct a_0 production and its production through f_0. The maximal values of the differential cross section may also occur at $\theta_{\rm c.m.} = 0^\circ$ depending on the sign of the coefficient C_1 in Eq. (36).

It follows from Fig. 15 in either case that the isospin-violation parameter $A_{\rm b}(\theta)$ for $\theta_{\rm c.m.} = 180^\circ$ may be quite large, i.e.,

$$A_{\rm b}(180^\circ) = 0.86 - 0.96 \text{ or } 0.9 - 0.98 \qquad (43)$$

for $R(f_0/a_0) = 1.46$ or 2.3, respectively. Note that the asymmetry depends rather weakly on $R(f_0/a_0)$. It might be more sensitive to the relative phase of a_0 and f_0 contributions.

5.2.3. Background. The dash-dotted curve in Fig. 13 shows our estimates of possible background from nonresonant $\pi^0\eta$ production in the reaction $pn \to d\pi^0\eta$ at $T_{\rm lab} = 2.6$ GeV (see also [63]). The background amplitude was described by the diagram shown in Fig. 11*e*, where η and π mesons are created through the intermediate production of $\Delta(1232)$ (in the amplitude $\pi N \to \pi N$) and $N(1535)$ (in the amplitude $\pi N \to \eta N$). The total cross section of the nonresonant $\pi\eta$ production due to this mechanism was found to be $\sigma_{\rm bg} \simeq 0.8$ μb for a cutoff in the OPE $\Lambda_\pi = 1$ GeV.

The background is charge-symmetric and cancels in the difference of the cross sections $\sigma(\theta) - \sigma(\pi - \theta)$. Therefore, the complete separation of the background is not crucial for a test of isospin violation due to the a_0–f_0 mixing. There will also be some contribution from π–η mixing as discussed in [57, 58]. According to the results of [57], this mechanism yields a charge-symmetry breaking in the ηNN system of about 6%:

$$R = d\sigma(\pi^+ d \to pp\eta)/d\sigma(\pi^- d \to nn\eta) = 0.938 \pm 0.009.$$

A similar isospin violation due to π–η mixing can also be expected in our case.

The best strategy to search for isospin violation is a measurement of the forward–backward asymmetry for different intervals of $M_{\pi^0\eta}$. As follows from Fig. 13, we have $\sigma_{a_0}(\sigma_{\rm bg}) = 0.3(0.4)$, 0.27(0.29), and

0.19(0.15) μb for $M_{\pi^0\eta} \geq 0.85$, 0.9, and 0.95 GeV, respectively. For $M_{\pi^0\eta} \leq 0.7$ GeV, the resonance contribution is rather small and the charge-symmetry breaking will be mainly related to π–η mixing and, therefore, will be small. On the other hand, in the interval $M_{\pi^0\eta} \geq 0.95$ GeV, the background does not exceed the resonance contribution and we expect a comparatively large isospin breaking due to a_0–f_0 mixing.

5.3. Reaction $pn \to df_0 \to d\pi\pi$

The isospin-violation effects can also be measured in the reaction

$$pn \to df_0 \to d\pi^+\pi^-, \tag{44}$$

where, due to mixing, the f_0 may also be produced via the a_0. The corresponding differential cross section is shown in Fig. 16. The differential cross section for f_0 production is expected to be substantially larger than for a_0 production, but the isospin-violation effect turns out to be smaller than in the $\pi\eta$-production channel. Nevertheless, the isospin-violation parameter A is expected to be about 10–30% and can be detected experimentally.

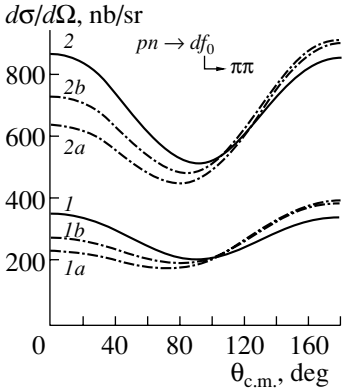

Fig. 16. Differential cross section of the reaction $pn \to df_0$ at $T_{\rm lab} = 2.6$ GeV as a function of $\theta_{\rm c.m.}$. The solid curves correspond to the case of isospin conservation, i.e., $|\xi|^2 = 0$. The dash-dotted curves include the mixing effect with $|\xi|^2 = 0.05$ for the lower curves (*1a* and *2a*) and $|\xi|^2 = 0.11$ for the upper curves (*1b* and *2b*). The curves *1, 1a, 1b* and *2, 2a, 2b* have been calculated for $R(f_0/a_0) = 1.46$ and 2.3, respectively.

5.4. Reactions $pd \to {}^3\mathrm{H}\,a_0^+$ and $pd \to {}^3\mathrm{He}\,a_0^0$

We continue with pd reactions and compare the final states ${}^3\mathrm{H}\,a_0^+$ (c) and ${}^3\mathrm{He}\,a_0^0$ (d). Near the threshold, the amplitudes of these reactions can be written as

$$T(pd \to {}^3\mathrm{H}\,a_0^+) = \sqrt{2}D_a\mathbf{S}_A \cdot \mathbf{e}, \tag{45}$$

$$T(pd \to {}^3\mathrm{He}\,a_0^0) = (D_a + \xi D_f)\mathbf{S}_A \cdot \mathbf{e}, \tag{46}$$

with $\mathbf{S}_A = \phi_A^T\sigma_2\boldsymbol{\sigma}\phi_N$. D_a and D_f are the scalar S-wave amplitudes describing the a_0 and f_0 production in the case of $\xi = 0$. The ratio of the differential cross sections for reactions (d) and (c) is then given by

$$R_{\rm dc} = \frac{|D_a + \xi D_f|^2}{2|D_a|^2} = \frac{1}{2} + \frac{2\mathrm{Re}(D_a^*\xi D_f) + |\xi D_f|^2}{|D_a|^2}. \tag{47}$$

The magnitude of the ratio $R_{\rm dc}$ now depends on the relative value of the amplitudes D_a and D_f. If they are comparable ($|D_a| \sim |D_f|$) or $|D_f|^2 \gg |D_a|^2$, the deviation of $R_{\rm dc}$ from 0.5 (which corresponds to isospin conservation) might be 100% or more. Only in the case $|D_f|^2 \ll |D_a|^2$ will the difference of $|R_{\rm dc}|^2$ from 0.5 be small. However, this seems to be very unlikely.

Using the two-step model for the reactions $pd \to {}^3\mathrm{He}\,a_0^0$ and $pd \to {}^3\mathrm{He}\,f_0$, involving the subprocesses $pp \to d\pi^+$ and $\pi^+n \to p\,a_0/f_0$ (cf. [64, 65]), we find

$$\frac{\sigma(pd \to {}^3\mathrm{He}\,a_0^0)}{\sigma(pd \to {}^3\mathrm{He}\,f_0)} \simeq \frac{\sigma(\pi^+n \to p\,a_0^0)}{\sigma(\pi^+n \to p\,f_0)}. \tag{48}$$

According to the calculations in [18], we expect $\sigma(\pi^+n \to pa_0^0) = \sigma(\pi^-p \to na_0^0) \simeq 0.5$–$1$ mb at 1.75–2 GeV/c. A similar value for $\sigma(\pi^-p \to nf_0)$ can be found using the results from [41]. According to the latter study, $\sigma(\pi^-p \to nf_0 \to nK^+K^-) \simeq 6$–$8$ μb at 1.75–2 GeV/c and $\mathrm{Br}(f_0 \to K^+K^-) \simeq 1\%$, which implies that $\sigma(\pi^-p \to nf_0) \simeq 0.6$–$0.8$ mb. Thus, we expect that near threshold $|D_a| \sim |D_f|$. This would imply that the effect of isospin violation in the ratio $R_{\rm dc}$ can become quite large.

Recently, the cross section of the reaction $pd \to {}^3\mathrm{He}\,K^+K^-$ has been measured by the MOMO collaboration at COSY (Jülich) [66]. It was found that $\sigma = 9.6 \pm 1.0$ and 17.5 ± 1.8 nb for $Q = 40$ and 56 MeV, respectively. The authors note that the invariant K^+K^- mass distributions in those data contain a broad peak which follows phase space. However, as was shown in [19], the form of the invariant mass spectrum, which follows phase space, cannot be distinguished from the a_0-resonance contribution at such small Q. Therefore, the events from the broad peak in [66] can also be related to a_0 and/or f_0. Moreover, due to the phase-space behavior near the threshold, one would expect a dominance of two-body reactions. Thus, the real cross section of the reaction $pd \to {}^3\mathrm{He}\,a_0^0 \to {}^3\mathrm{He}\,\pi^0\eta$ is not expected to be substantially smaller than its upper limit of about 40–70 nb at $Q = 40$–60 MeV, which follows from the MOMO data [66].

5.5. Reaction $dd \to {}^4\mathrm{He}\,a_0^0$

The direct production of a_0 in the reaction $dd \to {}^4\mathrm{He}\,a_0^0$ is forbidden. It thus can only be observed due

to the f_0–a_0 mixing:

$$\frac{\sigma(dd \to {}^4\mathrm{He}\, a_0^0)}{\sigma(dd \to {}^4\mathrm{He} f_0)} = |\xi|^2. \quad (49)$$

Therefore, it will be very interesting to study the reaction

$$dd \to {}^4\mathrm{He}(\pi^0\eta) \quad (50)$$

near the f_0-production threshold. Any signal of the reaction (50) then will be related to isospin breaking. It is expected to be much more pronounced near the f_0 threshold as compared to the region below this threshold.

In summarizing this section, we have discussed the effects of isospin violation in the reactions $pN \to da_0$, $pn \to df_0$, $pd \to {}^3\mathrm{He}({}^3\mathrm{H})a_0$, and $dd \to {}^4\mathrm{He}\, a_0$, which can be generated by f_0–a_0 mixing. It has been demonstrated that, for a mixing intensity of about $(8 \pm 3)\%$, the isospin violation in the ratio of the differential cross sections of the reactions $pp \to da_0^+ \to d\pi^+\eta$ and $pn \to da_0^0 \to d\pi^0\eta$ as well as in the forward–backward asymmetry in the reaction $pn \to da_0^0 \to d\pi^0\eta$ not far from the threshold may be about 50–100%. Such large effects are caused by the interference of direct a_0 production and its production via the f_0 (the former amplitude is suppressed close to threshold due to the P-wave amplitude, whereas the latter is large due to the S-wave mechanism). A similar isospin violation is expected in the ratio of the differential cross sections of the reactions $pd \to {}^3\mathrm{H}\, a_0^+(\pi^+\eta)$ and $pd \to {}^3\mathrm{He}\, a_0^0(\pi^0\eta)$. Finally, we have also discussed the isospin violation effects in the reactions $pn \to df_0(\pi^+\pi^-)$ and $dd \to {}^4\mathrm{He}a_0$. All reactions together—once studied experimentally—are expected to provide detailed information on the strength of the f_0–a_0 mixing. Corresponding measurements are now in preparation for the ANKE spectrometer at COSY (Jülich) [67].

ACKNOWLEDGMENTS

The authors are grateful to J. Ritman for stimulating discussions and useful suggestions and to V. Baru for providing the parametrization of the FSI enhancement factor.

This work is supported by Deutsche Forschungsgemeinschaft and by the Russian Foundation for Basic Research (project no. 00-02-04025).

REFERENCES

1. F. E. Close *et al.*, Phys. Lett. B **319**, 291 (1993).
2. M. Genovese *et al.*, Nuovo Cimento A **107**, 1249 (1994).
3. G. Janssen, B. Pierce, K. Holinde, and J. Speth, Phys. Rev. D **52**, 2690 (1995).
4. V. V. Anisovich *et al.*, Phys. Lett. B **355**, 363 (1995).
5. N. A. Törnqvist, Phys. Rev. Lett. **49**, 624 (1982).
6. K. Maltman, Nucl. Phys. A **675**, 209 (2000).
7. S. Narison, Nucl. Phys. B (Proc. Suppl.) **86**, 242 (2000).
8. L. Montanet, Nucl. Phys. B (Proc. Suppl.) **86**, 381 (2000).
9. V. V. Anisovich, L. Montanet, and V. N. Nikonov, Phys. Lett. B **480**, 19 (2000).
10. S. Narison, Nucl. Phys. B (Proc. Suppl.) **96**, 244 (2001).
11. N. N. Achasov, S. A. Devyanin, and G. N. Shestakov, Phys. Lett. B **88B**, 367 (1979).
12. N. N. Achasov and G. N. Shestakov, Phys. Rev. D **56**, 212 (1997).
13. T. Barnes, Phys. Lett. B **165B**, 434 (1985).
14. O. Krehl, R. Rapp, and J. Speth, Phys. Lett. B **390**, 23 (1997).
15. B. O. Kerbikov and F. Tabakin, Phys. Rev. C **62**, 064601 (2000).
16. F. E. Close and A. Kirk, Phys. Lett. B **489**, 24 (2000).
17. V. Yu. Grishina, L. A. Kondratyuk, M. Büscher, *et al.*, Phys. Lett. B **521**, 217 (2001).
18. V. Yu. Grishina, L. A. Kondratyuk, E. L. Bratkovskaya, *et al.*, Eur. Phys. J. A **9**, 277 (2000); J. Phys. G (in print).
19. E. L. Bratkovskaya *et al.*, nucl-th/0107071.
20. V. Chernyshev *et al.*, COSY Proposal No. 55 "Study of a_0^+ Mesons at ANKE" (1997), http://www.fz-juelich.de/ikp/anke; L. A. Kondratyuk *et al.*, Preprint No. 18-97, ITEP (Moscow, 1997).
21. M. Büscher *et al.*, Beam-Time Request for COSY Proposal #55 "Study of a_0^+ Mesons at ANKE" (2000); http://www.fz-juelich.de/ikp/anke.
22. M. Büscher *et al.*, Status Report for COSY Experiment #55 "Study of a_0^+ Mesons at ANKE" and Proposal "Investigation of Neutral Scalar Mesons a_0^0/f_0 with ANKE" http://www.fz-juelich.de/ikp/anke
23. S. Flatté, Phys. Lett. B **63B**, 224 (1976).
24. Particle Data Group (C. Caso *et al.*), Eur. Phys. J. C **15**, 1 (2000).
25. A. Abele *et al.*, Phys. Rev. D **57**, 3860 (1998).
26. WA102 Collab. (D. Barberis *et al.*), Phys. Lett. B **440**, 225 (1998).
27. R. Machleidt, K. Holinde, and Ch. Elster, Phys. Rep. **149**, 1 (1987).
28. V. Mull and K. Holinde, Phys. Rev. C **51**, 2360 (1995).
29. M. Kirchbach and D. O. Riska, Nucl. Phys. A **594**, 419 (1995).
30. D. L. Cheshire *et al.*, Phys. Rev. Lett. **28**, 520 (1972).
31. A. B. Kaidalov, Yad. Fiz. **53**, 1410 (1991) [Sov. J. Nucl. Phys. **53**, 872 (1991)].
32. L. A. Kondratyuk *et al.*, Phys. Rev. C **48**, 2491 (1993).
33. W. D. Apel *et al.*, Yad. Fiz. **41**, 126 (1985) [Sov. J. Nucl. Phys. **41**, 80 (1985)]; D. Alde *et al.*, Phys. Lett. B **205**, 397 (1988).

34. D. Alde *et al.*, Yad. Fiz. **59**, 1027 (1996) [Phys. At. Nucl. **59**, 982 (1996)]; S. Sadovsky, in *Proceedings of the 6th International Conference on Hadron Spectroscopy "Hadron'95,"* Ed. by M. C. Birse *et al.* (World Sci., Singapore, 1996), p. 445.
35. A. R. Dzierba, in *Proceedings of the Second Workshop on Physics and Detectors for DAΦNE'95, Frascati, 1995,* Ed. by R. Baldini *et al.*, Frascati Phys. Ser. **4**, 99 (1996).
36. R. Kokoski and N. Isgur, Phys. Rev. D **35**, 907 (1987).
37. A. B. Kaidalov, Surv. High Energy Phys. **13**, 265 (1999).
38. *Landolt-Börnstein: Numerical Data and Functional Relationships in Science and Technology, New Series,* Ed. by H. Schopper (Springer-Verlag, Berlin, 1988), Vol. I/12.
39. A. A. Sibirtsev, W. Cassing, and C. M. Ko, Z. Phys. A **358**, 101 (1997).
40. O. I. Dahl *et al.*, Phys. Rev. **163**, 1377 (1967).
41. E. L. Bratkovskaya, W. Cassing, L. A. Kondratyuk, and A. Sibirtsev, Eur. Phys. J. A **4**, 165 (1999).
42. T. Hippchen, J. Haidenbauer, K. Holinde, and V. Mull, Phys. Rev. C **44**, 1323 (1991); V. Mull, J. Haidenbauer, T. Hippchen, and K. Holinde, Phys. Rev. C **44**, 1337 (1991).
43. W. S. Chung, G. Q. Li, and C. M. Ko, Nucl. Phys. A **625**, 371 (1997).
44. K. Nakayama, A. Szczurek, C. Hanhart, *et al.*, Phys. Rev. C **57**, 1580 (1998).
45. V. Baru, A. Kudryavtsev, V. Tarasov, and V. Chernyshev, Preprint No. 30-00, ITEP (Moscow, 2000).
46. V. Baru, A. M. Gasparian, J. Haidenbauer, *et al.*, nucl-th/0006075; Yad. Fiz. **64**, 633 (2001) [Phys. At. Nucl. **64**, 579 (2001)].
47. K. Nakayama, nucl-th/0108032.
48. T. Feuster and U. Mosel, Phys. Rev. C **58**, 457 (1998); **59**, 460 (1999).
49. M. A. Abolins *et al.*, Phys. Rev. Lett. **25**, 469 (1970).
50. F. Balestra *et al.*, Phys. Rev. C **63**, 024004 (2001).
51. C. Quentmeier *et al.*, Phys. Lett. B **515**, 276 (2001).
52. A. D. Martin, Nucl. Phys. B **179**, 33 (1981).
53. J. Cugnon, P. Deneye, and J. Vandermeulen, Phys. Rev. C **41**, 1701 (1990).
54. J. C. M. Armitage *et al.*, Nucl. Phys. B **123**, 111 (1977).
55. H. Müller, Eur. Phys. J. A **11**, 113 (2001).
56. M. Atkinson *et al.*, Phys. Lett. B **138B**, 459 (1984).
57. W. B. Tippens *et al.*, Phys. Rev. D **63**, 052001 (2001).
58. A. Magiera and H. Machner, Nucl. Phys. A **674**, 515 (2000).
59. A. Kudryavtsev *et al.*, nucl-th/0203034; Phys. Rev. C **66**, 015207 (2002).
60. A. Kudryavtsev and V. E. Tarasov, Pis'ma Zh. Éksp. Teor. Fiz. **72**, 589 (2000) [JETP Lett. **72**, 410 (2000)].
61. V. Yu. Grishina *et al.*, Phys. Lett. B **475**, 9 (2000).
62. V. Yu. Grishina, L. A. Kondratyuk, and M. Büscher, Yad. Fiz. **63**, 1913 (2000) [Phys. At. Nucl. **63**, 1824 (2000)].
63. V. Yu. Grishina *et al.*, in *IKP Annual Report 2000,* Berichte des Forschungszentrums Jülich, Jül-3852, ISSN 0944-2952, p. 30.
64. G. Fäldt and C. Wilkin, Phys. Lett. B **354**, 20 (1995).
65. L. A. Kondratyuk and Yu. N. Uzikov, Pis'ma Zh. Éksp. Teor. Fiz. **63**, 3 (1996) [JETP Lett. **63**, 1 (1996)].
66. F. Belleman *et al.*, in *IKP Annual Report 2000,* Berichte des Forschungszentrums Jülich, Jül-3852, ISSN 0944-2952, p. 62.
67. M. Büscher *et al.*, COSY Proposal #97 "Investigation of Neutral Scalar Mesons with ANKE" (2001); http://www.fz-juelich.de/ikp/anke

Physics of Atomic Nuclei, Vol. 66, No. 1, 2003, pp. 17–29. Translated from Yadernaya Fizika, Vol. 66, No. 1, 2003, pp. 19–31.

100th ANNIVERSARY OF I.V. KURCHATOV'S BIRTH

Investigation of ^{138}Ba in the $(n, n'\gamma)$ Reaction

L. I. Govor, A. M. Demidov, and I. V. Mikhailov

Russian Research Centre Kurchatov Institute, pl. Kurchatova 1, Moscow, 123182 Russia

Received June 20, 2002

Abstract—For the reaction ^{138}Ba$(n, n'\gamma)$ induced by a beam of fast reactor neutrinos, the gamma spectrum, the angular distributions of gamma radiation, and its linear polarizations are measured, along with the half-lives of the excited states involved. The known diagram of energy levels and gamma transitions is supplemented. The multipole-mixture ratios δ are found for many transitions between the energy levels in question, and half-lives are determined for some excited states. © *2003 MAIK "Nauka/Interperiodica".*

The ^{138}Ba nucleus is of interest because it belongs to the chain of nuclei having the magic number of neutrons that is equal to $N = 82$, the levels of these nuclei up to an energy of 3 to 4 MeV being determined primarily by proton excitations. In $(n, n'\gamma)$ reactions, the ^{140}Ce and ^{142}Nd isotopes, which are members of this chain and for which excitations of the type in question must be controlled, in just the same way as for ^{138}Ba, by the interaction of protons occurring in the $1g_{7/2}$ and $2d_{5/2}$ shells, were previously explored in [1] and [2], respectively.

The bulk of information about the diagram of energy levels and gamma transitions in ^{138}Ba was obtained from the investigation of the beta decay of ^{138}Cs and the relevant (n, γ) reaction. The latest survey of available experimental data on ^{138}Ba can be found in [3], whence one can deduce that there are many uncertainties in the features of the levels and that reliable information about multipole mixtures in gamma transitions is scanty.

In this article, the results obtained by studying the spectrum of gamma rays from the reaction ^{138}Ba$(n, n'\gamma)$ induced by fast reactor neutrons and the angular distributions and linear polarizations of these gamma rays are presented along with the measured lifetimes of the levels involved. In relation to [4], where the investigation was performed only for the angular distributions of gamma rays from this reaction, the investigation reported here has a higher statistical accuracy; moreover, it also includes an analysis of the possible errors in determining multipole mixtures in [4]. As a result, information about multipole mixtures in gamma transitions is substantially supplemented; in addition, the features of many levels in ^{138}Ba, including their half-lives, are determined unambiguously.

1. RESULTS OF THE MEASUREMENTS

The measurements were performed at the IR-8 reactor installed at the Russian Research Centre Kurchatov Institute. A detailed account of the experimental and data-processing procedures used was given in [5]. In forming a beam of fast neutrons, a set of filters—it included 1 mm of Cd, 10 mm of B_4C, 50 mm of metallic uranium, and a replaceable filter formed by 10 mm of ^{10}B powder—was arranged to remove thermal and low-energy resonance neutrons from the beam and gamma radiation from the reactor-core region. The germanium detectors used to record gamma radiation had an efficiency of 10% and a resolution of 2.0 keV at $E_\gamma = 1.3$ MeV. A $^{138}BaCO_3$ sample of mass 28.7 g and thickness 1.7 g/cm^2 enriched in ^{138}Ba to 99.8% (the concentrations of the $A = 136$ and 137 barium isotopes were 0.04 and 0.16%, respectively) was taken for a target. The gamma-ray spectra were measured at angles of 90°, 105°, 115°, 125°, 135°, 142°, and 150° with respect to the neutron beam. The self-absorption of gamma rays in the sample was taken into account. In order to normalize the intensities of gamma radiation at different angles, dedicated measurements with a natural mixture of barium isotopes were performed, which made it possible to use the isotropic 0^+–2^+ gamma transition of energy 760.49 keV in ^{136}Ba. The angular distributions that we obtained exhibit a systematic deviation from those reported by Dioszegi *et al.* [4], which is probably due to a difference in normalization. Unfortunately, those authors did not describe their normalization method, nor did they present their results on the angular distribution for the 0^+–2^+ gamma transition of energy 754 keV. Possibly, the 191.9-keV gamma transition was taken as an isotropic one in [4] for normalization, but its isotropy is not confirmed by our data. In all probability, the

1063-7788/03/6601-0017$24.00

orientation of a ^{138}Ba nucleus in $BaCO_3$ cannot be lost completely within the lifetime of the level from which the transition occurs (its half-life is 0.8 μs). It is obvious that an error in normalization entails errors in all multipole-mixture ratios δ.

The linear polarization of the gamma rays in question was measured by a two-crystal Compton polarimeter [5].

Table 1 presents the values that we obtained for the energy (at an angles of $\theta = 90°$ between the direction of gamma-radiation detection and the neutron-beam axis) and the relative intensities (at $\theta = 125°$) of gamma transitions in ^{138}Ba. Given in the third column of Table 1 are the energies (E_i) of ^{138}Ba levels from which these gamma transitions occur.

The diagram of energy levels and gamma transitions in ^{138}Ba that was composed on the basis of our results and data compiled in the review article of Tuli [3] is given in Table 2. Also quoted in this table are the values that we obtained for the coefficients a_2 and a_4 in the expansion of the angular distributions of gamma radiation in Legendre polynomials $[W(\theta) = A_0(1 + a_2P_2(\cos\theta) + a_4P_4(\cos\theta))]$, the relative populations of levels in the relevant $(n, n'\gamma)$ reaction induced by fast reactor neutrons ($P_s = \sum I_\gamma^{\text{in}} - \sum I_\gamma^{\text{out}}$), and the values found for the multipole-mixture parameter δ or for the multipolarity ML (see [5]). The uncertainties in a_2, a_4, and δ correspond to a 68% confidence level. The uncertainties in the δ values and their signs are given according to the system adopted in [3].

The results obtained by measuring the linear polarization P_γ of gamma rays for ^{138}Ba are quoted in Table 3. In order to select δ unambiguously (of two possible values) by using measurements of gamma-ray angular distributions (with respect to the neutron-beam axis) alone, very small uncertainties in determining the coefficient a_4 were required in some cases. If this could not be achieved, data on the linear polarization of gamma rays were invoked to select one of the two values of δ. Accordingly, the last column of Table 3 presents the conclusion concerning the δ-ellipse branch on which the sought value of δ occurs ($a_4 \sim 0$ or $|a_4| > 0$, which usually corresponds to small or large values of $|\delta|$).

Experimental results for the half-lives of the ^{138}Ba levels involved are quoted in Table 4. These results were obtained from measurements with a metallic-barium sample containing a natural isotope mixture that were based on a method that employs the attenuation of the Doppler shift of gamma-transition energies in inelastic fast-neutron scattering. For the details of the procedure used, the interested reader is referred to [6–9]. The measurements were performed at three gamma-ray emission angles of 90°, 125°, and 150° simultaneously with a measurement of the gamma-ray spectrum of a radioactive ^{56}Co source. This made it possible to take into account possible time variations in the parameters of the spectrometric channel.

Experimental results for the factor F characterizing the attenuation of the Doppler shift of gamma-transition lines due to the moderation of ^{138}Ba recoil nuclei in a sample material are given in the fourth column of Table 4. On the basis of these values, the half-lives $T_{1/2}$ of the levels involved were calculated according to Blaugrund–Lindhard–Scharff–Shiott theory [9]. For the correction factor f_{nucl} taking into account inconsistencies between the theory of nuclear losses and the actual moderation processes, we employed the value of $f_{\text{nucl}} = 1.47$, which was determined in [6]. The problem of assessing this factor was discussed anew in connection with the emergence of a new study that was devoted to a resonance excitation of some levels in ^{138}Ba [10]. Use was made of all known values of $(\Gamma^0)^2/\Gamma$ (where Γ and Γ^0 are, respectively, the total level width and the partial width with respect to the transition to the ground state) and of the diagram of deexcitation of the 2218-, 3339-, and 3367-keV levels. The data available in the literature for the 2218-keV level are quite consistent both in $(\Gamma^0)^2/\Gamma$ and in the diagram of deexcitation of this state (Γ^0/Γ is 0.98 according to [3] and 0.97 according to our results). Data on the 3339- and 3367-keV states are characterized by a significant scatter. In all of the preceding studies, the ratio Γ^0/Γ was set to 0.77(4) for the 3339-keV level. This value relies on the investigation of ^{138}Cs beta decay in [11], where the intensity of the second (1903.0-keV) transition from the 3339-keV level was determined with a very large uncertainty (30%). Our measurements yield the value of $\Gamma^0/\Gamma = 0.901(15)$. The validity of this result is confirmed by the fact that it leads to consistent values for the lifetimes of the 3339- and 3367-keV levels in all studies, with the exception of that reported by Metzger in [12], who explored the resonance excitation of ^{138}Ba levels. This is also in accord with the results of our experiment (the factors F and the half-lives for the two levels in question agree to a high precision), which are independent of the diagram of excited-state deexcitation. The values found in [10, 12, 13] for the half-life $T_{1/2}$ of the 3339-keV level exhibit rather wide variations, between 30.1 and 44.1 fs if our value of Γ^0/Γ is taken into account, the average half-life value being $T_{1/2} = 34.5(51)$ fs in this case. According to data available from the literature, the average half-life value for the 3367-keV level, which is deexcited through a single transition to the ground state, is 36.2(38) fs. The choice of $f_{\text{nucl}} =$

1.47 corresponds to optimum agreement between our data on the lifetimes and the results of studies that are devoted to the resonance excitation of the 2218-, 3339-, and 3367-keV levels.

2. DISCUSSION OF THE RESULTS

Examining the dependence $P_s(E_i)$ and considering that the most intense transitions have already been included in the diagram of levels and gamma transitions, one can state that, at energies below 3 MeV, there are no $J \leq 5$ levels (J is the total angular momentum) in ^{138}Ba other than those that are quoted in Table 2.

For some specific levels, the results obtained in the present study are discussed immediately below.

Level at 1899 keV. An angular distribution of gamma rays that is characterized by a value of $a_2 \approx 0.32$ is expected for the 4^+-2^+ gamma transitions in an experiment employing fast reactor neutrons. A reduction of this value for the 462.79-keV gamma transition to $a_2 = 0.233$ is due to a higher cascade population and the half-life of 2.17 ns.

Level at 2091 keV. A value of $a_2 \approx 0.3$ is expected for the 6^+-4^+ gamma transition. The smoothing of the angular distribution to that which is characterized by $a_2 = +0.074$ is caused primarily by a very long half-life of 0.8 μs.

Level at 2190 keV. That the angular distribution of 754.05-keV gamma rays is isotropic and that the population P_s of this level is low make it possible to establish reliably its spin–parity of $J^\pi = 0^+$. There is no 2190-keV gamma transition in the gamma-ray spectrum—an upper limit on its intensity does not exceed 0.02 relative units.

Level at 2203 keV. The 304.0-keV gamma transition that was found in our study and which is characterized by a low intensity is possibly associated with the deexcitation of this level. For the 112.51-keV gamma transition, the second value of $\delta = +0.60(10)$ is improbable because of a small value of a_4.

Level at 2307 keV. Data on a_4 and on polarization for the 408.96-keV transition rule out the ambiguity in δ. The value of $\delta = -0.23$, which is quoted in the review article of Tuli [3], would correspond to $a_2 = +0.20$ here; at the same time, the observed value is $a_2 = +0.322(11)$.

Level at 2415 keV. An unambiguous value of δ for the 516.70-keV gamma transition follows from data on a_4 and P_γ. The value of $\delta(516.70\ \text{keV}) = -0.11$ given in [3] would correspond to $a_2 = -0.4$ here, but the observed value is $a_2 = -0.121(10)$. The value of P_γ for the 324.83-keV transition favors the small value of δ; however, the value of $\delta = -4.0(4)$ cannot be ruled out definitively in view of experimental errors. For the 212.28-keV transition, the second value of $\delta = -6.4 + 6 - 8$ is incompatible with a small value of a_4.

Level at 2445 keV. The values of P_γ and a_4 make it possible to find unambiguously the value of δ for the 1009.70- and 546.93-keV gamma transitions.

Level at 2583 keV. In experiments employing fast reactor neutrons, values of $a_2 \approx +0.28$ and $a_2 \approx -0.09$ are expected for the 2^+-0^+ and the $1-0^+$ transition, respectively. Accordingly, the gamma line at 2582.92 keV corresponds to the $1-0^+$ transition. This expected distinction between the angular distributions for the $1-0^+$ and 2^+-0^+ transitions makes it possible to select unambiguously angular-momentum values for the levels at 2639, 2931, 3050, 3339, 3367, 3442, 3504, 3601, 3643, 3734, 3800, 4001, 4026, and 4323 keV as well. Since the second value of $\delta = -2.0 + 6-7$ is less probable because of the value of P_γ for the gamma line at 1147.16 keV, we do not present it in the table.

Level at 2779 keV. The angular distribution for the 1343.54-keV gamma transition is somewhat smoothed ($a_2 = +0.234$ instead of the expected value of +0.32). In all probability, the peak at 1343.54 keV in the gamma-ray spectrum corresponds to two unresolved lines. The second line may be associated with the deexcitation of the level at 3242 keV. On the basis of the population expected for the level at 2779 keV, we have $I_\gamma \approx 1.7$ for the transition to the level at 1436 keV.

Level at 2796-keV? In the (n, γ) reaction, a 2795.68–5815.77 keV cascade of the observed gamma lines can be composed, which gives sufficient grounds to assume the presence of a level at 2796 or at 5816 keV. A population of $P_s \approx 2$ must be observed for the 2796-keV level in the $(n, n'\gamma)$ reaction; however, the 2796-keV gamma transition is not seen in the spectrum ($I_\gamma < 0.03$ relative units). We were unable to find other gamma lines for the deexcitation of the level at 2796 keV. In view of this, we can state that there is no level at 2796 keV in ^{138}Ba.

Level at 2881 keV. The values of a_4 and P_γ make it possible to rule out a large contribution of $M2$ radiation for the 1444.86-keV gamma transition.

Level at 2917 keV? This level was introduced in studying the (n, γ) reaction in view of the possible 2916.86–5694.56 keV cascade. The intensity of the 2917-keV gamma line in the $(n, n'\gamma)$ reaction is less than 0.01 relative units (the expected value is $P_s \approx 1.5$). Therefore, there is no level at 2917 keV in ^{138}Ba.

Level at 2931 keV. Data on a_4 and P_γ for the 1495.59-keV transition proved to be insufficient for pinpointing a single value of δ for this transition.

Table 1. Energies and intensities of ^{138}Ba gamma lines

$E_\gamma(\Delta E_\gamma)$, keV	$I_\gamma(\Delta I_\gamma)$, rel. units	E_i, keV	$E_\gamma(\Delta E_\gamma)$, keV	$I_\gamma(\Delta I_\gamma)$, rel. units	E_i, keV
107.8(2)	0.20(3)	2415	980.7(3)	0.070(12)	3184
112.51(3)	2.87(20)	2203	1009.70(2)	3.7(3)	2446
138.10(7)	0.32(3)	2446	1028.7(2)	0.096(12)	
191.95(2)	8.8(6)	2091	1033.1(2)	0.086(11)	
193.9(2)	0.115(10)	2639	1040.42(4)	0.52(4)	3486
212.28(3)	0.93(7)	2415	1054.2(2)	0.091(11)	3935
227.71(6)	0.214(17)	2446	1064.20(9)	0.20(3)	3155
304.0(2)	0.057(9)	2203	1068.27(8)	0.296(25)	3286?
324.83(2)	1.69(12)	2415	1082.8(3)	0.108(13)	
333.68(8)	0.199(16)	2779	1093.1(3)	0.166(16)	3184
363.88(4)	0.51(4)	2779	1116.66(8)	0.33(3)	3562
365.10(11)	0.227(19)	2583	1147.16(3)	1.81(13)	2583
375.6(2)	0.051(7)	3155	1151.38(14)	0.252(21)	3050
385.1(2)	0.066(9)		1158.1(2)	0.293(24)	
408.96(2)	3.60(25)	2308	1177.0(2)	0.106(14)	
421.41(11)	0.206(16)	2639	1186.9(3)	0.179(18)	
436.0(2)	0.049(6)	2852?	1203.6(2)	0.11(2)	2839
438.3(3)	0.040(7)	3622	1251.7(3)	0.092(15)	3442?
449.2(3)	0.033(6)	3633	1256.25(11)	0.249(22)	3155
462.79(2)	33.2(23)	1899	1264.63(12)	0.34(3)	3163
516.70(2)	2.55(18)	2415	1279.2(7)	0.061(10)	
524.5(2)	0.057(7)		1284.4(3)	0.229(19)	4165?
546.93(3)	1.39(10)	2446	1307.9(3)	0.107(11)	
648.1(2)	0.035(7)		1337.0(2)	0.114(11)	
669.3(3)	0.040(9)		1343.54(2)	2.12(15)	2779 + 3242?
683.65(7)	0.31(2)	2991	1358.80(6)	0.32(2)	3257
717.67(17)	0.103(11)	3163	1387.0(4)	0.096(10)	3286?
735.85(9)	0.240(19)		1392.9(2)	0.113(11)	
739.44(19)	0.130(13)	3155	1407.1(4)	0.038(8)	3610
754.05(2)	1.90(13)	2190	1415.71(3)	1.88(13)	2852
760.8(2)	0.076(9)		1426.3(3)	0.055(8)	
766.09(14)	0.182(16)	3647	1435.86(2)	100(7)	1436
773.16(5)	0.39(3)	2991	1444.86(2)	2.8(2)	2881
775.0(5)	0.053(11)		1478.28(17)	0.168(15)	3377
782.12(10)	0.27(2)	2218	1481.24(10)	0.33(3)	3380?
792.8(3)	0.043(8)		1490.8(3)	0.075(8)	
796.7(3)	0.051(8)	3242	1495.59(3)	1.48(10)	2931
813.0(4)	0.080(10)		1500.6(3)	0.043(7)	
855.7(3)	0.072(9)	3163	1507.9(5)	0.037(8)	
871.68(2)	3.9(3)	2308	1512.9(2)	0.080(10)	
880.70(15)	0.23(3)	2779	1515.8(4)	0.042(9)	3931
921.1(6)	0.063(13)		1536.2(5)	0.031(9)	
930.3(3)	0.061(8)		1541.0(2)	0.076(10)	
934.77(9)	0.258(20)	3242	1555.25(4)	0.66(5)	2991
944.7(3)	0.21(17)	3360	1566.2(2)	0.070(10)	
952.90(11)	0.267(22)	2852	1572.2(2)	0.072(9)	

Table 1. (Contd.)

$E_\gamma(\Delta E_\gamma)$, keV	$I_\gamma(\Delta I_\gamma)$, rel. units	E_i, keV	$E_\gamma(\Delta E_\gamma)$, keV	$I_\gamma(\Delta I_\gamma)$, rel. units	E_i, keV
1582.0(4)	0.041(7)	3800	2232.0(4)	0.055(7)	
1587.6(4)	0.039(7)	3486	2240.6(4)	0.058(9)	
1596.8(4)	0.037(7)		2373.3(2)	0.048(9)	
1605.4(2)	0.110(10)	3504	2391.4(5)	0.046(9)	
1614.08(3)	1.89(13)	3050	2402.8(7)	0.064(10)	
1620.5(4)	0.071(11)		2437.1(5)	0.067(8)	
1627.8(4)	0.071(9)	3935	2447.7(5)	0.050(7)	
1649.0(4)	0.089(12)		2486.1(8)	0.028(8)	3922
1653.5(3)	0.207(18)		2499.3(3)	0.070(8)	3935
1655.9(2)	0.131(14)		2511.3(5)	0.041(7)	
1663.2(5)	0.055(10)	3562	2582.92(10)	0.36(3)	2583
1674.8(3)	0.095(10)		2639.39(3)	2.64(19)	2639
1684.3(2)	0.119(11)		2731.8(9)	0.045(10)	4630
1727.03(6)	0.62(4)	3163	2753.1(6)	0.062(10)	
1743.95(18)	0.212(18)	3642.6?	2806.3(11)	0.069(8)	4242
1746.9(3)	0.097(12)		2831.2(6)	0.097(12)	
1750.5(6)	0.031(9)		2931.3(3)	0.100(15)	2931
1806.80(18)	0.202(16)	3242	3027.8(6)	0.045(7)	
1821.31(8)	0.49(4)	3257	3049.42(11)	0.42(3)	3050
1832.2(4)	0.126(12)		3061.2(6)	0.059(8)	
1850.30(10)	0.32(2)	3286?	3150.4(5)	0.050(10)	
1903.0(4)	0.067(9)	3339	3157.0(8)	0.052(10)	
1909.3(6)	0.059(11)		3179.62(15)	0.258(20)	4615
1914.3(3)	0.125(15)		3338.81(8)	0.61(4)	3339
1940.80(9)	0.44(3)	3377	3366.73(7)	0.57(4)	3367
1960.9(3)	0.158(14)	3860?	3437.0(7)	0.055(10)	
1993.0(4)	0.054(8)		3442.12(18)	0.201(18)	3442
1999.5(4)	0.051(8)		3504.1(2)	0.204(17)	3504
2023.5(3)	0.180(16)	3922	3539.9(6)	0.063(10)	
2032.6(3)	0.139(14)	3931	3600.7(3)	0.104(11)	3601
2068.1(4)	0.107(12)	3504	3642.8(2)	0.29(2)	3643
2071.8(5)	0.064(11)		3684.6(3)	0.139(13)	3685
2092.1(5)	0.064(8)		3734.3(3)	0.155(14)	3734
2136.4(5)	0.062(9)		3800.1(3)	0.159(14)	3800
2164.8(3)	0.121(12)	3601	4001.2(4)	0.126(13)	4001
2182.0(4)	0.111(10)	3618	4012.9(9)	0.041(9)	
2197.8(3)	0.073(8)		4025.8(4)	0.137(14)	4026
2210.9(3)	0.097(9)	3647	4051.3(9)	0.070(10)	
2217.86(2)	9.2(6)	2218	4323.2(4)	0.110(12)	4323

Level at 2991 keV. For the 1555.25-keV gamma transition, the small value of $\delta = +0.32(2)$ is ruled out by data on a_4 and P_γ.

Level at 3050 keV. On the basis of P_γ, we presented, in Table 2, the small value of δ for the 1614.08-keV gamma transition, ruling out the value of $\delta = +1.58(8)$.

Level at 3085 keV? This level was introduced in studying the (n, γ) reaction. For a level at this energy, the value of P_s is expected to be about 1.5. Since we were unable to find gamma lines of this total intensity

Table 2. Diagram of levels and gamma transitions in ^{138}Ba

E_i, keV	J_i^π	E_γ, keV	I_γ, rel. units	E_f, keV	J_f^π	P_s	a_2	a_4	$\delta \pm \Delta\delta$; ML
1435.87(2)	2_1^+	1435.86	100	0	0^+	41	+0.261(9)	−0.095(12)	$E2$
1898.66(3)	4_1^+	462.79	33.2	1436	2^+	14.3	+0.233(9)	−0.047(12)	$E2$
2090.61(4)	6_1^+	191.95	8.8	1899	4^+	3.5	+0.074(8)	−0.001(12)	
			(10.6)**						
2189.92(3)	0_2^+	754.05	1.9	1436	2^+	1.70	+0.001(13)	−0.009(20)	Isotropic
2203.12(5)	6_2^+	304.0*	0.057	1899	4^+	3.8			
		112.51	2.87	2091	6^+		+0.31(2)	−0.01(3)	$+0.03 \pm 7$
			(5.0)**						
2217.88(2)	2_2^+	2217.86	9.2	0	0^+	8.1	+0.270(9)	−0.092(12)	$E2$
		782.12	0.27	1436	2^+		+0.17(5)	−0.02(7)	-0.02 ± 8 or $+2.5 + 7 - 4$
2307.58(3)	4_2^+	871.68	3.9	1436	2^+	5.7	+0.311(11)	−0.067(15)	$E2$
		408.96	3.6	1899	4^+		+0.322(11)	+0.002(15)	$+0.03 \pm 2$
2415.40(4)	5_1^+	516.70	2.55	1899	4^+	4.6	−0.121(10)	+0.029(15)	$+0.059 \pm 7$
		324.83	1.69	2091	6^+		0.00(9)	0.00(8)	-0.10 ± 2
			(1.75)**						
		212.28	0.93	2203	6^+		−0.03(2)	+0.03(3)	-0.07 ± 2
			(1.04)**						
		107.8	0.20	2308	4^+		−0.17(21)	+0.02(33)	
			(0.36)**						
2445.58(3)	3_1^+	1009.70	3.7	1436	2^+	4.5	−0.181(9)	−0.002(14)	$+0.018 \pm 7$
		546.93	1.39	1899	4^+		+0.021(13)	−0.012(19)	-0.13 ± 2
		227.71	0.214	2218	2^+		−0.12(7)	+0.10(10)	$+0.01 \pm 8$
			(0.24)**						or $-5.6 + 18 - 46$
		138.10	0.32	2308	4^+				
			(0.48)**						
2583.03(4)	1_1^+	2582.92	0.36	0	0^+	2.4	−0.10(4)	0.00(6)	$M1$
		1147.16	1.81	1436	2^+		+0.014(14)	−0.001(21)	-0.19 ± 11
		365.10	0.227	2218	2^+		0.00(8)	0.00(12)	-0.1 ± 6 or $-2.6 + 18 - \infty$
2639.42(3)	2_3^+	2639.39	2.64	0	0^+	3.1	+0.276(11)	−0.082(15)	$E2$
		1203.6	0.11	1436	2^+				
		421.41	0.206	2218	2^+		+0.15(7)	+0.01(11)	-0.08 ± 12 or $+2.9 + 18 - 9$
		193.9	0.115	2446	3^+				
			(0.135)**						
2779.37(3)	4_3^+	1343.54	∼1.7	1436	2^+	∼ 2.6	+0.234(12)	−0.074(17)	$(E2)$
		880.70	0.23	1899	4^+				
		363.88	0.51	2415	5^+		+0.02(4)	+0.03(6)	-0.11 ± 3 or $-4.7 + 6 - 9$
		333.68	0.199	2446	3^+				
2851.58(4)	4_4^+	1415.71	1.88	1436	2^+	2.2	+0.349(14)	−0.083(19)	$E2$
		952.90	0.267	1899	4^+		−0.28(6)	−0.10(9)	-1.5 ± 5 (the other is $-5 + 2 - 9$)
		436.0*?	0.049	2415	5^+				
2880.74(3)	3_1^-	1444.86	2.8	1436	2^+	2.2	−0.164(10)	+0.001(15)	$+0.04 \pm 2$
2931.47(4)	2_4^+	2931.3	0.100	0	0^+	1.58	+0.21(9)	−0.08(12)	$E2$

Table 2. (Contd.)

E_i, keV	J_i^π	E_γ, keV	I_γ, rel. units	E_f, keV	J_f^π	P_s	a_2	a_4	$\delta \pm \Delta\delta$; ML
		1495.59	1.48	1436	2^+		−0.183(11)	−0.048(17)	-0.75 ± 4 (or $-4.2 + 4 - 5$)
2991.11(4)	3_2^+	1555.25	0.66	1436	2^+	1.36	+0.19(2)	+0.10(3)	$+9.8 + 21 - 14$
		773.16	0.39	2218	2^+		−0.40(4)	+0.03(6)	-2.5 ± 3 (or -0.18 ± 4)
		683.65	0.31	2308	4^+		+0.14(5)	+0.04(7)	-2.5 ± 5 (or -0.27 ± 6)
3049.96(4)	2_5^+	3049.82	0.42	0	0^+	2.6	+0.30(4)	−0.08(5)	$E2$
		1614.08	1.89	1436	2^+		+0.255(14)	−0.063(19)	$+0.16 \pm 2$
		1151.38	0.252	1899	4^+		+0.12(14)	−0.01(19)	
3154.91(11)	4_5^+	1256.25	0.249	1899	4^+	0.71?	−0.18(7)	−0.07(10)	$-1.0 + 2 - 3$ or $1/\delta = 0.00 \pm 1$
		1064.20	0.20	2091	6^+				
		739.44	0.130	2415	5^+				
		375.6*	0.051	2779	4^+				
3162.99(6)	2_6^+	1727.03	0.62	1436	2^+	1.14	+0.22(3)	−0.02(4)	$+0.05 \pm 5$ (or $+2.0 + 5 - 3$)
		1264.63	0.34	1899	4^+		+0.09(7)	+0.04(10)	($E2$)
		855.7	0.072	2308	4^+				
		717.67	0.103	2446	3^+				
3183.8(3)	8_1^+	1093.1	0.166	2091	6^+	0.16			
		980.7	0.070	2203	6^+				
3242.42(9)	3_3^+	1806.80	0.202	1436	2^+	∼0.9	+0.01(6)	+0.05(9)	$+0.17 \pm 5$ or $-28 + 16 - \infty$
		1343.5?	∼0.4	1899	4^+				
		934.77	0.258	2308	4^+		−0.31(6)	−0.01(8)	$+0.25 \pm 7$ or $+8 + 6 - 3$
		796.7*	0.051	2446	3^+				
3257.34(7)	$3^+, (4^+)$	1821.31	0.49	1436	2^+	0.81	+0.28(4)	0.00(5)	$+0.46 \pm 4$ or $+4.2 + 7 - 6$
		1358.80	0.32	1899	4^+		−0.17(5)	+0.02(7)	$+0.11 \pm 6$ or $-50 + 40 - 600$
3286.16(8)*?	$(2^+, 3^+)$	1850.30	0.32	1436	2^+	0.71	+0.34(5)	−0.12(7)	$+0.7 \pm 5$ ($J_i^\pi = 2^+$)
		1387.0	0.096	1899	4^+				
		1068.27	0.296	2218	2^+		−0.01(6)	−0.15(9)	
3338.85(8)	2^+	3338.81	0.61	0	0^+	0.68	+0.27(3)	−0.09(4)	$E2$
		1903.0	0.067	1436	2^+				
3360.1(3)	(7_1^+)	944.7	0.210	2415	5^+	0.21	+0.25(8)	−0.06(11)	($E2$)
3366.77(7)	2^+	3366.73	0.57	0	0^+	0.57	+0.27(3)	−0.06(4)	$E2$
3376.68(9)*	3^+	1940.80	0.44	1436	2^+	0.61	+0.47(4)	+0.01(6)	$+0.9 + 4 - 3$
		1478.28	0.168	1899	4^+		−0.02(10)	−0.09(14)	-0.13 ± 12 or $-4 + 1 - 6$
3379.90(10)*?	(5^+)	1481.24	0.33	1899	4^+	0.33	+0.37(5)	+0.12(7)	$+3.0 \pm 4$
3442.17(18)	2^+	3442.12	0.201	0	0^+	0.29?	+0.24(7)	−0.06(9)	$E2$
		1251.7*?	0.092	2190	0^+				
3486.00(5)*		1040.42	0.52	2446	3^+	0.56			
		1587.6	0.039	1899	4^+				

Table 2. (Contd.)

E_i, keV	J_i^π	E_γ, keV	I_γ, rel. units	E_f, keV	J_f^π	P_s	a_2	a_4	$\delta \pm \Delta\delta$; ML
3504.1(2)	2^+	3504.1	0.204	0	0^+	0.42	+0.25(7)	−0.09(9)	$E2$
		2068.1*	0.107	1436	2^+		+0.27(12)	0.00(18)	
		1605.4*	0.110	1899	4^+				
3562.24(8)	$(4)^-$	1663.2*	0.055	1899	4^+	0.38			
		1116.66*	0.33	2446	3^+		−0.14(7)	+0.01(11)	$+0.07 \pm 4$
3600.7(3)	1	3600.7	0.104	0	0^+	0.23	−0.07(12)	0.00(18)	$E1$ or $M1$
		2164.8*	0.121	1436	2^+		+0.10(15)	0.00(20)	
3610.2(4)	$(7^+, 8^+)$	1407.1	0.038	2203	6^+	0.04			
3617.9(4)	(0^+)	2182.0	0.111	1436	2^+	0.11	0.00(8)	−0.03(12)	
3622.1(4)	10_1^+	438.3	0.040	3184	8^+	0.04			
3633.0(4)	(9_1^-)	449.2	0.033	3184	8^+	0.03			
3642.9(2)	2^+	3642.8	0.29	0	0^+	0.29	+0.30(5)	−0.06(7)	$E2$
3642.62(18)?		1743.95	0.212	1899	4^+	0.21	+0.22(7)	+0.09(10)	
3646.83(14)	$(3)^-$	2210.9	0.097	1436	2^+	0.28			
		766.09	0.182	2881	3^-		+0.23(8)	+0.01(11)	-0.07 ± 10 or $+1.5 \pm 6$
3684.6(3)*	1	3684.6	0.139	0	0^+	0.14	+0.01(9)	0	$E1$ or $M1$
3694.1(4)		1387.0	0.096	2308	4^+	0.18			
		813.0	0.080	2881	3^-				
3734.3(3)*	2^+	3734.3	0.155	0	0^+	0.16	+0.29(11)	−0.24(16)	$E2$
3800.0(3)*	2^+	3800.1	0.159	0	0^+	0.20	+0.27(11)	−0.08(15)	$E2$
		1582.0	0.041	2218	2^+				
3859.6(3)?	$(5)^-$	1960.9*	0.158	1899	4^+	0.16	−0.19(11)	+0.01(17)	$(E1)$
3922.2(3)	$(3)^-$	2486.1	0.028	1436	2^+	0.21			
		2023.5	0.180	1899	4^+		−0.14(9)	−0.03(12)	$(E1)$
3931.3(3)*	$3^+, 4^+, 5$	2032.6	0.139	1899	4^+	0.18	+0.04(11)	+0.01(16)	
		1515.8	0.042	2415	5^+				
3935.0(2)	(2^+)	2499.3	0.070	1436	2^+	0.23			
		1627.8*	0.071	2308	4^+				
		1054.2	0.091	2881	3^-				
4001.2(4)*	2^+	4001.2	0.126	0	0^+	0.13	+0.26(15)	−0.16(19)	$E2$
4025.8(4)	1^-	4025.8	0.137	0	0^+	0.14	−0.17(9)	0.00(13)	$E1$
4165.1(3)	$(4)^-$	1284.4*?	0.229	2881	3^-	0.23			
4242.2(11)		2806.3	0.069	1436	2^+	0.07			
4323.2(4)	$(1)^-$	4323.2	0.110	0	0^+	0.11	−0.14(13)	+0.01(18)	$E1$
4615.32(15)*		3179.62	0.258	1436	2^+	0.26	−0.02(7)	−0.02(9)	
4630.5(9)		2731.8	0.045	1899	4^+	0.05			

* Values established for the first time.

** Transition intensities with allowance for conversion.

for the deexcitation of the level at 3085 keV, we deem that there is no such level in ^{138}Ba.

Level at 3163 keV. The spin–parity of $J^\pi = 3^+$ is impossible for this level because of a small value of $|a_4|$ and the value of P_γ for the 1727.03-keV gamma transition, while the spin–parity of $J^\pi = 3^-$ is ruled out by the value of a_2—for an E1 transition, it corresponds to $\delta = +0.40$, which is improbable for ^{138}Ba. The angular distribution of 1264.63-keV gamma rays is compatible with that which is expected for the 2^+–4^+ quadrupole transition.

Level at 3242 keV. The spin–parity of $J^\pi = 4^+$ is ruled out by the value of a_2 for the 1806.80-keV gamma transition, while the spin–parity of $J^\pi = 2^+$

Table 3. Linear polarization of gamma rays in the ^{138}Ba$(n, n'\gamma)$ reaction

E_γ, keV	J_i^π	J_f^π	P_γ^{calc}		P_γ^{expt}	Conclusions
			$a_4 \sim 0$	$\lvert a_4\rvert > 0$		
324.83	5_1^+	6_1^+	0.62(2)	0.46(2)	0.9(2)	$a_4 \sim 0$?
408.96	4_2^+	4_1^+	3.30(4)	0.94(4)	3.1(+12, −4)	$a_4 \sim 0$
462.79	4_1^+	2_1^+		2.17(9)	2.1(+6, −2)	Corresponds to $E2$
516.70	5_1^+	4_1^+	0.51(1)	1.20(1)	0.68(10)	$a_4 \sim 0$
546.93	3_1^+	4_1^+	0.69(1)	0.47(1)	0.75(16)	$a_4 \sim 0$
773.16	3_2^+	2_2^+	0.70(3)	1.62(1)	1.2(+7, −4)	$\lvert a_4\rvert > 0$?
782.12	2_2^+	2_1^+	1.93(5)	0.73(1)	1.1(+10, −6)	
871.68	4_2^+	2_1^+		3.2(2)	3.5(+15, −7)	Corresponds to $E2$
952.90	4_4^+	4_1^+	1.1(2)	0.60(+16, −9)	1.2(+10, −6)	$a_4 \sim 0$
1009.70	3_1^+	2_1^+	0.56(1)	1.52(1)	0.60(11)	$a_4 \sim 0$
1147.16	1_1^+	2_1^+	0.93(2)	0.81(1)	1.0(2)	
1343.54	4_3^+	2_1^+		2.2(3)	3.3(+18, −8)	Corresponds to $E2$
1415.71	4_4^+	2_1^+		3.9(4)	2.7(+14, −7)	Corresponds to $E2$
1435.86	2_1^+	0_1^+		2.32(11)	2.4(+7, −4)	Corresponds to $E2$
1444.86	3_1^-	2_1^+	1.9(2)		1.6(+5, −3)	Corresponds to $E1$
1495.59	2_4^+	2_1^+	1.74(3)	0.98(2)	1.4(+5, −3)	$a_4 \sim 0$?
1555.25	3_2^+	2_1^+	0.34(1)	1.21(3)	4(+7, −2)	$\lvert a_4\rvert > 0$
1614.08	2_5^+	2_1^+	1.77(4)	0.76(1)	1.4(+6, −4)	$a_4 \sim 0$
1727.03	2^+	2_1^+	1.92(6)	0.73(2)	1.5(+22, −9)	$J_i^\pi = 2^+, a_4 \sim 0$
	3^+	2_1^+	0.32(2)			

is incompatible with the a_2 value observed for the 934.77-keV gamma transition. A negative parity is unlikely because of the value of δ for the 934.77-keV gamma transition.

Level at 3257 keV. The spin–parity of $J^\pi = 2^+$ is excluded by the value of a_2 for the 1358.80-keV gamma transition, while the spin–parity of $J^\pi = 3^-$ is at odds with the value of δ for the 1821.31-keV gamma transition. The quantum numbers $J^\pi = 4^+$ are questioned because of the value of a_4 for the 1821.31-keV gamma transition (the value of $a_4 = -0.075$ is expected for the 4^+–2^+ transition). The value of δ in Table 2 is given for the $J^\pi = 3^+$ initial state.

Level at 3286 keV? This level can be introduced on the basis of the energies of three gamma transitions. The most probable spin–parity assignment for this level would be that of 2^+ or that of 3^+. However, the 1850.30- and the 1068.27-keV transition have been observed neither in studying the beta decay of ^{138}Ba nor in studying the relevant (n, γ) reaction, in which case the population of the 2^+ level is expected; therefore, the existence of a $J^\pi = 2^+$ level at this energy is questionable. The values of a_4 for the transitions in question are incompatible with $J^\pi = 3^+$.

Level at 3352 keV? A 3352.6-keV transition of low intensity was discovered in studying the beta decay of ^{138}Cs, and the level at the same energy was introduced on this basis. In the spectrum for the $(n, n'\gamma)$ reaction, the intensity of the 3352.6-keV transition is equal to 0.030(10) at the expected population P_s of this level about 0.5. In all probability, this transition proceeds to the first 2^+ level, in which case the energy of the initial state is 4789 keV. A 3823.56-keV transition that could correspond to a transition from a capture state to this level was discovered in the relevant (n, γ) reaction.

Level at 3360 keV. The angular distribution of 944.7-keV gamma rays is consistent with the spin–parity assignment of 7^+ for this level.

Table 4. Measured half-lives of some ^{138}Ba levels in the $(n, n'\gamma)$ reaction

E_{lev}, keV	J^π	E_γ, keV	F	$T_{1/2}$, ps	
				our study	[3]**
2189.92	0^+	754.05	−0.019(56)	≥0.8	–
2217.88	2^+	2217.86	0.257(14)*	0.140(10)	0.123(14)
2445.58	3^+	1009.70	0.035(31)	≥0.7	5(4)
		546.93	0.050(88)		
2583.03	1^+	2582.92	0.27(11)	0.134(+42, −29)	≤7
		1147.16	0.270(52)		
2639.42	2^+	2639.39	0.103(20)	0.42(+12, −8)	0.30(8)
2851.58	4^+	1415.71	−0.001(31)	≥1.5	≤11
2880.74	3^-	1444.86	0.491(26)	0.055(6)	≤11
2931.47	2^+	1495.59	0.21(4)	0.19(+5, −4)	–
3049.96	2^+	3049.82	0.21(10)	0.33(+14, −8)	–
		1614.08	0.124(36)		
3162.99	2^+	1727.03	0.15(9)	0.28(+55, −12)	–
3338.85	2^+	3338.81	0.650(65)	0.031(+9, −8)	0.029(6)**
3366.77	2^+	3366.73	0.650(74)	0.031(+10, −8)	0.070(13)**
3504.1	2^+	3504.1	0.19(19)	≥0.2	–
3600.7	1	3600.7	0.37(33)	≥0.09	–
3642.9	2^+	3642.8	0.75(13)	0.019(+16, −11)	0.024(10)
3734.3	2^+	3734.3	0.42(21)	0.08(+13, −4)	–
3800.1	2^+	3800.1	0.38(23)	0.09(+21, −6)	–
4025.8	1^-	4025.8	0.87(25)	≤35 fs	0.54(19) fs

* A partial population of this level by cascade gamma transitions from higher levels [6] is taken into account.

** See main body of the text.

Level at 3377 keV. The value of a_2 for the 1940.80-keV gamma transition is not compatible with the spin–parity values of 1, 2^+, 3^-, and 4^+ for this level; in addition, it unambiguously determines the value of δ (the value of δ corresponding to the experimental results for a_2 and a_4 occurs at the extremely right point of the δ ellipse).

Level at 3380 keV? We have proposed this level to ensure the placement of the 1481.24-keV transition. The intensity of this transition complies well with the population expected for the $J^\pi = 5^+$ level at this energy value. The angular distribution for the 1481.24-keV transition is at odds with the spin–parity values of $J^\pi = 2^+$ and 4^+, and the population is not consistent with $J^\pi = 3^+$.

Level at 3437 keV? The level was introduced because of the presence of a 3437.5(6)-keV gamma transition in the beta decay of ^{138}Cs and the 3436.18(9)-keV gamma transition in the (n, γ) reaction. The 3437.0(7)-keV transition of low intensity in the $(n, n'\gamma)$ reaction ($I_\gamma = 0.055$) is unable to ensure a value of $P_s \approx 0.4$ expected for this level, but it may be involved in the deexcitation of the 4872.9(7)-keV level to the first 2^+ level. The 3738.22(7)-keV transition observed in the (n, γ) reaction may be a transition from a capture state to this level.

Level at 3442 keV. This level was found in studying the (n, γ) reaction. Its population determined here is somewhat lower than that which is expected for a 2^+ level at this energy value. Possibly, there is a transition that proceeds to the level at 2639.42 keV

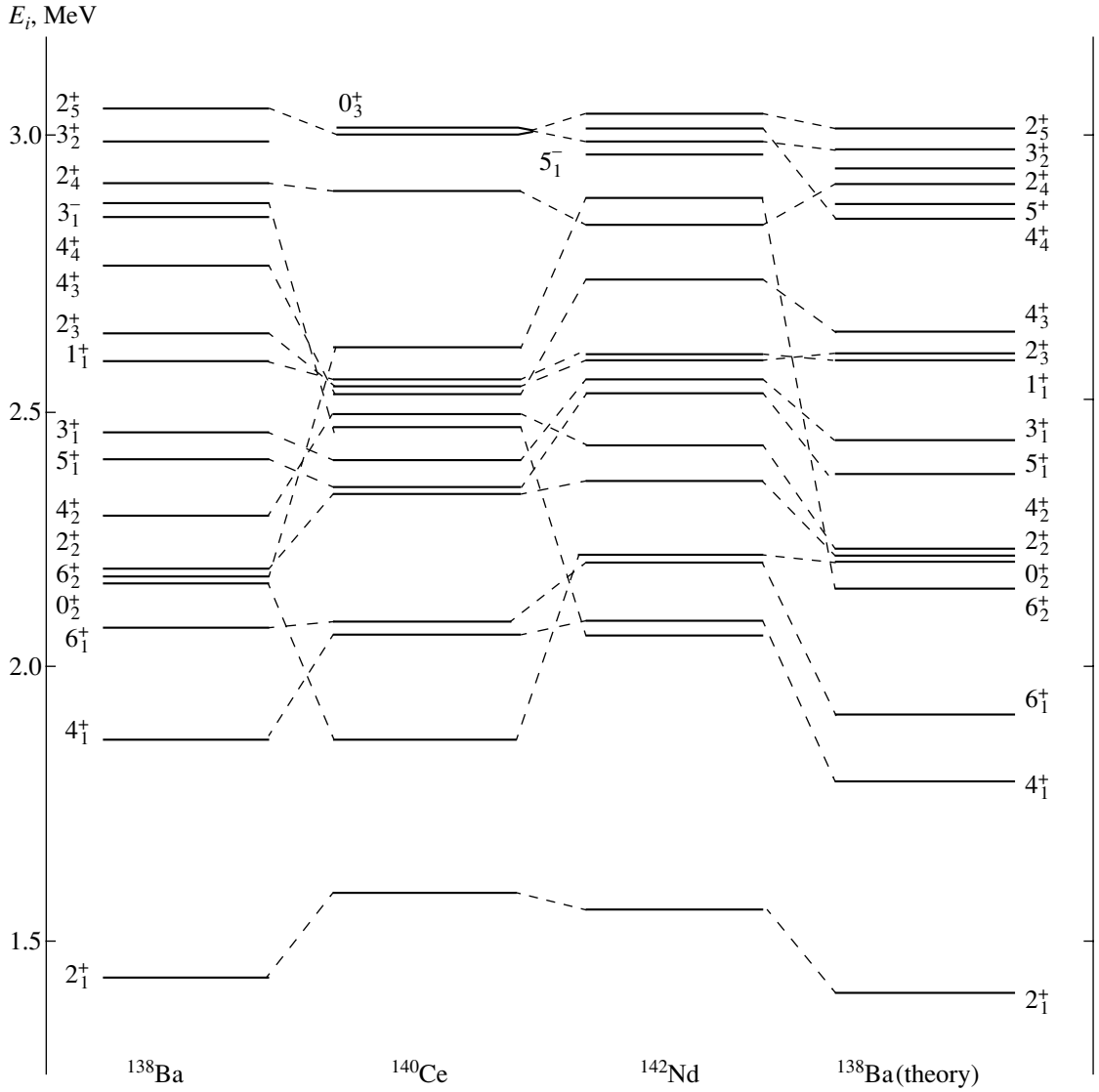

Energy-level diagrams for ^{138}Ba, ^{140}Ce, and ^{142}Nd along with the energy-level diagram computed for ^{138}Ba in [4] on the basis of the shell model.

and which coincides, in the measured spectrum, with the intense background line of lead at 803 keV.

Level at 3486 keV. We have introduced this level on the basis of the 1040.42-keV transition, which has a relatively high intensity. Because of its intensity, this transition cannot be associated with the deexcitation of a higher lying level (in particular, the level at 3922.5 keV, as was assumed in [3]). In the energy-level diagram, there is also no placement for it at energies below 2.5 MeV.

Level at 3562 keV. The $J^\pi = (4)^-$ level was introduced upon studying the (d, p) reaction. The intensity of the gamma line at 1116.66 keV complies well with the P_s value expected for a level at this energy. The angular distribution of 1116.66-keV gamma rays agrees with that which is expected for a $4^- - 3^+$ transition.

Level at 3618 keV. A $J^\pi = 0^+$ level at 3612 keV was found in the (t, p) reaction. The 2182.0-keV transition is a good candidate for that which could deexcite the 0^+ level at this energy since the intensity I_γ of this transition has an appropriate value and since it produces gamma rays distributed isotropically. The discrepancy between the energies is within the errors in determining them in the (t, p) reaction.

Level at 3643 keV. The value of a_2 for 1743.95-keV gamma rays is slightly greater than that which is expected for the $2^+ - 4^+$ transition, and this transition is observed neither in the beta decay of ^{138}Cs nor in the (n, γ) reaction. At the same time, the 3643.6-keV transition was discovered in these processes. The

Table 5. Values of δ in the deexcitation of some levels in ^{138}Ba, ^{140}Ce, and ^{142}Nd

Transition $J_i^\pi - J_f^\pi$	$^{138}_{56}Ba_{82}$	$^{140}_{58}Ce_{82}$ [1]	$^{142}_{60}Nd_{82}$ [2]
$2_2^+ - 2_1^+$	-0.02 ± 8 or $+2.5 + 7 - 4$	$+0.5 + 6 - 2$	$+0.16 + 6 - 5$
$2_3^+ - 2_1^+$	–	-0.17 ± 2	-0.28 ± 3
$2_4^+ - 2_1^+$	$-4.2 + 4 - 5$ or -0.75 ± 4	$-1.5 + 4 - 10$	$-0.6 + 2 - 3$ or $-6 + 3 - 29$
$2_5^+ - 2_1^+$	$+0.16 \pm 2$ or $+1.58 \pm 8$	$+0.7 \pm 3$	$+0.1 < \delta < +1.5$
$3_1^+ - 2_1^+$	$+0.018 \pm 7$	-0.056 ± 12	-0.07 ± 2
$3_1^+ - 4_1^+$	-0.13 ± 2	$+0.19 \pm 4$ or $+13 + 11 - 5$	-0.08 ± 2
$4_2^+ - 4_1^+$	$+0.03 \pm 2$	$+0.5 + 3 - 4$	-0.09 ± 3
$4_3^+ - 4_1^+$	–	-0.04 ± 2	-0.08 ± 4
$5_1^+ - 4_1^+$	$+0.059 \pm 7$	-0.069 ± 15	-0.038 ± 10
$5_1^+ - 6_1^+$	-0.10 ± 2	-0.19 ± 10	-0.06 ± 2 or $-7.0 + 10 - 15$
$6_2^+ - 6_1^+$	$+0.03 \pm 7$	-0.19 ± 4	-0.13 ± 4

Table 6. Experimental and theoretical values of δ for gamma transitions in ^{138}Ba

Transition $J_i^\pi - J_f^\pi$	Experiment		Theory [4]
	Our study	[3, 4]	
$3_1^+ - 2_1^+$	$+0.018 \pm 7$	-2.90 ± 15	-0.41
$3_2^+ - 2_1^+$	$+9.8 + 21 - 14$	$+0.21 \pm 4$	$+0.81$
$3_2^+ - 2_2^+$	-2.5 ± 5	-2.0 ± 6	-1.92
$4_2^+ - 4_1^+$	$+0.03 \pm 2$	-0.23 ± 7	$+0.01$
$5_1^+ - 6_1^+$	-0.10 ± 2	-7.8 ± 18	-1.25
$6_2^+ - 6_1^+$	$+0.03 \pm 7$	-0.27 ± 12	-0.02

total intensity I_γ of the two transitions in question is overly great for the level at the energy value being considered. Possibly, there are two levels at this energy.

Level at 3685 keV. The 3684.6-keV transition can be associated only with the deexcitation of this level to the ground state because, even for the transition to the 2_1^+ level, the expected intensity must be 2 to 3 times lower [according to the regularities in the behavior of $P_s(E_i)$ for the fast-reactor-neutron-induced reaction in question, which, for ^{138}Ba, are reflected in Table 2 (column P_s)]. Using this argument, we have also introduced levels at 3734.3, 3800.0, 4001.2, and 4615.32 keV.

3. COMPARISON OF THE RADIATIVE PROPERTIES OF ^{138}Ba, ^{140}Ce, AND ^{142}Nd LEVELS

The energy-level diagrams for ^{138}Ba, ^{140}Ce [1], and ^{142}Nd [2] are shown in the figure for the excitation-energy region extending up to about 3 MeV. Also given there is the energy-level diagram for ^{138}Ba according to the shell-model calculations in [4]. From the figure, it is obvious that, up to an excitation energy of about 3 MeV, all $J < 5$ levels have been revealed in these nuclei. (Only the position of the 0_3^+ level in ^{138}Ba has not yet been fixed.)

The values of δ that correspond to the deexcitation of some levels in the nuclei being considered are quoted in Table 5. In comparing these values, it is necessary to pay special attention to the sign of

δ, because it must greatly depend on the structure of excited states involved in a given transition. For the $J^\pi = 2^+$ levels, the sign of δ remains unchanged in going over from one nucleus of the above set to another and the value of this parameter changes insignificantly, while, for the majority of the levels characterized by different values of J, the sign of δ may be different for the different nuclei. In this case, the sign of δ must be affected by different contributions of the $2d_{5/2}$ and $1g_{7/2}$ proton states. We emphasize the opposite signs of δ for the $2_2^+ - 2_1^+$ and $2_3^+ - 2_1^+$ transitions in ^{140}Ce and ^{142}Nd, since this is peculiar to the majority of medium-mass even–even nuclei [14].

In Table 6, the values of δ that were computed in [4] on the basis of the shell model are contrasted against their experimental counterparts found in [4] and in our present study. The model used in those calculations explains only half of our data on δ values.

REFERENCES

1. L. I. Govor, A. M. Demidov, and V. A. Kurkin, Yad. Fiz. **56** (12), 15 (1993) [Phys. At. Nucl. **56**, 1625 (1993)].
2. L. I. Govor, A. M. Demidov, and V. A. Kurkin, Yad. Fiz. **59**, 1733 (1996) [Phys. At. Nucl. **59**, 1675 (1996)].
3. J. K. Tuli, Nucl. Data Sheets **69**, 69 (1993).
4. I. Dioszegi, A. Veres, W. Enghardt, and H. Prade, J. Phys. G **10**, 969 (1984).
5. A. M. Demidov, L. I. Govor, and K. A. Baskova, in *Investigation of Excited States in Nuclei* (Nauka, Alma-Ata, 1986), p. 70.
6. L. I. Govor, A. M. Demidov, O. K. Zhuravlev, *et al.*, Yad. Fiz. **54**, 330 (1991) [Sov. J. Nucl. Phys. **54**, 196 (1991)].
7. Yu. G. Kosyak, in *Investigation of Excited States in Nuclei* (Nauka, Alma-Ata, 1986), p. 4.
8. M. K. Georgieva, D. V. Elenkov, D. P. Lefterov, and G. Kh. Tumbev, Fiz. Élem. Chastits At. Yadra **20**, 930 (1989) [Sov. J. Part. Nucl. **20**, 393 (1989)].
9. A. E. Blaugrund, Nucl. Phys. **88**, 501 (1966).
10. R. D. Herzberg, I. Bauske, P. Von Brentano, *et al.*, Nucl. Phys. A **592**, 211 (1995).
11. G. H. Carlson, W. L. Talbert, and J. R. McConnell, Phys. Rev. C **9**, 283 (1974).
12. F. R. Metzger, Phys. Rev. C **18**, 2138 (1978).
13. C. P. Swann, Phys. Rev. C **15**, 1967 (1977).
14. A. M. Demidov, L. I. Govor, V. A. Kurkin, and I. V. Mikhaĭlov, Yad. Fiz. **60**, 581 (1997) [Phys. At. Nucl. **60**, 503 (1997)].

Translated by A. Isaakyan

Physics of Atomic Nuclei, Vol. 66, No. 1, 2003, pp. 172–181. From Yadernaya Fizika, Vol. 66, No. 1, 2003, pp. 175–184.

ELEMENTARY PARTICLES AND FIELDS
Theory

Three-Body Dispersion-Relation N/D Equations for the Coupled Decay Channels $\bar{p}p(J^{PC} = 0^{-+}) \to \pi^0\pi^0\pi^0$, $\eta\pi^0\pi^0$, $\eta\eta\pi^0$, $\bar{K}K\pi^{0*}$

A. V. Anisovich[**]

Petersburg Nuclear Physics Institute, Russian Academy of Sciences, Gatchina, St. Petersburg, 188350 Russia

Received February 1, 2001; in final form, May 10, 2001

Abstract—For several years the data on different $\bar{p}p(J^{PC} = 0^{-+}) \to 3$ mesons channels presented by the Crystal Barrel collaboration were successfully analyzed by extracting the leading amplitude singularities—pole singularities—with the aim of obtaining information about two-meson resonances. But these analyses do not take three-body final-state interactions into account in an explicitly correct way. This paper is devoted to the consideration of this problem. It is shown how the coupled three-body equations could be written for the $\pi^0\pi^0\pi^0$, $\eta\pi^0\pi^0$, $\eta\eta\pi^0$, and $\bar{K}K\pi^0$ channels in the $\bar{p}p$ annihilation at rest using the three-body dispersion-relation N/D method. © *2003 MAIK "Nauka/Interperiodica"*.

1. INTRODUCTION

For several years Crystal Barrel collaboration has presented high-statistics data on the three-meson production from $\bar{p}p$ annihilation at rest. These data were successfully analyzed (see, for example, [1–4]) with the aim of searching for new meson resonances in the 1000–1600 MeV region using the K-matrix formalism or a simplified dispersion N/D method. There is a strong expectation based on QCD [5], as well as on lattice calculations [6] that the lowest scalar glueball is located in this region. Thus, the identification of scalar resonances in the mass region 800–2000 MeV and their classification in $\bar{q}q$ nonets should be done to trap the lightest scalar glueball. The quark–gluon structure of these resonances can be determined from the analysis of coupling constants of these states to pseudoscalar mesons [7]. The question is whether the K-matrix approximation—or the simplified N/D method—is sufficient for this purpose.

In this paper the three-body dispersion N/D method is presented, which is based on the two-body unitarity condition and allows one to take into account the final-state interaction (FSI) of three mesons. The basic principles of this technique were developed in 1960s and they were applied to the calculation of FSI in the K-meson decay into three pions (see [8, 9] and references therein). Recently this technique was used for the calculation of the $\eta \to 3\pi$ decay [10] and ϕ-meson production in $p\bar{p}$ annihilation at rest [11].

This paper is organized as follows. In Section 2, the two-particle discontinuity of the decay amplitude is written out, and the integral equation is derived. It is shown how to take into account not only the S-wave binary interactions, but also interactions with higher angular momentum (P and D waves). In Section 3, this technique is generalized for the resonance and nonresonance two-particle interactions. The complete three-body dispersion equation is written so that may be used for the analysis of various three-particle reactions. In Section 4, it is shown how the coupled three-body equations could be written for $\pi^0\pi^0\pi^0$, $\eta\pi^0\pi^0$, $\eta\eta\pi^0$, and $\bar{K}K\pi^0$ channels in $\bar{p}p$ annihilation from the 0^{-+} state.

2. TWO-PARTICLE DISCONTINUITY OF THE DECAY AMPLITUDE

Let us start with the consideration of the decay of a scalar particle with the mass M and momentum P into three scalar particles with masses m_1, m_2, and m_3 and momenta k_1, k_2, and k_3. I would like to show that the energy dependence of this transition amplitude may be derived from the unitarity and analyticity. The imaginary part of the amplitude A_n for the transition $1 \to n$ is given by

$$\mathrm{Im}M_n = \frac{1}{2}\sum_{n'}(2\pi)^4\delta\left(P - \sum_{i=1}^{n'} k_i\right) T^*_{n'n}M_{n'}, \quad (1)$$

where $T_{n'n}$ is the scattering matrix. Equation (1) may be simplified if the approximation is used, where (i) binary interactions of particles are taken into account, neglecting three-particle forces; and (ii) there are no transitions through intermediate states with

[*] This article was submitted by the author in English.

[**] e-mail: aanisovi@iname.com

more than three particles. It is also supposed that there are no transitions through intermediate states involving other particles; still, this is not a crucial restriction. Below it is shown how the production of new particles in the intermediate state may be taken into account. In this approximation, one can write Eq. (1) as follows:

$$\mathrm{Im}M_3 = \frac{1}{2}(2\pi)^4\delta(P-k_1-k_2-k_3)T_{33}^*M_3. \quad (2)$$

Neglecting three-particle forces, the amplitude M_3 for the three-particle production is a sum of four terms: (i) the direct production amplitude $\lambda(s_{12},s_{13},s_{23})$, which is assumed, for the sake of simplicity, to be free of singularities; (ii) the amplitude a_{12}, where the last interaction is that of particles 1 and 2; likewise, there are similar terms (iii) a_{13}, and (iv) a_{23}. Taken into account are FSI with different orbital angular momenta L. Hence, the amplitude a_{ij} can be expressed through the L-wave amplitudes $A_{ij}^L(s_{ij})$ and is written as follows:

$$a_{ij} = \sum_L F_L A_{ij}^L(s_{ij}). \quad (3)$$

Here, s_{ij} is the two-particle invariant mass squared, $s_{ij}=(k_i+k_j)^2$. The function F_L defines the angular distribution of decaying particles. In the case of the S-wave binary interaction $F_0=1$, but for the higher wave interaction the amplitude depends on the angle between interacting and spectator particles as well.

2.1. S-Wave Interaction

Let us begin with the S-wave pair interactions. The decaying amplitude is given by

$$M(s_{12},s_{13},s_{23}) = \lambda(s_{12},s_{13},s_{23}) + A_{12}^0(s_{12}) \quad (4)$$
$$+ A_{13}^0(s_{13}) + A_{23}^0(s_{23}).$$

The connected part of the matrix T_{33} is not known, so the contribution from three-particle intermediate state into the imaginary part of M cannot be directly calculated and writing down the corresponding dispersion integral is impossible. So, the two-particle unitarity condition will be explored, in order to derive the integral equation for the amplitude A_{ij}^0. This method was described in detail in [8]. The idea of such an approach is that one should consider the case of small external mass $M < m_1+m_2+m_3$ when only the scattering reactions are physically possible. A simple relation can be written in this case, and then the analytic continuation of the final equation over the mass M back to the decay region is performed. Let us stress that the obtained expression differs from the contribution from the disconnected part of T in the imaginary part M satisfying the three-body unitarity condition, in which the three particles interact only in pairs [12].

Thus, an ordinary unitarity condition for the scattering in the channel of particles 1 and 2 is written down. This means that $(M+m_3) < s_{12}$ is assumed. The discontinuity of the amplitude is equal to

$$\mathrm{disc}_{12}M(s_{12},s_{13},s_{23}) = \frac{1}{2}\int d\Phi_{12}(k_1,k_2) \quad (5)$$
$$\times(\lambda + A_{12}^0(s_{12}) + A_{13}^0(s_{13}) + A_{23}^0(s_{23}))A_{2\to2}^{0*}(s_{12}),$$

where $d\Phi_{12}(k_1,k_2)$ is the phase volume of particles 1 and 2:

$$d\Phi_{12}(k_1,k_2) = (2\pi)^4\delta^4(P-k_1-k_2) \quad (6)$$
$$\times\frac{d^4k_1d^4k_2}{(2\pi)^6}\delta(m_1^2-k_1^2)\delta(m_2^2-k_2^2).$$

$A_{2\to2}^0$ is the S-wave two-particle scattering amplitude, which can be written in the dispersion N/D method as a series

$$A_{2\to2}^0(s) = G_0^L(s)G_0^R(s) + G_0^L(s)B_0(s)G_0^R(s) \quad (7)$$
$$+ G_0^L(s)B_0^2(s)G_0^R(s) + \ldots = \frac{G_0^L(s)G_0^R(s)}{1-B_0(s)}.$$

Here, G_0^L and G_0^R are the left and right vertex functions and $B_0(s)$ is the dispersion representation of the loop diagram:

$$B_0(s) = \int\limits_{(m_i+m_j)^2}^{\infty}\frac{ds'}{\pi}\frac{G_0^L(s')\rho_{ij}(s')G_0^R(s')}{s'-s}, \quad (8)$$

where ρ_{ij} is the two-particle phase space

$$\rho_{ij}(s) = \frac{1}{16\pi s}\sqrt{[s-(m_i+m_j)][s-(m_i-m_j)]}. \quad (9)$$

The vertex functions contain left-hand singularities related to the t-channel exchange diagrams, while the B function has singularities due to the elastic scattering. It is not specified from the consideration of the scattering amplitude $A_{2\to2}^0$ of (6) whether both vertices G_0^L and G_0^R have these singularities or only one of them. In the case of three-body decay the situation is quite the opposite. On the first sheet the decay amplitude has only singularities at $s_{ij}=(m_i+m_j)^2$, which are associated with the elastic scattering in the subchannel of particles i and j. This means that the vertex G_0^R is an analytic function. For the sake of simplicity,

$$G_0^R = 1. \quad (10)$$

Now return to Eq. (6). Since the λ functions do not have the two-particle threshold singularity and thus do not have a discontinuity, the left-hand side of (6) is

$$\mathrm{disc}_{12}M(s_{12},s_{13},s_{23}) = \mathrm{disc}_{12}A_{12}^0(s_{12}). \quad (11)$$

As was stressed in [13], only one rescattering of particles 1 and 2 can be considered in the final state and a full set of binary rescatterings can be taken into account multiplying by $(1 - B_0(s_{12}))^{-1}$. Thus, the two-particle discontinuity in this special case of one rescattering is defined as

$$\mathrm{disc}_{12}A^0_{12}(s_{12}) = \frac{1}{2}\int d\Phi_{12}(k_1,k_2) \qquad (12)$$
$$\times\,(\lambda(s_{12},s_{13},s_{23}) + A^0_{13}(s_{13}) + A^0_{23}(s_{23}))G^L_0(s_{12}).$$

It is convenient to perform the phase-space integration in Eq. (12) in the c.m.s. of particles 1 and 2. In this frame,

$$s_{13} = m_1^2 + m_3^2 - 2k_{10}k_{30} + 2z_{13}|\mathbf{k}_1||\mathbf{k}_3|, \qquad (13)$$
$$k_{10} = \frac{s_{12}+m_1^2-m_2^2}{2\sqrt{s_{12}}}, \quad |\mathbf{k}_1| = \sqrt{k_{10}^2 - m_1^2},$$
$$k_{30} = \frac{s_{12}+m_3^2-s}{2\sqrt{s_{12}}}, \quad |\mathbf{k}_3| = \sqrt{k_{30}^2 - m_3^2},$$

where $z_{13} = \cos\theta_{13}$, θ_{13} is the angle between particles 1 and 3 in the c.m.s. of particles 1 and 2, and $s = M^2$. The expression for s_{23} is obtained from Eq. (13) by the replacement $1 \leftrightarrow 2$. From Eq. (12) one has

$$\mathrm{disc}_{12}A^0_{12}(s_{12}) = (\lambda_S(s_{12}) + \langle A^0_{13}(s_{13})\rangle_0 \qquad (14)$$
$$+ \langle A^0_{23}(s_{23})\rangle_0)G^L_0(s_{12})\rho_{12}(s_{12}),$$

where the following notation is used:

$$\langle A^0_{i3}(s_{i3})\rangle_0 = \int\limits_{C_i(s_{12})} \frac{dz_{i3}}{2}A^0_{i3}(s_{i3}). \qquad (15)$$

λ_S is the S-wave projection of λ:

$$\lambda_S(s_{12}) = \int\limits_{-1}^{1}\frac{dz_{13}}{2}\lambda(s_{12},s_{13},s_{23}). \qquad (16)$$

Analytic continuation over external mass M from the scattering to the decay region allows one to define correctly the rules of integration over z. This integration should be carried out along the contour $C_i(s_{12})$, whose position at different s_{12} is described in detail in [8]. Here, note that only at small s_{12},

$$(m_1+m_2)^2 \le s_{12} \le \frac{m_i s}{m_i+m_3} \qquad (17)$$
$$+\frac{m_3}{m_i+m_3}(m_1+m_2-m_i)^2 - m_i m_3,$$

which coincides with the phase-space integration contour

$$-1 \le z_{i3} \le 1, \qquad (18)$$

and contains an additional piece at larger s_{12}.

Equation (14) allows us to write down the dispersion integral for the amplitude with one pair rescattering in the final state:

$$A^0_{12}(s_{12}) = \lambda_S(s_{12})B_0(s_{12}) + \int\limits_{(m_1+m_2)^2}^{\infty}\frac{ds'_{12}}{\pi} \qquad (19)$$
$$\times\,\frac{\rho_{12}(s'_{12})G^0_L(s'_{12})}{s'_{12}-s_{12}}(\langle A^0_{13}(s'_{13})\rangle_0 + \langle A^0_{23}(s'_{23})\rangle_0).$$

Here, λ_S is excluded from the dispersion integral, but it is also possible to include it: in both cases the unitarity is satisfied but with different behavior of the amplitude at infinity, which cannot be defined by the unitarity and analyticity only. After the transition from one rescattering to the full set of binary interactions in the final state, one has

$$A^0_{12}(s_{12}) = \frac{\lambda_S(s_{12})B_0(s_{12})}{1-B_0(s_{12})} + \frac{1}{1-B_0(s_{12})} \qquad (20)$$
$$\times\int\limits_{(m_1+m_2)^2}^{\infty}\frac{ds'_{12}}{\pi}\frac{\rho_{12}(s'_{12})G^L_0(s'_{12})}{s'_{12}-s_{12}}$$
$$\times\,(\langle A^0_{13}(s'_{13})\rangle_0 + \langle A^0_{23}(s'_{23})\rangle_0).$$

Let us now check that the extraction of the FSI does not violate the unitarity condition (6). To calculate the left-hand side of (6), the Eq. (20) is rewritten as follows:

$$A^0_{12}(s_{12}) = \frac{1-B^*_0(s_{12})}{|1-B_0(s_{12})|^2}(b^\lambda(s_{12}) + J(s_{12})), \qquad (21)$$

where

$$b^\lambda(s_{12}) = \lambda_S(s_{12})B_0(s_{12}), \qquad (22)$$

$$J(s_{12}) = \int\limits_{(m_1+m_2)^2}^{\infty}\frac{ds'_{12}}{\pi}\frac{\rho_{12}(s'_{12})G^L_0(s'_{12})}{s'_{12}-s_{12}} \qquad (23)$$
$$\times\left(\langle A^0_{13}(s'_{13})\rangle_0 + \langle A^0_{23}(s'_{23})\rangle_0\right).$$

Thus,

$$\mathrm{disc}_{12}A^0_{12}(s_{12}) \qquad (24)$$
$$= \frac{1}{|1-B_0(s_{12})|^2}(\mathrm{Im}B_0(s_{12})b^\lambda(s_{12})$$
$$+ (1-B_0(s_{12}))\mathrm{Im}b^\lambda(s_{12}) + \mathrm{Im}B_0(s_{12})J(s_{12})$$
$$+ (1-B_0(s_{12}))\mathrm{disc}J(s_{12})).$$

Taking into account that

$$\mathrm{disc}B_0(s_{12}) = \mathrm{Im}B_0(s_{12}) = \rho_{12}(s_{12})G^L_0(s_{12}), \qquad (25)$$
$$\mathrm{disc}b^\lambda(s_{12}) = \mathrm{Im}b^\lambda(s_{12}) = \rho_{12}(s_{12})G^L_0(s_{12})\lambda_S,$$
$$\mathrm{disc}J(s_{12}) = \rho_{12}(s_{12})G^L_0(s_{12})\langle A^0_{13} + A^0_{23}\rangle_0,$$

the result is the right-hand side of (6); hence, the unitarity condition is fulfilled.

2.2. P-Wave Interaction in the Final State

First, let us determine the structure of the amplitude, where particles 1 and 2 interact in the P wave and the particle 3 is a spectator. The easiest way to do this is to transform the decay amplitude into the scattering amplitude. To perform this transformation the antiparticle 3 with the momentum $(-k_3)$ is considered instead of particle 3 itself. The assumed form of the amplitude is $O_{1\mu}Q_{1\mu}A^1_{12}(s_{12})$.Operator Q_1 describes the P-wave angular distribution of particles 1 and 2 in the final state and is defined as the relative momentum of these particles:

$$Q_{1\mu} = k_{1\mu} - k_{2\mu} - \frac{m_1^2 - m_2^2}{s_{12}}(k_1 + k_2)_\mu. \qquad (26)$$

Operator O_1 should be constructed as the relative momentum of the initial state and antiparticle 3. Taking into account the fact that $Q_{1\mu}(k_1 + k_2)_\mu = 0$, one can define O_1 as

$$O_{1\mu} = k_{3\mu}. \qquad (27)$$

As is seen from (3),

$$F_1 = O_{1\mu}Q_{1\mu}, \qquad (28)$$

and it is easy to find that F_1 is proportional to z_{13} in the c.m.s. of particles 1 and 2.

Hereafter, the procedure of the above section is used to write down the two-particle unitarity condition and the integral equation for A^1. The P-wave two-particle scattering amplitude of particles 1 and 2 in the N/D method can be written as

$$A^1_{2\to 2}(s_{12}) = Q_{1\mu}\frac{G_1^L(s_{12})}{1 - B_1(s_{12})}Q_{1\mu}, \qquad (29)$$

where the B function is equal to

$$B_1(s_{ij}) = \int\limits_{(m_i+m_j)^2}^{\infty} \frac{ds'}{\pi}\frac{G_1^L(s')\rho_{ij}(s')\langle Q_{1\mu}Q_{1\mu}\rangle}{s' - s_{ij}} \qquad (30)$$

and $\langle\cdots\rangle$ means the averaging over space angle.

As the first step, one should consider a triangle diagram with one P-wave rescattering of particles 1 and 2. The discontinuity of this diagram is equal to:

$$\begin{aligned}&\mathrm{disc}_{12}A^1_{12}(s_{12}) \qquad (31)\\ &= \frac{1}{2}\int d\Phi_{12}(k_1,k_2)a_{13}(s_{13},z_{13})Q_{1\mu}G_1^L(s_{12})\\ &= G_1^L(s_{12})\rho_{12}(s_{12})\int\frac{d\Omega}{4\pi}Q_{1\mu}a_{13}(s_{13},z_{13}).\end{aligned}$$

The integration over the space angle is performed in the c.m. frame of particles 1 and 2. In this frame, Q_1 turns into $\mathbf{k}_{12}$. With the z axis directed along $\mathbf{k}_3$, the components of $\mathbf{k}_{12}$ are equal to

$$\begin{aligned}k_{12x} = k_{12}\sin\theta_{13}\cos\phi, \quad k_{12y} = k_{12}\sin\theta_{13}\sin\phi,\\ k_{12z} = k_{12}\cos\theta_{13},\\ k_{12} = \sqrt{\frac{1}{s_{12}}[s_{12} - (m_1+m_2)^2][s_{12} - (m_1-m_2)^2]},\end{aligned} \qquad (32)$$

where ϕ is azimuthal angle. The integration over ϕ in (32) keeps the only components of $Q_{1\mu}$ with $\mu = z$:

$$\begin{aligned}\int\frac{d\Omega}{4\pi}Q_{1x}\ldots = \int\frac{d\Omega}{4\pi}Q_{1y}\ldots = 0, \qquad (33)\\ \int\frac{d\Omega}{4\pi}Q_{1z}\ldots = k_{12}\int\frac{dz_{13}}{2}z_{13}\ldots.\end{aligned}$$

Let us introduce the vector $k_3^\perp$ with only z component unequal to zero in the c.m.s.:

$$k^\perp_{3\mu} = k_{3\mu} - p_\mu\frac{pk_3}{p^2}, \qquad (34)$$

where $p = k_1 + k_2$. Then it follows from (32):

$$\begin{aligned}\mathrm{disc}_{12}A^1_{12}(s_{12}) = k^\perp_{3\mu}\rho_{12}(s_{12})G_1^L(s_{12})\frac{k_{12}}{\sqrt{-(k_3^\perp)^2}} \qquad (35)\\ \times\int\limits_{C_3(s_{12})}\frac{dz_{13}}{2}z_{13}a_{13}(s_{13},z_{13}),\end{aligned}$$

where

$$-(k_3^\perp)^2 = \frac{[(M-m_3)^2 - s_{12}][(M+m_3)^2 - s_{12}]}{4s_{12}}. \qquad (36)$$

The invariant part of the P-wave amplitude can be written as a dispersion integral over the energy squared of particles 1 and 2 in the intermediate state, while $k_3^\perp$ in (35) defines the operator structure of the P-wave amplitude. Thus, the P-wave triangle diagram is equal to

$$k^\perp_{3\mu}\int\limits_{(m_1+m_2)^2}^{\infty}\frac{ds'_{12}}{\pi}\frac{\rho_{12}(s'_{12})G_1^L(s'_{12})}{s'_{12} - s_{12}}\langle a_{13}(s_{13},z)\rangle_1, \qquad (37)$$

where

$$\begin{aligned}\langle a_{13}(s_{13},z)\rangle_1 \qquad (38)\\ = \frac{k_{12}}{\sqrt{-(k_3^\perp)^2}}\int\limits_{C_3(s_{12})}\frac{dz}{2}za_{13}(s_{13},z).\end{aligned}$$

Equation (37) should be multiplied by the operator Q_1 which describes angular distribution of particles 1

and 2 in the final state. Using $k_{3\mu}^{\perp}Q_{1\mu} = O_{1\mu}Q_{1\mu}$, one may conclude that the operator part of a_{12} is correctly reconstructed. To take into account binary rescattering in the final state, it is necessary to multiply (37) by the factor $(1 - B_1(s_{12}))^{-1}$.

The same steps should be done if a_{13} is replaced by the direct production term $\lambda(s_{12}, s_{13}, s_{23})$. Still, the energy dependence of λ is not usually known; therefore, a simpler assumption is used. Let us introduce the constants λ_{ij}^{P}, which define the direct production amplitude of particles i and j in the P wave. Then the following integral equation for the amplitude A_{12}^{1} can be written as

$$A_{12}^{1}(s_{12}) = \frac{\lambda_{12}^{P}B_1(s_{12})}{1 - B_1(s_{12})} + \frac{1}{1 - B_1(s_{12})} \tag{39}$$

$$\times \int\limits_{(m_1+m_2)^2}^{\infty} \frac{ds'_{12}}{\pi} \frac{\rho_{12}(s'_{12})G_1^L(s'_{12})}{s'_{12} - s_{12}}(\langle a_{13}\rangle_1 + \langle a_{23}\rangle_1).$$

2.3. D-Wave Interaction in the Final State

Likewise, the case of D-wave interaction in the final state may be investigated. The amplitude, where particles 1 and 2 have the last interaction in the D wave, has the form $O_2Q_2A_{12}^{2}(s_{12})$. The operator Q_2 is a traceless tensor of the range 2 made up of the relative momenta of particles 1 and 2:

$$Q_{2\mu\nu} = k_{12\mu}k_{12\nu} - \frac{1}{3}k_{12}^{2}g_{\mu\nu}^{\perp}, \tag{40}$$

where

$$k_{12\mu} = k_{1\mu} - k_{2\mu} - \frac{m_1^2 - m_2^2}{s_{12}}(k_1 + k_2)_\mu, \tag{41}$$

$$g_{\mu\nu}^{\perp} = g_{\mu\nu} - \frac{p_\mu p_\nu}{p^2}. \tag{42}$$

Another operator, O_2, can be defined as

$$O_{2\mu\nu} = k_{3\mu}k_{3\nu}. \tag{43}$$

Below, it will be proved that O_2 can be defined in this way. Let us note here that the operator part of the D-wave decaying amplitude is proportional to $3z_{13}^2 - 1$.

Let us define the D-wave scattering amplitude of particles 1 and 2 in N/D representation as

$$A_{2\to2}^{2}(s_{12}) = Q_{2\mu\nu}\frac{G_2^L(s_{12})}{1 - B_2(s_{12})}Q_{2\mu\nu}. \tag{44}$$

Here, the definition of B_2 is similar to (30), with the replacement $Q_{1\mu} \to Q_{2\mu\nu}$. The discontinuity of the triangle diagram with the D-wave rescattering of particles 1 and 2 is equal to

$$\mathrm{disc}_{12}A_{12}^{2}(s_{12}) = \frac{1}{2} \tag{45}$$

$$\times \int d\Phi_{12}(k_1, k_2)a_{13}(s_{13}, z_{13})Q_{2\mu\nu}G_2^L(s_{12})$$

$$= G_2^L(s_{12})\rho_{12}(s_{12}) \int \frac{d\Omega}{4\pi}Q_{2\mu\nu}a_{13}(s_{13}, z_{13}).$$

The integration over the space angle is performed in the c.m. frame of particles 1 and 2. Equation (32) is used, and only the following components of the tensor $k_{12\mu}k_{12\nu}$ are not equal to zero:

$$\int \frac{d\Omega}{4\pi}k_{12x}k_{12x}\ldots = \int \frac{d\Omega}{4\pi}k_{12y}k_{12y}\ldots \tag{46}$$

$$= k_{12}^{2}\int \frac{dz_{13}}{4}(1 - z_{13}^2)\ldots,$$

$$\int \frac{d\Omega}{4\pi}k_{12z}k_{12z}\cdots = k_{12}^{2}\int \frac{dz_{13}}{2}z_{13}^2\ldots.$$

To perform the space integration in the invariant form, let us define the tensor $g_{\mu\nu}^{\perp\perp}$ as

$$g_{\mu\nu}^{\perp\perp} = g_{\mu\nu} - \frac{p_\mu p_\nu}{p^2} - \frac{k_{\mu3}^{\perp}k_{\nu3}^{\perp}}{(k_3^{\perp})^2}. \tag{47}$$

In the c.m. frame of particles 1 and 2, the tensor $g_{\mu\nu}^{\perp\perp}$ has only two nonzero diagonal elements:

$$g_{\mu\nu}^{\perp\perp} \to \mathrm{diag}(0, -1, -1, 0). \tag{48}$$

Thus, Eq. (47) can be rewritten as

$$\int \frac{d\Omega}{4\pi}k_{12\mu}k_{12\nu}\ldots \tag{49}$$

$$= -g_{\mu\nu}^{\perp\perp}k_{12}^{2}\int \frac{dz_{13}}{4}(1 - z_{13}^2)\ldots$$

$$- \frac{k_{\mu3}^{\perp}k_{\nu3}^{\perp}}{(k_3^{\perp})^2}k_{12}^{2}\int \frac{dz_{13}}{2}z_{13}^2\ldots$$

Equation (49) should be placed into (45) for the discontinuity of triangle diagrams. Taking into account that this expression must be multiplied by the external operator Q_2, one can see that only the third term in Eq. (49) contributes to (45). Moreover, one could replace $k_3^{\perp}$ by k_3. Finally, as follows from (45),

$$\mathrm{disc}_{12}A_{12}^{2}(s_{12}) = k_{3\mu}k_{3\nu}\rho_{12}(s_{12}) \tag{50}$$

$$\times G_2^L(s_{12})\langle a_{13}(s_{13}, z)\rangle_2,$$

where

$$\langle a_{13}(s_{13}, z)\rangle_2 \tag{51}$$

$$= \frac{k_{12}^2}{(k_3^{\perp})^2}\int\limits_{C_3(s_{12})} \frac{dz}{4}(1 - 3z^2)a_{13}(s_{13}, z).$$

The invariant part of the D-wave amplitude can be written as a dispersion integral, and a full set of binary rescatterings in the final state is defined by the factor

$(1 - B_2(s_{12}))^{-1}$. The result is the following integral equation for the amplitude A_{12}^2:

$$A_{12}^2(s_{12}) = \frac{\lambda_{12}^D B_2(s_{12})}{1 - B_2(s_{12})} \tag{52}$$
$$+ \frac{1}{1 - B_2(s_{12})} \int\limits_{(m_1+m_2)^2}^{\infty} \frac{ds'_{12}}{\pi} \frac{\rho_{12}(s'_{12}) G_2^L(s'_{12})}{s'_{12} - s_{12}}$$
$$\times (\langle a_{13}(s_{13}, z)\rangle_2 + \langle a_{23}(s_{23}, z)\rangle_2),$$

where the constant λ_{ij}^D stands for the direct production amplitude of particles i and j in the D wave.

3. DISPERSION EQUATIONS WITH THE RESONANCE AND NONRESONANCE PRODUCTION OF PARTICLES

In this section a realistic case is considered, when there are resonance and nonresonance interactions between two particles. This situation happens, for example, in the 0^{++} wave of the pion–pion amplitude, where there is a nonresonance background and a set of resonances at energies above 1 GeV. Figuring out the dispersion representation of the two-particle amplitude is the first step for this particular case. For the sake of simplicity, we consider the S-wave one-channel amplitude. The first resonance term of the amplitude can be written as

$$\sum_\alpha \frac{g^{(\alpha)2}(s)}{M_\alpha^2 - s}, \tag{53}$$

where M_α is a pure (nonphysical) mass of resonance α, and the function $g^{(\alpha)}(s)$ describes its decay into two particles. Below, we assume a universal s-dependence of $g^{(\alpha)}$:

$$g^{(\alpha)}(s) = g^{(\alpha)}\phi(s). \tag{54}$$

The second term of the amplitude with one virtual loop is equal to

$$\sum_{\alpha\alpha'} \frac{g^{(\alpha)2}(s)}{M_\alpha^2 - s} g^{(\alpha)} g^{(\alpha')} b(s) \frac{g^{(\alpha')2}(s)}{M_{\alpha'}^2 - s}, \tag{55}$$

where $b(s)$ is the loop diagram with the cutoff function. The behavior of $\phi(s)$ at large s (or at small distances r) is not known, and a simple way to avoid the uncertainties is to assume that the contribution from $r < r_0$ is equal to zero. Then the cutoff function $\Lambda(s)$ is defined as follows:

$$\Lambda(s) = \int d^3 r e^{i\mathbf{k}\cdot\mathbf{r}} \Theta(r - r_0) \int \frac{d^3 k'}{(2\pi)^3} e^{-i\mathbf{k}'\cdot\mathbf{r}} \phi^2(s'); \tag{56}$$

and $b(s)$ is equal to

$$b(s) = i\rho(s) + P\int \frac{ds'}{\pi} \frac{\rho(s')}{s' - s} \Lambda(s'). \tag{57}$$

The phase space ρ is given by (9), with $m_i = m_j \equiv m_\pi$. Summing up the terms with different number of loops, one obtains the following expression for the amplitude:

$$A = \frac{\sum\limits_\alpha \dfrac{g^{(\alpha)2}(s)}{M_\alpha^2 - s}}{1 - b(s)\sum\limits_\alpha \dfrac{g^{(\alpha)2}(s)}{M_\alpha^2 - s}}. \tag{58}$$

For nonresonance interaction of particles defined by the vertex function $f(s)$, Eq. (58) should be rewritten as follows:

$$A = \frac{\sum\limits_\alpha \dfrac{g^{(\alpha)2}(s)}{M_\alpha^2 - s} + f(s)}{1 - \left\{ b(s)\sum\limits_\alpha \dfrac{g^{(\alpha)2}(s)}{M_\alpha^2 - s} + b_f(s) \right\}}, \tag{59}$$

where

$$b_f(s) = i\rho(s) + P\int \frac{ds'}{\pi} \frac{\rho(s')}{s' - s} \Lambda_f(s'), \tag{60}$$

and $\Lambda_f(s)$ is given by (56) with the replacement of $\phi^2(s)$ by $f(s)$. It should be noted here that if ϕ and f are constants, then the cutoff functions are equal to zero, and the dispersion representation coincides with the K-matrix approach. Equation (59) can easily be generalized for the case of the two-particle interaction with orbital angular momentum L:

$$A_L = Q_{L,\mu} \frac{\sum\limits_\alpha \dfrac{g^{(\alpha)2}(s)}{M_\alpha^2 - s} + f(s)}{1 - \left\{ b(s)\sum\limits_\alpha \dfrac{g^{(\alpha)2}(s)}{M_\alpha^2 - s} + b_f(s) \right\}} Q_{L,\mu}, \tag{61}$$

where $b(s)$ and $b_f(s)$ are given by Eqs. (57) and (60), with the cutoff functions $\Lambda(s)$ and $\Lambda_f(s)$, respectively, which are equal to

$$\Lambda(s) = \int d^3 r e^{i\mathbf{k}\cdot\mathbf{r}} \Theta(r - r_0) \tag{62}$$
$$\times \int \frac{d^3 k'}{(2\pi)^3} e^{-i\mathbf{k}'\cdot\mathbf{r}} \phi^2(s') \langle Q_{L,\mu} Q_{L,\mu}\rangle,$$

$$\Lambda_f(s) = \int d^3 r e^{i\mathbf{k}\cdot\mathbf{r}} \Theta(r - r_0) \tag{63}$$
$$\times \int \frac{d^3 k'}{(2\pi)^3} e^{-i\mathbf{k}'\cdot\mathbf{r}} f(s') \langle Q_{L,\mu} Q_{L,\mu}\rangle.$$

The same formalism can be applied to the case of a multichannel amplitude. The decay of resonance α into particles m and n is given by the function $g^{(\alpha)}_{mn}(s) = g^{(\alpha)}_{mn}\phi_{mn}(s)$, and the nonresonance transition from the channel with particles m and n to the channel with particles m' and n' is given by $f_{mn;m'n'}(s)$. Here, the expression for multichannel amplitude is not given in an explicit form; its composition can be found in detail, for example, in [14]. Note that the denominator of (59), which describes the rescattering of particles in multichannel case, has the matrix form $(\hat{I} - \hat{B})^{-1}$, where $\hat{I}$ is an identity matrix and the B-matrix element is equal to

$$B_{mn;m'n'} = b_{mn;m'n'}(s)\sum_{\alpha}\frac{g^{(\alpha)}_{mn}g^{(\alpha)}_{m'n'}}{M^2_\alpha - s} + \beta_{mn;m'n'}(s), \tag{64}$$

$$b_{mn;m'n'}(s) = i\rho_{mn}(s) + P\int\frac{ds'}{\pi}\frac{\rho_{mn}(s')}{s'-s}\Lambda_{mn;m'n'}(s'), \tag{65}$$

where

$$\beta_{mn;m'n'}(s) = i\rho_{mn}(s) + P\int\frac{ds'}{\pi}\frac{\rho_{mn}(s')}{s'-s}\Lambda_{f,mn;m'n'}(s'). \tag{66}$$

Let us generalize the results of the previous sections and write the dispersion equations for the three-particle decay amplitude. The amplitude for the production of three different particles k, m, and n, which is denoted as M_{kmn}, is as follows:

$$M_{kmn} = a_{km;n}(s_{12}, z) + a_{nm;k}(s_{23}, z) + a_{kn;m}(s_{13}, z), \tag{67}$$

where the first term in the right-hand side gives the amplitude with the last interaction between particles k and m, and so on. The interaction of two particles, for example, n and m, can happen in different channels. Here, the isospin is neglected (let $I = 0$), so the two-particle momentum describes the type of interaction. Hence, the amplitude $a_{nm;k}$ can be written as

$$a_{nm;k} = \sum_J F_J A^{0J}_{nm;k}, \tag{68}$$

where $A^{0J}_{nm;k}$ is the amplitude of the last interaction of particles n and m with the angular momentum J and isospin $I = 0$. The integral equation for $A^{0J}_{nm;k}$ can be written as a generalization of Eqs. (20), (39), and (52). First, we use the term where only the particles m and n interact with each other and the particle k is a spectator. The resonance and nonresonance production of these particles from the initial state is

$$\lambda^{0J}_{mn;k}(s) = \sum_\alpha = \frac{C^{(\alpha)}_k g^{(\alpha)}_{mn}(s)}{M^2_\alpha - s} + \Phi^{0J}_{mn;k}, \tag{69}$$

where $C^{(\alpha)}_k$ is the production constant of resonance α and particle k, $\Phi^{0J}_{mn;k}$ corresponds to the direct production of the particles m and n with the relative momentum J. The rescattering of particles m and n gives the following amplitude:

$$\sum_{(m'n')}\lambda^{0J}_{m'n';k}\{(\hat{I} - \hat{B})^{-1}\}^{0J}_{m'n';nm}, \tag{70}$$

where the summation over intermediate states with the production of m' and n' particles is performed. The expression for triangle diagram can be written in the same way. Finally, the result is the following three-body dispersion relation:

$$\begin{aligned} A^{0J}_{mn;k} = {} & \sum_{(m'n')}\lambda^{0J}_{m'n';k}\{(\hat{I} - \hat{B})^{-1}\}^{0J}_{m'n';mn} \\ & + \sum_{(m'n')}\sum_{(m''n'')}\{(\hat{I} - \hat{B})^{-1}\}^{0J}_{m''n'';mn} \\ & \times \int\frac{ds'_{12}}{\pi}\frac{\rho_{m'n'}(s'_{12})N^{0J}_{m'n';m''n''}(s'_{12}, s_{12})}{s'_{12} - s_{12}} \\ & \times (\langle a_{n'k;m'}(s'_{13}, z)\rangle_J + \langle a_{m'k;n'}(s'_{23}, z)\rangle_J), \end{aligned} \tag{71}$$

where

$$N^{0J}_{m'n';mn}(s'_{12}, s_{12}) = \Lambda_{f,m'n';mn} + \sum_\alpha\frac{g^{(\alpha)}_{m'n'}(s'_{12})g^{(\alpha)}_{mn}(s_{12})}{M^2_\alpha - s_{12}}\bar{\Lambda}(s'_{12}), \tag{72}$$

and $\bar{\Lambda}(s')$ is the cutoff function obtained in (62) with the help of $\phi_{m'n'}(s)$.

4. DISPERSION EQUATIONS FOR THE COUPLED DECAY CHANNELS $\bar{p}p(0^{-+}) \to \pi^0\pi^0\pi^0$, $\eta\pi^0\pi^0$, $\eta\eta\pi^0$, $\bar{K}K\pi^0$

The proton–antiproton annihilation in the state $J^{PC} = 0^{-+}$ can originate from the two isospin states $I = 0$ and $I = 1$. Due to isospin conservation in strong interactions, there exist two integral equations for the following decay channels:

$$\bar{p}p(IJ^{PC} = 10^{-+}) \to \pi^0\pi^0\pi^0, \quad \eta\eta\pi^0, \quad \bar{K}K\pi^0$$

and

$$\bar{p}p(IJ^{PC} = 00^{-+}) \to \eta\pi^0\pi^0, \quad \bar{K}K\pi^0.$$

Let us write the integral equations for the decay from $I = 1$ state.

4.1. The Reaction $\bar{p}p$ $(10^{-+}) \to \pi^0\pi^0\pi^0$

For this reaction the only difference from the analysis given above is that one should take into account the isospin structure of the amplitude. The same analysis has been done in [10, 13], where the unitarity condition in the $\pi\pi$ channel was used to derive the amplitude for the $\eta \to 3\pi^0$ decay. This decay goes with the violation of isospin symmetry; therefore, the initial states have the same quantum numbers in both cases. Because of that, the results of [10] and [13] are reproduced here, and the contribution from the $\eta\eta$ and $\bar{K}K$ states is also taken into account. The annihilation amplitude into $3\pi^0$ is

$$M_{\pi^0\pi^0\pi^0} = a_{\pi^0\pi^0;\pi^0}(s_{12}, z) + a_{\pi^0\pi^0;\pi^0}(s_{13}, z) + a_{\pi^0\pi^0;\pi^0}(s_{23}, z), \tag{73}$$

where

$$a_{\pi^0\pi^0;\pi^0} = a^0_{\pi\pi;\pi^0} + \frac{4}{3}a^2_{\pi\pi;\pi^0}, \tag{74}$$

and $a^I_{\pi\pi;\pi^0}$ is the amplitude with the last pions interacting in the isospin state I. It should be noted that, due to the C invariance, there is no term in (74) with pion interactions in the state $I = 1$. For the channel with isospin $I = 0$, the S- and D-wave interactions should be taken into account; this allows one to properly calculate the production of f_0 and f_2 resonances, so

$$a^0_{\pi\pi;\pi^0} = A^{00}_{\pi\pi;\pi^0} + F_2 A^{02}_{\pi\pi;\pi^0}. \tag{75}$$

In the channel with isospin $I = 2$, only the S-wave interaction should be taken into account; therefore,

$$a^2_{\pi\pi;\pi^0} = A^{20}_{\pi\pi;\pi^0}. \tag{76}$$

The integral equations for $A^{0J}_{\pi\pi;\pi^0}$ have the following form:

$$A^{0J}_{\pi\pi;\pi^0} = \lambda^{0J}_{\pi\pi;\pi^0}\{(\hat{I} - \hat{B})^{-1}\}^{0J}_{\pi\pi;\pi\pi} + \{(\hat{I} - \hat{B})^{-1}\}^{0J}_{\pi\pi;\pi\pi}\int \frac{ds'_{12}}{\pi} \times \frac{\rho_{\pi\pi}(s'_{12})N^{0J}_{\pi\pi;\pi\pi}(s'_{12}, s_{12})}{s'_{12} - s_{12}} \times \left(\left\langle \frac{2}{3}a^0_{\pi\pi;\pi^0}(s'_{13}, z)\right\rangle_J + \left\langle \frac{20}{9}a^2_{\pi\pi;\pi^0}(s'_{23}, z)\right\rangle_J + \left\langle \frac{4}{3}a^1_{\pi\pi;\pi^0}(s'_{23}, z)\right\rangle_J\right) + \Delta_{\eta\eta} + \Delta_{\bar{K}K}, \tag{77}$$

where the contributions from the $\eta\eta$ and $\bar{K}K$ intermediate states are:

$$\Delta_{\eta\eta} = \lambda^{0J}_{\eta\eta;\pi^0}\{(\hat{I} - \hat{B})^{-1}\}^{0J}_{\eta\eta;\pi\pi} + \{(\hat{I} - \hat{B})^{-1}\}^{0J}_{\eta\eta;\pi\pi}\int \frac{ds'_{12}}{\pi} \times \frac{\rho_{\eta\eta}(s'_{12})N^{0J}_{\eta\eta;\pi\pi}(s'_{12}, s_{12})}{s'_{12} - s_{12}}\langle 2a_{\pi^0\eta;\eta}(s'_{13}, z)\rangle_J, \tag{78}$$

$$\Delta_{\bar{K}K} = \lambda^{0J}_{\bar{K}K;\pi^0}\{(\hat{I} - \hat{B})^{-1}\}^{0J}_{\bar{K}K;\pi\pi} + \{(\hat{I} - \hat{B})^{-1}\}^{0J}_{\bar{K}K;\pi\pi}\int \frac{ds'_{12}}{\pi} \times \frac{\rho_{\bar{K}K}(s'_{12})N^{0J}_{\bar{K}K;\pi\pi}(s'_{12}, s_{12})}{s'_{12} - s_{12}}\langle 2a_{\pi^0 K;\bar{K}}(s'_{13}, z)\rangle_J. \tag{79}$$

The amplitude $a^1_{\pi\pi;\pi^0}$ in (77) can be found only from the $\bar{p}p$ annihilation into charged pions; theferore, in our approach it could be simply replaced by the direct production amplitude of $\rho^+\pi^-$. In the integral equation for $A^{20}_{\pi\pi;\pi^0}$, only $\pi\pi$ intermediate states are taken into account, so one has:

$$A^{20}_{\pi\pi;\pi^0} = \lambda^{20}_{\pi\pi;\pi}\{(\hat{I} - \hat{B})^{-1}\}^{20}_{\pi\pi;\pi\pi} + \{(\hat{I} - \hat{B})^{-1}\}^{20}_{\pi\pi;\pi\pi}\int \frac{ds'_{12}}{\pi} \times \frac{\rho_{\pi\pi}(s'_{12})N^{20}_{\pi\pi;\pi\pi}(s'_{12}, s_{12})}{s'_{12} - s_{12}}(\langle a^0_{\pi\pi;\pi^0}(s'_{13}, z)\rangle_0 + \left\langle \frac{1}{3}a^2_{\pi\pi;\pi^0}(s'_{23}, z)\right\rangle_0 + \langle a^1_{\pi\pi;\pi^0}(s'_{23}, z)\rangle_0). \tag{80}$$

4.2. The Reactions $\bar{p}p(0^{-+}) \to \eta\eta\pi^0$

In the $\eta\pi^0$ channel the S- and D-wave interactions with the production of a_0 and a_2 resonances are taken into consideration. The annihilation amplitude is as follows:

$$M_{\eta\eta\pi^0} = a_{\eta\eta;\pi^0}(s_{12}, z) + a_{\eta\pi^0;\eta}(s_{13}, z) + a_{\eta\pi^0;\eta}(s_{23}, z), \tag{81}$$

where

$$a_{\eta\eta;\pi^0} = A^{00}_{\eta\eta;\pi^0} + F_2 A^{02}_{\eta\eta;\pi^0}, \tag{82}$$

$$a_{\eta\pi^0;\eta} = A^{10}_{\eta\pi^0;\eta} + F_2 A^{12}_{\eta\pi^0;\eta}. \tag{83}$$

The integral equation for the $A^{0J}_{\eta\eta;\pi^0}$ amplitude has the following form:

$$A^{0J}_{\eta\eta;\pi^0} = \lambda^{0J}_{\pi\pi;\pi^0}\{(\hat{I} - \hat{B})^{-1}\}^{0J}_{\pi\pi;\eta\eta} + \{(\hat{I} - \hat{B})^{-1}\}^{0J}_{\pi\pi;\eta\eta}\int \frac{ds'_{12}}{\pi} \times \frac{\rho_{\pi\pi}(s'_{12})N^{0J}_{\pi\pi;\eta\eta}(s'_{12}, s_{12})}{s'_{12} - s_{12}}\left(\left\langle \frac{2}{3}a^0_{\pi\pi;\pi^0}(s'_{13}, z)\right\rangle_J + \left\langle \frac{20}{9}a^2_{\pi\pi;\pi^0}(s'_{23}, z)\right\rangle_J + \left\langle \frac{4}{3}a^1_{\pi\pi;\pi^0}(s'_{23}, z)\right\rangle_J\right) + \Delta_{\eta\eta} + \Delta_{\bar{K}K}, \tag{84}$$

where contributions from the $\eta\eta$ and $\bar{K}K$ intermediate states are:

$$\Delta_{\eta\eta} = \lambda^{0J}_{\eta\eta;\pi^0}\{(\hat{I}-\hat{B})^{-1}\}^{0J}_{\eta\eta;\eta\eta} + \{(\hat{I}-\hat{B})^{-1}\}^{0J}_{\eta\eta;\eta\eta}\int\frac{ds'_{12}}{\pi} \times \frac{\rho_{\eta\eta}(s'_{12})N^{0J}_{\eta\eta;\eta\eta}(s'_{12},s_{12})}{s'_{12}-s_{12}}\langle 2a_{\pi^0\eta;\eta}(s'_{13},z)\rangle_J, \quad (85)$$

$$\Delta_{\bar{K}K} = \lambda^{0J}_{\bar{K}K;\pi^0}\{(\hat{I}-\hat{B})^{-1}\}^{0J}_{\bar{K}K;\eta\eta} + \{(\hat{I}-\hat{B})^{-1}\}^{0J}_{\bar{K}K;\eta\eta}\int\frac{ds'_{12}}{\pi} \times \frac{\rho_{\bar{K}K}(s'_{12})N^{0J}_{\bar{K}K;\eta\eta}(s'_{12},s_{12})}{s'_{12}-s_{12}}\langle 2a_{\pi^0K;K}(s'_{13},z)\rangle_J. \quad (86)$$

Here, $2a_{\pi^0K;K} = a_{\pi^0K;\bar{K}} + a_{\pi^0\bar{K};K}$. The integral equation for the $A^{1J}_{\eta\pi^0;\eta}$ amplitude is

$$A^{1J}_{\eta\pi^0;\eta} = \lambda^{1J}_{\eta\pi^0;\eta}\{(\hat{I}-\hat{B})^{-1}\}^{1J}_{\eta\pi^0;\eta\pi^0} + \{(\hat{I}-\hat{B})^{-1}\}^{1J}_{\eta\pi^0;\eta\pi^0}\times\int\frac{ds'_{12}}{\pi} \times \frac{\rho_{\eta\pi^0}(s'_{12})N^{1J}_{\eta\pi^0;\eta\pi^0}(s'_{12},s_{12})}{s'_{12}-s_{12}}(\langle a_{\eta\eta;\pi^0}(s'_{13},z)\rangle_J + \langle a_{\eta\pi^0;\eta}(s'_{23},z)\rangle_J). \quad (87)$$

4.3. Reactions $\bar{p}p(0^{-+}) \to \bar{K}K\pi^0$

These annihilation amplitudes are

$$M_{\pi^0\bar{K}K} = a_{\pi^0K;\bar{K}}(s_{12},z) + a_{\pi^0\bar{K};K}(s_{13},z) + a_{\bar{K}K;\pi^0}(s_{23},z). \quad (88)$$

As before, in the $\bar{K}K$ channel the S- and D-wave interactions and K^* resonances in the $K\pi$ channel are accounted for. So, one has

$$a_{\bar{K}K;\pi^0} = A^{00}_{\bar{K}K;\pi^0} + F_2A^{02}_{\bar{K}K;\pi^0}, \quad (89)$$

$$a_{\bar{K}\pi^0;K} = A^{1/2,1}_{\bar{K}\pi^0;K}. \quad (90)$$

Here, the isotopic spin $I = 1/2$. For these amplitudes, one can get the following integral equations:

$$A^{1/2,1}_{\bar{K}\pi^0;K} = \lambda^{1/2,1}_{\bar{K}\pi^0;K}\{(\hat{I}-\hat{B})^{-1}\}^{1/2,1}_{\pi^0K;\pi^0K} + \{(\hat{I}-\hat{B})^{-1}\}^{1/2,1}_{\pi^0K;\pi^0K}\int\frac{ds'_{12}}{\pi} \times \frac{\rho_{\pi^0K}(s'_{12})N^{1/2,1}_{\pi^0K;\pi^0K}(s'_{12},s_{12})}{s'_{12}-s_{12}}(\langle a_{\bar{K}\pi^0;K}(s'_{13},z)\rangle_J + \langle a_{\bar{K}K;\pi^0}(s'_{23},z)\rangle_J). \quad (91)$$

The integral equation for the $A^{0J}_{\bar{K}K;\pi^0}$ amplitude has the following form:

$$A^{0J}_{\bar{K}K;\pi^0} = \lambda^{0J}_{\pi\pi;\pi^0}\{(\hat{I}-\hat{B})^{-1}\}^{0J}_{\pi\pi;\bar{K}K} + \{(\hat{I}-\hat{B})^{-1}\}^{0J}_{\pi\pi;\bar{K}K}\int\frac{ds'_{12}}{\pi} \times \frac{\rho_{\pi\pi}(s'_{12})N^{0J}_{\pi\pi;\bar{K}K}(s'_{12},s_{12})}{s'_{12}-s_{12}}\left(\left\langle\frac{2}{3}a^0_{\pi\pi;\pi^0}(s'_{13},z)\right\rangle_J + \left\langle\frac{20}{9}a^2_{\pi\pi;\pi^0}(s'_{23},z)\right\rangle_J + \left\langle\frac{4}{3}a^1_{\pi\pi;\pi^0}(s'_{23},z)\right\rangle_J\right) + \Delta_{\eta\eta} + \Delta_{\bar{K}K}, \quad (92)$$

where contributions from the $\eta\eta$ and $\bar{K}K$ intermediate states are as follows:

$$\Delta_{\eta\eta} = \lambda^{0J}_{\eta\eta;\pi^0}\{(\hat{I}-\hat{B})^{-1}\}^{0J}_{\eta\eta;\bar{K}K} + \{(\hat{I}-\hat{B})^{-1}\}^{0J}_{\eta\eta;\bar{K}K}\int\frac{ds'_{12}}{\pi} \times \frac{\rho_{\eta\eta}(s'_{12})N^{0J}_{\eta\eta;\eta\eta}(s'_{12},s_{12})}{s'_{12}-s_{12}}\langle 2a_{\pi^0\eta;\eta}(s'_{13},z)\rangle_J, \quad (93)$$

$$\Delta_{\bar{K}K} = \lambda^{0J}_{\bar{K}K;\pi^0}\{(\hat{I}-\hat{B})^{-1}\}^{0J}_{\bar{K}K;\bar{K}K} + \{(\hat{I}-\hat{B})^{-1}\}^{0J}_{\bar{K}K;\bar{K}K}\int\frac{ds'_{12}}{\pi} \times \frac{\rho_{\bar{K}K}(s'_{12})N^{0J}_{\bar{K}K;\bar{K}K}(s'_{12},s_{12})}{s'_{12}-s_{12}}\langle 2a_{\pi^0K;K}(s'_{13},z)\rangle_J. \quad (94)$$

A set of integral equations for the reactions $\bar{p}p(IJ^{PC} = 00^{-+}) \to \eta\pi^0\pi^0, \bar{K}K\pi^0$ may be written in the same way.

5. CONCLUSION

To summarize, the two-particle discontinuity of the decay amplitude is written, and the integral equation is obtained which takes into account not only the S-wave binary interactions, but also interactions with higher angular momenta (P and D wave). These equations are generalized for the resonance and nonresonance types of two-particle interactions. A complete three-body dispersion equation is derived, which may be used for the analysis of various three-particle reactions. It was demonstrated how the coupled three-body equations can be written for the $\pi^0\pi^0\pi^0$, $\eta\pi^0\pi^0$, $\eta\eta\pi^0$, and $\bar{K}K\pi^0$ channels in $\bar{p}p$ annihilation at rest.

ACKNOWLEDGMENTS

This work was supported by the Russian Foundation for Basic Research, project no. 01-02-17861.

REFERENCES

1. C. Amsler *et al.*, Phys. Lett. B **355**, 425 (1995); **342**, 433 (1995).
2. C. Amsler *et al.*, Phys. Lett. B **333**, 277 (1994); V. V. Anisovich *et al.*, Phys. Lett. B **323**, 233 (1994).
3. V. V. Anisovich, D. V. Bugg, A. V. Sarantsev, and B. S. Zou, Phys. Rev. D **50**, 4412 (1994).
4. V. V. Anisovich and A. V. Sarantsev, Phys. Lett. B **413**, 137 (1997).
5. J. Paton and N. Isgur, Phys. Rev. D **31**, 2910 (1985); J. F. Donoghue, K. Johnson, and B. A. Li, Phys. Lett. B **99B**, 416 (1981); R. L. Jaffe and K. Johnson, Phys. Lett. B **60B**, 201 (1976).
6. G. S. Bali *et al.*, Phys. Lett. B **309**, 378 (1993); I. Chen *et al.*, Nucl. Phys. B (Proc. Suppl.) **34**, 357 (1994).
7. S. S. Gershtein, A. K. Likhoded, and Yu. D. Prokoshkin, Z. Phys. C **24**, 305 (1984); C. Amsler and F. E. Close, Phys. Lett. B **353**, 385 (1995); V. V. Anisovich, Phys. Lett. B **364**, 195 (1995).
8. V. V. Anisovich and A. A. Anselm, Usp. Fiz. Nauk **88**, 287 (1966) [Sov. Phys. Usp. **9**, 117 (1966)].
9. I. J. R. Aitchison, Phys. Rev. **137**, 1070 (1965).
10. A. V. Anisovich and H. Leutwyler, Phys. Lett. B **375**, 335 (1996).
11. A. V. Anisovich and E. Klempt, Z. Phys. A **354**, 197 (1996).
12. I. J. R. Aitchison and R. Pasquier, Phys. Rev. **152**, 1274 (1966).
13. A. V. Anisovich, Yad. Fiz. **58**, 1467 (1995) [Phys. At. Nucl. **58**, 1383 (1995)].
14. V. V. Anisovich, D. V. Bugg, and A. V. Sarantsev, Nucl. Phys. A **537**, 501 (1992).

Physics of Atomic Nuclei, Vol. 66, No. 1, 2003, pp. 182–190. Translated from Yadernaya Fizika, Vol. 66, No. 1, 2003, pp. 185–194.

ELEMENTARY PARTICLES AND FIELDS
Theory

Hadronization as Valon Confinement in the Course of Nuclear-Matter Cooling

I. I. Royzen* **and O. D. Chernavskaya****

Lebedev Institute of Physics, Russian Academy of Sciences, Leninskiĭ pr. 53, Moscow, 117335 Russia

Received March 6, 2002

Abstract—The updated three-phase concept of nuclear-matter evolution in the course of cooling—from a quark–qluon plasma (QGP) through an intermediate phase involving massive constituent quarks Q (valons), pions, and kaons ($Q\pi K$) to hadronic matter (H)—is exploited to describe relative hadronic yields from the midrapidity region in heavy-ion collisions at high energies. Attention is given primarily to the $Q\pi K$ phase, which is argued to permit a correct description within the ideal-gas approximation. This phase must exist until the mean spacing between valons approaches the confinement radius (at the temperature of $T_H \simeq 115 \pm 10$ MeV), in which case valons begin fusing to form final hadrons. The hadronic yields obtained by means of a thermodynamical treatment of the $Q\pi K$ phase and a simple combinatorial approach to the hadron-production process are shown to fit available experimental data from AGS, SPS, and RHIC quite well. This approach provides an alternative insight into the actual origin of the observed relative hadronic yields; it is free, to a considerable extent, from well-known puzzles inherent in conventional models that assume an early (high-temperature) chemical freeze-out of hadronic matter. (Within those models, the ideal-gas approximation is in fact employed to describe hadronic matter where hadrons have to be tightly packed and even overlap, which seems doubtful.) Many predictions for the yields of other hadrons that could be observed at these facilities, as well as at the LHC accelerator (under construction in CERN), are made. © *2003 MAIK "Nauka/Interperiodica".*

1. INTRODUCTION

The conventional way of describing heavy-ion collisions at high energies incorporates quark–gluon plasma (QGP) as a short-lived initial phase of nuclear matter formed in the central rapidity region as soon as the nuclei involved collide. After that, cooling down to the temperature of the chiral-breakdown transition, $T_c \simeq 200$ MeV, occurs fast, whereupon hot and dense hadronic matter is formed and is finally converted into experimentally observed free hadrons. Relative yields of different species of these hadrons depend on the equation of state (EoS) of nuclear matter from which they originate. It was indicated in [1] that SPS data on hadronic yields are quite compatible with the assumption of "early chemical freeze-out," which implies that, at a relatively high temperature of $T_{\rm ch} \simeq 170$ MeV (it is rather close to the chiral-breakdown temperature), the chemical content of the hadronic matter appears to be fixed. Here, one has to assume that this "frozen" hadronic matter is an ideal gas of crucially modified in-medium hadrons, so that their effective radii do not exceed about 0.3 fm![1)] It was also shown [2] that a similar thermodynamic description can be used to clarify AGS and SIS data as well, if it is assumed that the chemical freeze-out temperature $T_{\rm ch}$ is to vary along with the baryonic chemical potential of the fireball (that is, an expanding nuclear medium), this potential being about 110 and 60 MeV for AGS and SIS, respectively. As a result, a doubtful suggestion that a low-temperature QGP can exist was put forth and then discussed in some more detail [2, 3]. Both attributes of this approach—crucially modified (but still surviving!) in-medium hadrons and a low-temperature chiral transition—seem rather controversial and mysterious. That is why a feeling of dissatisfaction remains, and searches for some more consistent description of what occurs as nuclear matter undergoes cooling seems quite reasonable.

In this connection, it is reasonable to recall the rather old-fashioned notion of massive constituent

* e-mail: royzen@lpi.ru
** e-mail: chernav@lpi.ru

[1)] A straightforward estimation shows that a nearly ideal gas of slightly modified hadrons could not exist at corresponding particle (hadron) densities, since the wave functions for ordinary hadrons would overlap substantially.

quarks (valons), Q, linked properly to corresponding current quarks; first of all, we imply light valons $Q(q)$, $q \equiv u, d$ ($m_{Q(u,d)} \equiv m_{Q(q)} \simeq 330$ MeV), and strange ones $Q(s)$ ($m_{Q(s)} \simeq 480$ MeV)—that is, hypothetical particles that had been widely and fruitfully exploited before QCD was developed as a consistent field theory not incorporating valons as its inalienable entities. Until now, however, QCD has in fact remained quite a workable theory of hard processes, but it suffers from the lack of even qualitative results for processes at low and intermediate energies—that is, precisely for those that proceed within nuclear matter below the temperature T_c of the chiral-breakdown transition. Thus, embedding the valons unambiguously into the body of QCD is perhaps still waiting for its turn, although known attempts were futile [4]. Qualitative physical arguments in favor of the possibly important role of the valonic mass scale and of an intermediate phase involving valons and separating QGP and hadronic ones were put forth long ago [5–8]. It is worth noting that an experimentally observed significant excess of the low-mass dilepton (e^+e^-) yield in nucleus–nucleus collisions in relation to what is obtained by naively extrapolating data on proton–nucleus collisions can be described quite well within the approach allowing for the $Q\pi K$ phase [9].

Recently, a general idea was put forth [10] that could provide deeper insight into the physical reasons behind the unified thermal description of yields of various hadron species observed in heavy-ion collisions. In the present study, we show in more detail how valons could aid in describing relative hadronic yields, getting rid of the aforementioned curiosities inherent in the conventional approaches. The theory is constructed against the available results from AGS, SPS, and RHIC; in addition, many other ratios of hadronic yields are predicted (for LHC as well).

2. GENERAL MOTIVATION AND PROBLEMS

In all probability, nuclear matter admits a dual description just below the temperature of chiral-symmetry breakdown [9]: it can be treated either as a highly compressed "hadronic liquid" or as a state where most of the hadronic species cannot survive (with the exception of pions and kaons—see below), so that valons rather than hadrons become dominant degrees of freedom.[2)] Of course, one can choose either. To take the first way, however, one is supposed to know, at least, the relevant EoS of the medium under consideration. But who knows it? Actually, one has to postulate an EoS. A basic point of the second approach suggested here is that the valons produced in the course of chiral-symmetry breakdown must be reasonably treated as an ideal gas from the very beginning (in contrast to hadrons!) because of their actually small size [11], $r \simeq 0.3$ fm. Even at $T = 170$–200 MeV, the particle density within the ideal Boltzmann valonic gas is indeed about

$$\frac{12T^3}{\pi^2}\left[2\left(\frac{m_{Q(q)}}{T}\right)^2 K_2\left(\frac{m_{Q(q)}}{T}\right)\cosh(\mu_{Q(q)}/T)\right.$$
$$\left.+\left(\frac{m_{Q(s)}}{T}\right)^2 K_2\left(\frac{m_{Q(s)}}{T}\right)\cosh(\mu_{Q(s)}/T)\right] \simeq 1\ \mathrm{fm}^{-3}.$$

For the chemical potentials $\mu_{Q(q)}$ and $\mu_{Q(s)}$ of $Q(q)$ and $Q(s)$ valons, respectively, use is made here of values typical of heavy-ion collisions.[3)] Hence, the "valonic bodies" themselves occupy only about 10% of the total volume. This, rather optimistic, estimate becomes noticeably less favorable upon taking into account a certain balancing fraction of "large-sized" pions and kaons, which inevitably exist as the chemical equilibrium sets in[4)] (see Fig. 1). Fortunately,

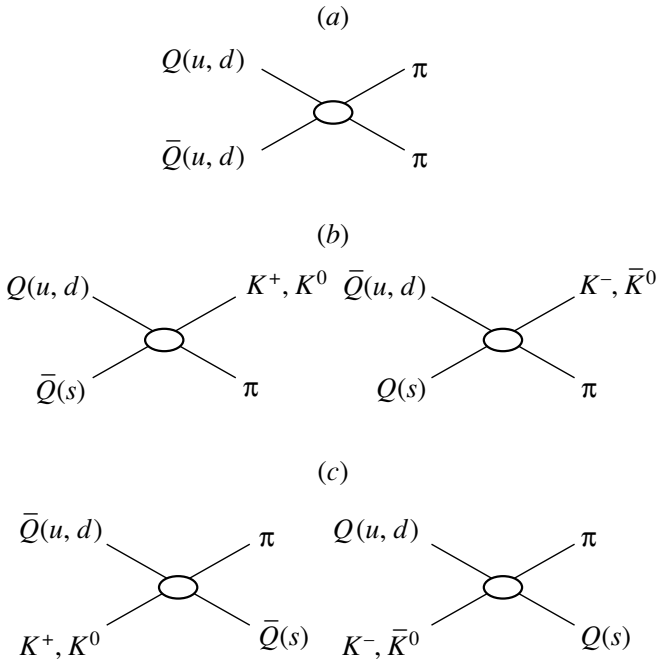

Fig. 1. Processes that are taken into account in deriving the detailed-balance equation (see Appendix) controlling the relative content of different components in a $Q\pi K$ gas. The diagrams in Figs. 1*b* and 1*c* actually correspond to two cross channels of the same diagram.

[2)] The presence of massive valons is indicative of chiral-symmetry breakdown.

[3)] We disregard here the distinction between the chemical potentials of $Q(u)$ and $Q(d)$ valons that is due to the difference in the proton and neutron content of heavy colliding nuclei, but, at low energies and large values of $\mu_{Q(q)}/T$ (SIS, AGS), this may lead to a noticeable effect.

Comparison of experimental and theoretical data (ratio of total yields of various hadronic species, N_i/N_j)

i/j	AGS Au + Au, $E_{\text{lab}} = 11$ GeV			SPS Pb + Pb, $E_{\text{lab}} = 160$ GeV				RHIC Au + Au, $\sqrt{s} = 130$ GeV			LHC $\sqrt{s} \simeq 5.5$ GeV	
	expt.	M1	M2	expt.	M*	M1	M2	expt.	M1	M2	M1	M2
p/π	1	0.78	0.86	0.228	0.238	0.209	0.240		0.15	0.158	0.1	0.08
$\overline{p}/p$	5×10^{-4}	4.7×10^{-4}	4.7×10^{-4}	0.067	0.055	0.084	0.08	0.67	0.67	0.67	1	1
K^+/π	0.175	0.196	0.177	0.16		0.165	0.17		0.183	0.143	0.119	0.107
K^-/π	0.034	0.044	0.035	0.085		0.106	0.091	0.16	0.156	0.127	0.119	0.107
K_S^0/π		0.123	0.107	0.125	0.137	0.136	0.133		0.169	0.136	0.119	0.107
η/π		0.097	0.097	0.081	0.087	0.09	0.09		0.097	0.097	0.097	0.097
Λ/π		0.061	0.058	0.077	0.096	0.069	0.073		0.051	0.034	0.033	0.027
Λ/K_S^0		0.5	0.54	0.63	0.76	0.52	0.47		0.29	0.23	0.28	0.25
K^+/K^-	5.14	4.45	4.89	1.85	1.9	1.54	1.89	1.1	1.07	1.12	1	1
$\bar{\Lambda}/\Lambda$		0.001	0.001	0.131	0.1	0.103	0.102	0.8	0.725	0.725	1	1
Ξ^-/Λ		0.09	0.093	0.101	0.11	0.109	0.107		0.168	0.148	0.121	0.121
$\Xi^+/\bar{\Lambda}$		0.478	0.478	0.188	0.185	0.21	0.22		0.197	0.174	0.121	0.121
Ξ^+/Ξ^-		0.002	0.002	0.232	0.228	0.2	0.2	0.85	0.852	0.852	1	1
Ω^+/Ω^-		0.013	0.013	0.383	0.53	0.385	0.382		1	1	1	1
ϕ/π		0.008	0.0076	0.021	0.019	0.013	0.013		0.014	0.015	0.018	0.008
Δ^2		0.17	0.035		0.36	0.42	0.49		0.04	0.04		
M1, M2	$\mu_q/T_H = 1.4$ $\mu_s/T_H = 0.59$ $T_H = 115 \pm 10$ MeV			$\mu_q/T_H = 0.47$ $\mu_s/T_H = 0.16$ $T_H = 115 \pm 10$ MeV				$\mu_q/T_H = 0.026$ $\mu_s/T_H \simeq 0$ $T_H = 115 \pm 10$ MeV			$\mu_q/T_H \simeq 0$ $\mu_s/T_H \simeq 0$ $T_H = 110$ MeV	
T_f^{ThHD}				115 ± 5 MeV				105 ± 5 MeV				
M*	$\mu_q/T_{\text{ch}} = 1.47$ $\mu_s/T_{\text{ch}} = 0.6$ $T_{\text{ch}} = 125$ MeV			$\mu_q/T_{\text{ch}} = 0.52$ $\mu_s/T_{\text{ch}} = 0.14$ $T_{\text{ch}} = 170$ MeV				$\mu_q/T_{\text{ch}} = 0.04$ $\mu_s/T_{\text{ch}} \leq 0.01$ $T_{\text{ch}} = 190$ MeV			$\mu_q \simeq 0$ $\mu_s \simeq 0$ $T_{\text{ch}} = ?$	

Notes: M* stands for the model from [1, 2], while M1 and M2 represent two versions of our model at $\langle j \rangle_1 = 0.5$ and $0.7 \leq j_2 \leq 1$ (see main body of the text); T_f^{ThHD} is the kinetic freeze-out temperature obtained from thermal hydrodynamical models.

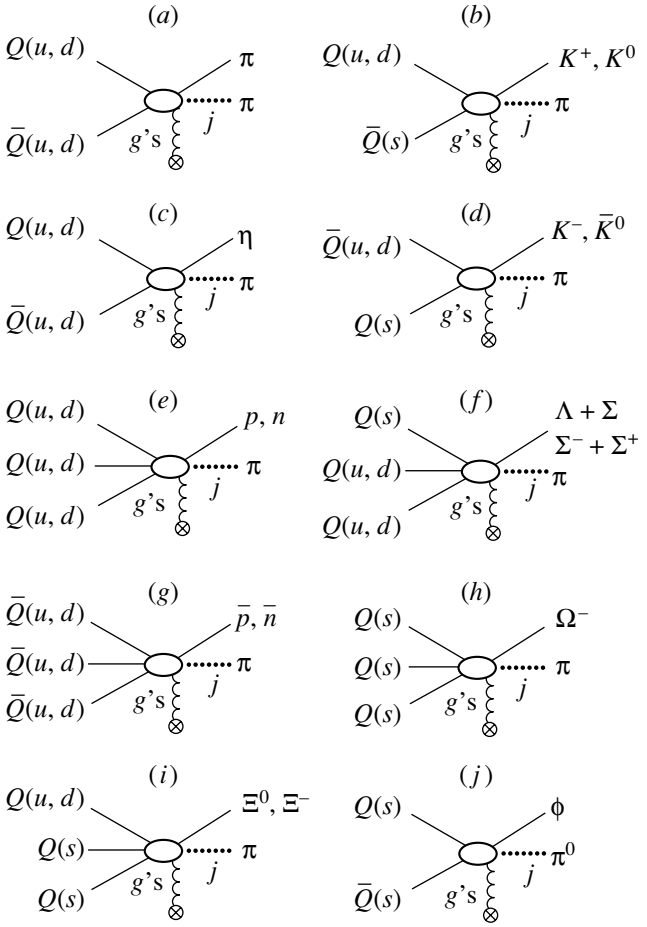

Fig. 2. Typical processes that accompany the hadronization phase transition ($T \simeq T_H$). The dotted and wavy lines represent attendant pions and gluons, respectively, the latter being absorbed by a medium.

this hadronic fraction never exceeds 25% (see below); therefore, this three-component $Q\pi K$ phase can still be treated reasonably as a gas,[5)] although quasi-ideality of this gas becomes somewhat more questionable. That is why we rely below, as far as possible, on a more general consideration based exclusively on chemical kinetics and then contrast the results against what one can obtain in the self-consistent ideal-gas approximation. We will see a posteriori that the results obtained by these two methods are quite compatible.

Thus, the general pattern of evolution of a hot nuclear fireball that is produced in the course of heavy-ion collisions is as follows. While expanding and cooling down from T_c to T_H, nuclear matter is gradually enriched in pions and kaons and impoverished in valons. The situation changes dramatically as soon as the mean spacing between valons becomes commensurate with the confinement radius. As a result, the gradually increasing color-screening length approaches the critical value, and hadrons themselves rather than valons (since they are to be bound into color-singlet objects) become dominant degrees of freedom. The bulk of hadrons are formed in precisely this way. The process described above is a phase transition if hadronization proceeds at the same temperature near $T \simeq T_H$ (or at close temperatures); otherwise, this is a phase crossover. Lattice calculations indicate that the special features of the phase transition and even its occurrence are controlled by the chemical potential (or by the net baryonic density) within nuclear matter. Here, we do not dwell upon this delicate question but concentrate on the pattern linked to a certain phase transition. This pattern is shown below to face no obvious contradictions with the available data within the existing accuracy (see table). Relevant hadron-production diagrams are depicted in Fig. 2.

[5)] What is the most relevant in the context of the problem under discussion is that this is especially true near the hadronization temperature T_H.

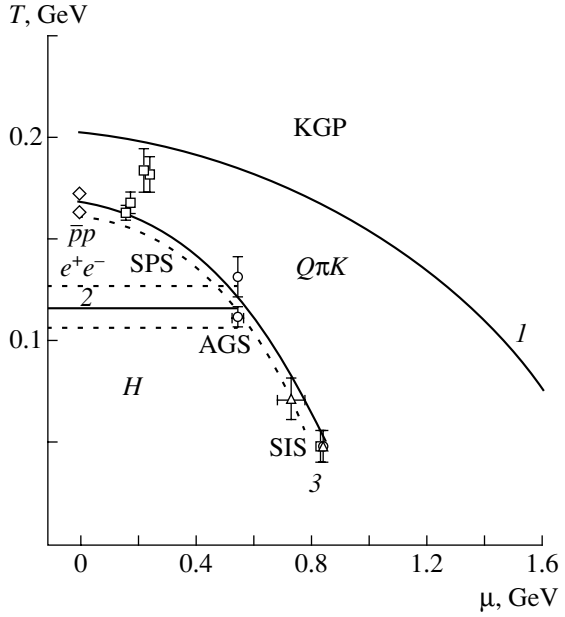

Fig. 3. μT phase diagram allowing for the $Q\pi K$ phase. The solid line *1* refers to the QGP $\rightarrow Q\pi K$ phase transition; the strip *2* between two dashed lines is our prediction for the temperature interval around $T = 115$ MeV where the $Q\pi K \rightarrow$ H phase transition is expected to occur; and two lines *3* (the solid and dashed ones correspond to $\langle E\rangle/N = 1.0$ and 0.94 GeV, respectively) were borrowed from [2] and are related to an early chemical freeze-out within the assumption of direct QGP $\rightarrow$ H phase transition.

3. CALCULATIONS AND RESULTS

In the course of the hadronization phase transition ($T = T_H$), all hadron species are generally produced in the same manner. In contrast to what we have in the $Q\pi K$ phase, the correlation length here remains large in relation to the mean spacing between the particles (or even infinite, if there occurs a second-order phase transition) over the entire stage of this phase transition. Therefore, multiparticle interactions dominate at this stage. One can also assume reasonably that, here, all hadrons, once created, survive because the confinement mechanism comes into play, suppressing disintegration.

Thus, final (observable) pions and kaons are produced in two ways at two stages of fireball evolution: first, there are equilibrium (primary) pions and kaons mentioned above (those that are accumulated in the course of the evolution of the $Q\pi K$ phase before overall hadronization—see Fig. 1); second, there are pions coming from $Q(q)\bar{Q}(q) \rightarrow \pi + X$ reactions and kaons coming similarly from $Q(q)\bar{Q}(s) \rightarrow K^+(K^0) + X$ and $Q(s)\bar{Q}(q) \rightarrow K^-(\bar{K}^0) + X$ reactions precisely at $T = T_H$. The latter are produced only at the stage of hadronization, just like other hadron species (see Fig. 2). The number of primary pions is

$$n_\pi \simeq \frac{bn}{1-b}, \tag{1}$$

where n is the total number of color particles within the fireball and b is the pionic fraction, which is calculated in the Appendix [see Eqs. (A.1)–(A.6)] on the basis of taking into account direct and inverse reactions shown in Fig. 1*a*. The numerical value of b appeared to be rather stable for SPS, RHIC, and LHC ($b \simeq 0.22$), but it was considerably lower for AGS ($b \simeq 0.13$). Making use of the diagrams in Figs. 1*b* and 1*c*, we can similarly estimate the number of primary kaons [see (A.7)]. The result is

$$n_{K^+} \simeq n_{K^0} \simeq \frac{4n_\pi + 3n_{Q(q)}}{6(4n_\pi + 3n_{\bar{Q}(q)})}\, n_{\bar{Q}(s)}, \tag{2}$$

where $n_{Q(q)}$ ($n_{\bar{Q}(q)}$) is the number of $Q(q)$ ($\bar{Q}(q)$) and $n_{\bar{Q}(s)}$ is the number of $\bar{Q}(s)$. The number of K^- ($\bar{K}^0$) is obtained by making here the substitution $Q \leftrightarrow \bar{Q}$.

As to secondary pions, their number can be estimated by tracing the fate of a valon $Q(q)$ [an antivalon $\bar{Q}(q)$] within nuclear matter undergoing hadronization. While moving over the mean free path, it coalesces with an antivalon (valon) with the probability[6] $n_{\bar{Q}(q)}/n$ ($n_{Q(q)}/n$), the total rate of such collisions thus being $n_{Q(q)}n_{\bar{Q}(q)}/n$. Each collision results in the $\pi + X$ state, where X may also include a number j of pions (see Fig. 2), the same being true for the production of other hadrons. With allowance for Eq. (1), the total yield of negative pions, which is assumed to be equal to one-third of the total pion rate, is

$$N_{\pi^-} \simeq \frac{1}{3}\left[\frac{bn}{1-b} + \frac{(1+\langle j\rangle)n_{Q(q)}n_{\bar{Q}(q)}}{n}\right] + \frac{\langle j\rangle}{3}[N_B + N_{\bar{B}} + (N_K - n_K) + \ldots], \tag{3}$$

where N_B ($N_{\bar{B}}$) and N_K are the total yields of baryons (antibaryons) and kaons, respectively; $\langle j\rangle$ is the mean value of j [it can easily be estimated to be within the range $0 \le j \le 1$ because the phase space is bounded[7]]; and the ellipsis stands for small terms whose inclusion is meaningless within the available accuracy of both the theory and the data. Following

[6] It is natural to assume that, at the hadronization stage, any valonic interaction that could result in the production of a hadron does indeed produce it. As to valon–hadron interaction, it is insignificant at this stage.

[7] The results appear to be weakly sensitive to the value of $\langle j\rangle$ within this range.

a similar line of reasoning and making use of (2), we find for the K-meson yield that

$$N_{K^+} \simeq N_{K^0} \simeq \frac{4n_\pi + 3n_{Q(q)}}{6(4n_\pi + 3n_{\bar{Q}(q)})} n_{\bar{Q}(s)} + \frac{n_{Q(q)} n_{\bar{Q}(s)}}{2n}. \quad (4)$$

We also have

$$N_{K_S^0} \simeq N_{K_L^0} \simeq 0.5(N_{K^0} + N_{\bar{K}^0}). \quad (5)$$

As to N_{K^-} and $N_{\bar{K}^0}$, they were obtained in the same way as before [see (2)]. The yields of some other mesons can easily be estimated by means of similar combinatorial and/or relevant cross-section considerations. For example, we have

$$N_\phi \simeq \frac{n_{Q(s)} n_{\bar{Q}(s)}}{n}. \quad (6)$$

The relative η-meson yield N_η/N_{π^0} can be immediately calculated by comparing the corresponding cross sections, since the two channels involved, $Q(q)\bar{Q}(q) \to \pi\pi^0$ and $Q(q)\bar{Q}(q) \to \pi\eta$ (see Fig. 2*c*), directly compete with each other. Apart from the distinction between the masses of these mesons—this alone results in the contraction of the $\pi\eta$ final phase space by a factor of about 2 to 3 in relation to the $\pi\pi^0$ phase space at the relevant energies/temperatures—one must consider that no ρ-meson intermediate state is allowed in the $\pi^+\eta$ channel. Being integrated with respect to energy, the corresponding excess of the $\pi\pi$ yield results in an extra factor of about 4 to 5, thus making finally $N_\eta/N_{\pi^0} \simeq 0.08$–$0.1$. Unfortunately, this estimate admits rather wide variations.

Some additional special features must be taken into account in deriving formulas for the baryon rates.

(i) In calculating the number of collisions, one must avoid double (or triple) counting for the same (anti)valons treated as a target and a projectile; for this, it is sufficient to introduce the factor $(1 + 2n^2_{Q(q)}/n^2)^{-1}$ for nucleons, the factor $(1 + n_{Q(q)}n_{Q(s)}/n^2)^{-1}$ for Λ and Ξ hyperons, and the factor $(1 + 2n^2_{Q(s)}/n^2)^{-1}$ for a Ω^- hyperon (here, $Q \to \bar{Q}$ for corresponding antiparticles).[8)]

(ii) One should bear in mind that, on one hand, Λ ($\bar{\Lambda}$) particles detected experimentally represent actually the sum $\Lambda(\bar{\Lambda}) + \Sigma^0(\bar{\Sigma})$ [since Σ^0 ($\bar{\Sigma}^0$) decays into $\Lambda(\bar{\Lambda}) + \gamma$ within about 10^{-19} s]; on the other hand, the same initial states can produce either Λ or Σ hyperons, with the final phase spaces being different (see the above comment on the η/π^0 yield ratio), along with the corresponding combinatorial factors for the production of neutral and charged hyperons (see the diagram in Fig. 2*h*).[9)] Thus, we arrive at

$$N_p \simeq N_n \simeq \frac{n^3_{Q(q)}}{2n^2(1 + 2n^2_{Q(q)}/n^2)}, \quad (7)$$

$$N_{\bar{p}} \simeq N_{\bar{n}} \simeq \frac{n^3_{\bar{Q}(q)}}{2n^2(1 + 2n^2_{\bar{Q}(q)}/n^2)};$$

$$N_\Lambda + N_{\Sigma^+} + N_{\Sigma^-} \simeq \frac{n_{Q(s)} n^2_{Q(q)}}{n^2(1 + n_{Q(q)}n_{Q(s)}/n^2)} \simeq 1.6N_\Lambda, \quad (8)$$

$$N_{\bar{\Lambda}} + N_{\bar{\Sigma}^+} + N_{\bar{\Sigma}^-} \simeq \frac{n_{\bar{Q}(s)} n^2_{\bar{Q}(q)}}{n^2(1 + n_{\bar{Q}(q)}n_{\bar{Q}(s)}/n^2)} \simeq 1.6N_\Lambda; \quad (9)$$

$$N_{\Xi^0} \simeq N_{\Xi^-} \simeq \frac{n_{Q(q)} n^2_{Q(s)}}{2n^2(1 + n_{Q(q)}n_{Q(s)}/n^2)}, \quad (10)$$

$$N_{\bar{\Xi}^0} \simeq N_{\bar{\Xi}^+} \simeq \frac{n_{\bar{Q}(q)} n^2_{\bar{Q}(s)}}{2n^2(1 + n_{\bar{Q}(q)}n_{\bar{Q}(s)}/n^2)};$$

$$N_{\Omega^-} \simeq \frac{n^3_{Q(s)}}{n^2(1 + 2n^2_{Q(s)}/n^2)}, \quad (11)$$

$$N_{\bar{\Omega}^+} \simeq \frac{n^3_{\bar{Q}(s)}}{n^2(1 + 2n^2_{\bar{Q}(s)}/n^2)};$$

and so on.

A comparison of the above predictions for the baryon and antibaryon rates with experimental data requires a more careful discussion (especially for antibaryons at AGS). A theoretical consideration of antibaryon production is a subtle point of any model because it implies the details of the evolution dynamics of nuclear matter undergoing hadronization. In contrast to mesons, which, once produced in the course of hadronization, retain their identity until final (kinetic) freeze-out (they undergo virtually no interactions other than elastic scattering), (anti)baryons begin to annihilate immediately after their production, the lower being T, the larger the annihilation cross section. A rather high density of surrounding baryons (large chemical potential) at AGS and a very large annihilation cross section, $\sigma_{p\bar{p}} \simeq 100$ mb, favor very strong absorption, which crucially diminishes the number of antibaryons before hadrons scatter away and stop interacting—only those that remain then hit the detectors used. Of course, this effect is disregarded in the above formulas. However, the $\bar{p}/\pi^+$

[8)] Actually, these factors may be significant only for nucleon production (and antinucleon production at RHIC and LHC).

[9)] As a result, the rate of $\Lambda(\bar{\Lambda})$ production turns out to be almost twice as large as that of both $\Sigma^\pm$ and $\bar{\Sigma}^\pm$ hyperons.

yield measured at AGS [13] involving a small number of nucleons participating in the formation of the nuclear fireball (about 20) is about twice as large as that in central collisions (that is, in the case where about 80 to 100 nucleons participate). This can be explained under the assumption that about half of product antiprotons have time to annihilate in the process of large-fireball cooling from the hadronization temperature T_H to kinetic freeze-out at T_f; in the case of a small, rapidly expanding fireball, this is impossible. The simplest (of course, naive) estimate shows that this assumption is quite reasonable. Indeed, we can easily estimate the dynamics of the number of antiprotons for $T_f \le T \le T_H$ as

$$N_{\bar{p}}(t) \simeq N_{\bar{p}}(0)\exp(-v\rho_p\sigma_{\bar{p}p}t),$$

where $\rho_p \simeq [V_0(1+N_\pi/N_p)]^{-1}$, V_0 being the mean volume per particle, and v is mean thermal velocity of nucleons. Using here the values of $N_p/N_\pi \simeq 0.8$ (see table), $V_0 \simeq (4\pi/3)(1.1\text{ fm})^3$ (this corresponds to the mean nucleon density in nuclei), and $v \simeq 2/3$, we obtain

$$N_{\bar{p}}(t) \simeq N_{\bar{p}}(0)\exp(-0.7t),$$

where the time is measured in fm units. Hence, the experimental result reported in [13] can be explained if the difference of the times of large- and small-fireball expansion is $\Delta t \simeq 1$ fm (for example, if the first is about 1 fm, while the second is much less than 1 fm). These were precisely the values adopted in composing the table. At SPS, the $\bar{p}/\pi$ yield ratio appeared to be virtually independent of the fireball size [14]. Most probably, this was caused by a considerable increase in the pion fraction among product hadrons and a decrease in the chemical potential (either of these factors "dilutes" the baryon content and reduces the probability of proton–antiproton collisions) rather than by a fast expansion of the fireball. At RHIC and LHC, the absorption of antiprotons (and of protons as well, their number being nearly equal there to the number of antiprotons) must not play any noticeable role.

The results of our calculations are quoted in the table (M1 column). The ratios $n_{Q(q)}/n_{\bar{Q}(q)}$, $n_{Q(s)}/n_{\bar{Q}(s)}$, and $n_{Q(q)}/n_{Q(s)}$ and the value of $\langle j\rangle$ were found by minimizing the sum of squared deviations,

$$\Delta^2 \simeq \min\left[\sum_{i=0}^{k}\left(1-\frac{a^i_{\text{theor}}}{a^i_{\text{expt}}}\right)^2\right],$$

where k is the number of measured relative yields of various species.

It should be noted that, so far, we have made no specific assumptions concerning the properties of the $Q\pi K$ gas. The assumption of its quasi-ideality becomes unavoidable if we try to extract the hadronization temperature T_H from ideal-gas formulas. We then have

$$\frac{n_{Q(q)}}{n_{\bar{Q}(q)}} = \exp(2\mu_{Q(q)}/T), \quad \frac{n_{Q(s)}}{n_{\bar{Q}(s)}} = \exp(2\mu_{Q(s)}/T),$$

$$\frac{n_{Q(q)}}{n_{Q(s)}} \simeq \left(\frac{m_{Q(q)}}{m_{Q(s)}}\right)^{3/2}\exp\left[\frac{m_{Q(s)}-m_{Q(q)}}{T}\right] \times \exp\left[\frac{\mu_{Q(q)}-\mu_{Q(s)}}{T}\right].$$

On doing this, we obtain nearly the same temperature, $T_H \simeq (115\pm 10)$ MeV (see Fig. 3), for all of the experiments under consideration—namely, for AGS, SPS, and RHIC. The predictions given in the table for future experiments at LHC were obtained for the same hadronization temperature T_H and zero values of all chemical potentials (see Fig. 3), $\mu_i = \mu = 0$.

4. DISCUSSION AND CONCLUDING REMARKS

It is worth mentioning that the above results are quite similar to those that one can obtain without precautions, describing the $Q\pi K$ phase as an ideal gas from the very beginning instead of employing detailed-balance equations (compare the columns M1 and M2 in the table). This implies either that the valon–pion–kaon gas is indeed similar to an ideal gas or that the relative content of different components in this gas is a crude characteristic (this seems quite plausible) that is rather insensitive to its fine tuning. Anyway, the compatibility of the results seems indicative of the validity of the approach itself.

It is important that the hadronization-temperature value of $T_H \simeq 115$ MeV found here is quite close to the thermal-freeze-out temperature (at which strong interactions cease to occur and free divergence begins) as estimated in [15] on the basis of thermal hydrodynamic models by analyzing the transverse-momentum spectra of hadrons. For SPS and RHIC, it appears to be about 105–115 MeV. If so, then fireball evolution from T_H to T_f occurs within a rather short time (of a few fm), and one can qualitatively understand why antiproton absorption in the course of and just after hadronization is crucially significant only for AGS (in which case the relative content of nucleons is very high). In particular, this is the reason why we do not need a special (and artificial) antiproton-regeneration mechanism (see, for example, [16]), but such a mechanism is mandatory within any approach assuming early freeze-out of hadronic matter.

That the hadronization temperature takes approximately the same value in the experiments at AGS,

SPS, and RHIC, although the corresponding chemical potentials differ substantially, which is expected to result in different EoS's, is yet another point that deserves a dedicated discussion. As a matter of fact, we cannot state that this result is quantitatively correct. The minimization of Δ^2 can hardly be considered as a reliable method for treating the data from AGS and RHIC, since the number of parameters to be varied is only slightly less than the number of fitted experimental results presently obtained at these accelerators. Moreover, very small values of Δ^2 should not be taken too seriously because the accuracy of data is insufficient.

The possible dependence of the hadronization temperature on the valonic chemical potential (and, hence, on the energy of colliding ions) is closely related to the very interesting hypothesis [7] that the color (more precisely, valonic) deconfinement is reasonably expected to occur even at very low interaction energies (the ion kinetic energy in the laboratory frame being as low as about 300 MeV) because the matter density in nucleons is only about three times larger than that in a normal nucleus, and only a small amount of effort is required in order that valous stop distinguishing "their original nucleons" from their neighbors (this means that the color-screening length is less than the confinement radius). If this is so, then, in particular, a thermal treatment of hadron production must be applicable even at such low energies. The success of such an approach would be a direct indication of the validity of the very notion of the valon itself. Of course, a high-luminosity machine equipped with high-precision detectors is required for implementing attempts at searches for relevant manifestations.

Thus, we can conclude that the proposed approach provides quite a successful treatment of available data on hadron yields, as well as on low-mass-dilepton production [9], in heavy-ion collisions. At the same time, it is free from crucial inconsistencies inherent in some conventional approaches, although some significant questions still remain unanswered.

ACKNOWLEDGMENTS

We are grateful to E.L. Feinberg for numerous stimulating discussions and permanent interest in our study.

The work was supported in part by the Russian Foundation for Basic Research (project no. 00-02-017250) and a grant (no. 00-15-96696) for "Leading Scientific Schools."

APPENDIX

Being averaged over particle distributions, the detailed-balance equation takes the form

$$\nu_{Q(q)}(T)\overline{\Omega_\pi}(T) \simeq \nu_\pi(T)\overline{\Omega_{Q(q)}}(T), \qquad (A.1)$$

where $\overline{\Omega_i}$ are the mean values of the corresponding final-state phase spaces.[10] Since each antivalon $\bar{Q}(q)$ of specific color and flavor encounters the corresponding valon $Q(q)$ with the probability $n_{Q(q)}/(n + n_\pi)$, the rate of $Q(q)\bar{Q}(q)$ collisions is

$$d\nu_{Q(q)} = \frac{(1-b)n_{Q(q)}n_{\bar{Q}(q)}}{n}\frac{dt}{\langle t\rangle}, \qquad (A.2)$$

$\langle t\rangle$ being the mean free time between successive collisions. Quite similarly, a π^0 meson encounters another π meson with the probability b, the total rate of $\pi^0\pi$ collisions being therefore $(2/9)bn_\pi dt/\langle t\rangle$ ($\pi^0\pi^+$ collisions) plus $(bn_\pi/18)dt/\langle t\rangle$ ($\pi^0\pi^0$ collisions); the number of $\pi^+\pi^-$ collisions is obviously equal to $(bn_\pi/9)dt/\langle t\rangle$.

Of course, $\pi^+\pi^+$ and $\pi^-\pi^-$ collisions are out of the game in the detailed-balance-principle equation (within the above approximation), since they never result in a two-valonic final state. For the total rate of $\pi\pi$ collisions to be taken into account, one therefore has

$$d\nu_\pi = \frac{7}{18}bn_\pi\frac{dt}{\langle t\rangle}. \qquad (A.3)$$

The averaged valonic and pionic phase spaces are, respectively,

$$\overline{\Omega_{Q(q)}} \simeq N_f^2(2S_Q+1)^2N_c\overline{p^2_{Q(q)}} \qquad (A.4)$$

and

$$\overline{\Omega_\pi} \simeq (2I_\pi+1)^2\overline{p_\pi^2},$$

where S_Q is the valonic spin; I_π is the pionic isospin; $p_{Q(s)(p_\pi)}$ is the valonic or pionic momentum in the c.m. frame of two interacting valons or pions; and N_c and N_f are the numbers of, respectively, colors and flavors [N_c appears in (A.4) instead of N_c^2, since only the color-singlet sector of the total two-valon phase space is considered]. For the mean energy of a particle of mass m, a straightforward averaging over the Boltzmann distribution yields

$$\overline{E^2(m,T)} = T^2\left[3\frac{m}{T}\frac{K_1(m/T)}{K_2(m/T)} + 12 + \frac{m^2}{T^2}\right], \quad (A.5)$$

[10] Only binary reactions are considered, because $2 \to 4$ reactions are substantially suppressed by limitations on the typical thermal final-state phase space at $T \simeq T_H$.

where $K_{1,2}$ are the corresponding Bessel functions. The c.m. value of $\overline{p_\pi^2}$ ($\overline{p_{Q(q)}^2}$) of each particle in the pionic (valonic) final state is obviously obtained by substituting $m = m_\pi$ ($m = m_{Q(q)}$) into this expression, subtracting m_π^2 ($m_{Q(q)}^2$), and taking half of this difference. Combining Eqs. (A.1)–(A.5), we easily obtain

$$b \simeq \left[1 + 2.5\left(\frac{n_{Q(q)}n_{\bar{Q}(q)}}{n^2}\frac{\overline{p_\pi^2}}{\overline{p_{Q(q)}^2}}\right)^{-1/2}\right]^{-1}, \quad \text{(A.6)}$$

where $\overline{p_i^2}$ are taken from (A.5).

We now consider the equilibrium kaon fraction and estimate the $K^{0,+}$-meson content in the $Q\pi K$ medium. In order to do this, one must take into account the diagrams in Figs. 1*b* and 1*c*. It is easy to verify that, at relevant temperatures, the mean squares of c.m. momenta are nearly equal for all four states under consideration; therefore, the corresponding detailed-balance equation takes the form[11)]

$$\frac{(2I_K+1)}{(2I_\pi+1)}n_\pi n_{\bar{Q}(s)} + \frac{(2I_K+1)(2I_\pi+1)}{(2S_Q+1)^2} \times \frac{n_{\bar{Q}(s)}n_{Q(q)}}{N_c} \simeq \frac{(2I_\pi+1)}{(2I_K+1)}n_{\bar{Q}(q)}n_K + \frac{(2S_Q+1)^2N_c}{(2I_K+1)(2I_\pi+1)}n_\pi n_K, \quad \text{(A.7)}$$

where K stands for K^+ or K^0 and I_i is the relevant isospin. This leads to Eq. (2).

Making use of these formulas, one can easily find that the kaon-induced correction to the value of b is indeed quite small—for example, $\frac{\delta b}{b} \simeq +(4-5)\times 10^{-2}$ for SPS—and that it is undoubtedly absorbed into the inaccuracy of the approach itself.

REFERENCES

1. P. Braun-Munzinger, I. Heppe, and J. Stachel, nucl-th/9903010.
2. J. Cleymans and K. Redlich, Nucl. Phys. A **661**, 379 (1999); nucl-th/9903063.
3. B. Müller and J. Rafelski, Phys. World **12** (3), 23 (1999).
4. K. G. Wilson, Phys. Rev. D **10**, 2445 (1974); K. G. Wilson and D. G. Robertson, hep-th/9411007.
5. O. D. Chernavskaya and E. L. Feinberg, in *Proceedings of International Conference "Hot Hadronic Matter: Theory and Experiment,"* Ed. by J. Letessier and J. Rafelski (Plenum, New York, 1995); J. Mosc. Phys. Soc. **6**, 37 (1996); E. L. Feinberg, in *Proceedings of the 2nd International Sakharov Conference,* Ed. by I. M. Dremin and A. M. Semikhatov (World Sci., Singapore, 1997), p. 6.
6. E. V. Shuryak, Phys. Lett. B **107B**, 103 (1981).
7. E. L. Feĭnberg, Usp. Fiz. Nauk **139**, 3 (1983) [Sov. Phys. Usp. **26**, 1 (1983)], and references therein; Preprint No. 197, FIAN (Lebedev Institute of Physics, USSR Academy of Sciences, Moscow, 1989); E. L. Feinberg, in *Proceedings of the International Conference "Relativistic Heavy Ion Collisions,"* Ed. by L. P. Chernai and D. D. Strottman (World Sci., Singapore, 1991).
8. A. V. Bochkarev and M. E. Shaposhnikov, Nucl. Phys. B **268**, 220 (1986); J. Cleymans, K. Redlich, H. Satz, and E. Suhonen, Z. Phys. C **33**, 151 (1986); D. V. Anchishkin, K. A. Bugaev, and M. I. Gorenstein, Z. Phys. C **45**, 687 (1990); S. P. Baranov and L. V. Fil'kov, Z. Phys. C **57**, 149 (1993).
9. O. D. Chernavskaya, E. L. Feinberg, and I. I. Royzen, Yad. Fiz. **65**, 167 (2002) [Phys. At. Nucl. **65**, 161 (2002)]; hep-ph/0011009.
10. O. D. Chernavskaya, E. L. Feinberg, and I. I. Royzen, hep-ph/0101063.
11. V. V. Anisovich *et al.*, Usp. Fiz. Nauk **144**, 553 (1984) [Sov. Phys. Usp. **27**, 901 (1984)]; B. L. Ioffe and V. A. Khoze, *Hard Processes* (North-Holland, Amsterdam, 1984), Vol. 1.
12. V. L. Eletsky *et al.*, Eur. J. Phys. A **3**, 381 (1998); Nucl. Phys. A **661**, 514 (1999).
13. E802 Collab. (Y. Akiba *et al.*), Nucl. Phys. A **610**, 139 (1996).
14. NA49 Collab. (F. Sikler *et al.*), Nucl. Phys. A **661**, 45 (1999).
15. N. Xu and M. Kaneta, Nucl. Phys. A **698**, 306 (2002); S. Panitkin, in *Proceedings of the 3rd International Sakharov Conference on Physics, Moscow, Lebedev Institute of Physics, 2002.*
16. R. Rapp and E. V. Shuryak, hep-ph/0008326.

Translated by O. Chernavskaya

[11)] Here, it is assumed that the matrix elements for the two processes involved are similar in absolute value.

Physics of Atomic Nuclei, Vol. 66, No. 1, 2003, pp. 191–194. Translated from Yadernaya Fizika, Vol. 66, No. 1, 2003, pp. 195–198.

ELEMENTARY PARTICLES AND FIELDS
Theory

Using a Chiral Anomaly to Determine the Number of Colors

R. N. Rogalyov*

Institute for High Energy Physics,
Protvino, Moscow oblast, 142281 Russia

Received January 17, 2002

Abstract—The N_c dependence of $PPP\gamma$ vertices, where P is a pseudoscalar meson and N_c is the number of colors, is analyzed with allowance for the N_c dependence of the quark charges. It is shown that the reactions $K\gamma \to K\pi$ and $\pi^{\pm}\gamma \to \pi^{\pm}\eta$ and the decay $\eta \to \pi^+\pi^-\gamma$ are the best processes for determining N_c. The cross section $\sigma(\pi^-\gamma \to \pi^-\eta)$ as measured by using the VES facility at IHEP agrees with the value of $N_c = 3$. © *2003 MAIK "Nauka/Interperiodica".*

A chiral anomaly [1] is a fundamental property of quantum field theories involving chiral fermions, such as the Standard Model (SM). It is a quantum-mechanical violation of a classical chiral symmetry such that its manifestations at the hadronic scale are unambiguously determined. This property distinguishes a chiral anomaly from other predictions of the SM; as a matter of fact, it is the only effect of quark–lepton interactions at short distances that admits a description in terms of hadronic fields without introducing additional phenomenological parameters. For this reason, experimental investigation of the chiral anomaly would provide a test of theoretical foundations of elementary particle physics.

Phenomenological implications of the chiral anomaly can be taken into account by supplementing the Lagrangian of chiral perturbation theory with the Wess–Zumino–Witten (WZW) functional [2, 3][1)]

$$S[U,\ell,r]^{(N_c=3)}_{\rm WZW} = -\frac{iN_c}{48\pi^2} \times \int d^4x\varepsilon^{\mu\nu\alpha\beta}\Big\langle U\ell_\mu\ell_\nu\ell_\alpha U^\dagger r_\beta + \frac{1}{4}U\ell_\mu U^\dagger r_\nu U\ell_\alpha U^\dagger r_\beta + iU\partial_\mu\ell_\nu\ell_\alpha U^\dagger r_\beta + i\partial_\mu r_\nu U\ell_\alpha U^\dagger r_\beta - i\Sigma^L_\mu\ell_\nu U^\dagger r_\alpha U\ell_\beta + \Sigma^L_\mu U^\dagger\partial_\nu r_\alpha U\ell_\beta - \Sigma^L_\mu\Sigma^L_\nu U^\dagger r_\alpha U\ell_\beta + \Sigma^L_\mu\ell_\nu\partial_\alpha\ell_\beta + \Sigma^L_\mu\partial_\nu\ell_\alpha\ell_\beta - i\Sigma^L_\mu\ell_\nu\ell_\alpha\ell_\beta + \frac{1}{2}\Sigma^L_\mu\ell_\nu\Sigma^L_\alpha\ell_\beta - i\Sigma^L_\mu\Sigma^L_\nu\Sigma^L_\alpha\ell_\beta\Big\rangle - (L\leftrightarrow R), \quad (1)$$

where N_c is the number of colors ($N_c = 3$); the angular brackets $\langle\dots\rangle$ denote the trace over the flavor indices;

$$\Sigma^L_\mu = U^\dagger\partial_\mu U; \qquad \Sigma^R_\mu = U\partial_\mu U^\dagger; \quad (2)$$
$$U = \exp\left(i\Phi\sqrt{2}/F\right);$$

$$r_\mu = \ell_\mu = eA_\mu Q = eA_\mu\,\mathrm{diag}\left(\frac{2}{3}, -\frac{1}{3}, -\frac{1}{3}\right); \quad (3)$$

A_μ is the electromagnetic field; $F = 93$ MeV;

$$\Phi = \begin{pmatrix} \frac{\pi^0}{\sqrt{2}} + \frac{\eta^8}{\sqrt{6}} + \frac{\eta^0}{\sqrt{3}} & \pi^+ & K^+ \\ \pi^- & -\frac{\pi^0}{\sqrt{2}} + \frac{\eta^8}{\sqrt{6}} + \frac{\eta^0}{\sqrt{3}} & K_0 \\ K^- & \bar{K}_0 & -\frac{2\eta^8}{\sqrt{6}} + \frac{\eta^0}{\sqrt{3}} \end{pmatrix};$$

and the symbol $(L\leftrightarrow R)$ denotes the substitutions $U \leftrightarrow U^\dagger$, $\ell_\mu \leftrightarrow r_\mu$, and $\Sigma^L_\mu \leftrightarrow \Sigma^R_\mu$.

The functional in (1) determines the low-energy behavior of the amplitudes of the reactions $\pi^0 \to \gamma\gamma$, $\eta \to \gamma\gamma$, $\eta \to \pi^+\pi^-\gamma$, $\pi^+\gamma \to \pi^+\pi^0$, $\pi^+\gamma \to \pi^+\eta$, $K^+\gamma \to K^+\pi^0$, and so on. Some of these reactions ($\pi^0 \to \gamma\gamma$, $\eta \to \gamma\gamma$, $\eta \to \pi^+\pi^-\gamma$, and $\pi^+\gamma \to \pi^+\pi^0$) were used to determine the number of colors N_c.

However, a recent analysis of $PPP\gamma$ and $P\gamma\gamma$ vertices (P is a pseudoscalar meson) revealed [4] that, in a self-consistent theory, the $\pi^0\gamma\gamma$ and $\pi^0\pi^+\pi^-\gamma$ vertices are independent of N_c, although it is precisely these vertices that were used to determine N_c. Moreover, it was stated in any textbook on elementary particle physics (see, for example, [5]) that the width with respect to the decay $\pi^0 \to \gamma\gamma$ is proportional to N_c^2; therefore, the width $\Gamma(\pi^0 \to \gamma\gamma)$ is considered

*e-mail: rogalyov@mx.ihep.su

1)In (1), it is assumed that the charge matrix is given by expression (3) for all N_c; however, it is shown below that this assumption is incorrect. For this reason, expression (1) is valid only for $N_c = 3$.

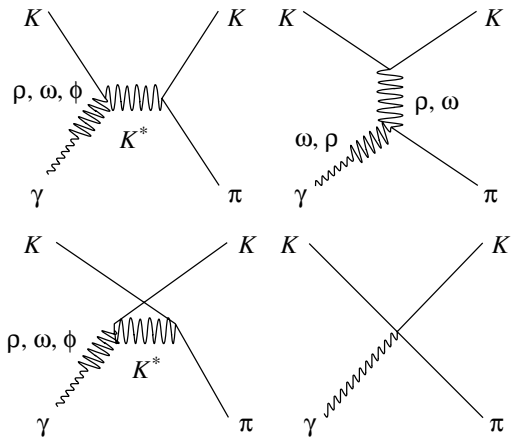

Diagrams contributing to the amplitudes of $K\gamma \to K\pi$ reactions.

as an important source of experimental information about the value of N_c. The point is that the statement that the amplitudes $\mathcal{A}_{\pi^+\gamma\to\pi^+\pi^0}$ and $\mathcal{A}_{\pi^0\to\gamma\gamma}$ are dependent on N_c stems from an implicit (and erroneous) assumption that the quark charges $Q_u = 2/3$, $Q_d = -1/3$, and $Q_s = -1/3$ are independent of N_c. If this assumption were true, the triangle anomalies in the quark sector (at $N_c + 3$) would not cancel those in the lepton sector, with the result that the SM would not be renormalizable. But assuming renormalizability of the SM for all N_c, we find that N_c and the quark charges are related by the equations

$$Q_u = \frac{1}{2}\left(\frac{1}{N_c} + 1\right), \quad Q_d = \frac{1}{2}\left(\frac{1}{N_c} - 1\right). \qquad (4)$$

On the basis of these equations, one can show that the amplitudes of processes involving only π mesons and having an anomalous G parity (such as $\pi^0 \to \gamma\gamma$, $\pi^+\gamma \to \pi^+\pi^0$, and $\eta \to \gamma\gamma$) are independent of N_c. The anomalous $\gamma\pi^0\pi^+\pi^-$ and $\gamma\eta\pi^+\pi^-$ vertices were studied theoretically (in the case of $N_c = 3$) in [6] and experimentally in processes that lead to the Coulomb production of π^0 [7] and η [8] mesons on nuclei at the IHEP facility. It should be noted that the experiment reported in [7] and devoted to measuring the cross section $\sigma(\pi^+\gamma \to \pi^+\pi^0)$ was motivated by the desire to determine the number of colors; however, this could not be done in this experiment according to the above. At the same time, experimental data obtained by Amelin *et al.* [8] can well be used to determine N_c. As of now, the only vertex involving light mesons that has been used to determine the number of colors N_c is $\eta\pi^+\pi^-\gamma$. It was studied in the decay $\eta \to \pi^+\pi^-\gamma$ [9] and in the scattering process $\pi^+\gamma \to \pi^+\eta$ [8]. The expression for this vertex for an arbitrary value of N_c is presented below. With allowance for this expression, the experiments mentioned immediately above favor $N_c = 3$.

The present study, as well as that of Bär and Wiese [4], is not aimed at questioning the entire body of experimental data indicating that $N_c = 3$; here, we pursue rather unpretentious goals. Bär and Wiese [4] propose that, in lending experimental support to the fact that there are three colors in our world, the decay $\eta \to \pi^+\pi^-\gamma$ should replace the textbook examples $\pi^0 \to \gamma\gamma$, and $\eta \to \gamma\gamma$ because the width with respect to the decay $\eta \to \pi^+\pi^-\gamma$ depends on N_c, whereas the widths with respect to the decays $\pi^0 \to \gamma\gamma$ and $\eta \to \gamma\gamma$ and the cross section for the reaction $\pi^+\gamma \to \pi^+\pi^0$ do not. In this study, we analyze the N_c dependence of the cross sections for the reactions $K\gamma \to K\pi$ and $K\gamma \to K\eta$, which can also be used to determine N_c. A detailed study of the relevant amplitudes is required because the ultimate expressions obtained in [4] for $PPP\gamma$ vertices {formulas (5.11) in [4]} are erroneous despite the fact that the analysis in [4] of the N_c dependence of the vertices of the anomalous Lagrangian is rather sophisticated and comprehensive. For instance, formulas (5.11) taken at $N_c = 3$ disagree with those obtained from the WZW functional (1). This error may stem from an improper antisymmetrization in formulas (5.12), where the authors of [4] deal with expressions antisymmetric in two operators instead of three operators that should be involved in the case of four-point Green's functions.

The effective Lagrangian for $PPP\gamma$ vertices can be calculated by either of the following two methods:

(i) The first consists in straightforwardly computing the group-theoretical coefficients of quark diagrams contributing to the respective Green's function with antisymmetrization in axial currents and with allowance for relations (4). Strictly speaking, this procedure yields only the ratios of coefficients of the same type, the known $\pi^0\gamma\gamma$ and $\pi^+\pi^-\pi^0\gamma$ vertices being used as reference values.

(ii) The second involves substituting the explicit expression for the matrix U [formula (2)] into the expression obtained by generalizing the WZW Lagrangian (1) to the case of $N_c \neq 3$. This generalization, proposed in [4], has the form

$$S = S^{(N_c=3)} + \left(1 - \frac{N_c}{3}\right) S_{\mathrm{GW}}, \qquad (5)$$

where S_{GW} is the Goldstone–Wilczek current [10],

$$S_{\mathrm{GW}}[U, A_\mu] = \frac{e}{48\pi^2} \qquad (6)$$
$$\times \int d^4x \varepsilon^{\mu\nu\alpha\beta} A_\mu \mathrm{tr}[(U^\dagger\partial_\nu U)(U^\dagger\partial_\alpha U)(U^\dagger\partial_\beta U)]$$
$$- \frac{ie^2}{32\pi^2} \int d^4x \varepsilon^{\mu\nu\alpha\beta} A_\mu F_{\nu\alpha} \mathrm{tr}[Q(\partial_\beta U U^\dagger + U^\dagger\partial_\beta U)].$$

In considering $PPP\gamma$ vertices, the third line in (6) can be omitted.

The results of the calculations by these two methods coincide; the required vertices have the form

$$\mathcal{L}^{PPP\gamma}_{\mathrm{WZW}} = \frac{ie}{4\pi^2F^3}\varepsilon^{\mu\nu\alpha\beta}A_\beta\Big(\partial_\mu\pi^0\partial_\nu\pi^+\partial_\alpha\pi^- + \frac{N_c}{3\sqrt{3}}\partial_\mu\eta^8\partial_\nu\pi^+\partial_\alpha\pi^- + \frac{N_c+3}{6}\partial_\mu\pi^0\partial_\nu K^+\partial_\alpha K^- + \frac{N_c-1}{2}\partial_\mu\pi^0\partial_\nu K^0\partial_\alpha\bar{K}^0 + \frac{9-N_c}{6\sqrt{3}}\partial_\mu\eta^8\partial_\nu K^+\partial_\alpha K^- - \frac{\sqrt{3}(N_c-1)}{2}\partial_\mu\eta^8\partial_\nu K^0\partial_\alpha\bar{K}^0 - \frac{N_c-3}{3\sqrt{2}}\partial_\mu\pi^-\partial_\nu K^+\partial_\alpha\bar{K}^0 + \frac{N_c-3}{3\sqrt{2}}\partial_\mu\pi^+\partial_\nu K^-\partial_\alpha K^0 + \frac{\sqrt{6}}{9}\partial_\mu\eta^0\partial_\nu K^+\partial_\alpha K^- + \frac{N_c\sqrt{6}}{9}\partial_\mu\eta^0\partial_\nu\pi^+\partial_\alpha\pi^-\Big), \quad (7)$$

where η^0 and η^8 are the singlet and octet states:

$$\eta = \eta^8\cos\theta_P - \eta^0\sin\theta_P, \qquad \eta' = \eta^8\sin\theta_P + \eta^0\cos\theta_P, \quad \theta_P \simeq 20^\circ. \quad (8)$$

Formula (7) is the main result of the present study. It should be noted that the $K^+K^0\pi^-\gamma$ and $K^-\bar{K}^0\pi^+\gamma$ vertices do not appear in the anomalous action[2)] only in the case of $N_c = 3$. For this reason, the threshold behavior of the cross sections for the reactions $K^+\gamma \to K^0\pi^+$ and $K^0\gamma \to K^+\pi^-$ serves as a good indicator of a deviation of the parameter N_c from the value of $N_c = 3$. To put it differently, only at $N_c = 3$ does the chiral anomaly make a contribution to the amplitudes of the reactions $K^+\gamma \to K^+\pi^0$ and $K^0\gamma \to K^0\pi^0$ and make no contribution to the amplitudes of the reactions $K^+\gamma \to K^0\pi^+$ and $K^0\gamma \to K^+\pi^-$. As a consequence, the cross sections for the reactions $K^+\gamma \to K^+\pi^0$ and $K^0\gamma \to K^0\pi^0$ near the threshold are one to two orders of magnitude larger than the cross sections for the reactions $K^+\gamma \to K^0\pi^+$ and $K^0\gamma \to K^+\pi^-$. These cross sections were calculated (in the case of $N_c = 3$) in [11], where the possibility of experimentally studying them was also discussed. Measurement of the cross sections for the reactions $K^+\gamma \to K^+\pi^0$, $K^0\gamma \to K^0\pi^0$, $K^+\gamma \to K^0\pi^+$, and $K^0\gamma \to K^+\pi^-$ is of particular interest because of their N_c dependence presented in (7).

However, formulas (7) describe correctly the amplitudes only at sufficiently low momenta. To describe the reactions $K\gamma \to K\pi$ and $\pi^\pm\gamma \to \pi^\pm\eta$ and the decay $\eta \to \pi^+\pi^-\gamma$ at physical values of momenta and masses, it is necessary to take into account the contribution of the 1^{--} resonances. This can be done on the basis of the vector-meson-dominance model. In what follows, we use the version of the vector-meson-dominance model from [12] because it is precisely this version of the model that reduces to chiral perturbation theory in the chiral limit and because the formalism proposed in [12] is well suited for taking the chiral anomaly into consideration. The Lagrangian of this model and its application to the above-mentioned processes can be found in [11–13]; here, we only comment on its dependence on the number of colors. In the normal part of this Lagrangian, the N_c dependence is entirely absorbed in the effective coupling g. The anomalous terms must be multiplied by $N_c/3$ in order to obtain the WZW Lagrangian in the vicinity of the chiral limit; the quark charges are considered to be functions of N_c according to (4). Within the vector-meson-dominance model, the reactions $\pi^\pm\gamma \to \pi^\pm\eta$ and the decay $\eta \to \pi^+\pi^-\gamma$ were analyzed in [6]. From the expressions presented in [6], it follows that both diagrams for these processes are proportional to $N_c(Q_u - Q_d) = N_c$, so that the dependence of the amplitudes on N_c is readily determined.

As to $K\gamma \to K\pi$ reactions, they present a challenge: a straightforward computation of the amplitudes is needed. The respective Feynman diagrams are shown in the figure.

The calculations were performed with the FORM package [14]. The result has the form

$$A_{K\gamma\to K\pi} = \frac{-ie}{16\pi^2F^3}\varepsilon^{\mu\nu\alpha\beta}q^\mu p_b^\nu p_2^\alpha\varepsilon^\beta \times \left(C_0 + \frac{C_sM_{K^*}^2}{s - M_{K^*}^2 + i\Gamma_{K^*}\sqrt{s}} + \frac{C_tM_\rho^2}{t - M_\rho^2} + \frac{C_uM_{K^*}^2}{u - M_{K^*}^2}\right), \quad (9)$$

where ε is the photon polarization vector; the momenta q, p_b, and p_2 are defined in the table; $s = (q + p_b)^2$; $t = (p_b - p_2)^2$; $u = (q - p_2)^2$; M_{K^*} and M_ρ are the masses of the K^* and ρ mesons; and Γ_{K^*} is the K^*-meson width. The coefficients C_0, C_s, C_t, and C_u for specific processes are presented in the table as functions of N_c.

Thus, measurement of the cross sections for the reactions $K^+\gamma \to K^+\pi^0$ and $K^+\gamma \to K^0\pi^+$ would compensate for a deficiency that arises in experimental facts giving evidence for $N_c = 3$ upon the exclusion of the decays $\pi^0 \to \gamma\gamma$ and $\eta \to \gamma\gamma$ and the reaction $\pi^+\gamma \to \pi^+\pi^0$ from the experimental-data sample

[2)] The $K^+K^0\pi^-\gamma$ and $K^-\bar{K}^0\pi^+\gamma$ vertices are not presented in [4].

Coefficients C_0, C_s, C_t, and C_u in formula (9)

Reaction	C_0	C_s	C_t	C_u
$K^+(p_b)\gamma(q) \to K^+(p_2)\pi^0(p_1)$	$\frac{N_c+3}{3}$	1	N_c+1	1
$K^+(p_b)\gamma(q) \to K^0(p_2)\pi^+(p_1)$	$\frac{\sqrt{2}(N_c-3)}{3}$	$\sqrt{2}$	$\sqrt{2}(N_c-2)$	$-2\sqrt{2}$
$\pi^+(p_b)\gamma(q) \to \pi^+(p_2)\eta(p_1)$	$\frac{2N_c\sqrt{3}}{9}P_\theta$	0	$\frac{2N_c\sqrt{3}}{3}P_\theta$	0

Note: Allowance for the η–η' mixing (8) gives rise to the factor [6] $P_\theta = (F/F_8)\cos\theta_P - (F/F_0)\sin\theta_P$, where the distinctions between the decay constants $F_{\pi^\pm} = F$, F_0, and F_8 must also be taken into consideration. The quantity F_0 (F_8) parametrizes the matrix element of the axial current between vacuum and purely singlet (octet) state. A calculation in the one-loop approximation of chiral perturbation theory yields $F_0 \approx 1.04F$ and $F_8 \approx 1.30F$ [15]; the mixing angle is $\theta_P = 20^\circ$. All this makes theoretical predictions for the decays $\eta \to \pi^+\pi^-\gamma$ and $\eta' \to \pi^+\pi^-\gamma$ and the reactions $\pi^\pm\gamma \to \pi^\pm\eta(\eta')$ less precise than the predictions for the reactions $K\gamma \to K\pi$.

used to determine N_c. Moreover, measurement of the cross sections for the reactions $K\gamma \to K\pi$ would make it possible to test phenomenological implications of the chiral anomaly in the world with three (rather than two) light quarks. This is of importance because the WZW Lagrangian was derived under the assumption that there are precisely three light quarks.

ACKNOWLEDGMENTS

I am grateful to M.I. Polikarpov for interest in this study.

REFERENCES

1. J. Bell and R. Jackiw, Nuovo Cimento **60**, 47 (1969); S. Adler, Phys. Rev. **177**, 2426 (1969); W. A. Bardeen, Phys. Rev. **184**, 1848 (1969).
2. J. Wess and B. Zumino, Phys. Lett. B **37B**, 95 (1971).
3. E. Witten, Nucl. Phys. B **223**, 422 (1983).
4. O. Bär and U.-J. Wiese, Nucl. Phys. B **609**, 225 (2001); hep-ph/0105258.
5. C. Itzykson and J. B. Zuber, *Introduction to Quantum Field Theory* (McGraw-Hill, New York, 1980; Mir, Moscow, 1984); T.-P. Cheng and L.-F. Li, *Gauge Theory of Elementary Particle Physics* (Clarendon, Oxford, 1984; Mir, Moscow, 1987).
6. B. R. Holstein, Phys. Rev. D **53**, 4099 (1996); E. P. Venugopal and B. R. Holstein, Phys. Rev. D **57**, 4397 (1998); A. V. Kiselev and V. A. Petrov, Yad. Fiz. **63**, 571 (2000) [Phys. At. Nucl. **63**, 499 (2000)].
7. Y. M. Antipov *et al.*, Phys. Rev. D **36**, 21 (1987).
8. D. V. Amelin *et al.*, Yad. Fiz. **62**, 496 (1999) [Phys. At. Nucl. **62**, 454 (1999)].
9. M. Gormley *et al.*, Phys. Rev. D **2**, 501 (1970).
10. J. Goldstone and F. Wilczek, Phys. Rev. Lett. **47**, 986 (1981).
11. R. N. Rogalyov, Yad. Fiz. **64**, 72 (2001) [Phys. At. Nucl. **64**, 68 (2001)].
12. M. Bando, T. Kugo, and K. Yamawaki, Phys. Rep. **164**, 217 (1988).
13. T. Fujiwara *et al.*, Prog. Theor. Phys. **73**, 926 (1985).
14. J. A. M. Vermaseren, *Symbolic Manipulation with FORM, Version 2* (CAN, Amsterdam, 1991).
15. J. Gasser and H. Leutwyler, Nucl. Phys. B **250**, 465 (1985).

Translated by R. Rogalyov

Physics of Atomic Nuclei, Vol. 66, No. 1, 2003, pp. 195–202. Translated from Yadernaya Fizika, Vol. 66, No. 1, 2003, pp. 199–206.

ELEMENTARY PARTICLES AND FIELDS
Theory

Photoproduction as the Limiting Case of Inelastic Scattering

A. A. Petrukhin and D. A. Timashkov

Moscow Engineering Physics Institute (State University), Kashirskoe sh. 31, Moscow, 115409 Russia

Received August 2, 2001; in final form, November 23, 2001

Abstract—On the basis of the vector-dominance model and Regge theory, formulas are derived that make it possible to obtain a unified description of the photoproduction cross section and the nucleon structure functions determining the cross section for inelastic lepton scattering at low Q^2. © *2003 MAIK "Nauka/Interperiodica".*

INTRODUCTION

Inelastic photon–hadron interaction is one of the simplest inelastic processes in elementary-particle physics, and investigation of this interaction is of great interest. At the same time, photoproduction can be interpreted as an extreme case of electroproduction at low momentum transfers in the quasistatic limit for $Q^2 \to 0$, where perturbative QCD ceases to be applicable. The Feynman diagram for photoproduction on a proton is equivalent to the hadronic vertex of the diagram for inelastic charged-lepton (electron or muon) scattering on hadrons (see Fig. 1). Therefore, investigation into photoproduction makes it possible to deduce important information not only about the interaction of high-energy photons with matter but also about the limiting behavior of the cross sections for inelastic lepton–proton processes and about the proton structure functions.

With the aim of obtaining simple formulas that would describe the cross sections for photo- and electroproduction processes and relations between them, we analyze here various phenomenological models of these processes.

1. BASIC RELATIONS

The photoproduction cross section is determined by the hadronic tensor identical to that which appears in the cross section for inelastic lepton–proton interaction; that is,

$$\sigma(\gamma p \to X) = \frac{4\pi^2\alpha_e}{K}\varepsilon^{\mu *}\varepsilon^{\nu}W_{\mu\nu}, \qquad (1)$$

where α_e is the fine-structure constant. For a real photon, $K = E_\gamma$ and the polarization vectors ε^μ and ε^ν lie in the plane orthogonal to the photon momentum. If we are dealing with a virtual photon, its transverse polarizations do not exhaust the possible states of this photon; moreover, the choice of the flux factor K is ambiguous in this case. Usually, it is taken to be

$$K = \nu - \frac{Q^2}{2M}. \qquad (2)$$

As is well known (see [1]), the hadronic tensor depends on the hadron and virtual-photon 4-momenta and two dimensionless structure functions

$$F_1 = MW_1 = \frac{M\nu}{4\pi^2\alpha_e}(1-x)\sigma_T, \qquad (3)$$

$$F_2 = \nu W_2 = \frac{Q^2}{4\pi^2\alpha_e}(1-x)\frac{1+\sigma_L/\sigma_T}{1+Q^2/\nu^2}\sigma_T. \qquad (4)$$

By x, we hereafter imply the Bjorken variable

$$x = \frac{Q^2}{2M\nu}. \qquad (5)$$

In the limit of photoproduction, the cross section σ_T for a transversely polarized photon reduces to $\sigma_{\gamma p}$, while the cross section σ_L for a longitudinally polarized photon vanishes. From Eqs. (3) and (4), one can deduce that, in this case, the structure functions F_1 and F_2 satisfy the simple relation

$$F_1 = \frac{F_2}{2x}, \qquad (6)$$

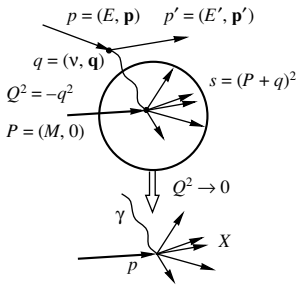

Fig. 1. Feynman diagrams for electro- and photoproduction: basic conventions.

1063-7788/03/6601-0195$24.00

which is known as the Callan–Gross relation [2] and which can be obtained on the basis of the quark–parton model for inelastic scattering at high Q^2.

Formulas (1), (3), and (4) reveal a close relation between the processes of photo- and electroproduction. However, this relation, which manifests itself at the level of Feynman diagrams and form factors, does not admit a direct transition from electro- to photoproduction for $Q^2 \to 0$, if for no other reasons than the fact that different particles are involved in these processes. This is also reflected in the kinematical constraint on the minimum momentum transfer in inelastic scattering:

$$Q^2 > Q^2_{\min} = \frac{m_l^2 y^2}{1-y}. \tag{7}$$

Here, m_l is the lepton (incident particle) mass and $y = \nu/E$ is the energy-transfer fraction. With allowance for relation (7), the limit of photoproduction in inelastic lepton–proton scattering is reached only for $y \to 0$, which, at a given value of the energy transfer ν, implies $E \to \infty$.

The inelastic-scattering cross section can be expressed in terms of the cross section for virtual-photon scattering on a proton as [3]

$$\frac{d\sigma_{\text{in}}}{dQ^2 d\nu} = \alpha_e \Gamma_T \sigma_{\gamma^* p}, \tag{8}$$

where Γ_T is the flux factor (see [3]) and

$$\sigma_{\gamma^* p} = \sigma_T + \epsilon \sigma_L. \tag{9}$$

If the lepton mass is disregarded, the polarization factor is usually defined at low Q^2 as

$$\epsilon = \left(1 + \frac{Q^2 + \nu^2}{2EE' - Q^2/2}\right)^{-1}, \tag{10}$$

while the flux factor is defined as

$$\Gamma_T = \frac{1}{\pi Q^2 \nu}\left(1 - y + y^2/2\right). \tag{11}$$

Here, the parenthetical expression can vary from 1/2 to 1. It was mentioned above that, in the limit of low Q^2, the cross section for a longitudinally polarized photon can be disregarded against the cross section for a transversely polarized photon. In this case, relation (9) takes the form

$$\sigma_{\gamma^* p} \approx \sigma_T.$$

Considering that the limit of photoproduction corresponds to low y and that the parenthetical expression in (11) is close to unity in this case, we can represent the inelastic-scattering cross section in the region of low Q^2 as

$$\frac{d\sigma_{\text{in}}}{dQ^2 d\nu} \approx \frac{\alpha_e}{\pi}\frac{\sigma_T(Q^2,\nu)}{Q^2\nu}. \tag{12}$$

The photoproduction process and inelastic electron (muon) scattering on a proton at low Q^2 is usually described on the basis of the vector-meson-dominance model and various modifications of this model that enable one to sidestep difficulties arising in QCD at low momentum transfers and to derive boundary conditions determining the behavior of the proton structure functions in the limit $Q^2 \to 0$.

2. VECTOR-MESON-DOMINANCE MODELS

The first model that described inelastic real-photon (or virtual-photon) scattering on a proton was the rho-dominance model. First, the idea that there is a hadronic component in the photon wave function was applied to describe photoproduction [4]. Further, Sakurai [5] employed this idea to describe virtual-photon interaction with a proton.

Since the rho-dominance model had been unable to ensure the required value of the cross section for virtual-photon scattering, the contributions of heavier vector mesons were included in order to describe the cross section $\sigma_{\gamma^* p}$ more accurately; that is, this cross section was taken in the form

$$\sigma_{\gamma^* p} = \sum_V \frac{\alpha_e}{\alpha_V}\frac{\sigma_{Vp}}{(1 + Q^2/m_V^2)^2}, \tag{13}$$

where α_V stands for the photon–meson coupling constants, m_V is the mass of a vector meson, and σ_{Vp} is the cross section for the interaction of a vector meson with a proton.

If, however, one took only a finite number of vector mesons (ρ, ω, φ), the structure function F_2 would decrease with increasing momentum transfer, but this would contradict the scaling behavior that was discovered at high Q^2 in electron–proton scattering at SLAC [6]. In view of this, the generalized vector-meson-dominance model, where summation in (13) is performed over the entire infinite mass spectrum of vector mesons, was proposed in the early 1970s [7, 8]. According to this model, the cross section for the scattering of a transversely polarized photon on a proton varies in proportion to $1/Q^2$, which is in accord with the scaling behavior of the structure functions.

As was shown in [9], the infinite sum in expression (13) can be replaced by an integral, whereupon one arrives at

$$\sigma_{\gamma^* p}(Q^2,\nu) = \alpha_e \int_{m_0^2}^{\infty} \frac{\rho(m^2,\nu)}{(1 + Q^2/m^2)^2} dm^2, \tag{14}$$

where $\rho(m^2,\nu)$ is the dynamical density of vector meson states.

The dynamical density is normalized to the photoproduction cross section as

$$\alpha_e \int_{m_0^2}^{\infty} \rho\left(m^2, \nu\right) dm^2 = \sigma_{\gamma p}. \quad (15)$$

We note that $\nu = K = E_\gamma$ for the case of photoproduction. From a dimensional analysis, it follows that the dependence ρ on m^2 must have the form $\rho \sim 1/m^4$.

Formulas proposed in [10, 11] to describe the cross section for virtual-photon scattering,

$$\sigma_{\gamma^* p}(Q^2, \nu) = \frac{\sigma_{\gamma p}(K)}{1 + Q^2/m_0^2}, \quad (16)$$

correspond to the choice of density function in the simplest form

$$\rho \sim \sigma_{\gamma p}/m^4. \quad (17)$$

In those studies, the value of m_0^2 was determined from a fit to experimental data and was set approximately to 0.4 GeV^2.[1)]

The value of this lower limit of integration in (14) can be obtained more accurately by invoking rather simple considerations. By definition, m_0 is the lower boundary of the mass spectrum of vector mesons. The lightest of these, the ρ meson, has the mass of $m_\rho = 0.77$ GeV and the width of $\Gamma_\rho = 0.151$ GeV, whence it follows that, for the lower boundary of the meson spectrum, one can take the value

$$m_0^2 = (m_\rho - \Gamma_\rho/2)^2 = 0.483 \text{ GeV}^2. \quad (18)$$

It should be noted that the values of m_0^2 obtained in [10–12] agree well with the value in (18).

3. PHOTOPRODUCTION CROSS SECTION

In order to determine the form of the dependence $\rho(m^2, \nu)$ on both variables m^2 and ν, we use the method of Regge poles. In Regge theory [15], the amplitude for the elastic scattering of two high-energy particles can be represented as

$$A(s, t) \sim s^{\alpha(t)}, \quad (19)$$

where s is the square of the c.m. energy and t is the 4-momentum transfer. The optical theorem relates the imaginary part of the amplitude for elastic scattering in the forward direction to the total cross section as

$$\mathrm{Im}A = s\sigma, \quad (20)$$

the cross section being expressed in terms of the Regge trajectories at $t = 0$ (so-called intercepts). Two intercepts are usually considered in the case of inelastic scattering: that of a Reggeon, $\alpha_R = 1/2$, and that of a Pomeron, $\alpha_\mathrm{P} \approx 1$. Therefore, we have

$$\sigma = \sum_{i=R,\mathrm{P}} c_i s^{\alpha_i - 1}. \quad (21)$$

By using the Regge method for photoproduction and by assuming that the exchanges of a Reggeon and a Pomeron are dominant in the limiting cases of, respectively, low and high energies, we can express the photoproduction cross section in terms of one intercept weakly dependent on the photon energy; that is,[2)]

$$\sigma_{\gamma p} \sim s^{\alpha(s)-1}, \quad (22)$$

$$s = M^2 + 2ME_\gamma. \quad (23)$$

We also have

$$\alpha(E_\gamma \to 0) \to \alpha_R, \quad (24)$$

$$\alpha(E_\gamma \to \infty) \to \alpha_\mathrm{P}. \quad (25)$$

The intercept cannot depend on energy more strongly than a logarithm of energy (otherwise, the pole concept loses meaning); therefore, we choose the dependence $\alpha(s)$ in such a way as to ensure fulfillment of relations (24) and (25); that is,

$$\alpha(s) = \alpha_R + (\alpha_\mathrm{P} - \alpha_R)\frac{f(s)}{1 + f(s)}, \quad (26)$$

$$f(s) = \ln\sqrt{1 + \frac{s - M^2}{m^2}} = \ln\sqrt{1 + \frac{2ME_\gamma}{m^2}}. \quad (27)$$

It follows that, with allowance for the asymptotic behavior in the form (22) (see, for example, [17]) and for the results of a dimensional analysis, the dynamical density of meson states can be represented as

$$\rho(m^2, s) = \frac{\pi^3}{m^4}\left(\frac{s}{m^2}\right)^{\alpha(s)-1}. \quad (28)$$

Upon substituting expressions (26)–(28) into Eq. (15) and making the change of variables

$$u = m^2/s, \quad (29)$$

[1)] In order to attain a higher precision, one can take either two terms corresponding to the contribution of light ($m_1^2 = 0.54$ GeV^2) and heavy ($m_2^2 = 1.8$ GeV^2) vector mesons [12] or a greater number of terms [13]. As was shown in [14], however, even the formulas obtained on the basis of the simplest model specified by Eq. (17) describe well the cross section for inelastic scattering and muon energy losses induced by this process if one uses a sufficiently accurate expression for $\sigma_{\gamma p}$.

[2)] The concept of an effective intercept taking into account the contributions of varoius trajectories was used previously (see, for example, [16]).

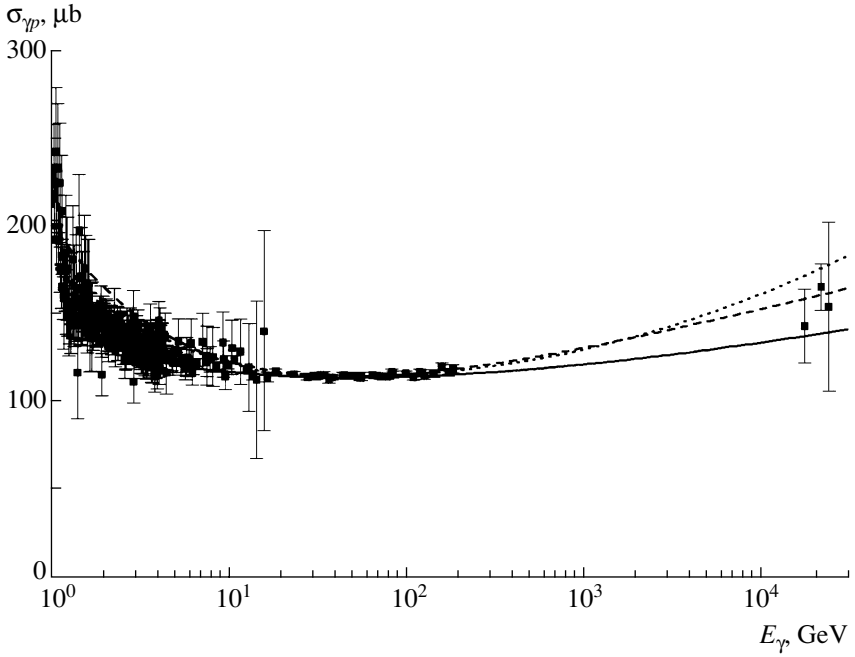

Fig. 2. Photoproduction cross section as a function of the photon energy: (solid curve) result of the calculation by formula (30) at $\alpha_{\mathrm{P}} = 1.065$, (dashed curve) fit from [19], and (dotted curve) result of the calculation by the formulas from [12]. Experimental data were borrowed from [18].

we obtain

$$\sigma_{\gamma p} = \frac{\pi^3 \alpha_e}{s} \int\limits_{u_0}^{\infty} \frac{du}{u^{1+\alpha(u)}}, \qquad (30)$$

where

$$u_0 = \frac{m_0^2}{s}, \qquad (31)$$

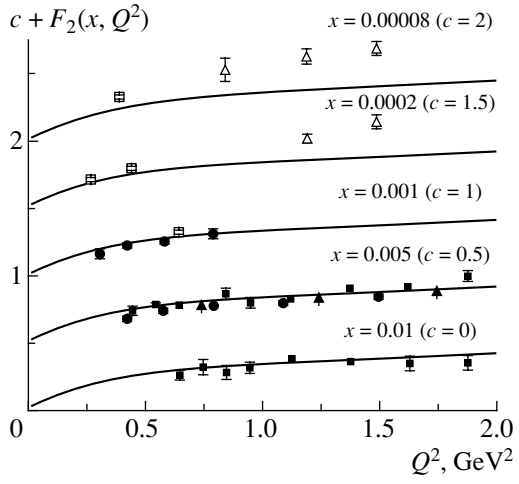

Fig. 3. Proton structure function F_2 (38) at low Q^2: (■) data from [21], (▲) data of the NMC collaboration [22], (□) data of the ZEUS collaboration [23], and (△) data of the H1 collaboration [24].

$$\alpha(u) = \frac{\alpha_R + \alpha_{\mathrm{P}} f(u)}{1 + f(u)}, \qquad (32)$$

$$f(u) = \ln \sqrt{1 + u^{-1}(1 - M^2/s)}.$$

The photoproduction cross section (30) as a function of the photon energy is displayed in Fig. 2, along with relevant experimental data from [18]. Also given in this figure are the main fits to $\sigma_{\gamma p}$ that were proposed previously in [12, 19]. Corrections in the low-energy region [20] were taken into account in the formula from [12].

It can seen from Fig. 2 that the cross section (30), which was obtained on the basis of the vector-meson-dominance model and Regge theory, faithfully reproduces experimental data both in the region adjacent to resonances (around a few GeV) and at high energies. In order to describe the resonance region, one can use standard Breit–Wigner formulas (see Appendix).

4. INELASTIC SCATTERING IN THE LIMIT OF LOW Q^2

Let us consider the case of a virtual photon. The relevant scattering cross section is given by expression (14) with the density function in the form (28).

Instead of the variable s, which, in the case of photoproduction, is equal to the square of the sum of the real-photon and proton 4-momenta, we will use

the variable W^2 defined as the square of the sum of the virtual-photon and proton 4-momenta,

$$W^2 = M^2 + 2M\nu - Q^2.$$

Both W^2 and s have the meaning of the square of the mass of the final hadron state, and we have $W^2 = s$ in the limit of photoproduction.

Substituting expression (28) into the integral in (14) and making the change of variable according to (29), we obtain the cross section for virtual-photon scattering on a nucleon in the form

$$\sigma_{\gamma^* p} = \frac{\pi^3 \alpha_e}{W^2} \int\limits_{u_0}^{\infty} \frac{u^{1-\alpha(u)} du}{(u + Q^2/W^2)^2}. \qquad (33)$$

In the limit of low Q^2, the cross sections for scattering of a real and a virtual photon are related by the equation

$$\sigma_{\gamma^* p} = \sigma_{\gamma p} \int\limits_{u_0}^{\infty} \frac{u^{1-\alpha(u)} du}{(u + Q^2/W^2)^2} \Bigg/ \int\limits_{u_0}^{\infty} \frac{du}{u^{1+\alpha(u)}}. \quad (34)$$

The structure functions for inelastic scattering are given by (3) and (4). Disregarding the contribution of the longitudinal component and assuming that $Q^2 \ll \nu^2$, we express the proton structure function F_2 in terms of the cross section for virtual-photon scattering as

$$F_2 = \frac{Q^2}{4\pi^2 \alpha_e} (1 - x) \sigma_{\gamma^* p}. \qquad (35)$$

Using relation (33) and disregarding the square of the 4-momentum transfer Q^2 in the expression for W^2, we represent F_2 as a function of x and Q^2:

$$F_2\left(x, Q^2\right) = \frac{\pi}{4} \frac{x}{1 + xM^2/Q^2} \qquad (36)$$
$$\times \int\limits_{u_0}^{\infty} \frac{u^{1-\alpha(u)} du}{\left(u + x/(1 + xM^2/Q^2)\right)^2}.$$

In the limit of low Q^2, the proton structure function F_2 depends on the variable

$$x_T = \frac{x}{1 + xM^2/Q^2} \qquad (37)$$

rather than on Q^2 and x individually, and we can write

$$F_2\left(x_T\right) = \frac{\pi}{4} x_T \int\limits_{u_0}^{\infty} \frac{u^{1-\alpha(u)} du}{\left(u + x_T\right)^2}. \qquad (38)$$

The structure function F_1 can be obtained from (35)–(38) with the aid of relation (6).

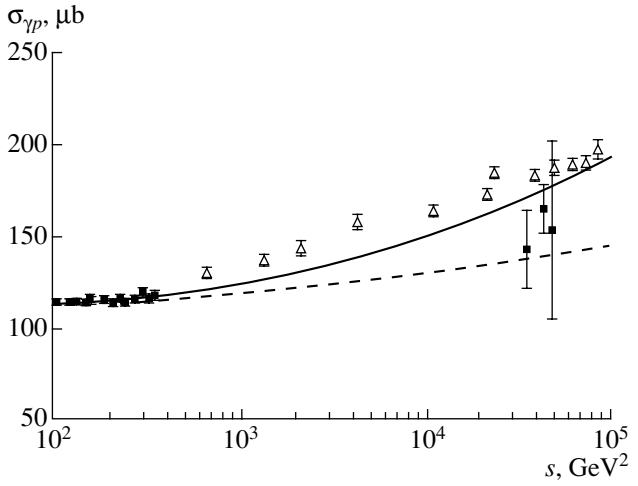

Fig. 4. Photoproduction cross section at high energies: (solid curve) results of the calculation with α_P given by (39), (dashed curve) results of the calculation with the constant value of $\alpha_P = 1.065$, (open triangles) experimental data of the ZEUS collaboration [40], and (closed boxes) experimental data from [18].

In Fig. 3, the behavior of the proton structure function F_2 in the region of low Q^2 is depicted along with experimental data obtained both with fixed targets (closed symbols) and with colliding beams (open symbols). It can be seen from Fig. 1 that, in the region of x values above 0.001, the results of the calculations agree well with the experimental data. The growth of the structure function with increasing Q^2 in the region of very low x is caused by the anomalous growth of the Pomeron intercept at high energies and momentum transfers (see next section).

5. HIGH-ENERGY REGION

In Regge theory, the behavior of the cross section at high energies is controlled by the Pomeron intercept—that is, by a pole that is characterized by the vacuum quantum numbers ($\alpha_P \approx 1$). However, the values of α_P that are obtained from a fit to data on inelastic scattering in the region of low x are greater. It is important to note that the broadening of the experimentally explored region toward higher interaction energies leads to greater values of the Pomeron intercept. The value of α_P as determined on the basis of data from [25–27] in the region $x > 10^{-4}$, which corresponds to energy transfers satisfying the condition $\nu < 1$ TeV, was 1.06 (ALLM91 parametrization [28]). In order to describe the first data obtained at the HERA collider in the region $x > 10^{-5}$ ($\nu < 10$ TeV) [29–32], α_P was taken to be close to 1.08 (see parametrizations in [33, 34]). Still greater values of $\alpha_P = 1.2$ (see the review article

of Kaidalov [35]) and 1.4 [36] were deduced from analyses of HERA data in the energy-transfer region extending up to a few tens of TeV (50 TeV).

Thus, the lower the value of x—that is, the higher the energy transfer—the greater the Pomeron intercept value that is obtained from a fit to experimental data on inelastic interaction. Qualitatively, this can be explained by the fact that, with increasing energy, more complicated mechanisms of Pomeron exchange (double Pomeron, perturbative Pomeron, triple Pomeron, etc., mechanisms) come into play. In order to describe such behavior of α_P quantitatively, one can therefore use the concept of an effective Pomeron intercept that is weakly dependent on energy. This effective Pomeron intercept will go over to a soft Pomeron ($\alpha_P \approx 1.06$–1.07) at low energies and a hard Pomeron ($\alpha_P \approx 1.2$–1.4) at high energies, and so on.

The effective Pomeron intercept depending on kinematical variables (on Q^2) was used previously to describe the anomalous growth of F_2 at low x [37]. But in that case, it was assumed that the intercept depends only on Q^2 and that only the soft Pomeron contributes to the photoproduction cross section. In recent years, however, it was sometimes hypothesized that a hard Pomeron may manifest itself even for $Q^2 \to 0$ [38]. This can be understood if the photoproduction limit is considered as a nonperturbative component in the low-x region. Since the regions of low Q^2 and x intersect for $Q^2 \to 0$, it would be reasonable to make an attempt at describing them in a unified manner with the aid of an effective Pomeron intercept.

It is known that, in the perturbative region, the dependence of α_P on x (and, hence, on energy) is used in the form of the square root of a logarithm [39]. Assuming that, in the limit of low Q^2, the effective Pomeron intercept exhibits the same functional growth with increasing energy, we can write

$$\alpha_P^{\text{eff}} = 1 + k_0\sqrt{\ln(s/M^2)}. \qquad (39)$$

In order to illustrate the potential of this formula, we compare the cross section $\sigma_{\gamma p}$ calculated on the basis of expression (39) with new experimental data on the photoproduction cross section that were obtained by the ZEUS collaboration at the HERA collider [40]. These data were deduced by rescaling the inelastic-electroproduction cross section measured in the low-Q^2 region ($\sim$0.5 GeV^2) to the value of $Q^2 = 0$ and are possibly plagued by some methodological error since there is a jumplike discrepancy between the ZEUS data and the results of other photoproduction experiments. Nevertheless, it can be seen from Fig. 4 that the energy dependence of the cross section is much stronger than that which is ensured by a soft Pomeron (dashed curve). The solid curve represents the cross section corresponding to the effective Pomeron intercept (39) at $k_0 = 0.028$.

Since there is no complete theory of Pomeron exchanges and inelastic processes in the low-x region, the energy dependence of α_P^{eff} can be chosen in some other form that does not contradict experimental data. In our opinion, however, the choice of α_P^{eff} in the form (39) gives hopes to develop a unified approach to describing the low-x region both for $Q^2 \to 0$ and for $\nu \to \infty$.

CONCLUSION

On the basis of the generalized vector-meson-dominance model and Regge theory, we have derived formulas that provide a unified description of the photoproduction cross section and structure functions in the limit of low Q^2.

The approach used here makes it possible to supplement, if necessary, the formula for the photoproduction cross section with resonance terms. In addition, it has been shown that the anomalous growth of the structure functions for inelastic scattering at low x and of the photoproduction cross section in the region of high energies can be described by using an effective Pomeron intercept.

In the present study, we have also obtained a formula for the virtual-photon-interaction cross section and a formula for the proton structure function at low Q^2 [Eqs. (33) and (38), respectively]. These formulas may serve as a guideline in ensuing searches for a unified approach to describing the inelastic-scattering cross section over the entire allowed region of kinematical variables.

APPENDIX

Region of Nucleon Resonances

In order to take into account the contributions of resonances, we represent the photoproduction cross section in the form

$$\sigma_{\gamma p}(E_\gamma) = \left\{\varphi(E_\gamma)\frac{\pi^3\alpha_e}{s}\int\limits_{u_0}^{\infty}\frac{du}{u^{1+\alpha(u)}}\right. \qquad (A.1)$$

$$\left. + \frac{1}{m_0^2}\sum_i A_i K_{\text{BW}}^{(i)}\right\}\theta(E_\gamma - m_{\text{thr}}),$$

where $\theta(x)$ is the Heaviside step function and

$$K_{\text{BW}}^{(i)} = \frac{(E_i^{\text{res}}\Gamma_i)^2}{(s-(E_i^{\text{res}})^2)^2 + (E_i^{\text{res}}\Gamma_i)^2} \qquad (A.2)$$

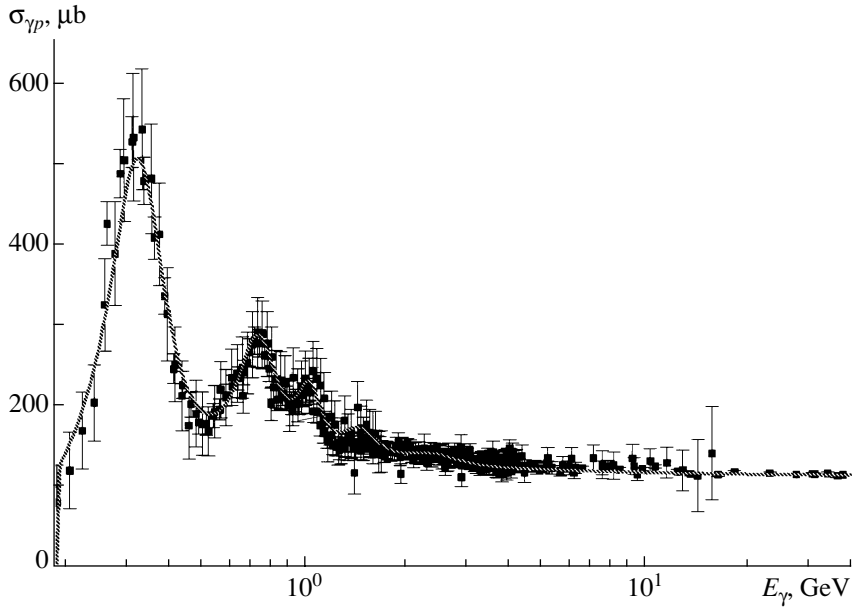

Fig. 5. Photoproduction cross section in the resonance region.

stands for functions that describe Breit–Wigner curves.

The function $\varphi(E_\gamma)$ specifies the threshold behavior of the cross section, its parameters usually being determined from a fit to experimental data (see, for example, [41]). If $\varphi(E_\gamma)$ is represented in the form

$$\varphi(E_\gamma) = \frac{E_\gamma - m_{\rm thr}}{E_b + E_\gamma - m_{\rm thr}}, \qquad \text{(A.3)}$$

then $m_{\rm thr}$ and E_b can be expressed in terms of the Δ-resonance parameters as

$$m_{\rm thr} = \frac{(M_\Delta - \Gamma_\Delta)^2 - M^2}{2M} \approx 190\ \text{MeV}, \qquad \text{(A.4)}$$

$$E_b = \frac{(M_\Delta + \Gamma_\Delta)^2 - M^2}{2M} \approx 505\ \text{MeV}. \qquad \text{(A.5)}$$

In Eq. (A.1), the number of terms that must be retained in order to describe the photoproduction cross section in the resonance region depends on the required accuracy. By way of example, available experimental data are contrasted in Fig. 5 against the results of the calculations by formula (A.1) that take into account five terms corresponding to the Δ resonance (P_{33}); the total contribution of the P_{11}, D_{13}, and S_{11} excitations; the F_{15} resonance; the total contribution of the S_{31}, F_{35}, and F_{37} resonances; and the contribution of heavy nucleon resonances, the values of the parameters Γ_i (in MeV), $E_i^{\rm res}$ (in MeV), and A_i being the following:

$$\begin{aligned}
&E_1^{\rm res} = 1220, \quad \Gamma_1 = 120, \quad A_1 = 0.55;\\
&E_2^{\rm res} = 1500, \quad \Gamma_2 = 160, \quad A_2 = 0.20;\\
&E_3^{\rm res} = 1680, \quad \Gamma_3 = 115, \quad A_3 = 0.10;\\
&E_4^{\rm res} = 1900, \quad \Gamma_4 = 230, \quad A_4 = 0.05;\\
&E_5^{\rm res} = 2300, \quad \Gamma_5 = 500, \quad A_5 = 0.02.
\end{aligned} \qquad \text{(A.6)}$$

From Fig. 5, it can be seen that good agreement with experimental data can be achieved by taking into account these five terms. If a higher precision is necessary, any number of resonances may be included in Eq. (A.1) by using the same procedure.

REFERENCES

1. S. D. Drell and J. D. Walecka, Ann. Phys. (N.Y.) **28**, 18 (1964).
2. G. Callan and D. J. Gross, Phys. Rev. Lett. **22**, 156 (1969).
3. L. N. Hand, Phys. Rev. **129**, 1834 (1963).
4. L. Stodolsky, Phys. Rev. Lett. **18**, 135 (1967).
5. J. J. Sakurai, Phys. Rev. Lett. **22**, 981 (1969).
6. I. Friedman and H. W. Kendal, Annu. Rev. Nucl. Part. Sci. **22**, 203 (1972).
7. J. J. Sakurai and D. Schildknecht, Phys. Lett. B **40B**, 121 (1972).
8. A. Bramon *et al.*, Phys. Lett. B **41B**, 609 (1972).
9. G. Shaw, Phys. Lett. B **228**, 25 (1989).
10. V. V. Borog and A. A. Petrukhin, in *Proceedings of the XIV International Cosmic Ray Conference, ICRC, 1975,* Vol. 6, p. 1949.
11. H. Fraas *et al.*, Nucl. Phys. B **86**, 346 (1975).

12. L. B. Bezrukov and É. V. Bugaev, Yad. Fiz. **32**, 1636 (1980) [Sov. J. Nucl. Phys. **32**, 847 (1980)].
13. G. Gounaris and S. Sarantakos, Phys. Rev. D **18**, 670 (1978).
14. R. P. Kokoulin and A. A. Petrukhin, in *Proceedings of Vulcano Workshop-1996 "Frontier Objects in Astrophysics and Particle Physics,"* Conf. Proc. Italian Phys. Soc. **57**, 379 (1997).
15. P. D. B. Collins, *An Introduction to Regge Theory and High Energy Physics* (Cambridge Univ. Press, Cambridge, 1977; Atomizdat, Moscow, 1980).
16. A. C. Irving and R. P. Worden, Phys. Rep. C **34**, 117 (1977).
17. G. Kerley and G. Shaw, Phys. Rev. D **56**, 7291 (1997).
18. Particle Data Group, Phys. Rev. D **54**, 182 (1996).
19. D. O. Caldwell *et al.*, Phys. Rev. Lett. **40**, 1222 (1978).
20. L. B. Bezrukov and É. V. Bugaev, Yad. Fiz. **33**, 1195 (1981) [Sov. J. Nucl. Phys. **33**, 635 (1981)].
21. B. A. Gordon *et al.*, Phys. Rev. D **20**, 2645 (1979).
22. M. Arneodo *et al.*, Nucl. Phys. B **483**, 3 (1997).
23. J. Breitweg *et al.*, hep-ex/0005018.
24. C. Adloff *et al.*, hep-ex/0012053.
25. M. Arneodo *et al.*, Nucl. Phys. B **333**, 1 (1990).
26. A. C. Benvenuti *et al.*, Phys. Lett. B **223**, 485 (1989).
27. L. W. Whitlow *et al.*, Phys. Lett. B **282**, 475 (1992).
28. H. Abramowicz *et al.*, Phys. Lett. B **269**, 465 (1991).
29. S. Aid *et al.*, Nucl. Phys. B **470**, 3 (1996).
30. C. Adloff *et al.*, Nucl. Phys. B **497**, 3 (1997).
31. M. Derrick *et al.*, Z. Phys. C **72**, 399 (1996).
32. J. Breitweg *et al.*, Phys. Lett. B **407**, 432 (1997).
33. A. Donnachie and P. V. Landshoff, Z. Phys. C **61**, 139 (1994).
34. H. Abramowicz and A. Levy, Preprint No. 97-251, DESY (1997).
35. A. B. Kaidalov, hep-ph/0103011.
36. J. G. Contreras *et al.*, Phys. Rev. D **62**, 034006 (2000).
37. A. Capella *et al.*, Phys. Lett. B **343**, 403 (1995).
38. P. V. Landshoff, hep-ph/0010315.
39. E. Gotsman *et al.*, Nucl. Phys. B **539**, 535 (1999).
40. C. Amelung, Nucl. Phys. B (Proc. Suppl.) **79**, 176 (1999).
41. S. Boffi *et al.*, Nucl. Phys. A **606**, 421 (1996).

Translated by A. Isaakyan

Physics of Atomic Nuclei, Vol. 66, No. 1, 2003, pp. 30–43. From Yadernaya Fizika, Vol. 66, No. 1, 2003, pp. 32–46.

Condensates in Quantum Chromodynamics*

B. L. Ioffe**

Institute of Theoretical and Experimental Physics,
Bol'shaya Cheremushkinskaya ul. 25, Moscow, 117218 Russia

Received March 6, 2002

Abstract—The paper presents a short review of our knowledge today on vacuum condensates in quantum chromodynamics (QCD). The condensates are defined as vacuum averages of the operators which arise due to nonperturbative effects. The important role of condensates in determining physical properties of hadrons and of their low-energy interactions in QCD is underlined. The special value of the quark condensate, connected to the existence of baryon masses, is mentioned. Vacuum condensates induced by external fields are discussed. QCD at low energy is checked on the basis of the data on hadronic τ decay. In theoretical analysis, the terms of perturbation theory (PT) up to α_s^3 are accounted for; in the operator product expansion (OPE), those up to dimension 8. The total probability of the decay $\tau \to$ hadrons (with zero strangeness) and of the τ-decay structure functions are best described at $\alpha_s(m_\tau^2) = 0.330 \pm 0.025$. It is shown that the Borel sum rules for τ-decay structure functions along the rays in the q^2-complex plane are in agreement with experiment, having an accuracy of $\sim 2\%$ at the values of the Borel parameter $|M^2| > 0.8$ GeV^2. The magnitudes of dimension 6 and 8 condensates were found, and the limitations on gluon condensates were obtained. The sum rules for the charmed-quark vector-current polarization operator were analyzed in three loops (i.e., in order α_s^2). The value of the charmed-quark mass (in an $\overline{MS}$ regularization scheme) was found to be $\overline{m}_c(\overline{m}_c^2) = 1.275 \pm 0.015$ GeV, and the value of gluon condensate was estimated as $\langle 0|(\alpha_s/\pi)G^2|0\rangle = 0.009 \pm 0.007$ GeV^4. The general conclusion is that the QCD described by PT + OPE is in good agreement with experiment at $Q^2 \gtrsim 1$ GeV^2. © *2003 MAIK "Nauka/Interperiodica".*

1. A FEW WORDS ABOUT IGOR' VASIL'EVICH

It is a great honor and at the same time a great pleasure for me to write a paper for the issue of *Physics of Atomic Nuclei* dedicated to 100th anniversary since the birth of Igor' Vasil'evich Kurchatov. Kurchatov was a very extraordinary person: an organizer of the highest class; I know of no one with such excellent organizational abilities. Without him, the Soviet atomic project would most likely not have been realized, at the least not in such short a time. Kurchatov had the strongest sense of responsibility not only for the work entrusted to him—the atomic project—but much wider—for the good of science in our country and, moreover, for the good of all whole mankind. I shall relate an episode not well known. As A.P. Aleksandrov witnessed [1], Kurchatov was deeply depressed when returning from the tests of the first hydrogen bomb (those who were present at the tests noticed the same). He said, "What a terrible thing we have made. The only thing we should worry about is to forbid all of this and to exclude nuclear war." In March 1954, Kurchatov, Alikhanov, Kikoin, and Vinogradov wrote a paper in which they concluded that mankind faces the menace of the end of all of life on earth. The paper was also signed by the Minister of the Medium Machine Building V.A. Malyshev, who sent it to Malenkov, Khrushchev, and Molotov. Khrushchev, however, rejected the paper, calling the words on the possible ruin of world civilization "theoretically wrong and politically harmful" (see [2]). The position of the Soviet leaders remained as before: world war should lead to the fall of the capitalism.

The same responsibility was inherent to Kurchatov when constructing atomic reactors and atomic power stations—I gave examples of this earlier [3]. I think that, if Kurchatov were alive, RBMK reactors, principally unsafe as physical systems, would not have been built and we would have avoided the Chernobyl catastrophe. However, on the other hand, Igor' Vasil'evich was a person of his time... (see [3]).

He liked science and, first of all, his main specialty—nuclear physics. He was deeply interested in the development of elementary particle physics, and he thought it necessary to develop such investigations in the Soviet Union. He supported the suggestion of Alikhanov and Vladimirsky to construct the 7-GeV hard-focusing proton accelerator at the Institute of

*This article was submitted by the author in English.

**e-mail: ioffe@vitep1.itep.ru

Theoretical and Experimental Physics (ITEP), and then, using the ITEP project, of the 50-GeV proton accelerator (later, 70 GeV) near Serpukhov. In 1954, such a decision was adopted at the meeting of the Scientific-Technical Council at the Ministry of Medium Machine Building chaired by Kurchatov.

2. INTRODUCTION

Nowadays, it has been reliably established that the true (microscopic) theory of strong interaction is quantum chromodynamics (QCD), a gauge theory of interacting quarks and gluons. It has also been established that, unlike, e.g., quantum electrodynamics (QED), a vacuum in QCD has a nontrivial structure: due to nonperturbative effects, i.e., not admitting expansion in the interaction constant (even if it is small), nonzero fluctuations of gluon and quark fields persist in a QCD vacuum. (Examples of such nonperturbative fields are instantons [4]—classical solutions of equations for a gluon field, which realize the minimum of actions in the QCD Lagrangian.)[1)] The nontrivial structure in QCD manifests itself in the presence of vacuum condensates, analogous to those in condensed matter physics (for instance, spontaneous magnetization). Vacuum condensates are very important in elucidating the QCD structure and in describing hadron properties at low energies. Condensates, in particular, quark and gluon, have been investigated since the 1970s. Here, first should be noted the QCD sum rule method by Shifman, Vainshtein, and Zakharov [5], which is based on the idea of the leading role of condensates in the calculation of masses of the low-lying hadronic states. In the papers of 1970s–1980s, it was adopted that the perturbative interaction constant is comparatively small (e.g., $\alpha_s(1\ \mathrm{GeV}) \approx 0.3$), so that it is enough to restrict oneself to the first-order terms in α_s and sometimes even disregard perturbative effects in the region of masses larger than 1 GeV. At present, it is clear that α_s is considerably larger ($\alpha_s(1\ \mathrm{GeV}) \sim 0.6$). In a number of cases, there have appeared results of perturbative calculations in orders α_s^2 and α_s^3. New, more precise experimental data at low energies were obtained. Thereby, on one hand, it is necessary, and on the other, it appears possible, to compare QCD with experiment in the low energy region on a higher level of precision. The results of such a comparison are presented in this paper.

In Section 3, I define condensates, describe their properties, and give numerical values obtained previously. In Section 4, the data on hadronic decays of a τ lepton are compared with theoretical expectations obtained on the basis of the operator product expansion in QCD with perturbative terms up to α_s^3 taken into account. The values of condensates and the coupling constant $\alpha_s(m_\tau^2)$ are obtained. In Section 5, the polarization operator of the vector current of charmed quarks is analyzed in the three-loop approximation (i.e., taking into account terms $\sim\alpha_s^2$), the value of the charmed quark and the value of gluon condensate are found. Section 6 presents our conclusions.

3. DEFINITION OF CONDENSATES AND THEIR MAIN PROPERTIES

In QCD (or in the more general case, in quantum field theory) by condensates are meant the vacuum mean values $\langle 0|O_i|0\rangle$ of local (i.e., taken at a single spacetime point) operators $O_i(x)$, which arise due to nonperturbative effects. The latter point is very important and needs clarification. When determining vacuum condensates, averaging only over nonperturbative fluctuations is implied. If, for some operator O_i, the nonzero vacuum mean value appears also in perturbation theory, it should not be taken into account in determining the condensate—in other words, when determining condensates the perturbative vacuum mean values should be subtracted in the calculation of the vacuum averages. One more specification is necessary. The perturbation theory series in QCD are asymptotic. So, vacuum mean operator values may appear due to one or another summing of asymptotic series. Such vacuum mean values are commonly referred to as vacuum condensates.

Separation of perturbative and nonperturbative contributions to vacuum mean values has some arbitrariness. Usually [6, 7], this arbitrariness is avoided by introduction of some normalization point μ^2 ($\mu^2 \sim 1\ \mathrm{GeV}^2$). Integration over momenta of virtual quarks and gluons in the region below μ^2 is referred to as condensates; above μ^2, to perturbative theory. In such a formulation, condensates depend on the normalization point μ: $\langle 0|O_i|0\rangle = \langle 0|O_i|0\rangle_\mu$. Other methods for determining condensates are also possible (see below).

In perturbation theory, corrections to the condensates appear as a series in the coupling constant $\alpha_s(\mu)$:

$$\langle 0|O_i|0\rangle_Q = \langle 0|O_i|0\rangle_\mu \sum_{n=0}^{\infty} C_n^{(i)}(Q,\mu)\alpha_s^n(\mu). \quad (1)$$

The running coupling constant α_s on the right-hand side of (1) is normalized at the point μ. The left-hand side of (1) represents the value of the condensate normalized at the point Q. Coefficients $C_n^{(i)}(Q,\mu)$

[1)] This statement refers to Euclidean space; in the Minkowski space, instantons realize tunneling transitions between Hilbert spaces with different topological quantum numbers.

may have logarithms $\ln Q^2/\mu^2$ in powers up to n for $C_n^{(i)}$. Summing up the terms with highest powers of logarithms leads to the appearance of the so-called anomalous dimension of operators, so that in a general form it can be written as

$$\langle 0|O_i|0\rangle_Q = \langle 0|O_i|0\rangle_\mu \left(\frac{\alpha_s(\mu)}{\alpha_s(Q)}\right)^\gamma \times \sum_{n=0}^{\infty} c_n^{(i)}(Q,\mu)\alpha_s^n(\mu), \quad (2)$$

where γ is an anomalous dimension (number) and $c_n^{(i)}$ already has no leading logarithms. If there exist several operators of the given (canonical) dimension, then their mixing is possible in perturbation theory. Then (1), (2) become matrix relations.

In their physical properties, condensates in QCD have much in common with condensates appearing in condensed matter physics such as superfluid liquid (Bose condensate) in liquid ^{4}He, a Cooper pair condensate in a superconductor, and spontaneous magnetization in magnets. This is why, analogous to effects in the physics of condensed matter, it can be expected that if one considers QCD at a finite temperature T, with T increasing at some $T = T_c$, there will be a phase transition and condensates (or a part of them) will be destroyed. Particularly, such a phenomenon must hold for condensates responsible for spontaneous symmetry breaking—at $T = T_c$ they should vanish and symmetry must be restored. (In principle, surely, QCD may have a few phase transitions.)

Condensates in QCD are divided into two types: conserving and violating chirality. As is known, the masses of u, d, s light quarks in the QCD Lagrangian are small compared to the characteristic scale of hadronic masses $M \sim 1$ GeV. In neglecting light quark masses, the QCD Lagrangian becomes chiral-invariant: left-hand and right-hand (in chirality) light quarks do not interact with each other, and both vector and axial currents are conserved (except for a flavor-singlet axial current, the nonconservation of which is due to an anomaly). The accuracy of neglecting light quark masses corresponds to the accuracy of isotopical symmetry, i.e., a few percent in the case of u and d quarks and of the accuracy of SU(3) symmetry, i.e., 10–15% in the case of s quarks. In the case of condensates violating chiral symmetry, perturbative vacuum mean values are proportional to light quark masses and are zero within $m_u = m_d = m_s = 0$. So, such condensates are determined in the theory much better than those conserving chirality and, in principle, may be found experimentally with higher accuracy.

Among chiral-symmetry-violating condensates of most importance is the quark condensate $\langle 0|\bar{q}q|0\rangle$ ($q = u, d$ are the fields of u and d quarks). $\langle 0|\bar{q}q|0\rangle$ may be written in the form

$$\langle 0|\bar{q}q|0\rangle = \langle 0|\bar{q}_L q_R + \bar{q}_R q_L|0\rangle, \quad (3)$$

where q_L, q_R are the fields of left-hand and right-hand (in chirality) quarks. As follows from (3), the nonzero value of quark condensate means the transition of left-hand quark fields into right-hand ones and its not small value would mean chiral-symmetry violation in QCD. (If chiral symmetry is not violated, then, at small m_u, m_d, $\langle 0|\bar{q}q|0\rangle \sim m_u, m_d$.) By virtue of isotopical invariance,

$$\langle 0|\bar{u}u|0\rangle = \langle 0|\bar{d}d|0\rangle. \quad (4)$$

For a quark condensate there holds the Gell-Mann–Oakes–Renner relation [8]

$$\langle 0|\bar{q}q|0\rangle = -\frac{1}{2}\,\frac{m_\pi^2 f_\pi^2}{m_u + m_d}. \quad (5)$$

Here m_π, f_π are the mass and constant of π^+-meson decay ($m_\pi = 140$ MeV, $f_\pi = 131$ MeV); m_u and m_d are the masses of u and d quarks. Relation (5) is obtained in the first order in m_u, m_d, m_s (for its derivation, see, e.g., [9]). To estimate the value of a quark condensate, one may use the values of quark masses $m_u = 4.2$ MeV, $m_d = 7.5$ MeV [9]. (These values were suggested by Weinberg [10]; within the errors they coincide with other estimates—see, for example, [11].) Substituting these values into (5) we get

$$\langle 0|\bar{q}q|0\rangle = -(243\ \text{MeV})^3. \quad (6)$$

Value (6) has a characteristic hadronic scale. This shows that chiral symmetry, which is fulfilled with good accuracy in the light quark Lagrangian ($m_u, m_d/M \simeq 0.01$, M is hadronic mass scale, $M \sim 0.5$–1 GeV), is spontaneously violated in the hadronic-state spectrum.

Another argument in favor of spontaneous violation of chiral symmetry in QCD is the existence of massive baryons. Indeed, in the chiral-symmetry theory, all fermionic states should be either massless or parity-degenerate. Obviously, baryons, in particular, nucleons, do not possess this property. It can be shown [9, 12] that both these phenomena—the presence of the chiral-symmetry-violating quark condensate and the existence of massive baryons—are closely connected with each other. According to the Goldstone theorem, the spontaneous symmetry violation leads to the appearance of massless particles in the physical-state spectrum—of Goldstone bosons. In QCD, Goldstone bosons can be identified with a π-meson triplet within $m_u, m_d \to 0$, $m_s \neq 0$ (SU(2) symmetry) or with an octet of pseudoscalar mesons (π, K, η) within the limit $m_u, m_d, m_s \to 0$ (SU(3)

symmetry). The presence of Goldstone bosons in QCD makes it possible to formulate the low-energy chiral effective theory of strong interactions (see reviews [9, 13, 14]).

A quark condensate may be considered as an order parameter in QCD corresponding to spontaneous violation of chiral symmetry. At the temperature of restoration of the chiral symmetry $T = T_c$ it must vanish. The investigation of the temperature dependence of quark condensate in chiral effective theory [15] (see also the review [9]) shows that $\langle 0|\bar{q}q|0\rangle$ vanishes at $T = T_c \approx 150$–200. Similar indications were obtained also in the lattice calculations [16].

Thus, the quark condensate (1) has the lowest dimensions ($d = 3$) as compared with other condensates in QCD, (2) determines masses of usual (nonstrange) baryons, and (3) is the order parameter in the phase transition between the phases of violated and restored chiral symmetry. These three facts determine its important role in low-energy hadronic physics.

Let us estimate the accuracy of the numerical value of (6). The Gell-Mann–Oakes–Renner relation is derived up to correction terms linear in quark masses. In the chiral effective theory, one succeeds in estimating the correction terms and thereby the accuracy of Eq. (5) appears of order 10%. However, it is not a single origin of errors in determining the quark condensate value. The quark condensate, as well as quark masses, depends on the normalization point and has anomalous dimensions equal to $\gamma_m = -\gamma_{\bar{q}q} = \frac{4}{9}$. In the mass values taken above, normalization point μ was not fixed exactly (in fact, it was taken as $\mu \sim 1$ GeV). In addition, the accuracy of the above value of $m_u + m_d = 11.7$ MeV which enters into (5) seems to be on the order of 10–20%. The value of the quark condensate may be also found from the sum rules for the proton mass. Analysis [17] gave for it a value very close to (6) (with a 3% difference) at normalization point $\mu = 1$ GeV. The accuracy of these sum rules seems to be on the order of 10–15%. Concludingly, it may be believed that the value of the quark condensate is given by (6) at normalization point $\mu = 1$ GeV with 10–20% accuracy. The quark condensate of strange quarks somewhat differs from $\langle 0|\bar{u}u|0\rangle$. In [12] it was found that

$$\langle 0|\bar{s}s|0\rangle/\langle 0|\bar{u}u|0\rangle = 0.8 \pm 0.1. \qquad (7)$$

The next, in dimension ($d = 5$), condensate violating chiral symmetry is quark gluonic one:

$$-g\left\langle 0\left|\bar{q}\sigma_{\mu\nu}\frac{\lambda^n}{2}G^n_{\mu\nu}q\right|0\right\rangle \equiv m_0^2\langle 0|\bar{q}q|0\rangle. \qquad (8)$$

Here $G^n_{\mu\nu}$ is the gluon field strength tensor, λ^n are the Gell-Mann matrices, and $\sigma_{\mu\nu} = (i/2)(\gamma_\mu\gamma_\nu - \gamma_\nu\gamma_\mu)$. The value of parameter m_0^2 was found in [18] from the sum rules for baryonic resonances,

$$m_0^2 = 0.8 \text{ GeV}^2. \qquad (9)$$

Consider now condensates conserving chirality. Playing the fundamental role here is the gluon condensate of the lowest dimension:

$$\left\langle 0\left|\frac{\alpha_s}{\pi}G^n_{\mu\nu}G^n_{\mu\nu}\right|0\right\rangle. \qquad (10)$$

Due to the fact that the gluon condensate is proportional to the vacuum mean value of the trace of the energy–momentum tensor $\theta_{\mu\nu}$, its anomalous dimension is zero. The existence of the gluon condensate was first indicated by Shifman, Vainshtein, and Zakharov [5]. They also obtained, from the sum rules for charmonium, its numerical value:

$$\left\langle 0\left|\frac{\alpha_s}{\pi}G^n_{\mu\nu}G^n_{\mu\nu}\right|0\right\rangle = 0.012 \text{ GeV}^4. \qquad (11)$$

As was shown by the same authors, the nonzero and positive value of gluon condensate means that the vacuum energy is negative in QCD: the vacuum energy density in QCD is given by $\varepsilon = -(9/32)\langle 0|(\alpha_s/\pi)G^2|0\rangle$. Therefore, if a quark is embedded in the vacuum, this results in its excitation, i.e., in increasing energy. In this way, the explanation of the bag model could be obtained in QCD: in the domain around the quark there appears an excess of energy, which is treated as the energy density B in the bag model [although the magnitude of B probably does not agree with the value of ε that follows from (11)]. In [5], perturbative effects were taken into account only in the order α_s, the value for α_s being taken twice smaller than the modern one. Later, many attempts were made to determine the value of the gluon condensate by studying various processes and applying various methods. However, the results of different approaches were inconsistent with each other and with (11), and sometimes the difference was even very large—the values of the condensate appeared to be severalfold larger. All of this requires reanalyzation of $\langle 0|\frac{\alpha_s}{\pi}G^2|0\rangle$ determination based on contemporary values which will be performed in Sections 4 and 5.

The $d = 6$ gluon condensate has the form

$$g^3 f^{abc}\langle 0|G^a_{\mu\nu}G^b_{\nu\lambda}G^c_{\lambda\mu}|0\rangle \qquad (12)$$

(f^{abc} are structure constants of the SU(3) group). There are no reliable methods to determine it from experimental data. There is only an estimate which follows from the method of dilute instanton gas [19]:

$$g^3 f^{abc}\langle 0|G^a_{\mu\nu}G^b_{\nu\lambda}G^c_{\lambda\mu}|0\rangle = \frac{4}{5}(12\pi^2) \qquad (13)$$

$$\times \frac{1}{\rho_c^2}\left\langle 0\left|\frac{\alpha_s}{\pi}G_{\mu\nu}^2\right|0\right\rangle,$$

where ρ_c is the instanton effective radius in the given model (for an estimation, one may take $\rho_c \sim 1/3{-}1/2$ fm).

The general form of $d = 6$ condensates is

$$\alpha_s\langle 0|\bar{q}_i O_\alpha q_i \cdot \bar{q}_k O_\alpha q_k|0\rangle, \tag{14}$$

where q_i, q_k are quark fields of u, d, s quarks and O_α are Dirac and $SU(3)$ matrices. Following [5], Eq. (14) is usually factorized: in the sum over the intermediate state in all channels (i.e., if necessary, after Fierz transformation), only the vacuum state is taken into account. The accuracy of such an approximation is $\sim 1/N_c^2$, where N_c is the number of colors, i.e., $\sim 10\%$. After factorization Eq. (14) reduces to

$$\alpha_s\langle 0|\bar{q}q|0\rangle^2. \tag{15}$$

The anomalous dimension of (15) is $1/9$, and it can be approximately set to zero. Finally, the $d = 8$ quark condensates, assuming factorization, reduce to

$$\alpha_s\langle 0|\bar{q}q|0\rangle \cdot m_0^2\langle 0|\bar{q}q|0\rangle. \tag{16}$$

(The notation of (8) is used.) It should be noted, however, that the factorization procedure in the $d = 8$ condensate case is uncertain. For this reason, it is necessary to require that their contribution be small.

Let us also dwell on one more type of condensates—those induced by external fields. The meaning of such condensates can be easily understood by comparison with analogous phenomena in the physics of condensed media. If the above-considered condensates can be compared, for instance, with ferromagnets, where magnetization is present even in the absence of external magnetic field, condensates induced by external field are similar to dia- or paramagnetic materials. Consider the case of the constant external electromagnetic field $F_{\mu\nu}$. In its presence there appears a condensate induced by external field (in the linear approximation in $F_{\mu\nu}$):

$$\langle 0|\bar{q}\sigma_{\mu\nu}q|0\rangle_F = e_q\chi F_{\mu\nu}\langle 0|\bar{q}q|0\rangle. \tag{17}$$

As was shown in [20], in a good approximation, $\langle 0|\bar{q}\sigma_{\mu\nu}q|0\rangle_F$ is proportional to e_q—the charge of quark q. The field-induced vacuum expectation value $\langle 0|\bar{q}\sigma_{\mu\nu}q|0\rangle_F$ violates chiral symmetry. So, it is natural to separate $\langle 0|\bar{q}q|0\rangle$ as a factor in Eq. (17). The universal quark-flavor-independent quantity χ is called the magnetic susceptibility of the quark condensate. Its numerical value was found in [21] using a special sum rule:

$$\chi = -(5.7 \pm 0.6)\ \mathrm{GeV}^{-2}. \tag{18}$$

Another example is external constant axial isovector field A_μ, the interaction of which with light quarks is described by the Lagrangian

$$L' = (\bar{u}\gamma_\mu\gamma_5 u - \bar{d}\gamma_\mu\gamma_5 d)A_\mu. \tag{19}$$

In the presence of this field, there appear condensates induced by it:

$$\langle 0|\bar{u}\gamma_\mu\gamma_5 u|0\rangle_A = -\langle 0|\bar{d}\gamma_\mu\gamma_5 d|0\rangle_A = f_\pi^2 A_\mu, \tag{20}$$

where $f_\pi = 131$ MeV is the constant of $\pi \to \mu\nu$ decay. The right-hand side of Eq. (20) is obtained assuming $m_u, m_d \to 0$, $m_\pi^2 \to 0$ and follows directly from consideration of the polarization operator of axial currents $\Pi_{\mu\nu}^A(q)$ in the limit $q \to 0$, when the nonzero contribution to $\Pi_{\mu\nu}^A(q)_{q\to 0}$ emerges only from a one-pion intermediate state. Equality (20) was used to calculate the axial coupling constant q_A in β decay [22]. A relation analogous to (20) holds in the case of an octet axial field. Of special interest is the condensate induced by the singlet (in flavors) constant axial field,

$$\langle 0|j_{\mu 5}^{(0)}|0\rangle = 3f_0^2 A_\mu^{(0)}, \tag{21}$$

$$j_{\mu 5}^{(0)} = \bar{u}\gamma_\mu\gamma_5 u + \bar{d}\gamma_\mu\gamma_5 d + \bar{s}\gamma_\mu\gamma_5 s, \tag{22}$$

and the Lagrangian of interaction with external field has the form

$$L' = j_{\mu 5}^{(0)} A_\mu^{(0)}. \tag{23}$$

Constant f_0 cannot be calculated by the method used when deriving Eq. (20), since the singlet axial current is not conserved by virtue of anomaly and the singlet pseudoscalar meson η' is not a Goldstone particle. Constant f_0^2 is proportional to the topological susceptibility of a vacuum [23],

$$f_0^2 = \frac{4}{3}N_f^2\chi'(0), \tag{24}$$

where N_f is the number of light quarks, $N_f = 3$, and the topological susceptibility of the vacuum $\chi(q^2)$ is defined as

$$\chi(q^2) = i\int d^4x e^{iqx}\langle 0|T\{Q_5(x), Q_5(0)\}|0\rangle. \tag{25}$$

$$Q_5(x) = \frac{\alpha_s}{8\pi}G_{\mu\nu}^n(x)G_{\mu\nu}^n(x). \tag{26}$$

Using the QCD sum rule, one may relate f_0^2 to the part of proton spin Σ carried by quarks in polarized ep (or μp) scattering [23]. The value of f_0^2 was found from the self-consistency condition of the sum rule obtained (or from the experimental value of Σ):

$$f_0^2 = (2.8 \pm 0.7) \times 10^{-2}\mathrm{GeV}^2. \tag{27}$$

The related value of the derivative at $q^2 = 0$ of vacuum topological susceptibility $\chi'(0)$ (more precisely, its nonperturbative part) is equal to

$$f_0^2 = (2.8 \pm 0.7) \times 10^{-2}\ \mathrm{GeV}^2. \qquad (28)$$

The value $\chi'(0)$ is of essential interest for studying vacuum properties in QCD.

4. TEST OF QCD AT LOW ENERGIES ON THE BASIS OF τ DECAY: DETERMINATION OF $\alpha_s(m_\tau^2)$ AND CONDENSATE VALUES

Recently, collaborations ALEPH [24], OPAL [25] and CLEO [26] measured with good accuracy the relative probability of hadronic decays of τ lepton $R_\tau = B(\tau \to \nu_\tau + \text{hadrons})/B(\tau \to \nu_\tau e\overline{\nu}_e)$ and the vector (V) and axial (A) spectral functions. Below I present the results of the theoretical analysis of these data based on the operator product expansion (OPE) in QCD [27, 28]. In the perturbation theory series, the terms up to α_s^3 will be taken into account; in OPE, the operators up to dimension 8.

Consider the polarization operator of hadronic currents,

$$\Pi^J_{\mu\nu}(q) = i\int e^{iqx}\langle TJ_\mu(x)J_\nu(0)^\dagger\rangle dx \qquad (29)$$

$$= (q_\mu q_\nu - g_{\mu\nu}q^2)\Pi_J^{(1)}(q^2) + q_\mu q_\nu \Pi_J^{(0)}(q^2),$$

where

$$J = V, A; \quad V_\mu = \bar{u}\gamma_\mu d, \quad A_\mu = \bar{u}\gamma_\mu\gamma_5 d.$$

The spectral functions measured in τ decay are imaginary parts of $\Pi_J^{(1)}(s)$ and $\Pi_J^{(0)}(s)$, $s = q^2$,

$$v_1/a_1(s) = 2\pi\mathrm{Im}\Pi^{(1)}_{V/A}(s + i0), \qquad (30)$$

$$a_0(s) = 2\pi\mathrm{Im}\Pi_A^{(0)}(s + i0).$$

Functions $\Pi_V^{(1)}(q^2)$ and $\Pi_A^{(0)}(q^2)$ are analytical functions in the q^2 complex plane with a cut along the right-hand semiaxis starting from $4m_\pi^2$ for $\Pi_V^{(1)}(q^2)$ and $9m_\pi^2$ for $\Pi_A^{(0)}(q^2)$. Function $\Pi_A^{(1)}(q^2)$ has kinematical pole at $q^2 = 0$. This is a specific feature of QCD following from chiral symmetry within massless u and d quarks and from spontaneous violation of it. The kinematical pole appears due to the one-pion state contribution to $\Pi_A(q)$, which has the form [27]

$$\Pi^A_{\mu\nu}(q)_\pi = -\frac{f_\pi^2}{q^2}(q_\mu q_\nu - g_{\mu\nu}q^2) - \frac{m_\pi^2}{q^2}q_\mu q_\nu \frac{f_\pi^2}{q^2 - m_\pi^2}. \qquad (31)$$

Consider first the ratio of the total probability of hadronic decays of τ leptons into states with zero strangeness to the probability of $\tau \to \nu_\tau e\overline{\nu}_e$. This ratio is given by the equality [29]

$$R_{\tau,V+A} = \frac{B(\tau \to \nu_\tau + \text{hadrons}_{S=0})}{B(\tau \to \nu_\tau e\bar{\nu}_e)} \qquad (32)$$

$$= 6|V_{ud}|^2 S_{\mathrm{EW}} \int\limits_0^{m_\tau^2} \frac{ds}{m_\tau^2}\left(1 - \frac{s}{m_\tau^2}\right)^2$$

$$\times \left[\left(1 + 2\frac{s}{m_\tau^2}\right)(v_1 + a_1 + a_0)(s) - 2\frac{s}{m_\tau^2}a_0(s)\right],$$

where $|V_{ud}| = 0.9735 \pm 0.0008$ is the matrix element of the Kobayashi–Maskawa matrix; $S_{\mathrm{EW}} = 1.0194 \pm 0.0040$ is the electroweak correction [30]. Only the one-pion state practically contributes to the last term in (32) and it appears to be small:

$$\Delta R_\tau^{(0)} = -24\pi^2 \frac{f_\pi^2 m_\pi^2}{m_\tau^4} = -0.008. \qquad (33)$$

Denote

$$\omega(s) \equiv v_1 + a_1 + a_0 \qquad (34)$$

$$= 2\pi\mathrm{Im}[\Pi_V^{(1)}(s) + \Pi_A^{(1)}(s) + \Pi_A^{(0)}(s)] \equiv 2\pi\mathrm{Im}\Pi(s).$$

As follows from Eq. (31), $\Pi(s)$ has no kinematical pole, but only a right-hand cut. It is convenient to transform the integral in Eq. (32) into that over the circle of radius m_τ^2 in the complex s plane [31–33]:

$$R_{\tau,V+A} = 6\pi i|V_{ud}|^2 S_{\mathrm{EW}} \oint\limits_{|s|=m_\tau^2} \frac{ds}{m_\tau^2}\left(1 - \frac{s}{m_\tau^2}\right)^2 \qquad (35)$$

$$\times \left(1 + 2\frac{s}{m_\tau^2}\right)\Pi(s) + \Delta R_\tau^{(0)}.$$

Calculate first the perturbative contribution to Eq. (35). To this end, use the Adler function $D(Q^2)$:

$$D(Q^2) \equiv -2\pi^2 \frac{d\Pi(Q^2)}{d\ln Q^2} = \sum_{n\geq 0} K_n a^n, \qquad (36)$$

$$a \equiv \alpha_s/\pi, \qquad Q^2 \equiv -s,$$

the perturbative expansion of which is known up to terms of $\sim \alpha_s^3$. In the $\overline{MS}$ regularization scheme, $K_0 = K_1 = 1$, $K_2 = 1.64$ [34], $K_3 = 6.37$ [35] for three flavors, and for K_4 there is the estimate $K_4 = 25 \pm 25$ [36]. The renormalization-group equation yields

$$\frac{da}{d\ln Q^2} = -\beta(a) = -\sum_{n\geq 0}\beta_n a^{n+2} \qquad (37)$$

$$\to \ln\frac{Q^2}{\mu^2} = -\int\limits_{a(\mu^2)}^{a(Q^2)} \frac{da}{\beta(a)}.$$

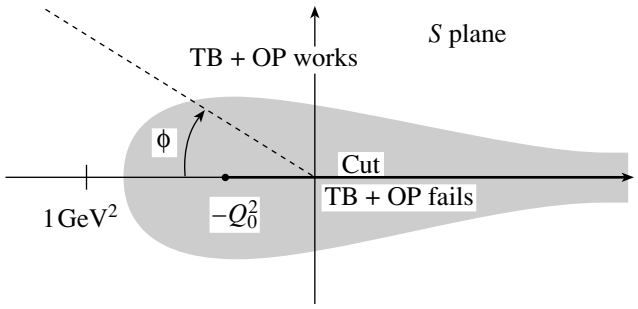

Fig. 1. The applicability region of PT and OE in the complex plane s. In the dashed region, PT + OE does not work.

In the $\overline{MS}$ scheme for three flavors $\beta_0 = 9/4$, $\beta_1 = 4$, $\beta_2 = 10.06$, $\beta_3 = 47.23$ [37, 38]. Integrating over Eq. (36) and using Eq. (38) we get

$$\Pi(Q^2) = \frac{1}{2\pi^2} \int\limits_{a(\mu^2)}^{a(Q^2)} D(a) \frac{da}{\beta(a)}. \qquad (38)$$

Set $\mu^2 = m_\tau^2$ and choose some (arbitrary) value $a(m_\tau^2)$. With the help of Eq. (37) one may then determine $a(Q^2)$ for any Q^2 and by analytical continuation for any s in the complex plane. Then, calculating (38), find $\Pi(s)$ in the whole complex plane. Substitution of $\Pi(s)$ into Eq. (35) determines R_τ for the given $a(m_\tau^2)$ up to power corrections. Thereby, knowing R_τ from experiment, it is possible to find the $a(m_\tau^2)$ corresponding to it. Note that, with such an approach, there is no need to expand the denominator in Eqs. (37) and (38) in the inverse powers of $\ln Q^2/\mu^2$. Particularly, there is no expansion on the right-hand semiaxis in powers of the parameter $\pi/\ln(Q^2/\mu^2)$, which is not small in the investigated region of Q^2. Advantages of transformation of the integral over the real axis (32) in the contour integral are as follows. It can be expected that the applicability region of the theory presented as PT + OPE in the complex s plane is off the shadowed region in Fig. 1. It is evident that at positive and comparatively small s, PT + OPE do not work. At negative $s = -Q^2$ in the α_s order, a nonphysical pole appears; in higher orders, according to (9), it is replaced by a nonphysical cut, which starts from point $-Q_0^2$, determined by the formula

$$\ln \frac{Q_0^2}{\mu^2} = - \int\limits_{a(\mu^2)}^{\infty} \frac{da}{\beta(a)}. \qquad (39)$$

Integration over the contour allows one to obviate the dashed region in Fig. 1 [except for the vicinity of the positive semiaxis, the contribution of which is suppressed by the factor $(1 - \frac{s}{m_\tau^2})^2$ in Eq. (6)], i.e., to work in the applicability region of PT + OPE. The OPE terms, i.e., power corrections to the polarization operator, are given by formula (5):

$$\Pi(s)_{\text{nonpert}} = \sum_{n\geq 2} \frac{\langle O_{2n}\rangle}{(-s)^n}\left(1 + c_n \frac{\alpha_s}{\pi}\right) \qquad (40)$$

$$\times \frac{\alpha_s}{6\pi Q^4}\langle G^a_{\mu\nu} G^a_{\mu\nu}\rangle \left(1 + \frac{7}{6}\frac{\alpha_s}{\pi}\right) + \frac{128}{81 Q^6}\pi\alpha_s \langle \bar{q}q\rangle^2$$

$$\times \left[1 + \left(\frac{29}{24} + \frac{17}{18}\ln\frac{Q^2}{\mu^2}\right)\frac{\alpha_s}{\pi}\right] + \frac{\langle O_8\rangle}{Q^8}$$

(α_s corrections to the first and second terms in Eq. (39) were calculated in [39] and [40], respectively). Contributions of the operator with $d = 2$ proportional to m_u^2, m_d^2 and of the condensate $2(m_u + m_d)\langle 0|\bar{q}q|0\rangle$ are neglected. (The latter is an order of magnitude smaller than the gluon condensate contribution.) In calculating the $d = 6$ term, factorization hypothesis was used. It can be readily seen that $d = 4$ condensates (up to small α_s corrections) give no contribution to the integral over contour in Eq. (35). The contribution from the condensate $\langle O_8\rangle$ may be estimated as $|\langle O_8\rangle| < 10^{-3}$ GeV^8 and appears to be negligibly small. $R_{\tau,V+A}$ may be represented as

$$R_{\tau,V+A} = 3|V_{ud}|^2 S_{\text{EW}}\left(1 + \delta'_{\text{em}} + \delta^{(0)} + \delta^{(6)}_{V+A}\right) \qquad (41)$$

$$+ \Delta R^{(0)} = 3.475 \pm 0.022,$$

where $\delta'_{em} = (5/12\pi)\alpha_{em}(m_\tau^2) = 0.001$ is the electromagnetic correction [41], $\delta^{(6)}_{A+V} = -(5 \pm 2) \times 10^{-3}$ is the contribution of the $d = 6$ condensate (see below), and $\delta^{(0)}$ is the PT correction. The right-hand side presents the experimental value obtained as a difference between the total probability of hadronic decays $R_\tau = 3.636 \pm 0.021$ [42] and the probability of decays in states with the strangeness $S = -1 R_{\tau,s} = 0.161 \pm 0.007$ [43, 44]. For perturbative correction it follows from Eq. (41) that

$$\delta^{(0)} = 0.206 \pm 0.010. \qquad (42)$$

Employing the above-described method in [28], the constant $\alpha_s(m_\tau^2)$ was found from (42):

$$\alpha_s(m_\tau^2) = 0.355 \pm 0.025. \qquad (43)$$

The calculation was made taking into account terms $\sim\alpha_\tau^3$; the estimate of the effect of the terms $\sim\alpha_s^4$ is accounted for in the error. Perhaps the error is underestimated (by 0.010–0.015), since the theoretical and experimental errors were added in quadratures.

I determine now the values of condensates based on the data [24–26] on spectral functions. It is convenient first to consider the difference $\Pi_V - \Pi_A$, which is not contributed by perturbative terms and there remains only the OPE contribution:

$$\Pi_V^{(1)}(s) - \Pi_A^{(1)}(s) = \sum_{d\geq 4} \frac{O_d^{V-A}}{(-s)^{d/2}} \left(1 + c_d \frac{\alpha_s}{\pi}\right). \quad (44)$$

The gluon-condensate contribution falls out in the $V - A$ difference, and only the following condensates with $d = 4, 6, 8$ remain:

$$O_4^{V-A} = 2(m_u + m_d)\langle \bar{q}q\rangle = -f_\pi^2 m_\pi^2, \quad (45)$$

$$O_6^{V-A} = 2\pi\alpha_s \langle (\bar{u}\gamma_\mu \lambda^a d)(\bar{d}\gamma_\mu \lambda^a u) \quad (46)$$
$$- (\bar{u}\gamma_5\gamma_\mu \lambda^a d)(\bar{d}\gamma_5\gamma_\mu \lambda^a u)\rangle = -\frac{64\pi\alpha_s}{9}\langle \bar{q}q\rangle^2,$$

$$O_8^{V-A} = 8\pi\alpha_s m_0^2 \langle \bar{q}q\rangle^2, \quad (47)$$

where m_0^2 is determined in Eq. (9). In the right-hand side of (46), (47), factorization hypothesis was used. Calculation of the coefficients at α_s in Eq. (44) gave $c_4 = 4/3$ [39] and $c_6 = 89/48$ [40]. The value of $\alpha_s(m_\tau^2)$ (43) corresponds to $\alpha_s(1\ \mathrm{GeV}^2) = 0.60$. Thus, if we take for the quark condensate at the normalization point $\mu^2 = 1\ \mathrm{GeV}^2$ the value (6), then vacuum condensates taking into account α_s corrections appear to be equal (at $\mu^2 = 1\ \mathrm{GeV}^2$):

$$O_4 = -4.22 \times 10^{-4}\ \mathrm{GeV}^4, \quad (48)$$

$$O_6 = -3.75 \times 10^{-3}\ \mathrm{GeV}^6, \quad (49)$$

$$O_8 = 2.5 \times 10^{-3}\ \mathrm{GeV}^8. \quad (50)$$

(In what follows, indices $V - A$ will be omitted and O_D will mean condensates with the account of α_s corrections.)

Our aim is to compare OPE theoretical predictions with experimental data on $V - A$ structure functions measured in τ decay, and the values of O_6 and O_8 found from experiment with Eqs. (49) and (50). Numerical values of O_6 and O_8 in (49) and (50) do not differ strongly. This indicates that OPE asymptotic series (44) at $Q^2 = -s \sim 1\ \mathrm{GeV}^2$ converge badly and maybe even diverge, and the role of higher dimension operators may be substantial. Therefore, it is necessary either to work at larger Q^2, where, however, experimental errors increase, or to improve the convergence of the series. The most plausible method is to use the Borel transformation. Write for $\Pi_V^{(1)} - \Pi_A^{(1)}$ the subtractionless dispersion relation

$$\Pi_V^{(1)}(s) - \Pi_A^{(1)}(s) = \frac{1}{2\pi^2}\int_0^\infty \frac{v_1(t) - a_1(t)}{t - s}dt + \frac{f_\pi^2}{s} \quad (51)$$

(the last term on the right-hand side is the kinematic pole contribution). We now set $s = s_0^{i\phi}$ ($\phi = 0$ on the upper edge of the cut) and perform the Borel transformation in s_0. As a result, we get the following sum rules for the real and imaginary parts of (51):

$$\int_0^\infty \exp\left(\frac{s}{M^2}\cos\phi\right)\cos\left(\frac{s}{M^2}\sin\phi\right) \quad (52)$$
$$\times (v_1 - a_1)(s)\frac{ds}{2\pi^2} = f_\pi^2 + \sum_{k=1}^\infty (-1)^k \frac{\cos(k\phi) O_{2k+2}}{k! M^{2k}},$$

$$\int_0^\infty \exp\left(\frac{s}{M^2}\cos\phi\right)\sin\left(\frac{s}{M^2}\sin\phi\right) \quad (53)$$
$$\times (v_1 - a_1)(s)\frac{ds}{2\pi^2 M^2} = \sum_{k=1}^\infty (-1)^k \frac{\sin(k\phi) O_{2k+2}}{k! M^{2k+2}}.$$

The use of the Borel transformation along the rays in the complex plane has a number of advantages. The exponent index is negative at $\pi/2 < \phi < 3\pi/2$. Choose ϕ in the region $\pi/2 < \phi < \pi$. In this region, on one hand, the shadowed area in Fig. 1 in the integrals (52), (53) is touched to a lesser degree, and, on other hand, the contribution of large s, particularly, $s > m_\tau^2$, where experimental data are absent, is exponentially suppressed. At definite values of ϕ, the contribution of some condensates vanishes, which may be also used. In particular, the condensate O_8 does not contribute to (52) at $\phi = 5\pi/6$ or to (53) at $\phi = 2\pi/3$, while the contribution of O_6 vanishes at $\phi = 3\pi/4$. Finally, a well-known advantage of the Borel sum rules is factorial suppression of higher dimension terms of OPE. Figures 2 and 3 present the results of the calculations of the left-hand sides of Eqs. (52) and (53) on the basis of the ALEPH [24] experimental data compared with OPE predictions—the right-hand side of these equations.

The experimental data are best described at the values [27]

$$O_6 = -(6.8 \pm 2.1) \times 10^{-3}\ \mathrm{GeV}^6, \quad (54)$$

$$O_8 = -(7 \pm 4) \times 10^{-3}\ \mathrm{GeV}^8. \quad (55)$$

When estimating errors in (54) and (55), an uncertainty of the higher dimension–operator contribution was taken into account in addition to experimental errors. (For details see [27].)

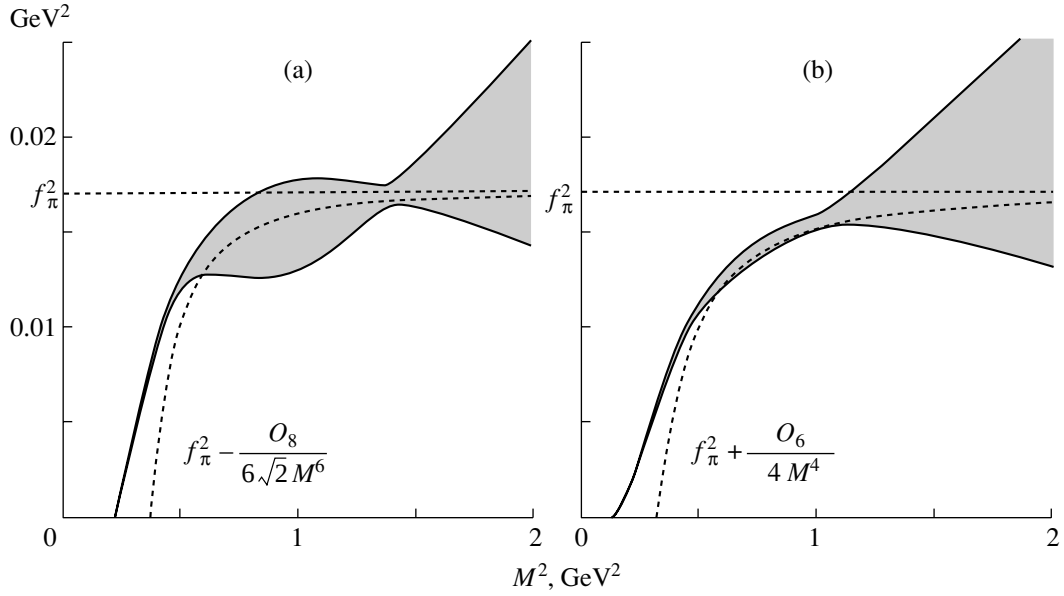

Fig. 2. Equation (52): the left-hand side is obtained based on the experimental data and the shaded region corresponds to experimental errors; the right-hand side—the theoretical one—is represented by the dotted curve and numerical values of condensates are taken to be equal to the central values of Eqs. (54) and (55); (a) $\phi = 3\pi/4$; (b) $\phi = 5\pi/6$.

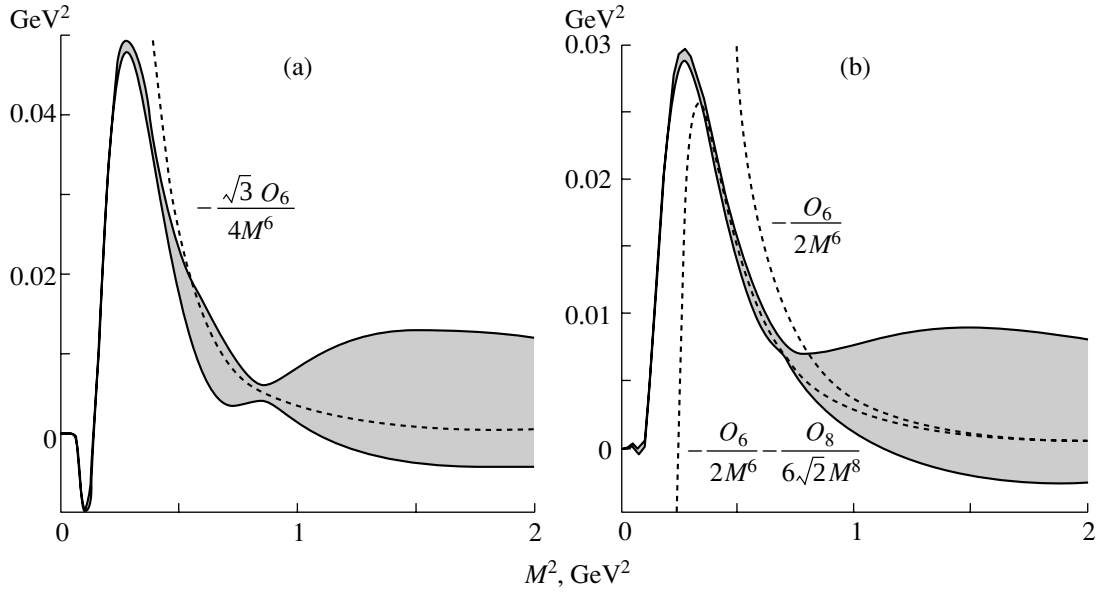

Fig. 3. The same for Eq. (53): (a) $\phi = 2\pi/3$; (b) $\phi = 3\pi/4$.

As is seen from the figures, at these values of condensates, good agreement with experiment starts rather early—at $M^2 > 0.5$ GeV^2. In paper [27], the sum rules for the moments and the Gaussian sum rules were also considered. All of them agree with the condensate values in (54) and (55), but the accuracy of their determination is worse. The values in (54) and (55) are by a factor of 1.5–2 larger than those in (49) and (50). As was discussed above, the accuracy of (49) and (50) is on the order of 50%. Therefore, most plausible is that the real value of condensates O_6, O_8 is somewhere close to the lower edge of errors in (54) and (55).

Consider now the polarization operator $\Pi(s)$ defined in (34) and condensates entering into the OPE for $\Pi(s)$ (see (40)). In principle, the perturbative terms contribute to chirality-conserving condensates. If we follow the separation method of perturbative

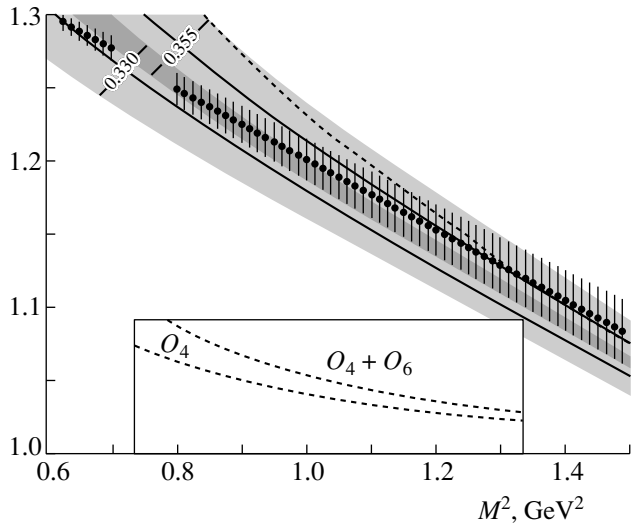

Fig. 4. The results of the Borel transformation of $V + A$ correlator for two values $\alpha_s(m_\tau^2 = 0.355$ and $\alpha_s(m_\tau^2) = 0.330$. The widths of the bands correspond to PT errors; dots with errors, to experimental data. The dotted curve is the sum of the perturbative contribution at $\alpha_s(m_\tau^2) = 0.330$ and O_4, O_6 condensates.

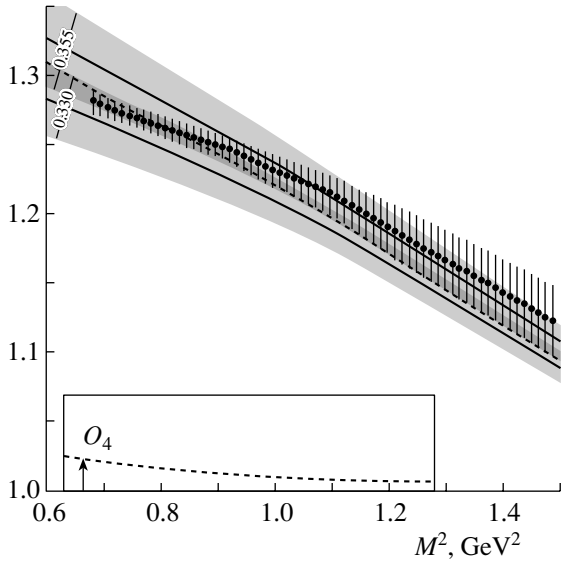

Fig. 5. The result of the Borel transformation along the ray at $\phi = 5\pi/6$. The dotted line corresponds to the central value of gluon condensate (56), added to the PT curve with $\alpha_s(m_\tau^2) = 0.330$.

and nonperturbative contributions by introducing infrared cutoff [6, 7], then such a contribution would actually appear due to the region of virtualities smaller than μ^2. In the present paper, according to [28], another method is exploited, when the β function is expanded only in the number of loops (see Eq. (11) and the text following it) but not in $1/\ln Q^2$. So, the dependence of condensates on normalization point μ^2 is determined only by perturbative corrections, as is seen in (40). Condensates determined in such a way may be called n-loop ones (in the given case, three-loop). Consider the Borel transformation of the sum $\Pi(s)_{\text{pert}} + \Pi(s)_{\text{nonpert}}$, where $\Pi(s)_{\text{pert}}$ is given by Eq. (38), and $\Pi(s)_{\text{nonpert}}$, by Eq. (13). Figure 4 presents the results of three-loop calculation for two values of $\alpha_s(m_\tau^2)$—0.355 and 0.330. The widths of the bands correspond to theoretical error taken to be equal to the last accounted term $K_3 a^2$ in the Adler function (36). (The same result for the error is obtained if one takes four loops in the β function and sets $K_4 = 50 \pm 50$.) The dotted line corresponds to the sum of contributions of gluon condensate (11) and condensate O_6^{V+A} in (13) with a numerical value corresponding to O_6^{V-A} (54). The dots with errors represent experimental data. (The contribution of the $d = 4$ and $d = 6$ operators is given separately in the inset.)

It is seen that the curve with $\alpha_s(m_\tau^2) = 0.330$ and condensate contributions can be matched with experiment starting from $M^2 = 1.1$ GeV^2, the agreement being improved at smaller values $\langle 0|\frac{\alpha_s}{\pi}G^2|0\rangle$ than (11). The curve with $\alpha_s(m_\tau^2) = 0.355$ taking into account condensates coincides with experiment only at $M^2 > 1.5$ GeV^2. The same tendency persists for the Borel sum rules taken along the rays in the s complex plane at various ϕ. Figure 5 gives the sum rule for $\phi = 5\pi/6$. From consideration of this and of other sum rules, the estimation for gluon condensate follows:

$$\left\langle 0\left|\frac{\alpha_s}{\pi}G^a_{\mu\nu}G^a_{\mu\nu}\right|0\right\rangle = 0.006 \pm 0.012 \text{ GeV}^4. \quad (56)$$

The best agreement of the theory with experiment in the low Q^2 region (up to $\sim$2% at $M^2 > 0.8$ GeV^2) is obtained at $\alpha_s(m_\tau^2) = 0.330$, which corresponds to $\alpha_s(m_z^2) = 0.118$.

Let us now make some remarks on modifications of QCD in the low-energy region.

1. Analytical perturbative QCD [45, 46]. It is assumed that $\alpha_s(q^2)$ is an analytical function of q^2 [45], or, in a more general case, it is supposed that the perturbative part of the polarization operator is an analytical function of q^2. The comparison of this approach with the τ-decay data showed [28] that in the analytical QCD,

$$\alpha_s^{\text{anal}}(m_z^2) = 0.140, \quad (57)$$

which strongly disagrees with the world mean value $\alpha_s(m_z^2) = 0.119 \pm 0.002$.

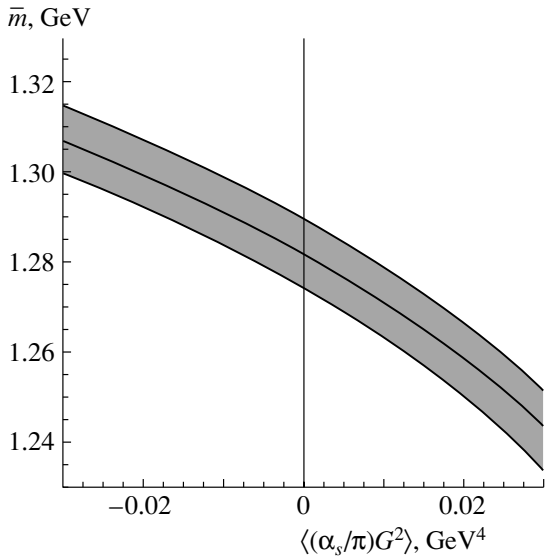

Fig. 6. The dependence of $\overline{m}(\overline{m})$ on $\langle 0|\alpha s/\pi)G^2|0\rangle$ obtained at $n = 10$, $Q^2 = 0.98 \cdot 4m^2$ and $\alpha_s(Q^2 + \overline{m}^2)$.

2. Renormalon summing leading to the tachion mass λ^2 in gluon propagator [47]. The restriction to the tachion mass

$$-\lambda^2 = 0.1 \pm 0.15 \text{ GeV}^2 \tag{58}$$

was found from τ-decay.

3. Instantons. It was shown [28] that in the dilute-instanton-gas approximation [48], instantons barely affect determination of $\alpha_s(m_\tau^2)$ and the Borel sum rules. Their effect, however, appears to be considerable and strongly dependent on the value of the instanton radius ρ_c in the sum rules obtained by integration over closed contours in the complex plane s at the radii of the contours $s < 2$ GeV^2.

5. SUM RULES FOR CHARMONIUM AND GLUON CONDENSATE

The value of the gluon condensate was found by Shifman, Vainstein, and Zakharov from the sum rules for the polarized operator of vector currents of charmed quarks [5], but in these calculations, the constant α_s was taken as comparatively small ($\alpha_s(1 \text{ GeV}^2) \approx 0.3$; $\Lambda^{(3)}_{\text{QCD}} = 100$ MeV) and perturbative corrections were taken into account only in the first order. It is clear now that $\alpha_s(Q^2)$ in the region $Q^2 \sim 1$–10 GeV^2 is approximately twice as large, so that taking into account higher order corrections became necessary. (In what follows, I formulate the main results of [49].)

Consider the polarization operator of charmed vector currents,

$$i\int dx e^{iqx}\langle TJ_\mu(x)J_\nu(0)\rangle = (q_\mu q_\nu - g_{\mu\nu}q^2)\Pi(q^2), \tag{59}$$

$$J_\mu = \bar{c}\gamma_\mu c.$$

The dispersion representation for $\Pi(q^2)$ has the form

$$R(s) = 4\pi \text{Im}\Pi(s + i0), \tag{60}$$

$$\Pi(q^2) = \frac{q^2}{4\pi^2}\int\limits_{4m^2}^{\infty}\frac{R(s)ds}{s(s-q^2)},$$

where $R(\infty) = 1$ in the partonic model. In the approximation of infinitely narrow widths of resonances, $R(s)$ can be written as sums of contributions from resonances and the continuum:

$$R(s) = \frac{3\pi}{Q_c^2\alpha^2_{\text{em}}(s)}\sum_\psi m_\psi\Gamma_{\psi\to ee}\delta(s-m_\psi^2) + \theta(s-s_0), \tag{61}$$

where $Q_c = 2/3$ is the charge of charmed quarks, s_0 is the continuum threshold (in what follows, $\sqrt{s_0} = 4.6$ GeV), $\alpha(s)$ is the running electromagnetic constant, and $\alpha(m^2_{J/\psi}) = 1/133.6$. Following [5], to suppress the contribution of higher states and the continuum, we study the polarization operator moments

$$M_n(Q^2) \equiv \frac{4\pi^2}{n!}\left(-\frac{d}{dQ^2}\right)^n\Pi(-Q^2) = \int\limits_{4m^2}^{\infty}\frac{R(s)ds}{(s+Q^2)^{n+1}}. \tag{62}$$

According to (61), the experimental values of moments are determined by the equality

$$M_n(Q^2) = \frac{27\pi}{4\alpha^2_{\text{em}}}\sum_{\psi=1}^{6}\frac{m_\psi\Gamma_{\psi\to ee}}{(m_\psi^2+Q^2)^{n+1}} + \frac{1}{n(s_0+Q^2)^n}. \tag{63}$$

It is reasonable to consider the ratios of moments $M_{n1}(Q^2)/M_{n2}(Q^2)$ from which the uncertainty due to error in $\Gamma_{J/\psi\to ee}$ markedly falls out. The theoretical value for $\Pi(q^2)$ is presented as a sum of perturbative and nonperturbative contributions. It is convenient to express the perturbative contribution via $R(s)$, making use of (60) and (62):

$$R(s) = \sum_{n\geq 0}R^{(n)}(s,\mu^2)a^n(\mu^2), \tag{64}$$

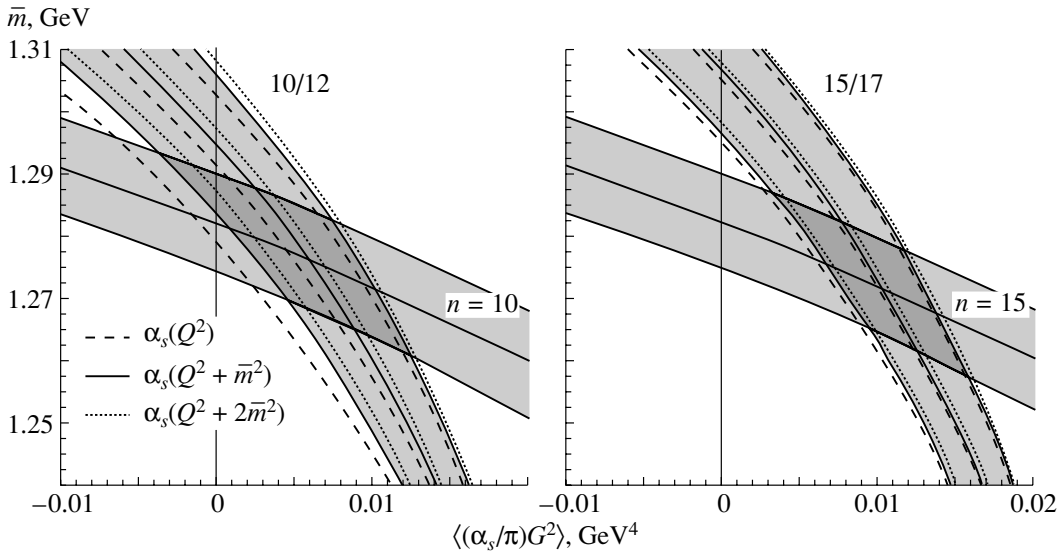

Fig. 7. The dependence of $\overline{m}(\overline{m})$ on $\langle 0|(\alpha s/\pi)G^2|0\rangle$ obtained from the moments (horizontal bands) and their ratios (vertical bands) at different α_s. The left-hand figure: $Q^2 = 4\overline{m}^2$, $n = 10$, M_{10}/M_{12}; the right-hand figure: $Q^2 = 8\overline{m}^2$, $n = 15$, M_{15}/M_{17}.

where $a(\mu^2) = \alpha_s(\mu^2)/\pi$. At present, three terms of expansion in (64) are known: $R^{(0)}$ [51], $R^{(1)}$ [52], and $R^{(2)}$ [53]. They are represented as functions of quark velocity $v = \sqrt{1 - 4m^2/s}$, where m is the pole mass of the quark. Since they are cumbersome, I will not present them here.

Nonperturbative contributions to the polarization operator have the form (restricted by $d = 6$ operators)

$$\Pi_{\text{nonpert}}(Q^2) = \frac{1}{(4m^2)^2}\left\langle 0\left|\frac{\alpha_s}{\pi}G^2\right|0\right\rangle \times [f^{(0)}(z) + af^{(1)}(z)] + \frac{1}{(4m^2)^3}g^3 f^{abc} \times \langle 0|G^a_{\mu\nu}G^b_{\nu\lambda}G^c_{\lambda\mu}|0\rangle F(z), \quad z = -Q^2/4m^2. \tag{65}$$

Functions $f^{(0)}(z)$, $f^{(1)}(z)$, and $F(z)$ were calculated in [5], [54], and [55], respectively. The use of the quark pole mass is, however, unacceptable. The matter is that in this case, the PT corrections to moments are very large in the region of interest and the perturbative series seems to diverge. For instance, at

$$\frac{M^{(1)}}{M^{(0)}} = 13.836, \quad \frac{M^{(2)}}{M^{(0)}} = 193.33, \quad \frac{M^{(G,1)}}{M^{(G,0)}} = 13.791 \tag{66}$$

(here $M^{(k)}$ mean the coefficients at the contributions of terms $\sim a^k$ to the moments; $M^{(G,k)}$ are similar coefficients for the gluon condensate contribution. In the region of interest $a \sim 0.1$). At $Q^2 = 0$, the situation is even worse. So, it is reasonable to turn to the $\overline{MS}$ mass $\overline{m}(\mu^2)$, taken at the point $\mu^2 = \overline{m}^2$. After turning to the $\overline{MS}$ mass $\overline{m}(\overline{m}^2)$ we get instead of (66)

$$\frac{\bar{M}^{(1)}}{\bar{M}^{(0)}} = 0.045, \quad \frac{\bar{M}^{(2)}}{\bar{M}^{(0)}} = 1.136, \tag{67}$$

$$\frac{\bar{M}^{(G,1)}}{\bar{M}^{(G,0)}} = -1.673. \tag{68}$$

At $a \sim 0.1$ and at the ratios of moments given by (67), there is good reason to believe that the PT series converges well. Such a good convergence holds (at $n > 5$) only in the case of sufficiently large Q^2; at $Q^2 = 0$, one does not succeed in finding such n that perturbative corrections, α_s corrections to gluon condensates, and contribution of the term $\sim\langle G^3\rangle$ would simultaneously be small.

It is also necessary to choose a scale—normalization point μ^2 where $\alpha_s(\mu^2)$ is taken. In (64), $R(s)$ is a physical value and cannot depend on μ^2. Since, however, we take into account in (64) only three terms, with an unsuitable choice of μ^2, such a μ^2 dependence may arise due to neglected terms. At large Q^2, the natural choice is $\mu^2 = Q^2$. It can be thought that at $Q^2 = 0$ the reasonable scale is $\mu^2 = \overline{m}^2$, though some numerical factor is not excluded in this equality. This is why it is reasonable to take the interpolation form

$$\mu^2 = Q^2 + \overline{m}^2, \tag{69}$$

but one must check the dependence of final results on a possible factor at $\overline{m}^2$. Equating the theoretical value of some moment at fixed Q^2 (in the region where $M_n^{(1)}$

and $M_n^{(2)}$ are small) to its experimental value, one can find the dependence of $\overline{m}$ on $\langle(\alpha_s/\pi)G^2\rangle$ (neglecting the terms $\sim\langle G^3\rangle$). Such a dependence for $n=10$ and $Q^2/4m^2=0.98$ is presented in Fig. 6.

To fix both $\overline{m}$ and $\langle(\alpha_s/\pi)G^2\rangle$ one should, except for moments, take their ratios. Figure 7 shows the value of $\overline{m}$ obtained from the moment M_{10} and the ratio M_{10}/M_{12} at $Q^2=4m^2$ and from the moment M_{15} and the ratio M_{15}/M_{17} at $Q^2=8m^2$. The best values of the masses of a charmed quark and the gluon condensate are obtained from Fig. 7:

$$\bar{m}(\bar{m}^2)=1.275\pm0.015\ \text{GeV}, \qquad (70)$$
$$\left\langle\frac{\alpha_s}{\pi}G^2\right\rangle=0.009\pm0.007\ \text{GeV}^4.$$

Up to now, the corrections $\sim\langle G^3\rangle$ have not been taken into account. It appears that, in the region of n and Q^2 used to find $\overline{m}$ and the gluon condensate, they are comparatively small and, hardly not changing $\overline{m}$, increase $\langle(\alpha_s/\pi)G^2\rangle$ by 10–20% if the term $\sim\langle G^3\rangle$ is estimated according to (13) at $\rho_c=0.5$ fm.

It should be noted that improvement of the accuracy of $\Gamma_{J/\psi\to ee}$ would make it possible to refine the value of the gluon condensate: the widths of the horizontal bands in Fig. 7 are determined mainly just by this error. In particular, this, perhaps, would allow one to exclude the zero value of the gluon condensate, which would be extremely important. Unfortunately, Eq. (69) does not allow one to do this for sure. Reduction of theoretical errors which determine the width of vertical bands seems to be less realistic.

6. CONCLUSIONS

In this paper I compared the results of the recent precise measurements of τ-lepton hadronic decays [24–26] with QCD predictions in the low-energy region. The perturbative terms up to α_s^3 and the terms of the OPE up to $d=8$ were taken into account. It is shown that QCD taking into account OPE terms agrees with experiment up to $\sim$2% at the values of the complex Borel parameter $|M^2|>0.8$–1.0 GeV^2 in the left-hand half-plane of the complex plane. The following was found:

1. The values of the QCD coupling constant $\alpha_s(m_\tau^2)=0.355\pm0.025$ from the total probability of τ decays and $\alpha_s(m_\tau^2)=0.330$ from the sum rules at low energies. (The latter value corresponds to $\alpha_s(m_z^2)=0.118$.)

2. The value of the quark condensate squared (assuming factorization)

$$\alpha_s\langle0|\bar\psi\psi|0\rangle^2=(2.25\pm0.70)\times10^{-4}\ \text{GeV}^6$$

and of quark-gluon condensate of $d=8$.

3. The value of the gluon condensate

(a) from the τ-decay data,

$$\left\langle0\left|\frac{\alpha_s}{\pi}G^2\right|0\right\rangle=0.006\pm0.012\ \text{GeV}^4;$$

(b) from the sum rules for charmonium,

$$\left\langle0\left|\frac{\alpha_s}{\pi}G^2\right|0\right\rangle=0.009\pm0.007\ \text{GeV}^4.$$

It was shown that the sum rules for charmonium are in agreement with experiment when accounting for perturbative corrections $\sim\alpha_s^2$ and for OPE terms proportional to $\langle(\alpha_s/\pi)G^2\rangle$ and to $\langle G^3\rangle$.

The main conclusion is that in the range of low-energy phenomena under consideration, perturbation theory and operator expansion, i.e., the idea of vacuum condensates in QCD, are in excellent agreement with experiment starting from $Q^2\sim1$ GeV^2.

ACKNOWLEDGMENTS

I am deeply indebted to K.N. Zyablyuk, who had performed the main calculations in papers [27, 28], the results of which I used here.

The paper is supported by the following grants: CRDF RP2-2247, INTAS-2000-587 and the Russian Foundation for Basic Research (project no. 00-02-17808).

REFERENCES

1. P. A. Aleksandrov, *Academician Anatoliĭ Petrovich Aleksandrov: Direct Speech* (Nauka, Moscow, 2001), p. 177.
2. D. Holloway, *Stalin and the Bomb: the Soviet Union and Atomic Energy, 1939–1956* (Yale Univ. Press, New Haven, 1994; Sibirskiĭ Khronograf, Novosibirsk, 1997), Chap. 15, Sect. 6.
3. B. L. Ioffe, Novyĭ Mir, No. 6, 161 (1999).
4. A. A. Belavin, A. M. Polyakov, A. S. Schwarz, and Yu. S. Tyupkin, Phys. Lett. B **59B**, 85 (1975).
5. M. A. Shifman, A. I. Vainstein, and V. I. Zakharov, Nucl. Phys. B **147**, 385, 448 (1979).
6. V. A. Novikov, M. A. Shifman, A. I. Vainstein, and V. I. Zakharov, Nucl. Phys. B **249**, 445 (1985).
7. M. A. Shifman, *Lecture at 1997 Yukawa International Seminar, Kyoto, 1997,* Prog. Theor. Phys. Suppl. **131**, 1 (1998).
8. M. Gell-Mann, R. J. Oakes, and B. Renner, Phys. Rev. **175**, 2195 (1968).
9. B. L. Ioffe, Usp. Fiz. Nauk **171**, 1273 (2001).
10. S. Weinberg, Trans. N. Y. Acad. Sci., Ser. 2 **38**, 185 (1977).
11. H. Leutwyler, J. Mosc. Phys. Soc. **6**, 1 (1996).
12. B. L. Ioffe, Nucl. Phys. B **188**, 317 (1981); Erratum: **192**, 591 (1981).

13. H. Leutwyler, in *At the Frontier of Particle Physics: Handbook of QCD, Boris Ioffe Festschrift,* Ed. by M. Shifman (World Sci., Singapore, 2001), Vol. 1, p. 271.
14. U. Meissner, in *At the Frontier of Particle Physics: Handbook of QCD, Boris Ioffe Festschrift,* Ed. by M. Shifman (World Sci., Singapore, 2001), Vol. 1, p. 417.
15. P. Gerber and H. Leutwyler, Nucl. Phys. B **321**, 387 (1989).
16. P. Chen *et al.*, Phys. Rev. D **64**, 014503 (2001).
17. B. L. Ioffe, *Lecture at St. Petersburg Winter School on Theoretical Physics, 1998*, Surv. High Energy Phys. **14**, 89 (1999).
18. V. M. Belyaev and B. L. Ioffe, Zh. Éksp. Teor. Fiz. **83**, 876 (1982) [Sov. Phys. JETP **56**, 493 (1982)].
19. V. A. Novikov, M. A. Shifman, A. I. Vainstein, and V. I. Zakharov, Phys. Lett. B **86B**, 347 (1979).
20. B. L. Ioffe and A. V. Smilga, Nucl. Phys. B **232**, 109 (1984).
21. V. M. Belyaev and Ya. I. Kogan, Yad. Fiz. **40**, 1035 (1984) [Sov. J. Nucl. Phys. **40**, 659 (1984)]; Ya. Ya. Balitskiĭ, A. V. Kolesnichenko, and A. V. Yung, Yad. Fiz. **41**, 282 (1985) [Sov. J. Nucl. Phys. **41**, 178 (1985)].
22. V. M. Belyaev and Ya. I. Kogan, Pis'ma Zh. Éksp. Teor. Fiz. **37**, 611 (1983) [JETP Lett. **37**, 730 (1983)].
23. B. L. Ioffe and A. G. Oganesian, Phys. Rev. D **57**, R6590 (1998).
24. ALEPH Collab. (R. Barate *et al.*), Eur. Phys. J. C **4**, 409 (1998).
25. OPAL Collab. (K. Ackerstaff *et al.*), Eur. Phys. J. C **7**, 571 (1999); G. Abbiendi *et al.*, Eur. Phys. J. C **13**, 197 (2002).
26. CLEO Collab. (S. J. Richichi *et al.*), Phys. Rev. D **60**, 112002 (1999).
27. B. L. Ioffe and K. N. Zyablyuk, Nucl. Phys. A **687**, 437 (2001).
28. B. V. Geshkenbein, B. L. Ioffe, and K. N. Zyablyuk, Phys. Rev. D **64**, 093009 (2001).
29. A. Pich, in *Proceedings of QCD94 Workshop, Montpellier, 1994,* Nucl. Phys. B (Proc. Suppl.) **39**, 396 (1995).
30. W. J. Marciano and A. Sirlin, Phys. Rev. Lett. **61**, 1815 (1988).
31. E. Braaten, Phys. Rev. Lett. **60**, 1606 (1988); Phys. Rev. D **39**, 1458 (1989).
32. S. Narison and A. Pich, Phys. Lett. B **211**, 183 (1988).
33. F. Le Diberder and A. Pich, Phys. Lett. B **286**, 147 (1992).
34. K. G. Chetyrkin, A. L. Kataev, and F. V. Tkachov, Phys. Lett. B **85B**, 277 (1979); M. Dine and J. Sapirshtein, Phys. Rev. Lett. **43**, 668 (1979); W. Celmaster and R. Gonsalves, Phys. Rev. Lett. **44**, 560 (1980).
35. L. R. Surgaladze and M. A. Samuel, Phys. Rev. Lett. **66**, 560 (1991); S. G. Gorishny, A. L. Kataev, and S. A. Larin, Phys. Lett. B **259**, 144 (1991).
36. A. L. Kataev and V. V. Starshenko, Mod. Phys. Lett. A **10**, 235 (1995).
37. O. V. Tarasov, A. A. Vladimirov, and A. Yu. Zharkov, Phys. Lett. B **93B**, 429 (1980); S. A. Larin and J. A. M. Vermaseren, Phys. Lett. B **303**, 334 (1993).
38. T. van Ritbergen, J. A. M. Vermaseren, and S. A. Larin, Phys. Lett. B **400**, 379 (1997).
39. K. G. Chetyrkin, S. G. Gorishny, and V. P. Spiridonov, Phys. Lett. B **160B**, 149 (1985).
40. L.-E. Adam and K. G. Chetyrkin, Phys. Lett. B **329**, 129 (1994).
41. E. Braaten and C. S. Li, Phys. Rev. D **42**, 3888 (1990).
42. Particle Data Group (K. Hagiwara *et al.*), Phys. Rev. D **66**, 010001 (2002).
43. ALEPH Collab. (R. Barate *et al.*), Eur. Phys. J. C **11**, 599 (1999).
44. OPAL Collab. (G. Abbiendi *et al.*), Eur. Phys. J. C **19**, 653 (2001).
45. I. L. Solovtsov and D. V. Shirkov, Phys. Rev. Lett. **79**, 1209 (1997); I. L. Solovtsov and D. V. Shirkov, Teor. Mat. Fiz. **120**, 1210 (1999).
46. B. V. Geshkenbein and B. L. Ioffe, Pis'ma Zh. Éksp. Teor. Fiz. **70**, 167 (1999) [JETP Lett. **70**, 161 (1999)].
47. K. G. Chetyrkin, S. Narison, and V. I. Zakharov, Nucl. Phys. B **550**, 353 (1999).
48. T. Shafer and E. V. Shuryak, Rev. Mod. Phys. **70**, 323 (1998).
49. B. L. Ioffe and K. N. Zyablyuk, hep-ph/0207183.
50. V. B. Berestetskiĭ and I. Ya. Pomeranchuk, Zh. Éksp. Teor. Fiz. **29**, 864 (1955) [Sov. Phys. JETP **2**, 580 (1956)].
51. J. Schwinger, *Particles, Sources, and Fields* (Addison-Wesley, Reading, 1970; Mir, Moscow, 1976), Vol. 2.
52. A. H. Hoang, J. H. Kuhn, and T. Teubner, Nucl. Phys. B **452**, 173 (1995); K. G. Chetyrkin, J. H. Kuhn, and M. Steinhauser, Nucl. Phys. B **482**, 213 (1996); K. G. Chetyrkin *et al.*, Nucl. Phys. B **503**, 339 (1997); Eur. Phys. J. C **2**, 137 (1998).
53. D. J. Broadhurst *et al.*, Phys. Lett. B **329**, 103 (1994).
54. S. N. Nikolaev and A. V. Radyushkin, Yad. Fiz. **39**, 147 (1984) [Sov. J. Nucl. Phys. **39**, 91 (1984)].

Physics of Atomic Nuclei, Vol. 66, No. 1, 2003, pp. 44–46. Translated from Yadernaya Fizika, Vol. 66, No. 1, 2003, pp. 47–50.

NUCLEI
Experiment

Measurements of the Partial Cross Section for the Reaction ^{48}Ti(n, γ_1)^{49}Ti and Estimation of the Radiative Strength Functions for $E1$ and $M1$ Transitions

A. V. Voinov*, D. G. Serov, Yu. P. Popov, N. A. Gundorin, A. P. Kobzev, and S. S. Parzhitski

Joint Institute for Nuclear Research, Dubna, Moscow oblast, 141980 Russia

Received March 22, 2002

Abstract—The partial cross section for radiative neutron capture by ^{48}Ti nuclei was measured as a function of neutron energy. The method of neutron spectrometry used is based on the shift in the energy of the primary γ transition in response to a change in the energy of the captured neutron. The reaction ^{7}Li(p, n)^{7}Be was used as a neutron source. Protons were accelerated by a Van de Graaff electrostatic generator up to energies of 60 keV above the reaction threshold, which provided neutron energies in the range from 10 to 120 keV. The partial widths of some resonances were determined. The radiative strength functions of $E1$ and $M1$ transitions to the first excited state were calculated. © *2003 MAIK "Nauka/Interperiodica".*

INTRODUCTION

At present, there is a large body of experimental data on the parameters of neutron resonances in nuclei, as well as experimental and evaluated data on the cross sections for radiative neutron capture. At the same time, there is a large deficit in data on the partial cross sections. This is because the partial cross sections for the reactions under discussion are small, are difficult to measure by standard methods, and require using high-efficiency experimental methods with spectrometry of the accompanying γ radiation. In this study, we measured the partial cross sections for radiative neutron capture by a method based on the proportionality between the incident-neutron energy and the energy of the primary γ transition to a low-lying level of the nucleus [1–3]. Previously, we used Fe and Ni samples for which the partial γ widths of the strongest resonances were measured by the time-of-flight method. This provided us with referencing to absolute values in the cross-section measurements. Here, we continue our studies using the reaction ^{48}Ti(n, γ_1)^{49}Ti. The corresponding γ decay is schematically shown in Fig. 1.

DESCRIPTION OF THE EXPERIMENT

In our experiment, we recorded the primary γ transitions populating the first excited state of the ^{49}Ti daughter nucleus. The spin and parity of the final state is $3/2^-$; thus, the multipolarities of the primary γ transition are $E1$ for s-wave resonances and $M1$ for p-wave resonances. The layout of the experiment is shown in Fig. 2. A ring-shaped sample made of a natural titanium mixture is 4 mm thick. The sample was irradiated with a neutron flux from the reaction ^{7}Li(p, n)^{7}Be. Protons were accelerated by a Van de Graaff electrostatic generator up to energies of 60 keV above the reaction threshold, which provided the sample irradiation with neutrons of energy in the range from 10 to 120 keV. A lead block shielded the germanium detector from hard γ radiation of the ^{7}Li(p, γ)^{8}Be reaction. The compact geometry of the experiment allowed an optimum efficiency to be achieved both for detecting γ-ray photons and for irradiating the sample with neutrons.

The measurements were carried out in short (one-hour-long) series. The resulting spectra were summed after prior electronic-gain-drift correction. The background spectrum was measured with a graphite sample instead of a titanium one. The sample

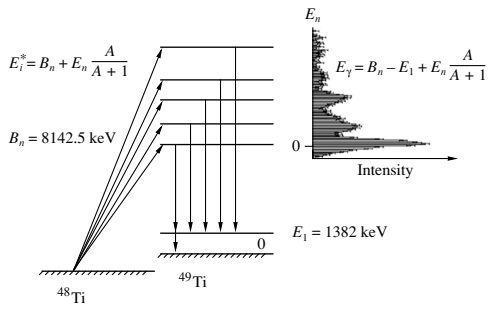

Fig. 1. Diagram of the γ decay of a compound ^{49}Ti nucleus after neutron capture.

*e-mail: voinov@nf.jinr.ru

1063-7788/03/6601-0044$24.00

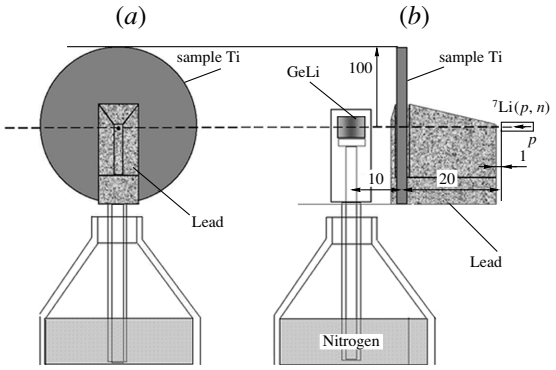

Fig. 2. Layout the experimental setup: (*a*) front view and (*b*) side view.

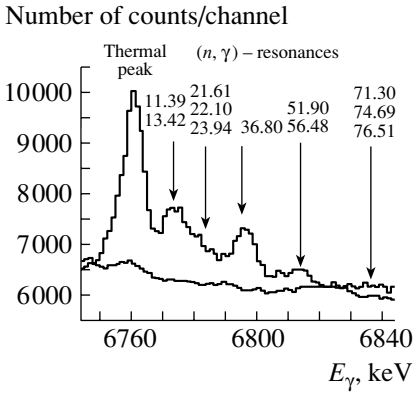

Fig. 3. Part of the γ spectrum including the ^{48}Ti$(n, \gamma_1)^{49}$Ti resonance structure.

thickness was chosen to provide equivalent neutron scattering.

The energy resolution of the method was determined by the resolution of the germanium detector, which, in turn, was about 8 keV in the spectral range under study. Part of the experimental spectrum for the γ transition to the first excited state (1381.6 keV, $3/2^-$) of the daughter nucleus is shown in Fig. 3. The corresponding background is also shown in the figure; we see no background peaks that could distort the effect. The arrows in Fig. 3 indicate the positions of the known (n, γ) resonances for the isotope under study and their energies (in keV). The thermal peak in this spectrum was produced by the capture of thermal neutrons that are present abundantly in the experimental hall. This peak provides a good possibility of determining the zero reference point for the neutron energies.

RESULTS AND THEIR ANALYSIS

The area of the peak corresponding to the ith resonance for a thin sample can be expressed by the formula

$$A_i \sim k\phi_i\varepsilon_i g_i \frac{\Gamma_{ni}\Gamma^p_{\gamma i}}{\Gamma_i}, \qquad (1)$$

where Γ_{ni} is the neutron width of the ith resonance, $\Gamma^p_{\gamma i}$ is the partial radiative width, Γ_i is the total resonance width, ϕ_i is the neutron flux, g_i is the spin factor, and k is the coefficient used below for the absolute normalization of the cross sections {k was determined from additional measurements for the reaction ^{58}Ni$(n, \gamma_0)^{59}$Ni whose partial cross section is known from our previous experiments [4]}.

The effective spectrum of incident neutrons was calculated from the kinematics of the reaction ^{7}Li$(p, n)^7$Be [5] with allowance made for the configuration of the setup (Fig. 4).

The partial cross section for the reaction ^{48}Ti(n, γ_1) (see Fig. 5) was calculated after the background subtraction. The area under the peak of each resonance was determined through computer fitting with the fixed peak positions corresponding to the neutron-resonance energies according to the expression cited in Fig. 1. This allowed us to calculate the partial resonance parameters of the reaction.

In addition to the strong resonances responsible for the formation of the peaks, the experimental spectrum includes a large number of weak resonances. These weak resonances were assumed to form a continuous intensity distribution of γ transitions in the region of well-resolved strong peaks. Therefore, the adjustable function used in the fit was defined as the sum of Gaussian peaks and smooth functions.

The partial parameters $g\Gamma_{ni}\Gamma^p_{\gamma i}/\Gamma_i$ calculated by using formula (1) are listed in the table, where the errors are purely statistical. The resonance energies, well-known data from [6], and our experimental data are given in the first, fourth and fifth columns of the table, respectively.

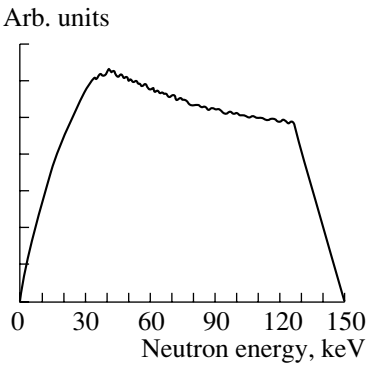

Fig. 4. Effective spectrum of the neutrons involved in the reaction on the sample.

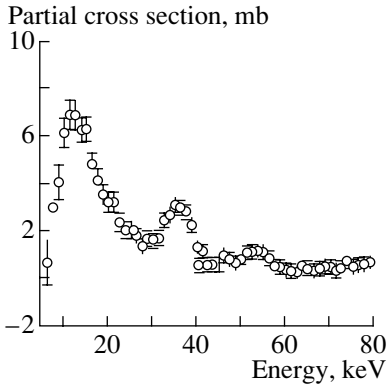

Fig. 5. Partial cross section for the reaction ^{48}Ti(n, γ_1).

Hence, the radiative strength functions for $E1$ and $M1$ transitions can be estimated as

$$S_\gamma(E1) = \frac{\langle \Gamma_\gamma^p(E1)\rangle}{D_0 E_\gamma^3}, \qquad (2)$$

$$S_\gamma(M1) = \frac{\langle \Gamma_\gamma^p(M1)\rangle}{D_1 E_\gamma^3},$$

where $D_0 = 13$ keV and $D_1 = 8.5$ keV are the mean level spacings calculated from the systematic data of other authors [5] and $E_\gamma = (8142 - 1382) = 6760$ keV is the energy of the γ transition of the compound nucleus to the first excited state.

The radiative strength functions obtained for the first time for ^{48}Ti are

$$S_\gamma(M1) = (5.0 \pm 4.0) \times 10^{-8}\ \text{MeV}^{-3},$$

$$S_\gamma(E1) = (2.5 \pm 2.0) \times 10^{-8}\ \text{MeV}^{-3}.$$

For comparison, we used systematic data from [7]: for the nuclei with a mass of about 48, the values of the radiative strength functions are 2×10^{-8} MeV^{-3} for $E1$ transitions and 1×10^{-8} MeV^{-3} for $M1$ transitions. Thus, we may conclude that the values of the radiative strength functions determined by our method are in agreement with the systematic data of other authors.

The significant errors for the radiative strength functions are attributable to the small number of resonances over which they were averaged.

Data on the resonance parameters of the ^{48}Ti(n, γ_1) reaction

E_n, keV	J^π	l	$g\Gamma_n\Gamma_\gamma/\Gamma$, meV [6]	$g\Gamma_n\Gamma_\gamma^p/\Gamma$, meV
11.49	−	1	280	68 ± 20
13.42	−	1	320	73 ± 30
17.60	$1/2^+$	0	2600	54 ± 20
21.61	−	1	190	58 ± 10
36.80	$1/2^+$	0	3000	190 ± 10
51.9	$1/2^+$	0	1500	64 ± 10

CONCLUSION

The potential of the new neutron-spectrometry method demonstrated above showed its value in investigating one more isotope. This study uncovered hitherto unknown information that can be used in other studies. Although the energy resolution (and, hence, the accuracy) of this method is largely determined by the HPGe-detector resolution in the energy range used in our measurements ($\sim$6 MeV), there are ways for improving the capabilities of this method. In our subsequent studies, we plan to use background-suppression methods to increase the sensitivity of the method in measurements and to reduce its statistical error.

ACKNOWLEDGMENTS

We thank I.A. Chepurchenko and the entire staff of the EG-5 Van de Graaff electrostatic generator for stable and reliable operation of the setup.

This work was supported by the Russian Foundation for Basic Research, project no. 00-02-17310.

REFERENCES

1. Yu. P. Popov, P. V. Sedyshev, and M. V. Sedysheva, JINR Rapid Commun. No. 6[80]-96, 79 (1996).
2. Yu. P. Popov *et al.*, in *Proceedings of ISINN-6* (JINR, Dubna, 1999); Phys. At. Nucl. **62**, 827 (1999).
3. V. J. Thompson, A. V. Lopez, W. V. Prestivich, *et al.*, Nucl. Instrum. Methods Phys. Res. **126**, 263 (1975).
4. Yu. P. Popov *et al.*, Phys. At. Nucl. **63**, 525 (2000).
5. J. H. Gibbons and H. W. Newson, in *Fast Neutron Physics*, Ed. by J. B. Marion and J. L. Fowler (Interscience, New York, 1960), Vol. 1, p. 133.
6. S. I. Sukhoruchkin, Z. N. Soroko, and V. V. Deriglazov, *Table of Neutron Resonance Parameters* (Landolt-Börnstein/New Series, Vol. 16/B), Ed. by H. Schopper (Springer-Verlag, Berlin, 1998).
7. J. Kopecky and M. Uhl, in *Proceedings of Specialists Meeting on Measurement, Calculation, and Evaluation of Photon Production Data, Bologna, Italy, 1994,* p. 119.

Translated by V. Bukhanov

Physics of Atomic Nuclei, Vol. 66, No. 1, 2003, pp. 47–55. Translated from Yadernaya Fizika, Vol. 66, No. 1, 2003, pp. 51–58.

NUCLEI
Experiment

Refractive Effects in the Reaction $^{13}C(^3He, t)^{13}N$ at an Energy of 60 MeV

N. Burtebaev[1)], A. Duisebaev[1)], and S. B. Sakuta

Russian Research Centre Kurchatov Institute, pl. Kurchatova 1, Moscow, 123182 Russia

Received August 22, 2001

Abstract—In the angular range 10°–120°, the angular distributions of tritons from the reaction $^{13}C(^3He, t)^{13}N$ induced by ^3He nuclei of energy 60 MeV are measured for transitions to the ground state ($J^\pi = 1/2^-$) of the ^{13}N nucleus and to its excited states at $E_x = 2.365$ MeV ($1/2^+$) and $E_x = 3.51$ MeV ($3/2^-$) + 3.55 MeV ($5/2^+$). A theoretical analysis of these data is performed within the distorted-wave method under the assumption of the one-step charge-exchange mechanism. This analysis employs a microscopic form factor that takes into account the central and tensor components of nucleon–nucleon interaction. It is shown that an acceptable description of the experimental data in question is achieved with potentials whose volume integrals do not exceed 300 MeV fm^3. © *2003 MAIK "Nauka/Interperiodica".*

1. INTRODUCTION

Charge-exchange reactions—in particular, $(^3He, t)$ reactions—provide the most universal means for studying the spin–isospin structure of nuclei, since it is possible in this case to perform investigations over the entire excitation-energy region, including the region inaccessible to beta-decay explorations. In describing such reactions, use is usually made of the microscopic distorted-wave method, where effective interaction is represented as the sum of interactions between projectile and target nucleons [1–6]. In principle, this model furnishes the possibility of deducing information about the structure of nuclei, but this possibility can actually be realized only in the case where the reaction under study proceeds through the one-step charge-exchange mechanism and where the effective interaction is well known.

Yet another difficulty involved in the calculation of cross sections on the basis of the distorted-wave method is that which is associated with the ambiguity in choosing optical potentials. For a long time since the studies reported in [7, 8], it seemed that the discrete-ambiguity problem had been removed and that, by analyzing elastic scattering measured at fairly high projectile energies, in which case nuclear-rainbow effects caused by the refractive properties of the potential clearly manifest themselves in angular distributions, the potential could be determined nearly unambiguously. Later on, there appeared, however, a large number of studies [6, 9, 10–12], where it was shown that some degree of ambiguity remains because of a correlation between the real and the imaginary part of the potential. By way of example, we indicate that, in exploring the elastic scattering of ^3He on ^{13}C at energies of 50 and 60 MeV, eight potentials were found in [9] that describe equally well the measured angular distributions over the entire region of angles. An analysis revealed that the experimental cross sections can be reproduced at nearly all values of the volume integral J_V of the real part of the potential that lie in the range 200–450 MeV fm^3; therefore, the value of J_V cannot be determined from scattering data alone without imposing additional constraints on its parameters. Despite a distinct manifestation of nuclear-rainbow effects in scattering, the ambiguity in choosing potentials remains because of a strong correlation between their imaginary and real parts, which makes it possible to compensate for variations in a real part, even within a rather wide region, by the appropriate variations in the corresponding imaginary part (and vice versa) without spoiling the quality of a fit.

The present article reports on studying the reaction $^{13}C(^3He, t)^{13}N$ at a projectile energy of 60 MeV. Our attention was focused primarily on the following questions:

(i) How do refractive effects manifest themselves in this charge-exchange reaction?

(ii) Is it possible to reduce the ambiguity in choosing optical potentials by supplementing the analysis of elastic scattering with the analysis of the charge-exchange reaction in question?

[1)]Institute of Nuclear Physics, National Nuclear Center of the Republic of Kazakhstan, Almaty, 480082 Republic of Kazakhstan.

1063-7788/03/6601-0047$24.00

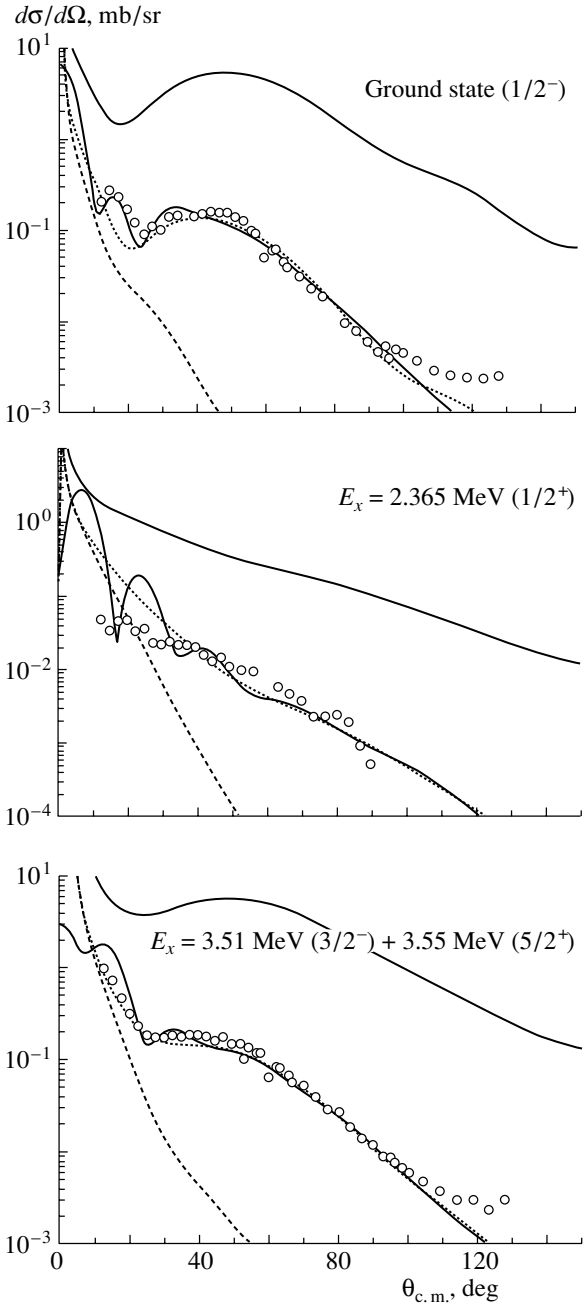

Fig. 1. Angular distributions of tritons from the reaction ^{13}C(^{3}He, t)^{13}N induced by 60-MeV ^{3}He nuclei that proceeds through the channels involving transitions to the ground state ($J^\pi = 1/2^-$) of the ^{13}N nucleus and to its excited states at 2.365 MeV ($1/2^+$) and 3.51 MeV ($3/2^-$) + 3.55 MeV ($5/2^+$). The solid curves represent the results of the calculation by the distorted-wave method under the assumption of the one-step charge-exchange mechanism. The dashed and dotted curves were obtained by decomposing the cross sections into the near and the far component, respectively. The upper solid curves correspond to the calculation for the far component with zero imaginary part of the optical potential. Points (open circles) represent experimental data of our present study.

2. EXPERIMENTAL PROCEDURE AND EXPERIMENTAL RESULTS

The (^{3}He, t) reaction in question was explored at the isochronous cyclotron of the Institute of Nuclear Physics (National Nuclear Center of the Republic of Kazakhstan), the beam energy being 60 MeV in this experiment. For a target, we used a self-supporting carbon film of thickness 1.2 mg/cm^2 enriched in the ^{13}C isotope to 86%. Charged reaction products were recorded by a telescope consisting of a thin (200-μm-thick) surface-barrier silicon detector and a thick Ge(Li) detector whose sensitive region had a depth of up to 7 mm. The product tritons were identified by employing a computer-based system for a ΔE–E two-dimensional analysis. The energy resolution was not poorer than 600 keV and was determined primarily by the beam-energy spread and the target thickness. The angular distributions of tritons for transitions to the ground state ($J^\pi = 1/2^-$) of the ^{13}N nucleus and to its excited states at $E_x =$ 2.365 MeV ($J^\pi = 1/2^+$) and $E_x = 3.51$ MeV ($J^\pi = 3/2^-$) + 3.55 MeV ($J^\pi = 5/2^+$) were obtained in the angular range 10°–120°. The results are displayed in Fig. 1. It can be seen from this figure that, for transitions to the ground state ($1/2^-$) and to the states at 3.51 MeV ($3/2^-$) + 3.55 MeV ($5/2^+$), which are unresolved in our experiment, the angular distributions in question have a broad maximum in the angular range 40°–50° and exhibit a monotonic exponential decrease at larger angles. With respect to the rainbow maximum that was observed in the elastic scattering of ^{3}He by ^{13}C at the same energy in [9], the above maximum is shifted by 10°–15° toward smaller angles. In the case of the transition to the $1/2^+$ state at 2.365 MeV, there are no structures of the above type in the angular range 40°–50°.

3. ANALYSIS OF THE RESULTS

It was assumed that the reaction (^{3}He, t) proceeds through the one-step charge-exchange mechanism. In calculating the differential cross sections, we relied on the distorted-wave method and employed a microscopic form factor. Within this method, the amplitude of the process has the form

$$T_{if} = \int dr\, \chi_f^{(-)*}(\mathbf{k}_f, \mathbf{r}) F(\mathbf{r})\, \chi_i^{(+)}(\mathbf{k}_i, \mathbf{r}),$$

where $\chi_{i(f)}$ represents distorted waves that describe the relative motion of participant nuclei in the input (output) channel and r is the distance between the centers of mass of colliding nuclei. Within a microscopic model, the reaction form factor can be written as

$$F(\mathbf{r}) = \sum_{i,j} \langle bB|v_{ij}|aA\rangle,$$

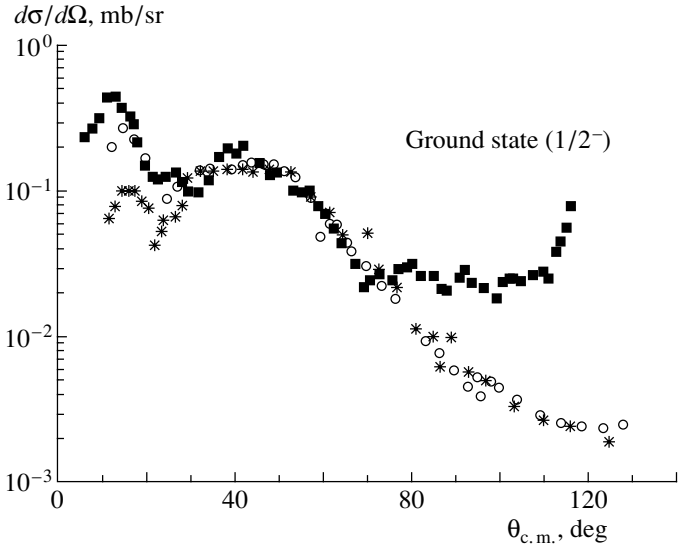

Fig. 2. Experimental angular distributions for the reaction ^{13}C(^{3}He, t)^{13}N proceeding through transitions to the ground state of the ^{13}N nucleus at the beam energies of (closed boxes) 40, (open circles) 60, and (asterisks) 72 MeV. The scale of angles was reduced to the energy of 60 MeV ($\theta' = \theta(E_i/60)$ MeV).

where aA and bB are the internal wave functions for, respectively, the initial- and the final-state nuclei and v_{ij} is the effective interaction between the ith nucleon of the projectile nucleus and the jth nucleon of the target nucleus.

The effective interaction between the nucleons of colliding nuclei included the central and the tensor component; that is,

$$v_{ij}(r_{ij}) = \{[V_\tau + V_{\sigma\tau}(\boldsymbol{\sigma}_i \cdot \boldsymbol{\sigma}_j)]g(r_{ij}) + V_T S_{ij} g_T(r_{ij})\}(\boldsymbol{\tau}_i \cdot \boldsymbol{\tau}_j),$$

where V_τ, $V_{\sigma\tau}$, and V_T are the strength parameters of, respectively, the isospin, the spin–isospin, and the tensor interaction; $S_{ij} = (3/r^2)(\boldsymbol{\sigma}_i \cdot \mathbf{r}_{ij})(\boldsymbol{\sigma}_j \cdot \mathbf{r}_{ij}) - (\boldsymbol{\sigma}_i \cdot \boldsymbol{\sigma}_j)$ is the relevant tensor operator; and $\mathbf{r}_{ij} = \mathbf{r} + \mathbf{r}_i - \mathbf{r}_j$, $\mathbf{r}_{i(j)}$ being the nucleon coordinates with respect to the center of mass of nucleus a (A). The radial dependence of the central interaction was chosen in the Yukawa potential form $g(r) = \exp(-\mu r)/(\mu r)$, with the parameter being set to $\mu = 0.7$ fm^{-1}. The tensor interaction was taken in the form of the one-pion-exchange potential with the same value of μ. The strength parameters had the values of $V_\tau = 6.0$ MeV, $V_{\sigma\tau} = 4.0$ MeV, and $V_T = 2.0$ MeV. A normalization factor was introduced in order to fit the absolute values of the theoretical cross sections to the experimental results. The interaction-parameter values indicated above are close to those from [5]. The volume integrals for the central interaction ($J_\tau = 219.8$ MeV fm^3, $J_{\sigma\tau} = 146.5$ MeV fm^3) comply with the corresponding values obtained from an analysis of the relevant (p, n) reaction by using the Yukawa potential at $\mu = 1.0$ fm^{-1} [13].

The calculations were performed with the aid of the standard DWUCK4 code [14] implementing the distorted-wave method and disregarding the dimensions of a projectile particle, its internal wave function being taken in the delta-function form.

The transitions from the ground state of the ^{13}C nucleus to the excited states of the ^{13}N nucleus at 2.365 MeV ($1/2^+$) and 3.51 MeV ($3/2^-$) + 3.55 MeV($5/2^+$) were considered as the transitions of a nucleon from the $1p_{1/2}$ shell, respectively, to the $2s_{1/2}$ shell and to the $1p_{3/2}$ and $1d_{5/2}$ shells. The single-particle wave functions were computed for the Woods–Saxon potential at the radius values set to $r_0 = 1.25$ fm and $r_C = 1.30$ fm and the diffuseness parameter set to $a = 0.65$ fm. The depth of the potential was determined from a fit to the nucleon binding energy. For each of the transitions being considered, the selection rules for the one-step charge-exchange mechanism admit two values of the total-angular-momentum transfer. These are $\Delta J^\pi = 0^+, 1^+$; $\Delta J^\pi = 0^-, 1^-$; and $\Delta J^\pi = 1^+, 2^+$ for the transitions to the ground state, the excited state at 2.365 MeV ($1/2^+$), and the excited state at 3.51 MeV ($3/2^-$), respectively.

In order to describe the distortions of the relative motion of the nuclei, the same phenomenological potentials whose radial dependence involves the Woods–Saxon form and its derivative were used both for the input and for the output channel. These potentials are given by

$$U(r) = V f_R(r) + i(W f_I(r) + 4W_D a_D df_D(r)/dr)$$

Parameters of the optical potential used in calculating distortions in the reaction ^{13}C(^{3}He, t)^{13}N

$-V$, MeV	r_V, fm	a_V, fm	$-W$, MeV	r_W, fm	a_W, fm	W_D, MeV	r_D, fm	a_D, fm	V_{so}, MeV	r_{so}, fm	a_{so}, fm	J_V^*, MeV fm^3
142.6	0.67	0.81	3.95	2.58	0.42	6.35	1.1	0.48	6.84	0.38	1.24	215

* This is the volume integral per pair of interacting particles (a projectile and a target nucleus).

$$+ (h/(m_\pi c))^2 V_{so}(1/r)(df_{so}(r)/dr)(\mathbf{L}\cdot\boldsymbol{\sigma}) + V_C(r),$$

where $f_i(r) = [1 + \exp((r - R_i)/a_i)]^{-1}$ is the Woods–Saxon form factor, with $R_i = r_i A^{1/3}$ and a_i being its radius and diffuseness parameter; V, W, W_D, and V_{so} are the depths of the real, the volume imaginary, the surface imaginary, and the spin–orbit potential, respectively; and V_C is the Coulomb potential of a uniformly charged sphere of radius $R_C = 1.3A^{1/3}$.

4. DISCUSSION OF THE RESULTS

It was indicated above that, for the transitions to the ground state of the ^{13}N ($1/2^-$) nucleus and to its excited states at 3.51 MeV ($3/2^-$) + 3.55 MeV ($5/2^+$), the experimental angular distributions of tritons have a broad maximum in the angular range 40°–50° and exhibit a sharp exponential decrease at larger angles. This behavior of the cross sections is similar to the behavior of the elastic-scattering cross section measured in [9] at the same energy value. The only difference is that, in elastic scattering, the maximum in question is observed at an angle of about 60°. It is well known that this maximum owes its existence to the refractive properties of the nuclear potential. In classical physics, it corresponds to the boundary deflection angle, also known as the rainbow-scattering angle. We will now show that the maxima observed in the (^{3}He, t) reaction and in elastic scattering are of the same origin. We will illustrate this statement by merely comparing the experimental angular distributions for the reaction ^{13}C(^{3}He, t)^{13}N that are measured at different values of the ^{3}He energy. In the semiclassical approximation, the differential cross sections are described by the Airy function in the vicinity of the rainbow maximum, the position of the maximum changing with energy according to the $1/E$ law. We note that the shift of ordinary oscillations with energy is in inverse proportion to the square root of it. The angular distributions of tritons from the reaction ^{13}C(^{3}He, t)^{13}N proceeding via the transition to the ground state of the ^{13}N nucleus are given in Fig. 2, where the cross sections measured in [5] at energies of 40 and 72 MeV are shown in addition to our data. For the clarity of presentation, the scale of energy is reduced to the energy value of 60 MeV ($\theta' = \theta(E_i/60\ \text{MeV})$). In doing this, no additional normalization of the cross sections was performed. As might have been expected, the cross sections at all three energy values agree in the region of the rainbow bump. Distinctions are observed only at small angles, in the region of Fraunhofer oscillations, and at large angles (there, the experimental points corresponding to the energy of 40 MeV lie considerably higher). A rainbow character of the angular distributions in (^{3}He, t) reactions was predicted in [15, 16] and, for the first time, was comprehensively explored in [5, 6]. It should be noted, however, that rainbow effects do not manifest themselves in the transition to the state at $E_x = 2.365$ MeV ($1/2^+$). The reason for this will be discussed below.

Our calculations were performed with potentials that were found from an analysis of the elastic scattering of ^{3}He on ^{13}C at an energy of 60 MeV. Their parameters are given in [9]. In order to reproduce experimental data, the calculated cross sections were increased by a factor of 2.5 for the transition to the ground state of the ^{13}N nucleus, by a factor of 2 for the transition to its excited state at 2.365 MeV ($1/2^+$), and by a factor of 1.5 for the transition to its excited states at 3.51 MeV ($3/2^-$) + 3.55 MeV ($5/2^+$). These normalization factors do not exhibit a sizable dependence on the potential used. However, the shape of the angular distributions is described well only in the case where the volume integral of the real part of a potential does not exceed 300 MeV fm^3. Calculations with potentials of greater strength ($J_V \sim$ 400 MeV fm^3) predict the rainbow-maximum position in the vicinity of 60° (that is, in the region where it occurs in elastic scattering), but this is at odds with the experimental differential cross sections for the (^{3}He, t) reaction in question. Figure 1 shows the computed differential cross sections along with their experimental counterparts. The optical potential that provides the best fit to experimental data is specified in the table. At present, values of the volume integral J_V around 400 MeV fm^3 are thought to be the most reasonable for the interaction of ^{3}He nuclei and alpha particles with p-shell nuclei. This follows both from the predictions of folding models and from data of a global phenomenological analysis of elastic scatter-

ing in the energy range between 10 and 200 MeV [17, 18].

Proceeding to discuss previous investigations of $(^3He, t)$ reactions, we would like to emphasize that by no means is it always possible to obtain an acceptable description of such a reaction by using potentials found from an analysis of elastic scattering. For example, Ball and Cerny [2], who studied $(^3He, t)$ reactions on p-shell nuclei at an energy of about 40 MeV, found that cross sections calculated with such potentials do not reproduce a deep minimum observed in the angular range 35°–45° for transitions involving an angular-momentum transfer of $L = 0$. Agreement with experimental data was attained only upon a 7% reduction of the real part of the optical potential.

In order to reproduce the shapes of the angular distributions of tritons in the angular range 20°–40° that originate from the $(^3He, t)$ reactions on nuclei from ^{12}C to ^{90}Zr, Van der Wef *et al.* [4] had to reduce the depth of the real and the imaginary potential for the output channel by 15%.

In order to match the computed and measured cross sections for the transitions to the states at 2.31 MeV (0^+) and 3.95 MeV (1^+) of the ^{14}N nucleus in the reaction $^{14}C(^3He, t)^{14}N$, the depth of the real potential for the triton was reduced by 30% in relation to that for ^3He [6]. As to the case of the transition to the ground state, only by modifying the form factor in the surface region could one achieve there agreement with respective experimental data [6]. The distinction between the nuclear potentials for ^3H and ^3He is due to their isospin dependence—by and large, the potential is shallower for ^3H than for ^3He. However, this distinction (about 2 to 3%) is not as great as that which is required for a satisfactory description of experimental data. As to the case of the mirror reaction $^{13}C(^3He, t)^{13}N$, the optical potentials for ^3H and ^3He are identical there. In the above examples, where the parameters of the optical potentials that were found from an analysis of elastic scattering had to be modified in order to attain agreement with experimental data, the volume integrals J_V were greater than 300 MeV fm^3. Thus, the data of our analysis and the results of previous investigations indicate that, by studying the reaction $(^3He, t)$, the ambiguity in choosing optical potentials can be reduced in a sense that data on this reaction are compatible only with those potentials whose volume integrals do not exceed $J_V = 300$ MeV fm^3.

Apart from the full results for the calculated cross sections, Fig. 1 displays the cross sections corresponding to the decomposition of the reaction amplitude into the near (dashed curves) and the far (dotted curves) component [19]. It can be seen that the various types of behavior of the experimental differential cross sections for the transitions to the ground and excited states of the ^{13}N nucleus in the rainbow-maximum region and at large angles are well reproduced by the far component. In terms of classical mechanics, this component is associated with trajectories going on the farther side of the target nucleus, corresponding to particle scattering by a nuclear field at negative angles. Both the theoretical and the experimental cross sections have broad maxima in the angular range 40°–50° for the transitions to the ground state $(1/2^-)$ and to the excited states at $E_x =$ 3.51 MeV $(3/2^-) + 3.55$ MeV $(5/2^+)$, but they do not exhibit such a maximum for the transition to the excited state at 2.365 MeV $(1/2^+)$. These distinctions

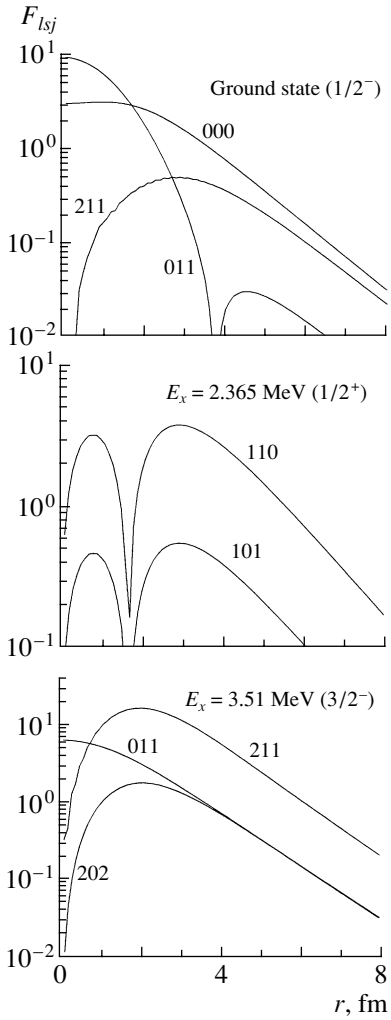

Fig. 3. Theoretical charge-exchange form factors for transitions to the ground state $(J^\pi = 1/2^-)$ of the ^{13}N nucleus and to its excited states at 2.365 MeV $(1/2^+)$ and 3.51 MeV $(3/2^-)$. The relevant quantum numbers lsj are indicated on the curves.

are the most pronounced in the behavior of the cross sections that were calculated for the far components at W, $W_D = 0$ and which are represented by the upper solid curves in Fig. 1. From Fig. 1, it can also be seen that the point of intersection of the cross-section curves corresponding to the near and the far component lies in the vicinity of 0°; in the case of elastic scattering, it occurs at 25° [9]. This shift can be explained in the following way: the amplitude of the charge-exchange reaction in question is determined by short-range nuclear forces, whence one can conclude that the interaction region does not extend beyond the nuclear volume even if the final particle is emitted at small angles; in the case of elastic scattering, however, the long-range Coulomb field, which plays the role of a scattering lens, shifts the characteristic structure of the angular distributions toward larger angles. This is precisely the reason why the rainbow maximum in the reaction ^{13}C(^{3}He, t)^{13}N is shifted with respect to the maximum in the corresponding elastic-scattering process.

The structures observed in the angular distributions can be explained by the distinctions between the charge-exchange form factors for the transitions being considered (see Fig. 3). The form factor for the transition to the ground state ($1/2^-$) of the ^{13}N nucleus and the form factor for the transition to its excited state at 3.51 MeV ($3/2^-$) contain three components each, which are specified by the quantum numbers lsj (as usual, l, s, and j are, respectively, the orbital-angular-momentum transfer, the spin transfer, and the total-angular-momentum transfer) of 000, 011, and 211 for the former and 011, 211, and 202 for the latter. The monopole components ($lsj = 000, 011$) enhance the role of central trajectories, and rainbow maxima in the angular range 40°–50° clearly manifest themselves in the angular distributions of tritons. On the contrary, the form factor for the transition to the excited state at 2.365 MeV ($1/2^+$) is determined by the orbital-angular-momentum transfer of $l = 1$, and this leads to the reduction of the contribution from trajectories at distances of 1.5 to 2.5 fm. It is not surprising that, in this case, the far component of the cross section features no structures in the angular range 40°–50°. The role of central trajectories in the formation of the rainbow maximum is demonstrated by the calculations for the transition to the ground state of the ^{13}N nucleus that involve a cutoff form factor (Fig. 4): a cutoff up to $r = 1$ fm has virtually no effect on the shapes of the angular distributions, but, even at $r = 1.5$–2.5 fm, the rainbow maximum disappears, which is accompanied by the emergence of diffractive oscillations over the entire interval of angles.

Thus, the description of (^{3}He, t) reactions is highly sensitive to the behavior of the relevant form factor; if this form factor is known to an insufficiently high precision, this may lead to inadequate results in describing experimental data with potentials found from an analysis of elastic scattering. The reliability of the form factor used in analyzing charge-exchange reactions depends on whether the internal nuclear wave functions and the effective interaction are known quite well. Demyanova *et al.* [20], who studied the reaction (^{6}Li,^{6}He) at an energy of 93 MeV, showed that, by modifying the form factor, one can improve agreement with experimental data for potentials whose volume integral J_V is greater than 300 MeV fm^3. However, it is hardly possible to refine the form factor empirically because of the ambiguity in choosing optical potentials.

Analyzing the results, we did not go beyond the one-step charge-exchange mechanism. In considering the possible contribution of two-step processes, it is necessary, above all, to take into account the mechanism of sequential one-nucleon transfers according to the ^{3}He–d–t and ^{3}He–α–t schemes. The calculations performed in [3] reveal that the shapes of the angular distributions for the one-step mechanism may differ significantly from those for the two-step mechanism. The theoretical cross sections for the one-step mechanism decrease more sharply. Therefore, the two-step mechanism can no longer be taken into account implicitly by renormalizing the calculated cross sections. Similar results were also obtained in studying different charge-exchange reactions, (^{7}Li, ^{7}Be) in [21] and (^{6}Li, ^{6}He) in [22].

Let us estimate the relationship between the one- and the two-step mechanism in (^{3}He, t) reactions. In order to evaluate the cross section for the two-step mechanism (σ_s), we make use of the rough approximation

$$\sigma_s = \frac{A\sigma_1\sigma_2}{\sqrt{E}},$$

where σ_1 and σ_2 are the cross sections for one-nucleon transfer at, respectively, the first and the second step of the reaction; E is the projectile energy; and A is a constant. In the case being considered, σ_1 stands for the cross sections for the (^{3}He, α) and (^{3}He, d) reactions, while σ_2 represents the cross sections for the (α, t) and (d, t) reactions. This energy dependence is confirmed by more rigorous calculations (see, for example, [23, 24]) in which sequential nucleon transfer was taken into account within the coupled-channel method. The cross sections measured for (^{3}He, α) [25–27], (α, t) [28, 29], (^{3}He, d) [30–32], and (d, t) [33, 34] reactions in the energy range between 15 and 60 MeV change only slightly

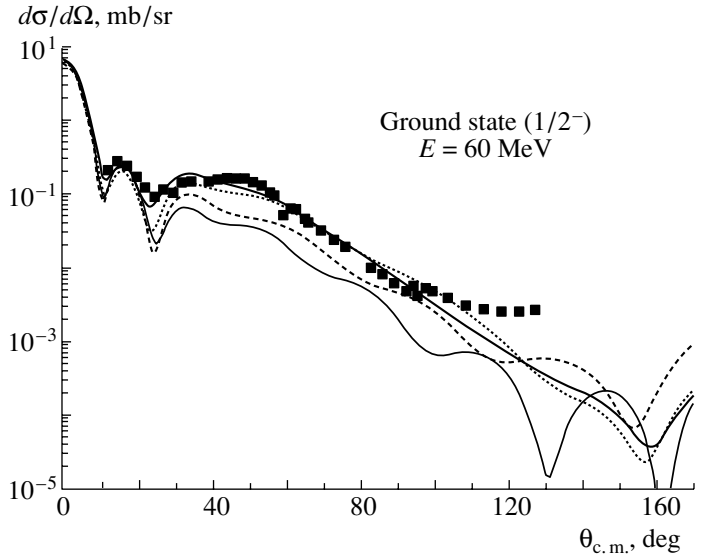

Fig. 4. Shapes of the computed cross sections for the transition to the ground state of the ^{13}N nucleus in the reaction $^{13}C(^3He, t)^{13}N$ for various values of the cutoff radius in the charge-exchange form factor. The dotted, the dashed, and the lower solid curve correspond to the cutoff at $r = 1.5$, 2.0, and 2.5 fm, respectively. The upper solid (thick) curve represents the results of the cutoff-free calculation.

with energy at small angles and, at zero angle, are approximately equal to 10–15 mb/sr. Therefore, σ_1 and σ_2 can also be treated, to a high precision, as constants. For an absolute normalization of the cross section, we make use of the experimental value ($\sigma =$ 2 mb/sr) measured in the (^{3}He, t) reaction at an energy of 14 MeV [35], assuming that it is fully determined by the two-step mechanism. The energy dependence obtained in this way is represented by the solid curve in Fig. 5.

The energy dependence of the cross section for the direct charge-exchange process was borrowed from [36]. According to the calculations presented in [36], the cross section for direct charge exchange in the reaction $^{12}C(^{12}C,^{12}N)^{12}B$ grows exponentially with energy, reaching saturation at an energy of $E = 40$ MeV per nucleon. It is expected that the cross sections for (^{3}He, t) reactions depend similarly on energy per nucleon. The dotted curve in Fig. 5 represents the energy dependence of the cross sections for the reaction $^{13}C(^3He, t)^{13}N_{g.s.}$. These results were normalized to the experimental cross sections for zero angle that were measured at the ^{3}He-beam energies of 200 [37] and 600 MeV [38] under conditions ensuring the one-step character of the process. From Fig. 5, it can be seen that the contribution of the two-step mechanism realized through sequential nucleon transfer is negligible at ^{3}He energies in excess of 100 MeV, but that it may become as great as 50% at 60–70 MeV.

It follows that more rigorous calculations involving both mechanisms may significantly change the shape of the theoretical angular distribution; taking this into consideration, one can imagine that agreement with experimental data will also become possible with physically reasonable potentials characterized by $J_V > 300$ MeV fm^3.

At present, however, it is still unclear why data

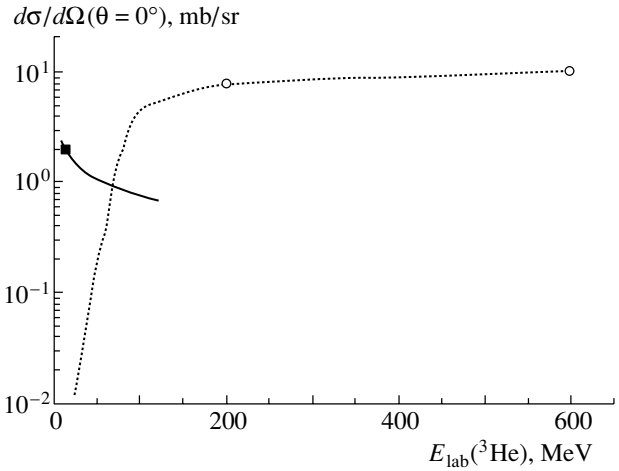

Fig. 5. Estimates of the energy dependences of the cross sections for the one- and for the two-step mechanism of the reaction $^{13}C(^3He, t)^{13}N$ proceeding via the transition to the ground state of the ^{13}N nucleus. The solid and the dotted curve represent the results for the two-step process and the direct charge-exchange process, respectively. Points correspond to the experimental cross sections for zero angle at energies of (closed box) 14 MeV [35], (open circle) 200 MeV [37], and (open circle) 600 MeV [38].

on (^{3}He, t) reactions favor, among potentials found from analyses of elastic scattering, those that are unphysical according to current ideas.

In order to draw definitive conclusions, it is necessary to perform additional investigations that would make it possible to estimate directly the possible contribution of two-step processes to the reaction being considered.

5. CONCLUSION

The reaction ^{13}C(^{3}He, t)^{13}N induced by ^{3}He projectiles of energy 60 MeV has been investigated at the isochronous cyclotron of the Institute of Nuclear Physics (National Nuclear Center of the Republic of Kazakhstan). The angular distributions of tritons in the angular range 10°–120° have been measured for transitions to the ground state ($1/2^-$) of the ^{13}N nucleus and to its excited states at $E_x =$ 2.365 MeV ($1/2^+$) and $E_x = 3.51$ MeV ($3/2^-$) + 3.55 MeV ($5/2^+$). For the transitions to the negative-parity states, the angular distributions exhibit a broad maximum in the angular range 40°–50°. This maximum, which owes its existence to the refractive properties of the nuclear potential, is shifted by 10° to 15° toward smaller angles with respect to the rainbow maximum in the elastic scattering of ^{3}He on ^{13}C at the same energy. No special features in the angular distributions for the transition to the state at 2.365 MeV ($1/2^+$) have been observed in the angular range 40°–50°.

Our analysis has been based on the distorted-wave method and has been performed with a microscopic form factor under the assumption of the one-step charge-exchange mechanism. In calculating distortions, use has been made of the potentials found from an analysis of the elastic scattering of ^{3}He on ^{13}C at an energy of 60 MeV. It has been shown that an acceptable description of the angular distributions in question can be achieved only with potentials whose volume integrals do not exceed 300 MeV fm^3. However, it is currently thought that J_V values around 400 MeV fm^3 are the most reasonable for the interaction of ^{3}He and alpha particles with p-shell nuclei.

Distinctions between the shapes of the angular distributions for the transitions studied here have been explained by special features of the relevant charge-exchange form factors. In (^{3}He, t) reactions, the rainbow effect disappears if the form factor does not involve $l = 0$ components.

So far, it has remained unclear why the (^{3}He, t) reaction considered here selects, among the potentials found from an analysis of elastic scattering, unphysical ones characterized by the volume integral of the real part in the region $J_V < 300$ MeV fm^3.

Dedicated investigations are required in order to answer this question; first of all, it is desirable to take into account, via calculations based on the coupled-channel method, the possible contribution of two-step processes to the reaction in question.

REFERENCES

1. F. A. Gareev, S. N. Ershov, A. A. Ogloblin, and S. B. Sakuta, Fiz. Élem. Chastits At. Yadra **20**, 1293 (1989) [Sov. J. Part. Nucl. **20**, 541 (1989)].
2. G. C. Ball and J. Cerny, Phys. Rev. **177**, 1466 (1969).
3. T. Tanabe, M. Yasue, K. Sato, *et al.*, Nucl. Phys. A **311**, 38 (1978).
4. S. Y. van der Weff *et al.*, Nucl. Phys. A **496**, 305 (1989).
5. A. S. Demyanova, A. A. Ogloblin, S. N. Ershov, *et al.*, Phys. Scr. **32**, 89 (1990).
6. A. S. Demyanova, A. A. Ogloblin, Yu. A. Lyashko, *et al.*, Phys. Rev. C **38**, 1975 (1988).
7. D. A. Goldberg and S. M. Smith, Phys. Rev. Lett. **29**, 500 (1972).
8. D. A. Goldberg, S. M. Smith, and G. F. Burdzik, Phys. Rev. C **10**, 1362 (1974).
9. N. Burtebaev, A. Duĭsebaev, B. A. Duĭsebaev, and S. B. Sakuta, Yad. Fiz. **63**, 625 (2000) [Phys. At. Nucl. **63**, 562 (2000)].
10. K. B. Baktybaev, A. D. Duĭsebaev, and A. B. Kabulov, Izv. Akad. Nauk Kaz. SSR, Ser. Fiz.-Mat., No. 6, 68 (1974).
11. L. Freindl, H. Dabrowski, K. Grotowski, and R. Planeta, Raport No. 1059/PL, IFJ (Krakow, 1979).
12. P. L. Roberson, Phys. Rev. C **22**, 482 (1980).
13. S. M. Austin, in *Proceedings of the Conference "The (p,n) Reaction and the Nucleon–Nucleon Force,"* Ed. by C. D. Goodman *et al.* (Plenum, New York, 1980), p. 203.
14. P. D. Kunz, Code DWUCK4 (unpublished).
15. Yu. A. Berezhnoĭ and V. V. Pilipenko, Dokl. Akad. Nauk Ukr. SSR, Ser. A, No. 5, 52 (1984).
16. Yu. A. Berezhnoy and V. V. Pilipenko, J. Phys. G **11**, 1161 (1985).
17. R. Görgen, F. Hinterberger, R. Jahn, *et al.*, Nucl. Phys. A **320**, 296 (1979).
18. H.-J. Trost, P. Lezoch, and U. Strohbusch, Nucl. Phys. A **462**, 333 (1987).
19. R. C. Fuller, Phys. Rev. C **12**, 1561 (1975).
20. A. S. Demyanova, J. M. Bang, F. A. Gareev, *et al.*, Nucl. Phys. A **501**, 336 (1989).
21. S. B. Sakuta, Yu. A. Glukhov, A. T. Rudchik, *et al.*, Nucl. Phys. A **587**, 355 (1995).
22. S. B. Sakuta, Yu. A. Glukhov, A. T. Rudchik, *et al.*, Nucl. Phys. A **639**, 599 (1998).
23. H. G. Bohlen, H. Lenske, and H. H. Wolter, *Jahresbericht Hahn-Meitner-Institut* (Berlin, 1987), p. 1.
24. W. von Oertzen, Preprint HMI-P 87/9 (1987).

25. K. P. Artemov, V. Z. Gol'dberg, V. P. Rudakov, and I. N. Serikov, Yad. Fiz. **7**, 500 (1968) [Sov. J. Nucl. Phys. **7**, 314 (1968)].
26. V. V. Adodin, N. T. Burtebaev, and A. D. Duĭsebaev, Yad. Fiz. **55**, 577 (1992) [Sov. J. Nucl. Phys. **55**, 319 (1992)].
27. V. Burjan, J. Ceipek, J. Fojtu, *et al.*, Phys. Rev. C **49**, 977 (1994).
28. P. Gaillard, R. Bouche, L. Feurrais, *et al.*, Nucl. Phys. A **131**, 353 (1969).
29. G. Hauser, R. Lohken, G. Nowicki, *et al.*, Nucl. Phys. A **182**, 1 (1972).
30. C. H. Holbrow, R. Middleton, W. Focht, *et al.*, Phys. Rev. **183**, 880 (1969).
31. P. V. Drumm, O. Karban, A. K. Basak, *et al.*, Nucl. Phys. A **448**, 93 (1986).
32. P. Bem, V. Burjan, V. Kroha, *et al.*, Phys. Rev. C **62**, 024320 (2000).
33. M. Gaillard, R. Bouche, L. Feurrais, *et al.*, Nucl. Phys. A **119**, 161 (1968).
34. F. Hinterberger, G. Mairle, U. Schmidt-Rohr, *et al.*, Nucl. Phys. A **106**, 161 (1968).
35. F. Nüsslin and P. Braun-Munzinger, Z. Phys. **240**, 217 (1970).
36. J. S. Winfield, N. Anantaraman, Sam. M. Austin, *et al.*, Phys. Rev. C **33**, 1333 (1986).
37. J. Jänecke, F. D. Becchetti, A. M. Van den Berg, *et al.*, Nucl. Phys. A **526**, 1 (1991).
38. I. Bergqvist, A. Brockstedt, L. Carlén, *et al.*, Nucl. Phys. A **469**, 648 (1987).

Translated by A. Isaakyan

Physics of Atomic Nuclei, Vol. 66, No. 1, 2003, pp. 56–60. From Yadernaya Fizika, Vol. 66, No. 1, 2003, pp. 59–63.

NUCLEI
Experiment

Neutron Scattering in Argon and *ne* Interaction*

T. L. Enik , V. A. Ermakov†, R. V. Kharjuzov, L. V. Mitsyna, V. G. Nikolenko, S. S. Parzhitski, A. B. Popov, G. S. Samosvat, and V. A. Vtjurin

Joint Institute for Nuclear Research, Dubna, Moscow oblast, 141980 Russia

Received August 13, 2001; in final form, January 10, 2002

Abstract—As a preparation for the new experiment to measure the ne scattering length a_{ne}, the total neutron cross section of gaseous argon has been obtained by the time-of-flight method at the Dubna booster IBR-30 in the energy range from ∼5 eV to ∼30 keV. A combined one-level analysis of the newly obtained and other known data on cross sections of Ar and ^{36}Ar has made it possible to improve some neutron parameters and calculate the scattering cross section σ_s and the scattering length a separately for ^{36}Ar and ^{40}Ar at any energy. © *2003 MAIK "Nauka/Interperiodica"*.

1. IMPROVED METHOD FOR ne SCATTERING LENGTH MEASUREMENT

A historically first, rather difficult, way of observing the ne interaction by neutron scattering in a gas [1] successfully resulted in obtaining one of the best estimates of the ne scattering length a_{ne} [2]. Since then, there have been no other attempts to use this method. It seems, however, that the resources of the method are far from being exhausted and it can be significantly improved as shown in [3]. Actually, at slow neutron scattering, the ne interaction leads to a rise of a small forward–backward asymmetry against the background of a stronger asymmetry because of kinematics as illustrated in Fig. 1 by the example of the ratio R of scattering intensities at two angles ϑ_1 and $\vartheta_2 = \pi - \vartheta_1$.

Using the cadmium difference method alone, the authors of [2] could only obtain $\langle R\rangle$, i.e., the integral effect of a_{ne} over the entire thermal neutron spectrum. A much more informative way is to obtain the differential effect $R(E)$ as a function of the neutron energy E by the time-of-flight method.

To extract a_{ne} from $\langle R\rangle$ or $R(E)$, it is necessary (i) to take into account the anisotropy caused by the movement of the center of mass (see [2, 3]) and (ii) to use precise values of the quantities entering into combination determining the ne effect in $\langle R\rangle$ and $R(E)$:

$$K = \frac{a^N_{\rm coh} Z a_{ne}}{\sigma^N_s}\frac{A+1}{A}\left[f(E,\vartheta_1) - f(E,\vartheta_2)\right],$$

where $a^N_{\rm coh}$ is the coherent nuclear scattering length; σ^N_s is the total nuclear scattering cross section; and A, Z, and $f(E,\vartheta)$ are the mass number, number of electrons, and the electron form factor of the atom.

Of the four noble gases, we chose argon for the first experiments. It has K/a_{ne}(∼0.13 fm^{-1}), which is a little larger than that of krypton (∼0.10 fm^{-1}) and a little smaller than that of xenon (∼0.15 fm^{-1}). On the other hand, argon has an advantage of a weaker neutron capture: the ratio of thermal-neutron-capture cross section to neutron scattering cross section is approximately 1, 3, and 5 for argon, krypton, and xenon, respectively.

2. MEASUREMENTS

The total neutron cross section of Ar was measured by the time-of-flight method at the Dubna booster IBR-30. A neutron beam ∼30 mm in diameter is alternately transmitted through a vacuum tube and an identical tube with natural argon at ∼50 atm. The argon-sample thickness is 995.9 mm or 0.1241 ± 0.0005 b^{-1}.

The neutron detector is installed on the 242-m flight path and is a battery of ^{3}He counters divided into 16 units providing 16 independent neutron spectra. The instantaneous counting rate in each spectrum does not exceed 3×10^3 s^{-1}, which removes the necessity of any dead-time correction.

One of the combinations of the filters B_4C, Al, Ti, MnO, Co, Ni, W, and Au was permanently in the beam.

The measuring process is controlled by a PC and consists of alternating 20-min exposures with and without argon in the beam and the summing up of the accumulated spectra and counts from beam monitors.

†Deceased.
*This article was submitted by the authors in English.

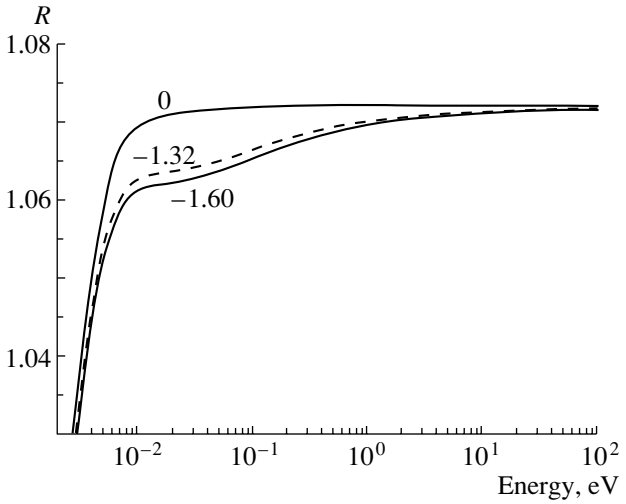

Fig. 1. The calculated ratio R of scattering intensities at angles 45° and 135° in ^{40}Ar for the indicated a_{ne} values in 10^{-3} fm.

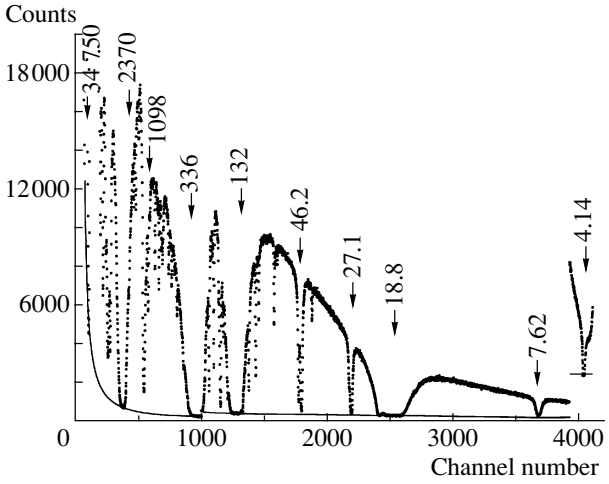

Fig. 2. The spectrum of counts taken in 21 h with an open beam and the curve of the background. The channel width is 1 μs for the channel interval 1–1000, 2 μs for the interval 1001–3916, and 16 μs for the 3917–4096 channels. The energies of some resonances are shown in eV.

3. OBTAINING THE TOTAL CROSS SECTION

Let N_i^0 and N_i be the counts of neutrons in the time channel i going through the vacuum and argon tubes, respectively, and being normalized to monitors. For the transmission of argon, we then have

$$T_i = \frac{N_i - B_i}{N_i^0 - B_i^0}, \qquad (1)$$

where B_i^0 and B_i are the corresponding background counts. To determine B_i^0 and B_i, curves of the form

$$B_i = \frac{a}{i-d} + b + ci, \quad B_i^0 = \frac{a_0}{i-d_0} + b_0 + c_0 i \quad (2)$$

were drawn through deep resonance minima in both spectra, N_i and N_i^0. An example of the spectrum N_i and the curve B_i is shown in Fig. 2.

We have, however, found an alternative method for taking into account the background in the T calculation. It follows from a different form of Eq. (1),

$$N_i = T_i N_i^0 + B_i - T_i B_i^0, \qquad (3)$$

and it consists in application of the least-squares method to the spectra N_i and N_i^0 by Eq. (3). Namely, the left-hand sides of the equations are the experimental points, and the right-hand sides are the function describing them.

For a sufficiently narrow energy interval of channels where T_i can be considered to be constant, the difference $B_i - T_i B_i^0$ is even more likely to be constant since the two backgrounds are described with two close curves of the type of Eq. (2). Thus, instead of (3), we have a problem with two constant parameters:

$$N_i = TN_i^0 + C, \qquad (4)$$

where the standard error $\sqrt{2N_i} \approx \sqrt{N_i + TN_i^0}$ should be assigned to every experimental point N_i.

It is important to emphasize that the first method works well for absolutely "black" resonances and it cannot guarantee the correct background far from such resonances. On the other hand, the second method can only be applied if spectra in the given interval have large steep rises or falls. Our spectra only have five or six "black" resonances in 4096 channels, but they have a large number of sharp

Table 1

E, eV	σ_t, mb
5.2	711(19)
10.6	707(10)
25	680(8)
46	689(7)
86	683(8)
186	669(9)
420	668(11)
790	678(19)
1500	557(13)
3200	565(13)
5900	521(23)
10000	427(18)
18600	354(30)
30100	281(21)

intensity jumps. That is why the T values giving the total cross section in barns as $\sigma_t = -0.1241^{-1} \ln T$ are obtained in the present work using the second method, which removes the necessity of fitting a pair of background curves. As for the first method, it gives T values that agree with those of the second method for $E < 7$ keV (for the channel numbers >220), that is, only if the backgrounds B_i^0 and B_i vary not too quickly. For instance, C values for five parts of the channel interval from 1001 to 3916 channels fluctuate within the limits from −27 to −14 with the mean error ∼5, while the B_i^0 value varies approximately from 500 to 250 (see Fig. 2).

The results on σ_t for different average neutron energies E are shown in Table 1 (the statistics are collected for 195 h).

4. OTHER DATA AND ANALYSIS

To carry out an impartial analysis, we summarized all known data on the neutron cross sections of argon up to the energy ∼40 keV. They are σ_t of ^{36}Ar from [4] and σ_t of Ar from [5–7] (the data [7] are reported in [8] and are averaged over six intervals by us) together with the scattering (σ_s [2, 9]) and capture (σ_γ [9, 10]) cross sections of ^{36}Ar and Ar for thermal neutrons ($E = 0.0253$ eV). The whole collection of σ_t for natural argon together with our results is illustrated in Fig. 3.

A combined analysis of all data is done using ordinary one-level expressions for the cross sections of nuclei with a zero spin, including ne scattering:

$$\sigma_s = \frac{4\pi}{k^2}\left\{\sin^2\delta_0 + 3\sin^2\delta_1 + \sum \frac{\Gamma_n\left[\Gamma_n/4 - (\Delta E\cos\delta_0 + (\Gamma/2)\sin\delta_0)\sin\delta_0\right]}{\Delta E^2 + \Gamma^2/4}\right\} + 8\pi a a_{ne} Z f(k), \quad (5)$$

$$a = \frac{1}{2k}\left[-\sin 2\delta_0 + \sum \frac{\Gamma_n\left(\Delta E\cos 2\delta_0 + (\Gamma/2)\sin 2\delta_0\right)}{\Delta E^2 + \Gamma^2/4}\right], \quad (6)$$

$$\sigma_\gamma = \frac{\pi}{k^2}\sum \frac{\Gamma_n\Gamma_\gamma}{\Delta E^2 + \Gamma^2/4}, \quad (7)$$

$$\sigma_t = \sigma_s + \sigma_\gamma, \quad (8)$$

where k is the neutron wave number; $\delta_0 = -kR_0'$ and $\delta_1 = -k^3R^2R_1'/3$ are the phase shifts for s and p wave determined by the corresponding scattering radii R_0' and R_1'; $R = 1.35A^{1/3}$ fm; $\Delta E = E - E_0$ is the deviation from the resonance energy; $\Gamma_n = \Gamma_n^0\sqrt{E[\text{eV}]}$, Γ_γ, and $\Gamma = \Gamma_n + \Gamma_\gamma$ are the neutron, radiative, and total widths of the resonance, respectively; and $f(k) = (q_0/k)^2\left[\sqrt{1 + 12(k/q_0)^2} - 1\right]/6$ is the electron form factor averaged over ϑ [11] ($q_0 = 4.45 \times 10^{-5}$ fm^{-1} for argon).

The cross sections of ^{36}Ar are described by formulas (5)–(8), which contain the parameters of only one known resonance at $E_0 = -10$ keV [10] under the sum sign. Every cross section of Ar nuclei is a weighted sum of those of ^{36}Ar and ^{40}Ar with the weight numbers 0.00337 and 0.99663, respectively. The ^{38}Ar isotope admixture of 0.063%, whose thermal $\sigma_s = (1.5 \pm 1.5)$ b [2], is neglected. As for the resonances of ^{40}Ar, we try to include from zero to eight resonances taken from [12] in the sums.

The main aim of the present analysis is to find such parameters in (5)–(7) that would describe the data best and make it possible to calculate any cross section and scattering length a for both isotopes at any energy.

5. RESULT OF ANALYSIS

We start the analysis with the following values of parameters from [10, 12]:

$$\begin{gathered}\text{for } ^{36}\text{Ar}, R_0' = 3.4(3)\text{ fm}, E_0 = -10(1)\text{ keV}, \quad (9)\\ \Gamma_n^0 = 91.3(10.0)\text{ eV}, \Gamma_\gamma = 1.32(30)\text{ eV};\\ \text{for } ^{40}\text{Ar}, R_0' = 2.7(2)\text{ fm}, E_0 = -1000\text{ eV},\\ \Gamma_n^0 = 0.0573\text{ eV}, \Gamma_\gamma = 1\text{ eV},\end{gathered}$$

plus seven resonances at 70–600 keV with $\Gamma_\gamma = 1$ eV.

As for $R_1' = 8$ fm (obtained by extrapolation from [13]) and $a_{ne} = -1.43 \times 10^{-3}$ fm (being nearly the center of the experimental values for bound atoms [3]), they do not vary because their contributions to σ_s [second and last terms in (5)] are small: 2.3 mb at 30 keV and −6.5 mb at ∼0.025 eV, respectively. This results in the dashed curve for σ_t of Ar in Fig. 3 and $\chi^2 = 4240$ for 72 experimental points of all data. Three points from [5] that are marked by us with large errors are in contradiction with the $1/v$ law and are not included in the fitting.

In the process of fitting,

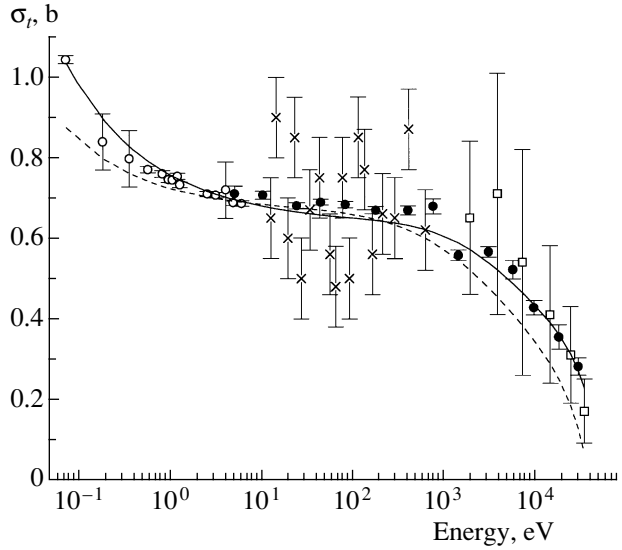

Fig. 3. The total cross section σ_t for natural argon. Points are the data from [5] (open circles), [6] (crosses), and [7, 8] (open squares), and black points are the present data. The dashed curve is the data description with the initial parameters (9); the solid curve is the same with the fitted parameters (10).

(1) it has come to light that one negative and just one positive resonance of ^{40}Ar are necessary and sufficient for the description of the data;

(2) the negative resonance changes most and moves much closer to a zero energy;

(3) the other values experience moderate changes or remain unchanged.

We thus conclude that

$$\text{for } ^{36}\text{Ar}, R'_0 = 2.84(10)\text{ fm}, E_0 = -10\text{ keV}, \quad (10)$$
$$\Gamma_n^0 = 91.3\text{ eV}, \Gamma_\gamma = 1.32\text{ eV};$$
$$\text{for } ^{40}\text{Ar}, R'_0 = 2.405(7)\text{ fm}, E_0 = -100\text{ eV},$$
$$\Gamma_n^0 = 1.08(2)\text{ meV}, \Gamma_\gamma = 1.32\text{ eV},$$
$$E_0 = 76486\text{ eV}, \Gamma_n^0 = 20.509\text{ eV}, \Gamma_\gamma = 1.32\text{ eV},$$

corresponding to the solid curve in Fig. 3 and $\chi^2 = 178$ (errors of fitted parameters are in brackets).

As is seen in Fig. 3, at 5–6 eV, there is a jump of ~30 mb between our data and data from [5]. A very likely reason for that is a mistaken thickness of the sample in one of the papers or in both. Therefore, we did two additional fittings: with σ_t from [5] multiplied by 1.04 and with our σ_t divided by 1.04. This resulted in a decrease of χ^2 to 158 and 96, respectively, and in just a ~2% change of R'_0 for ^{40}Ar.

Table 2

$a^N_{\rm coh}$, fm	σ^N_s, b	$a^N_{\rm coh}/\sigma^N_s$, fm^{-1}
1.880(7)	0.656(4)	0.02867(9)
1.908(7)	0.669(4)	0.02854(9)
1.865(7)	0.649(4)	0.02873(9)
1.873(8)	0.653(3)	0.02868(17)

6. CONCLUSIONS

1. The main result of the investigation is shown in Table 2. It presents the coherent scattering length $a^N_{\rm coh} = \sum \rho a$ and the scattering cross section $\sigma^N_s = 4\pi \sum \rho a^2$ calculated at $E = 0.0253$ eV and averaged over ^{36}Ar and ^{40}Ar, where ρ is the isotope abundance and a is given by (6). The results calculated using the parameters of our main fit are the first line; the second and third lines are the results of additional fittings. It is interesting to compare them with the results of [2], obtained using σ_s of ^{36}Ar and Ar measured in a thermal neutron beam, which are the last line in Table 2. An excellent agreement of the parameters $a^N_{\rm coh}/\sigma^N_s$ that are of most interest for us is obvious, which raises the reliability of the future a_{ne} results. At the same time, the present accuracy of ratio $a^N_{\rm coh}/\sigma^N_s$ allows one, in principle, to reduce the error of the a_{ne} value by a factor of 3–4 compared to the best results.

2. Our next experiment will be an attempt to observe the interference phenomenon of the neutron waves scattered by neighboring atoms of argon. Such an effect is calculated in [13] and can be the next hindrance to the a_{ne} extraction from the $R(E)$ results, especially if the gas pressure is not low. Thus, it is very important to check calculations by an experiment.

ACKNOWLEDGMENTS

This work was supported by the Russian Foundation for Basic Research, project no. 00-02-17814.

REFERENCES

1. E. Fermi and L. Marschall, Phys. Rev. **72**, 1139 (1947).
2. V. E. Krohn and G. R. Ringo, Phys. Rev. **148**, 1303 (1966); Phys. Rev. D **8**, 1305 (1973).
3. G. G. Bunatian, V. G. Nikolenko, A. B. Popov, *et al.*, Z. Phys. A **359**, 337 (1997).
4. R. E. Chrien, A. P. Jain, and H. Palevsky, Phys. Rev. **125**, 275 (1962).
5. D. C. Rorer, B. M. Ecker, and R. O. Akyuz, Nucl. Phys. A **133**, 410 (1969).
6. E. Melkonian, Phys. Rev. **76**, 1750 (1949).
7. H. I. Liou, J. Rainwater, G. Hacken, and U. N. Singh, Phys. Rev. C **11**, 457 (1975).
8. V. McLane, C. L. Dunford, and P. F. Rose, *Neutron Cross Sections* (Academic, New York, 1988), Vol. 2.

9. R. Genin, H. Beil, C. Signarbieux, *et al.*, J. Phys. **24**, 21 (1963).
10. S. F. Mughabghab, M. Divadeenam, and N. E. Holden, *Neutron Cross Sections* (Academic, New York, 1981), Vol. 1, Part A.
11. V. F. Sears, Phys. Rep. **141**, 281 (1986).
12. S. I. Sukhoruchkin, Z. N. Soroko, and V. V. Deriglazov, *Landolt-Börnstein: Numerical Data and Functional Relationships in Science and Technology, New Series,* Ed. by H. Schopper (Springer-Verlag, Berlin, 1998), Vol. 16B.
13. G. S. Samosvat, Fiz. Élem. Chastits At. Yadra **26**, 1567 (1995) [Phys. Part. Nucl. **26**, 655 (1995)].

Physics of Atomic Nuclei, Vol. 66, No. 1, 2003, pp. 6–16. Translated from Yadernaya Fizika, Vol. 66, No. 1, 2003, pp. 8–18.

100th ANNIVERSARY OF I.V. KURCHATOV'S BIRTH

Search for Neutron Resonances in the ^{178m_2}Hf Isomer and Their Investigation

G. V. Muradian, O. Ya. Shatrov, M. A. Voskanian, L. P. Yastrebova, V. L. Volkov, Ch. Briançon[1], M. Hussonnois[2], Yu. Ts. Oganessian[3], S. A. Karamian[3], and O. Constantinescu[3]

Russian Research Centre Kurchatov Institute, pl. Kurchatova 1, Moscow, 123182 Russia

Received June 27, 2002

Abstract—Experiments aimed at detecting and investigating neutron resonances in the ^{178m_2}Hf isomer are described, and the results obtained in these experiments are presented. The investigations in question are of great interest since the structure of this isomer—it is interpreted as the ($\pi 7/2^+$, $\pi 9/2^+$, $\nu 7/2^+$, $\nu 9/2^+$) configuration—and its high spin of $J = 16$ differ significantly from the structure and spin of nuclei studied previously. The experiments performed at the Kurchatov Institute employed a neutron source based on the FAKEL linear electron accelerator and a multisection detector from NaI(Tl) crystals that was able to ensure a 4π coverage. This equipment made it possible to study gamma-ray cascades in radiative neutron capture versus neutron energy. Despite an extremely small number of isomer nuclei, a low content of the isomer in the target used, and its high radioactivity, resonances were discovered that arise upon neutron capture by a high-spin ^{178m_2}Hf nucleus. The parameters of these resonances were found. The mean spacing between the revealed resonances is about 1 eV, which is consistent with calculations based on the Fermi gas model. This indicates that the Fermi gas model describes well the density of both low- and high-spin levels. At the same time, the above agreement suggests that, upon the formation of a compound nucleus, the structure of the isomeric state is destroyed completely. On the other hand, glaring discrepancies between experimental data and the predictions of the statistical model were found: gamma transitions from high-spin resonances ($J = 31/2^+, 33/2^+$) populate predominantly the low-spin ground state ($J = 9/2^+$) rather than the high-spin state of the ^{179m_2}Hf isomer ($J = 25/2^-$); the radiative width is approximately one-third as great as that which is predicted by the statistical model; and the properties of gamma cascades are different for different resonances, this difference being beyond statistical fluctuations. The results of the present investigation make it possible to reveal special features in the behavior of the quantum number K at high excitation energies. © *2003 MAIK "Nauka/Interperiodica".*

1. INTRODUCTION

The discovery of man-made isomers was a commonly recognized achievement of I.V. Kurchatov [1]. In the present article, we describe experiments aimed at searches for neutron resonances in the man-made ^{178m_2}Hf isomer and their investigation and present the results obtained in this way. The ^{178m_2}Hf isomer is characterized simultaneously by a high excitation energy ($E^* = 2.5$ MeV) and by a long half-life ($T = 31$ yr). In 1936, when Kurchatov definitively discovered the phenomenon of man-made nuclear isomerism, one could hardly imagine that long-lived isomers of such high energy would be obtained. And still fainter were hopes for accumulating so large a number of isomeric nuclei and for constructing such neutron spectrometers that experiments seeking neutron resonances in isomers and investigating these resonances would become feasible. The first experiments of this type were launched at the institute organized by Kurchatov. As to ^{178m_2}Hf isomeric nuclei themselves, they were obtained at the Flerov laboratory of the Joint Institute for Nuclear Research, whose foundation was initiated by Kurchatov and implemented by his disciples. These investigations proved to be possible owing to an international collaboration with two French institutions [Centre de Spectrometrie Nucleaires et de Spectrometrie en Mass (CSNSM) and Institut de Physique Nucleaire (IPN)], where the chemical purification and the mass separation of the ^{178m_2}Hf isomer were performed.

Experimental investigation of neutron resonances

[1]Centre de Spectrometrie Nucleaires et de Spectrometrie en Mass (CSNSM), IN2P3–CSRS, F91405 Orsay Campus, France.

[2]Institut de Physique Nucleaire (IPN), F91406 Orsay, France.

[3]Joint Institute for Nuclear Research, Dubna, Moscow oblast, 141980 Russia.

in isomers is of crucial importance for developing the theory of highly excited nuclear states. It is well known that individual properties of highly excited nuclear states can be explored by studying neutron resonances. Numerous investigations of this kind have been performed up to the present time. Regularities established in them admit an interpretation of compound states on the basis of a statistical approach. However, available data cover only a rather narrow class of compound states, those that are characterized by rather low angular momenta; moreover, only states whose spins differ insignificantly (by about unity) could be explored in each individual nucleus. In this connection, it is of great interest to detect and investigate neutron resonances in the ^{178m_2}Hf isomer, since its structure, which is interpreted as the $(\pi 7/2^+, \pi 9/2^+, \nu 7/2^+, \nu 9/2^+)$ configuration [2], and its high spin of $J = 16$ differ sharply from the structure and spin of nuclei studied previously. In order to detect and explore neutron resonances in ^{178m_2}Hf, we investigated gamma-ray cascades arising upon neutron capture. The diagram of neutron capture by a ^{178}Hf nucleus in the ground and in the isomeric state is displayed in Fig. 1, along with the gamma-ray cascades being studied. On the basis of the results of these experiments, one can test basic concepts of a theory that describes the production and decay of highly excited states. First, one can compare the mean spacing D between resonances for the same nucleus at two sharply different values of the spin, 1/2 and 33/2 or 31/2. The mean spacing for the ground state of ^{178}Hf is well known. It is $D(1/2) = 62$ eV [3], which agrees well with the estimate within the Fermi gas model at the corresponding excitation energy E^* equal to the neutron-binding energy S_n, $E^* = S_n = 6.099$ MeV. The mean spacing $D(31/2, 33/2)$ between isomer resonances is highly sensitive to deviations from statistical concepts of compound states—in particular, to the degree of decay of an isomeric state upon the formation of a compound nucleus. By way of example, we indicate that, if the structure of the ^{178m_2}Hf isomeric state is completely destroyed upon neutron capture, the level density can be described on the basis of the Fermi gas model at the excitation energy of $E^* = S_n + E_{\rm is} = 6.099 + 2.446 = 8.545$ MeV, where $E_{\rm is}$ is the isomer excitation energy. For $D(31/2, 33/2)$, this yields the value of 1.46 eV. But if the structure of the isomeric state is not destroyed upon neutron capture, the Fermi gas excitation energy is $E^* = S_n = 6.099$ MeV, with the result that D will take a value approximately equal to that for the resonances of the target nucleus ^{178}Hf in the ground state (that is, 62 eV) [3]. Thus, the mean spacing between the resonances of an isomer can furnish information about the degree to which

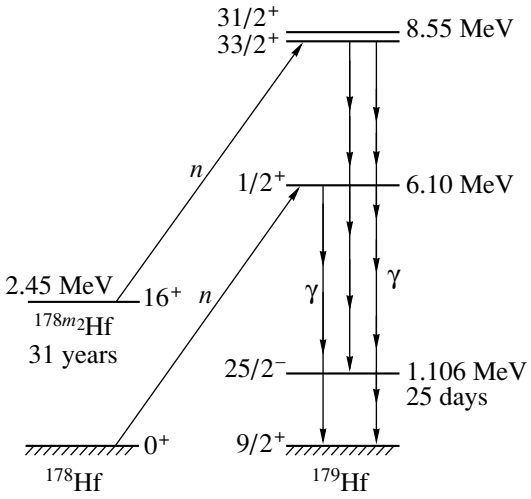

Fig. 1. Diagram of neutron capture by a ^{178}Hf nucleus in the ground and in the isomeric state.

the structural features of an isomer excited state are destroyed upon neutron capture.

From the results obtained by studying gamma-ray cascades, one can deduce rather interesting information about the behavior of the quantum number K. From Fig. 1, it can be seen that the gamma-ray cascades in question can populate both the ground state of the ^{179}Hf nucleus $(9/2^+)$ and its $25/2^-$ isomeric state characterized by the excitation energy of 1106 keV and half-life of $T = 25$ d. According to the laws of statistics, gamma transitions from high-spin resonances will populate predominantly the $25/2^-$ high-spin isomeric state because of a small difference of spins between these states. If, however, some values of the quantum number K are favored in highly excited states, the populations determined experimentally for the $9/2^+$ and $25/2^-$ states may deviate significantly from expected values, since these states differ strongly in K ($K = 9/2$ in the ground state, but it is 25/2 in the isomeric state). The populations of these states can be measured directly owing to the difference in the energy release and in the multiplicity of gamma rays in the corresponding cascades.

2. TARGET FROM THE ^{178m_2}Hf ISOMER

Macroscopic amounts of the ^{178m_2}Hf isomer were obtained by irradiating a ^{176}Yb target with a 100- to 150-μA flux of alpha particles of energy about 36 MeV at the U-200 cyclotron installed at the Joint Institute for Nuclear Research (JINR, Dubna). In order to prevent, during the irradiation process, the formation of the ^{172}Hf and ^{175}Hf isotopes, which are radioactive, the target from ^{176}Yb was enriched to 99.998% at the PARIS mass separator (CSNSM,

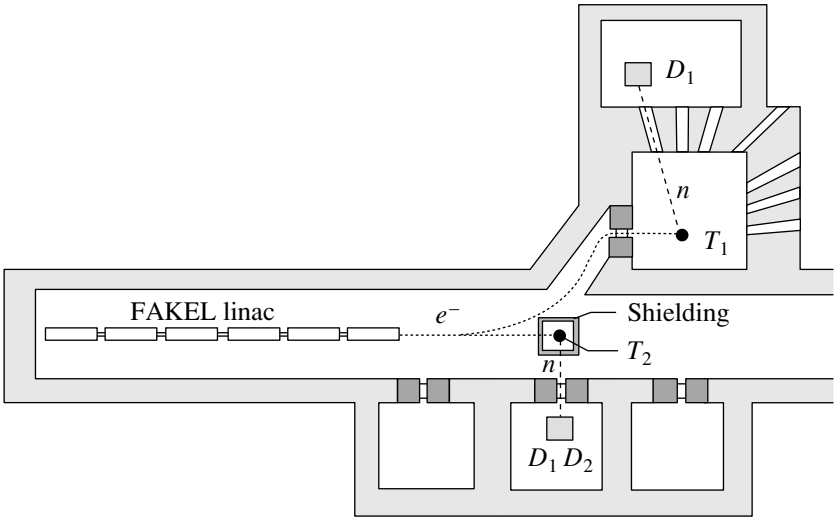

Fig. 2. Layout of neutron spectrometers employed at the FAKEL linear electron accelerator: (T_2) neutron target of a new spectrometer, (T_1) neutron target of the spectrometer used previously, and (D_1, D_2) multisection gamma-ray detectors ensuring a 4π coverage.

Orsay, France). In implementing this procedure, use was made of ultrapure substrate materials and of the chemically purified oxide $^{176}Yb_2O_3$. The product isomeric material was stored for three months after irradiation, whereupon it was subjected to a chemical purification from admixtures by the chromatographic method with an efficiency of 95%, the degree of purification being 10^7. After that, targets containing $n \sim 2 \times 10^{14}$ isomer nuclei were manufactured [4, 5]. In these targets, the numbers of nuclei of the stable isotopes ^{178}Hf and ^{177}Hf were, respectively, 100 and 150 times greater than the number of isomer nuclei. Experiments performed with these targets revealed that low-energy resonances of ^{177}Hf strongly complicate observation of isomer resonances. In view of this, a new target was prepared that was purified from this isotope with an efficiency of 20 to 25% by using the PARIS mass separator. This target contained $n = 1.2 \times 10^{14}$ nuclei of the ^{178m_2}Hf isomer, 1.2×10^{16} nuclei of ^{178}Hf, and 1.2×10^{15} nuclei of ^{177}Hf. The diameter of the target was 3 mm. A 0.005-mm-thick foil of ultrapure aluminum (99.999%) served as a substrate and, simultaneously, as a means for fastening the target to the sample holder. The total thickness of aluminum in the detector along the neutron beam was 0.015 mm.

3. EXPERIMENTAL FACILITY AND MEASUREMENTS

Investigations of neutron resonances in ^{178m_2}Hf with the aid of the relevant (n, γ) reaction were begun at the FAKEL linear electron accelerator of the Kurchatov Institute immediately after the fabrication of the target [4, 5]. The spectrometry of neutrons was based on the time-of-flight technique. The main difficulty in detecting and investigating neutron resonances of the ^{178m_2}Hf isomer was associated with an extremely small amount of the isomer ($n \sim 10^{14}$, 30 ng) and with a heavy intrinsic radioactive background ($\sim 10^6$ photons per second). It is sufficient to indicate that, in studying resonances of stable nuclei, the effect-to-background ratio is about 1000 for the case where the weight of the nuclei in the sample used is about 1 g; accordingly, this ratio will be as low as about 3×10^{-5} for 30 ng, and this is the reason why experiments of the type being discussed are extremely difficult. The procedure developed at the Kurchatov Institute for the spectrometry of gamma-ray cascades on the basis of a multisection detector of 4π coverage from NaI(Tl) crystals was used to study (n, γ) reactions [6]. This procedure makes it possible to measure the spectrum of gamma-ray cascades induced by neutron capture versus the incident-neutron energy; in addition, it has a high sensitivity and enables one to suppress the background significantly by imposing various conditions in selecting gamma-ray cascades.

The first experiments aimed at detecting neutron resonances in ^{178m_2}Hf [7, 8] were performed for the neutron-spectrometer flight base of $L = 10.6$ m, which was the minimum possible at that time. Only strong-low energy resonances of stable hafnium isotopes, whose content in the target under study was about 100 to 150 times greater than the content of the isomer, were detected as the result of nearly 100-h measurements. This was due to a small magnitude of the effect and to a relatively heavy background, which was commensurate with the effect for the detected

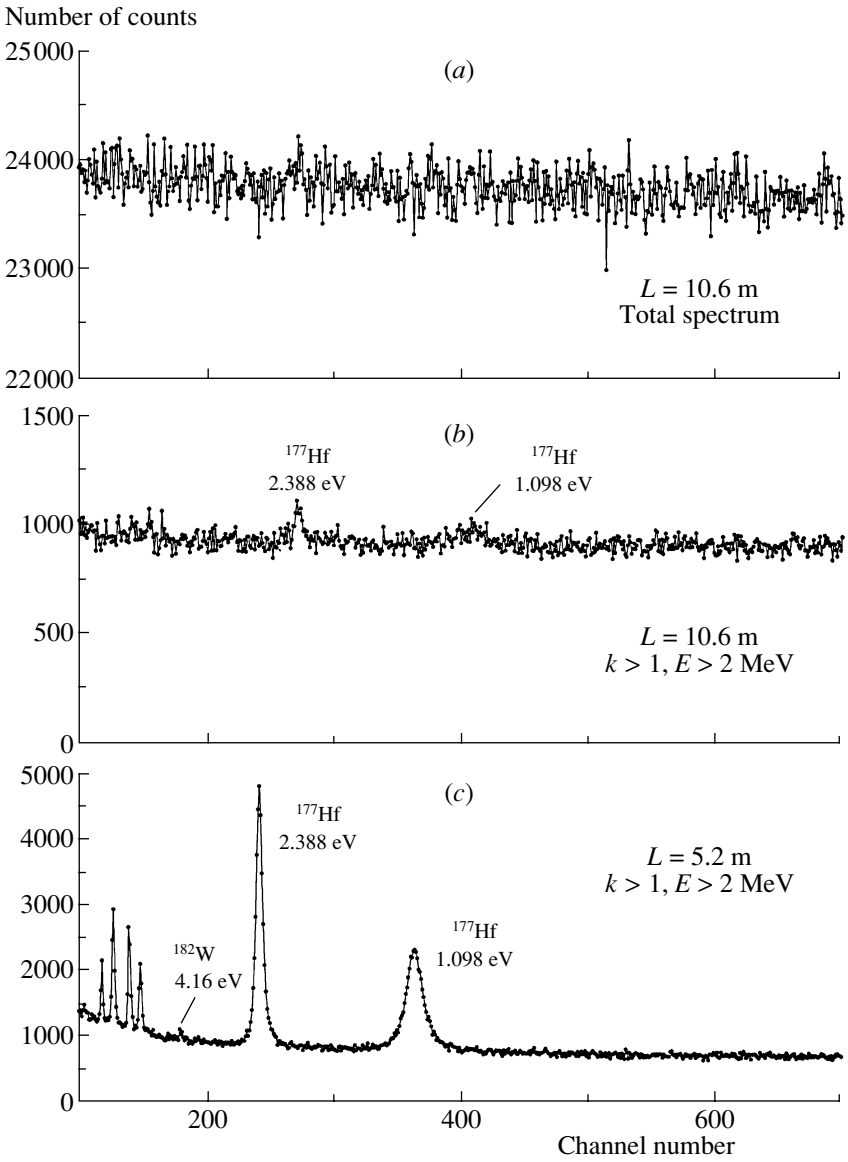

Fig. 3. Time-of-flight spectra for a ^{178m_2}Hf target not subjected to purification that were obtained as the result of 40-h measurements with a 16-section detector by using (*a*, *b*) the old (employed previously) and (*c*) the new spectrometer.

resonances. Obviously, it was next to impossible to reveal isomer resonances under such conditions.

In this connection, the possibility of significantly increasing the efficiency of investigations that are performed by the time-of-flight method under the conditions of a heavy background was analyzed in [9]. In the absence of background that is not associated with the operation of a pulsed neutron source, the efficiency (ε) is given by the obvious expression

$$\varepsilon_0 = C_0 \frac{Q}{L^2},$$

where Q is the neutron-source intensity, L is the flight base, and C_0 is a constant. But under the conditions where the background is much greater than

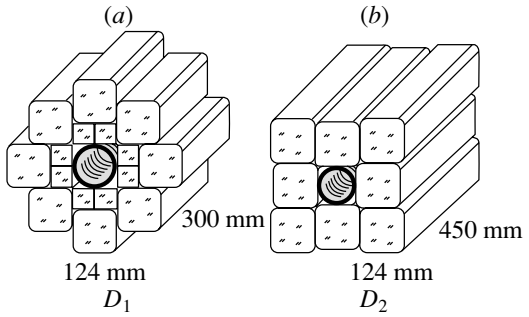

Fig. 4. Multisection detectors of 4π coverage on the basis of NaI(Tl) crystals: (*a*) 16-section detector D_1 and (*b*) 8-section detector D_2. The circle in boldface type represents a ^{10}B layer.

the sought effect, the dependence of ε on Q and L is radically different [9]; that is,

$$\varepsilon_F = C_F \frac{Q^2}{L^5},$$

where C_F is a constant. Thus, the efficiency of investigations of the type being discussed is in inverse proportion to the fifth power of the flight path and in direct proportion to the square of the neutron-source intensity. In view of this, a new neutron spectrometer with a flight base of 5.2 m, which is one-half as long the flight base of the previous spectrometer, was constructed in order to improve considerably the efficiency of such investigations [9]. In contrast to the neutron target of the spectrometer used previously, the neutron target of the new spectrometer was arranged in the direct electron beam, where the mean current is higher by a factor of about 3 (see Fig. 2). Even the first experiment with the ^{178m_2}Hf isomer demonstrated that the efficiency of the new spectrometer is much higher than the efficiency of the old spectrometer. The time-of-flight spectra obtained with a sample containing $n = 1.4 \times 10^{14}$ isomer nuclei are displayed in Fig. 3 for measurements based on (Figs. 3*a*, 3*b*) the old and (Figs. 3*c*) the new spectrometer and performed with the same 16-section spectrometer (see Fig. 4*a*). The spectrum in Fig. 3*a* involves all events recorded by the detector as a discrete unit. The spectrum in Fig. 3*b* was obtained by selecting events according to the multiplicity of pulses from the detector sections and according to the energies deposited in them. In the spectrum that is shown in Fig. 3*c* and which was obtained under the same event-selection conditions as the spectrum in Fig. 3*b*, all resonances of admixed nuclei of stable hafnium isotopes are clearly seen at neutron energies below 20 eV (above 20 eV, the isomer resonances could not be revealed because of a decrease in the neutron flux and in the resonance cross section). We note that the channel width for the spectrum in Fig. 3*c* was chosen to be one-half as great as that for the spectra in Figs. 3*a* and 3*b*. This was done in order to ensure that the resonance positions were approximately identical in the measurements with the two spectrometers. A comparison of the results obtained with the new and the old spectrometer showed that the efficiency of detection of weak resonance peaks with a new spectrometer is higher by a factor of about 470, which corresponds to a decrease in the flight base and the increase in the intensity of the electron flux [9].

A new target purified from stable hafnium isotopes at the PARIS mass separator was manufactured with the aim of obtaining a more pronounced effect. The target contained $n = 1.2 \times 10^{14}$ nuclei of the ^{178m_2}Hf isomer. Moreover, a new detector for the spectrometry of multiplicities was constructed in order to improve the efficiency of measurements still further. The detector contained eight identical sections from NaI(Tl) crystals, each section having dimensions of $124 \times 124 \times 450$ mm^3 (see Fig. 4*b*). In order to shield the scintillator from neutrons scattered on the target under study, a ^{10}B layer of thickness about 1 g/cm^2 was arranged between the target and the crystals. In relation to the 16-section detector used in the previous experiment (see Fig. 4*a*) with the new spectrometer, the detector in question had a higher efficiency and a lower background. The measurements were performed at the electron-pulse duration of $\tau = 300$ ns, the pulse-repetition frequency of $\nu = 450$ Hz, and the electron-beam power of $P = 2$ kW. The duration of the measurements was 120 h.

For each recorded event, the information-storage system enabled one to save 17 words: the instant of detection (with respect to the first detected photon from a cascade), the energy deposition in each of the eight sections of the detector, and the time of flight of the neutron that induced a given event (the instant of emergence of the first recorded photon from each cascade of gamma transitions with respect to the accelerator start).

4. RESULTS OF THE MEASUREMENTS

In order to reveal and investigate neutron resonances, time-of-flight spectra corresponding to various values of the coincidence multiplicity k and the total energy deposition E in the detector that were determined within a 60-ns time interval were composed from accumulated events. In doing this, only those events in which the energy deposition exceeded 1 MeV in at least one section were selected and only those sections in which the energy deposition exceeded 0.22 MeV were considered. This selection made it possible to suppress the radioactive background of the sample to a considerable extent. The results are presented in Figs. 5 and 6 in the form of the dependence of the time-of-flight spectra on k and E, respectively.

From the set of peaks, five resonances—at 0.75, 1.80, 3.10, 3.72, and 4.52 eV—that admit an identification with resonances in the ^{178m_2}Hf isomer can be singled out with a more or less acceptable reliability. Indeed, these resonances do not coincide in energy position with strong resonances of any nuclei [3]. They are not weak resonances of admixed nuclei either, since even strong resonances of such nuclei manifest themselves only slightly—for example, this is so for the strong resonance of the ^{182}W nucleus at 4.155 eV (see Figs. 5, 6). The parameters of the detected resonances were determined from a fit of a Breit–Wigner curve to the experimental data with

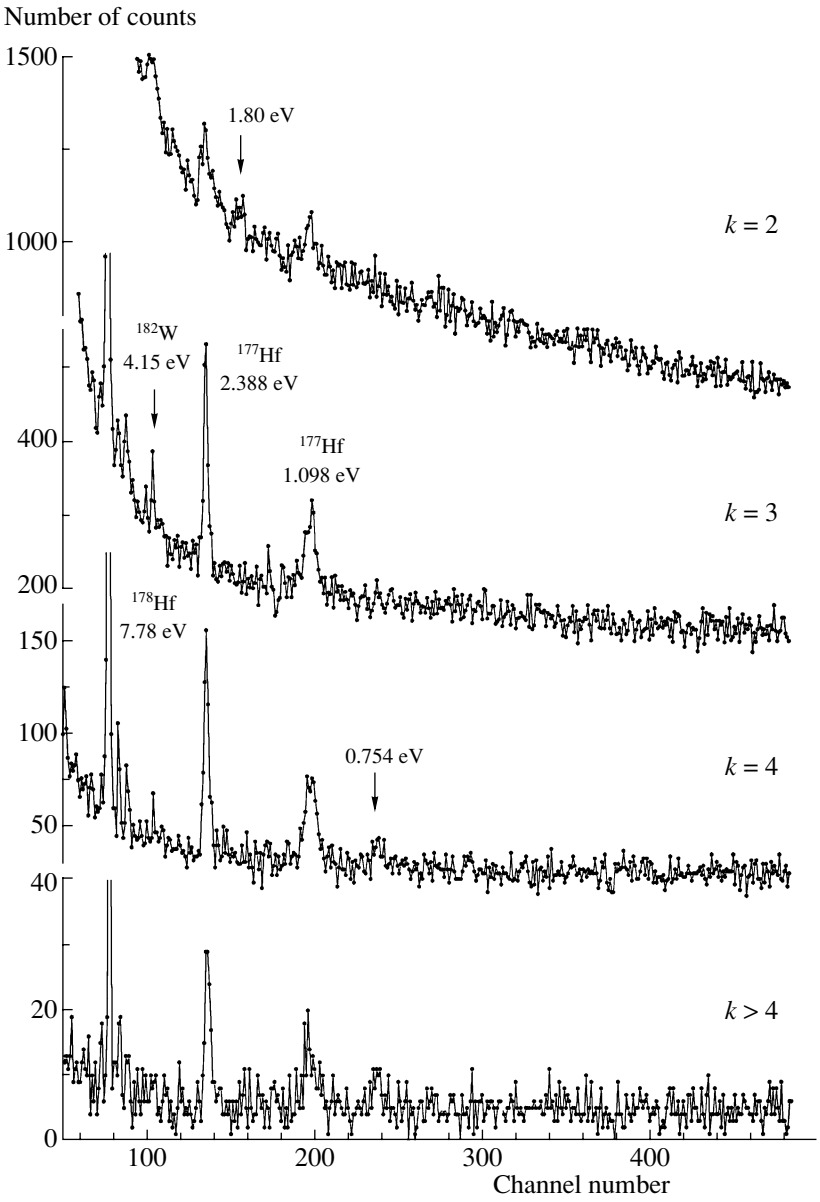

Fig. 5. Time-of-flight spectra in measurements with ^{178m2}Hf for various values of the coincidence multiplicity k at a total energy deposition in excess of 4.8 MeV.

allowance for the Doppler effect and spectrometer resolution. Figure 7 shows such a fit for the resonance at 0.75 eV. For this resonance, the radiative width estimated on the basis of the maximum-likelihood method is 25 ± 10 meV. For other resonances of the isomer, the values of $2g\Gamma_n$ were determined under the assumption of $\Gamma_\gamma = 54$ meV (mean value of Γ_γ for the resonances in ^{178}Hf) or at $\Gamma_\gamma = 80$ meV (the value of Γ_γ according to the calculation on the basis of the statistical model). In these calculations, the flux of neutrons incident on the sample was calibrated by using the resonances in ^{177}Hf and ^{178}Hf, the numbers of their nuclei being determined in independent measurements: $(1.16 \pm 0.26) \times 10^{15}$ for ^{177}Hf and $(1.20 \pm 0.08) \times 10^{16}$ for ^{178}Hf. In the calibration procedure employed, a simulation of gamma-ray cascades and of the recording of these cascades in the detector was performed in order to take into account the distinctions between their spectra for isomer resonances and for the resonances in ^{177}Hf. The values obtained for the resonance parameters are given in the table.

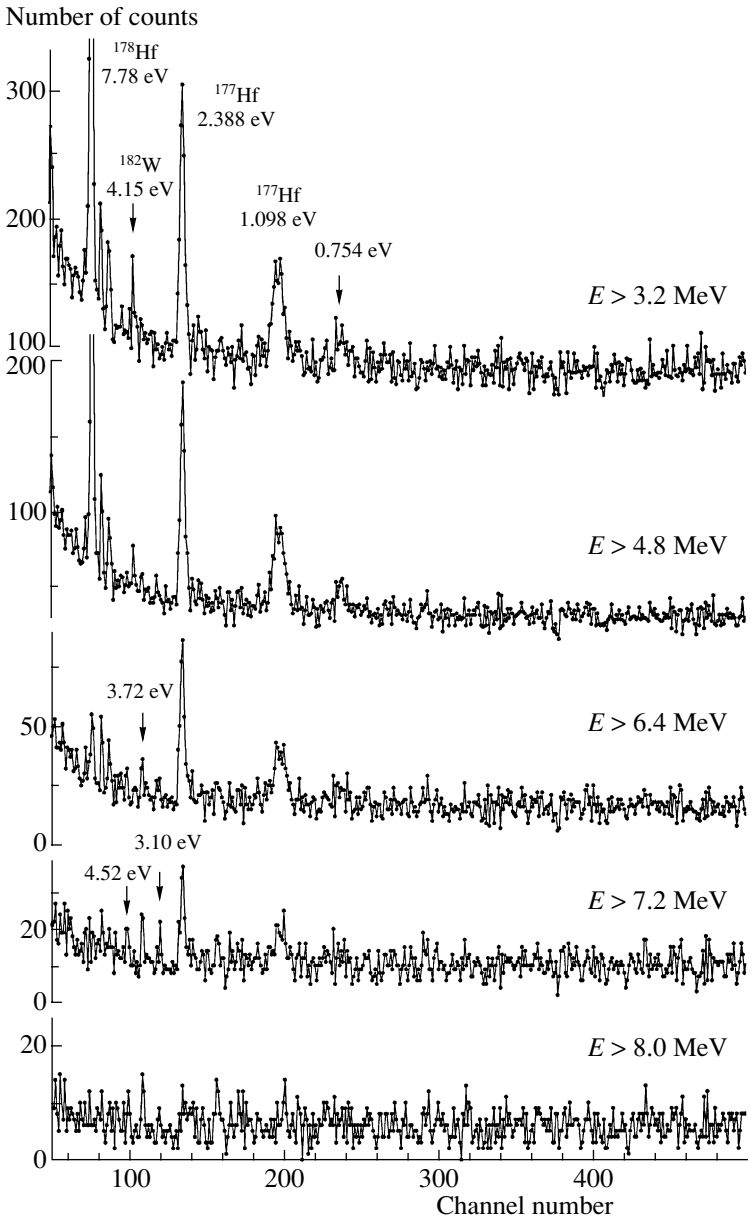

Fig. 6. Time-of-flight spectra in measurements with ^{178m_2}Hf for various values of the total energy deposition E at a coincidence multiplicity in excess of three.

5. ANALYSIS OF THE RESULTS

5.1. Spacing between the Levels

On the basis of the data quoted in the table, the mean spacing between the resonances of the ^{178m_2}Hf isomer can be estimated at $0.94^{+0.6}_{-0.3}$ eV (the errors were determined according to the procedure used in [10]).

We note that, in calculating the mean spacing D between levels on the basis of the Fermi gas model, use is usually made of the traditional formula for the level density. This formula was obtained in the approximation of low angular momenta, in which case the energy of rotation is much less than the excitation energy; however, the neutron resonances of the hafnium isomer have high spins ($J = 31/2, 33/2$) and, accordingly, a higher energy of rotation (about 2.2 MeV). Therefore, a more precise estimate can be obtained without recourse to this approximation by numerically computing $\rho(U, J)$ as the difference of the densities of states; that is,

$$\rho(U, J) = \omega(U, M = J) - \omega(U, M = J + 1), \quad (1)$$

where $U = S_n + E_{\rm is} - \Delta$ is the excitation energy with allowance for pair correlations (Δ) and M is the projection of the angular momentum onto a fixed axis. In

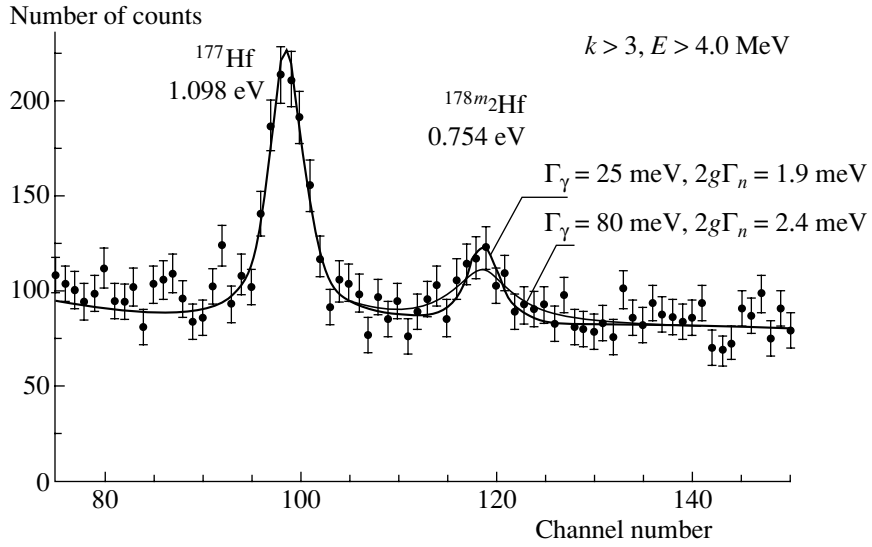

Fig. 7. Fit of a Breit–Wigner curve to experimental data at various values of the radiative width.

accordance with [11], we have

$$\omega(U,M) = \frac{1}{12\sqrt{2g\bar{m}^2}\,[U - M^2/(2g\bar{m}^2)]^{3/2}} \times \exp\left[2\sqrt{a\left(U - \frac{M^2}{2g\bar{m}^2}\right)}\right], \quad (2)$$

where $\bar{m}^2$ is the mean square of the single-particle angular momentum and g is the density of single-particle states at the Fermi energy. By using the value of $\bar{m}^2$ from [12], we obtain the mean spacing of $D = 1.46$ eV, which, within the experimental errors, agrees with the measured value of $0.94^{+0.6}_{-0.3}$ eV. It should be noted that the measured value of D also complies well with the estimate $D = 0.86$ eV, which was obtained of the basis of the microscopic approach developed by Ignatyuk [13].

The agreement between the theoretical and experimental results indicates that the Fermi gas model describes well the densities of both low- and high-spin levels. At the same time, this agreement suggests that, upon the formation of a compound nucleus, the energy of the isomer is converted into the neutron binding energy and the Fermi gas energy; that is, the isomeric state is destroyed completely.

5.2. Radiative Transitions

The radiative width could be measured only for the resonance at 0.75 eV. The most probable value of this width is 25 meV. In order to perform a comparison with the prediction of the statistical model, we performed a calculation that relies on the procedure and parameter values recommended in the Reference Input Parameter Library [14].

The radiative width was calculated in terms of the sum of the probabilities of all gamma transitions from the resonance state i to all possible final states f satisfying selection rules in spin and parity; that is,

$$\Gamma_\gamma^{\rm stat} = k\sum_{J_f}\int_0^{E^*} E_\gamma^{2l+1} f_{E(M)l}\frac{\rho(E_f,J_f)}{\rho(E_i,J_i)}dE, \quad (3)$$

where E* is the excitation energy of the nucleus, E_γ is the transition energy, $f_{E(M)l}$ is the radiative strength function, and k is a normalization factor. In the calculation, we took into account only $E1$, $M1$, and $E2$ transitions, since the contribution of higher multipoles is negligible. In calculating the $E1$ radiative strength function, use was made of a generalized Lorentzian distribution that takes into account the energy and temperature dependence of giant dipole resonances [15]. A standard Lorentzian distribution [16] was employed for $E2$ and $M1$ transitions. By using the measured value of $\bar{\Gamma}_\gamma = 54$ meV for the mean radiative width of resonances in ^{178}Hf and the values of $\Gamma_\gamma^{\rm stat}$ that were calculated by formula (3), one can obtain an estimate of Γ_γ for the isomer resonances that is independent of the normalization factor k. For the 31/2- and 33/2-spin resonances of ^{178m_2}Hf, this yielded the values of 83 and 77 meV, respectively.

Figure 7 shows a fit of the Breit–Wigner curve at $\Gamma_\gamma = 25$ meV and $\bar{\Gamma}_\gamma^{\rm stat} = 80$ meV (the calculated radiative width that is averaged for two spin states, those characterized by the spin values of 31/2 and 33/2) to experimental data. It can be seen that the value of 80 meV agrees poorly with experimental data. The ratio of the likelihood functions for the above values of Γ_γ is about 5.

Parameters of neutron resonances in ^{178m_2}Hf

E_0, eV	$2g\Gamma_n$, meV	Γ_γ, meV	I_γ, b	$\sigma_\gamma^{\text{th}}$, b ($E_n = 0.025$ eV)	$2g\Gamma_n^0$, meV
0.754	1.9 ± 0.4	25 ± 10	6360 ± 1340	212 ± 96	2.5 ± 0.5
1.80	5.2 ± 1.5	(54)	2990 ± 860	132 ± 38	2.9 ± 0.8
	5.0 ± 1.4	(80)	2990 ± 860	196 ± 56	
3.10	4.4 ± 1.8	(54)	865 ± 354	28 ± 12	1.4 ± 0.6
	4.3 ± 1.8	(80)	870 ± 356	43 ± 17	
3.72	8.2 ± 2.5	(54)	1050 ± 320	33 ± 10	2.2 ± 0.7
	7.8 ± 2.4	(80)	1050 ± 320	49 ± 15	
4.52	9.5 ± 3.8	(54)	805 ± 322	24 ± 9	2.1 ± 0.8
	8.9 ± 3.6	(80)	805 ± 322	34 ± 14	
0.025 [8]	–	–	800 ± 130	51 ± 10	
0.025 [17]	–	–	–	46 ± 5	

Thus, the statistical model yields an exaggerated value of the radiative width.

5.3. Population of Low-Lying States

Let us consider the populations of low-lying states in ^{179}Hf. For thermal neutrons ($E_n = 0.025$ eV), the table presents the contributions of the ^{178m_2}Hf resonances to the resonance integral I_γ and to the capture cross section $\sigma_\gamma^{\text{th}}$ according to calculations that employ the resonance parameters. Given in the last two rows of the table are the values $(I_\gamma)^*$ and $(\sigma_\gamma^{\text{th}})^*$ corresponding to the population of the ^{179m_2}Hf isomer ($I = 25/2^-$) that were measured directly by the activation method [8, 17]. The values of I_γ and $\sigma_\gamma^{\text{th}}$ that were obtained in the present study correspond to the total effect of the population of the isomeric ($I = 25/2^-$) and the ground state of ^{179}Hf. It is therefore natural that $\sum I_\gamma > (I_\gamma)^*$ and $\sum \sigma_\gamma^{\text{th}} > (\sigma_\gamma^{\text{th}})^*$. It can be seen that even the values of $I_\gamma = 6360 \pm 1340$ b and $\sigma_\gamma^{\text{th}} = 212 \pm 96$ b, which were obtained for a single resonance at 0.75 eV, are much greater than the values of $(I_\gamma)^* = 800 \pm 130$ b and $(\sigma_\gamma^{\text{th}})^* = 51 \pm 10$ b, which were measured by the activation method. The distinction between the values of the resonance integral is especially pronounced.

The values of I_γ and $\sigma_\gamma^{\text{th}}$ can be matched with $(I_\gamma)^*$ and $(\sigma_\gamma^{\text{th}})^*$ if one assumes that, in more than 90% of events, the decay of this resonance states leads to the population of the ground state of ^{179}Hf and, accordingly, that, in less than 10% of events, this decay leads to the population of its $25/2^-$ isomeric state. However, this contradicts the results of the calculation based on the statistical model. According to this calculation, the population of the $25/2^-$ state is about 80%, which is an order of magnitude greater than the value obtained from a comparison of the results of our present measurements and the results presented in [8, 17].

Similar contradictions, albeit less pronounced, are observed for the resonance at 1.80 eV as well, for which the I_γ and $\sigma_\gamma^{\text{th}}$ values obtained in our study are much greater than $(I_\gamma)^*$ and $(\sigma_\gamma^{\text{th}})^*$.

Thus, there is a glaring contradiction between the predictions of the statistical model and the measured ratio of the cross sections for the population of the ground state of ^{179}Hf ($9/2^+$) and its $25/2^-$ isomeric state.

5.4. Gamma-Ray Cascades

Because of low statistics, it is reasonable to characterize the spectrum of gamma-ray cascades by a small number of parameters. For such parameters, one can take the multiplicity of coincidences and the total energy deposition. Figures 5 and 6 display the measured time-of-flight spectra at various values of the coincidence multiplicity k and the total energy deposition E. As can be seen from these figures, the isomer resonances differ considerably from one another. The resonance at 0.75 eV is clearly seen in a spectrum of high multiplicity ($k > 3$) at a relatively low total energy deposition ($E > 4.8$ MeV), no other resonance being manifested here. The resonance at 1.8 eV has

an anomalously low multiplicity. In practice, it is seen only at $k = 2$, but no other isomer resonance can be observed at this multiplicity. The resonances at 3.10, 3.72, and 4.52 eV manifest themselves at large values of the total energy deposition ($E > 7.2$ MeV; see Figs. 5, 6) and the coincidence multiplicity ($k > 3$), in which case one cannot see other isomer resonances. So sharp a distinction between gamma-ray cascades associated with the resonances is at odds with known systematics of neutron resonances and their statistical description. Indeed, the expected fluctuations of the intensity of various cascades are small because of a wide set of intermediate transitions. They are on the same order of magnitude as the fluctuations of the total radiative width—that is, about 5 to 10%. The observed distinctions between the intensities are much greater.

6. DISCUSSION

From the analysis performed in this study, it follows that the mean spacing between the neutron resonances of the isomer considered here agrees well with the prediction of the Fermi gas model. The agreement between this theory and experimental data indicates that the Fermi gas model describes well the densities of both low- and high-spin levels. At the same time, this implies that, upon the formation of a compound nucleus, the isomer energy is converted into the neutron binding energy and the Fermi gas energy; that is, the isomeric state is destroyed completely. Concurrently, the probabilities of gamma transitions associated with the resonances in question are not described by the predictions of the statistical model. Specifically, the discrepancies here are the following: (i) Although the resonances are characterized by a high spin, gamma-ray cascades starting from them populate predominantly the low-spin ground state ($J = 9/2$) rather than the ^{179m_2}Hf isomeric state of high spin ($J = 25/2$). (ii) The measured radiative width is approximately one-third as great as the value obtained within the statistical model. (iii) Gamma-ray cascades induced by the decay of the ^{178m_2}Hf isomer do not comply with the statistical model—they are different for different resonances.

An attempt at explaining the observed deviations by the effect of the quantum number K seems the most natural. It is well known that K is a good quantum number at relatively low energies. According to available data for ^{179}Hf, this is so in the excitation-energy region $E^* < 3$ MeV. At higher energies, available data on neutron resonances in various nuclei indicate that gamma transitions to low-lying states characterized by different values of K are of a statistical character. However, the levels of the ^{179}Hf nucleus that are involved in the formation of a gamma cascade have a very high spin; as a result, the distribution of wave-function components characterized by different values of K at fixed J^π may deviate significantly from a statistical distribution.

We will now address the question of how one could qualitatively explain the observed contradictions on the basis of additional assumptions on the quantum number K at excitation energies in excess of 3 MeV.

In order to explain contradictions in the populations of the low-lying $9/2^+$ and $25/2^-$ states (the ground state and the isomeric state at 1106 keV, respectively), it is sufficient to assume that, in the energy region $E^* > 3$ MeV, the set of high-spin levels through which a gamma-ray cascade proceeds is, on average, dominated by low-K ($K < 17/2$) states. During the emission of a gamma-ray cascade, the nucleus occurring in a low-K state then undergoes transitions within its band; from the specific diagram of levels and transitions, it follows that, in the region $E^* < 3$ MeV, such transitions populate the ground state, missing the $25/2^-$ state. It is precisely for this reason that the population of the ground state is enhanced in relation to that which is expected within the statistical model.

The other two contradictions can be explained by assuming that levels at $E^* \sim 8.5$ MeV (neutron resonances) may have, at some values of K, large wave-function components that change from one resonance to another. Because of selection rules in K, this would result in different gamma-ray cascades for different resonances and in a reduction of the effective number of levels to which the first gamma transition may proceed. The latter would lead to a decrease in the radiative width.

We would like to emphasize that the above qualitative explanation does not exhaust all possibilities for explaining the experimental results that we obtained. In order to explore more reliably the problem of deviations of the properties of high-spin resonances from the predictions of the statistical model, it is necessary to perform further, more precise, investigations with the ^{178m_2}Hf isomer; it is also desirable to study the special features of gamma-ray cascades involving resonances of high-spin nuclei.

ACKNOWLEDGMENTS

We are grateful to S.T. Belyaev, A.Yu. Rumyantsev, and N.A. Chernoplekov for support of these investigations. Thanks are also due to the personnel of the FAKEL accelerator for generous technical assistance in performing experiments and to I.N. Mikhailov for enlightening discussions on the results presented in this article.

REFERENCES

1. I. V. Kurchatov, B. V. Kurchatov, L. V. Mysovsky, and L. I. Rusinov, C. R. He. Acad. Sci. **200**, 1201 (1935).
2. V. G. Soloviev, *Theory of Complex Nuclei* (Pergamon, Oxford, 1976), p. 149.
3. S. F. Mughabghab, in *Neutron Cross Sections Series,* Vol. 1: *Neutron Resonance Parameters and Thermal Cross Sections* (Academic, New York, 1984).
4. Yu. Ts. Oganessian *et al.*, J. Phys. G **17**, 393 (1991).
5. Yu. Ts. Oganessian *et al.*, in *Proceedings of the Workshop on Application of Lasers in Atomic Nuclear Research, Dubna, 1990*, D15-91-410, p. 55.
6. G. V. Muradian *et al.*, Nucl. Sci. Eng. **90**, 60 (1985).
7. G. V. Muradian *et al.*, in *Proceedings of the 2nd International Seminar on Interaction of Neutrons with Nuclei (ISINN-2), Dubna, Russia, 1994,* E3-94-419, p. 214.
8. Yu. Ts. Oganessian *et al.*, in *Proceedings of International Conference "Nuclear Physics of Our Times," Sunnybell Island, Florida, 1992.*
9. G. V. Muradian *et al.*, Nucl. Instrum. Methods Phys. Res. A **411,** 396 (1998).
10. G. V. Muradian and Yu. V. Adamchuk, Nucl. Phys. **68**, 549 (1965).
11. Yu. V. Sokolov, *Level Density in Nuclei* (Énergoatomizdat, Moscow, 1990).
12. A. Gilbert and A. G. W. Cameron, Can. J. Phys. **43**, 1446 (1965).
13. A. V. Ignatyuk, Yad. Fiz. **17**, 502 (1973) [Sov. J. Nucl. Phys. **17**, 258 (1973)].
14. *Reference Input Parameter Library* (IAEA, Vienna, 1997).
15. J. Kopecky and R. E. Chrien, Nucl. Phys. A **468**, 285 (1987).
16. M. Uhl and J. Kopecky, Report INDC(NDS)-335, IAEA (Vienna, 1995), p. 157.
17. Ch. Briançon *et al.*, in *Proceedings of the 8th International Symposium "Capture γ-ray Spectroscopy and Related Topics," Fribourg, 1993,* Ed. by J. Kern (World Sci., Singapore, 1993), p. 192.

Translated by A. Isaakyan

Physics of Atomic Nuclei, Vol. 66, No. 1, 2003, pp. 61–74. Translated from Yadernaya Fizika, Vol. 66, No. 1, 2003, pp. 64–76.

NUCLEI
Theory

Exact Solutions to the Three-Body Problem For *S*-Wave Interactions of the Centrifugal Type

V. V. Pupyshev*

Joint Institute for Nuclear Research, Dubna, Moscow oblast, 141980 Russia

Received March 19, 2001; in final form, February 5, 2002

Abstract—The simplest exact solutions to the Schrödinger and Faddeev equations for S-wave pair interactions of the centrifugal type are constructed and investigated for the case of zero total orbital angular momentum of three particles. © *2003 MAIK "Nauka/Interperiodica".*

1. INTRODUCTION

A comprehensive investigation of the problem of three particles p_1, p_2, and p_3 coupled by pair interactions of the centrifugal type,

$$V_{ij}(r_{ij}) = \alpha_{ij}/r_{ij}^2, \quad i \neq j = 1,2,3, \qquad (1)$$
$$\alpha_{ij} = \text{const},$$

where r_{ij} is the distance between particles p_i and p_j, is of interest from the physical and theoretical points of view and for applications.

Interactions of the type in (1), as well as all known interactions, with the exception of Coulomb ones, are model interactions, but, in the physically important extreme cases of short ($r_{ij} \to 0$) and long ($r_{ij} \to \infty$) distances, they describe leading terms of the asymptotic expressions for realistic interactions. By way of example, it can be recalled that, for $r_{ij} \to 0$, the Bonn potential [1], which is one of the modern model nucleon–nucleon interactions, has an $O(r_{ij}^{-2})$ singularity identical to that in (1). Another example is provided by the interaction of the electric dipole [2] formed by particles p_i and p_j in an excited bound state with the third charged particle p_k. For $r_{ij} \to \infty$, this interaction decreases in just the same way as the interaction in (1) (in proportion to r_{ij}^{-2}).

Further, it is well known from [3] that, under the Efimov conditions [4], the effective interaction in the pair of heavy particles p_i and p_j loosely bound by a light particle p_k has the same asymptotic behavior (r_{ij}^{-2} for $r_{ij} \to \infty$). Efimov proved that, in the limit of a long scattering length of the binary subsystem, there arises the spectrum of three-body bound states that condenses logarithmically toward zero. The situation in the system of three ^{4}He atoms, which was recently the subject of intensive investigations [5, 6], is similar. In this system, the pair interaction is described by various modifications of the model potential proposed by Aziz *et al.* [7], which, in just the same way as any interaction of the van der Waals type [2], increases fast at short distances and decreases slowly at long distances. Interactions of the type in (1) for $\alpha_{ij} > 0$ have a qualitatively similar behavior.

Thus, there exists a rather broad class of three-body systems, whose total Hamiltonian in the limits $r_{ij} \to 0, \infty$ coincides or is qualitatively close to the total Hamiltonian of the three-particle problem governed by the interactions in (1). In view of this, the problem considered here is of interest from the physical point of view; its exact solutions can be used to simulate wave functions of actual three-body systems, at least in the asymptotic regions.

The criterion of existence of physically acceptable solutions to the problem of N particles whose interaction potentials have $O(r_{ij}^{-2})$ asymptotic behavior for $r_{ij} \to 0$ or $r_{ij} \to \infty$ (or in both limiting cases) is known only for $N = 2$. Even for $N = 3$, the theorem of existence and uniqueness of such solutions in scattering theory for few-body systems [8] has not yet been proven. From the viewpoint of extending the theory to the case of singular interactions, it would therefore be of interest to find a criterion of existence and to analyze exact solutions for $N = 3$.

Exact solutions to any model three-particle problem [in particular, that which is specified by interactions of the type in (1)] are undoubtedly of use from the viewpoint of applications as well—for example, in testing algorithms for numerically solving the three-body Faddeev and Schrödinger equations in coordinate space.

In the pioneering mesh algorithm [9] for numerically solving Faddeev equations in coordinate space, use was made of a finite-difference approximation of

*e-mail: pupyshev@thsun1.jinr.ru

1063-7788/03/6601-0061$24.00

the sought Faddeev components on a finite mesh of nodes. Later, there appeared more efficient discretization methods based on the approximation of these components by bicubic Hermitian splines [10]; C^2-class splines [11]; and quintet basis splines, which were first applied in [12] and then in [6].

We would now like to list the reasons for which, despite advances made in practically studying Faddeev equations, a reliable and universal algorithm for integrating these equations has yet to be constructed definitively.

First, all known schemes for discretizing Faddeev equations in coordinate space have been realized only for problems of three-particle bound states or for problems of the scattering of a particle by the pair of the remaining particles rather than for the problem of $3 \to 3$ scattering. So far, no such algorithm for the last problem in question has been constructed because of very complicated boundary conditions at long distances.

Second, all known methods based on finite-difference or spline approximations are mathematically incomplete, since within none of these could one prove analytically that the calculated solution to Faddeev equations converges point by point to an exact solution as the maximum step h of some mesh is reduced. It is difficult to prove this statement for two-dimensional integro-differential Faddeev equations [8] because of the presence of integral operators in them and for three-dimensional differential Faddeev equations [13] because of the presence of unknown functions whose arguments, albeit being known, are nonlinear functions of independent variables.

Since there were no asymptotic estimates of convergence for $h \to 0$, it was necessary to demonstrate the reliability and accuracy of the proposed mesh methods by testing the numerical stability of integrated three-body characteristics, such as bound-state energies, phase shifts, or scattering cross sections. For the same reason, the question of point-by-point convergence, which, in contrast to integral convergence, is precisely a criterion of accuracy and reliability of a numerical method, remains open, as a rule. A satisfactory answer to this question can be obtained by using, as a reference solution, a known exact solution to a model problem that is qualitatively the closest to the problem being investigated. To get an idea of the point-by-point convergence of the algorithm being tested, it is sufficient to compare an exact solution to the model problem with its numerical solution on an arbitrary sequence of points that is quite large, on one hand, and which, on the other hand, contains points occurring in physically important asymptotic regions such as vicinities of the points of ternary and binary collisions and the region of long distances.

Such a comparison is of particular importance in the case of interactions featuring a strong repulsion at short distances and slowly decreasing at long distances—for example, interactions of the van der Waals type. The point is that, in this case, it is very difficult to perform a stable numerical integration of Faddeev equations; this can be done only by means of special recently proposed numerical methods. For such a method, a transformation of the hyperradius and the tensor representation of matrices were used in [10] for three-body calculations and the boundary-condition model and potentials introduced by Aziz *et al.* [7] were invoked in [5] to calculate bound and scattering states in the system formed by three ^{4}He atoms; in [6], it was proposed to modify the discrete-problem matrix in such a way as to ensure the absence of large eigenvalues in its spectrum and this construction was realized for the problem of calculating bound states of the same system (helium trimer).

Since interactions of the van der Waals type and interactions of the type in (1) for $\alpha_{ij} > 0$ behave similarly at long and short distances, exact solutions to the three-particle problem for interactions of the type in (1) can be used as reference ones for testing both known and new algorithms for numerically solving the Schrödinger and Faddeev equations for systems consisting of three atoms or three molecules.

Thus, the construction of exact solutions to the three-body problem for interactions of the centrifugal type and an analysis of their properties is not only of interest but also of importance. For a first step, exact solutions are investigated here for the case where such interactions are included only in S waves, which is typical of nuclear physics.

2. BASIC NOTATION AND FORMULATION OF THE PROBLEM

Let us consider the Faddeev equations [8]

$$(H_0 - E)\Psi_i = -V_i\Psi, \quad \Psi = \sum_{k=1}^{3}\Psi_k, \qquad (2)$$
$$i = 1, 2, 3,$$

for the system of three particles p_1, p_2, and p_3 having arbitrary masses m_1, m_2, and m_3, respectively, and zero total orbital angular momentum. It is well known from [14–16] that, for the S-wave interactions

$$V_i(\mathbf{x}_i) = c_i I_i^0/x_i^2, \qquad I_i^0 \equiv |Y_{00}(\hat{x}_i)\rangle\langle Y_{00}(\hat{x}_i)|, \quad (3)$$
$$c_i = \text{const}, \qquad i = 1, 2, 3,$$

these equations have the exact solutions

$$\Psi_i(\mathbf{r}_i; p^2) = r^{-2}Z_p(z)F_i(\Omega_i; p^2), \quad \mathbf{r}_i = (r, \Omega_i), \quad (4)$$

$$z \equiv r\sqrt{E}, \qquad i = 1, 2, 3,$$

at an arbitrary total energy E, but at specific values of the constants c_1, c_2, c_3, and p^2. In these solutions, p^2 is the constant of separation of the hyperradius $r \equiv \sqrt{x_i^2 + y_i^2}$ and the hyperangles $\Omega_i = (\hat{x}_i, \hat{y}_i, \varphi_i)$ [17], while the function Z_p obeys the Bessel equation

$$(z^2\partial_z^2 + z\partial_z + z^2 - p^2)Z_p(z) = 0. \tag{5}$$

It is well known [18] that, in the case of $m_i = m_1$ and $c_i = c_1 < 0$, $i = 1, 2, 3$, which was investigated in [14], the functions F_1, F_2, and F_3 cannot generally be represented as finite linear combinations of the basis hyperharmonics [17]

$$Y^{00}_{Laa}(\Omega_i) = N_{La}(1 - v_i^2)^{a/2} P^{(a+1/2, a+1/2)}_{L/2-a}(v_i) P_a(u_i), \tag{6}$$

$$N_{La} \equiv \frac{(-1)^a\sqrt{2a+1}}{2^{a+3/2}\pi\Gamma(L/2+3/2)}$$
$$\times ((L+2)\Gamma(L/2-a+1)\Gamma(L/2+a+2))^{1/2},$$
$$L = 0, 2, \ldots, \quad a = 0, 1, \ldots, L/2,$$
$$v_i \equiv \cos 2\varphi_i, \quad u_i \equiv \mathbf{x}_i \cdot \mathbf{y}_i/(x_i y_i),$$

but it was shown in [6] that, at $p^2 = (t+2)^2$ and under specific conditions on all coefficients c_i and B^i_L, these functions can be written as

$$F_i(\Omega_i; p^2) = \sum_{L=0}^{t} B^i_L Y^{00}_{L00}(\Omega_i), \tag{7}$$
$$i = 1, 2, 3, \quad t < \infty,$$

at arbitrary masses of the particles involved.

The main objective of the present study is to analyze the properties of all exact ($t < \infty$) solutions and to tabulate the simplest ($t = 4$) solutions (4)–(7) to the Faddeev Eqs. (2) and (3) and the corresponding solutions Ψ to the Schrödinger equation.

It is especially important to solve this problem because, in the literature, there are no straightforwardly calculable reference Faddeev components whose asymptotic expressions are qualitatively similar to physical ones at an arbitrary energy E. We will now clarify this statement.

In six-dimensional coordinate space $\mathcal{R}^6$, the Faddeev Eqs. (2) have spurious solutions [18]. The spurious solution (Ψ_1, Ψ_2, Ψ_3) is exact, but, by definition, it carries no information about the coordinate dependence of pair interactions and corresponds to the trivial solution $\Psi \equiv 0$ to the Schrödinger equation. Therefore, the similarity of spurious solutions found analytically and those calculated by integrating the Faddeev equations is not a criterion of the accuracy of the numerical algorithm being tested.

Apart from spurious solutions and the exact solution for the case that is specified by the interaction in (3) and which is considered here, exact solutions to the Faddeev and Schrödinger equations in $\mathcal{R}^6$ are known only for oscillator interactions [18, 19]. In that case, there exist only three-particle bound states at $E > 0$. Therefore, the oscillator Faddeev components can be used as reference ones only in testing algorithms for numerically solving the problem of three-particle bound states for $E > 0$. The class of these problems is overly narrow, including only problems specified by locking pair interactions: $V_i(\mathbf{x}_i) \to \infty$, $x_i \to \infty$, $i = 1, 2, 3$.

If, for the function Z_p, we take the Hankel function $H^{(1)}_p(z)$ or the modified Bessel function $K_p(|z|)$, then, in the limit $r \to \infty$, exact solutions (4)–(7) will have asymptotic expressions that are qualitatively similar to physical ones [8], which oscillate for $E > 0$ or decrease exponentially for $E < 0$. Therefore, these exact solutions can be used both as model ones and as reference ones in testing algorithms for numerically solving the Faddeev and Schrödinger equations for the scattering problem and the problem of three-particle bound states.

Since the aforementioned exact solutions are universal and are of importance as reference ones, the method proposed previously in [16] for constructing them is extended in Section 3 to the case where one coupling constant in (3) is infinitely large in absolute value and to the case where this is so for two coupling constants; also, the method is supplemented with an alternative version that involves considering the generalized eigenvalue problem and studying partitions [20] of exact Faddeev components Ψ_i into physical terms (Ψ^u_i) determining the solution Ψ to the Schrödinger equation and spurious terms (Ψ^s_i) making no contributions to this solution:

$$\Psi_i = \Psi^u_i + \Psi^s_i, \quad \Psi = \sum_{k=1}^{3} \Psi_k = \sum_{k=1}^{3} \Psi^u_k \neq 0,$$
$$\sum_{k=1}^{3} \Psi^s_k \equiv 0, \quad i = 1, 2, 3.$$

In order to render a practical application of exact solutions comprehensible and straightforward, particular attention is paid in Section 4 to deriving and analyzing all formulas (without exception) necessary for constructing reference solutions and to representing these formulas in a form that is the most convenient for calculations; finally, tables and figures that provide clear illustrations of the process for constructing these solutions are also given there. The main results and their physical implications are discussed in Section 5.

3. EXACT SOLUTIONS

In order to reduce the Faddeev Eqs. (2) to a set of two systems of linear equations determining allowed values of the constants c_1, c_2, and c_3 and of all coefficients B_L^i in the exact solutions (4)–(7), we will need the following three hyperharmonics (6):

$$\left(\mathbf{L}^2 - L(L+4)\right) Y_{L00}^{00}(\Omega_i) = 0; \tag{8}$$

$$4\cos^2\varphi_i Y_{L00}^{00}(\Omega_i) = \sum_{L'=L_-(L)}^{L+2} (1+\delta_{LL'}) Y_{L'00}^{00}(\Omega_i), \tag{9}$$

$$L_-(L) \equiv \max\{0, L-2\};$$

$$K(\gamma_{ki}) Y_{L00}^{00}(\Omega_i) = \sum_{a=0}^{L/2} \langle aa|K(\gamma_{ki})|00\rangle_{L0} Y_{Laa}^{00}(\Omega_i). \tag{10}$$

Here, $\mathbf{L}$ is the 15-component vector operator of the grand-orbital momentum [17] and $K(\gamma)$ is the kinematical-transformation operator [18]. In the case of $\gamma = \gamma_{ki}$, where γ_{ki} is the kinematical angle,

$$\gamma_{ki} \equiv g_{ki} \arctan\left(\frac{m_j}{m_k m_i}(m_1+m_2+m_3)\right)^{1/2}, \tag{11}$$

$$g_{ki} = -g_{ik} = 1,$$

the operator $K(\gamma_{ki})$ coincides with the operator of the cyclic permutation of the numbers i, j, and k of particles p_i, p_j, and p_k such that, under this permutation, the indices i, j, and k go over to k, i, and j, respectively. The expansion in (10) describes the transformation of hyperharmonics under the above permutation and involves the Reynal–Revai coefficients $\langle aa|K(\gamma_{ki})|00\rangle_{L0}$. The dependence of these coefficients on the kinematical angles (11) is given by the well-known formulas [21]

$$\langle aa|K(\gamma_{ki})|00\rangle_{L0} = (-1)^a \langle aa|K(\gamma_{ik})|00\rangle_{L0} \tag{12}$$
$$= \frac{N_{La}}{2^a N_{L0}} \frac{(\sin 2\gamma_{ki})^a P_{L/2-a}^{(a+1/2,a+1/2)}(\cos 2\gamma_{ki})}{P_{L/2}^{(1/2,1/2)}(-1)}.$$

We will describe in detail the case of three different particles, whereupon we will consider the particular cases of two and three identical bosons.

Using the ansatz in (4) and the fact that Z_p is a solution to Eq. (5), we reduce the original Faddeev Eqs. (2) in $\mathcal{R}^6$ to equations of the Faddeev type on the five-dimensional unit hypersphere $\mathcal{S}^5$. The result is

$$\cos^2\varphi_i(\mathbf{L}^2(\Omega_i) + 4 - p^2) F_i(\Omega_i; p^2) \tag{13}$$
$$= -\mathrm{c}_i I_i^0 \sum_{k=1}^{3} F_k(\Omega_k; p^2), \quad i = 1,2,3.$$

We note that, upon making the substitution

$$F_i(\Omega_i; p^2) = \frac{4}{\sqrt{\pi}} \mathrm{cosec} 2\varphi_i \cdot U_i(\varphi_i; p^2) \mathcal{Y}_{00}^{00}(\Omega_i), \tag{14}$$
$$i = 1,2,3,$$

and taking the projection onto the bispherical harmonic $\mathcal{Y}_{00}^{00} = (4\pi)^{-1}$, these equations reduce to the one-dimensional integro-differential equations

$$(\cos^2\varphi_i(\partial_{\varphi_i}^2 + p^2) - c_i) U_i(\varphi_i; p^2) \tag{15}$$
$$= c_i \sum_{k\neq i} \int_a^b d\varphi_k U_k(\varphi_k; p^2)/|\sin 2\gamma_{ki}|,$$
$$a \equiv |\varphi_i - |\gamma_{ki}||, \; b \equiv \min\{\varphi_i + \gamma_{ki}, \pi - \varphi_i - |\gamma_{ki}|\}.$$

Further, it can be verified that, if the series in (7) satisfy Eq. (13), the series

$$U_i(\varphi_i; p^2) = \sum_{L=0}^{t} B_L^i \sin 2n\varphi_i, \tag{16}$$
$$i = 1,2,3, \qquad n = L/2+1,$$

will be solutions to Eqs. (15) by virtue of relations (14).

Under the same assumption, the corresponding exact solution Ψ to the Schrödinger equation can be constructed on the basis of the formulas

$$\Psi(\mathbf{r}_i; p^2) = \sum_{k=1}^{3} \Psi_k(\mathbf{r}_k; p^2) = r^{-2} Z_p(z) F(\Omega_i; p^2), \tag{17}$$

$$F(\Omega_i; p^2) \equiv F_i(\varphi_i; p^2) + \sum_{k\neq i} F_k(\varphi_k(\varphi_i, u_i; \gamma_{ki}); p^2), \tag{18}$$

$$\varphi_k(\varphi_i, u_i; \gamma_{ki}) = \arccos(\cos^2(\gamma_{ki} - \varphi_i)$$
$$+ (u_i - 1)\sin\gamma_{ki}\cos\gamma_{ki}\sin 2\varphi_i)^{1/2}.$$

With the aid of formulas (7) and (10), the functions $F(\Omega_i; p^2)$ can also be represented as a double sum,

$$F(\Omega_i; p^2) = \sum_{L=0}^{t} \sum_{a=0}^{L/2} {}^i B_{La} Y_{Laa}^{00}(\Omega_i), \tag{19}$$

$${}^i B_{La} \equiv \delta_{a0} B_L^i + \sum_{k\neq i} \langle aa|K(\gamma_{ki})|00\rangle_{L0} B_L^k. \tag{20}$$

By using the substitution in (7) at $p^2 = (t+2)^2$ in Eqs. (13), making the substitution

$$B_L^i = \frac{X_n^i}{n^2 - m^2}, \quad n = L/2+1 = 1,2,\ldots,m-1, \tag{21}$$

$$X_m^i = B_t^i, m = t/2 + 1,$$

and taking the projection onto the basis specified by Eq. (6), we now derive, with the aid of formulas (8)–(12), a set of matrix equations of dimension $m-1$,

$$D^1 X_1 + IX_2 = 0, \tag{22}$$
$$IX_{n-1} + D^n X_n + IX_{n+1} = 0,\ n = 2, 3, \ldots, m-2,$$
$$IX_{m-2} + D^{m-1} X_{m-1} = 0,$$

and the matrix equation

$$M^t X_m = -\frac{1}{4} IX_{m-1}. \tag{23}$$

Here, all matrices and sought columns X_n are three-dimensional; that is,

$$X_n \equiv (X_n^1, X_n^2, X_n^3)^T, \quad n = 1, 2, \ldots, m; \tag{24}$$
$$D_{ii}^n = 2 + \frac{c_i}{n^2 - m^2}, \quad D_{ik}^n = (D_{ii}^n - 2) K_n(\gamma_{ki}),$$
$$n = 1, 2, \ldots, m-1;$$
$$I_{ii} = 1, \quad I_{ki} = 0; \quad M_{ii}^t = c_i,$$
$$M_{ik}^t = c_i K_m(\gamma_{ki}), \quad k \neq i = 1, 2, 3,$$

where $K_n(\gamma_{ki})$ is the coefficient in (12) at $a = 0$ and $L = 2(n-1)$.

Let us represent the set of Eqs. (22) as one matrix equation

$$A^t X = 0, \quad X \equiv (X_1, X_2, \ldots, X_{m-1})^T, \tag{25}$$
$$\dim A^t = 3(m-1) = 3t/2.$$

Setting $\alpha_k \equiv c_k/c_2$, $k = 1, 2, 3$, and $R^t \equiv A^t$ at $c_1, c_2, c_3 = 0$, we recast this equation into the equivalent form

$$R^t X = c_2 T^t X, \tag{26}$$

where, by construction, R^t and T^t are, respectively, a block-tridiagonal and a block-diagonal matrix. The blocks of the principal diagonals of these matrices are the three-dimensional matrices $R^n = 2I$ and T^n,

$$T_{ii}^n = \frac{\alpha_i}{m^2 - n^2}, \quad T_{ik}^n = T_{ii}^n K_n(\gamma_{ki}), \tag{27}$$
$$k \neq i = 1, 2, 3, \quad n = 1, \ldots, m-1,$$

while each block of the upper and lower diagonals of the matrix R^t is the matrix I.

From the theorem of existence and uniqueness of solutions to finite homogeneous and nonhomogeneous systems of linear equations, which is known in linear algebra [22], it follows that the set of the conditions $\det M^t \neq 0$ and $\det A^t = 0$ is a criterion of a simultaneous and nontrivial consistency of the systems of Eqs. (23) and (25).

With the aid of Eqs. (11), (12), and (24), it can easily be shown that, at arbitrary particle masses and nonvanishing coupling constants, $\det M^t = 0$ at $t = 0, 2$ and $\det M^t \neq 0$ at $t \geq 4$. Therefore, we further assume that $t \geq 4$.

In order to analyze the condition $\det A^t = 0$, we apply, to the set of Eqs. (22), the substitution method [22], which is the most economical and convenient for operator accumulation: by consecutively expressing all columns $X_2, \ldots, X_{m-1}$ in terms of the column X_1, we reduce this set of equations to the equation $G^t X_1 = 0$ involving the three-dimensional matrix G^t and the condition $\det A^t = 0$ to the equivalent condition $\det G^t = 0$.

Further, we note that the elements (24) of the matrix A^t depend on the ratio of the particle masses through the kinematical angles (11) and on the interaction parameters. It follows that $\det A^t$ and $\det G^t$ are polynomials of degree $N \leq t/2$ in the argument q, which is one of the parameters c_1, c_2, and c_3, the coefficients C_n in this polynomial being dependent on the remaining two parameters and on two ratios of the particle masses. At $q = c_2$ and $m_3 = 1$, the analysis of the condition $\det G^t = 0$ reduces to studying all real-valued roots $c_2 = c_2^\nu(c_1; c_3, m_1, m_2)$ of the algebraic equation

$$\det G^t = \sum_{n=0}^{N \leq t/2} C_n(c_1; c_3, m_1, m_2) c_2^n = 0 \tag{28}$$

as functions of the argument c_1 and the parameters c_3, m_1, and m_2.

It should be noted that, if a chosen value of t is not large—at given finite values of c_1, c_3, m_1, and m_2, all roots c_2^ν of Eq. (28) are bounded—these roots can be found by solving the generalized eigenvalue problem specified by Eqs. (26) and (27) on the basis of known methods (see [22]) that make it possible to calculate simultaneously all eigenvectors X^ν and eigenvalues c_2^ν, $\nu = 1, 2, \ldots$, but, now, as functions of the parameters α_3, m_1, and m_2 [$c_2^\nu(\alpha_1; \alpha_3, m_1, m_2)$ α_1].

We now consider the case where, in the limit $c_1 \to \infty$, some root c_2^ν has a finite limit c_2^s. In order to calculate, to a high precision, the corresponding bounded limiting solutions X and X^m to Eqs. (22) and (23), it is necessary, first, to go over to the limit $c_1 \to \infty$ in these equations and, then, to solve the resulting limiting equations. In order to derive such equations, each equation in the sets of Eqs. (22) and (23) for the unknown quantities X_n^i that involves c_1 must be divided by c_1, whereupon it is necessary to set $c_1 = \infty$. As a result, we obtain sets of equations for determining the limiting values of the coefficients X_n^i. In the matrix form, these equations have the same form as the original Eqs. (22) and (23), but they

involve the matrices I, D^n, and M^t, whose first rows ($i = 1$; $k = 1, 2, 3$) can be calculated by the formulas

$$D^n_{ik} = [K_n(\gamma_{ki})]^{1-\delta_{ki}}/(n^2 - m^2), \qquad (29)$$
$$I_{ik} = 0, \quad M^t_{ik} = [K_m(\gamma_{ki})]^{1-\delta_{ki}};$$

their second and third rows are determined, as before, by Eqs. (24).

Let us investigate the structure of the series in (19) for the function F at $c_1 = \infty$ and $c_2 = c_2^s$. For this purpose, the first equation ($i = 1$) of each matrix equation of the limiting sets of equations as given by (22), (23), and (29) is reduced, with the aid of relations (21), to the equality

$$B^1_L + K_n(\gamma_{21})B^2_L + K_n(\gamma_{31})B^3_L = 0. \qquad (30)$$

According to the definition in (20), the left-hand side of (30) is equal to the coefficient ${}^1B_{L0}$, whence it follows that, in the limit under study, ${}^1B_{L0} = 0$ at all values of L. In the representation Ω_i, $i = 1$, the series in (19) does not therefore involve the hyperharmonics Y^{00}_{Laa} with $a = 0$; that is,

$$F(\Omega_i; p^2) = \sum_{L=2}^{t}\sum_{a=1}^{L/2} {}^iB_{La}Y^{00}_{Laa}(\Omega_i). \qquad (31)$$

Since $K_1(\gamma_{ki}) = 1$ at any value of γ_{ki}, it follows from Eqs. (20) and (30) at $n = 1$ that ${}^iB_{00} = 0$, $i = 1, 2, 3$. Hence, the limiting series (19) for the functions $F(\Omega_k; p^2)$, $k = 2, 3$, as well as the series in (31), do not contain the hyperharmonic Y^{00}_{000}, but, in general, they involve all other hyperharmonics of $L > 0$:

$$F(\Omega_k; p^2) = \sum_{L=2}^{t}\sum_{a=0}^{L/2} {}^kB_{La}Y^{00}_{Laa}(\Omega_k). \qquad (32)$$

Thus, we see that, in the limit $c_1 = \infty$ and at $c_2 = c_2^s$, the terms $B^i_0 Y^{00}_{000}$ of the series in (7) for the components F_i are spurious; that is, these terms cancel in summing these components into the hyperangular part [Eqs. (31), (32)] of the limiting solution Ψ to the Schrödinger equation.

Other limiting solutions can be analyzed by following a line of reasoning similar to that adopted above: if $|c_2^\nu| \to \infty$ at $c_1 \to c_1^s$ and if $|c_1^s| < \infty$, we set $i = 2$ in formulas (29) and (31) and $k = 1, 3$ in the series in (32); but if $|c_2^\nu| \to \infty$ for $|c_1| \to \infty$, it is necessary to employ the values of $i = 1, 2$ and $k = 3$ in the same formulas.

It only remains to describe two particular cases of physical significance.

Suppose that particles p_2 and p_3 are identical bosons. We denote by P_{23} the interchange operator and by I the identity operator. Therefore, $m_2 = m_3$ and $c_2 = c_3$; according to (11), we also have $\gamma_{12} = \gamma_{31}$. For the sought Faddeev components (4)–(7) and the function in (17) corresponding to these components to obey the permutation-symmetry conditions [8]

$$\Psi_1 = P_{23}\Psi_1, \quad \Psi_2 = P_{23}\Psi_3,$$
$$\Psi = P_{23}\Psi = \Psi_1 + (I + P_{23})\Psi_2,$$

we set $B^2_L = B^3_L$ for $L = 0, 2, \ldots, t$ and, according to formulas (21), $X^2_n = X^3_n$ at all values of n. Therefore, all columns and matrices of Eqs. (22) and (23) and the blocks of the matrices of Eq. (26) appear to be two-dimensional,

$$X_n \equiv (X^1_n, X^2_n)^T, \quad n = 1, 2, \ldots, m; \qquad (33)$$
$$I = \mathrm{diag}\{1, 1\};$$
$$D^n_{ii} = 2 + \frac{c_i}{n^2 - m^2}(1 + \delta_{i2}K_n(\gamma_{23})),$$
$$D^n_{ik} = \frac{c_i}{n^2 - m^2}(1 + \delta_{k2})K_n(\gamma_{12});$$
$$M^t_{ii} = c_i(1 + \delta_{i2}K_m(\gamma_{23})),$$
$$M^t_{ik} = c_i(1 + \delta_{k2})K_m(\gamma_{12}), \quad k \neq i = 1, 2,$$
$$R^n = 2I, \quad T^n_{ii} = \frac{\alpha_i}{m^2 - n^2}(1 + \delta_{i2}K_n(\gamma_{23})),$$
$$T^n_{ki} = \frac{\alpha_i}{m^2 - n^2}(1 + \delta_{k2})K_n(\gamma_{12}),$$

and formulas (20) are simplified to become

$$ {}^1B_{La} = (1 + (-1)^a)(\delta_{a0}B^1_L \qquad (34)$$
$$+ 2\langle aa|K(\gamma_{21})|00\rangle_{L0}B^2_L), \quad a = 1, 2, \ldots;$$
$$ {}^iB_{La} = \langle aa|K(\gamma_{12})|00\rangle_{L0}B^1_L$$
$$+ (\delta_{a0} + \langle aa|K(\gamma_{32})|00\rangle_{L0})B^2_L, \quad i = 2, 3.$$

Suppose that p_1, p_2, and p_3 are identical bosons. In this case, we have $m_k = m_1$, $c_k = c_2$, and $|\gamma_{ki}| = \pi/3$ for all $k \neq i = 1, 2, 3$. The complete-permutation-symmetry conditions [8]

$$\Psi_i = P_{ki}\Psi_k, \quad \Psi = P_{ki}\Psi = (I + P_{12} + P_{23})\Psi_i,$$
$$k \neq i = 1, 2, 3,$$

are satisfied for all sought Faddeev components (4)–(7) and the function in (17) corresponding to them if one sets $B^k_L = B^1_L$ and $X^k_n = X^1_n$ at arbitrary k, n, and L. It follows that, in Eqs. (22), (23), and (26), all block matrices are one-dimensional,

$$D^n = 2 + \frac{c_2}{n^2 - m^2}(1 + 2K_n(\pi/3)); \qquad (35)$$
$$M^t = c_2(1 + 2K_m(\pi/3));$$
$$X_n = X^1_n, \quad I = 1, \quad R^n = 2, \quad T^n = (D^n - 2)/c_2,$$
$$n = 1, \ldots, m - 1,$$

and that, by virtue of Eqs. (12) and the identities $B^i_n = B^1_n$, $i = 1, 2, 3$, formulas (20) take the form

$$ {}^iB_{La} = [\delta_{a0} + (1 + (-1)^a)\langle aa|K(\pi/3)|00\rangle_{L0}]\, B^1_L, \quad a = 1, 2, \ldots. \tag{36}$$

In order to highlight one special feature, we will consider the coefficients in (36) for even values of the index a. If $B^i_L \neq 0$, then ${}^iB_{La} = 0$ only at $L = 2$ and $a = 0$, because in no other case, as follows from Eqs. (12), do we have $\langle aa|K(\pi/3)|00\rangle_{L0} = -1/2$. Therefore, the series in (19) for the function F does not involve the hyperharmonic Y^{00}_{200} even in the case where this hyperharmonic appears in the series in (7) for the components F_i of the function F. Therefore, the term $B^i_2 Y^{00}_{200}$ in the component F_i is spurious at any c_2 and t.

4. REFERENCE SOLUTIONS

For reference solutions to the Faddeev Eqs. (2), it is reasonable to use the exact solutions (4) whose hyperspherical expansions involve a minimum possible number of terms. As was shown above, there are no nontrivial exact solutions at $t = 0$, 2. Therefore, we consider the case of $t = 4$, where $m = t/2 + 1 = 3$ and $p^2 = 36$ and where there are three unknown columns X_1, X_2, and X_3. In this case, the set of Eqs. (22) consists of two equations

$$D^1 X_1 + X_2 = 0, \quad X_1 + D^2 X_2 = 0,$$

which are equivalent to the equations

$$G^4 X_1 = 0, \quad G^4 = D^2 D^1 - I; \quad X_2 = -D_1 X_1;$$

the column X_3 is determined by Eq. (23); and the matrices D^1, D^2, and M^4 are given by formulas (24), (33), and (35), which correspond to this case.

4.1. Case of Three Different Particles

At $t = 4$, Eq. (28) is the quadratic equation

$$\det G^4 = \det(D^2 D^1 - I) = Ac_2^2 + Bc_2 + C = 0. \tag{37}$$

At arbitrary real-valued c_1, c_3, m_1, and m_2, its coefficients

$$\begin{aligned} A &\equiv 15 + 2(t_1^2 - 1)c_1 + 2(t_3^2 - 1)c_3, \qquad (38)\\ B &\equiv 2(t_1^2 - 1)c_1^2 + 2(t_3^2 - 1)c_3^2 - 390 \\ &- 2(16t_1^2 + 5t_1 - 36)c_1 - 2(16t_3^2 + 5t_3 - 36)c_3 \\ &+ \frac{2}{3}(4(t_1^2 + t_2^2 + t_3^2) + t_1 + t_2 + t_3 - 12)c_1 c_3 \\ &- \frac{2}{3}(\cos 2(\gamma_{12} - \gamma_{31}) + \cos 2(\gamma_{12} - \gamma_{23}) \\ &\quad + \cos 2(\gamma_{31} - \gamma_{23}))c_1 c_3, \end{aligned}$$

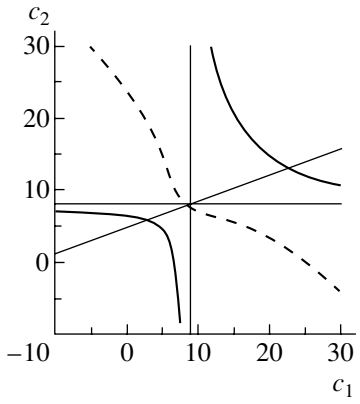

Fig. 1. Roots $c_2 = c_2^{\pm}(c_1; c_3, m_1, m_2)$ of Eq. (37) with the coefficients given by (38) versus the argument c_1 for the case of $c_3 = -2$, $m_1 = 2$, and $m_2 = 4$: (solid curves) c_2^+ and (dashed curve) c_2^-. The thin solid lines are the horizontal and vertical asymptotes (41), and the inclined straight line (42) was drawn through the points of their intersection.

$$\begin{aligned} C &\equiv 15(c_1^2 + c_3^2) + 2((t_2^2 - 1)(c_1 + c_3) \\ &- 16t_2^2 - 5t_2 + 36)c_1 c_3 - 390(c_1 + c_3) + 1800, \\ t_1 &\equiv \cos 2\gamma_{12}, \quad t_2 \equiv \cos 2\gamma_{31}, \quad t_3 \equiv \cos 2\gamma_{23}, \end{aligned}$$

are such that the discriminant $D \equiv B^2 - 4AC$ is positive. Therefore, there always exist two different real-valued roots c_2^+ and c_2^-:

$$c_2^{\pm}(c_1; c_3, m_1, m_2) = -\frac{B}{2A} \times \left(1 \pm \mathrm{sgn}(c_1^s - c_1)\left(1 - 4\frac{AC}{B^2}\right)^{1/2}\right). \tag{39}$$

In the (c_1, c_2) coordinate plane (for example, see Fig. 1), the graph of the function c_2^-, which is everywhere continuous, has the inclined asymptote

$$c_2 = -c_1 - \frac{1}{3}\left(7 + 4\frac{2m_1 + 2m_2 + 1}{(m_1 + m_2)^2}\right)c_3 + \frac{1}{2}\left(37 + 5\frac{m_1 + m_2 + 1}{m_1 m_2}\right), \tag{40}$$

while the graph of the function c_2^+, which has a discontinuity at the zero c_1^s of the coefficient A, has a vertical and a horizontal asymptote:

$$c_1 = c_1^s \equiv \frac{15 + 2(t_3^2 - 1)c_3}{2(1 - t_1^2)}, \qquad c_2 = c_2^s \equiv \frac{15 + 2(t_2^2 - 1)c_3}{2(1 - t_1^2)}. \tag{41}$$

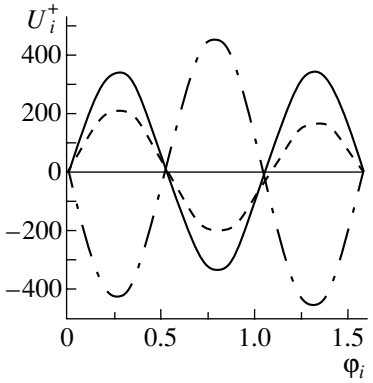

Fig. 2. Components (16) at $m_1 = 10$, $m_2 = 20$, $c_1 = -2$, $c_2 = c_2^+ = 14.7647$, and $c_3 = -40$: (solid curve) $U_1^+(\varphi_1; 36)$, (dashed curve) $U_2^+(\varphi_2; 36)$, and (dash-dotted curve) $U_3^+(\varphi_3; 36)$.

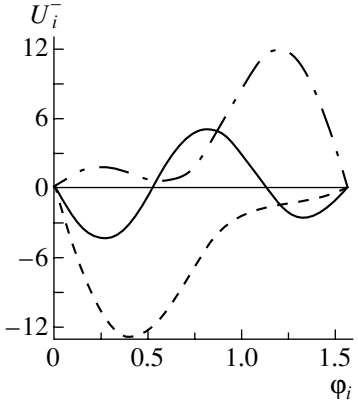

Fig. 3. Components (16) at $m_1 = 10$, $m_2 = 20$, $c_1 = -2$, $c_2 = c_2^- = 90.3522$, and $c_3 = -40$: (solid curve) $U_1^-(\varphi_1; 36)$, (dashed curve) $U_2^-(\varphi_2; 36)/3$, and (dash-dotted curve) $U_3^-(\varphi_3; 36)/3$.

The point (c_1^s, c_2^s) of their intersection lies on the straight line

$$c_2 = \frac{1 - t_2^2}{1 - t_3^2} c_1 + \frac{15}{2} \frac{t_2^2 - t_3^2}{(1 - t_1^2)(1 - t_3^2)}. \qquad (42)$$

At arbitrary fixed values of m_1, m_2, and c_3, we have the inequality $c_2^+ < c_2^s$ if $c_1 < c_1^s$ and the inequality $c_2^+ > c_2^s$ if $c_1 > c_1^s$. If c_3 increases or decreases, the point (c_1^s, c_2^s) therefore moves along this straight line downward or upward, respectively. The graphs of the functions $c_2^\pm$ exhibit similar shifts in response to variations in c_3.

In the case of $m_1 = 10$, $m_2 = 20$, $c_1 = -2$, and $c_3 = -40$, the roots $c_2^\pm$ calculated by formulas (38) and (39) to six decimal places are as follows: $c_2^+ = 14.7647$ and $c_2^- = 90.3522$; the corresponding values of the coefficients $B_L^{i\pm}$ in the series in (7) and (16) are compiled in Table 1, while the components $U_i^\pm(\varphi_i; 36)$ are displayed in Figs. 2 and 3 versus the angle φ_i, $i = 1, 2, 3$. This table and these figures illustrate the existence of two types of exact solutions to Eqs. (15). We now describe these types.

At moderate values of $c_2 = c_2^+ \ll |c_3|$, there exist solutions of the first type, (U_1^+, U_2^+, U_3^+). The expansions (16) of all their components U_i^+ are dominated ($B_L^{i+} \ll B_t^{i+}, i = 1, 2, 3; L = 0, 2$) by the basis function $\sin 2n\varphi_i$ characterized by the maximum possible value of $n = 3$ at the fixed value of $t = 4$ (see columns 2–4 in Table 1 and Fig. 2). Solutions of the second type (U_1^-, U_2^-, U_3^-) exist at $c_2 = c_2^-$ and c_3 whose absolute values are much greater than $|c_1|$. In the expansions of the components U_i^- of these solutions, all functions $\sin 2n\varphi_i$, $n = 1, 2, 3$, appear with commensurate coefficients ($|B_L^{i-}| \sim |B_4^{i-}|$, $i = 1, 2, 3$; $L = 0, 2$), but the component U_1^- is much less ($|U_1^-| \ll |U_k^-|, k = 2, 3$) than the others (see columns 5–7 in Table 1 and Fig. 3).

The solutions (U_1^+, U_2^+, U_3^+) generate the solution Ψ^+ that satisfies the Schrödinger equation and which is close to the solution of the free equation corresponding to it ($c_k = 0$, $k = 1, 2, 3$). We will now demonstrate this explicitly. Disregarding the coefficients B_L^{i+}, $L = 0, 2$, and using Eqs. (7), (17), (19), and (20), we do indeed obtain

$$\Psi^+(\mathbf{r}_i; 36) \approx r^{-2} Z_6(z) \sum_{a=0,1,2} {}^i B_{4a}^+ Y_{4aa}^{00}(\Omega_i).$$

The solution Ψ^- obeying the Schrödinger equation and corresponding to the solution (U_1^-, U_2^-, U_3^-) has a different physical property: the function $|\Psi^-|^2$ is expelled from that region of configuration space $\mathcal{R}^6$ where the total interaction V is repulsive and is localized in that region where this interaction is attractive. This property is a corollary of the particular angular dependence of the components U_1^-, U_2^-, and U_3^-, which is illustrated in Fig. 3. The component U_2^- of the pair of strongly repulsed ($c_2 = c_2^- \approx 90$) particles p_1 and p_3 is localized in the region $\varphi_2 < \pi/4$, which is far off their collision point $\varphi_2 = \pi/2$; on the contrary, the component U_3^- of the pair of strongly attracted ($c_3 = -40$) particles p_1 and p_2 is localized near the binary-collision point $\varphi_3 = \pi/2$. Because of a weak attraction ($c_1 = -2$) in the pair of particles p_2 and p_3, the remaining component U_1^- has three local extrema that are commensurate in magnitude and which are uniformly distributed over the entire interval $0 \le \varphi_1 \le \pi/2$.

Table 1. Coefficients $B_L^{i\pm}$ corresponding to the roots $c_2^+ = 14.7647$ and $c_2^- = 90.3522$ of Eq. (37) with coefficients (38) at $m_1 = 10$, $m_2 = 20$, $c_1 = -2$, and $c_3 = -40$

L	B_L^{1+}	B_L^{2+}	B_L^{3+}	B_L^{1-}	B_L^{2-}	B_L^{3-}
0	1.000000	−12.96196	7.038856	1.000000	−24.02648	17.83859
2	−1.230759	26.94059	16.86049	−1.124846	−16.86264	−15.58043
4	338.9026	190.3271	−445.3111	−3.942418	−6.419471	10.03177

Table 2. Coefficients B_L^i at $t = 4$, $m_1 = 10$, $m_2 = 20$, and $c_3 = -40$ for $|c_1| = \infty$ and $c_2 = c_2^s = 21.5152$ or for $|c_1| = c_1^s = 35.7374$ and $|c_2| = \infty$

L	B_L^1	B_L^2	B_L^3	B_L^1	B_L^2	B_L^3
	$\lvert c_1\rvert = \infty, \quad c_2 = c_2^s$			$c_1 = c_1^s, \quad \lvert c_2\rvert = \infty$		
0	1.000000	−0.594640	−0.405398	1.000000	−1.783493	0.783449
2	−0.136155	1.902848	1.297151	−3.200000	0.137848	−2.507177
4	14.02088	8.101168	−18.65622	−27.74264	−14.32074	35.71708

In the limiting case of $|c_1| = \infty$ and $c_2 = c_2^+ = c_2^s$, we solve analytically Eqs. (22) and (23) with the block matrices (29). By using relations (21), we then obtain the formulas

$$f_1 = 15 + c_3(2t_2^2 + t_3 - \cos 2(\gamma_{12} - \gamma_{31}) - 1), \quad (43)$$

$$B_0^1 = 1, \quad B_0^2 = \frac{1}{f_1}(2c_3(1 - t_2^2) - 15),$$

$$B_2^2 = -\frac{16}{5}B_0^2,$$

$$B_0^3 = -1 - B_0^2, \quad B_2^3 = -\frac{16}{5}B_0^3,$$

$$B_2^1 = -(t_1 B_2^2 + t_2 B_2^3);$$

$$g_1 = 2\sin 2\gamma_{31} + \sin 2(\gamma_{12} - \gamma_{23}) + \sin(4\gamma_{23} - 2\gamma_{31}),$$

$$B_4^2 = \frac{12}{f_1(1 - t_3^2)}(2t_2^2 - 2t_3 - \cos 2(\gamma_{12} - \gamma_{31}) + 1),$$

$$B_4^3 = \frac{24}{f_1 g_1}(\sin(4\gamma_{12} - 2\gamma_{31}) + 2\sin 2(\gamma_{12} - \gamma_{31}) - 3\sin 2\gamma_{12} - \sin 6\gamma_{12} - \sin 3\gamma_{31}),$$

$$B_4^1 = -K_3(\gamma_{12})B_4^2 - K_3(\gamma_{31})B_4^3,$$

which are convenient for consecutively calculating the limiting coefficients B_L^i. In this limit, the components in (7) involve spurious terms $B_0^i Y_{000}^{00}(\Omega_i)$, $i = 1, 2, 3$, while, in the representation Ω_i, $i = 1$, the series in (19) can be written, according to (31), in the simplest form

$$F(\Omega_i; 36) = \sum_{L=2}^{4} \sum_{a=1}^{L/2} {}^i B_{La} Y_{Laa}^{00}(\Omega_i) \neq 0. \quad (44)$$

In the case of $c_1 = c_1^s$ and $c_2 = c_2^+ = \pm\infty$, we similarly obtain

$$f_2 = 15 + 2c_3(t_3^2 - 1), \quad (45)$$

$$B_0^1 = 1, \qquad B_2^1 = -\frac{16}{5},$$

$$B_0^3 = \frac{c_3}{f_2}(t_2 - \cos 2(\gamma_{12} - \gamma_{31})),$$

$$B_0^2 = -1 - B_0^3, \qquad B_2^3 = -\frac{16}{5}B_0^3,$$

$$B_2^2 = \frac{16}{5}(t_1 + t_2 B_0^3);$$

$$g_2 = \sin 2(\gamma_{31} - \gamma_{12}) + \sin(2\gamma_{23} - 4\gamma_{31}) - 2\sin 2\gamma_{23},$$

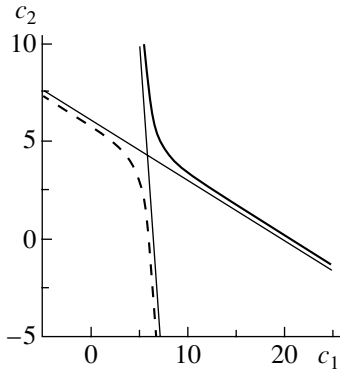

Fig. 4. Roots $c_2 = c_2^{\pm}(c_1; m_1)$ of Eq. (37) with coefficients (46) versus the argument c_1 at $m_1 = 2$: (solid curve) c_2^+ and (dashed curve) c_2^-. The thin solid lines are the inclined asymptotes (49).

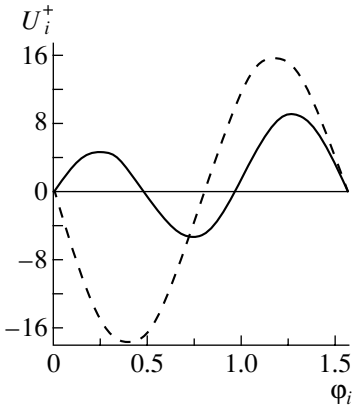

Fig. 5. Components (16) at $m_1 = 2$, $c_1 = -2$, and $c_2 = c_2^+ = 61.9400$: (solid curve) $U_1^+(\varphi_1; 36)$ and (dashed curve) $U_2^+(\varphi_1; 36)$.

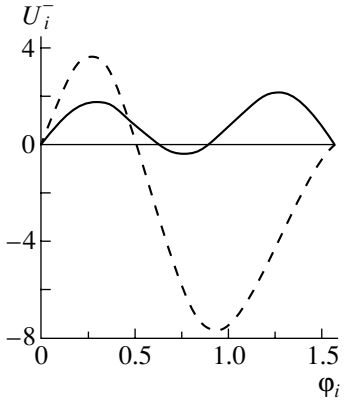

Fig. 6. Components (16) at $m_1 = 2$, $c_1 = -2$, and $c_2 = c_2^- = 6.93328$: (solid curve) $U_1^-(\varphi_1; 36)$ and (dashed curve) $U_2^-(\varphi_2; 36)$.

$$B_4^1 = \frac{12}{f_2(t_2^2-1)}(2t_3^2 - 2t_2 - \cos 2(\gamma_{12}-\gamma_{23})),$$
$$B_4^3 = \frac{24}{f_2 g_2}(2\sin 2(\gamma_{12}-\gamma_{31}) + \sin(4\gamma_{12}-2\gamma_{23}) - 3\sin 2\gamma_{12} - \sin 6\gamma_{12} - \sin 2\gamma_{23}),$$
$$B_4^2 = -K_3(\gamma_{12})B_4^1 - K_3(\gamma_{23})B_4^3.$$

In this limit, the spurious terms are the same as before ($B_0^i Y_{000}^{00}$), while the function $F(\Omega_2; 36)$ can be found by formula (44) at $i = 2$.

By way of example, the values of the coefficients in (43) and (45) are given in Table 2 for $m_1 = 10$, $m_2 = 20$, and $c_3 = -40$. It can be seen that, in either extreme case considered above, $|B_L^i| \ll |B_4^i|$, $i = 1, 2, 3$; $L = 0, 2$. Therefore, both limiting solutions (U_1, U_2, U_3) are those of the first type—that is, their expansions are dominated by the basis function $\sin 2n\varphi_i$ whose index takes the maximum possible value of $n = 3$.

In the remaining limiting cases, where, according to (40), $c_2^- \to \mp\infty$ for $c_1 \to \pm\infty$, the situation is different: if $B_0^{1\pm} = 1$, then $B_1^{2\pm} = -1$ and $B_L^{i\pm} = 0$ for all other values of i and L. Therefore, the limiting solutions to Eqs. (13) are identical,

$$F_i^\pm = (-1)^{1+i} Y_{000}^{00}, \quad i = 1, 2; \quad F_3^\pm \equiv 0,$$

and are spurious, since their sum in (18) is a trivial function: $F \equiv 0$.

Once we have found all coefficients B_L^i and have constructed the components F_i in the form of the series in (7), we can calculate the function F by formulas (18) or (19).

Table 3. Coefficients $B_L^{i\pm}$ corresponding to the roots $c_2^+ = 61.9400$ and $c_2^- = 6.93328$ of Eq. (37) with coefficients (46) at $m_1 = 2$ and $c_1 = -2$

L	B_L^{1+}	B_L^{2+}	B_L^{1-}	B_L^{2-}
0	1.000000	−1.347928	1.000000	−4.221037
2	−2.521657	−16.69492	−0.223170	3.991469
4	6.256621	−0.128311	1.408249	2.295875

4.2. Case of Two Identical Particles

Since $m_2 = m_3 = 1$ and $c_2 = c_3$, Eq. (28) reduces to the square Eq. (37) with the simpler coefficients

$$A \equiv 12t_1^2, \quad B \equiv 4((2t_1^2 - t_1 + 2)c_1 - 24t_1^2 - 15), \quad (46)$$
$$C \equiv 3(c_1^2 - 6)(c_1 - 20), \quad t_1 \equiv -(1+m_1)^{-1},$$

whereas the sought roots $c_2 = c_2^\pm(c_1; m_1)$ depend on one argument c_1 and one parameter m_1. If $m_1 < \infty$, then $A < 0$ and $D = B^2 - 4AC > 0$ at any value of c_1; therefore, there exist two different real-valued roots

$$c_2^\pm(c_1; m_1) = \frac{1}{6t_1^2}((t_1 - 2t_1^2 - 2)c_1 + 24t_1^2 + 15) \quad (47)$$
$$\pm \frac{1}{6t_1^2}[4(t_1^4 - t_1^3 - t_1 + 1)c_1^2 + 6(8t_1^3 - 16t_1^4 + 13t_1^2 + 5t_1 - 10)c_1 + 9(64t_1^4 - 40t_1^2 + 25)]^{1/2},$$

which are continuous in the argument c_1. For $c_1 \to \pm\infty$, these roots are unbounded:

$$c_2^+(c_1; m_1) = a^\pm c_1 + b^\pm + O(c_1^{-1}), \quad (48)$$
$$c_2^-(c_1; m_1) = a^\mp c_1 + b^\mp + O(c_1^{-1}),$$
$$a^\pm \equiv \frac{1}{6t_1^2}\left(t_1 - 2t_1^2 - 2 \pm 2(1-t_1)\sqrt{t_1^2 + t_1 + 1}\right),$$

$$b^{\pm} \equiv \frac{1}{2t_1^2}\left(8t_1^2 + 5 \pm \frac{16t_1^3 + 8t_1^2 - 5t_1 - 10}{2\sqrt{t_1^2 + t_1 + 1}}\right).$$

Therefore, their graphs (see, for example, Fig. 4) have the inclined asymptotes

$$c_2 = a^+c_1 + b^+, \quad c_2 = a^-c_1 + b^-. \qquad (49)$$

The straight line $c_2 = a^+c_1 + b^+$ is an asymptote of the graph of $c_2^+(c_1; m_1)$ for $c_1 \to -\infty$ and an asymptote of the graph of $c_2^-(c_1; m_1)$ for $c_1 \to \infty$. The straight line $c_2 = a^-c_1 + b^-$ is an asymptote of the graph of $c_2^+(c_1; m_1)$ for $c_1 \to \infty$ and an asymptote of the graph of $c_2^-(c_1; m_1)$ for $c_1 \to -\infty$.

Only at $m_1 = 3/5$ is the discriminant D the perfect square of the argument c_1, in which case the functions $c_2^{\pm}$ coincide with their asymptotic expressions:

$$c_2^+(c_1; 3/5) = 6(20 - c_1)/25, \qquad (50)$$
$$c_2^-(c_1; 3/5) = 8(6 - c_1)/16.$$

The case of $m_1 = \infty$ is a special one. Here, we have $A = 0$; therefore, there exists only one root undergoing a discontinuity at the point $c_1 = c_1^s = 15/2$:

$$c_2(c_1; \infty) = \frac{3}{4}\frac{(c_1 - 6)(c_1 - 20)}{15 - 2c_1}. \qquad (51)$$

The resulting family (47)–(51) of all roots of Eq. (37) with coefficients (46) has two special features: $c^+(20; m_1) = c^-(6; m_1) = 0$ at all values of m_1, but the values of $c_2^{\pm}$ at $c_1 = 0$ depend on m_1 as

$$c_2^{\pm}(0; m_1) = \frac{5}{2}m_1^2 + 5m_1 + \frac{13}{2} \pm \frac{1}{2}$$
$$\times (25m_1^4 + 100m_1^3 + 110m_1^2 + 20m_1 + 49)^{1/2}.$$

It follows that, as m_1 increases from 0 to ∞, the ordinate of the point where the graph of the root c_2^+ (c_2^-) intersects the ordinate axis increases from 10 to ∞ (3 to 6), while the point of intersection with the abscissa axis, $(20, 0)$ [$(6, 0)$], remains immobile.

At $B_0^{1\pm} = 1$, the coefficients corresponding to the roots in (47) are the following:

$$B_0^{2\pm} = -\frac{c_2^{\pm}}{2f^{\pm}}(c_1 - 10 + 2t_1(t_1c_2^{\pm} - 2)), \qquad (52)$$

$$B_2^{1\pm} = -\frac{4}{5f^{\pm}}(10(6 - c_2^{\pm}) + t_1(c_1 + 2t_1(c_2^{\pm} - 8))c_2^{\pm}),$$

$$B_2^{2\pm} = -\frac{2c_2^{\pm}}{5f^{\pm}}(10 - c_1 - 2t_1(c_2^{\pm} - 8)),$$

$$B_4^{1\pm} = \frac{15}{8g^{\pm}}((8t_1^2(t_1^2 - 1) + 3)c_2^{\pm}B_2^{1\pm}$$
$$+ (1 - 4t_1^2)c_1B_2^{2\pm}),$$

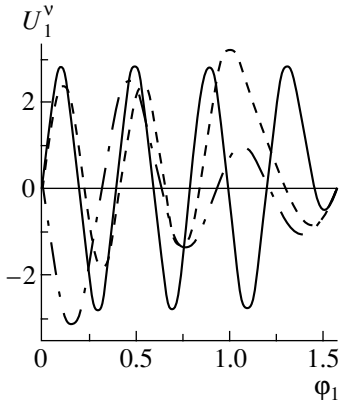

Fig. 7. Components (16) at $t = 14$ and the constant c_2 equal to $\sqrt{c_2^1}$, $\sqrt{c_2^3}$, or $\sqrt{c_2^6}$: (solid curve) $0.1U_1^1(\varphi_1; 256)$ at $c_2 = 5.81556$, (dashed curve) $U_1^3(\varphi_1; 256)$ at $c_2 = 31.8512$, and (dash-dotted curve) $0.02U_1^6(\varphi_1; 256)$ at $c_2 = 170.427$.

$$B_4^{2\pm} = \frac{15}{16g^{\pm}}((1 - 4t_1^2)c_2^{\pm}B_2^{1\pm} + 3c_1B_2^{2\pm});$$
$$f^{\pm} \equiv (c_1 - 10)(c_2^{\pm} - 6) + 2t_1^2c_2^{\pm}(c_2^{\pm} - 8),$$
$$g^{\pm} \equiv (1 - t_1^2)^2c_1c_2^{\pm}.$$

In the particular case of $m_1 = 2$ and $c_1 = -2$, it follows from formulas (47) that

$$c_2^{\pm} = (205 \pm \sqrt{27769})/6.$$

To six decimal places, we therefore have $c_2^+ = 61.9400$ and $c_2^- = 6.93328$; the coefficients in (52) that correspond to these values of c_2^+ and c_2^- are compiled in Table 3, while the components $U_i^{\pm}(\varphi_i; 36)$, $i = 1, 2$, calculated as the sums in (16) are depicted in Figs. 5 and 6. According to the data in Table 3, the component U_2^+ can be approximated by the second term of its series in (16).

If, in formulas (52), we replace the roots $c_2^{\pm}$ by their asymptotic expressions (48) and go over to the limits $c_1 \to \pm\infty$, we obtain the coefficients of the series in (7) for two limiting exact solutions $(F_1^{\pm}, F_2^{\pm})$ to Eqs. (13):

$$B_0^{1\pm} = 1, \quad B_2^{1\pm} = -\frac{1}{2}, \quad B_4^{1\pm} = B_4^{2\pm} = 0, \quad (53)$$

$$B_0^{2\pm} = -\frac{8}{5}$$
$$\times \frac{4t_1^3 - 3t_1^2 + 3t_1 - 4 \pm \mathrm{sgn}(c_1)\delta(4t_1^2 - 5t_1 + 4)}{8t_1^3 + 3t_1^2 - 2 \pm \mathrm{sgn}(c_1)\delta(8t_1^2 - 4t_1 + 2)},$$

$$B_2^{2\pm} = -\frac{1}{2t_1}B_0^{2\pm}; \quad \delta \equiv \sqrt{t_1^2 + t_1 + 1}.$$

These solutions are spurious. Indeed, all coefficients (34) in the series in (19) that represent the

Table 4. Eigenvalues c_2^ν of the problem specified by Eq. (26) and corresponding coefficients $B_L^{1\nu}$ at $t = 8, 10, 12, 14$

t	c_2^ν	$B_2^{1\nu}$	$B_4^{1\nu}$	$B_6^{1\nu}$	$B_8^{1\nu}$	$B_{10}^{1\nu}$	$B_{12}^{1\nu}$	$B_{14}^{1\nu}$
8	5.19375	−1.54375	2.55234	−4.0	−11.5523			
	12.0000	−0.57143	0.0	1.33333	1.66667			
	30.8062	2.11518	−7.05234	−4.0	−1.94766			
10	5.83831	−1.64016	2.59149	−3.61627	3.91018	7.36706		
	16.9905	−0.59464	0.11323	0.74190	−1.25685	−0.81371		
	39.4006	1.50631	−4.86681	1.14251	13.9297	3.88895		
	59.1039	3.35349	−9.24531	−7.72494	−11.4764	−2.13590		
12	6.06294	−1.72913	2.69056	−3.67033	4.21833	−5.07798	−8.46850	
	18.9525	−0.86983	0.75712	−0.21448	−0.92610	3.15382	1.68255	
	28.2394	−0.25070	−0.63591	1.33930	−0.25940	−2.78006	−0.99539	
	73.9381	2.79588	−7.49072	−2.43657	7.92538	3.96780	0.54260	
	106.807	4.98713	−12.4210	−16.8906	−45.6014	−13.5438	−1.28215	
14	5.81556	−1.80922	2.80194	−3.82010	4.59742	−5.68542	7.06801	24.3072
	17.0506	−1.24747	1.57629	−1.49307	0.47312	1.41442	−4.90285	−5.75092
	31.8512	−0.50744	−0.03831	0.69668	−0.80740	0.50382	1.28813	0.80885
	53.8113	0.59056	−2.43396	2.11098	2.60527	−7.87223	−5.62504	−2.09065
	108.377	3.31888	−8.38664	−3.86512	5.23021	4.20258	1.07618	0.19859
	170.427	6.42135	−15.1557	−27.1061	−89.5814	−31.1362	−4.60983	−0.54097

functions $F^\pm$ corresponding to these solutions are equal to zero; therefore, $F^\pm \equiv 0$.

4.3. Case of Three Identical Particles

We now have $m_k = 1$ and $c_k = c_2$ at all $k = 1, 2, 3$. Hence, Eq. (37) has the form $c_2 - 4 = 0$. Its root is $c_2 = 4$; the corresponding coefficients are $B_0^1 = 1$, $B_2^1 = -4/5$, and $B_4^1 = -1$, while the component in (16) has the form

$$U_1(\varphi; 36) = \sin 2\varphi - \frac{4}{5}\sin 4\varphi - \sin 6\varphi, \quad \varphi \equiv \varphi_1.$$

The special features of the structure of the components U_1 and F_1 for $t > 4$, as discussed below, have been deduced from a numerical analysis of the generalized eigenvalue problem specified by Eqs. (26) and (27) with the block matrices (35).

In the case of $t = 6$, there exist two eigenvalues $c_2^\pm = 9 \pm \sqrt{11}$ and two corresponding components (16):

$$U_1^\pm(\varphi; 64) = \sin 2\varphi - \frac{\sin 4\varphi}{4(c_2^\pm - 10)} + \frac{5}{21 - 2c_2^\pm} \times \left(3\sin 6\varphi + \frac{14}{c_2^\pm}\sin 8\varphi\right).$$

All eigenvalues c_2^ν, $\nu = 1, 2, \ldots, t/2 - 1$, of the problem specified by Eq. (26) and the corresponding values of the coefficients $B_L^{1\nu}$, $L = 2, 4, 6, t$ for $t = 8, 10, 12, 14$ are compiled in Table 4. Here, the following regularity can be observed: for the minimum root c_2^1, the amplitudes $B_L^{1\nu}$ of the hyperharmonics Y_{L00}^{00} in the series in (7) for the component $F_1^\nu(\varphi_1; (t+2)^2)$ increase with increasing grand-orbital momentum L, so that the hyperharmonic Y_{t00}^{00} corresponding to the maximum possible value of $L = t$ is dominant; for the maximum root $c_2^{t/2}$, the analogous series is dominated

by hyperharmonics characterized by medium values of the grand-orbital momentum, $L = t/4 - 1/2$. For this reason, the components U_1^ν, which are specified by the series in (16) and which are associated with the three increasing roots c_2^ν for $\nu = 1$, $t/4 - 1/2$, and $t/2 - 1$, have drastically different angular dependences. It can be seen from Fig. 7 that, as $c_2 = c_2^\nu$ grows—that is, as repulsion becomes stronger in all three boson pairs—the components U_1^ν normalized by the same condition $B_0^{1\nu} = 1$ are monotonically expelled from the half-vicinity of the binary-collision point ($\varphi = \pi/2$), the amplitudes of their oscillations increasing concurrently.

5. DISCUSSION OF THE MAIN RESULTS

For the purpose of discussion, we will first consider the isolated binary subsystem (p_1, p_3) of the three-particle system (p_1, p_2, p_3) under investigation.

Let e be the total energy of the (p_1, p_3) subsystem. It is well known [2] that, for $c_2 < 0$, all physically allowed wave functions $\psi(x_1; e)$ for this system are weakly singular at the origin $x_1 = 0$: $x_1\psi \to 0$ for $x_1 \to 0$; for $c_2 > -1/4$, the number of bound states is finite, while, for $c_2 < -1/4$, the number of bound states is infinite, the ground-state energy being $e = -\infty$. In this state, particles p_1 and p_3 occur in an infinitely small vicinity of their center of mass ($x_1 = 0$); therefore, it is common practice to say that there occurs a collapse of particles to the point $x_1 = 0$. Fulfillment of the inequality $c_2 < -1/4$ is the condition under which this phenomenon is realized.

In contrast to the case of two particles, sufficient conditions for the existence of all physically allowed solutions to the problem of three particles whose interaction is of the centrifugal type are not known [8]. To some extent, this gap is filled by the existence criterion proven in Section 3: for the case of zero total angular momentum and S-wave interactions of the centrifugal type in (3), the three-particle problem specified by Eq. (2) has an exact solution that can be represented in the form of the product (4) of a general solution to the Bessel Eq. (5) and the finite linear combination (7) of hyperharmonics (6) if—and only if—$t \geq 4$, $p^2 = (t+2)^2$, and there exists at least one solution (c_2, X) to the generalized eigenvalue problem (26) at fixed ratios $\alpha_1 = c_1/c_2$ and $\alpha_3 = c_3/c_2$.

The most significant result of Section 4 is the following: in the limit of two coupling constants that are indefinitely large in magnitude, the reference exact solutions ($t = 4$) to Faddeev equations go over to spurious solutions, while, in the limit of one coupling constant large in magnitude—for example, in the case where $c_2 = c_2^- \to -\infty$ and $c_1 = c_1^s$—they reduce to solutions of great physical interest. Indeed, such solutions are regular everywhere on $\mathcal{S}^5$—in particular, at the binary-collision point $x_1 = 0$. This is not the whole story, however: although the condition of collapse ($c_2 < -1/4$) of particles p_1 and p_3 to this point is satisfied in the absence of particle p_2, the collapse does not occur in the three-particle system because of the interactions V_1 and V_3 of particles p_3 and p_1 with particle p_2.

Since all hyperharmonics in (6) are regular on $\mathcal{S}^5$, all singular solutions satisfying Faddeev equations and describing the collapse of particles into binary-collision points must involve infinite hyperspherical series.

In conclusion, we would like to emphasize the particular numerical significance and adaptability of the exact solutions in question as reference ones. These solutions provide a unique possibility of estimating the point-by-point convergence of the tested numerical algorithm in the following extreme situations: in the limit of a small binding energy $E_b = -E$, where the Faddeev components Ψ_i decrease slowly for $r \to 0$; in the cases where these components increase sharply in magnitude for $r \to 0$ and (or) oscillate quickly for $\varphi_i \to 0$; and, finally, in the case of one or two coupling constants large in magnitude.

REFERENCES

1. R. Machleidt, K. Holinde, and Ch. Elster, Phys. Rep. **149**, 1 (1987).
2. L. D. Landau and E. M. Lifshitz, *Course of Theoretical Physics,* Vol. 3: *Quantum Mechanics: Non-Relativistic Theory* (Nauka, Moscow, 1974; Pergamon, Oxford, 1977).
3. F. M. Pen'kov, Zh. Éksp. Teor. Fiz. **106**, 1046 (1994) [JETP **79**, 568 (1994)].
4. B. N. Efimov, Yad. Fiz. **12**, 1080 (1970) [Sov. J. Nucl. Phys. **12**, 589 (1971)]; V. Efimov, Nucl. Phys. A **210**, 157 (1973).
5. A. K. Motovilov, S. A. Sofianos, and E. A. Kolganova, Chem. Phys. Lett. **275**, 168 (1997); Phys. Rev. A **56**, 1686 (1997); J. Phys. B **31**, 1279 (1998); A. K. Motovilov *et al.*, Eur. Phys. J. D **13**, 33 (2001).
6. V. A. Roudnev and S. L. Yakovlev, Comput. Phys. Commun. **126**, 162 (2000); Chem. Phys. Lett. **328**, 97 (2000).
7. R. A. Aziz *et al.*, J. Chem. Phys. **70**, 4330 (1979).
8. L. D. Faddeev and S. P. Merkuriev, *Quantum Scattering Theory for Several Particle Systems* (Kluwer, Dordrecht, 1993).
9. S. P. Merkuriev, G. Gignoux, and A. Laverne, Ann. Phys. (N.Y.) **99**, 30 (1976).
10. N. W. Schellingerhout, L. P. Kok, and G. D. Bosveld, Phys. Rev. A **40**, 5568 (1989).
11. V. V. Pupyshev, Yad. Fiz. **43**, 1318 (1986) [Sov. J. Nucl. Phys. **43**, 846 (1986)].

12. C.-Y. Hu, A. A. Kvitsinsky, and S. P. Merkuriev, Phys. Rev. A **45**, 2723 (1992).
13. V. V. Kostrykin, A. A. Kvitsinsky, and S. P. Merkuriev, Few-Body Syst. **6**, 97 (1989).
14. Y. Avishai, J. Math. Phys. **16**, 1491 (1975).
15. V. V. Pupyshev, Phys. Lett. A **140**, 151 (1989).
16. V. V. Pupyshev, Preprint R5-2000-296, OIYaI (Joint Insitute for Nuclear Research, Dubna, 2000).
17. R. I. Jibuti and N. B. Krupennikova, *Method of Hyperspherical Functions in Few-Body Quantum Mechanics* (Metsniereba, Tbilisi, 1984).
18. V. V. Pupyshev, Fiz. Élem. Chastits At. Yadra **30**, 1562 (1999) [Phys. Part. Nucl. **30**, 689 (1999)].
19. M. Moshinsky, *The Harmonic Oscillator in Modern Physics: From Atoms to Quarks* (Gordon and Breach, New York, 1969; Mir, Moscow, 1972).
20. V. V. Pupyshev, Teor. Mat. Fiz. **125**, 253 (2000).
21. Ya. A. Smorodinskiĭ and V. D. Éfros, Yad. Fiz. **17**, 210 (1973) [Sov. J. Nucl. Phys. **17**, 107 (1973)].
22. B. B. Voevodin, *Computational Principles of Linear Algebra* (Nauka, Moscow, 1977).

Translated by A. Isaakyan

Physics of Atomic Nuclei, Vol. 66, No. 1, 2003, pp. 75–80. From Yadernaya Fizika, Vol. 66, No. 1, 2003, pp. 77–82.

NUCLEI
Theory

Analytic Estimates of the Product Yields for Nuclear Reaction in the Ultralow Energy Range*

V. M. Bystritsky and **F. M. Pen'kov*****

Joint Institute for Nuclear Research, Dubna, Moscow oblast, 141980 Russia

Received November 27, 2001; in final form, April 17, 2002

Abstract—Simple analytic expressions for estimation of product yields from reactions between light nuclei in the ultralow collision energy range are given. It is shown that, even in the case of total absorption targets and large spread of incident beam energies, these expressions can be factorized and naturally define the effective target thickness and the range of particle collision energies in the entrance channel that in turn defines the yield of reaction products. © *2003 MAIK "Nauka/Interperiodica".*

1. INTRODUCTION

Importance of studying reactions between light nuclei in the ultralow energy range is shown in many papers [1–7]. This study allows not only verification of fundamental symmetries in strong interactions [1–4] but also solution to some astrophysical problems [5–7]. However, it is very difficult to study the processes in great depth because cross sections for nuclear reactions at ultralow energy and intensities of charged particle beams produced by classical accelerators are too small [8, 9]. In this connection, it was proposed [7, 10–12] to study the nuclear reactions by the method based on generation of radially converging ion fluxes in the course of liner plasma implosion. This method made it possible to obtain new experimental results for the dd reaction in the c.m. deuteron collision energy range 0.05–2.3 keV [12–17], on the one hand, and can be a basis for nuclear-physics diagnostics of plasma processes, on the other hand.

A procedure for finding the average astrophysical S factor and effective $d(d,n)^3$He reaction cross sections for the deuteron-collision energies in question is described in [16, 17]. Note that the experiments with a liner plasma (Z pinch) differ from the experiments at classical accelerators by an appreciably larger spread of incident energies and by stopping mechanisms in the target. In the liner plasma experiments, the target is completely polarized and the liner ion energy loss is due to elastic collisions with particles of the dense target plasma. In the accelerator experiments, the target is a condensed or gaseous medium, where energy loss at low energy is due to inelastic collisions of incident particles with atoms of the medium. Therefore, the procedure for extraction of dd-reaction parameters from the observed neutron yield included both numerical calculation of the effective target thickness providing a 90% neutron yield (for assessment of target transparency conditions) and calculation of the energy distribution of colliding deuterons contributing to the observed reaction-product yield. The energy distribution of accelerated liner deuterons, phenomenological dependence of the nuclear-reaction cross section on the deuteron-collision energy, and the model of Coulomb slowing-down of liner plasma ions during plasma–target interaction had to be taken into consideration. The above calculation scheme is cumbersome and admits some arbitrary interpretation of such experimentally significant parameters as effective reaction cross sections and effective target thicknesses, which hinders correct comparison of the experimental results obtained by different authors.

In this connection, the purpose of the present paper was to work out an approach to analysis of experimental data that could allow basic characteristics of nuclear reactions to be unambiguously found from reaction-yield measurements irrespective of the experimental procedure. In other words, it is necessary to find an expression for the nuclear-reaction yield in a general form that involves the same quantities of the same physical meaning, whatever the experimental procedure. These quantities are the reaction cross section at a particular collision energy of interacting particles, the effective target thickness corresponding to this energy, and the fraction of particles (from the total spectrum of particles incident on the target) participating in the interaction.

*This article was submitted by the authors in English.

** e-mail: bystvm@nusun.jinr.ru

*** e-mail: penkov@thsun1.jinr.ru

1063-7788/03/6601-0075$24.00

2. BASIC FORMULAS

Let us simplify calculations of the nuclear-reaction-product yield at low energy, where the reaction cross section σ admits parametrization

$$\sigma = (S/E_{\rm col})\exp(-\beta/\sqrt{E_{\rm col}}), \quad (1)$$

where S is the so-called astrophysical factor and $\beta/\sqrt{E_{\rm col}}$ is the Sommerfeld parameter in suitable form ($\beta = 2\pi Z_1 Z_2\sqrt{\mu/2}$, where μ is the reduced mass of colliding particles and Z_1 and Z_2 are their charges). By way of example, below we consider the dd reaction for which β is 31.29 at the c.m. collision energy $E_{\rm col}$ in keV. The astrophysical factor S is usually only slightly dependent on energy when the latter is well below nuclear energies ($\sim$ MeV).

Let the target be hit by a particle beam with a Gaussian energy distribution with the average energy $\bar{E}$ and spread $\sqrt{\sigma_0}$:

$$f(E) = \frac{1}{\sqrt{2\pi\sigma_0}}\exp\frac{(E-E)^2}{2\sigma_0}. \quad (2)$$

The yield of reaction products from the complete-stopping target can be written as

$$N = N_d n_t \varepsilon_n \int\limits_0^\infty f(E)dE \int\limits_0^{x_{\max}} \sigma(E'(E,x))dx, \quad (3)$$

where the maximum range $x_{\max}$ is defined by the complete stopping at the initial energy E, i.e., by the condition $E'(E, x_{\max}) = 0$, and the constants N_d, n_t, and ε_n correspond to the amount of incident particles, target density, and reaction-product-recording efficiency, respectively. It is convenient to pass to integration over E' varying from E to 0,

$$N = N_d n_t \varepsilon_n \int\limits_0^\infty f(E)dE \int\limits_0^E \sigma(E')\left(-\frac{dE'}{dx}\right)^{-1} dE', \quad (4)$$

and to change the order of integration,

$$N = N_d n_t \varepsilon_n \int\limits_0^\infty \sigma(E)\left(-\frac{dE}{dx}\right)^{-1} dE \int\limits_E^\infty dE' f(E'). \quad (5)$$

The specific-loss function dE/dx is defined by the conditions for stopping of incident particles in the target.

Using parametrization of cross section (1), we write (5) in the form

$$N = N_d n_t \varepsilon_n \int\limits_0^\infty S(E)\exp(-\beta/\sqrt{E})D(E)dE \quad (6)$$
$$\times \int\limits_E^\infty dE' f(E'),$$

where $D(E) = -(1/E)(dx/dE)$ is introduced for abbreviation. At low energy ($\beta/\sqrt{E_{\rm col}} \gg 1$), the function $\exp(-\beta/\sqrt{E})D(E)\int_E^\infty dE' f(E')$ has a sharp maximum, which makes it reasonable to introduce a new distribution function $P(E)$ defining the density of the reaction-product yield at the collision energy E:

$$P(E) = \frac{\exp(-\beta/\sqrt{E})D(E)\int\limits_E^\infty dE' f(E')}{\int\limits_0^\infty \exp(-\beta/\sqrt{E})D(E)dE\int\limits_E^\infty dE' f(E')}. \quad (7)$$

Then, the reaction product yield is expressed in terms of the average value

$$\bar{S} = \int\limits_0^\infty S(E)P(E)dE \quad (8)$$

of the smooth function $S(E)$:

$$N = N_d n_t \varepsilon_n \bar{S}\int\limits_0^\infty \exp(-\beta/\sqrt{E})D(E)dE\int\limits_E^\infty dE' f(E'). \quad (9)$$

If the function $S(E)$ is smoother than $P(E)$, we can make an obviously accurate replacement

$$\bar{S} \to S(\langle E\rangle),$$

where

$$\langle E\rangle = \int\limits_0^\infty EP(E)dE, \quad (10)$$

obtaining

$$\bar{S} = S(\langle E\rangle) + \left(\frac{1}{2}\frac{d^2S}{dE^2}(0)(\langle E^2\rangle - \langle E\rangle^2)\right) + \ldots$$

This expression shows that deviation of $\bar{S}$ from $S(\langle E\rangle)$ is defined by the condition of small variation in the first derivative at the dispersion scale of the $P(E)$ distribution (factor $\langle E^2\rangle - \langle E\rangle^2$).

Considering the latter remarks, we write the expression for the reaction product yield as

$$N = N_d n_t \varepsilon_n S(E_{\rm col})\int\limits_0^\infty \exp(-\beta/\sqrt{E})D(E)dE \quad (11)$$
$$\times \int\limits_E^\infty dE' f(E'),$$

where the average energy $\langle E\rangle$ is designated as $E_{\rm col}$. Below, when estimating analytically expression (11), we will obtain an explicit expression for dispersion of the distribution $P(E)$.

3. ANALYTIC ESTIMATION

To simplify analysis of experimental data, it is necessary to have an analytic form of the integral appearing in (11):

$$I = \int\limits_0^\infty \exp(-\beta/\sqrt{E})D(E)dE \int\limits_E^\infty dE' f(E'). \quad (12)$$

Note that the integrand has a pronounced maximum due to its exponential decrease at low energy (factor $\exp(-\beta/\sqrt{E})$) and, as a rule, even faster decrease in the function $\int_E^\infty dE' f(E')$ at high energy. Therefore, a natural form of approximation for integral (12) is based on the Laplace method (see, for example, [18]), which requires the following operations to take the integral

$$\tilde{I} = \int\limits_a^b F(x)dx$$

of the sharp function $F(x)$ with a single peak in the integration interval. The function $F(x)$ is replaced by the expression $\exp(\tilde{\varphi}(x))$ ($\tilde{\varphi}(x) = \ln(F(x))$). A point x_m where the function $\tilde{\varphi}(x)$ reaches its maximum, i.e., the equation $d\tilde{\varphi}(x)/dx = 0$ is solved for x, is sought. If $a < x_m < b$, the integral $\tilde{I}$ can be written in an approximate form

$$\tilde{I} \approx \int\limits_a^b \exp\left(\tilde{\varphi}(x_m) + \frac{1}{2}\tilde{\varphi}^{(2)}(x_m)(x - x_m)^2\right)dx.$$

If $-\tilde{\varphi}^{(2)}(x_m)x_m^2 \gg 1$, integration can be extended to the interval $(-\infty, \infty)$ and the integral can be calculated explicitly. Considering the terms of expansion in $\tilde{\varphi}^{(2)}(x_m)$ (see [18]) that define the relative error δ of the method, the approximate integral can be written as

$$\tilde{I} \approx F(x_m)\sqrt{\frac{2\pi}{-\tilde{\varphi}^{(2)}(x_m)}}(1+\delta), \quad (13)$$

$$\delta = \frac{1}{8}\frac{\tilde{\varphi}^{(4)}(x_m)}{(\tilde{\varphi}^{(2)}(x_m))^2}.$$

Following the method described, we represent the integral I as

$$I = \int\limits_0^\infty e^{\varphi(E)}dE,$$

$$\varphi(E) = -\beta/\sqrt{E} + \ln\left(\int\limits_E^\infty dE' f(E')\right) + \ln(D(E)).$$

Then, the equation for the maximum of the function $\varphi(E)$ is

$$\frac{\beta}{2E_m^{3/2}} - \frac{f(E_m)}{\int\limits_{E_m}^\infty dE' f(E')} + \frac{D^{(1)}(E_m)}{D(E_m)} = 0, \quad (14)$$

and, according to (13), the approximate expression for the integral I is factorized on condition that the correction δ is small:

$$I \approx \sqrt{\frac{2\pi}{-\varphi^{(2)}(x_m)}}\exp(-\beta/\sqrt{E_m})D(E_m) \quad (15)$$

$$\times \int\limits_{E_m}^\infty dE' f(E')(1+\delta), \quad \delta = \frac{1}{8}\frac{\varphi^{(4)}(E_m)}{(\varphi^{(2)}(E_m))^2}.$$

Note the obvious condition of expression (15) being stable against small perturbations of E_m. Since the first derivative of $\varphi(E)$ is zero, the errors Δ in determination of the extreme energy yield a correction to I quadratic in Δ, either because of approximate calculation of the root or because of neglect of some small terms in (14),

$$e^{\varphi(E_m+\Delta)} = \exp\left(\varphi(E_m) + \frac{1}{2}\varphi^{(2)}(E_m)\Delta^2 + \dots\right)$$

$$\approx e^{\varphi(E_m)}\left(1 + \frac{1}{2}\varphi^{(2)}(E_m)\Delta^2\right).$$

4. EXTRA SIMPLIFICATION

Smoothness of the function $D(E)$ as compared with other components of the integrand in (12) provides an extra possibility of considerably simplifying (14) and (15). For example, the energy loss from stopping of incident deuterons by plasma deuterons is described by the expression [19]

$$\frac{dx}{dE} = -\frac{2E}{\pi n_t e^4 L_d}, \quad (16)$$

where e is the elementary charge and L_d is the Coulomb logarithm equal to 12.8 (see [19]) for experimental conditions [17]. In this case, the function $D(E)$ is simply constant in E and does not contribute to the position of E_m. In the case of stopping by electrons with temperature T_e when $(m_d/m_e)T_e \gg E \gg T_e$, the stopping obeys the law [19]

$$\frac{dx}{dE} = -\frac{3}{8n_t L_e}\sqrt{\frac{2T_e^3 m_d}{\pi E m_e}}, \quad (17)$$

where m_d and m_e are the deuteron and electron masses, respectively, and L_e is the Coulomb logarithm for deuteron–electron collisions. Thus, the function $D^{(1)}(E)/D(E) = -3/(2E)$ for stopping of ions by plasma electrons at a collision energy well below $\beta^2/9$ is small compared to the first term in (14). For example, $\beta^2/9 \simeq 109$ keV for deuteron–electron stopping. Therefore, when collision energies are low and β is large, E_m is mainly governed by the first two terms in (14); i.e., the stopping law only slightly affects the position of the maximum. Let us find out when the function $D^{(1)}(E_m)/D(E_m)$ can be ignored. To this end, we assume it to be a small quantity shifting the position of E_m by Δ on condition that

$$\frac{\beta}{2E_m^{3/2}} - \frac{f(E_m)}{\int\limits_{E_m}^{\infty} dE' f(E')} = 0.$$

Then,

$$\Delta = -\frac{D^{(1)}(E_m)}{D(E_m)} \frac{1}{\varphi_0^{(2)}(E_m)}, \qquad (18)$$

where $\varphi_0 = \varphi - \ln(D(E))$. Thus, smallness of the contribution from stopping processes to the energy E_m is dictated by smallness of the ratio between the logarithmic derivative of $D(E)$ and the dispersions of the energy distribution of the integrand in the Gaussian approximation. As was mentioned above, the correction Δ does not make a linear contribution to the integral because of the stationarity condition. Therefore, the effect produced by the stopping force on the energy shift causes a relative change in the integral I by a value

$$\delta_D = \frac{1}{2\varphi_0^{(2)}(E_m)} \left(\frac{D^{(1)}(E_m)}{D(E_m)} \right)^2.$$

The correction δ_D was found for deuteron stopping, but its form is valid for stopping of any ions in plasma because only energy dependence of the function D matters.

Considering what was said above, the integral I can be written as

$$I \approx \sqrt{\frac{2\pi}{-\varphi_0^{(2)}(E_m)}} \exp(-\beta/\sqrt{E_m}) D(E_m) \qquad (19)$$

$$\times \int\limits_{E_m}^{\infty} dE' f(E')(1 + \delta + \delta_D), \quad \delta = \frac{1}{8} \frac{\varphi_0^{(4)}(E_m)}{(\varphi_0^{(2)}(E_m))^2},$$

$$\delta_D = \frac{1}{2\varphi_0^{(2)}(E_m)} \left(\frac{D^{(1)}(E_m)}{D(E_m)} \right)^2,$$

where

$$\varphi_0(E) = -\beta/\sqrt{E} + \ln\left(\int\limits_E^{\infty} dE' f(E') \right) \qquad (20)$$

and E_m is defined by the equation for the extreme point

$$\frac{\beta}{2E_m^{3/2}} - \frac{f(E_m)}{\int\limits_{E_m}^{\infty} dE' f(E')} = 0. \qquad (21)$$

In view of (21) and (2), the second derivative of the function $\varphi_0(E)$ at the point E_m appearing in (19) is

$$\varphi_0^{(2)}(E_m) = -\frac{3\beta}{4E_m^{5/2}} + \frac{E_m - \bar{E}}{\sigma_0} \frac{\beta}{2E_m^{3/2}} - \frac{\beta^2}{4E_m^3}. \qquad (22)$$

To estimate the accuracy of taking the integral I, it is also necessary to calculate the fourth derivative $\varphi_0^{(4)}(E_m)$. In view of (21) and (2), it has a simple though cumbersome form

$$\varphi_0^{(4)}(E_m) = -\frac{105\beta}{16E_m^{9/2}} - \frac{3\beta^4}{8E_m^6} \qquad (23)$$

$$+ \left(\frac{(E_m - \bar{E})^3}{\sigma_0^3} - 3\frac{E_m - \bar{E}}{\sigma_0^2} \right) \frac{\beta}{2E_m^{3/2}}$$

$$- \left(\frac{(E_m - \bar{E})^2}{\sigma_0^2} - \frac{1}{\sigma_0} \right) \frac{\beta^2}{E_m^3} + \frac{E_m - \bar{E}}{\sigma_0} \frac{3\beta^3}{2E_m^{9/2}}$$

$$- \left(\frac{E_m - \bar{E}}{\sigma_0} \right)^2 \frac{3\beta^2}{4E_m^3}.$$

Now the expression for the nuclear-reaction yield can be written in a simple analytic form

$$N_{\text{anal}} = N_d n_t \varepsilon_n \sigma(E_m) l_{\text{eff}}(E_m) K(E_m), \qquad (24)$$

where we made use of the fact that $S(E_{\text{col}}) = S(E_m) + O(S^{(2)}/|\varphi_0^{(2)}|)$ and denoted the fraction of the initial beam contributing to the reaction by the coefficient $K(E_m)$,

$$K(E_m) = \int\limits_{E_m}^{\infty} dE f(E) = \frac{2E_m^{3/2}}{\beta} f(E_m), \qquad (25)$$

and the quantity with the meaning of the effective thickness by l_{eff},

$$l_{\text{eff}} = \sqrt{\frac{2\pi}{-\varphi_0^{(2)}(E_m)}} \frac{dx}{dE}(E_m). \qquad (26)$$

The relative error of formula (24) is determined by the quantities δ and δ_D from (19). Note that the quantity $-1/\varphi^{(2)}(E_m)$ or its approximate value $-1/\varphi_0^{(2)}(E_m)$ plays the role of dispersion of the distribution function $P(E)$ in the Gaussian approximation.

Comparison of numerically (11) and analytically (24) calculated neutron yield in the $d(d,n)^3$He reaction under the experimental conditions [17] (all quantities with dimensions of energy are given in keV and with dimensions of length in cm)

$\bar{E}/W$	E_m	$\sigma(E_m)\times 10^{33}$	$n_t l_{\text{eff}}(E_m)$	$K(E_m)$	N_{anal}	δ	N
1.05/0.8	1.766	1.68	2.99×10^{18}	0.0224	1.17	−0.01	1.17
1.2/0.65	1.786	1.90	2.93×10^{18}	0.0383	2.22	−0.008	2.22
1.4/0.65	2.041	7.52	3.94×10^{18}	0.0487	14.94	−0.008	14.93
1.7/0.55	2.250	19.4	4.67×10^{18}	0.0831	77.73	−0.005	77.44

5. COMPARISON OF ANALYTIC ESTIMATES AND NUMERICAL CALCULATIONS

To find out how close analytic expression (24) is to (11), we compare them under real experimental conditions [17] of measuring the S factor for the $dd\to{}^3\text{He}+n$ reaction at implosion of the liner plasma. A supersonic hollow cylindrical deuterium jet with a current of ~ 1 MA through it was used as a liner. The liner plasma was accelerated toward the axis under the effect of its own magnetic field. The target was a CD_2 layer deposited on the surface of the metallic Cu cylinder placed along the liner axis. In the course of liner implosion, the target was heated to the state of completely ionized plasma. Under the experimental conditions [17], the temperature of the target was 20–30 eV, the deuteron-collision energy range was 1.05–1.7 keV, and the relative spread of liner deuteron energies W was 0.80–0.55. The quantity W was defined as the relative width at a half-maximum ($W=2.3548\sqrt{\sigma_0}/\bar{E}$).

These experimental conditions impose severe requirements to the accuracy of calculation in data processing by formula (11) because of the Coulomb factors ($\exp(-\beta/\sqrt{1\text{ keV}})\simeq 2.6\times 10^{-14}$). On the other hand, neutron yields calculated by (11) and (24) virtually coincide. Below, we give expressions for quantities appearing in (24) that are convenient for fast analysis of the experimental results. According to [20–22], only dd stopping was taken into account for the effective target thickness

$$n_t l_{\text{eff}} = 12.13E_m^2\left(\frac{\beta}{\sqrt{E_m}}\left(3.0+\frac{\beta}{\sqrt{E_m}}-11.09\frac{(E_m-\bar{E})E_m}{W^2\bar{E}^2}\right)\right)^{-1/2}\times 10^{18}, \quad (27)$$

$$K(E_m) = 1.879\frac{E_m^{3/2}}{\beta W\bar{E}}\exp\left(-2.7726\frac{(E_m-\bar{E})^2}{W^2\bar{E}^2}\right). \quad (28)$$

In addition, using two-dimensional fitting of the solution for (21), we give a simple dependence of the roots of this equation for the dd reaction ($\beta=31.29$):

$$E_m \simeq 0.0038+0.2770W+0.8496\bar{E} + 0.7312\bar{E}W+0.1282W^2\bar{E}-0.0641W\bar{E}^2. \quad (29)$$

Under the experimental conditions [17], the error in determination of E_m does not exceed 8 eV. Note that the maximum deviation is 43 eV at $\bar{E}=3.0$ keV and $W=0.2$ in the entire ranges of fitting in terms of $E_m=0.8$–3.0 keV and in terms of $W=0.2$–1.

The table compares neutron yields numerically calculated by (11) and analytically found by (24). The experimental conditions [17] set the parameter values $N_d=2.07\times 10^{18}$ and $\varepsilon_n=0.005$, while the astrophysical factor S was taken to be 50 b keV. It is evident from the table that the largest difference between the numerically and analytically estimated neutron yields is 0.38% with an error estimate of 0.5%. In [17] there are plots of the distribution functions $f(E)$ and $P(E)$ whose maxima are considerably shifted. Their numerical values $\bar{E}$ and E_m are given in the upper rows of the table. It is the large shift of these quantities (1.4–2 standard deviations) that is responsible for only small fractions of the incident deuteron flux contributing to the yield of final products of nuclear reactions (function $K(E_m)$): 2–8%. Note that the numerical estimate of the neutron yield fraction at the target thickness l_{eff} corresponds to about a 95% neutron yield.

6. CONCLUSION

Analytic estimates of product yields in nuclear reactions at ultralow collision energies show that a large spread of particle energies in the entrance channel and large target thicknesses do not prevent introducing the notions of the effective target thickness, cross section, and interaction energy with dispersion defined by the value of $\varphi^{(2)}(E_m)$. These quantities naturally appear in the factorized form of expression (24). In this case, there arises a factor with a simple meaning of a fraction of the initial flux of particles participating in the reactions. Note that it would

be much easier to compare experimental results if authors of publications gave experimental conditions for their investigation of nuclear reactions at ultralow energies in terms of expression (24).

REFERENCES

1. S. P. Merkuriev *et al.*, in *Proceedings of the International Conference on the Theory of Few Body and Quark–Hadron Systems,* Preprint No. D4-87-692, OIYaI (Joint Institute for Nuclear Research, Dubna, 1987), p. 6.
2. H. Paetz gen. Schieck, Few-Body Syst. **5**, 171 (1988).
3. V. F. Kharchenko *et al.*, Yad. Fiz. **55**, 86 (1992) [Sov. J. Nucl. Phys. **55**, 49 (1992)].
4. G. S. Chulick *et al.*, Nucl. Phys. A **551**, 255 (1993).
5. J. N. Bachall and M. H. Pinsonneault, Rev. Mod. Phys. **64**, 885 (1992).
6. W. A. Fowler, Rev. Mod. Phys. **56**, 149 (1984).
7. V. B. Belyaev *et al.*, Nukleonika **40**, 85 (1995).
8. F. Ajzenberg-Selove, Nucl. Phys. A **490**, 1 (1988).
9. Vit. Bystritskii *et al.*, in *Proceedings of the 10th IEEE International Pulsed Power Conference, Albuquerque, 1995,* Ed. by W. L. Baker and G. Copperstein (IEEE, New York, 1995), p. 1215.
10. V. B. Belyaev *et al.*, Preprint No. D15-92-324, OIYaI (Joint Institute for Nuclear Research, Dubna, 1992).
11. V. B. Belyaev *et al.*, Preprint No. D15-95-375, OIYaI (Joint Institute for Nuclear Research, Dubna, 1995).
12. V. M. Bystritsky *et al.*, Nukleonika **42**, 775 (1997).
13. T. L. Bulgakov *et al.*, Yad. Fiz. **60**, 1349 (1997) [Phys. At. Nucl. **60**, 1217 (1997)].
14. Vit. M. Bystritskii *et al.*, Preprint No. D15-96-11, OIYaI (Joint Institute for Nuclear Research, Dubna, 1996).
15. Vit. Bystritskii *et al.*, in *Proceedings of the 11th International Conference on High Power Particle Beams "Beams 96," Prague, 1996,* Vol. 2, p. 917.
16. V. M. Bystritsky *et al.*, Laser Part. Beam **18**, 1 (2000).
17. V. M. Bystritsky *et al.*, Yad. Fiz. **64**, 920 (2001) [Phys. At. Nucl. **64**, 855 (2001)].
18. M. F. Fedoryuk, *Method of Saddle Points* (Nauka, Moscow, 1977), p. 41.
19. D. V. Sivukhin, *Theoretical Problems of Plasma* (Atomizdat, Moscow, 1964), p. 81.
20. K. Nui and T. Abe, in *Proceedings of the 3rd International Conference on High Power Electron and Ion Beam, Novosibirsk, 1979,* Vol. 2, p. 518.
21. L. A. Artsimovich, *Controlled Thermonuclear Reactions* (Fizmatgiz, Moscow, 1961), p. 170.
22. Vit. Bystritskii *et al.*, in *Proceedings of the Second International Conference Dense Z-Pinches, Laguna Beach, 1988,* AIP Conf. Proc. **195**, 522 (1989).

Physics of Atomic Nuclei, Vol. 66, No. 1, 2003, pp. 81–86. From Yadernaya Fizika, Vol. 66, No. 1, 2003, pp. 83–88.

NUCLEI
Theory

nd Scattering at Low Energies in the Two-Body Potential Model*

Yu. V. Orlov and Yu. P. Orevkov

Institute of Nuclear Physics, Moscow State University, Vorob'evy gory, Moscow, 119992 Russia

Received August 30, 2001; in final form, January 31, 2002

Abstract—The S-wave phase shift $\delta(E)$ for the spin-doublet nd scattering at low energy E is calculated in the framework of the two-body approach. The effective-range-theory formula $k\cot\delta = (1 + k^2/\kappa_0^2)^{-1}(-1/a + C_2k^2 + C_4k^4)$ is used to obtain approximate analytical results with different potentials. The corresponding coefficients C_2 and C_4 are obtained from our previous calculations of the asymptotic normalization parameter function $C_t^2(a\kappa)$, where κ is the triton wave number and a is the doublet nd scattering length. The model reasonably describes $\delta(E)$, the results being quite sensitive to the choice of the effective nd potential. © *2003 MAIK "Nauka/Interperiodica".*

1. INTRODUCTION

The spin-doublet neutron–deuteron system is a classic example of application of the three-body Faddeev equation. It has been demonstrated in various studies that the nd system's physical characteristics (especially the doublet scattering length a_2) depend strongly on an NN-interaction model. A correlation has been found between a_2 and the triton binding energy ε_t (the Phillips line [1]) and the analogous one for the virtual-triton (t^*) "binding energy" ε_{t^*} as well as for the asymptotic normalization parameter of the triton C_t^2 (the Girard–Fuda lines [2]). An effective-range theory expression for $k\cot\delta$ with a pole taken into account (see, for example, [3]) also represents a correlation among the observables mentioned above. It does not include three-particle properties in an explicit way. The existence of correlations means that the doublet nd system at low energy is controlled by a few independent physical parameters, mainly by the scattering length a_2.

One could expect that three-body features of the nd system would be decisive even when its energy E is below the deuteron-breakup threshold because the deuteron binding energy ε_d is small in comparison with ε_t. But it has been shown by N/D-method calculations [4, 5] that the low-energy observables of the doublet nd system may be described reasonably well without taking into account the three-particle S-matrix cut in the complex energy plane.

It follows that the two-body potential model can also be applied in the low-energy region. An advantage of this model in comparison with the N/D method and the effective-range theory is that it is possible to calculate the form factors for the vertices $t \to n + d$ and $t^* \to n + d$ which can be applied in the nuclear reaction theory based on the Feynman diagram method. It is important in this application to have the right (experimental) values of ε_t (8.48 MeV) and a_2 (0.65 fm), which is ensured in the two-body potential model by fitting its parameters. But even modern Faddeev calculations with a realistic NN potential taking into account the charge-independence breaking still underestimate the binding energy ε_t. One needs to add three-nucleon ($3N$) interaction to get the proper values of ε_t and a_2 (see, for example, [6]).

The one-nucleon exchange Feynman diagram plays an important role in nd scattering because its pole is situated close to the physical region of the transfer momentum simply due to the smallness of ε_d. This is another theoretical argument in favor of the two-body model, because it is possible to imitate such singularity by using a Yukawa-type potential.

A two-body potential model was proposed for the doublet Nd system in [7, 8]. The Hulthén potential

$$V(r) = -V_0/[\exp(\mu r) - 1] \qquad (1)$$

was used by Petrov in [7]. It was shown that the model describes reasonably well a trend of the vertex nuclear constant G_t^2 in the Faddeev calculations that differ by the values of a_2 and ε_t. In addition, in [9, 10], the virtual pole position [the virtual-triton (t^*) binding energy ε_{t^*}], the vertex nuclear constant $G_{t^*}^2$, and the $k\cot\delta$ pole (or the partial scattering amplitude $f(k)$ zero) position ($-E_0$) [10] were reasonably well reproduced for the same model without additional parameter fitting. Let us bear in mind that the vertex nuclear constant G_t^2 can be written in terms of the asymptotic normalization parameter C_t^2 for the triton bound state radial wave function.

*This article was submitted by the authors in English.

1063-7788/03/6601-0081$24.00

All the characteristics mentioned above were calculated in [10] for the Yukawa potential

$$V(r) = -V_0(\mu r)^{-1}\exp(-\mu r) \qquad (2)$$

to determine their sensitivity to the concrete form of an effective nd potential. A reasonable agreement with the experimental data and with the results of calculations for the Hulthén potential was obtained.

One of the two potentials proposed by Tomio *et al.* [8] has the following form:

$$V(r) = -V_0(R/r)^2[\sin(r/R)]^2\exp(-\mu r). \qquad (3)$$

Three parameters V_0, R, and μ were fitted to the experimental values: a_2, ε_t, and the binding energy of ^{3}He. In [8], a theoretical estimation of the nuclear doublet pd scattering length was the main goal. The other characteristics of the doublet nd system discussed above were not considered. Whereas the oscillating factor in (3) was introduced to make the potential regular at zero range, the long-range factor $(1/r^2)$ was used following the conclusions reached by Efimov in [11]. In [12], we calculated all the above-mentioned low-energy observables for potential (3) and refitted the potential parameters. We compared the results of the calculations for potentials (1), (2), and (3) in a large region of the potential strength parameter $g = K_0^2/\mu^2$, where $K_0^2 = [(4/3)m/\hbar^2]V_0$ and m is the nucleon mass, in order to reveal their sensitivity to the potential asymptotic behavior. In [13], we proposed another potential with the proper (Faddeev) asymptotic form but without oscillations. We found that long-range effects are distinctly revealed in the calculation results of the asymptotic normalization parameter C_t^2, or the nuclear vertex constant G_t^2, for the virtual decay $t \to n + d$. The value of C_t^2 decreases, while $n(= 0, 1, 2)$ increases in the potential factor $(1/r^n)$. The effects are slightly weaker in the results for the position $(-E_0)$ of the $k\cot\delta$ pole ($f(k)$ zero).

The potential scaling allows us to reduce the problem from a two- to a one-parametric task and makes it easier to compare directly the results of physical values from different models. In [13], we compared the dependence of C_t^2 on $a_2\kappa_t$ (here, $\kappa_t = [(4/3)m(\varepsilon_t - \varepsilon_d)]^{1/2}$) for all the considered potentials in a large area of parameter $g = K_0^2/\mu^2$, which includes the lightest nuclear-bound systems: deuteron d, hypertriton $^3_\lambda$H, and triton ^{3}H (t). We compared the function $C_t^2(a_2\kappa_t)$ given by different approaches, including the effective-range theory [3] and the N/D method [2, 14]. We found that the results [2, 14] differ from all others in that there was a sharp rise $C_t^2(a_2\kappa_t)$. We explained this anomalous behavior. In addition, the form factor $g_t(q^2)$ for the vertex $t \to n + d$ was calculated with different nd potentials. The results for $g_t(q^2)$ turned out to be in reasonable agreement with the result of the Faddeev calculations [15, 16] obtained with the Malfliet–Tjon NN potential, especially in the case of potential (3).

Because of the considerable uncertainty of the value C_t^2, which results from analyses of experimental nuclear reaction data, one cannot select the best potential, in spite of quite large differences among the calculated results with the potentials used. However, it may be possible to do this by using the S-wave doublet phase shift $\delta(E)$ for nd scattering, which is known to a greater precision.

Thus, in this paper, the function $\delta(E)$ is calculated at low energy E in the framework of the two-body approach.

To obtain approximate analytic results for the phase shift $\delta(E)$, a generalized effective-range theory is used in the present article, clearly taking into account the $k\cot\delta$ pole. Such an approach is supported by the facts that the nd-separation energy is relatively small and the same approximation using Faddeev calculation results with some separable NN potential gives a successful description [3] of the whole set of observables for the doublet nd system.

Obviously, one can calculate phase shifts with a given two-body potential by numerical calculation of the Schrödinger equation. Instead, we prefer to use approximate formulas of the generalized effective-range theory to obtain results with a concrete potential in an analytical form. To estimate the uncertainty of such an approximation, we calculate the difference $\Delta\delta(E)$ between the approximate and the exact results obtained with the Hulthén potential, when the S-wave solution is known in an analytical form. An application of this approximate method to the $\delta(E)$ calculation is justified, in particular, because of the roughness of the two-body model used for the typical three-body task.

The main aims of this paper are the following:

(i) to investigate the validity of the two-body model for a $\delta(E)$ description at low energy with the potentials considered earlier;

(ii) to select, if possible, the best effective nd potential by comparing the results of the $\delta(E)$ calculation with experimental data and with Faddeev calculation results;

(iii) to estimate the uncertainty of the adopted method of the phase shift calculation as a function of energy in the considered region.

Coefficients C_2 and C_4 in the effective-range approximation in form (1), the $k\cot\delta$ pole position ($-\kappa_0^2$), and the asymptotic normalization constant C_t^2 for the triton wave function

The calculation object	$-C_2$, fm	C_4, fm^3	$\kappa_0^2\times10^3$, fm^{-2}	C_t^2
The phase shift $\delta(E)$ by using the function $C_t^2(\kappa)$ ($E\le0$) with the following *nd* potentials:				
Hulthén (1)	39.48	101.5	7.76	3.50
Yukawa (2)	32.63	160.3	6.32	2.74
Tomio *et al.* (3)	127.3	435.4	2.05	3.48
C_t^2 by using the phase shift $\delta(E)$ ($E\ge0$) in the case of the Hulthén potential	48.07	72.23	7.76	2.18
C_T^2 and $\delta(E)$ by Simenog *et al.* [3]	68.03	159.5	4.74	3.50

2. METHOD FOR CALCULATING THE PHASE SHIFT

All the potentials considered have a scaling property, so one can calculate the function $C_t^2(a\kappa)$. Here, a is the variable doublet *nd* scattering length (the index in a_2 is omitted for considerations of brevity), and κ is the wave number for the triton binding energy, treated below as an argument. At the experimental triton binding energy, $\kappa=\kappa_t$. Let us remember that C_t^2 and $a\kappa$ are invariants of a scaling transformation for coordinates (r) and momenta (p): $r\to\gamma r$, $p\to\gamma^{-1}p$, where γ is an arbitrary constant (see [10]).

At low energy, one can use the following formula for the generalized effective-range theory (see, for example, [3, 13]):

$$k\cot\delta=(1+k^2/\kappa_0^2)^{-1}(-1/a+C_2k^2+C_4k^4). \quad (4)$$

Here, the pole at the neutron–deuteron relative energy $E=-E_0$, $\kappa_0^2=(4/3)mE_0$, is explicitly included. The corresponding asymptotic normalization constant is given as (see [10] and references therein)

$$[C_t^2]_{\text{eff.range}}=(2/3)\times(1-\kappa^2/\kappa_0^2)/[1-3\kappa^2/\kappa_0^2-2\kappa(C_2-2C_4\kappa^2)]. \quad (5)$$

Expressions (4) and (5) are used for an analytic continuation from negative to positive energy. The coefficients C_2 and C_4 are found with concrete potentials at the experimental values $\kappa=\kappa_t$ and $a=a_2$ as well as at the fixed value κ_0, which is different for each potential, with the use of the function $C_t^2(a\kappa)$, calculated in our earlier papers [10, 12]. At the fixed value $a=a_2=0.65$ fm, the function $C_t^2(a\kappa)$ has one variable κ and we denote it as $C_t^2(\kappa)$. We use the following procedure to find the values of C_2 and C_4.

Let us determine a new function $\varphi(\kappa^2)$ in accordance with Eq. (5) by the expression

$$C_t^2(\kappa)=(2/3)\times(1-\kappa^2/\kappa_0^2)/[1-3\kappa^2/\kappa_0^2-2\kappa(\varphi(\kappa^2))]. \quad (6)$$

At small $t=\kappa^2$, one has

$$\varphi(t)\cong F(t),\quad F(t)=C_2-2C_4t. \quad (7)$$

The coefficients C_2 and C_4 are calculated with the potential given by setting functions $\varphi(t)$ and $F(t)$ and their derivatives $d\varphi(t)/dt$ and $dF(t)/dt$ equal to each other at the energy $E=-(\varepsilon_t-\varepsilon_d)$, i.e., from the following system of equations:

$$\varphi(\kappa_t^2)=C_2-2C_4\kappa_t^2,\qquad \{d/dt[\varphi(t)]\}_{t=\kappa_t^2}=-2C_4. \quad (8)$$

The exact function $\delta(E)$ with the Hulthén potential (1) is calculated by the formula ($N\to\infty$)

$$\delta(E)=\sum_{n=1}^{N}\ln\left|\frac{(-|x(E)|^2+n^2-g)+g|x(E)|/n}{(-|x(E)|^2+n^2-g)-g|x(E)|/n}\right|, \quad (9)$$

where $x(E)=2kR$, $g=(4/3)mV_0R^2$ (the values of the parameters V_0 and R are given in [7]). The summation in (9) can be cut at $N\ge300$ to obtain reasonable precision.

3. NUMERICAL RESULTS

The values of C_2 and C_4 found with each potential are given in the table, together with κ_0^2 and C_t^2. The corresponding values from [3], as well as C_{2+} and C_{4+} found at positive energy (see text below), are given for comparison. One can see great differences between the different sets of these parameters. The set for the

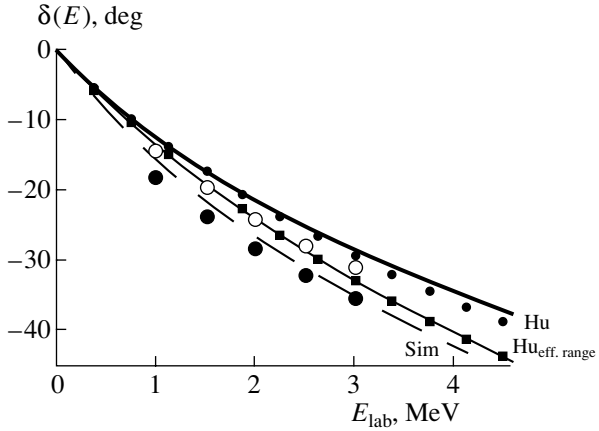

Fig. 1. The nd-scattering phase shift $\delta(E)$ in the S-wave spin-doublet state. Results obtained in the two-body model with the Hulthén potential (Hu) are shown by a thick solid curve for the exact calculation, by a dotted curve for the effective-range theory in form (4) in the positive energy region ($E \geq 0$), and by a curve with closed squares ($\mathrm{Hu}_{\mathrm{eff.range}}$) for the effective-range theory in form (4) with the use of Eq. (5) (see text) in the negative energy region ($E \leq 0$). A dashed curve (Sim) shows results obtained in the effective-range theory in form (4) with parameters from [3]. Big closed and open circles show the results of calculations borrowed from [17], based on the Faddeev equations with NN potential AV18 [18] and with the same potential plus three-body force added (AV18 + $3N$), respectively.

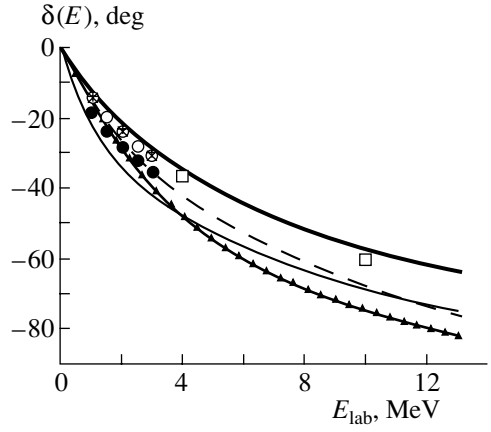

Fig. 2. Results of the nd-scattering phase-shift calculation in the form $\delta(E) = \delta(E)_{\mathrm{eff.range}} + \Delta\delta(E)$ for the S-wave spin-doublet state. The values of $\delta(E)_{\mathrm{eff.range.}}$ are obtained in the two-body model with the Yukawa potential (curve with closed triangles) and with the potential by Tomio *et al.* [8] (thin solid curve) by using the effective-range theory, Eqs. (4) and (5), with a correction $\Delta\delta(E)$, found for the Hulthén potential, taken into account. For comparison, some curves and points from Fig. 1 are given as well. (They include the thick solid curve for the Hulthén potential exact results and the dashed curve for the effective-range theory [3], the open and the closed circles for the Faddeev equations results with and without $3N$ forces, respectively.) In addition, the results borrowed from [14] are shown based on the N/D method with (+) and without (×) absorption effects taken into account; the three-body calculation results at energies of 4 MeV [19] and 10 MeV [20] are shown by open squares.

oscillating potential (3) from Tomio *et al.* especially stands out. We note a large spread of the κ_0^2 values as well. This parameter is very sensitive to the model and to the value of the product $a\kappa$. This is because the function $\kappa_0^2(a\kappa)$ has an infinite derivative at $a\kappa = 0$. Due to this fact, it is not easy to calculate the position of the $k\cot\delta$ pole with high precision, and it may be quite a problem to observe this pole in experiments for other physical systems.

The results of our $\delta(E)$ calculations with different potentials are shown in Figs. 1 and 2. They can be compared with each other and with the results of modern Faddeev calculations [17] with the realistic NN interactions AV18 (Argonne potential [18]) and AV18 + $3N$. The variant AV18 denotes NN forces with charge-dependence breaking taken into account, and AV18 + $3N$ means that three-nucleon forces (Urbana model) are included as well (see reference in [17]). The curve $\delta(E)$ calculated by formula (4) with the parameters taken from [3], which is in agreement with the results of a phase-shift analysis, is also displayed in the same figures.

The exact and approximate results calculated with the Hulthén potential are given in Fig. 1. The corresponding two curves have nearly the same shape, so the correction leads to an anticlockwise rotation of the approximate curve toward the exact one around the center of the coordinates. This correction, $\Delta\delta(E) = \delta(E) - \delta(E)_{\mathrm{eff.range}}$, increases monotonically with energy. At energy below the deuteron-breakup threshold, the value $\Delta\delta(E)$ is less than the three-body force effect (which is about 5°) found in the modern Faddeev calculations [17].

In Fig. 2, we show the calculation results $\delta(E) = \delta(E)_{\mathrm{eff.range}} + \Delta\delta(E)$ with different effective nd potentials when the correction is included. The function $\delta(E)_{\mathrm{eff.range}}$ is calculated by formula (4) with each potential with the coefficients C_2 and C_4 taken from the table. But the correction $\Delta\delta(E)$ is obtained with the Hulthén potential. Taking this correction into account leads to a narrowing of the bunch of curves $\delta(E)$ with different potentials and, correspondingly, to an improvement in their agreement with the experimental data and with the Faddeev calculation results. In Fig. 2, the N/D-method results borrowed from [14] are shown, calculated with and without absorption effects taken into account. One can see that the two-body model with the Hulthén and Yukawa potentials describes the experimental data at low energy reasonably well. The agreement is worse in the case of an oscillating potential from [8]. The Faddeev

calculation results [19, 20] for $\mathrm{Re}\delta(E)$ are also shown in Fig. 2.

We carried out an additional test of the effective-range theory in form (4) in the whole energy range considered (≈8.5 MeV) from the bound-state pole of triton at negative energy to the deuteron-breakup threshold at positive energy where triton decay into three nucleons is possible. With this in mind, we found the coefficients C_2 and C_4 for the Hulthén potential for positive energy E as well. The corresponding coefficients C_{2+} and C_{4+} (see the table) are found by fitting $\delta(E)$ from Eq. (4) to the exact phase shift (9) just near zero energy ($E \approx 0$). This approximation (see Fig. 1) gives much better agreement with the exact result in comparison with the calculation results using the formula (5) and information about the function $C_t^2(\kappa)$. However, the calculation of the asymptotic normalization constant C_t^2 by using Eq. (5) with the coefficients C_{2+} and C_{4+} leads to the value $C_t^2 = 2.18$, which can be compared with the exact value $C_t^2 = 3.5$ for the Hulthén potential. Quite a large difference between these figures means that the distance from the triton pole to the nd-scattering threshold (6.26 MeV) is too great for the effective-range approximation (4) to be valid with high precision for the two-body model with a given potential in the whole energy range considered. To improve this approximation, one can include in Eq. (4) the next term of the effective-range expansion (C_6k^6), but this procedure results in two more fitting parameters. In addition to the term C_6k^6, the other pole of the function $k\cot\delta$ should be taken into account as well to preserve the right asymptotic behavior of the partial scattering amplitude $f(k)$, in accordance with the relation

$$f(k) = (k\cot\delta - ik)^{-1}. \qquad (10)$$

The existence of a countable set of $k\cot\delta$ poles ($f(k)$ zeros) was established in [21] on the theorem level with the Yukawa-type potential. For a system having a bound and a virtual level, this is connected with the symmetry theorem proved in [22].

In all figures, we accept the definition $\delta(E) = 0$ at $E = 0$ as in some papers (see, for example, [17]). Actually, one should take $\delta(0) = \pi$, as follows from the Levinson theorem, because the nd system has one bound level (triton) in the spin-doublet S-wave state. This fact is taken into account in some other publications, for example, in [14].

4. CONCLUSION

It is shown that it is possible to describe reasonably well the low-energy behavior of the S-wave phase shift $\delta(E)$ for the spin-doublet nd scattering by using a simple two-body potential model with only the two fitting parameters mentioned above. It is well known that the nd interaction in the spin-quartet state for the S wave has a repulsive character, so the two-body approach considered is an obviously good approximation for this state as well. As a result, one can successfully use the two-body potential model in calculating the cross section for low-energy nd scattering.

The differences between curves $\delta(E)$ with different potentials turn out to be large enough to enable making a choice among the potentials used. The Hulthén potential appears to be the best one. The exact results of the $\delta(E)$ calculation for this potential slightly overestimate the experimental phase shift behavior, but the existence of the solution in analytical form is an additional argument in favor of its selection.

The phase shift $\delta(E)$ is obtained in this paper using a simple analytical approximation with the other potentials. Comparison of these results with the experimental data and with the Faddeev calculation results reveals reasonable agreement among them, which justifies a rigorous calculation in the framework of the two-body model with any effective nd potential.

It is shown that the effective-range theory in the form (4) does not permit a very precise description of the whole set of observables discussed above with a concrete potential. This result does not contradict the successful description of the experimental data by the same formula with parameters from [3]. In the case of the Hulthén potential, the uncertainty, $\Delta\delta(E)$, of this approximation is less than 5° at $E_{\mathrm{lab}} \leq 3$ MeV, i.e., below the deuteron-breakup threshold (E_{lab} denotes neutron energy in the laboratory system). This uncertainty is less than the three-body-force effect found in the modern Faddeev calculations [17].

ACKNOWLEDGMENTS

This work was supported in part by the Russian Foundation for Basic Research (project no. 01-02-16621) and by the Foundation for Basic Research: Russian Universities (project no. 02.03.003).

Note added. Recently, we have obtained a much better approximation of the scattering function $k\cot\delta$ with the coefficients C_2 and C_4 whose values were found by fitting the triton binding energy to the experimental value and the virtual-pole position to the value that we obtained earlier for specific potentials. The new set of C_2 and C_4 values does not change the main conclusions of this study. The new results will be published elsewhere.

REFERENCES

1. A. C. Phillips, Nucl. Phys. A **107**, 209 (1968).
2. B. A. Girard and M. G. Fuda, Phys. Rev. C **19**, 579 (1979); **19**, 583 (1979).
3. I. V. Simenog, A. I. Sitnichenko, and D. V. Shapoval, Yad. Fiz. **45**, 60 (1987) [Sov. J. Nucl. Phys. **45**, 37 (1987)].
4. J. S. Whiting and M. G. Fuda, Phys. Rev. C **14**, 18 (1976).
5. S. K. Adhikari, Phys. Rev. C **30**, 31 (1984).
6. A. Kievsky, M. Viviani, and S. Rosati, Phys. Rev. C **52**, R15 (1995).
7. N. M. Petrov, Yad. Fiz. **48**, 50 (1988) [Sov. J. Nucl. Phys. **48**, 31 (1988)].
8. L. Tomio, A. Delfino, and S. K. Adhikari, Phys. Rev. C **35**, 441 (1987).
9. Yu. V. Orlov, N. M. Petrov, and G. N. Teneva, Yad. Fiz. **55**, 38 (1992) [Sov. J. Nucl. Phys. **55**, 23 (1992)].
10. Yu. V. Orlov, Yu. P. Orevkov, and L. I. Nikitina, Izv. Akad. Nauk, Ser. Fiz. **60**, 152 (1996).
11. V. Efimov, Nucl. Phys. A **362**, 45 (1981).
12. Yu. V. Orlov, Yu. P. Orevkov, and L. I. Nikitina, Yad. Fiz. **63**, 394 (2000) [Phys. At. Nucl. **63**, 328 (2000)].
13. Yu. V. Orlov, Yu. P. Orevkov, and L. I. Nikitina, Yad. Fiz. **65**, 396 (2002) [Phys. At. Nucl. **65**, 371 (2002)].
14. A. N. Safronov, Yad. Fiz. **50**, 951 (1989) [Sov. J. Nucl. Phys. **50**, 593 (1989)].
15. V. B. Belyaev, B. F. Irgaziev, and Yu. V. Orlov, Preprint No. P4-81-58, OiYaI (Joint Institute for Nuclear Research, Dubna, 1974).
16. V. B. Belyaev, B. F. Irgaziev, and Yu. V. Orlov, Yad. Fiz. **24**, 44 (1976) [Sov. J. Nucl. Phys. **24**, 22 (1976)].
17. A. Kievsky, S. Rosati, W. Tornow, and M. Viviani, Nucl. Phys. A **607**, 402 (1996).
18. R. B. Wiringa, V. G. J. Stoks, and R. Schiavilla, Phys. Rev. C **51**, 38 (1995).
19. J. L. Friar *et al.*, Phys. Rev. C **42**, 2310 (1990).
20. G. L. Payne *et al.*, Phys. Rev. C **30**, 1132 (1984).
21. Yu. V. Orlov and L. I. Nikitina, Yad. Fiz. **61**, 833 (1998) [Phys. At. Nucl. **61**, 750 (1998)].
22. Yu. V. Orlov, Phys. Lett. B **163B**, 25 (1985).

Physics of Atomic Nuclei, Vol. 66, No. 1, 2003, pp. 87–98. Translated from Yadernaya Fizika, Vol. 66, No. 1, 2003, pp. 89–99.

NUCLEI
Theory

dt, d^3He, and $p\alpha$ Scattering in the Vicinity of the ^{5}He* and ^{5}Li* Resonances

A. V. Kulik and V. D. Mur

Moscow State Engineering Physics Institute (Technical University), Kashirskoe sh. 31, Moscow, 115409 Russia

Received November 19, 2001; in final form, March 4, 2002

Abstract—It is shown that the simplest strong-interaction models (those that employ the Breit boundary condition and a delta-function potential) involving only three free parameters describe adequately the properties of the dt and d^3He systems in the vicinity of the ^{5}He*$(3/2^+)$ and ^{5}Li*$(3/2^+)$ resonances—that is, at energies in the regions $E \lesssim 3E_C$ and $E \lesssim 2E_C$, where E_C is the corresponding Coulomb energy. For these systems, the complex values of the scattering length, of the effective range, and of the shape parameter are extracted from experimental data on the reaction cross section and proton polarization in $p\alpha$ scattering (in the case of the d^3He system). The astrophysical function is extrapolated to the low-energy region $(0 \le E < 0.1E_C)$, which is of importance for thermonuclear investigations, but which is hardly accessible to direct measurements. © *2003 MAIK "Nauka/Interperiodica".*

1. INTRODUCTION

Investigation of resonance Coulomb systems (pp, dt, d^3He, $p\alpha$, $\alpha\alpha$, etc.) is of great interest for astrophysics, the physics of thermonuclear fusion, and so on. Since the study of Landau and Smorodinsky [1], an effective-range expansion is used to describe low-energy scattering in a model-independent way. In the case of s-wave scattering, this expansion has the form [2]

$$K_{CS}(k^2) \equiv (\bar{K}_{CS}(k^2) + 2h(\eta))/a_B \quad (1)$$
$$= -1/a_{CS} + (1/2)r_{CS}k^2 - P_{CS}(r_{CS})^3k^4 + Q_{CS}(r_{CS})^5k^6 + ...,$$

where

$$\bar{K}_{CS}(k^2) = 2\pi D_C(\eta)\cot(\delta_{CS}),$$
$$D_C(\eta) = (\exp(2\pi\eta) - 1)^{-1}, \quad (2)$$
$$h(\eta) = [\psi(i\eta) + \psi(-i\eta) - \ln\eta^2]/2,$$

with $\psi(z)$ being the logarithmic derivative of the Euler gamma function. Here, $a_B = \hbar^2/(Z_1Z_2e^2\mu)$ is the Bohr radius of the system (see Table 1); $\eta = 1/(ka_B)$ is the Sommerfeld parameter; $\hbar k = (2\mu E)^{1/2}$, with E and μ being, respectively, the c.m. energy and the reduced mass; and $\delta_{CS}(k)$, a_{CS}, r_{CS}, and P_{CS} and Q_{CS} are, respectively, the nuclear–Coulomb phase shift for s-wave scattering, the scattering length, the effective range, and the shape parameters.

For the pp system, the scattering length and the effective range are known to a high precision, but the relative errors in the shape parameters are quite large [10, 11]:

$$a_{CS} = -7.8098 \pm 0.0023 \text{ fm}, \quad (3)$$
$$r_{CS} = 2.764 \pm 0.010 \text{ fm},$$
$$P_{CS} = 0.051 \pm 0.014,$$
$$Q_{CS} = 0.028 \pm 0.013.$$

Even in the case of the $\alpha\alpha$ system, however, where there is a narrow Breit–Wigner resonance ^{8}Be(0^+) of energy $E_R = E_r - i\Gamma/2$ [9],

$$E_r = 92.12 \pm 0.05 \text{ keV}, \quad \Gamma = 6.8 \pm 1.7 \text{ eV}, \quad (4)$$

it is impossible [12] to extract reliably, in a model-independent way, the low-energy parameters from experimental data [13–15] for $E < 11$ MeV (such an attempt was first made in [16]). Later, the quantities a_{CS}, r_{CS}, and P_{CS} were found in [17] on the basis of scattering data for $E < 1$ MeV and the experimental value of E_r; in addition, the value of $\Gamma = 3.6$ eV was obtained there for the width of the level, this value being different from its experimental counterpart by two standard deviations. In the case being discussed, it is difficult to determine the parameters of the expansion in (1) since, at low energies ($kr_0 \ll 1$), there is a large experimental error because of a small penetrability of the Coulomb barrier and since the inclusion of more precise data for $kr_0 > 1$ ($E > 1$ MeV) requires retaining higher terms in expansion (1), whereupon the result becomes more uncertain.

In [8, 18], the problem of reliably extracting the low-energy parameters of the $\alpha\alpha$ system was solved by using, along with the expansion in (1), extremely simple models of nuclear interaction. Resorting to

Table 1. Parameters of extremely light Coulomb systems

System	a_B, fm	r_0, fm	E_C, keV	E_r, keV	Γ, keV	$k_r r_0$
pp	57.62	1.62	24.99	−143	936	0.09
dt	24.04	3.63	59.89	48.1	72.2	0.20
$p\alpha$	18.03	2.48	79.85	209	270	0.28
d^3He	12.02	3.97	239.5	209	270	0.38
$\alpha\alpha$	3.627	3.34	1588	92.1	0.0058	0.31

Note: Here, $E_C = Z_1 Z_2 e^2/a_B$ is the Coulomb energy and r_0 is the sum of the charge radii of the particles involved [3–5]. The resonance energies $E_R = E_r - i\Gamma/2$ are determined from Eq. (A.14) (compare with the corresponding values from [6–9]); $\hbar k_r = (2\mu E_r)^{1/2}$.

models makes it possible to include experimental data at higher energies in the processing procedure and to take into account a greater number of terms in the expansion in (1) without increasing the number of independent parameters.

A simple realistic model of $\alpha\alpha$ interaction,

$$V_M(r) = \{\infty, r < r_c;$$
$$-U, r_c \le r \le r_N; \quad 4e^2/r, r > r_N\},$$

was proposed by Margenau [19]. The limit of a narrow and deep well ($r_c \to r_N$, $U \to \infty$) corresponds to the Breit model (B) [20, 21] with the coupling constant g equal to the aforementioned limit of the expression

$$\check{g} = r_N(2\mu U/\hbar^2)^{1/2}[(r_N - r_c)(2\mu U/\hbar^2)^{1/2} - \pi/2]; \quad (5)$$

that is, it corresponds to the statement that, at $r = r_N$, the radial wave function $R(r) = \chi(r)/r$ satisfies the boundary condition

$$r_N\chi'(r_N)/\chi(r_N) = -g, \chi(r) \equiv 0 \text{ for } r < r_N. \quad (6)$$

Another limiting case, that where Coulomb repulsion is dominant and where the wave function is localized in the vicinity of $r \sim r_N$ (see Table 5 in the second article quoted in [22]), leads to the delta-function model (D) of strong interaction: $V_S(r) = -[g\hbar^2/(2\mu r_N^2)]\delta(r - r_N)$, where g is a dimensionless constant. This model is equivalent to the boundary condition

$$r_N[(\chi'(r_N + 0) - \chi'(r_N - 0))/\chi(r_N)] = -g. \quad (7)$$

The results obtained by processing scattering data [13] for $E < 1.5$ MeV ($kr_N \le 1$) at the fixed value of $E_r = 92.1$ keV are illustrated in Fig. 1. The curves B and D correspond to solutions to the Schrödinger equation that satisfy conditions (6) and (7), respectively, with the parameters obtained in [8]. By varying the parameters of the potential V_M, one can displace the curve M over the entire region between the curves B and D. For the curve M shown in Fig. 1, we have

$$U = 6.676 \text{ MeV}, \quad r_N = 4.0 \text{ fm}, \quad r_c = 1.6 \text{ fm}, \quad (8)$$

which corresponds to the value of $\bar{g} = 1.216$ for the sign-reversed logarithmic derivative of the wave function at $r = r_N$. An estimation on the basis of Eq. (5) yields $\check{g} = 1.11$. These values are close to that of $g = 1.022$, which was obtained within the Breit model [8]. The dashed curve corresponds to retaining the first four terms of the expansion in (1) at [8, 18]

$$a_{CS} = -(2.03 \pm 0.10) \times 10^3 \text{ fm}, \quad (9)$$
$$r_{CS} = 1.107 \pm 0.006 \text{ fm},$$
$$P_{CS} = -0.226 \pm 0.007,$$
$$Q_{CS} = 0.19 \pm 0.02.$$

A comparison with (3) shows that the use of the above strong-interaction models leads to a higher relative precision in determining the shape factors P_{CS} and Q_{CS} from experimental data. For the width of the ^{8}Be(0^+) resonance, one obtains [8, 18] the value of $\Gamma = 5.81 \pm 0.31$ eV, which is in good agreement with the experimental value in (4). Since, in the vicinity of the ^{5}He*($3/2^+$) and ^{5}Li*($3/2^+$) low-energy resonances, the $l = 0$, $J^P = 3/2^+$ resonance wave plays a dominant role both in elastic dt and d^3He scattering and in the fusion reactions $dt \to n\alpha$ and $d^3\text{He} \to p\alpha$, all the aforesaid gives sufficient grounds to use, in simulating the low-energy properties of not only the $\alpha\alpha$ system but also the dt and d^3He systems, the phenomenological potentials that correspond to the boundary conditions (6) and (7).

The resonance nuclear reactions $dt \to n\alpha + 17.59$ MeV and $d^3\text{He} \to p\alpha + 18.35$ MeV, which are accompanied by a large energy release, play an important role in the problems of thermonuclear fusion, of the muon catalysis of nuclear reactions [23–25], and of primary nucleosynthesis [26]. To the best of our knowledge, the effective-range approximation for describing the reactions $dt \to n\alpha$ and $d^3\text{He} \to p\alpha$ in a model-independent way was first employed in [27], where it was found, in particular, that there is a significant ambiguity in determining a_{CS} and r_{CS} on the

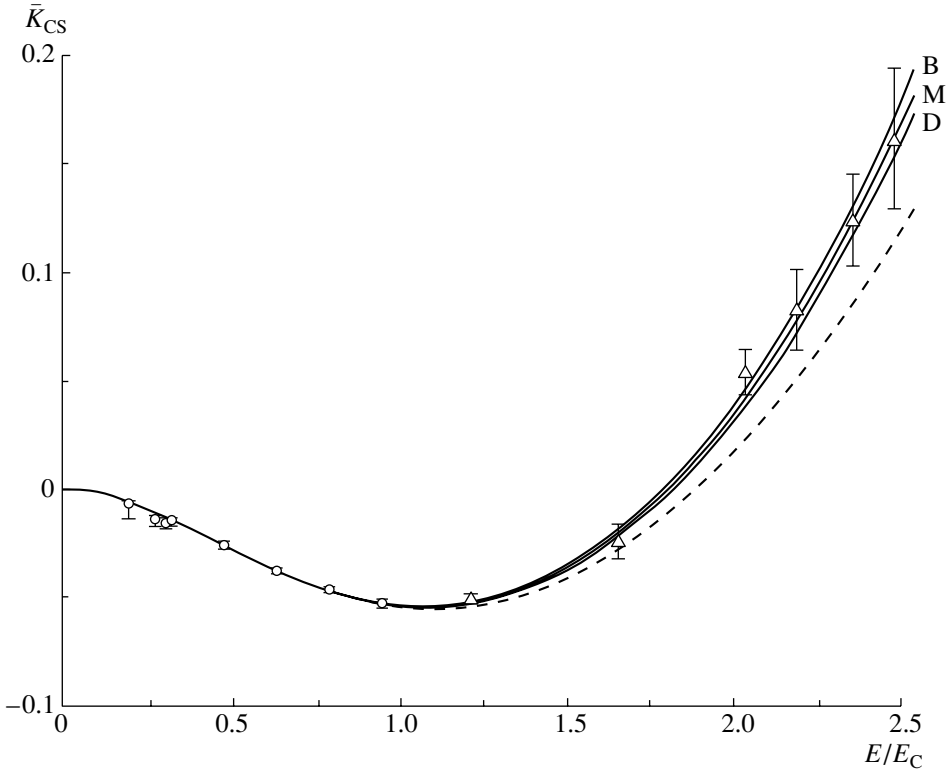

Fig. 1. Phase shifts for $\alpha\alpha$ scattering. The function $\bar{K}_{CS}$ was defined in (2). The solid curves B, M, and D correspond to exact solutions within, respectively, the Breit model, the Margenau model, and the model employing the δ-function potential, the relevant parameters being set to the values indicated in (8) and the values from [8]. The dashed curve corresponds to retaining the first four terms of the expansion in (1). Points represent experimental data from (circles) [13] and (triangles) [15].

basis of experimental data known at that time for the reaction cross section σ_r. The possibility of extracting low-energy parameters from data on the reaction cross section [28] arises owing to the interference between nuclear and Coulomb interactions; however, a self-consistent variation of the parameters admit their changes over rather wide intervals (see Table 1 in [29]). Therefore, some additional criteria (apart from the χ^2 criterion) for selecting values of the low-energy parameters are required. In particular, a constraint on the Coulomb renormalization of the effective range was taken into account in [22].

In the present study, this problem is solved through recourse to extremely simple models of nuclear interaction. Since difficulties arising in processing experimental data are similar to those that were indicated above for the $\alpha\alpha$ system, it is natural to use, as before, the strong-interaction-potential models specified by Eqs. (6) and (7). Because of absorption, there arises here an additional free parameter, since the coupling constant becomes complex-valued, $g = g_1 + ig_2$, $g_2 > 0$, which corresponds to an optical potential. Such an approach is implemented in Section 2 for dt scattering and in Section 3 for the d^3He system, precision polarization data for $p\alpha$ scattering also being used in the latter case. The results of our study are discussed in Section 4, and some technical details are explained in the Appendices.

2. dt SCATTERING IN THE VICINITY OF THE ^{5}He*$(3/2^+)$ RESONANCE

In the case of the dt system, only data [30–32] on the reaction cross section, which have a relative error less than 3% for energies in the range $0 < E < 3E_C$, are included in processing. The results obtained by fitting the parameters of the Breit model and the model employing a delta-function potential are given in Table 2 at the smallest value of χ^2, while the corresponding values of the expansion parameters (A.1) for dt scattering are presented in Table 3. The low-energy parameters appearing in (1) that are rescaled on this basis are

$$a_{CS} = -(82.5 \pm 4.5) - i(31.0 \pm 0.9)\ \text{fm}, \quad (10)$$
$$r_{CS} = (5.11 \pm 0.37) - i(0.14 \pm 0.02)\ \text{fm},$$
$$P_{CS} \times 10^2 = -(9.4 \pm 0.6) - i(0.2 \pm 0.03),$$
$$Q_{CS} \times 10^2 = (2.3 \pm 0.3) + i(0.1 \pm 0.03).$$

Table 2. Parameters of model strong-interaction potentials for the d^3H and d^3He systems

System	Model	r_N, fm	Re g	Im $g \times 10$	χ^2	a_S, fm	r_S, fm	$P_S \times 10$	$Q_S \times 10^2$	$E_R^{(S)}$, keV
d^3H	B	5.3 ± 0.5	0.279 ± 0.002	0.70 ± 0.07	0.83	$23.2 - 4.48i$	$8.43 - 0.386i$	$-0.52 - 0.02i$	$0.66 + 0.06i$	$-45 - 24i$
	D	7.1 ± 0.8	1.486 ± 0.007	1.13 ± 0.12	0.69	$21.0 - 3.22i$	$7.90 - 0.241i$	$-0.48 - 0.02i$	$0.54 + 0.05i$	$-60 - 26i$
d^3He	B	3.9 ± 0.7	0.247 ± 0.03	0.48 ± 0.15	1.4	$19.1 - 2.96i$	$6.35 - 0.208i$	$-0.51 - 0.014i$	$0.64 + 0.04i$	$-67 - 27i$
	D	5.2 ± 0.9	1.46 ± 0.04	0.7 ± 0.2	1.9	$16.2 - 1.68i$	$5.84 - 0.114i$	$-0.48 - 0.012i$	$0.52 + 0.03i$	$-104 - 29i$

Note: The low-energy parameters a_s, r_s, P_s, and Q_s and the resonance energy $E_R^{(s)} = E_r^{(s)} - i\Gamma^{(s)}/2$ refer to model potentials in the absence of Coulomb interaction [see Eqs. (A.15), (A.17), and (A.18)].

The accuracy of the experimental data used proved to be sufficient for determining, through resorting to extremely simple strong-interaction-potential models in order to stabilize results, not only the scattering length and the effective range but also the shape parameters $P_{\rm CS}$ and $Q_{\rm CS}$ to a precision commensurate with that of the results in (3), which were obtained in a model-independent way from data on elastic pp scattering.

The quality of the approximation of the astrophysical function [see also Eqs. (A.5) and (A.6)]

$$s(E) = \frac{3}{8}\frac{\mu E}{\hbar^2\pi^2}\frac{\sigma_r(E)}{D_{\rm C}(\eta)},$$

where σ_r is the reaction cross section and $D_{\rm C}(\eta)$ is the Coulomb barrier penetrability, which was defined in (2), is illustrated in Fig. 2*a*. It can be seen that the result in the effective-range approximation, which corresponds to retaining the first two terms of the expansion in (1), differs (within two standard deviations) from the exact result only in a close vicinity of the ^{5}He*$(3/2^+)$ resonance. The first three terms of the expansion in (1) reproduce the exact result over the entire energy region $E \lesssim 3E_{\rm C}$ considered here. Using the parameter values quoted in Table 3, one can calculate the astrophysical function $s(E)$ for $E < 0.2E_{\rm C}$; this region of extremely low energies is of interest, in particular, for calculating fusion reactions in mesic molecules [33], but it is hardly accessible to direct measurements (see Fig. 2*b*). With the aid of Eq. (A.6), it can be shown that, at such energies, the astrophysical function is given by

$$s(E) = (1.295 \pm 0.04) + (1.13 \pm 0.03)E/E_{\rm C} \quad (11)$$
$$+ (1.23 \pm 0.03)(E/E_{\rm C})^2.$$

For $E < 0.2E_{\rm C}$, the expansion in (11) is precise to within one percent. The value $s(0)$ of the astrophysical function at the origin is consistent with the results previously obtained in [29, 30, 33].

At the parameter values quoted in Table 2, the strong-interaction models specified by Eqs. (6) and (7) make it possible to describe the low-energy properties of the dt system over an energy range that is broader than that which was used in data processing. In particular, the low-energy parameters extracted from data on the fusion reaction $dt \to n\alpha$ alone make it possible to calculate the elastic-scattering cross section as well. Figure 3 displays the ratio $R(E)$ [see Eq. (A.4)] of the differential cross section for elastic dt scattering at an angle of 90° in the c.m. frame to the cross section for Rutherford scattering at the same angle. It can be seen that the results of the calculations based on the Breit model and the model employing a delta-function potential are close to each

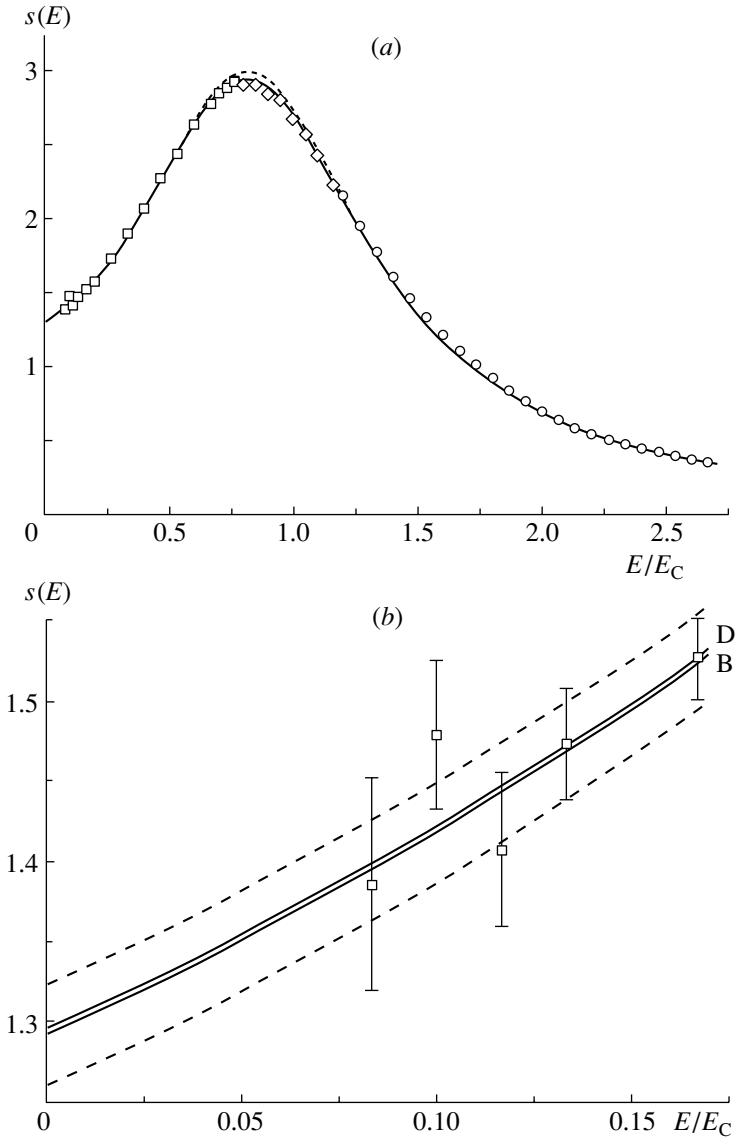

Fig. 2. Astrophysical function for the fusion reaction $dt \to n\alpha$. In Fig. 2*a*, the solid curve corresponds to the Breit model and the model employing a delta-function potential (the results based on these models are indistinguishable on the scale of the figure); the dashed curve represents the results in the effective-range approximation; and points stand for experimental data from (open boxes) [30], (open diamonds) [31], and (open circles) [32]. In Fig. 2*b*, the solid curves B and D correspond to the Breit model and the model of a delta-function potential, respectively, the parameters being indicated in Table 2; the dashed curves refer to models characterized by limiting values of χ^2 ; and points (open squares) represent data from [30].

other and that they are consistent (within one standard deviation) with available experimental data [34] at energies up to $5E_C$.

The sets of low-energy parameters of the dt system in Table 3 are close to the model-independent set with $\alpha_0 = 0.26$ in Table 1 of [29], but they do not of course coincide. In these sets, the values of the imaginary part of the effective range show the greatest distinctions (by more than a factor of 2), but, as such, this imaginary part is small. Such a distinction is quite natural, because there are three free parameters in each of the models specified by Eqs. (6) and (7), while four parameters were varied in [29] (the shape parameter was not used in [29]). In view of this, it was necessary to invoke additional selection criteria. The analysis in [35] took into account constraints on the Coulomb renormalization of the effective range, on one hand, and the results of the partial-wave analysis of $n\alpha$ scattering [36] in the vicinity of the ^{5}He$^*(3/2^+)$ resonance, on the other hand. Unfortunately, these data, as well as experimental data from [37] on the total cross section for $n\alpha$ scattering in the resonance region, are insufficiently precise for a reliable determination of the phase shift for potential $n\alpha$ scattering

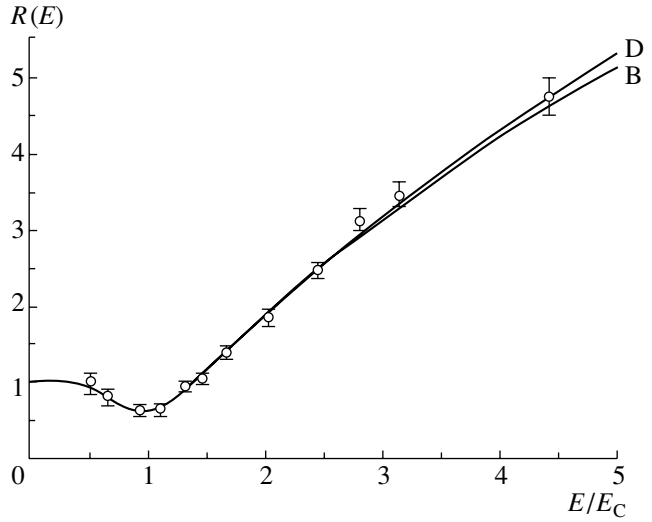

Fig. 3. Ratio $R(E)$ (A.4) of the differential cross section to the Rutherford cross section. The solid curves B and D correspond to the Breit model and the model of a delta-function potential, respectively, the parameter values being given in Table 3. Points (open circles) represent data from [34].

(an additional free parameter is present here). The situation is totally different for the d^3He system, which will be considered in the next section.

3. d^3He AND $p\alpha$ SCATTERING IN THE VICINITY OF THE ^{5}Li*$(3/2^+)$ RESONANCE

The errors in experimental data [38] on the fusion reaction $d^3\mathrm{He}\to p\alpha$ at low energies ($E < 0.75E_\mathrm{C}$) are 15–30% (see Fig. 4)—that is, they are quite large. At the same time, modern experiments (see [39]) have a precision of about 4% at higher energies. Apart from these data on the reaction cross section, we have used precision (the error is 2 to 3%) polarization data [40] for $p\alpha$ scattering in the vicinity of the ^{5}Li*$(3/2^+)$ resonance—more specifically, at the laboratory proton energies

$$E_p = 22.46, 22.71, 22.96, 23.16, \quad (12)$$
$$23.29, 23.48, 23.56 \text{ MeV}.$$

In rescaling these values to the c.m. frame, it is necessary here to take into account a relativistic correction; that is,

$$k^2 = 2m_\alpha(E_p - E_\mathrm{thr})/(m_p + m_\alpha),$$
$$E_\mathrm{thr} = \Delta(1 + m_p/m_\alpha)$$
$$+ \Delta^2/(2m_\alpha c^2) = 23.014 \text{ MeV}$$

($\Delta = 18.350$ MeV is the energy release in the fusion reaction $d^3\mathrm{He}\to p\alpha$). The results obtained by processing the experimental data in question (in all, we have taken into account 191 points) are quoted in Table 2. The phase shifts for potential $p\alpha$ scattering that are obtained within the Breit model and the model employing a delta-function potential are, respectively,

$$\varphi_{p\alpha} = 2.9^\circ \pm 0.8^\circ \quad \text{and} \quad 2.6^\circ \pm 0.9^\circ. \quad (13)$$

The expansion parameters (A.1) are given in Table 3; the low-energy parameters of the expansion in (1) that are rescaled from these values are

$$a_\mathrm{CS} = -(54.1 \pm 4.9) - i(8.6 \pm 1.4) \text{ fm}, \quad (14)$$
$$r_\mathrm{CS} = (3.17 \pm 0.29) - i(0.05 \pm 0.02) \text{ fm},$$
$$P_\mathrm{CS} \times 10^2 = -(11.8 \pm 1.4) - i(0.1 \pm 0.05),$$
$$Q_\mathrm{CS} \times 10^2 = (3.9 \pm 1.2) + i(0.1 \pm 0.07).$$

Since the accuracy of experimental data for the d^3He system is rather poor, the criterion $\bar{\chi}^2 = \chi^2_{0.3} + \chi^2_\mathrm{min}$, where $\chi^2_{0.3} = 1.15$ is the maximum value of χ for a given data set and χ^2_min is its minimum value, was used, as in [39], to select model-parameter values. The energy dependence of the astrophysical function is displayed in Fig. 4. In this case, the effective-range approximation leads to an overestimation of $s(E)$ for $E > 0.5E_\mathrm{C}$; at the same time, the first three terms of the expansion in (1) yield a result that is indistinguishable (on the scale of the figure) from exact solutions for $E \lesssim 2E_\mathrm{C}$. Thus, it is necessary to take into account the shape parameter for the d^3He system. For $E < 0.2E_\mathrm{C}$, the result for the astrophysical function is (see also Fig. 4*b*)

$$s(E) = (0.72 \pm 0.1) + (0.535 \pm 0.01)E/E_\mathrm{C} \quad (15)$$
$$+ (0.64 \pm 0.02)(E/E_\mathrm{C})^2.$$

Just as for dt scattering, the accuracy of this expansion is not poorer than 1% for $E < 0.2E_\mathrm{C}$. We

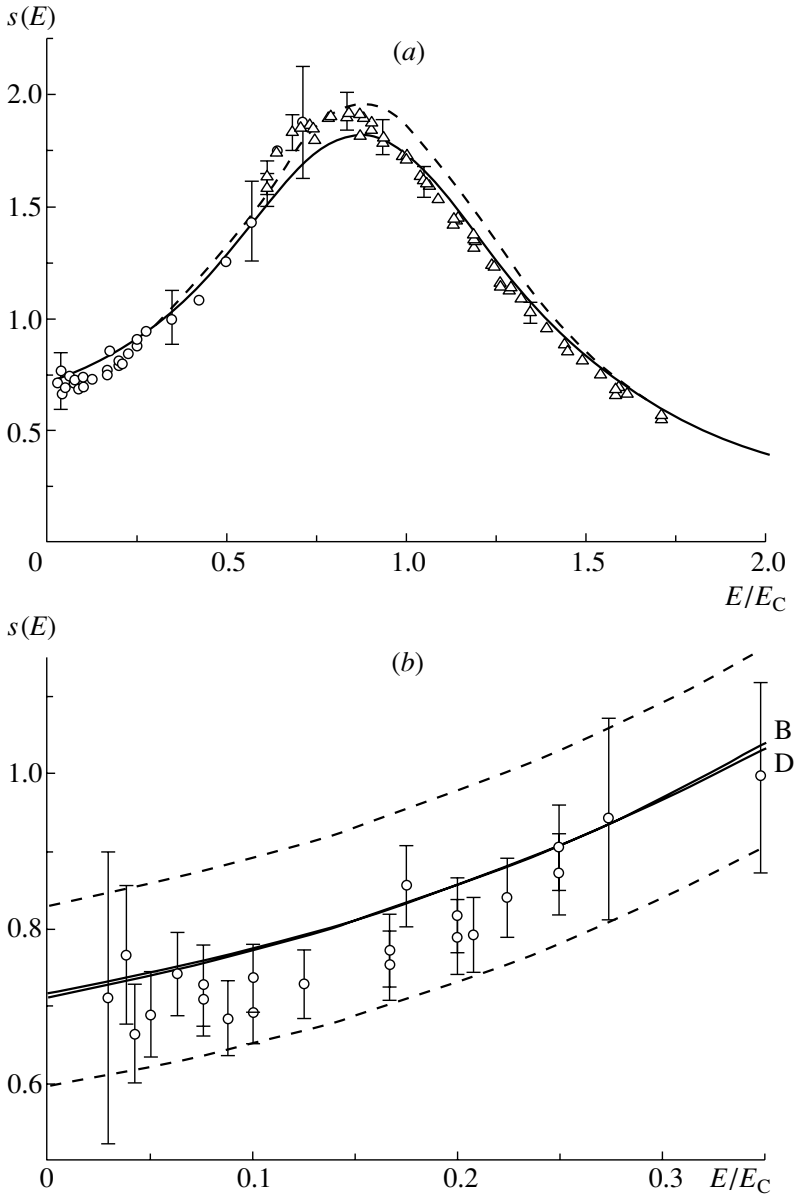

Fig. 4. Astrophysical function for d^3He scattering. In Fig. 4*a*, the solid curve corresponds to the Breit model and the model of a delta-function potential (the results based on these models are indistinguishable on the scale of the figure); the dashed curve represents the results obtained in the effective-range approximation; and points stand for data from (open circles) [38] and (open triangles) [39]. Errors are indicated only for some typical experimental points. In Fig. 4*b*, the upper solid curve for $E \to 0$ and the lower solid curve correspond to the delta-function potential and the Breit model, respectively, the parameter values being indicated in Table 2; the dashed curves refer to models characterized by limiting values of $\bar{\chi}^2$ (see main body of the text); and points (open circles) represent experimental data from [38].

note that the value that we obtained here for $s(0)$ is consistent with the value of $S(0) = 6.70$ MeV b [see Eq. (A.7) in the Appendix below] presented in [39] for the dimensional astrophysical function [it corresponds to $s(0) = 0.735$].

The set of low-energy parameters of the d^3He system that is the closest to the sets in Table 3 is that which corresponds to $\alpha_0 = 0.22$ in Table 1 of the second article quoted in [22] (the value of $\beta_2 = 0.0065$ chosen for this set is more than one order of magnitude greater than that given in Table 3). These parameters could be refined owing predominantly to taking into account polarization data in the vicinity of the ^{5}Li*$(3/2^+)$ resonance. The results obtained by calculating proton polarization according to Eqs. (A.8) and (A.9) with the parameter values from Table 3 are shown in Fig. 5 for the extreme values of the energy E_p in (12) for the data set used, in which case

Table 3. Expansion parameters (A.1) for the d^3H and d^3He systems

System	Model	$\alpha_0 \times 10$	$\beta_0 \times 10^2$	$\alpha_1 \times 10$	$\beta_1 \times 10^2$	$\alpha_2 \times 10^3$	$\beta_2 \times 10^4$	$\alpha_3 \times 10^5$	$\beta_3 \times 10^6$
d^3H	B	2.53	9.4	1.072	0.32	0.96	0.72	1.2	1.3
	D	2.57	9.8	1.052	0.25	0.84	0.39	0.85	0.47
d^3He	B	2.14	3.3	1.323	0.24	2.3	1.1	5.7	4.1
	D	2.19	3.5	1.311	0.19	2.1	0.63	4.3	1.6

Note: The results quoted here correspond to the central values of the radii r_N and of the coupling constants g from Table 2.

$|k|r_0 \approx 0.75$. Since nuclear–Coulomb phase shifts decrease fast with increasing orbital angular momentum, $\delta_l \propto (kr_0)^{2l+1}$, nonresonance phase shifts, which are known [41] to within 2–4%, were used in our calculations (in the resonance region, the error in the $^2D_{3/2}$ phase shift is about 10%). The agreement with experimental data is quite impressive.

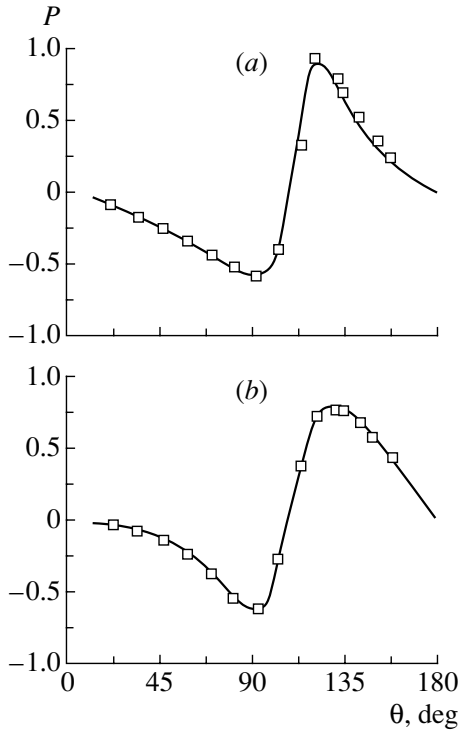

Fig. 5. Proton polarization in $p\alpha$ scattering at the laboratory proton energies of (*a*) $E_p = 22.46$ MeV (that is, $E = -1.85E_C$) and (*b*) $E_p = 23.56$ MeV (that is, $E = 1.82E_C$). The solid curves were calculated on the basis of Eq. (A.8) with the parameter values that are quoted in Table 3 and the phase shifts for potential scattering that are given in (13) (these are indistinguishable for the Breit model and the model of a delta-function potential). Points (open boxes) represent data from [40].

4. CONCLUDING REMARKS

(i) The use of the Breit model and of the model based on a delta-function potential, which are the simplest strong-interaction models and which involve only three independent parameters, make it possible to determine reliably the complex values of the scattering length, the effective range, and the shape parameter P_{CS} for the d^3H and d^3He systems and to extrapolate the astrophysical function to the low-energy region $E < 0.1E_C$, which is hardly accessible to direct measurements, but which is of paramount importance for thermonuclear investigations. The point is that treatment on the basis of specific nuclear-interaction models reduces uncertainties that arise in extracting low-energy parameters from experimental data and, at the same time, yields results that, as can be seen from Figs. 2–5, are virtually independent of the form of strong-interaction potential at $E \lesssim E_C$—that is, the corresponding description is nearly model-independent at low energies.

(ii) The existence of distinct ($\mathrm{Re}(a_{CS}/r_{CS}) \sim 10$) Coulomb resonances ^{5}He*$(3/2^+)$ and ^{5}Li*$(3/2^+)$ is possible only if channels of reactions that involve the production of the above compound nuclei are weakly coupled. This is consistent with the smallness of the ratio β_i/α_i ($\beta_i/\alpha_i \sim 0.1$) at $i = 0, 1, 2$ for the d^3H and d^3He systems (see Table 3).

(iii) A comparison of the signs of the real parts of a_S and a_{CS}, as well of $E_r^{(S)}$ and E_r, for the dt and d^3He systems shows that Coulomb interaction pushes out the bound state into a continuum (if absorption in the system is disregarded).

(iv) Since the nuclear–Coulomb effective range satisfies the condition $r_{CS} < (1/3)a_B$ (see [22]) in the resonance case and since the ratio r_N/a_B is $r_N/a_B \approx 1/4$ for the mirror systems being considered—that is, it is close to a limiting value—Coulomb renormalization in these systems is of importance not only for the scattering length but also for the effective range. It should be emphasized that by no means

can one consider a significant distinction between the effective ranges r_{CS} for dt and d^3He scattering—to say nothing of the corresponding values of the scattering length a_{CS} [see the values in (10) and (14)]—as evidence of violation of the isotopic invariance of nuclear forces, since the structure of both the dt and the d^3He system is controlled to a considerable extent by Coulomb interaction.

ACKNOWLEDGMENTS

We are grateful to B.M. Karnakov and V.S. Popov for stimulating discussions of the results presented here.

This work was supported in part by the Russian Foundation for Basic Research (project nos. 00-02-16354 and 01-02-16850).

APPENDIX A

Resonance Approximation in the Two-Channel Problem

The ^{5}Li*$(3/2^+)$ resonance plays a dominant role not only in the s wave of low-energy d^3He scattering (first channel) but also in the d wave of $p\alpha$ scattering (second channel) near the threshold E_{thr} for the reaction $p\alpha \to d^3$He. For such a two-channel system, the scattering-matrix elements for the $3/2^+$ state can be expressed in terms of the low-energy parameters of the d^3He system by using the analyticity and unitarity conditions and by taking into account invariance under time reversal. If there is absorption in the system—that is, if open inelastic channels are taken into account—the effective-range function and the low-energy parameters are complex-valued:

$$a_B K_{CS}(k^2) = \alpha(k^2) - i\beta(k^2), \quad \text{(A.1)}$$
$$\alpha(k^2) = \alpha_0 + \alpha_1(ka_B)^2 + \alpha_2(ka_B)^4 + \alpha_3(ka_B)^6 + \ldots,$$
$$\beta(k^2) = \beta_0 + \beta_1(ka_B)^2 + \beta_2(ka_B)^4 + \beta_3(ka_B)^6 + \ldots.$$

The scattering length, the effective range, and the shape parameters are expressed in terms of the real-valued coefficients α_i and β_i as

$$a_B/a_{CS} = -\alpha_0 + i\beta_0,$$
$$r_{CS}/a_B = 2(\alpha_1 - i\beta_1),$$
$$P_{CS} = -(1/8)(\alpha_2 - i\beta_2)(\alpha_1 - i\beta_1)^{-3},$$
$$Q_{CS} = (1/32)(\alpha_3 - i\beta_3)(\alpha_1 - i\beta_1)^{-5}.$$

For the scattering-matrix elements S_{ik}, we have

$$S_{11} = \exp(2i\sigma_0)[a(k) - ib_-(k)]/[a(k) - ib_+(k)], \quad \text{(A.2)}$$
$$S_{12} = S_{21} = 2i\exp(i(\sigma_0 + \sigma_2 + \varphi)) \times (2\pi\beta D_C)^{1/2}/[a(k) - ib_+(k)],$$
$$S_{22} = \exp(2i(\sigma_2 + \varphi)) \times [a(k) + ib_-(k)]/[a(k) - ib_+(k)], E_p > E_{thr},$$
$$S_{22} = \exp(2i(\sigma_2 + \varphi)) \times [A(k) + i\beta(k^2)]/[A(k) - i\beta(k^2)], E_p < E_{thr},$$

where $\sigma_l(k) = \arg\Gamma(l + 1 + i\eta)$ is the Coulomb phase shift in the state characterized by the orbital angular momentum l; φ is the phase shift for potential scattering through the second channel—in the energy region being considered, it can be assumed to be constant;

$$a(k) = \alpha(k^2) - 2h(\eta), \quad \text{(A.3)}$$
$$b_\pm(k) = \beta(k^2) \pm 2\pi D_C(\eta),$$
$$A(k) = \alpha(-\lambda^2) - 2g(\lambda),$$
$$g(\lambda) = \psi(1/\lambda) + \lambda/2 + \ln\lambda,$$

with λ being $\lambda = -ika_B$; and the functions $D_C(\eta)$ and $h(\eta)$ were defined in (2). For the ratio of the differential cross section for elastic scattering through the first channel at an angle of $\pi/2$ to the Rutherford cross section, one can find from the above relations that [28]

$$R(E, \theta = \pi/2) = 1 \quad \text{(A.4)}$$
$$- (4/3)ka_B D_C(\eta)(a^2(k) + b_+^2(k))^{-1} \times [a(k)\cos[\ln 2/(ka_B)] + b_+(k)\sin[\ln 2/(ka_B)] - (ka_B)D_C(\eta)/2].$$

For the reaction cross section, we accordingly have

$$\sigma_r = (2\pi/3)k^{-2}(1 - |S_{11}|^2) \quad \text{(A.5)}$$
$$= (16\pi^2/3)k^{-2}D_C(\eta)s(E).$$

Here, $s(E)$ is the so-called astrophysical function defined as

$$s(E) = \beta(k^2)/(a^2(k) + b_+^2(k)) \quad \text{(A.6)}$$
$$= s_0 + s_1(E/E_C) + s_2(E/E_C)^2 + \ldots$$

with

$$s_0 = \beta_0/(\alpha_0^2 + \beta_0^2),$$
$$s_1 = (2s_0/\beta_0)[\beta_1 - 2s_0(\bar\alpha_1\alpha_0 + \beta_1\beta_0)],$$
$$s_2 = (4s_0/\beta_0) \times \left[\beta_2 - 2s_0\left(\bar\alpha_2\alpha_0 + \beta_2\beta_0 + \frac{1}{2}\bar\alpha_1^2 + \frac{1}{2}\beta_1^2\right) - \frac{\beta_1}{2}\frac{s_1}{s_0} + \frac{\beta_0}{4}\frac{s_1^2}{s_0^2}\right],$$

where $\bar\alpha_1 = \alpha_1 - 1/6$ and $\bar\alpha_2 = \alpha_2 - 1/60$.

Often use is made of the dimensional astrophysical function $S(E)$, which is related to the dimensionless

astrophysical function $s(E)$ defined in (A.5) by the equation

$$S(E) = (8\pi^2/3)E_C a_B^2 s(E)/[1 - \exp(-2\pi\eta)]. \quad (A.7)$$

For the polarization of scattered protons, we have

$$P = 2\mathrm{Re}(gf^*)/[|g|^2 + |f|^2], \quad (A.8)$$

where the amplitudes $g(\theta,k)$ and $f(\theta,k)$ for, respectively, non-spin-flip and spin-flip elastic $p\alpha$ scattering at an angle θ can be represented in the form [42]

$$\exp(-2i\sigma_0)g(\theta,k) \quad (A.9)$$
$$= \eta^2\exp[-2i\eta\ln(\sin(\theta/2))]/[2\sin^2(\theta/2)]$$
$$+ (\eta/2i)\sum_{l=0}^{\infty}[(l+1)(\tau_l^+\exp(2i\delta_l^+) - 1)$$
$$+ l(\tau_l^-\exp(2i\delta_l^-) - 1)]\exp(2i\Phi_l)P_l(\cos(\theta)),$$
$$\exp(-2i\sigma_0)f(\theta,k)$$
$$= (\eta/2)\sum_{l=1}^{\infty}[\tau_l^+\exp(2i\delta_l^+) - \tau_l^-\exp(2i\delta_l^-)]$$
$$\times \exp(2i\Phi_l)P_l^1(\cos(\theta)).$$

Here, $P_l^m(\cos(\theta))$ are associated Legendre polynomials, $\Phi_l = \sigma_l - \sigma_0 = \sum_{m=1}^{l}\arctan(\eta/m)$ is the difference of the nonrelativistic Coulomb phase shifts in the l ($l \geq 1$) and s waves, $\tau_l^{\pm}$ are the inelasticity parameters in states characterized by specific values of the orbital angular momentum l and the total angular momentum $J = l \pm 1/2$, and $\delta_l^{\pm}$ are the nuclear–Coulomb phase shifts in these states. In particular, the result obtained for the amplitude $D_{3/2}$ according to (A.2) is

$$\tau_2^-\exp(2i\delta_2^-) = \exp(2i(\sigma_2 + \varphi)) \quad (A.10)$$
$$\times [a(k) + ib_-(k)]/[a(k) - ib_+(k)], \quad E_p > E_{\mathrm{thr}},$$
$$\tau_2^-\exp(2i\delta_2^-) = \exp(2i(\sigma_2 + \varphi))$$
$$\times [A(k) + i\beta(k^2)]/[A(k) - i\beta(k^2)], \quad E_p < E_{\mathrm{thr}},$$

where the inelasticity parameter is $\tau_2^- = |S_{11}| = |S_{22}| = \exp(-2\mathrm{Im}\delta_2^-)$. In addition to three parameters of the strong-interaction-potential models, there then arises, in the threshold region, yet another free parameter, the phase shift φ for potential scattering. Finally, we note that Eqs. (A.2)–(A.10) are valid for the dt system as well, in which case there is no Coulomb interaction in the second channel. One must then set $\sigma_2(\eta) \equiv 0$.

APPENDIX B

Effective-Range Expansion for Exactly Solvable Models

In the Breit model, which is specified by Eq. (6), the effective-range-expansion function has the form

$$r_N K_{\mathrm{CS}}(k^2) = -v_0(r_N,k^2)/u_0(r_N,k^2) \quad (A.11)$$
$$+ \{u_0(r_N,k^2)[(1+g)u_0(r_N,k^2)$$
$$+ r_N du_0(r_N,k^2)/dr_N]\}^{-1}$$

(compare with [22]). Here, the functions $u_0(r,k^2)$ and $v_0(r,k^2)$ defined as

$$u_0 = (krC_0(\eta))^{-1}F_0(kr,\eta), \quad (A.12)$$
$$v_0 = C_0(\eta)G_0(kr,\eta) - 2\eta h(\eta)C_0^{-1}(\eta)F_0(kr,\eta),$$

where $C_0^2(\eta) = 2\pi\eta D_C(\eta)$, are analytic functions of k^2 (see, for example, [43]), in contrast to the Coulomb functions F_0 and G_0, which are, respectively, regular and irregular at the origin. Expansion (A.11) in powers of k^2 yields

$$a_{\mathrm{CS}}/a_B = [2gI_1(\rho) + \rho I_0(\rho)]/4[2gK_1(\rho) - \rho K_0(\rho)],$$
$$r_{\mathrm{CS}}/a_B = 1/3 \quad (A.13)$$
$$- \rho^2[4(g+1)^2 - \rho^2]/[12(2gI_1(\rho) + \rho I_0(\rho))^2]$$

with

$$\rho = (8r_N/a_B)^{1/2}$$

{see the second article quoted in [22]; here, we take the opportunity of correcting a misprint there: in Eq. (A.20) of that article, the coefficient of the product I_0I_1 of Macdonald functions is equal to 2 (not 4), and that formula is completely in accord with (A.13)}. The next terms of the expansion in question are cumbersome, and we do not present them explicitly for this reason. The energy $E_R = E_r - i\Gamma/2$ of Breit–Wigner resonances is determined from the equation

$$(1/a_B)(2\pi i D_C(\eta) + 2h(\eta)) \quad (A.14)$$
$$= -1/a_{\mathrm{CS}}$$
$$+ \frac{1}{2}r_{\mathrm{CS}}k^2 - P_{\mathrm{CS}}(r_{\mathrm{CS}})^3k^4 + Q_{\mathrm{CS}}(r_{\mathrm{CS}})^5k^6.$$

If the Coulomb potential is switched off, $u_0(r,k^2) \to \sin(kr)/kr$, $v_0(r,k^2) \to \cos(kr)$, and it follows from (A.11) that

$$r_N K_S(k^2) = -z\cot(z) + z^2/[\sin^2(z)(g + z\cot(z))], \quad (A.15)$$

$$z = kr_N,$$
$$a_S/r_N = (g+1)/g,$$
$$r_S/r_N = (2/3)(g^2 + 3g + 3)(g+1)^{-3},$$
$$P_S = (-3/40)(g+1)^3$$

$$\times (g^3 + 6g^2 + 15g + 15)(g^2 + 3g + 3)^{-3},$$
$$Q_S = (9/1120)(g+1)^6$$
$$\times (2g^4 + 18g^3 + 72g^2 + 147g + 126)$$
$$\times (g^2 + 3g + 3)^{-5}.$$

For a delta-function potential at a sphere of radius $r = r_N$ [see Eq. (7)], one has [43]

$$r_N K_{\rm CS}(k^2) \qquad (A.16)$$
$$= -v_0(r_N, k^2)/u_0(r_N, k^2) + 1/[g u_0^2(r_N, k^2)],$$
$$a_{\rm CS}/a_{\rm B} = gI_1(\rho)^2(4gK_1(\rho)I_1(\rho) - 2)^{-1},$$
$$r_{\rm CS}/a_{\rm B} = 1/3 - \rho^2[gI_1(\rho) - \rho I_2(\rho)]/(12gI_1(\rho)^3).$$

For $a_{\rm B} \to \infty$, we find from (A.16) that

$$r_N K_S(k^2) = -z\cot(z) + z^2/[g\sin^2(z)], \quad (A.17)$$
$$a_S/r_N = g/(g-1), \quad r_S/r_N = (2/3)(g+1)/g,$$
$$P_S = (-3/40)g^2(g+3)/(g+1)^3,$$
$$Q_S = (9/560)g^4(g+5)/(g+1)^5.$$

The equations for determining the resonance energy $E_R^{(S)} = E_r^{(S)} - i\Gamma^{(S)}/2$ within the Breit model and the model employing a delta-function potential are, respectively,

$$z/[\sin^2(z)(g + z\cot(z))] - \cot(z) = i \qquad (A.18)$$

and

$$z/[g\sin^2(z)] - \cot(z) = i.$$

By solving Eqs. (A.18) with the parameter values quoted in Table 2, we obtain the positions of the resonances and their widths. The results are also presented in this table.

REFERENCES

1. L. D. Landau and Ya. A. Smorodinskiĭ, Zh. Éksp. Teor. Fiz. **14**, 272 (1944).
2. H. A. Bethe, Phys. Rev. **76**, 38 (1949).
3. A. Bohr and B. R. Mottelson, *Nuclear Structure*, Vol. 1: *Single-Particle Motion* (Benjamin, New York, 1969; Mir, Moscow, 1971).
4. D. K. Tilley, H. R. Weller, and H. H. Hasan, Nucl. Phys. A **474**, 1 (1987).
5. F. Aisenberg-Selove, Nucl. Phys. A **490**, 1 (1988).
6. L. R. Kok, Phys. Rev. Lett. **45**, 427 (1980).
7. B. M. Karnakov, V. D. Mur, S. G. Pozdnyakov, and V. S. Popov, J. Mosc. Phys. Soc. **2**, 103 (1992).
8. A. V. Kulik, Yad. Fiz. **59**, 217 (1996) [Phys. At. Nucl. **59**, 199 (1996)].
9. J. Benn, E. B. Dalley, H. H. Muller, *et al.*, Nucl. Phys. A **106**, 296 (1968).
10. G. E. Brown and A. D. Jackson, *The Nucleon–Nucleon Interaction* (North-Holland, Amsterdam, 1976).
11. O. Dumbrajs, R. Kock, G. C. Oades, *et al.*, Nucl. Phys. B **216**, 277 (1983).
12. T. A. Tombrello, Phys. Lett. **23**, 106 (1966).
13. N. R. Heydenburg and G. M. Temmer, Phys. Rev. **104**, 123 (1956).
14. R. Nilson, W. K. Jentschke, G. R. Briggs, *et al.*, Phys. Rev. **109**, 850 (1958).
15. T. A. Tombrello and L. S. Senhouse, Phys. Rev. B **129**, 2252 (1963).
16. J. L. Russell, G. C. Phillips, and C. W. Reich, Phys. Rev. **104**, 135 (1956).
17. B. M. Karnakov, V. D. Mur, S. G. Pozdnyakov, and V. S. Popov, Pis'ma Zh. Éksp. Teor. Fiz. **54**, 131 (1991) [JETP Lett. **54**, 127 (1991)].
18. B. M. Karnakov, A. V. Kulik, V. D. Mur, and V. S. Popov, J. Mosc. Phys. Soc. **8**, 291 (1998).
19. H. Margenau, Phys. Rev. **59**, 37 (1941).
20. G. Breit and W. G. Bouricius, Phys. Rev. **74**, 1546 (1948).
21. G. Breit, *Theory of Resonance Reactions* (in Handbuch der Physik XLI/1 Springer, Berlin, 1959; Inostrannaya Literatura, Moscow, 1961).
22. V. D. Mur, B. M. Karnakov, S. G. Pozdnyakov, and V. S. Popov, Pis'ma Zh. Éksp. Teor. Fiz. **56**, 133 (1992) [JETP Lett. **56**, 127 (1992)]; Yad. Fiz. **56** (2), 125 (1993) [Phys. At. Nucl. **56**, 217 (1993)].
23. Ya. B. Zel'dovich and S. S. Gershteĭn, Usp. Fiz. Nauk **71**, 581 (1960) [Sov. Phys. Usp. **3**, 593 (1960)].
24. S. S. Gerstein and L. I. Ponomarev, Phys. Lett. B **72B**, 80 (1977).
25. P. Ackerbauer, J. Werner, W. H. Breunlich, *et al.*, Nucl. Phys. A **652**, 311 (1999).
26. S. Burles and D. Tytler, Astrophys. J. **499**, 699 (1998).
27. I. Ya. Barit and V. A. Sergeev, Tr. Fiz. Inst. Akad. Nauk SSSR **44**, 3 (1969).
28. B. M. Karnakov, V. D. Mur, S. G. Pozdnyakov, and V. S. Popov, Pis'ma Zh. Éksp. Teor. Fiz. **51**, 352 (1990) [JETP Lett. **51**, 399 (1990)]; Yad. Fiz. **52**, 1540 (1990) [Sov. J. Nucl. Phys. **52**, 973 (1990)].
29. V. S. Popov, B. M. Karnakov, and V. D. Mur, Zh. Éksp. Teor. Fiz. **110**, 1537 (1996) [JETP **83**, 849 (1996)].
30. N. J. Jarmie, R. E. Brown, and R. A. Hardekopf, Phys. Rev. C **29**, 2031 (1984).
31. R. E. Brown, N. J. Jarmie, and G. M. Hale, Phys. Rev. C **35**, 1999 (1987).
32. A. P. Kobzev, V. I. Salatskiĭ, and S. A. Telezhnikov, Yad. Fiz. **3**, 1060 (1966) [Sov. J. Nucl. Phys. **3**, 774 (1966)].
33. L. N. Bogdanova, V. E. Markushin, V. S. Melezhik, and L. I. Ponomarev, Zh. Éksp. Teor. Fiz. **81**, 829 (1981) [Sov. Phys. JETP **54**, 442 (1981)]; Yad. Fiz. **34**, 1191 (1981) [Sov. J. Nucl. Phys. **34**, 662 (1981)].
34. Yu. G. Balashko, Tr. Fiz. Inst. Akad. Nauk SSSR **33**, 66 (1965).
35. V. D. Mur, B. M. Karnakov, S. G. Pozdnyakov, and V. S. Popov, Yad. Fiz. **57**, 820 (1994) [Phys. At. Nucl. **57**, 769 (1994)].
36. B. Hoop and H. H. Barschall, Nucl. Phys. **83**, 65 (1966).

37. B. Haesner, W. Heeringa, H. O. Klages, *et al.*, Phys. Rev. C **28**, 995 (1983).
38. A. Krauss, H. W. Becker, H. P. Trautvetter, *et al.*, Nucl. Phys. A **465**, 150 (1987).
39. W. H. Geist, C. R. Brune, H. J. Karwowski, *et al.*, Phys. Rev. C **60**, 054003 (1999).
40. A. D. Bacher, G. R. Plattner, H. E. Conzett, *et al.*, Phys. Rev. C **5**, 1147 (1972).
41. G. R. Plattner, A. D. Bacher, and H. E. Conzett, Phys. Rev. C **5**, 1158 (1972).
42. H. Foote, O. Chamberlain, E. H. Rogers, and H. M. Steiner, Phys. Rev. **122**, 959 (1961).
43. V. D. Mur and V. S. Popov, Teor. Mat. Fiz. **65**, 238 (1985).

Translated by A. Isaakyan

Physics of Atomic Nuclei, Vol. 66, No. 1, 2003, pp. 99–104. Translated from Yadernaya Fizika, Vol. 66, No. 1, 2003, pp. 100–106.

NUCLEI
Theory

Results of Numerically Solving an Integral Equation for a Two-Fermion System

N. B. Skachkov* **and T. M. Solov'eva****

Joint Institute for Nuclear Research, Dubna, Moscow oblast, 141980 Russia

Received July 10, 2001; in final form, January 8, 2002

Abstract—A two-particle system is described by integral equations whose kernels are dependent on the total energy of the system. Such equations can be reduced to an eigenvalue problem featuring an eigenvalue-dependent operator. This nonlinear eigenvalue problem is solved by means of an iterative procedure developed by the present authors. The energy spectra of a two-fermion system formed by particles of identical masses are obtained for two cases, that where the total spin of the system is equal to zero and that where the total spin of the system is equal to unity. The splitting of the ground-state levels of positronium and dimuonium, the frequency of the transition from the ground state of orthopositronium to its first excited state, and the probabilities of parapositronium and paradimuonium decays are computed. The results obtained in this way are found to be in good agreement with experimental data. © *2003 MAIK "Nauka/Interperiodica"*.

1. INTRODUCTION

A description of the energy spectrum of two-particle bound states is an important physical problem. In order to solve this problem, use is extensively made of three-dimensional relativistic quasipotential equations whose kernels are constructed from the Feynman matrix elements of the interaction amplitude by equating the times of two particles. Upon going over to the single-time formalism, the interaction operator (kernel of an integral equation) appears to be dependent on the total energy of the system. Thus, the problem of finding the energy spectrum of the system becomes nonlinear. An iterative procedure for solving these nonlinear integral equations was proposed and justified in [1]. The results obtained by numerically calculating the energy spectrum of a system of two scalar particles were also presented there for the case of scalar-photon exchange. The objective of this study is to perform similar calculations for the spin case.

2. TWO-FERMION SYSTEM

Relativistic integral equations describing the interaction of two fermions within the single-time formalism were obtained in [2]. In the present study, we restrict ourselves to the case of zero orbital angular momentum ($l = 0$) and consider a two-particle system characterized by the total-spin values of zero ($S = 0$) and unity ($S = 1$). We assume that the masses of the fermions are identical, $m_1 = m_2 = m$, and that the mass of the particle mediating the interaction is zero. In the c.m. frame ($|\mathbf{p}_1| = |\mathbf{p}_2| = p$), the relativistic integral equation for the wave function can then be written in the form [3]

$$2\sqrt{m^2+p^2}(M-2\sqrt{m^2+p^2})\psi(p) = \frac{\alpha}{\pi}\int\limits_0^\infty \frac{m^2 dk}{\sqrt{m^2+k^2}} V_l^S(p,k,M)\psi(k). \quad (1)$$

Here, we use the relativistic units of measurement where $\hbar = c = 1$. In this equation, p and k are the absolute values of the fermion momenta in the initial and final states, respectively; $\psi(p)$ is the wave function for the two-fermion system; M is the sought mass of this system, $M = 2m + E$; E is the sought binding energy; V_l^S is the quasipotential constructed from the matrix elements of the interaction amplitude that was calculated within QED; and $\alpha = 1/137.0359895$ is the fine-structure constant [4].

Within the one-photon-exchange approximation, the corresponding formula for the kernel $V_0^0(p,k,M)$ ($S = 0$) has the form {see [2, formula (2.36)]}

$$V_0^0(p,k,M) = 2(m^2 - 2\sqrt{m^2+p^2}\sqrt{m^2+k^2}) \times \ln\left|\frac{p+k+\sqrt{m^2+p^2}+\sqrt{m^2+k^2}-M}{|p-k|+\sqrt{m^2+p^2}+\sqrt{m^2+k^2}-M}\right|, \quad (2)$$

while the kernel $V_0^1(p,k,M)$ ($S = 1$) is {see [2, formula (3.25)]}

*e-mail: skachkov@cv.jinr.ru
**e-mail: tanyusha@cv.jinr.ru

$$V_0^1(p,k,M)=\left\{4R_1\ln\left|\frac{p+k+\sqrt{m^2+p^2}+\sqrt{m^2+k^2}-M}{|p-k|+\sqrt{m^2+p^2}+\sqrt{m^2+k^2}-M}\right|+R_2+R_3+R_4\right\}pk/2, \qquad (3)$$

where

$$R_1=\frac{\gamma^2-1}{\gamma-\gamma'}\left(\frac{m(2\sqrt{m^2+p^2}+\sqrt{m^2+k^2})}{pk}+\gamma\left(\frac{m}{\sqrt{m^2+p^2}+m}+2\right)\right)+\gamma\left(2\gamma+\frac{m^2}{pk}\right),$$

$$R_2=2\frac{\gamma'^2-1}{\gamma'-\gamma}\left(\frac{m(2\sqrt{m^2+p^2}+\sqrt{m^2+k^2})}{pk}+\gamma'\left(\frac{m}{\sqrt{m^2+p^2}+m}+2\right)\right)$$
$$\times\ln\left|\frac{m^2+\sqrt{m^2+p^2}\sqrt{m^2+k^2}+pk}{m^2+\sqrt{m^2+p^2}\sqrt{m^2+k^2}-pk}\right|,$$

$$R_3=4\frac{\gamma'^2-1}{\gamma'-\gamma}\left(\frac{m(2\sqrt{m^2+p^2}+\sqrt{m^2+k^2})}{pk}+\gamma'\left(\frac{m}{\sqrt{m^2+p^2}+m}+2\right)\right)$$
$$\times\frac{\sqrt{m^2+p^2}+\sqrt{m^2+k^2}-M}{(2\sqrt{m^2+p^2}\sqrt{m^2+k^2}+2m^2-p^2-k^2)^{1/2}}\left[\mathrm{arctg}\frac{(2\sqrt{m^2+p^2}\sqrt{m^2+k^2}+2m^2-p^2-k^2)^{1/2}}{p+k}\right.$$
$$\left.-\mathrm{arctg}\frac{(2\sqrt{m^2+p^2}\sqrt{m^2+k^2}+2m^2-p^2-k^2)^{1/2}}{|p-k|}\right],$$

$$R_4=\frac{|p-k|^3-(p+k)^3}{3p^2k^2}\frac{m(\sqrt{m^2+p^2}+\sqrt{m^2+k^2}-M)}{\sqrt{m^2+p^2}+m}+\frac{(p+k-|p-k|)(\sqrt{m^2+p^2}+\sqrt{m^2+k^2}-M)}{2pk}$$
$$\times\left[\frac{-4m^2}{pk}-8\left(\gamma+\frac{p^2+k^2}{2pk}\right)+4m\frac{2\sqrt{m^2+p^2}+\sqrt{m^2+k^2}}{pk}+4\left(\frac{m}{\sqrt{m^2+p^2}+m}+2\right)\right.$$
$$\left.\times\left(\gamma+\frac{(\sqrt{m^2+p^2}+\sqrt{m^2+k^2})^2}{2pk}\right)\right]+\frac{4m^2}{pk}+8\gamma-4m\frac{2\sqrt{m^2+p^2}+\sqrt{m^2+k^2}}{pk}$$
$$-4\left(\frac{m}{\sqrt{m^2+p^2}+m}+2\right)(\gamma+\gamma'),$$

$$\gamma=(p^2+k^2-$$
$$(\sqrt{m^2+p^2}+\sqrt{m^2+k^2}-M)^2)/(2pk),$$
$$\gamma'=(\sqrt{m^2+p^2}\sqrt{m^2+k^2}+m^2)/(pk).$$

3. ITERATIVE PROCEDURE FOR SOLVING AN INTEGRAL EQUATION INVOLVING A NONLINEAR DEPENDENCE ON THE EIGENVALUE

Integral equations involving a nonlinear dependence on the total energy of the system reduce to a nonlinear spectral problem. In [1], an iterative procedure for solving such spectral problems involving an eigenvalue-dependent operator was described in detail and a mathematically rigorous validation of this procedure was given. The distinction between this iterative procedure and the known methods for solving nonlinear integral equations lies in the fact that the quantity iterated in [1] is an eigenvalue rather than an eigenfunction.

Briefly, the idea of the method is as follows. At each iteration step, the eigenvalue labeled with a fixed number k and chosen from the set of eigenvalues calculated at the preceding step of the iterative procedure is substituted into the kernel of the integral operator. At the first iteration step, an input approximation of the sought eigenvalue is substituted into the kernel. If there is no information about the distribution of eigenvalues, the input-approximation value is chosen arbitrarily. On the basis of the physical formulation of the problem being considered, this can be done, however, in such a way as to improve the convergence of the iterative process. Unknown wave functions are

Table 1. Spectrum of binding energies of a two-fermion system

	$S=0$	$S=1$
E_1/m	$-0.125837237(1)\times10^{-4}$	$-0.125820738(1)\times10^{-4}$
E_2/m	$-0.025983124(2)\times10^{-4}$	$-0.025981041(2)\times10^{-4}$
E_3/m	$-0.011648115(2)\times10^{-4}$	$-0.011647192(2)\times10^{-4}$
E_4/m	$-0.006613318(3)\times10^{-4}$	$-0.006613126(3)\times10^{-4}$

Table 2. Frequencies of transitions between positronium levels (in MHz)

	Experiment	Results of perturbation-theory calculations [8]	This study
$1^3S_1-1^1S_0$	203389.10(0.74)	203392.12(0.50)	203861(25)
$2^3S_1-1^3S_1$	1233607216.4(3.2)	1233607222.6(0.8)	1233609106(37)

Table 3. Frequencies of transitions between dimuonium levels (in MHz)

	Results of perturbation-theory calculations [10]	This study
$1^3S_1-1^1S_0$	$42333.5(2.7)\times10^3$	$42151.8(5.1)\times10^3$
$2^3S_1-2^1S_0$	$5290.07(0.34)\times10^3$	$5321.7(10.2)\times10^3$

calculated as the ordinary eigenfunctions of the linear spectral problem. For this, we use, in our calculations, the F02AGF code belonging to the NAGLIB library and realizing the QR algorithm [5]. Attainment of a small value of the difference ϵ between two eigenvalues calculated at two consecutive iteration steps is a criterion of closeness of our approximations to the sought eigenvalue. As this difference becomes smaller than the preassigned value characterizing the accuracy to which the problem must be solved, the iterative process is taken to be completed. The eigenvalue and the corresponding eigenfunction that were obtained at the final iteration step are assumed to be the sought solution to the problem.

4. RESULTS OF THE CALCULATIONS

The above method was used to obtain the energy spectra for a system of two bound fermions. These spectra are presented in Table 1. By multiplying the data in this table by the mass of a specific particle, we can obtain the spectrum of binding energies of the corresponding two-particle system (e^+e^-, $\mu^+\mu^-$, and so on).

Among all two-fermion systems, the positronium atom—a bound state of an electron and a positron—has received the most adequate study. The difference of the energies of the ortho- and parapositronium ground states and the difference of the energies of the orthopositronium ground and first excited states were measured experimentally in [6, 7]. Our results[1)] for the differences of the energy levels under investigation are presented in Table 2 (in MHz), along with the experimental data and theoretical results of other authors [8]. One can see from this table that the agreement between the results of the numerical calculation within the one-photon-exchange approximation and the experimental data is fairly good. The discrepancy with the results of [8] can be attributed to both the fact that the forms of the potentials applied in the one-photon approximation are different and the fact that higher order corrections of perturbation theory in the constant α were used in [8].

We now proceed to consider the $\mu^+\mu^-$ bound state. As in the case of positronium, we will refer to the singlet state of dimuonium as paradimuonium and to its triplet state as orthodimuonium. Experiments studying dimuonium are still under way. By solving the Bethe–Salpeter equations for bound states within perturbation theory, the authors of some studies (see [9, 10]) calculated, however, the differences of the energies of the ground and first excited states for ortho- and paradimuonium. In Table 3, the data

[1)] By using the Planck constant $\hbar = 6.6260755\times10^{-34}$ J s and the relation $1\,\text{eV} = 1.60217733\times10^{-19}$ J [4], we obtain $1\,\text{eV} = 241798834$ MHz. The electron mass is 510999.07 eV [4].

calculated in the present study (the muon-mass value of 105658389 eV [4] has been employed here) with the aid of the iterative procedure are displayed along with the data calculated in [10]. Our results are seen to be rather close to the results from [10].

5. PARAPOSITRONIUM AND PARAMUONIUM WIDTHS WITH RESPECT TO DECAYS INTO TWO PHOTONS

The probability of parapositronium decay into two photons can be determined with the aid of the expression [11]

$$\Gamma(e^+e^- \to 2\gamma) = \frac{8}{\pi}\alpha^2 m_e \left| \int_0^\infty d\chi \chi \psi(\chi) \right|^2, \quad (4)$$

where $\chi = \ln[(p + \sqrt{p^2 + m_e^2})/m_e]$ is the rapidity conjugate to the relative particle momentum and m_e is the electron mass.

In the case of an energy-dependent potential, the normalization condition for the wave function $\psi(p)$ is written in the form [12]

$$\frac{1}{(2\pi)^6} \int \psi(p) \left\{ \frac{\partial}{\partial M}[G_0^{-1}(p, M) - V_l^S(p, k, M)] \right\} \psi(k) dp dk = 2M,$$

where $G_0(p, M)$ is the free Green's function for Eq. (1):

$$G_0^{-1}(p, M) = 2\sqrt{m^2 + p^2}(M - 2\sqrt{m^2 + p^2}).$$

For the parapasitronium width with respect to decay into two photons, integration in (4) of the first eigenfunction (parapositronium ground state), which was derived by numerically solving Eq. (1) with the potential (2), yields

$$\Gamma(e^+e^- \to 2\gamma) = 7.9843(72) \times 10^9 \text{ s}^{-1}, \quad (5)$$

which is in good agreement with the experimental value measured in [13],

$$\Gamma^{\text{expt}}(e^+e^- \to 2\gamma) = 7.9909(17) \times 10^9 \text{ s}^{-1}. \quad (6)$$

Previously, we solved the relativistic quasipotential equation for two scalar particles by using the iterative procedure. The energy spectrum that was obtained in solving this equation is presented in [14]. We note that, in the scalar case, the quasipotential $V_0(p, k, M)$ has the form

$$V_0(p, k, M) \quad (7)$$
$$= 2\ln \left| \frac{|p - k| + \sqrt{m^2 + p^2} + \sqrt{m^2 + k^2} - M}{p + k + \sqrt{m^2 + p^2} + \sqrt{m^2 + k^2} - M} \right|.$$

By using the first eigenfunction obtained by solving Eq. (1) with the potential (7), we can calculate the probability of the decay of the positronium ground state in the scalar approximation. In this case, the numerical integration in formula (4) gives the value

$$\Gamma(e^+e^- \to 2\gamma) = 7.9782(72) \times 10^9 \text{ s}^{-1}. \quad (8)$$

If, in the calculation by formula (4), we use the first eigenfunction obtained by numerically solving the Schrödinger equation [15] with the Coulomb potential, the decay width in the nonrelativistic approximation is

$$\Gamma(e^+e^- \to 2\gamma) = 7.9635(72) \times 10^9 \text{ s}^{-1}. \quad (9)$$

By using the model relativistic wave function, the authors of [11] calculated the width with respect to parapositronium decay into two photons by formula (4). As a result, they obtained the value of 7.97×10^9 s^{-1}, which is close to the decay-width value that we calculated in the scalar approximation. By comparing the values in (5), (6), (8), and (9), one can see that the agreement between the numerically calculated and experimentally measured values of the decay width is improved if spin and relativistic corrections are taken into account in constructing the quasipotential. The parapositronium decay width was also calculated in [16–18]. Upon taking into account the contributions of diagrams corresponding to higher orders of perturbation theory, the result appears to be 7.9895×10^9 s^{-1} [18].

It was also noted in [11] that, if the $\mu^+\mu^-$ pair is assumed to form a loosely bound system—that is, in the limit where the binding energy tends to zero—the expression for the probability of paradimuonium decay into two photons will differ from that in (4) by the substitution $m_e \to m_\mu$ (m_μ is the muon mass):

$$\Gamma(\mu^+\mu^- \to 2\gamma) = \Gamma(e^+e^- \to 2\gamma)(m_\mu/m_e). \quad (10)$$

By using formulas (4) and (10), we can find that the decay probability for the ground state of the $\mu^+\mu^-$ bound system for the spinor equation with the potential (2) is

$$\Gamma(\mu^+\mu^- \to 2\gamma) = 1650.9(1.5) \times 10^9 \text{ s}^{-1}$$

and that the analogous probability for the relativistic scalar equation with the potential (7) is

$$\Gamma(\mu^+\mu^- \to 2\gamma) = 1649.6(1.5) \times 10^9 \text{ s}^{-1}.$$

Let us compare the values obtained for the decay probability by solving the nonlinear integral equations with the potentials (2) and (7) by the iterative procedure and the results of other authors. In [11], the width with respect to paradimuonium decay into two photons was calculated by formula (10) with a model relativistic wave function. The result obtained there, 1648×10^9 s^{-1}, is close to our result for the scalar case. Performing calculations by the formula $\Gamma^{(0)}(n^1S_0) = \alpha^5 m_\mu/2n^3$, which determines the decay width in the leading order of perturbation theory [19], we obtain the value of 1660.8×10^9 s^{-1} for the ground state. The decay width of $1680.3(0.5) \times 10^9$ s^{-1} was derived from the paradimuonium lifetime of $\tau(1^1S_0) = 0.59512(18) \times 10^{-12}$ s, which was calculated in [10] with allowance for higher order corrections in the constant α. Thus, our results are in good agreement with the results obtained by different methods.

In Table 4, we give the decay probabilities calculated in the present study for the first three excited states of parapositronium and paradimuonium. Here, n is the principal quantum number. In the calculations, we used the eigenfunctions of numbers 2, 3, and 4 as obtained in solving Eq. (1) with the potential (2) within the iterative procedure. Further experiments to study positronium and dimuonium will make it possible to test our results.

Table 4. Decay widths of excited states (numerical calculations)

n	Parapositronium, s^{-1}	Paradimuonium, s^{-1}
2	$0.94651(55) \times 10^9$	$195.71(11) \times 10^9$
3	$0.27763(47) \times 10^9$	$57.405(97) \times 10^9$
4	$0.10467(39) \times 10^9$	$21.642(81) \times 10^9$

6. CONCLUSION

On the basis of the method developed in our previous studies, integral equations for the wave function describing the system of two fermions of identical masses have been solved for the case of electromagnetic interaction (one-photon-exchange quasipotential). The fact that our results agree with available experimental data and with results obtained by other methods demonstrates a high efficiency of our iterative procedure for solving integral equations whose operator is dependent on the relevant eigenvalue—in the case being considered, on the total energy (or mass) of a composite system. The QED case chosen in the present study can be considered as a test problem that enables us to perform a comparison both with the results of other authors and with experimental data. In the future, our iterative method for solving nonlinear spectral problems can be employed to solve integral equations describing bound states in the system of two particles, first, in the case of different masses and, second, in the case where the mass of the particle mediating the interaction is nonzero. The application of the proposed procedure, upon an appropriate modification, to solving sets of integral equations whose kernels are eigenvalue-dependent seems promising. Such sets of equations arise, for example, in considering bound states in a two-particle system whose orbital angular momentum satisfies the condition $l \geq 1$.

APPENDIX

Errors in Calculating the Energy Levels and Decay Widths of Positronium and Dimuonium

The code based on the method that was developed for solving a nonlinear spectral problem and which is described in Section 3 involves an iterative procedure applied to discrete equations. Upon going over from an equation in a continuous variable to equations in a discrete variable in finite-dimensional space, the original problem reduces to a matrix eigenvalue problem whose solution can be constructed, in the linear case, by elaborate practical methods. The Bubnov–Galerkin projection method [20] provides one of the possible ways for implementing this transition. In the case under consideration, the error in calculating the eigenvalues and eigenfunctions of the nonlinear spectral problem therefore receives contributions from the error associated with an approximation of the continuous Eq. (1) by a set of discrete equations and the error introduced by the iterative method for solving the resulting nonlinear discrete spectral problem.

A set of numerical experiments has been performed in order to estimate the accuracy of discrete eigenvalues and eigenfunctions obtained here. We have considered Eq. (1) with the potentials (2), (3), and (7) and the Schrödinger equation involving the Coulomb potential [15] and having an exact solution that can be represented in an analytic form. The numerical calculations presented in [21] revealed that the errors in the eigenvalues and eigenfunctions due to the approximations used are close for all of the equations considered in the present study (one to two significant digits are coincident).

It was also shown in [21] that the error in calculating the eigenvalues and eigenfunctions of the nonlinear spectral problem by the above iterative method is

one to two orders of magnitude smaller than the error of the approximation. In calculating the decay widths by the method proposed in [11], an additional error stems from a numerical integration. It was proven in [21], however, that the error from a numerical integration is much less than the approximation error. In calculating the errors in the frequencies of the transitions between the energy levels and the errors in the positronium and dimuonium decay widths, we have therefore taken into account only the errors in the eigenvalues and eigenfunctions due to the approximation according to the Bubnov–Galerkin method.

REFERENCES

1. T. M. Solov'eva and E. P. Zhidkov, Comput. Phys. Commun. **126**, 168 (2000).
2. V. V. Dvoeglazov, N. B. Skachkov, *et al.*, Yad. Fiz. **54**, 658 (1991) [Sov. J. Nucl. Phys. **54**, 398 (1991)].
3. V. G. Kadyshevsky, R. M. Mir-Kasimov, and N. B. Skachkov, Nuovo Cimento A **55**, 232 (1968).
4. Particle Data Group, Phys. Rev. D **54**, 21 (1996); **54**, 65 (1996).
5. J. H. Wilkinson, *The Algebraic Eigenvalue Problem* (Clarendon, Oxford, 1965; Nauka, Moscow, 1970).
6. M. W. Ritter, P. O. Egan, *et al.*, Phys. Rev. A **30**, 1331 (1984).
7. M. S. Fee, A. P. Mills, *et al.*, Phys. Rev. Lett. **70**, 1397 (1993).
8. S. G. Karshenboim and K. Pachucki, Phys. Rev. Lett. **80**, 2101 (1998).
9. S. G. Karshenboim, U. D. Jentshura, *et al.*, Phys. Rev. A **56**, 4483 (1997).
10. S. G. Karshenboim, U. D. Jentshura, *et al.*, Phys. Lett. B **424**, 397 (1998).
11. G. A. Kozlov, S. P. Kuleshov, *et al.*, Teor. Mat. Fiz. **60**, 24 (1984).
12. R. N. Faustov and A. A. Khelashvili, Yad. Fiz. **10**, 1085 (1969) [Sov. J. Nucl. Phys. **10**, 619 (1970)].
13. A. H. Al-Ramadhan and D. W. Gidley, Phys. Rev. Lett. **72**, 1632 (1994).
14. B. N. Khoromskij, T. M. Makarenko, E. G. Nikonov, *et al.*, in *Proceedings of the International Conference on Programming and Mathematical Methods for Solving Physical Problems, Dubna, 1993,* Ed. by Yu. Yu. Lobanov *et al.* (World Sci., Singapore, 1994), p. 210.
15. V. A. Fock, Z. Phys. **98**, 145 (1935).
16. V. V. Dvoeglazov, R. N. Faustov, and Y. N. Tyukhtyaev, hep-ph/9306227.
17. R. N. Faustov and A. P. Martynenko, hep-ph/0002281.
18. A. Czarnecki, K. Melnikov, and A. Yelkhovsky, hep-ph/9910488.
19. J. Malenfant, Phys. Rev. D **36**, 863 (1987).
20. M. A. Krasnosel'skiĭ, G. M. Vaĭnikko, P. P. Zabrpeĭko, *et al.*, *Approximate Solution of Operator Equations* (Nauka, Moscow, 1969).
21. E. P. Zhidkov, N. B. Skachkov, and T. M. Solov'eva, Preprint No. P11-01-120, OIYaI (Joint Institute for Nuclear Research, Dubna, 2001).

Translated by A. Isaakyan